WORLD METEOROLOGICAL ORGANIZATION
GLOBAL OZONE RESEARCH AND MONITORING PROJECT—REPORT NO. 18

Report of the International Ozone Trends Panel 1988

VOLUME II

(NASA-TM-105119) REPORT OF THE INTERNATIONAL OZONE TRENDS PANEL 1988, VOLUME 2 (NASA) 404 p CSCL 13B
N92-15157
--THRU--
N92-15163
Unclas
G3/45 005343[illegible]

United Nations Environment Program
United Nations Headquarters
Gigiri
Nairobi, Kenya

World Meteorological Organization
41, Avenue Giuseppe Motta
Case Postale No. 5
CH-1211, Geneva 20, Switzerland

National Aeronautics and Space Administration
Office of Space Science and Applications
Earth Science and Applications Division
600 Independence Avenue, SW
Washington, DC 20546
USA

U.S. Department of Commerce
National Oceanic and Atmospheric Administration
14th Street and Constitution Avenue, NW
Hoover Building, Room 5128
Washington, DC 20230
USA

Federal Aviation Administration
Office of Environment
800 Independence Avenue, SW
Washington, DC 20591
USA

This document was published with the assistance of the Alternative Fluorocarbons Environmental Acceptability Study (AFEAS) as a service to the international science community.

WORLD METEOROLOGICAL ORGANIZATION
GLOBAL OZONE RESEARCH AND MONITORING PROJECT—REPORT NO. 18

Report of the International Ozone Trends Panel – 1988

VOLUME II

NATIONAL AERONAUTICS AND SPACE ADMINISTRATION
NATIONAL OCEANIC AND ATMOSPHERIC ADMINISTRATION
FEDERAL AVIATION ADMINISTRATION
WORLD METEOROLOGICAL ORGANIZATION
UNITED NATIONS ENVIRONMENT PROGRAM

Table of Contents

VOLUME I

Page

Chapter 1 Introduction **3**

1.0 Introduction 3
1.1 Background 3
1.2 Key Findings 4

Chapter 2 Spacecraft Instrument Calibration and Stability **7**

2.1 Introduction 11
2.2 Instrument Degradation 13
2.3 The Solar Backscatter Ultraviolet (SBUV) Experiment 17
2.4 The Total Ozone Mapping Spectrometer (TOMS) 45
2.5 The SAGE–I and SAGE–II INSTRUMENTS 52
2.6 Solar Mesosphere Explorer (SME) UV Ozone and Near Infrared (NIR) Airglow Instruments 65
2.7 The Limb Infrared Monitor of the Stratosphere (LIMS) 80
2.8 Other Instruments 92
2.9 Conclusions 97

Chapter 3 Information Content of Ozone Retrieval Algorithms **107**

3.0 Introduction 111
3.1 Profile Retrieval Concepts 112
3.2 Error Analysis Concepts 113
3.3 Retrieval Analysis for Individual Instruments 115
3.4 Alternative Strategies for Ozone Profile Trend Detection 171
3.5 Summary and Conclusions 174

Chapter 4 Trends in Total Column Ozone Measurements **179**

4.0 Introduction 183
4.1 Ground-Based Measurements of Ozone 184
4.2 Satellite Measurements of Total Ozone 202
4.3 Use of External Data To Diagnose Problems at Groundstations 205
4.4 Calibration of TOMS Using Dobson Data 232
4.5 Preliminary Examination of Ground-Based Total Ozone Measurements 236
4.6 Detailed Analysis of the Provisionally Revised Ground-Based Data 251
4.7 Analysis of TOMS Data Normalized to the Dobson Network 299
4.8 Summary 314
Appendix 317

Chapter 5 Trends in Ozone Profile Measurements **383**

5.1 Summary and Index 387
5.2 Solar Backscatter Ultraviolet Instrument (SBUV) 390

[illegible] ii INTENTIONALLY BLANK

PRECEDING PAGE BLANK NOT FILMED

Table of Contents (continued)

Page

5.3 Ozone Trends From Comparison of SAGE–I and SAGE–II 394
5.4 Solar Backscatter Ultraviolet II (SBUV–2) 410
5.5 Umkehr Measurements of Upper Stratospheric Ozone 412
5.6 SBUV, SAGE–I, and LIMS Ozone Intercomparison (Spring 1979) 427
5.7 Trends at Upper Boundary of the Stratosphere (SBUV, SME, SMM) 431
5.8 Rocket Ozonesonde (ROCOZ–A) 436
5.9 Conclusions 440

References .... follows page 442

VOLUME II

Chapter 6 Trends in Stratospheric Temperature 443

6.1 Introduction 447
6.2 Temperature Data Set Description 447
6.3 Data Analysis 462
6.4 Mechanisms for Atmospheric Temperature Trends 485
6.5 Conclusions 496

Chapter 7 Theory and Observations: Model Simulations of the Period 1955–1985 ... 499

7.0 Introduction 503
7.1 Atmospheric Scenarios for 1955–1990 503
7.2 The Models 508
7.3 Model Simulations of Ozone Change 521
7.4 Conclusions 539

Chapter 8 Trends in Source Gases 543

8.1 Introduction 547
8.2 Halocarbons: CCL_3F, CCl_2F_2, CH_3CCl_3, CCl_4 548
8.3 Other Chlorocarbons 555
8.4 Bromocarbon Species 558
8.5 Nitrous Oxide 559
8.6 Methane 562
8.7 Trace Gases Influencing Tropospheric Ozone and Hydroxyl Radical Concentrations 565
8.8 Conclusions 568

Chapter 9 Trends in Stratospheric Minor Constituents 571

9.1 Introduction 575
9.2 Odd Nitrogen 575

Table of Contents (continued)

Page

9.3 Halogens—Chlorine, Fluorine, Bromine (Cl, F, Br) 582
9.4 H_2O/HO_x 589
9.5 Summary 592

Chapter 10 Trends in Aerosol Abundances and Distributions 595

10.1 Introduction 599
10.2 Aerosols in the Middle and Lower Atmosphere 599
10.3 Long-Term Aerosol Data Bases 609
10.4 Aerosol Perturbations: El Chichón and Other Events 622
10.5 Aerosol Impact on Ozone Observations 632
10.6 Polar Stratospheric Clouds and the Ozone Hole 641
10.7 Conclusions 662

Chapter 11 Observations and Theories Related to Antarctic Ozone 665

11.1 Introduction 669
11.2 Observations 669
11.3 Transport Theories for the Antarctic Ozone Hole 704
11.4 Chemical Theories and Observations 725
11.5 Can We Explain the Observed Springtime Ozone Trend Over Antarctica in the Last 20 Years? 743
11.6 What Are the Implications for the Global Earth's System of the Ozone Changes Observed Over Antarctica? 744
11.7 Questions for the Future 745
11.8 Summary 746

Appendixes

A Statistical Approaches to Ozone Trend Detection 751
  1.0 Current Status of Statistical Analyses 755
  2.0 Temporal and Spatial Correlation 760
  3.0 Seasonality in Ozone Data 768
  4.0 Summary 772

B List of Contributors 773
C Ozone Trends Panel Working Group Meetings 781
D List of Figures 787
E List of Tables 811
F Major Acronyms 817
G Chemical Formulae and Nomenclature 823
H Pressure–Altitude Conversion Chart 827

References .... follows page 830

VOLUME II

45

53439

P-54

CHAPTER 6

N92-15458

Trends in Stratospheric Temperature

Panel Members

M. R. Schoeberl, Chapter Chair
P. A. Newman, Observations Subgroup Chair
J. E. Rosenfield, Modeling Subgroup Chair

J. Angell
J. Barnett
B. Boville NH 315709
S. Chandra
S. Fels
E. Fleming
M. Gelman
K. Labitzke F 7115851

A. J. Miller
J. Nash
V. Ramaswamy
F. Schmidlin
M. Schwarzkopf
K. Shine

PRECEDING PAGE BLANK NOT FILMED

Chapter 6

Trends in Stratospheric Temperature

Contents

6.1 INTRODUCTION 447

6.2 TEMPERATURE DATA SET DESCRIPTION 447

- 6.2.1 Radiosonde 447
  - 6.2.1.1 Introduction 447
  - 6.2.1.2 Radiosonde Errors 447
  - 6.2.1.3 Description of the Radiosonde Data Sets 448
- 6.2.2 Satellite 450
  - 6.2.2.1 Introduction 450
  - 6.2.2.2 Radiance Data 452
  - 6.2.2.3 NMC Analyses 454
- 6.2.3 Rocketsonde 458
  - 6.2.3.1 Introduction 458
  - 6.2.3.2 Corrections 458
  - 6.2.3.3 Rocket Data Base 459
  - 6.2.3.4 Accuracy and Precision 460
  - 6.2.3.5 Trend Detection 461
  - 6.2.3.6 Summary 461

6.3 DATA ANAYLSIS 462

- 6.3.1 Intercomparisons 462
- 6.3.2 Short-Term Change and Long-Term Trends 472

6.4 MECHANISMS FOR ATMOSPHERIC TEMPERATURE TRENDS 485

- 6.4.1 Global Ozone Changes 485
- 6.4.2 The Radiative Impact of Other Trace Gases 489
- 6.4.3 Solar Cycle 489
- 6.4.4 Aerosols 490
- 6.4.5 Dynamics 494
- 6.4.6 Radiative Photochemical Models 495

6.5 CONCLUSIONS 496

PAGE 444 INTENTIONALLY BLANK

PRECEDING PAGE BLANK NOT FILMED

6.1 INTRODUCTION

The purpose of this chapter is to examine stratospheric temperatures for long-term and recent trends, discuss the mechanisms that can produce atmospheric temperature trends, and determine if observed changes in upper stratospheric temperatures are consistent with observed ozone changes.

The long-term temperature trends are determined up to 30 mb from radiosonde analysis (since 1970) and rocketsondes (since 1969 and 1973) up to the lower mesosphere principally in the Northern Hemisphere. The more recent trends (since 1979) incorporate satellite observations.

Previously published stratospheric temperature trend analyses used a variety of statistical techniques and data bases; as a result, intercomparison has been difficult. Here, data sets from the Free University of Berlin, the U.S. National Meteorological Center (NMC) of the National Oceanic and Atmospheric Administration (NOAA), the United Kingdom Meteorological Office (UKMO), and radiosonde and selected rocketsonde information are compared. The data set descriptions, intercomparisons, and trends make up Sections 6.2 and 6.3 of this report.

In Section 6.4, the mechanisms that can produce recent temperature trends in the stratosphere are discussed. The following general effects have been considered: changes in ozone, changes in other radiatively active trace gases, changes in aerosols, changes in solar flux, and dynamical changes. Radiative equilibrium experiments have been performed with carefully calibrated radiative transfer codes to quantify the magnitude of the temperature changes expected with ozone and solar flux changes. In particular, computations have been made to estimate the temperature changes associated with the upper stratospheric ozone changes reported by the SBUV instrument aboard Nimbus–7 and the SAGE instruments. The conclusions of this report are given in Section 6.5.

6.2 TEMPERATURE DATA SET DESCRIPTION

6.2.1 Radiosonde

6.2.1.1 Introduction

Radiosondes continue to provide the basic upper air data for meteorological services. The users are a diverse group, including meteorologists who are involved in operational numerical weather analysis and forecasting, and climatologists who are interested in the long-term variations of quantities such as temperature. The accuracy of the temperature, pressure, and humidity measurements obtained from radiosondes is particularly important to these users. However, the accuracy required for day-to-day operations is not the same as that required for the study of long-term trends; understandably, it is the accuracy required by the former that has received the most attention.

6.2.1.2 Radiosonde Errors

Specification of the errors of the various radiosonde systems in regular worldwide use has proven difficult. A relatively inexpensive "standard" instrument for calibration purposes has never been developed; in the absence of a reference instrument, different methods have been used in an attempt to judge the quality of radiosonde instruments, including the evaluation of

PAGE 446 INTENTIONALLY BLANK

PRECEDING PAGE BLANK NOT FILMED

day–night differences in observational reports. A very useful method of comparing the measurement capabilities of radiosondes is instrumental intercomparison, whereby multiple radiosondes are carried aloft on a single balloon.

The most recent, and largest ever, series of radiosonde intercomparisons, organized by the WMO Commission on Instrument and Method of Observation (CIMO), was carried out at Bracknell, England, in 1984, and at Wallops Island, Virginia, USA, in 1985 (Nash and Schmidlin, 1987). The main findings, based on eight radiosonde types used in the intercomparisons, are:

- The reproducibility of temperature measurements was about 0.2K in most cases.
- The reproducibility of pressure measurements varied from 0.5 to about 2.0 mb.
- Different radiosonde instruments showed different time constants of response, which can lead to appreciable difference in temperature estimates at given levels.
- Performance of the pressure sensor can be critical to temperature estimates at heights above 20 mb (assignment of the temperature to an incorrect pressure level).

As an example of these problems, Figure 6.1 displays a plot of consistent temperature differences for a variety of radiosonde instruments (reprinted from Nash and Schmidlin, 1987). Above the 50 mb level, instrument differences can be larger than 1K. The number of different types of radiosonde in use at any time is not small (~17). Thus, the continuity and accuracy of long-term trends are also subject to errors caused by modifications in design, manufacture, and data reduction.

These findings have an obvious impact on operational analyses, in which accuracy is important, but their impact on trend analysis, in which precision is most important, may not be as great. What is important in trend measurement is that the observations at individual stations be consistent in time; in the attempt to improve accuracy based on the above findings, it is this consistency that is lost. It is not clear that the operational radiosonde network now in place will ever prove entirely satisfactory for the detection of long-term variations in quantities such as temperature. Nevertheless, radiosondes provide, and probably will continue to provide, the primary data set for long-term lower stratospheric temperature trend assessment.

6.2.1.3 Description of the Radiosonde Data Sets

Two radiosonde-based data series are readily available for the investigation of long-term temperature and geopotential height changes in the lower stratosphere, such as 30 mb. The Northern Hemisphere daily analyses, carried out by the Stratospheric Research Group of the Free University of Berlin, are based mainly on radiosonde observations at 00 and 12 UT (about 900 observations per day). Since 1980, these analyses have included satellite data taken over the oceans (Labitzke et al., 1985). Because these analyses are a research project, carried out only after all data have been received, consistency in time is achieved. The daily charts are digitized on a 10 by 10 latitude–longitude grid, and monthly zonal-mean temperatures are obtained. Over the middle latitudes, each monthly zonal mean value of temperature is based on approximately 3,000 observations, resulting in a extremely small sampling error. Another advantage of this technique is that errors of single stations on single days can be eliminated by comparison with other stations nearby, and missing data can be interpolated. This data set starts in July 1964 for most stratospheric pressure surfaces.

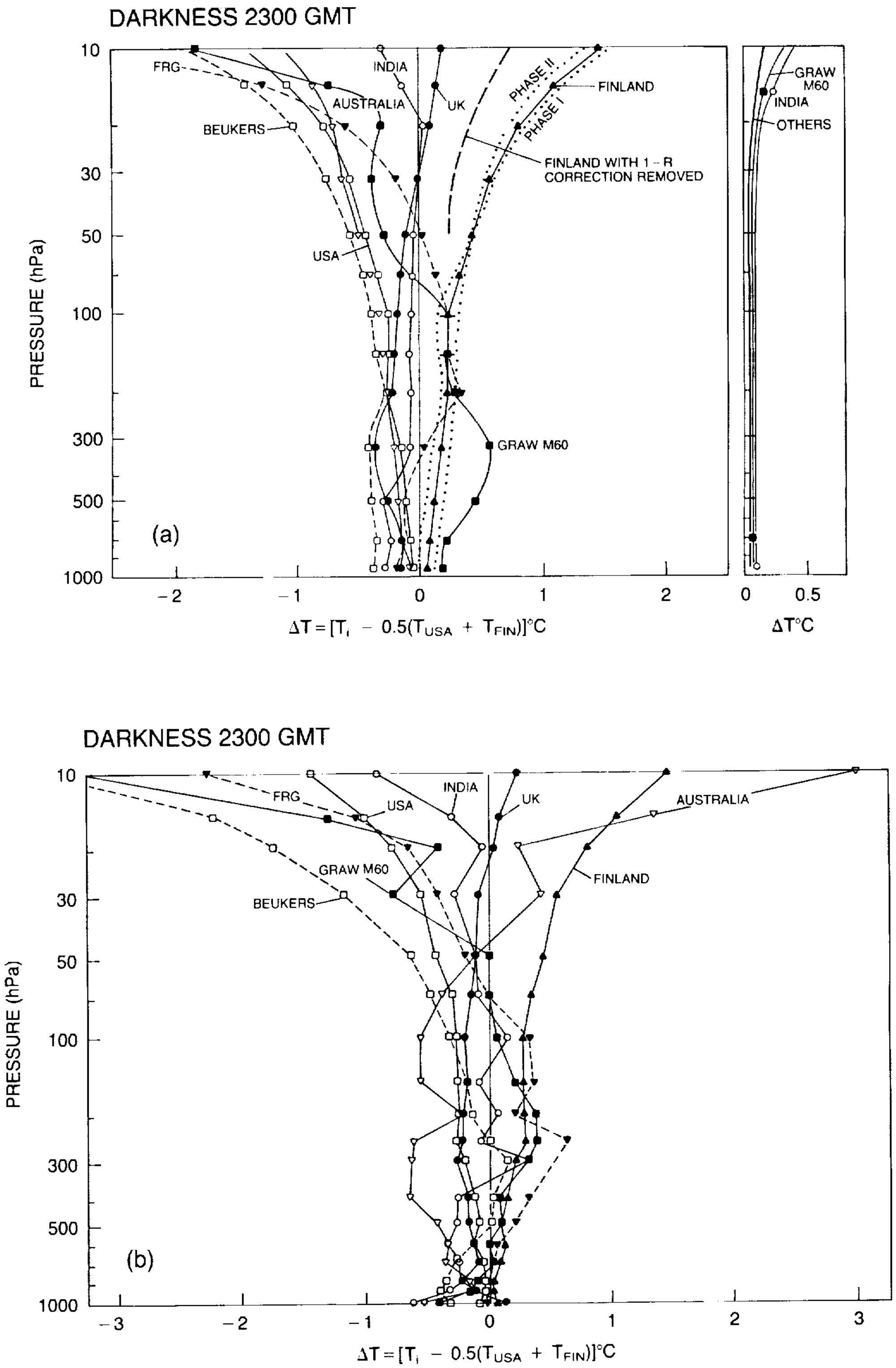

Figure 6.1 Intercomparison of different radiosondes at night (from Nash and Schmidlin, 1987). T_i is the temperature measured by the particular instrument. (a) Temperature differences from a standard defined by the U.S. and Finnish instruments. (b) As in (a), but reported on standard pressure surfaces. Note the increased error caused by the information in the pressure sensor.

The second temperature series, from Angell and Korshover (1983a), is based on the variation of height difference or thickness (proportional to mean temperature) between 100 and 30 mb at 63 radiosonde stations distributed worldwide, 45 of which are in the Northern Hemisphere. At each station for each year, the seasonal deviation of thickness from the long-term seasonal mean has been determined; these station deviations have then been averaged for polar, temperate, subtropical, and equatorial zones, as well as for both hemispheres and the world, by the use of area weighting. This data set generally begins in 1958, but because Soviet Union radiosonde data were not available before 1970, the temperature variations in north polar and north temperate climatic zones are not represented before that date. Because of the relatively small number of radiosonde stations used in this analysis, this technique is much more sensitive to erroneous station data or missing data than is the previous technique. The two data sets are intercompared in Section 6.3.1.

6.2.2 Satellite

6.2.2.1 Introduction

Before 1978, several satellite temperature sounders were in use with weighting functions in the stratosphere and mesosphere, including the Vertical Temperature Profile Radiometer (VTPR), the Selective Chopper Radiometer (SCR), and the Pressure Modulated Radiometer (PMR). Data from these have not been used for trend analysis because the available data are not of sufficient accuracy or record length. For example, the PMR data for the upper stratosphere and mesosphere would have been of particular interest but, although the instrument appeared to be stable, the data record extended only for 3 years.

The TIROS–N Operational Vertical Sounder (TOVS) Series began operation in late 1978. TOVS comprises three radiometers that provide observations of narrow bandwidth radiance, originating primarily from the stratosphere and troposphere. The radiometers are the High-resolution Infrared Sounder (HIRS–2), the Stratospheric Sounding Unit (SSU), and the Microwave Sounding Unit (MSU); their nominal performance is outlined in Smith et al. (1979). These instruments measure the thermal emission from layers of the atmosphere, as indicated by the weighting functions given in Figure 6.2a. The present series of the TIROS–N spacecraft is expected to remain in operation beyond 1990; hence, the current type of sounders has the potential to provide a monitor of stratosphere temperature trends over at least 10 years. However, because not all of the spacecraft will carry the principal stratosphere sounder, the SSU, the quality of trend information can be expected to diminish during the rest of the decade.

These emitted radiances from Earth's atmosphere may be individually converted to an equivalent temperature for each layer (known as the brightness temperature) or may be retrieved to obtain a temperature profile or layer mean temperature between fixed pressure levels. It should be noted that the measurements are obtained on a vertical pressure scale (as opposed to height).

Two methods for determining stratospheric temperature changes from the TOVS data will be discussed. Nash and Forrester (1986) used the zonal mean measurements from several radiometer channels. Their work was aimed primarily at trend-type studies, without performing any temperature retrieval. They established reproducibility and systematic drifts in both the radiometric (i.e., temperature) and the spectroscopic (i.e., weighting function) performance by careful comparison between different sounders in simultaneous operation and by careful prelaunch calibration. Estimates of temperature trends since late 1979 were derived for layers of

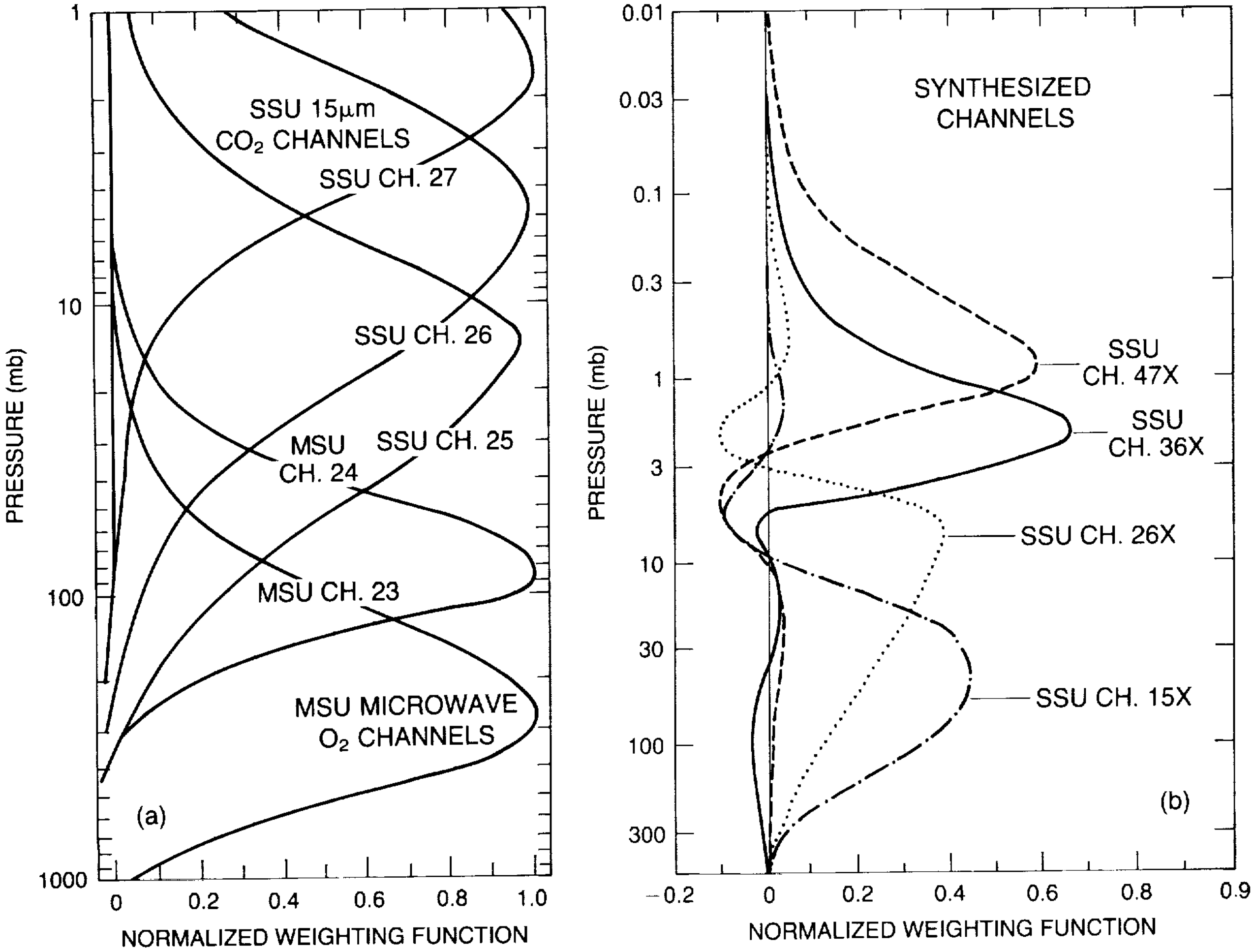

Figure 6.2 Weighting functions for satellite temperature instruments: (a) MSU, SSU; (b) Synthesized SSU channels from Nash (1987).

the atmosphere centered at pressures between 90 and 0.5 mb. Their method is discussed in detail in Section 6.2.2.2.

Gelman et al. (1986) use global stratospheric temperature fields derived as an operational product from the National Meteorological Center. In contrast to the Nash and Forrester method, a temperature retrieval process is used first to give temperatures as a function of latitude, longitude, and pressure. Because data from only one satellite are used at any one time, periods of overlap are not available for intercomparison. The fields were retrospectively adjusted (primarily using comparisons with rocketsonde data) to compensate for differences between the successive satellites in the TIROS–N series. This data set is discussed in Section 6.2.2.3.

6.2.2.2 Radiance Data

NOAA spacecraft have been in simultaneous operation for most of the time since late 1978. Comparison of observations obtained by the nominally identical TIROS Operational Vertical Sounders (TOVS) from two simultaneously operated spacecraft in the TIROS–N/NOAA series has allowed a check on the stability of their radiometer performance.

The comparison data used in this report were previously described by Nash and Forrester (1986) and were obtained by an extension of the methods used in earlier studies of SSU performance by Pick and Brownscombe (1981) and Nash and Brownscombe (1983).

The TOVS channels chosen for analysis have been limited to those with relatively high vertical resolution (i.e., 10 to 15 km), namely MSU and SSU. The stratospheric HIRS–2 channels have poor vertical resolution and contribute only redundant information. Processed radiance observations from these channels have been separated according to radiometer view angle and used to generate zonally averaged mean radiances for 10 latitude bands centered from 70°N to 70°S for each day. Radiances from the nadir or near-nadir views have been used in each case. Further independent information is obtained through a procedure described by Nash (1988) in which differences are taken between the zonal mean SSU radiances at 35° and 5° to nadir. The 35° weighting functions are at higher altitudes (because of limb effects), and combinations can be found that are either sharper than the contributing weighting functions or at higher altitudes. This technique provides the highest altitude weighting function, known as 47X, which is centered at about 0.5 mb (approximately 54 km). Figure 6.2b gives the weighting functions for these synthesized channels.

The consistency between the TOVS channels has been examined by computing the difference between the zonally averaged radiances obtained for the north- and southbound portions of the orbit at each latitude. Because the NOAA spacecraft are in Sun-synchronous orbits, the nadir-view observations at a given latitude are always for fixed local times, which are about 12 hours apart at most latitudes for a given spacecraft. Observation local times were about 0300 and 1500 hours for TIROS–N, NOAA–7, and NOAA–9, and about 0700 and 1900 hours for NOAA–6 and NOAA–8. The existence of diurnal and semidiurnal solar tides is a major complication because they lead to consistent biases between the measurements at these various local times. A solar diurnal tide will cause a difference between the north- and southbound zonal means, but will not affect their average except when their local times differ substantially from 12 hours. However, a solar semidiurnal tide has the reverse effect of causing a bias in the north/southbound average, but producing zero difference in the zonal means. The lunar semidiurnal tide has an effect similar to that of the solar semidiurnal tide, except that it has a 4-week periodicity; its effect was eliminated here by averaging over monthly periods. For the diurnal cycle, which has the largest amplitude at extratropical latitudes, solar tidal theory predicts maximum 12-hour differences of less than 0.3K at 100 mb, less than 0.5K at 20 mb, and rising to a peak of about 6K at 2 mb. The temperature is predicted to peak at about 1800 hours. The TOVS observations are compatible with this theory. Not only are the 12-hour differences as expected (larger for the 0700–1900 hour spacecraft), but so are the absolute differences between spacecraft.

For trend determination, it is important to distinguish between radiometric calibration and spectroscopic errors, which are largely independent. A single channel will measure radiance (or brightness temperature) corresponding to a weighting function. Radiometric calibration errors cause the measured radiance to be incorrect, directly causing a temperature error. Spectroscopic errors (such as errors in the filter wavelength or in the basic spectroscopic line data) will cause errors, such as a vertical shift, in the weighting function; this leads indirectly to temperature errors that will depend upon the lapse rate and, hence, upon the latitude and season. Both types of error have various components of systematic bias, but some of these will be common to all instruments of a given type or design. Thus, errors in spectral line data would be unimportant when intercomparing SSU's, but would matter when comparing an SSU with an MSU, since the two instruments view at quite different wavelengths. Nash and Forrester (1986) used measurements of natural atmospheric variations that are height dependent (e.g., the tidal 12-hour difference, seasonal variations) to intercompare the pressure levels viewed by different radiometers and by radiosondes, and so establish which channels were observing at the correct level. Residual differences were then described as biases. The latitudinal variation of bias between the different measurements for the same pressure level was also used as an indication of data quality and of the types of instrument problems that could be occurring. Of crucial importance was the apparent long-term stability of the NOAA–6 SSU and MSU. Although there were periods when this satellite was not operated (because of the failure of the HIRS–2), there was enough overlap of operation with other NOAA satellites to be confident of the long-term trends shown. Temperature values within these gaps were obtained from TOVS instruments on the other satellites, after adjustments were made for identifiable radiometric and spectroscopic differences.

The overall conclusions regarding the accuracy of TOVS data for long-term trend studies are:

- Single TOVS channels can, in some cases, measure monthly zonal mean brightness temperature to an accuracy of about 0.2K root mean square (rms) (1K for synthesized channels).
- The data sets obtained from several satellites indicate that the NOAA–6 SSU and MSU were stable over the period 1980–1986 to the same order of accuracy.

Because the atmospheric mixing ratio of carbon dioxide is increasing at a rate of about 0.4 percent per year, the weighting function for a spectroscopically stable SSU channel moves upwards, causing a change in the measured brightness temperature that depends on the lapse rate. Line-by-line calculations have been made of the effects of an 8 ppmv increase in the carbon dioxide mixing ratio, corresponding to the change from 1979–1980 to 1985–1986, for an annual mean 30°N temperature profiles. These changes (listed in Table 6.1) are substantially smaller than the trends observed, so it is concluded that these effects play only a minor role. Oxygen mixing ratios are proportionally much more stable than those of carbon dioxide, and any trend for the MSU weighting functions should be negligible. Another potential source of error is the effect of ozone upon absorption in the 15-micron carbon dioxide band used by the SSU and HIRS for temperature sounding. The use of gas correlation minimizes the effect of ozone on the SSU measurements to the extent that it is not considered necessary to make any correction. However,

Table 6.1 Sensitivity of Measured SSU Brightness Temperatures to 8 ppmv CO_2 Increase and 10 Percent Ozone Decrease at all Levels

Channel	Apparent Temperature Increase Due to 8 ppmv CO_2 Increase (K)	Apparent Temperature Increase Due to 10% Ozone Decrease (K)
47X	−0.289	−0.01
36X	−0.072	−0.04
27	0.00	0.00
26	0.12	−0.01
25	0.14	−0.02
26X	0.182	0.02
15X	0.085	0.05

Table 6.1 gives the calculated apparent temperature changes caused by a 10 percent decrease of ozone concentration. Any small ozone trend that might have occurred should have negligible effect on the temperature trend measurements over this period. The corrections indicated in Table 6.1 have not been incorporated into the data set's satellite.

6.2.2.3 NMC Analyses

The NOAA series of polar-orbiting satellites has provided temperature soundings in support of operational meteorological analyses for weather forecasting. As part of the regular operations of the NMC, global fields have been produced of geopotential height and temperature at stratospheric constant pressure levels 70, 50, 30, 10, 5, 2, 1, and 0.4 mb (corresponding to altitudes from 18 to 55 km). The analysis system for the fields is a modified Cressman for both 70 to 10 mb levels (Finger et al., 1985) and 5 to 0.4 mb levels (Gelman and Nagatani, 1977). The source of satellite data for the analysis, as well as the methodology for using these data in the analysis system, have changed as improvements have been developed (Gelman et al., 1983). Some changes were necessary because of instrumental failure or failure of specific instrument channels. Table 6.2 summarizes the principal changes that are relevant to a study of the stratospheric fields (70 to 0.4 mb) for the Northern and Southern Hemisphere analyses. The changes to the 70 to 10 mb system primarily have involved changes in the use of radiosonde data for the Southern Hemisphere and in first-guess derivation. Changes for the upper stratosphere (5 to 0.4 mb) analyses relate to changes in satellites as well as in the use of TOVS data. Before October 17, 1980, simple regression relationships from two channels of the VTPR or the SCR were used. Temperature retrievals produced from TOVS provide layer mean temperature between the standard pressure levels. Temperatures at the NMC analysis levels are found by linear interpolation in log pressure of the layer mean temperatures.

As indicated in Table 6.1, there have been seven changes (eight periods) since the initiation of the NMC global stratospheric analyses. Some basis must be provided for assuring stability of the NMC analyses for determining interannual changes in stratospheric structure and long-term trends in temperature. Therefore, meteorological rocketsonde and radiosonde temperatures have been compared with temperatures interpolated to the locations of the rocket stations from the analyzed field closest in time.

The error estimates for rocketsonde temperature data are 1–3K over the altitudes 35 to 55 km (see Section 6.2.3). Since both rocketsonde hardware and data observation procedures have been standardized for the stations in the Cooperative Meteorological Rocketsonde Network (CMRN)

Table 6.2 Global Daily 1200 GMT Temperature and Height Fields History of Changes

Period	Dates	Levels (mb)	Hem.	Data and Analysis Procedures
1	Sept. 24, 1978–Feb. 23, 1979	70–10	N	Rawinsonde data First guess 50% persistence, 50% regression upward
		70–10	S	Radiosonde and VTPR temperatures
		5–0.4	N,S	Regression from VTPR channels 1,2
2	Feb. 25, 1979–Oct. 16, 1980	70–10	N	Rawinsonde data
3	(2/25/79–1/20/80; TIROS–N) (1/21/80–10/16/80; NOAA–6)			First guess 50% persistence, 50% TOVS beginning Oct. 3, 1979
		70–10	S	Radiosonde and TOVS temperatures
		5–0.4	N,S	Regression from SSU channels 25,26
	Oct. 17, 1980–Present	70–10	N	Rawinsonde data
4	(10/17/80–9/1/81; NOAA–6)			First guess 100% TOVS beginning 17 June 1981
5	(9/2/81–9/1/83; NOAA–7)			TOVS first guess saved outside NMC octagon grid points beginning 29 Feb., 1984
6	(9/2/83–6/18/84; NOAA–8)			
7	(6/19/84–2/26/85; NOAA–7)			
8	(3/27/85; NOAA–9)			
		70–10	S	TOVS (no radiosonde)
		5–0.4	N,S	TOVS

since at least 1978, an inherent assumption is made that these rocketsonde data may be used as a reasonable and consistent standard against which to gauge the long-term stability of the NMC stratospheric temperature analyses.

Adjustments have been derived and applied to the archived NMC stratospheric analyses for 5 mb and above. The temperature adjustments are, at most, 9K; the largest adjustments occur nearest the Equator or the North and South Poles. The adjustments are recommended for application in the Southern as well as in the Northern Hemisphere, even though the rocketsonde stations used to derive the adjustments are almost exclusively in the Northern Hemisphere. This puts significant limitations on Southern Hemisphere trend estimates.

Another approach to deriving adjustments is to determine directly the difference between analyses obtained from the two data sources. It is best if an overlap period, during which comparisons can be made of the two analysis products, is available. This has not been possible in the past because of operational considerations at NMC. Furthermore, some changes needed as a result of the failure of an instrument or specific channels precluded such an overlap period. Therefore, Gelman et al. (1983) compared zonal average temperatures derived from the analyses immediately before and after each change and tried to determine the nonmeteorological change at each change date. This determination is most difficult at polar latitudes in winter and may not be possible when there is a lapse in analyses of more than a few days, as was the case at the beginning of period 8. Figure 6.3 shows these determinations (denoted by joint) for the Equator, 30°N, 30°S, 60°S, and 60°N for the 2-mb level over the eight adjustment periods (see Table 6.2). Figure 6.3 (denoted by Rocket) also shows the changes implied by the rocket comparisons.

Another method of estimating these changes is by statistical evaluation. Estimates based on this approach for 2 mb are also shown in Figure 6.3 (denoted by Step Regression) and are discussed in detail by Gelman et al. (1983). The pattern of relative agreement among the different methods depicted in Figure 6.3 is reasonably good. However, differences of 2–4K are common, and uncertainty in adjustments of this magnitude should be expected.

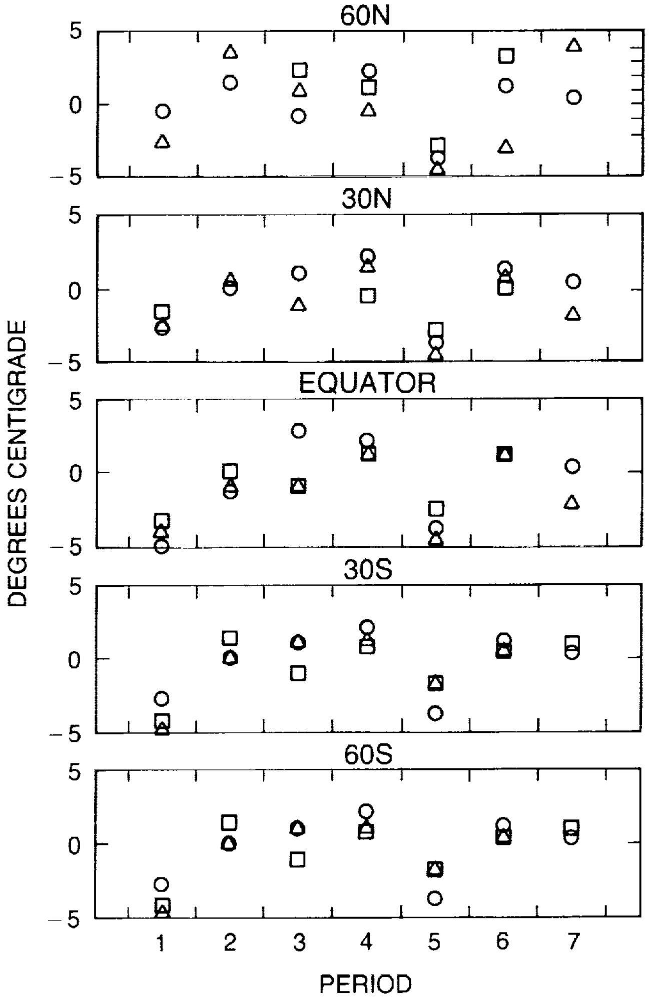

Figure 6.3 Temperature changes in the 2 mb NMC analyses, as inferred from rocket comparisons (○, Rocket), comparison of analyses around change dates (□, Joint), and regression (△, Step Regression), as explained in text.

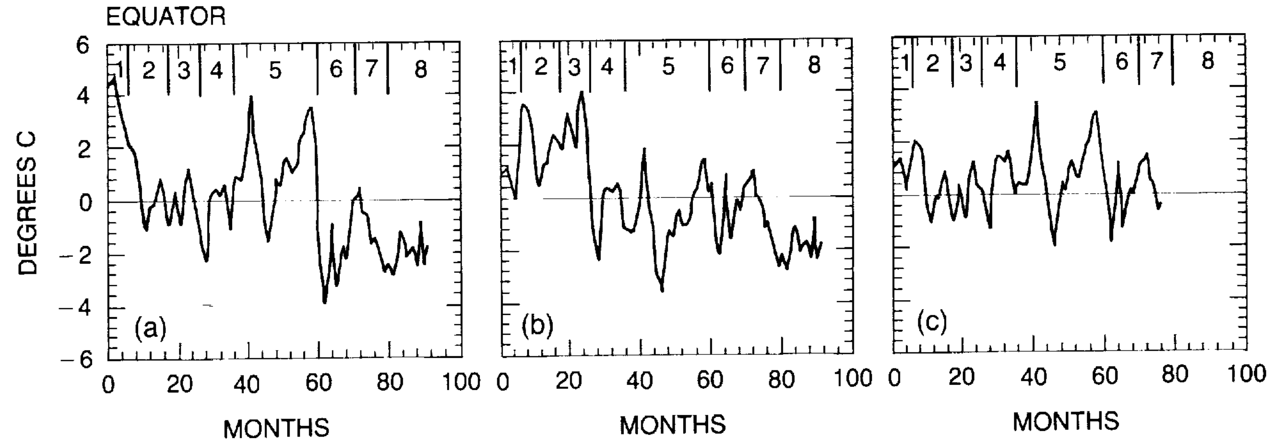

Figure 6.4 Monthly 2 mb average temperature (a, unadjusted; b, adjusted to rocket; c, adjusted to joints) deviations from the long-term monthly averages for the Equator. Time runs from October 1978 (month 1) to April 1986 (month 91).

Figure 6.4a shows the unadjusted 2-mb equatorial deviations for the 91-month period of record. Large changes in the level of deviations may be noted between several of the periods. In Figure 6.4b, the 2-mb equatorial deviations are shown after adjustments for rocket data comparisons have been applied. A jump of about 2K may be noted between periods 3 and 4; the reason is not yet known. Figure 6.4c shows the 2-mb equatorial deviations after the adjustments, using the method of joints (Gelman et al., 1983), have been applied. The jumps between periods have been largely eliminated by this method. However, no joint adjustment was derived between periods 7 and 8 because good analyses are lacking as a result of noisy SSU data on NOAA–9. It is also noted that this result is consistent with Figure 6.3, in which the changes from periods 3 to 4 are consistent between the joint and statistical methodologies, but differ from the rocketsondes. The cause of this discrepancy is under study, but it points out the need for consistent ground truth and the efficacy of a system of checks and balances. Figure 6.5 shows comparable information for 30°N. For this and other latitudes, after rocket adjustments have been applied, unexplained jumps are less apparent than for the Equator.

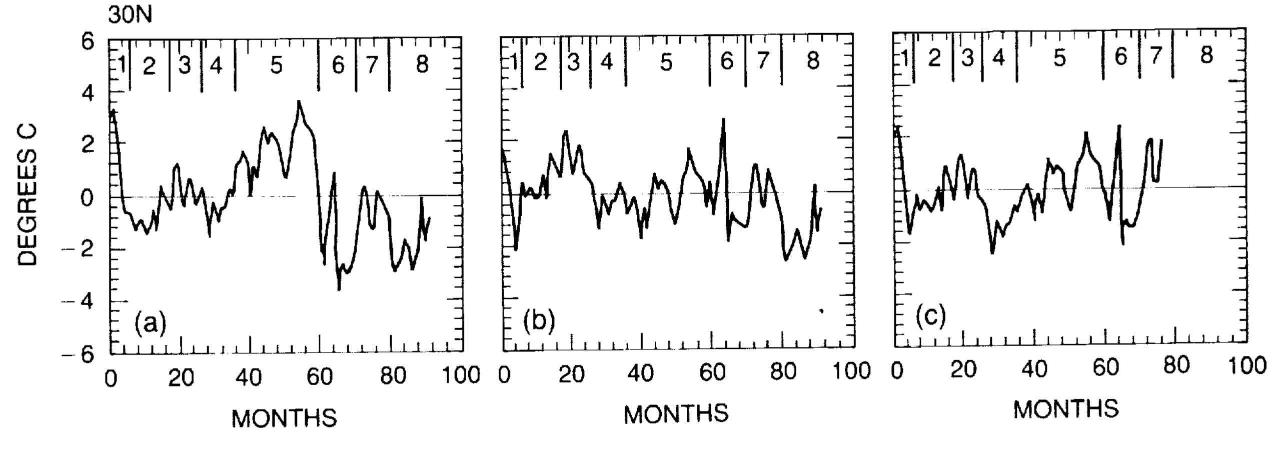

Figure 6.5 As in Figure 6.4, but for 30°N.

The underlying theme of this discussion has been to determine to what degree a trend in stratospheric temperature can be detected. On average, NMC analyses have had one major change a year with a confidence factor of 2–3K. Thus, if NMC stratospheric analyses with current adjustment techniques are used, a trend of less than 1.5K per decade over a decade would not be detected; however, a decadal change of 4–5K would be detectable.

6.2.3 Rocketsonde

6.2.3.1 Introduction

The number of rocketsonde launch sites operated by the United States increased from an initial 3 or 4 sites in 1958 to about 30 in 1965, and has since decreased to the present 9 sites. The number of rocketsondes launched in the U.S. has also decreased, from 3 to 5 per week to about 3 to 5 per month—a serious limitation for detecting long-term trends.

Despite the long period of rocketsonde measurements that exists for the U.S., many of the launch sites are unsuitable for trend analysis because of short, and often incomplete, data records. Nonetheless, the U.S. rocketsonde program has provided sufficient information from 14 launch sites (Table 6.3) to attempt an analysis of temperature trends. For this report, six sites with the most complete long-term records will be discussed.

6.2.3.2 Corrections

When properly applied, rocketsonde temperature corrections should improve the estimate of ambient temperature. Examples of optimal corrections applied to the Arcasonde and Datasonde instruments are presented in Table 6.4 and applied to the same temperature profile, independent of the instrument. The aerodynamic and radiation corrections are the dominant contribution to the total correction.

Table 6.3 Rocketsonde Launch Sites Having Data Available for Trend Analysis

Rocketsonde Site	Latitude	Longitude	Observational Period
Ascension Island	9°S	14°W	1969–1985
Kwajalein, MI	9°N	168°E	1979–1985
Ft. Sherman, CZ	9°N	80°W	1969–1979
Antigua, BWI	17°N	62°W	1969–1977
Barking Sands, HI	22°N	160°W	1969–1982
Cape Canaveral, FL	28°N	81°W	1969–1986
White Sands Missile Range, NM	32°N	106°W	1969–1982
Pt. Mugu, CA	34°N	119°W	1969–1982
Wallops Island, VA	38°N	75°W	1969–1980
Shemya, AK	53°N	174°E	1975–1985
Primrose Lake, Canada	55°N	110°W	1969–1982
Ft. Churchill, Canada	59°N	94°W	1971–1979
Poker Flat, AK	65°N	148°W	1969–1978
Thule, Greenland	77°N	69°W	1976–1981

NOTE: Data exist into 1986 for most of these sites. However, the reduction in the number of the U.S. rocketsonde launchings beginning in the late 1970's inhibits analysis outside of above dates.

Table 6.4 Example of Arcasonde and Datasonde Measurements of Same Temperature Profiles and Appropriate Corrections

	Temp. (K)	Aero. Heating	Lag.	Emissivity	Radiation	Correction	Ambient Temp.
	Alt. = 40 km						
Arcasonde	250.0	−0.4	−1.0	0.4	−0.4	−1.4	248.6
Datasonde	250.3	−0.4	−0.5	0.3	−1.1	−1.7	248.6
	Alt = 45 km						
Arcasonde	242.0	−0.9	−1.2	0.5	−0.4	−2.0	240.0
Datasonde	242.6	−0.9	−0.7	0.4	−1.4	−2.6	240.0
	Alt = 50 km						
Arcasonde	261.0	−2.1	−1.7	0.9	−0.5	−3.4	257.6
Datasonde	261.9	−2.2	−0.9	0.7	−1.9	−4.3	257.6

NOTE: Corrections are from Krumins and Lyons (1972).

The interpretation of the temperature trend between 1971 and 1973 given by Johnson and Gelman (1985) proposes that part of the sudden decrease in the temperature observed (~3K) could be attributed to a changeover in instrument design (i.e., from Arcasonde to Datasonde); however, the decrease is still present when only Datasonde profiles are used (Schmidlin, private communication). The Datasonde gradually replaced the Arcasonde at all U.S. ranges—at many before 1971. Krumins and Lyons (1972) published Datasonde corrections in 1972 that generally came into use at launch ranges in 1973. The initiation of corrections in 1973 might explain part of the decrease reported by Johnson and Gelman. The magnitude of the correction, if applied, would be about −1.0K at 40 km and about −1.6K at 45 km—approximately the amount of the difference noted between 1971 and 1973.

6.2.3.3 Rocket Data Base

All of the U.S. rocketsonde data available in the archive from 1969–1986 were examined. Data obtained before 1969 were not used because of the different data format. In addition, diverse instrument designs were used at some ranges until about 1971 and, in a few cases, even as late as 1973. Because the measurement quality of these systems varied from one instrument design to the other, the data from these instruments were not used. The rocket data base includes only Arcasonde and Datasonde data.

To eliminate the possibility of any discontinuity in the use of the corrections of Krumins and Lyons (1972) at any of the sites listed in Table 6.3, the data were examined for 1972 through 1986 to determine whether the standard U.S. correction was applied. If corrections had not been applied, they were incorporated. Furthermore, the temperature data obtained between 1969 and 1972 were also corrected using the same procedure. Thus, the temperature trend analyses presented here are produced from a consistent and homogeneous group of corrected temperature measurements extending from 1969 to the present.

It should be noted that even though the data set may now be considered uniform throughout, bad measurements were found in the profiles (as a result of bad calibrations or depressed sensors, for example) and had to be eliminated. The data from the 14 sites selected for analysis were plotted with the accompanying conjunctive rawinsonde. Profiles that showed differences of 3K or more throughout their overlapping altitudes were subsequently deleted. No attempt was made to determine whether the fault was in the radiosonde or the rocketsonde data. The consequence of this editing was a reduction in the number of observations available for analysis by about 35 percent. Despite the removal of a large number of observations, sufficient data were available with a reasonable temporal distribution to produce the monthly averages used in the trend analysis.

The steps followed to obtain a valid and consistent data set for trend analysis can be summarized as follows:

- Only Arcasonde and Datasonde profiles from 1969 through 1986 were selected for analysis.
- All rocketsonde profiles from 1969 to 1972 were edited and quality checked by comparing them with the supporting radiosonde; if temperature differences of 3K or more were present, the rocketsonde observation was deleted.
- All uncorrected profiles were corrected, using the standard method.

6.2.3.4 Accuracy and Precision

Direct analysis of accuracy is difficult for rocketsonde instruments because of the lack of a reference standard. Although occasional Datasonde instruments give data profiles that disagree with the conjunctive radiosonde profile, a number of instruments were recalibrated after 2 years and found unchanged (Schmidlin, 1981). Thus, any disagreement between the rocketsonde and radiosonde temperatures is usually the result of bad calibration, an improperly mounted thermistor, or a bad radiosonde measurement. Poor data from these sources were removed as far as possible. However, true inflight accuracy is difficult to specify; hence, the need for corrections. Corrections should be known well enough to enable ambient temperatures to be produced from the thermistor temperature.

The accuracy of the Datasonde temperature sensor has been estimated as 3–5K, based on comparisons between 1) various rocket techniques (Olsen et al., 1979; Schmidlin, 1984), 2) rocketsonde instrument designs (Finger et al., 1975; Olsen et al., 1979), and 3) satellite instruments (Barnett et al., 1974; Barnett and Corney, 1984; and Pick and Brownscombe, 1981). A recent comparison of overlapping Datasonde thermistor and falling sphere measurements between 30 and 60 km (Schmidlin, private communication) revealed excellent temperature agreement to within the limits of the variability in the measurements. The inflatable sphere's measurement is independent of the external influences that disturb thermistor measurements (e.g., aerodynamic heating and radiation errors), so that this agreement suggests that Datasonde accuracy is probably near 1K up to an altitude of 60 km.

An analysis of paired measurements (Schmidlin, 1981) using 21 pairs of Datasonde, with the instruments of each pair launched 5 minutes apart, gave an estimate of repeatability of 0.8K at 35 km and 1.3K at 50 km. Through the use of an indirect method for estimating errors found in Gandin (1963), the precision of the Datasonde was calculated to be 0.6K at 35 km and 0.9K at 50 km.

6.2.3.5 Trend Detection

Initial trend analysis carried out for the 40 and 45 km altitudes using unedited Wallops Island and Cape Canaveral observations, respectively, indicated a temperature decrease of approximately −0.35K per year. This rather large downward trend was determined for 1969–1986 using all of the data existing in the archive (including the unqualified rocketsondes, uncorrected profiles, and corrected profiles). Regression of the edited Cape Canaveral and Wallops Island monthly averages for the same altitudes showed trends of approximately −0.22° per year and −0.18° per year, respectively. Thus, the difference between the edited data used here and the unedited data can be very large.

Because of the sudden temperature decrease (between 1971 and 1973) reported by Johnson and Gelman (1985), it was considered important to attempt to determine whether the temperature drop originated from the Arcasonde to Datasonde changeover. Schmidlin (private communication) has separated Datasonde observations from all others in the 1970–1973 timeframe. From these Datasonde observations it is clear that a 2K drop in temperature still exists at most rocket stations. At the time of writing, it is still not clear whether this drop in temperature is due to undetected instrumental problems or to a real atmospheric change. Further work on this point is clearly warranted. Trends should be calculated separately for 1969–1986 and 1973–1986.

Since the sample size was reduced by about 35 percent after eliminating all suspect observations, as described above, there is some concern that the gaps between monthly averages were more frequent than desired and might lead to erroneous results. Consideration was given to using the longest complete data periods to reduce the error caused by the smaller segments of data. Only a handful of the 14 stations had sufficiently long data records to permit trend analyses. Trends were calculated between 1973 and the latest date possible for 4 of the 14 sites. The averages calculated for each altitude (30, 35, . . ., 55 km) are actually derived from 5-km vertical intervals (i.e., 30 km is an average of the temperatures between 28 and 32 km). Monthly averages are composed of the observations within a given month, with a minimum of three observations. When multiple observations occurred within the same day, only one observation for that day was included. Furthermore, it was important to reduce the effect that tidal activity might have had on the trend calculations. Therefore, only observations made in daylight were used. An attempt to use a more restricted time period of 2 or 4 hours centered about midday failed because then the sample size became too small.

6.2.3.6 Summary

A careful examination of the rocketsonde data for the 1969–1986 period, and elimination of the profiles that disagreed with the supporting radiosondes, reduced the data set by about 35 percent. If the standard U.S. correction had not been applied, the rocketsonde data were corrected following Krumins and Lyons (1972).

Monthly averages over the period 1969 to the end of the data set were calculated using daylight observations only; nighttime observations were avoided to reduce any biasing effect that might be created from the diurnal tide. Monthly averages comprise at least three observations. Johnson and Gelman (1983), using the unedited rocketsonde data, showed an average temperature decrease of 3.4K in the 25 to 30 km, 25° to 55°N region between 1970 and 1972, while the support radiosondes showed only a 2K change. However, the edited rocketsonde data set used here shows temperature decreases of 3.3K, 2.2K, 1.6K, 1.2K, and 2.9K at Cape Canaveral, White Sands, Pt. Mugu, Wallops Island, and Primrose Lake over a 28 to 32 km altitude range for the same period. The average of these stations is in better agreement with the support radiosonde change, suggesting that the editing of biased rocketsondes and the application of corrections to uncorrected data may have alleviated much of the difference.

6.3 DATA ANALYSIS

6.3.1 Intercomparisons

In previous studies of stratospheric temperature trends, little attempt was made to intercompare data sets. The object of this section is to make the comparisons among the various data sets available for trend assessments and to provide a data quality check for long-term trend computations.

In a previous intercomparison study, Labitzke et al. (1986b) compared the radiosonde-based data of Angell and Korshover (1983a) (hereafter referred to as AK) to the Berlin analyses used by Naujokat (1981) (hereafter referred to as N (see Section 6.2.1.3 for a description of both data sets). Labitzke et al. (1986b) showed that some of the large differences between AK and N resulted from the omission of Russian radiosondes (i.e., the stations Orenburg, 50°N, 50°E; Omsk, 60°N, 70°E; and Kirensk, 60°N, 110°E) from AK's data before 1970, and from a few short periods between 1970 and 1978. Figure 6.6 (from Labitzke et al., 1986b) displays AK's data in the north temperate zone (solid line), the average of the 50°N and 60°N zonal means from the Berlin data (dotted line), and the average of points from the Berlin data collocated to the AK selected radiosonde sites (dashed line). The Berlin collocated data correspond well to the Berlin zonal means. The AK data do not correspond well to the Berlin data before 1970 and during the summer 1973 to summer 1974 period because of the absence of the Russian stations. During the 1978 through 1982 period, serious deviations between AK and the Berlin data occur that are ascribed by Labitzke et al. to missing or bad data.

The data sets used herein to make detailed comparisons are described in Section 6.2.2. Two of the data sets (satellite and NMC data) start in 1979; hence, the data sets for six levels in the

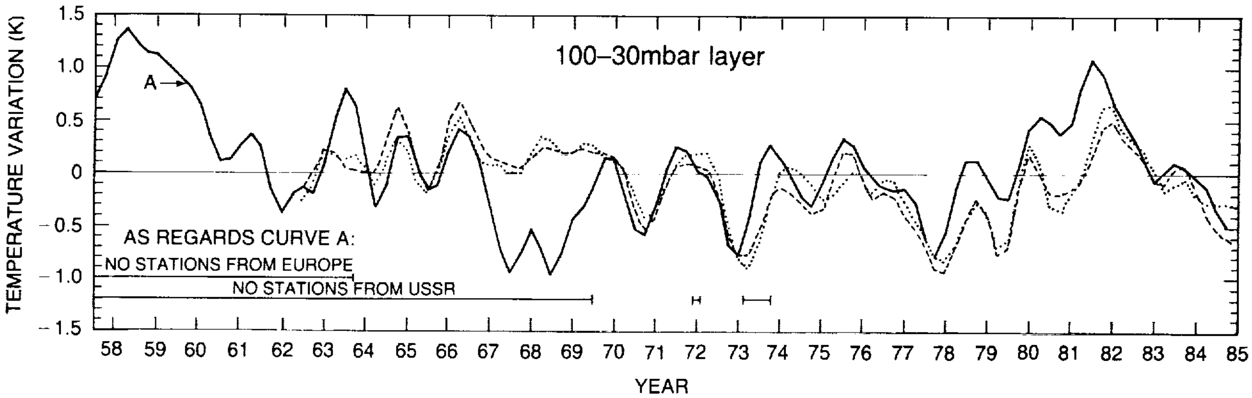

Figure 6.6 Temperature variation (K) in the 30–100 mb layer of "north temperate" latitudes, where a 1–2–1 weighting (1–1 at beginning and end of record) has been applied twice to successive seasonal deviations from the mean: —— all stations from Angell and Korshover /7/ (mean 1958–1977); ---- all nearby grid points from Berlin analyses; . . . . average of the zonal mean of 50°N and 60°N from Berlin grid point data (mean 1963–1977); (tick marks are for summer = J–J–A).

stratosphere are compared, beginning from 1979 through 1986. Each data set has had the long-term seasonal average removed; these deseasonalized data have been smoothed with a 1–2–1 filter. The stratosphere has been divided into six levels (100 to 50 mb, 100 to 30 mb, 30 to 10 mb, 10 to 5 mb, 5 to 1 mb, and 0.5 mb) for the comparisons. The data are compared globally, in the Northern Hemisphere, in the Southern Hemisphere, and in the Tropics (30°S to 30°N).

Level Comparisons

100 to 150 mb

Figures 6.7a–d display the 100 to 50 mb layer mean temperature anomalies of the 1979 through 1986 period; the brightness temperature anomalies from MSU channel 24 centered at 90 mb (200 to 50 mb layer) (see Nash and Forrester, 1986), are also plotted. A visual comparison of the data set differences indicates a general consistency within 0.5K, that gives confidence in their reliability. The largest deviations within the data occur in AK's radiosonde data during 1985 in the Southern Hemisphere (Figure 6.7b). This data set is colder than those of the NMC and MSU by at least 1K. All of the data sets display the strong positive anomaly in late 1982 that has been associated with the eruption of El Chichón.

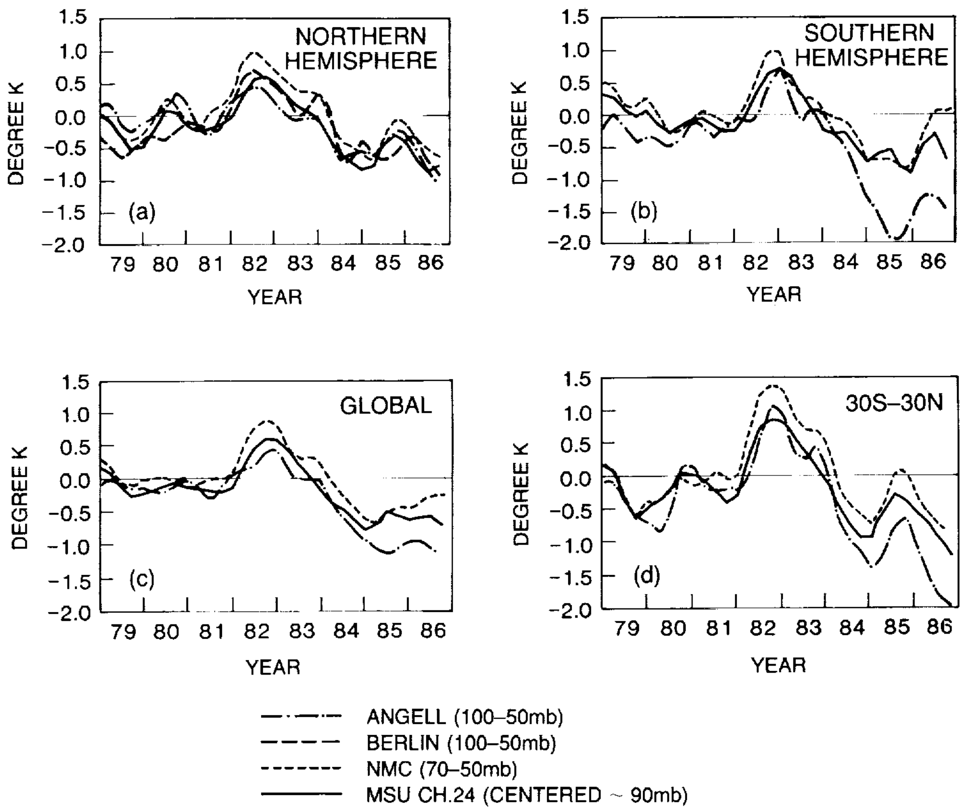

Figure 6.7 Seasonal temperatures with the long-term seasonal averages removed and smoothed 1–2–1 in time: Angell 100–50 mb radiosonde thickness (solid–dot); Berlin 100–50 mb thickness (long dash); NMC 70–50 mb thickness (short dash); and MSU channel 24 centered at approximately 90 mb (solid) for (a) Northern Hemisphere average, (b) Southern Hemisphere average, (c) global average, and (d) 30°S–30°N average. Berlin data were available only for the Northern Hemisphere. Tick marks on the abscissa correspond to the D–J–F seasons.

100 to 30 mb

Figures 6.8a–d display the 100 to 30 mb layer mean temperature anomalies for the 1979–1986 period. Two satellite channels are included here: MSU channel 24 (discussed previously), and SSU channel 15X centered at 50 mb (see Nash and Forrester, 1986). MSU-24 approximates the 200 to 50 mb layer mean temperature, while SSU-15X approximates the 150 to 20 mb layer mean temperature. These data are generally consistent to within 1K over the 8-year period. Comparisons between Figure 6.8 and Figure 6.7 show similar behavior. The most serious discrepancies between data sets occur with AK's data for 1985 (see Figure 6.7), and the SSU-15X data from 1980 and early 1981.

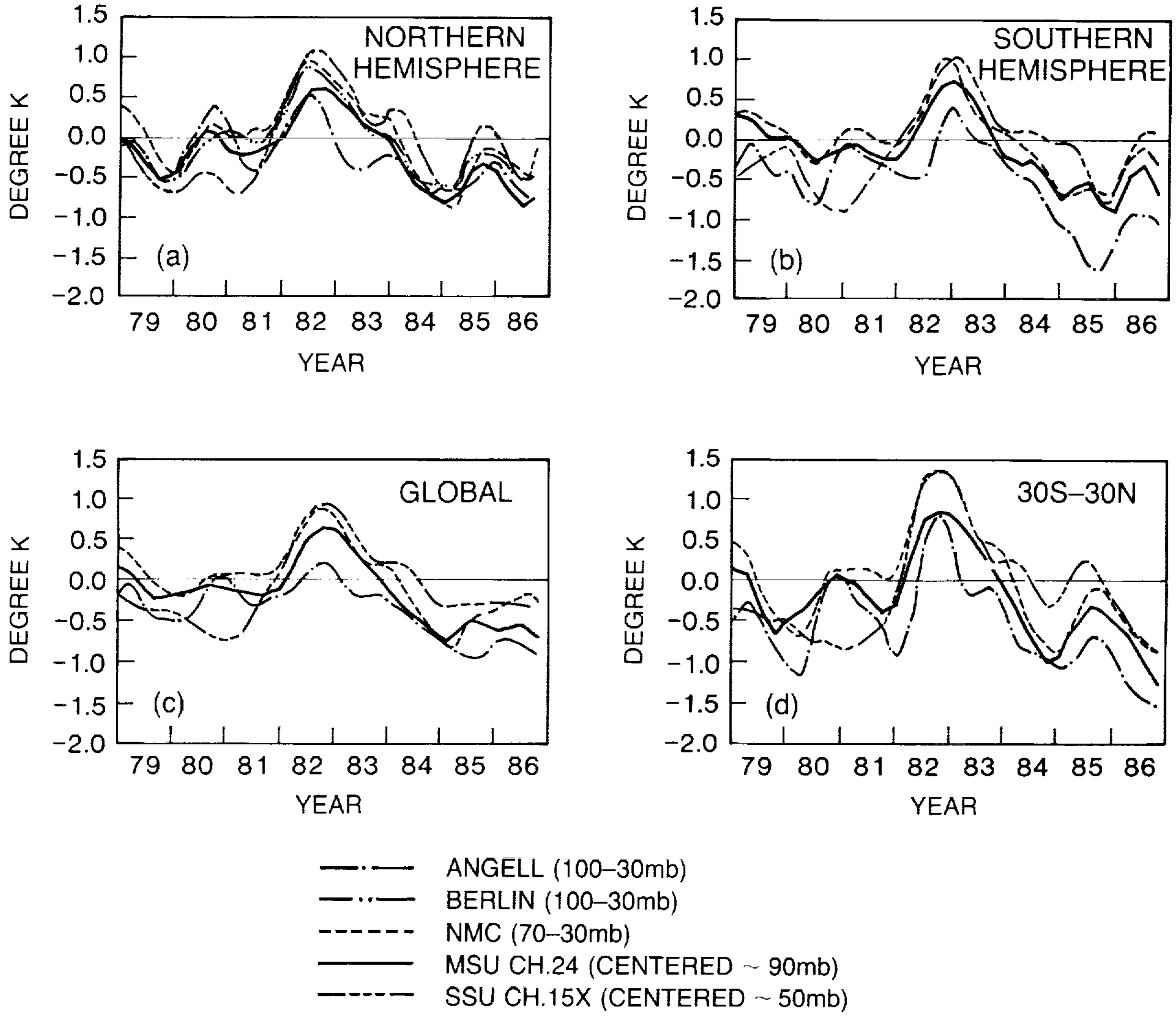

Figure 6.8 Seasonal temperatures with the long-term seasonal averages removed and smoothed 1–2–1 in time: Angell 100–30 mb radiosonde thickness (solid–dot); Berlin 100–30 mb thickness (long dash); NMC 70–30 mb thickness (short dash); MSU channel 24 centered at approximately 90 mb (solid); and SSU channel 15X centered at approximately 50 mb (solid–dot) for (a) Northern Hemisphere average, (b) Southern Hemisphere average, (c) global average, and (d) 30°S–30°N average. Berlin data were available only for the Northern Hemisphere. Tick marks on the abscissa correspond to the D–J–F seasons.

30 to 10 mb

Figure 6.9 displays the NMC 30 to 10 mb layer temperature anomalies for 1979–1986 and SSU channels 26X (centered at 20 mb, solid line) and 25 (centered at 15 mb, solid-dot line). SSU channel 26X approximates the 55 to 7 mb layer, while channel 25 approximates the 50 to 5 mb layer. These data are generally consistent to within 1K. The NMC data are generally warmer than the satellite data from 1979 to 1983; they also show an extremely cold period during the Southern Hemisphere summer of 1985/1986, which is weakly apparent in the SSU channels.

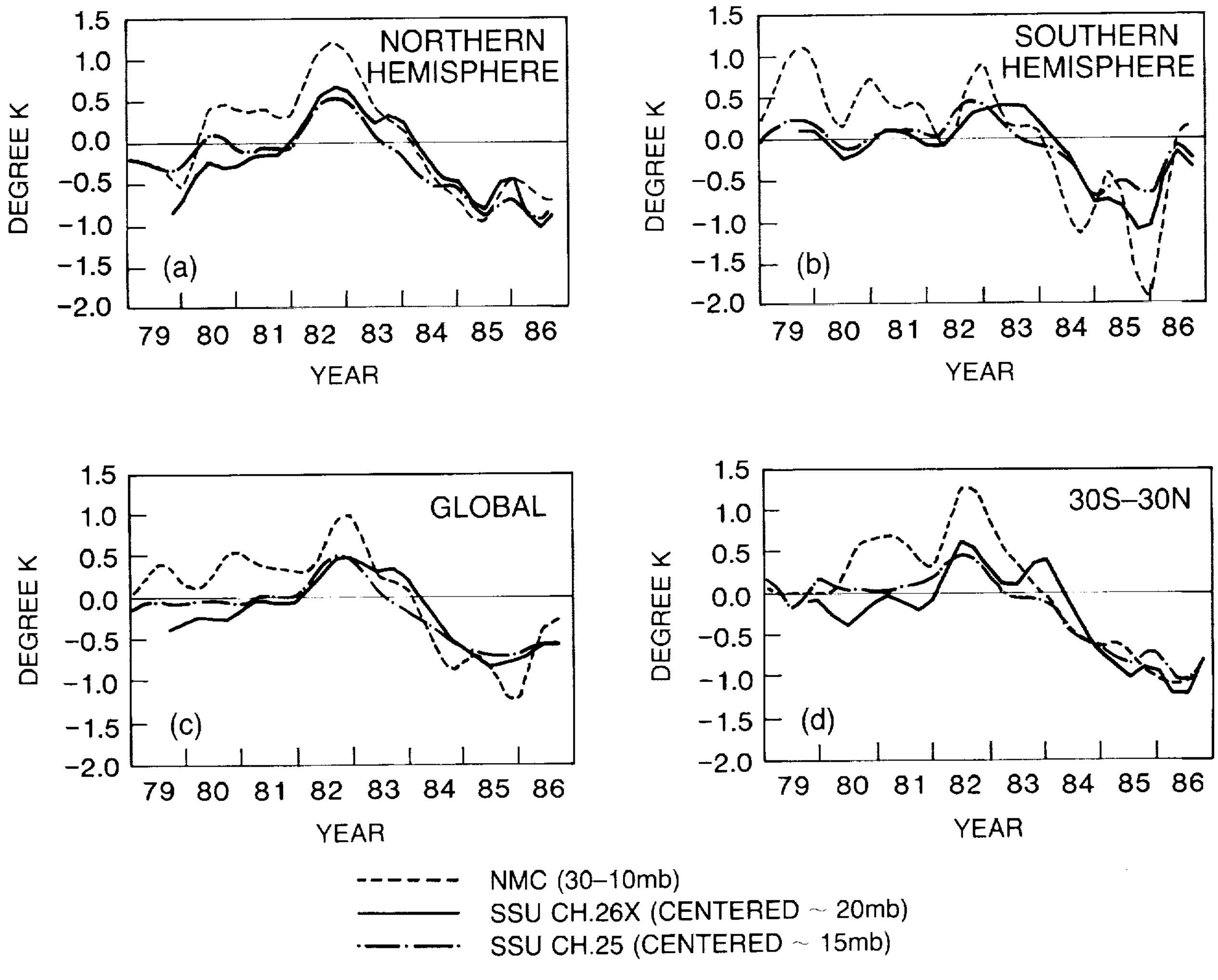

Figure 6.9 Seasonal temperatures with the long-term seasonal averages removed and smoothed 1–2–1 in time: NMC 30–10 mb thickness (dotted); SSU channel 26X centered at approximately 20 mb (solid); and SSU channel 25 centered at approximately 15 mb (three short dashes and a long dash) for (a) Northern Hemisphere average, (b) Southern Hemisphere average, (c) global average, and (d) 30°S–30°N average. Tick marks the abscissa correspond to the D–J–F seasons.

10 to 5 mb

Figure 6.10 displays the NMC 10 to 5 mb layer mean temperature anomalies and the SSU channel 26 data (centered at 6 mb and approximating the 20 to 2 mb layer). In general, the available data at this level are consistent only to 1–2K, and would produce radically different trends. For example, the NMC data show a 2K positive anomaly in both hemispheres during the 1982/1983 period, while the SSU data show weak positive anomalies on the order of 0.25–0.5K. Also note that a similar anomaly appears at lower levels in all of the data sets, but with a magnitude of only 1–1.5K.

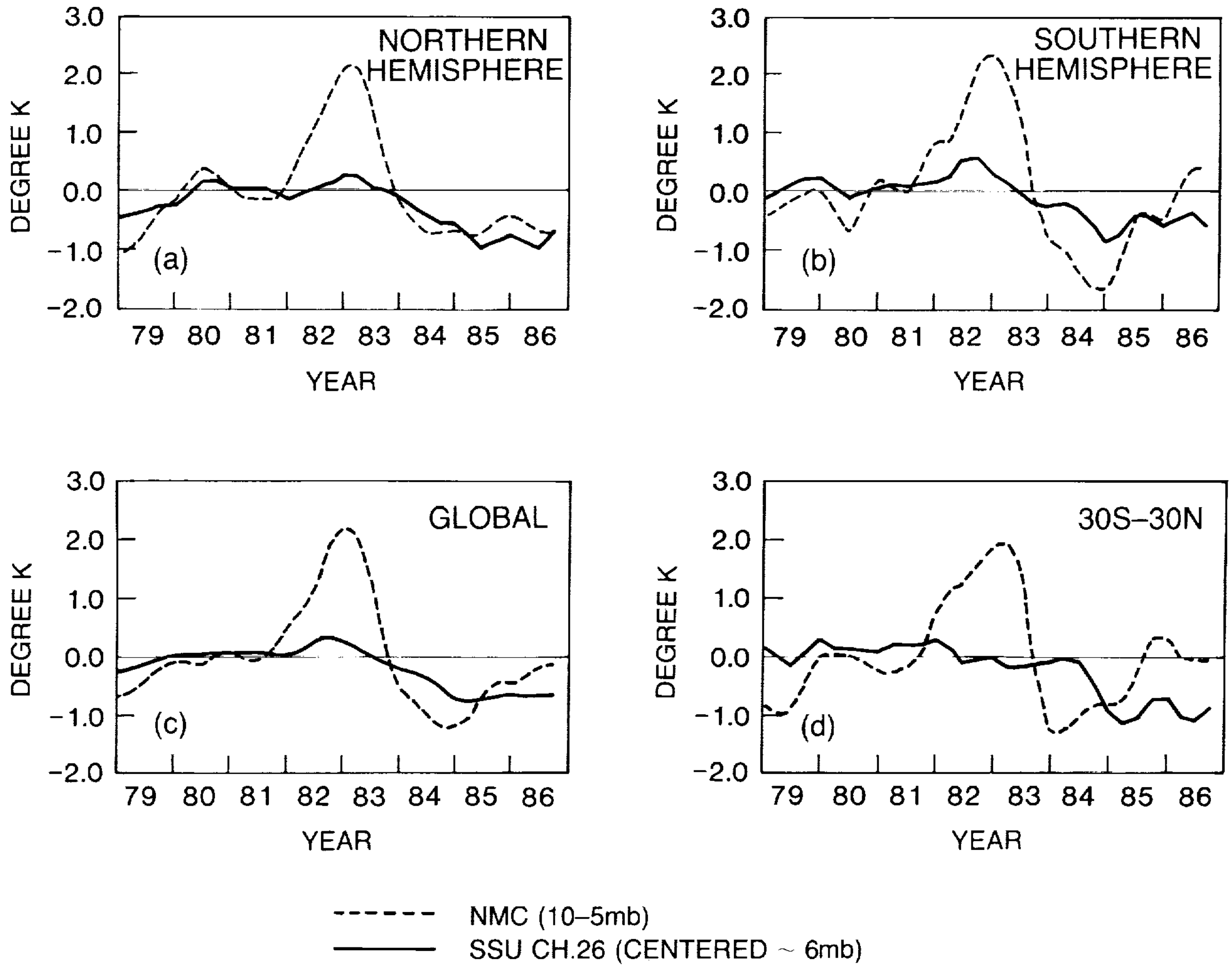

Figure 6.10 Seasonal temperatures with the long-term seasonal averages removed and smoothed 1–2–1 in time: NMC 10–5 mb thickness (dotted); and SSU channel 26 centered at approximately 6 mb (solid) for (a) Northern Hemisphere average, (b) Southern Hemisphere average, (c) global average, and (d) 30°S–30°N average. Tick marks on the abscissa correspond to the D–J–F seasons.

5 to 1 mb

Figure 6.11 displays the NMC 5 to 1 mb layer mean temperature anomalies with SSU channel 27 (centered at 2 mb and approximating the 5.7 to 0.5 mb layer, solid line) and 36X (centered at 1.5 mb and approximating the 4 to 0.5 mb layer, solid-dot line) brightness temperature anomalies. Again, the NMC data show a strong positive anomaly between 1982 and 1983 that is not evident in the satellite data. The SSU data are very consistent with one another. Except for the 1982/1983 period, the data are generally consistent to within 1K of one another, and show a cooling of 1–2K between 1979 and 1986.

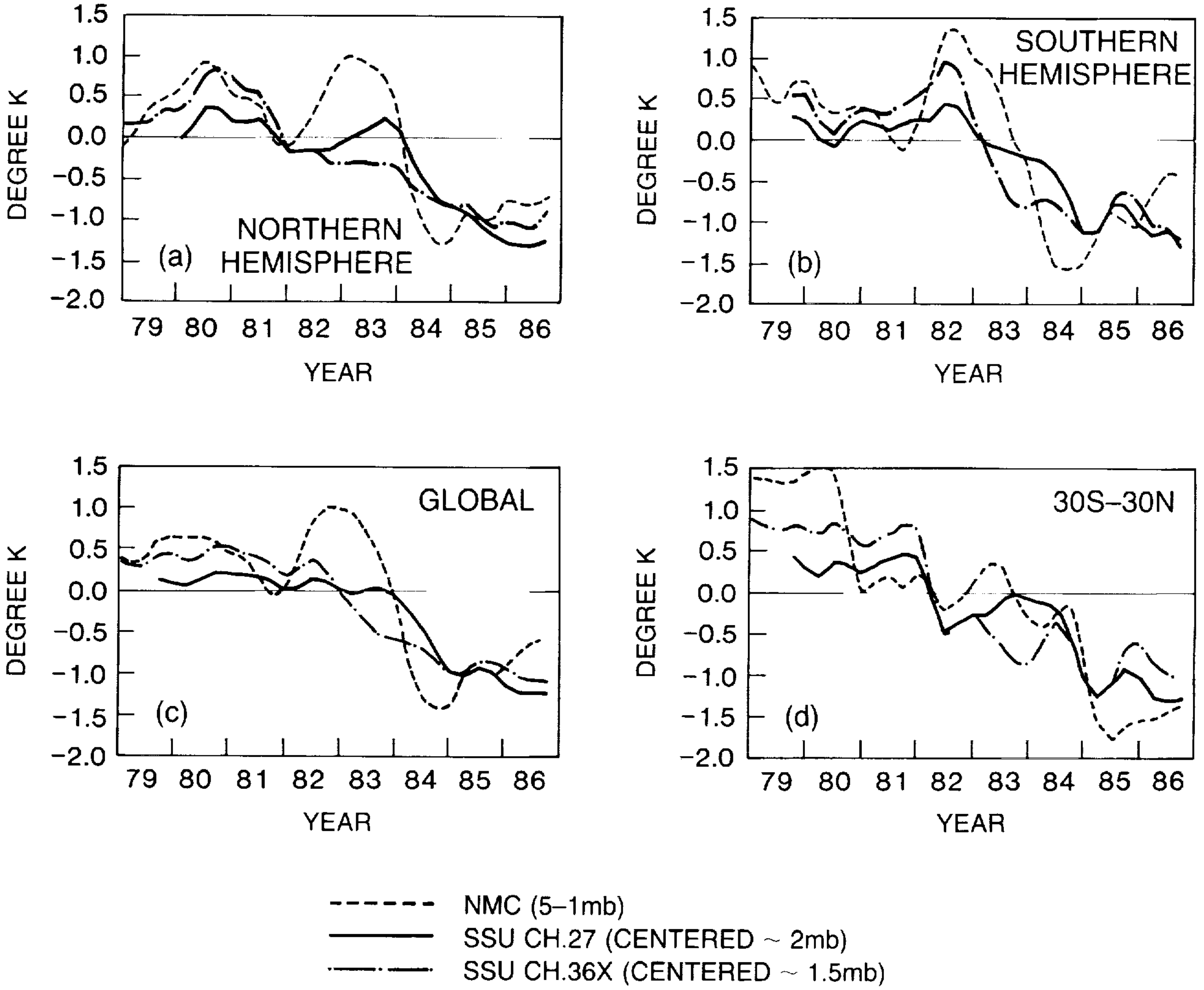

Figure 6.11 Seasonal temperatures with the long-term seasonal averages removed and smoothed 1–2–1 in time: NMC 5–1 mb thickness (dotted); SSU channel 27 centered at approximately 2 mb (solid); and SSU channel 36X centered at approximately 1.5 mb (solid–dot) for (a) Northern Hemisphere average, (b) Southern Hemisphere average, (c) global average, and (d) 30°S–30°N average. Tick marks on the abscissa correspond to the D–J–F seasons.

0.5 mb

Figures 6.12a–d display the SSU channel 47X data centered at 0.5 mb and approximating the 1.2 to 0.2 mb layer. Few reliable data were available for comparison at this level, with the exception of the irregularly spaced rocketsonde data (see the following discussion). These data show an almost linear cooling of 2.5K from late 1979 to late 1986. Nash and Forrester (1986) estimate this channel to have a standard error of about lK because of the sensitivity to changes in SSU channel 27's spectroscopic performance.

In addition to these conventional data sets, the data have also been compared to the rocketsondes (see Section 6.2.3). These rocketsonde data are irregularly spaced and are concentrated primarily in the Northern Hemisphere, with the exception of Ascension Island at 9°S, 14°W. Figures 6.13–16 display comparisons of rocketsonde and zonal mean satellite data from three stations at four different levels. These three stations (Ascension Island, 9°S to 14°W; Cape Canaveral, 28°N to 81°W; and Kwajalein Island, 9°N to 168°E) were chosen for the length and continuity of their data over 1979 to 1986.

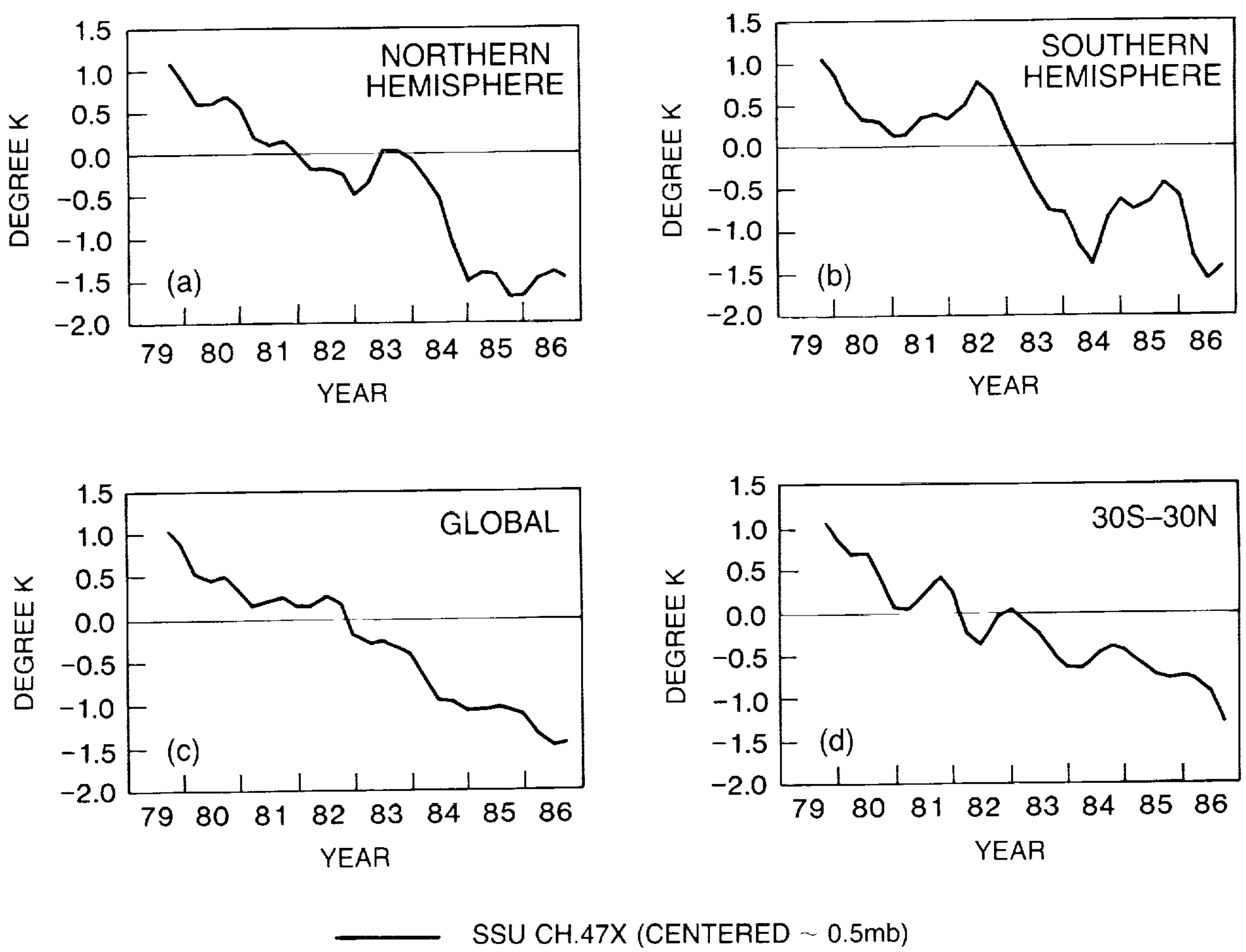

Figure 6.12 Seasonal temperatures with the long-term seasonal averages removed and smoothed 1–2–1 in time for SSU channel 47X centered at approximately 0.5 mb for (a) Northern Hemisphere average, (b) Southern Hemisphere average, (c) global average, and (d) 30°S–30°N average. Tick marks on the abscissa correspond to the D-J-F seasons.

Figures 6.13a–c display rocket data averaged from 27.5 km to 37.5 km in comparison to the SSU channel 25 zonal mean data. SSU channel 25 is centered at 15 mb (~30 km), with a weighting function width of about 17 km. The Cape Canaveral data are compared to the 30°N SSU zonal mean; the Ascension data are compared to the 10°S SSU data; and the Kwajalein data are compared to the 10°N SSU data. The rocketsonde data are processed by finding the deviation from the long-term monthly mean, interpolating missing months, averaging the deviations into seasons, and, finally, smoothing the seasonal deviations with a 1–2–1 filter. In general, the data on these plots are consistent to only 1–2K. This poor consistency could result from the comparison of single station data to the satellite data zonal means. For example, all three rocket data sets show a strong quasi-biennial oscillation (QBO) signal that is largely absent from the SSU data at 10°S (Figure 6.13a) and 10°N (Figure 6.13c). A visual averaging of Kwajalein and Ascension shows that two large minima would still appear at the tick marks between 80/81 and 82/83—QBO minima at both stations. Nastrom and Belmont (1975) showed that the QBO has a 2K amplitude and is vertically deep (~20 km) in the region of SSU channel 25's weighting function; thus, this channel should have peak anomalies in excess of 1K. It is not clear why SSU channel 25 cannot resolve the QBO.

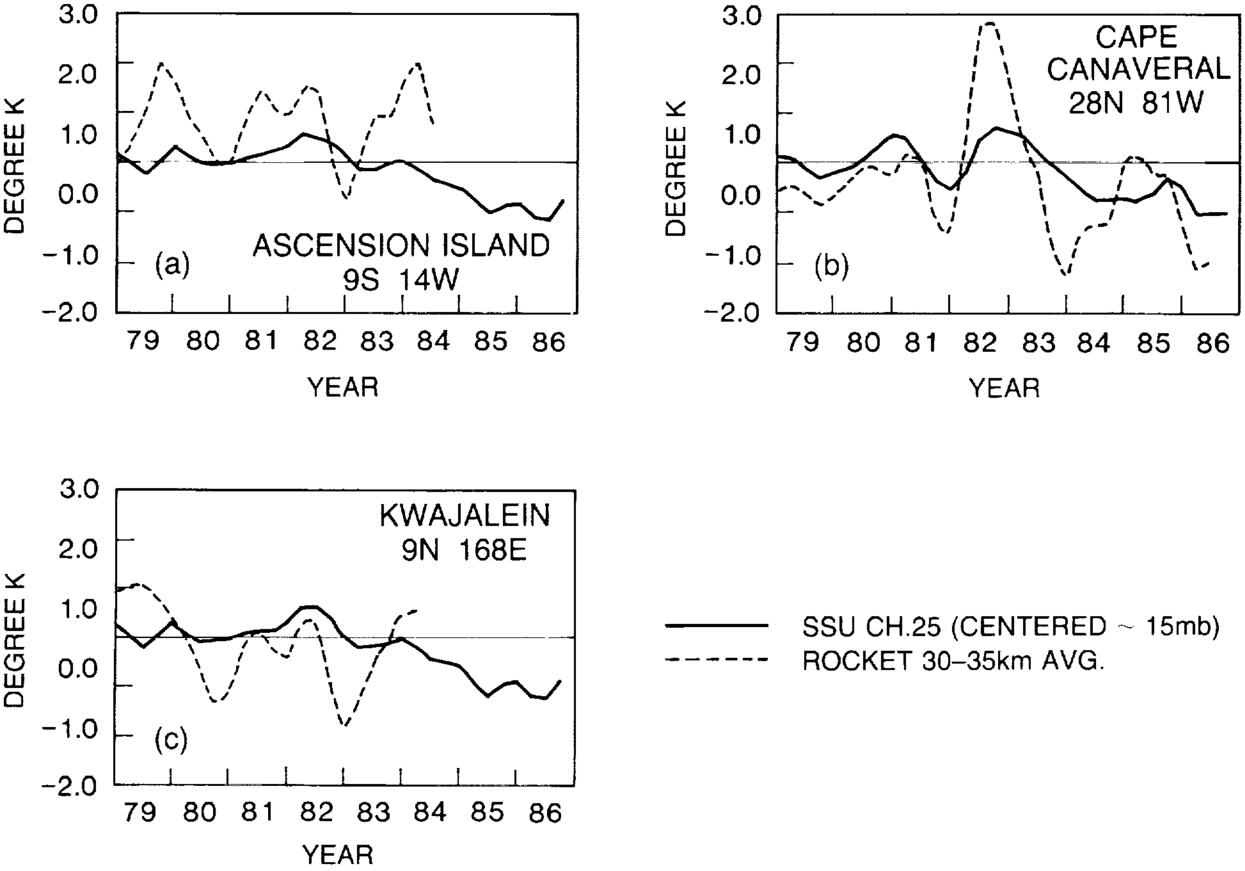

Figure 6.13 Seasonal temperatures with the long-term seasonal averages removed and smoothed 1–2–1 in time for the 30–35 km layer average of station rocket data (dotted) and the corresponding zonal average of SSU channel 25 centered at approximately 15 mb (solid) for (a) Ascension Island (9°S, 14°W), (b) Cape Canaveral (28°N, 81°W), and (c) Kwajalein (9°N, 168°E). Tick marks on the abscissa correspond to the D–J–F seasons.

Figure 6.14 displays the comparison of SSU channel 26 (centered at 6 mb or 35 km, with a weighting function width of 17 km) to the rocketsonde temperatures averaged from 27.5 km to 42.5 km. Again, the variations in this altitude range are greater in the rocketsonde data than in the satellite data, with a consistency of only 1–2K.

Figure 6.15 displays the SSU channel 27 (centered at 2 mb or 43 km, with a weighting function width of 17 km) layer temperature anomalies, SSU channel 36X (centered at 1.5 mb or 45 km, with a weighting function width of 12 km) layer temperature anomalies, and the 37.5 km to 52.5 km averaged rocketsonde temperature anomalies. These data sets are in very good agreement, with the exception of a strong positive anomaly at Cape Canaveral in mid-1982 that resulted from computer problems at Cape Canaveral in 1982 (K. Johnson, private communication). Coolings in all of the data sets from mid-1982 occur at both Ascension and Kwajalein in association with the El Chichón eruption. The data are consistent to 1K.

Figure 6.16 displays the SSU channel 47X (centered at 0.5 mb or 53 km, with a weighting function width of 17 km) layer mean temperature anomalies, and the 47.5 km to 57.5 km averaged rocketsonde temperature anomalies. The results of a comparison between these two data sets are not good; in general, they compare to within 1–2K.

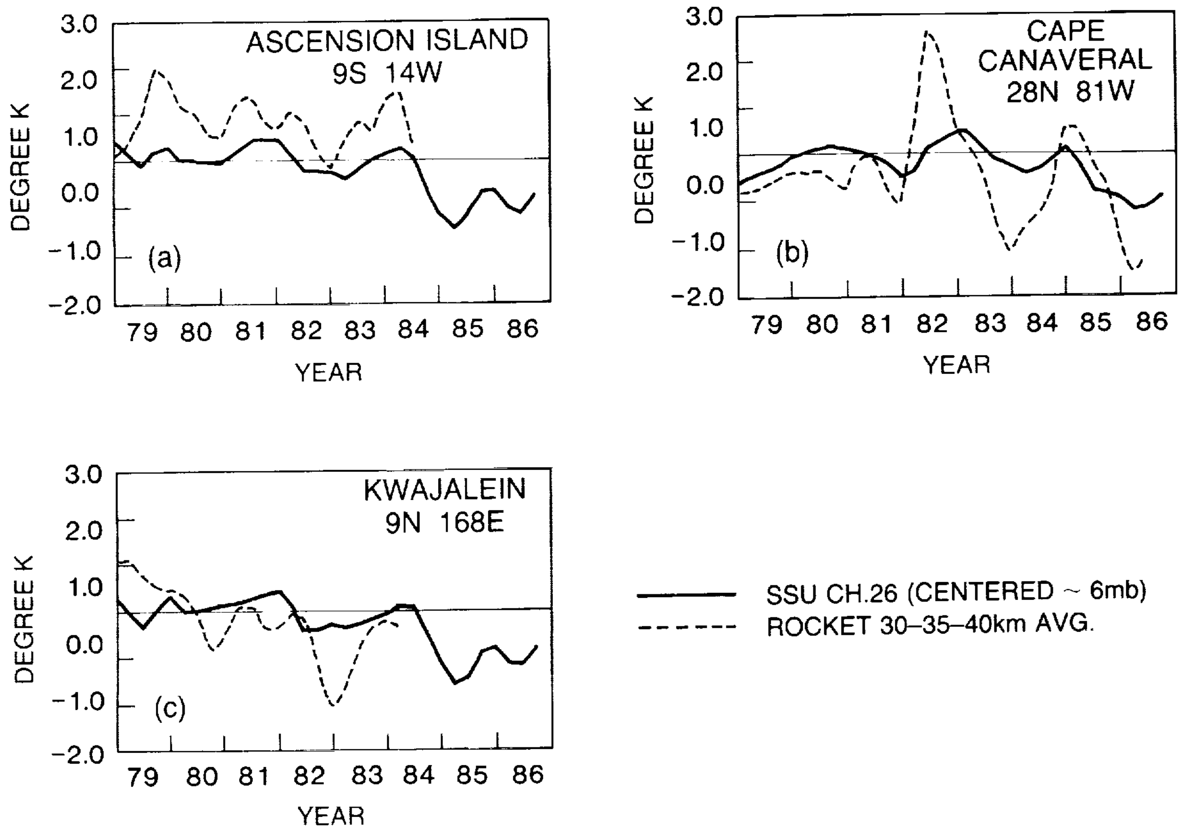

Figure 6.14 Seasonal temperatures with the long-term seasonal averages removed and smoothed 1–2–1 in time for the 30–35–40 km layer average of station rocket data (dotted) and the corresponding zonal average of SSU channel 26 centered at approximately 6 mb (solid) for (a) Ascension Island (9°S, 14°W), (b) Cape Canaveral (28°N, 81°W), and (c) Kwajalein (9°N, 168°E). Tick marks on the abscissa correspond to the D–J–F seasons.

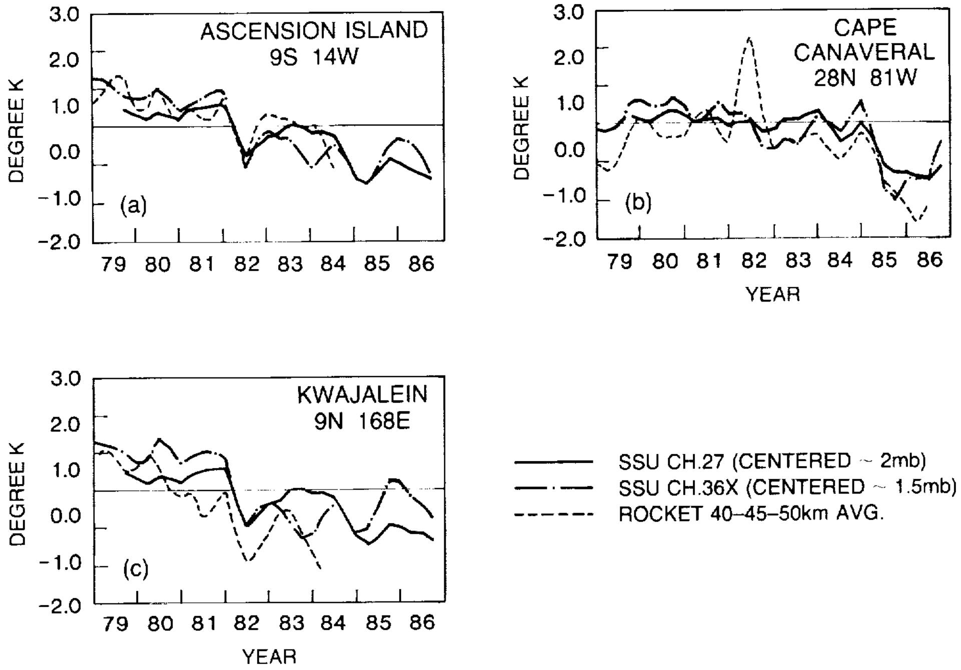

Figure 6.15 Seasonal temperatures with the long-term seasonal averages removed and smoothed 1–2–1 in time for the 40–45–50 km layer average of station rocket data (dotted) and the corresponding zonal average of SSU channel 27 centered at approximately 2 mb (solid) and SSU channel 36X centered at approximately 1.5 mb (solid–dot) for (a) Ascension Island (9°S, 14°W), (b) Cape Canaveral (28°N, 81°W), and (c) Kwajalein (9°N, 168°E). Tick marks on the abscissa correspond to the D–J–F seasons.

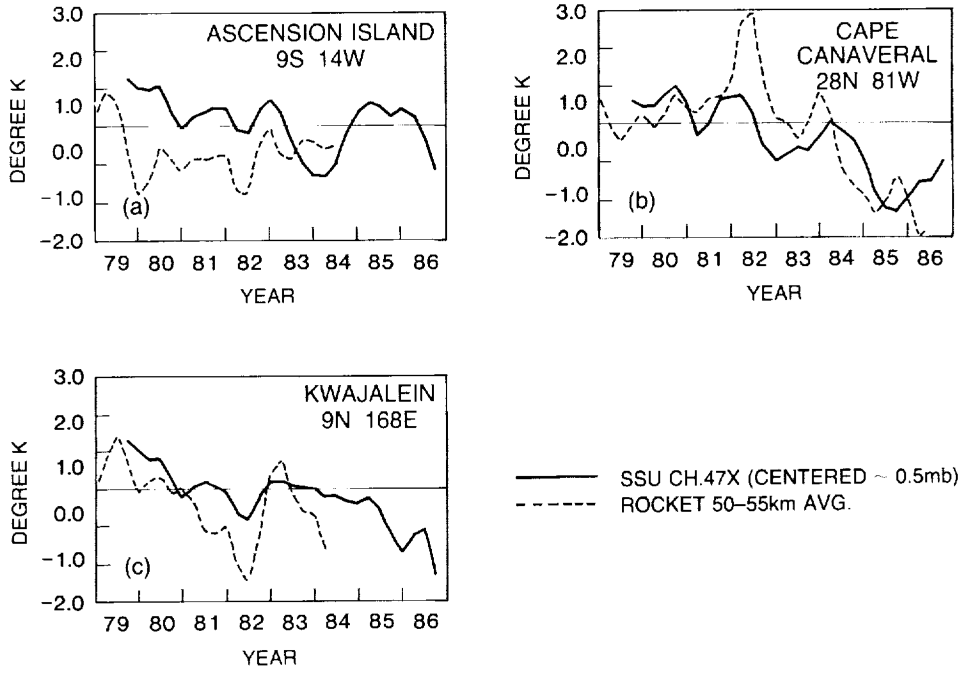

Figure 6.16 Seasonal temperatures with the long-term seasonal averages removed and smoothed 1–2–1 in time for the 50–55 km layer average of station rocket data (dotted) and the corresponding zonal average of SSU channel 47X centered at approximately 0.5 mb (solid) for (a) Ascension Island (9°S, 14°W), (b) Cape Canaveral (28°N, 81°W), and (c) Kwajalein (9°N, 168°E). Tick marks on the abscissa correspond to the D–J–F seasons.

6.3.2 Short-Term Change and Long-Term Trends

In the previous intercomparison section, effects on the data by the QBO and El Chichón are observed (e.g., see Figure 6.7d). These effects would tend to undermine trend computations. For example, the warming by El Chichón would tend to bias upward any trend computation that uses 1982 or 1983 data. Another technique for determining changes is to difference individual years; however, this technique would be biased by the respective phases of the QBO. To assess temperature changes that have occurred over the short period of 1979 to 1986, data from 1985 and 1986 have been averaged and differenced with the 1979 and 1980 average. This differencing avoids the 1982 and 1983 El Chichón event, while minimizing the QBO signal with the 2-year average.

The six levels used in the intercomparison section have been differenced; these differences are shown in Tables 6.5 to 6.10. The data sets used are the same as those shown in Section 6.3.1.

Figure 6.17 displays the global layer temperature changes over the 1979/1980 to 1985/1986 period as a function of altitude. The lower stratosphere shows a slight cooling of approximately 0.5K. The upper stratosphere (10 to 0.5 mb) shows coolings in excess of 1K. Recall that these changes are for layers that are on the order of 10 to 15 km deep. (See Figure 6.2 for the satellite weighting functions.)

Table 6.5 100–50 mb Layer Mean Temperature Changes 1986/1985–1980/1979

	N. Hem.	S. Hem.	Global	30°S–30°N
Angell Radiosonde	−0.6	−1.2	−1.0	−1.0
Berlin	−0.2			
NMC	−0.3	−0.6	−0.5	−0.2
MSU Channel 24 Centered at ~90 mb	−0.4	−0.6	−0.5	−0.5

Table 6.6 100–30 mb Layer Mean Temperature Changes 1986/1985–1980/1979

	N. Hem.	S. Hem.	Global	30°S–30°N
Angell Radiosonde	−0.3	−0.8	−0.6	−0.5
Berlin	−0.3			
NMC	−0.5	−0.5	−0.5	−0.4
MSU Channel 24 Centered at ~90 mb	−0.4	−0.6	−0.5	−0.5
SSU Channel 15X Centered at ~50 mb	0.2	0.1	0.1	0.2

Table 6.7 30–10 mb Layer Mean Temperature Changes 1986/1985–1980/1979

	N. Hem.	S. Hem.	Global	30°S–30°N
NMC	−0.6	−1.4	−1.0	−1.0
SSU Channel 26X Centered at ~20 mb[1]	−0.3	−0.6	−0.5	−0.8
SSU Channel 25 Centered at ~15 mb	−0.6	−0.6	−0.6	−0.9
Ascension Is.[2] (9°S, 14°W)	30 km			0.1
Cape Canaveral[3] (28°N, 81°W)	30 km			−0.7
Kwajalein[4] (9°N, 168°E)	30 km			−0.1

[1] The first period is the 2-year average September 1979–August 1981.
[2] The second period is the 2-year average August 1982–July 1984.
[3] The second period is the 2-year average September 1984–August 1986.
[4] The second period is the 2-year average July 1982–June 1984.

Table 6.8 10–5 mb Layer Mean Temperature Changes 1986/1985–1980/1979

	N. Hem.	S. Hem.	Global	30°S–30°N
NMC	−0.3	−0.2	−0.2	+0.3
SSU Channel 26 Centered at ~6 mb	−0.6	−0.6	−0.6	−1.0
Ascension Is.[1] (9°S, 14°W)	35 km			−0.1
Cape Canaveral[2] (28°N, 81°W)	35 km			−0.1
Kwajalein[3] (9°N, 168°E)	35 km			−1.3

[1] The second period is the 2-year average August 1982–July 1984.
[2] The second period is the 2-year average September 1984–August 1986.
[3] The second period is the 2-year average July 1982–June 1984.

Figure 6.18 displays the 30°S to 30°N layer temperature changes over the 1979/1980 average to 1985/1986 average period as a function of altitude. Three rocketsonde stations (Ascension Island, Cape Canaveral, and Kwajalein Island) are also included on this figure. Again, as in Figure 6.17, a small cooling is seen in the lower stratosphere, and a cooling of 1–2K in the upper stratosphere. The rocketsonde data tend to bracket the satellite data, thus illustrating the need for zonal averaging and showing that caution is needed when analyzing for trends at single stations.

The error bars used in Figures 6.17 and 6.18 are taken from the discussion in Section 6.2. The satellite data monthly zonal mean rms error is 0.2K (1K for synthesized channels), the daily

Table 6.9 5–1 mb Layer Mean Temperature Changes 1986/1985–1980/1979

	N. Hem.	S. Hem.	Global	30°S–30°N
NMC	−1.4	−1.5	−1.4	−2.8
SSU Channel 27 Centered at ~2 mb[1]	−1.3	−1.2	−1.2	−1.5
SSU Channel 36X Centered at ~1.5 mb	−1.4	−1.4	−1.4	−1.7
Ascension Is.[2]	40 km			−0.7
(9°S, 14°W)	45 km			−1.2
Cape Canaveral[3]	40 km			−0.3
(28°N, 81°W)	45 km			−0.5
Kwajalein[4]	40 km			−2.5
(9°N, 168°E)	45 km			−2.5

[1] The first period is the 2-year average September 1979–August 1981.
[2] The second period is the 2-year average August 1982–July 1984.
[3] The second period is the 2-year average September 1984–August 1986.
[4] The second period is the 2-year average July 1982–June 1984.

Table 6.10 0.5 mb Layer Mean Temperature Changes 1986/1985–1979/1980

	N. Hem.	S. Hem.	Global	30°S–30°N
SSU Channel 47X Centered at ~0.5 mb[1]	−2.1	−1.4	−1.7	−1.3
Ascension Is.[2]	50 km			−0.6
(9°S, 14°W)	55 km			0.4
Cape Canaveral[3]	50 km			−2.0
(28°N, 81°W)	55 km			−2.3
Kwajalein[4]	50 km			−1.2
(9°N, 168°E)	55 km			−1.0

[1] The first period is the 2-year average September 1979–August 1981.
[2] The second period is the 2-year average August 1982–July 1984.
[3] The second period is the 2-year average September 1984–August 1986.
[4] The second period is the 2-year average July 1982–June 1984.

radiosonde based data should have errors on the order of 0.5K (based on the reproducibility of measurements; see Figure 6.1), the daily rocketsonde data have a repeatability of 0.8K (35 km) to 1.3K (50 km), and the NMC data errors are estimated from the daily radiosonde errors (0.5K in lower stratosphere) and daily rocketsonde errors (1.3K in the upper stratosphere). Monthly averaging should reduce the random errors in these data; hence, the error estimates for the rocket, radiosonde, and NMC data are very conservative. NMC errors are 1.5K at the upper levels.

The only data sets available for the longer term stratospheric trends are the Angell and Korshover (AK) radiosonde data, the Berlin data (B), and the rocketsonde data (R). The AK and B data (lower stratosphere) have been available only since 1970 and 1962, respectively. The R data (upper stratosphere and lower mesosphere) have limited spatial coverage.

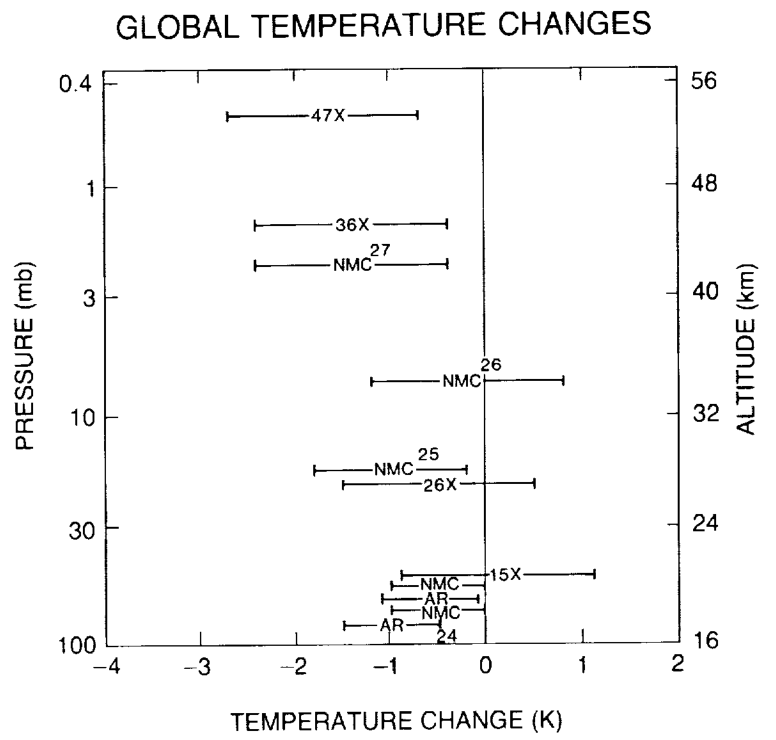

Figure 6.17 Summary of global stratospheric temperature differences (1985 and 1986 minus the average of 1979 and 1980). Symbols denote Angell's radiosonde data (AR), NMC data (NMC), and satellite data (channel numbers, see Figure 6.2). Error bars denote uncertainties (see text). Nash and Forrester (1986) estimate their satellite errors as 0.2 K rms (1 K rms for synthesized channels).

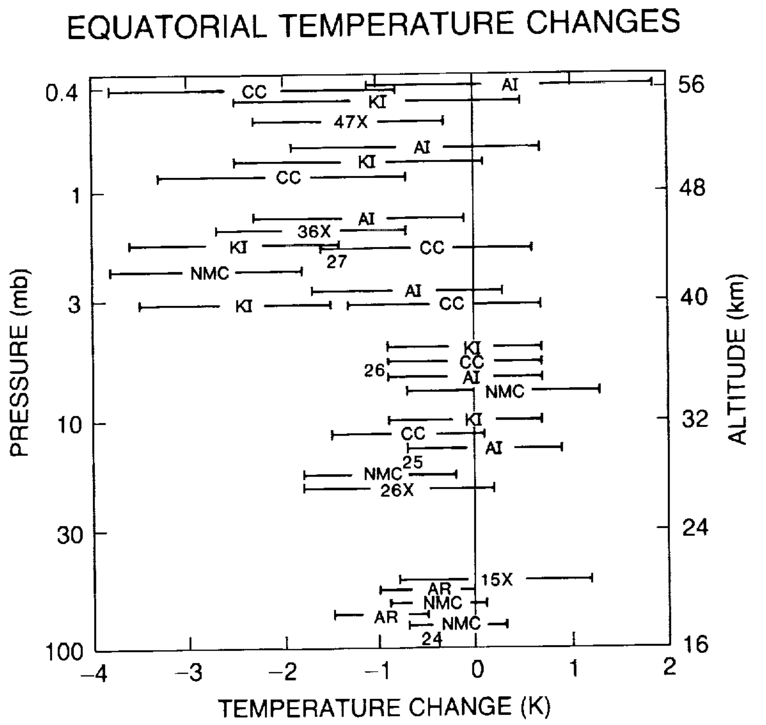

Figure 6.18 As in 6.17, except for Tropics and including rocket stations. Kwajalein Island (KI; 9°N, 168°E), Ascension Island (AI; 9°S, 14°W), and Cape Canaveral (CC; 28°N, 81°W).

Figure 6.19 displays the lower stratospheric trends of Angell and Korshover as well as the Berlin data. Both data sets are in good agreement within their error bounds. Figure 6.20 from Angell (1987) displays Northern Hemisphere combined radiosonde and rocketsonde trends from 1973 to 1985 for each season.

The trends above 25 km shown in Figure 6.20 are calculated from unedited rocketsonde data and are not in agreement with those computed from the edited data (see Section 6.2.3). In this report, trends computed from the edited rocket data are used. The monthly averaged edited data are processed by 1) computing the long-term monthly average, 2) removing those monthly averages, leaving the deviations from the monthly averages, 3) linearly interpolating missing data, 4) smoothing the data, and 5) using the smoothed data to compute two separate trends for the periods 1969 to data set end and 1973 to data set end. These monthly deviations (denoted by crosses), smoothed deviations (solid line), and least-square fits of the 1969–end smoothed deviations (straight line) are illustrated in Figures 6.21–26. The decadal trends for both 1969–end and 1973–end are shown in the lower right-hand corners of each graph.

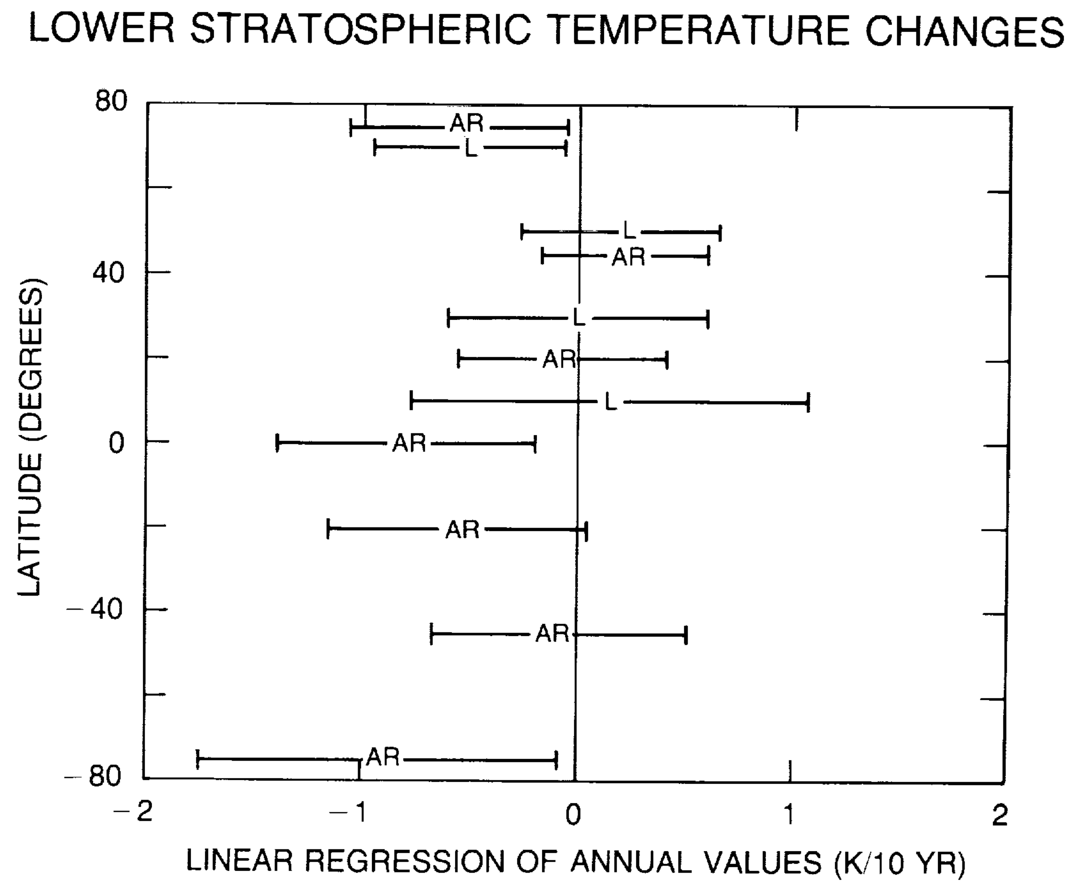

Figure 6.19 1970–1986 linear regressions from Free University of Berlin data at 30 mb (L), and Angell and Korshover (1983a) climate zones from the 100–30 mb thicknesses (AR). Error bars denote the 95 percent confidence limits of the regressions.

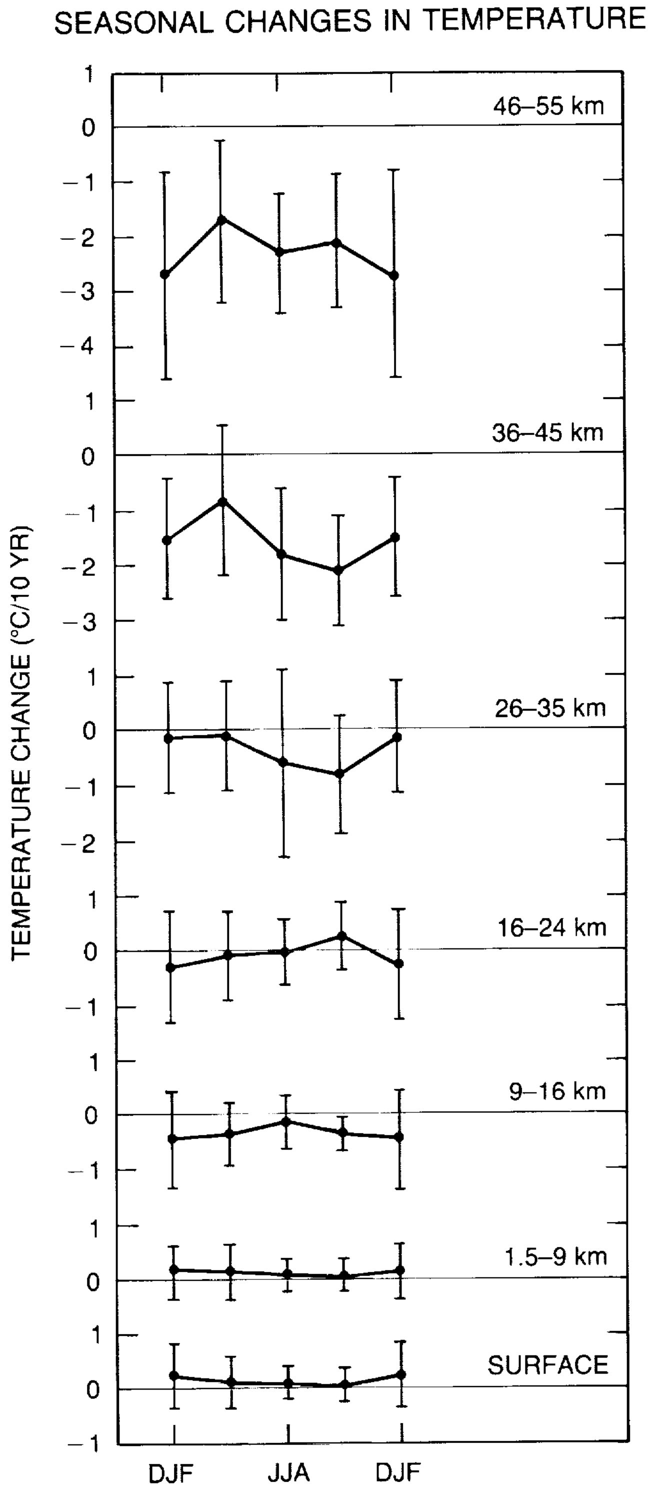

Figure 6.20 Seasonal changes in tropospheric and stratospheric Northern Hemisphere temperature (degrees Celsius per 10 years) between 1973 and 1985 (DJF is December–January– February, etc.) based on linear regression applied to rocketsonde data primarily in the Western Hemisphere (values above 25 km) and radiosonde data around the entire hemisphere. The vertical bars are 95 percent confidence limits for the seasonal changes, as estimated from the standard deviation of seasonal temperatures about the line of regression.

Ascension Island (8°S)

Figure 6.21 depicts the monthly data and the trend for each of the six levels at Ascension Island. The trends observed at 30, 35, and 40 kilometers are large and positive. The trend is about −0.1K per decade at 50 km and −1.0K per decade at 55 km over 1973–1985. The QBO signal is seen in the data, with an amplitude of about 2K.

Kwajalein, Marshall Islands (9°N)

The Kwajalein data show evidence of the QBO signal at altitudes below 45 km with an amplitude of 1 to 2K. The 1973–1985 temperature trends for Kwajalein are small, as seen in Figure 6.22. At 30 km, the trend is only 0.7K per decade, while at 35 km to 55 km, the trends are even smaller.

Barking Sands, Hawaii (22°N)

The 1973–1982 trends calculated for Barking Sands also are small. Figure 6.23 shows that the rate of temperature decrease is, at 30 km, 0.8K per decade; at 35 km, −0.6K per decade; at 40 km, 0.3K per decade; and at 45 and 50 km, 0.3K and 1.9K per decade, respectively. At 55 km, the rate of increase is larger: 1.0K per decade. The temporal temperature structure at Barking Sands shows the QBO with a 1 to 2K amplitude.

Cape Canaveral, Florida (28°N)

Weak downward trends from 1973–1985 are noted at all altitudes, with the exception of 55 km. For example, Figure 6.24 shows downward temperature trends of −0.2K per decade at 30 km, −0.6K per decade at 35 km, −1.0K per decade at 40 km, −0.7K per decade at 45 km, and −0.6K per decade at 50 km. The QBO is again clearly seen, with an amplitude of 1–3K.

Pt. Mugu, California (34°N)

The Pt. Mugu 1973–1982 temperature trends (Figure 6.25) vary between no trend at 35 km to a 2.3K per decade trend at 55 km. A weaker (1K amplitude), chaotic QBO signal is apparent at 30 km.

Primrose Lake, Canada (55°N)

Temperature trends from 1973–1985 at Primrose Lake are shown in Figure 6.26. The regression analysis, however, indicates downward as well as upward trends at the different altitudes. These varying trends may be a result of the large interannual variability in high latitudes combined with the missing data. For example, at 30 km, the trend is indicated as 1.5K per decade, while at 35 km it appears to be upward at a rate of 2.5K per decade. Essentially, the trends calculated for the Primrose Lake temperature data may be inconclusive because of the aforementioned large interannual variability and missing monthly average data.

The six rocketsonde sites show downward temperature trends in the stratosphere when the 1969, 1970, and 1971 data are included in the trend analysis. Since rocketsonde sites are uniquely located and few in number, it is impossible to determine a zonal or global trend from these data. There is still disagreement between researchers over differences in the rocketsonde data during the 1970–1972 period.

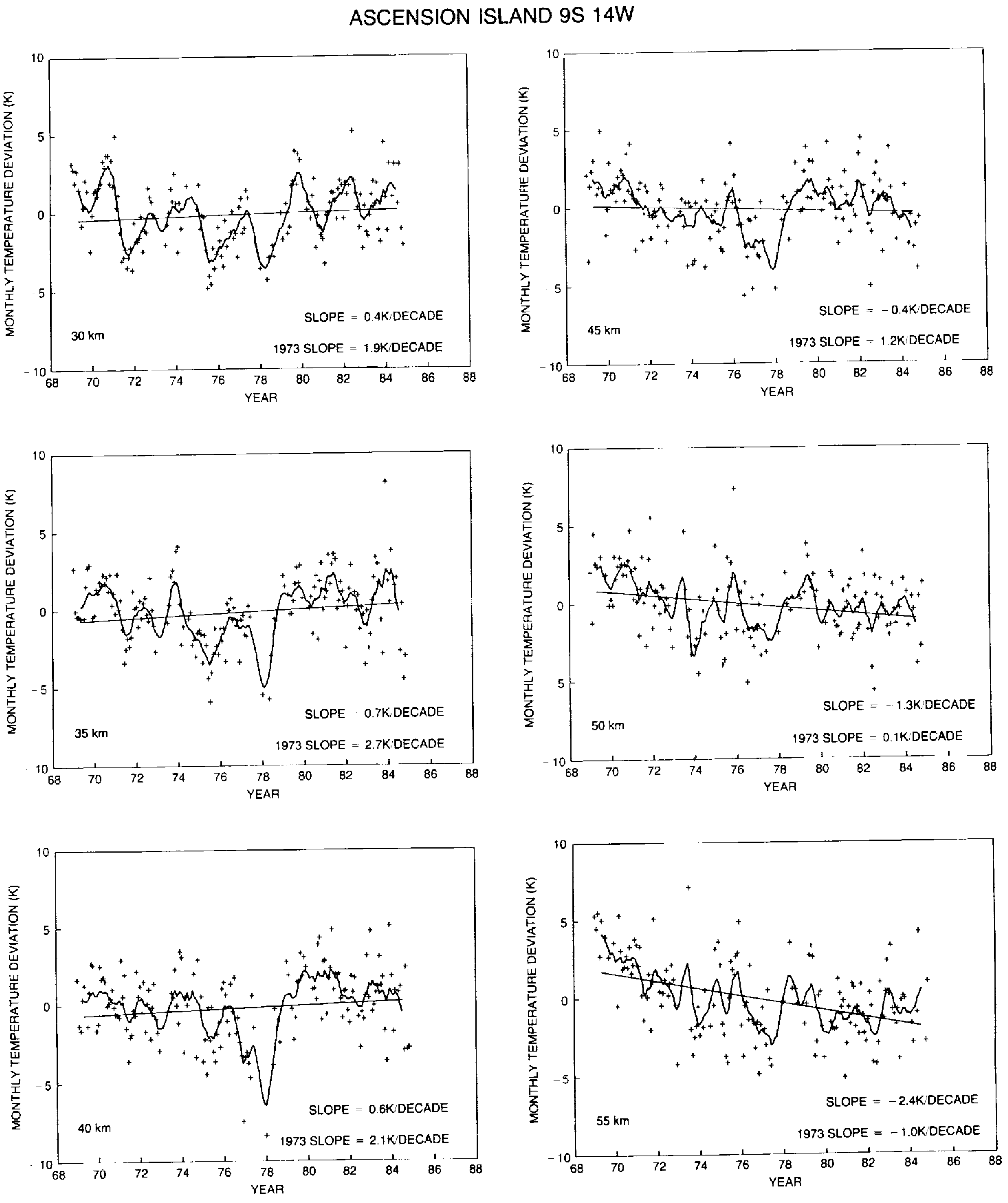

Figure 6.21 Rocket observations for 30–55 km region at Ascension Island. Solid line is smoothed data set (see text). Straight line is 1969–end trend. Crosses denote deviations from monthly mean. First slope is 1969–end of data set trends, second slope is 1973–end of data set trend.

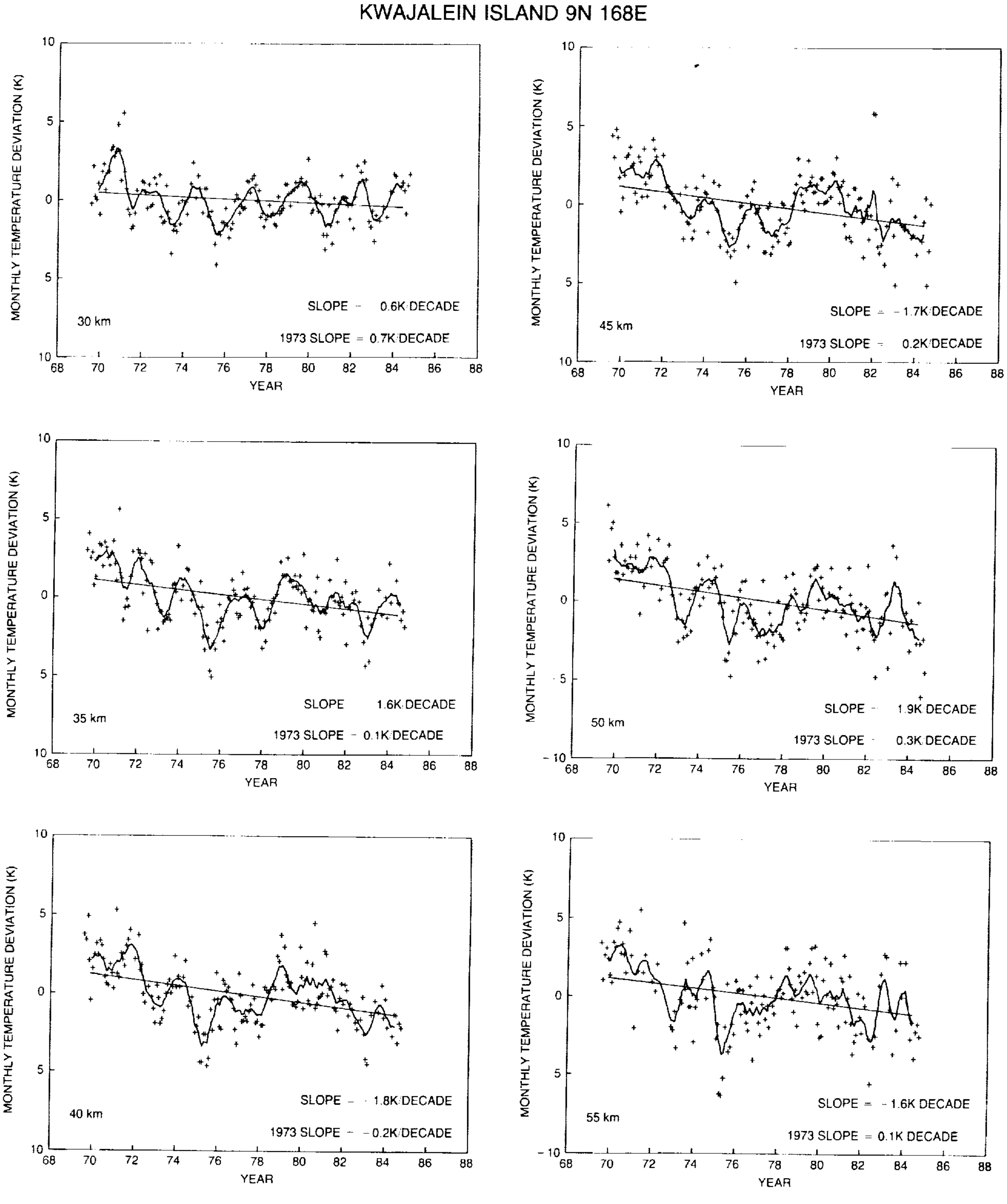

Figure 6.22 Same as 6.21 except for Kwajalein.

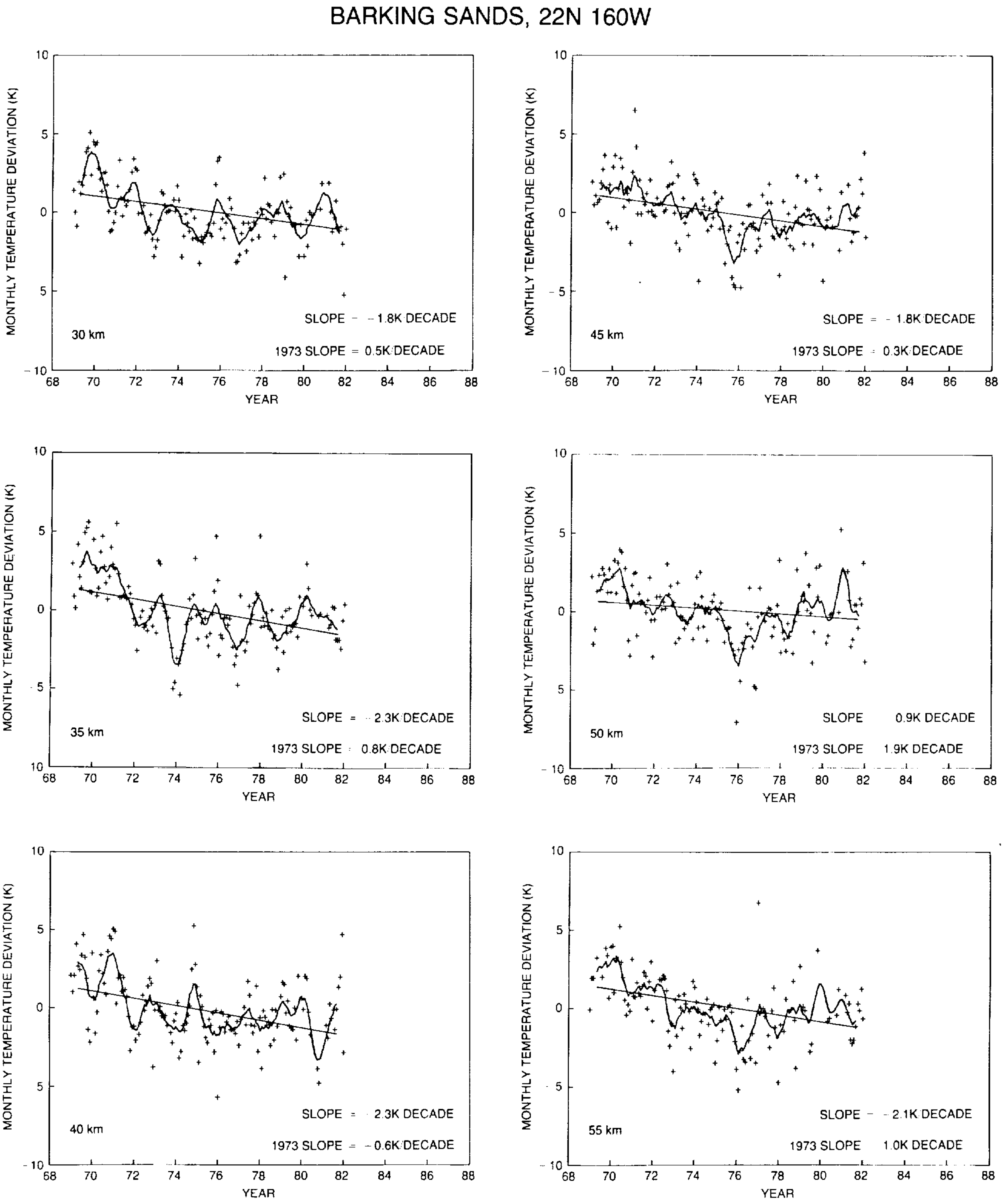

Figure 6.23 Same as 6.21 except for Barking Sands.

CAPE CANAVERAL 28N 81W

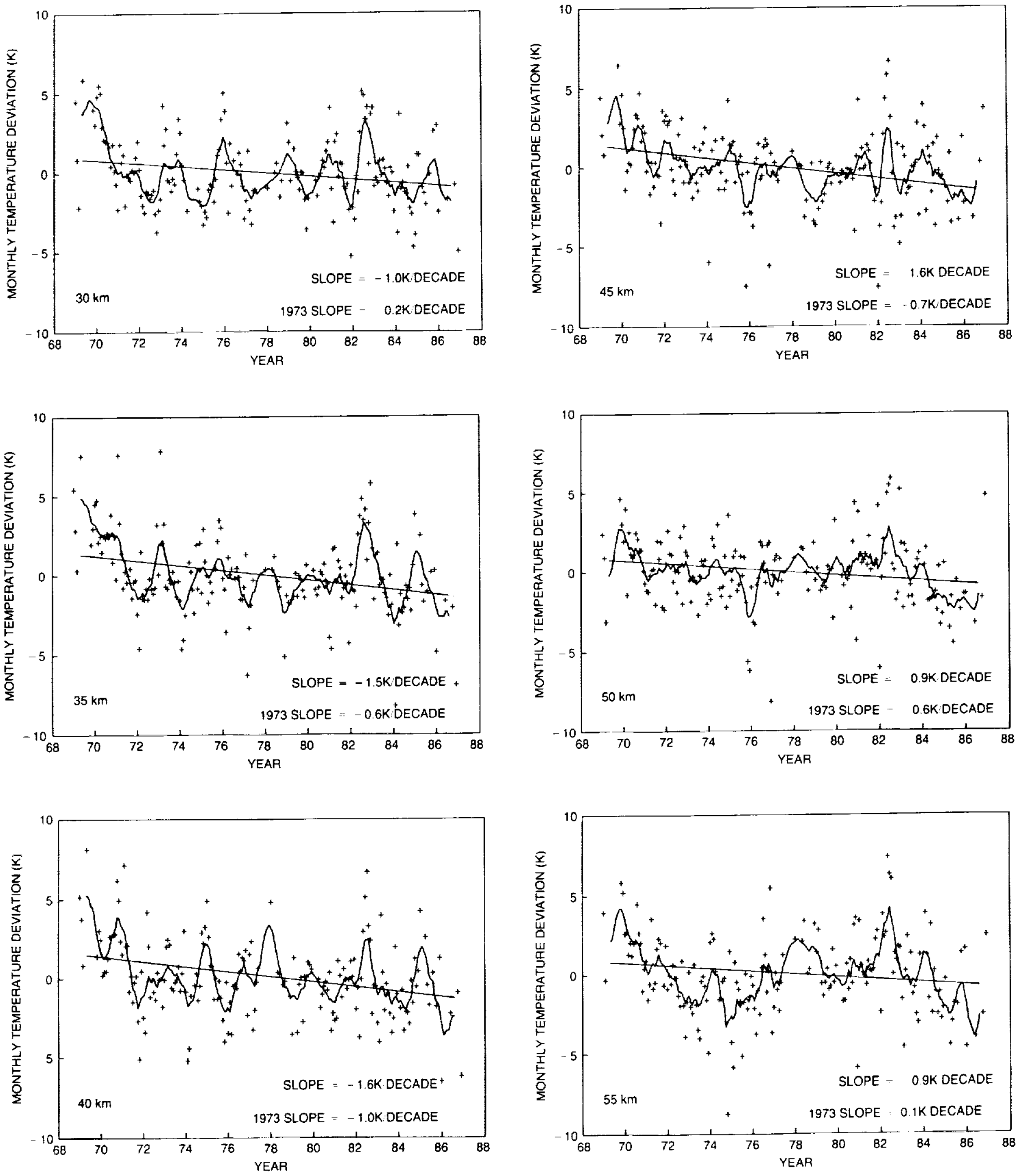

Figure 6.24 Same as 6.21 except for Cape Canaveral.

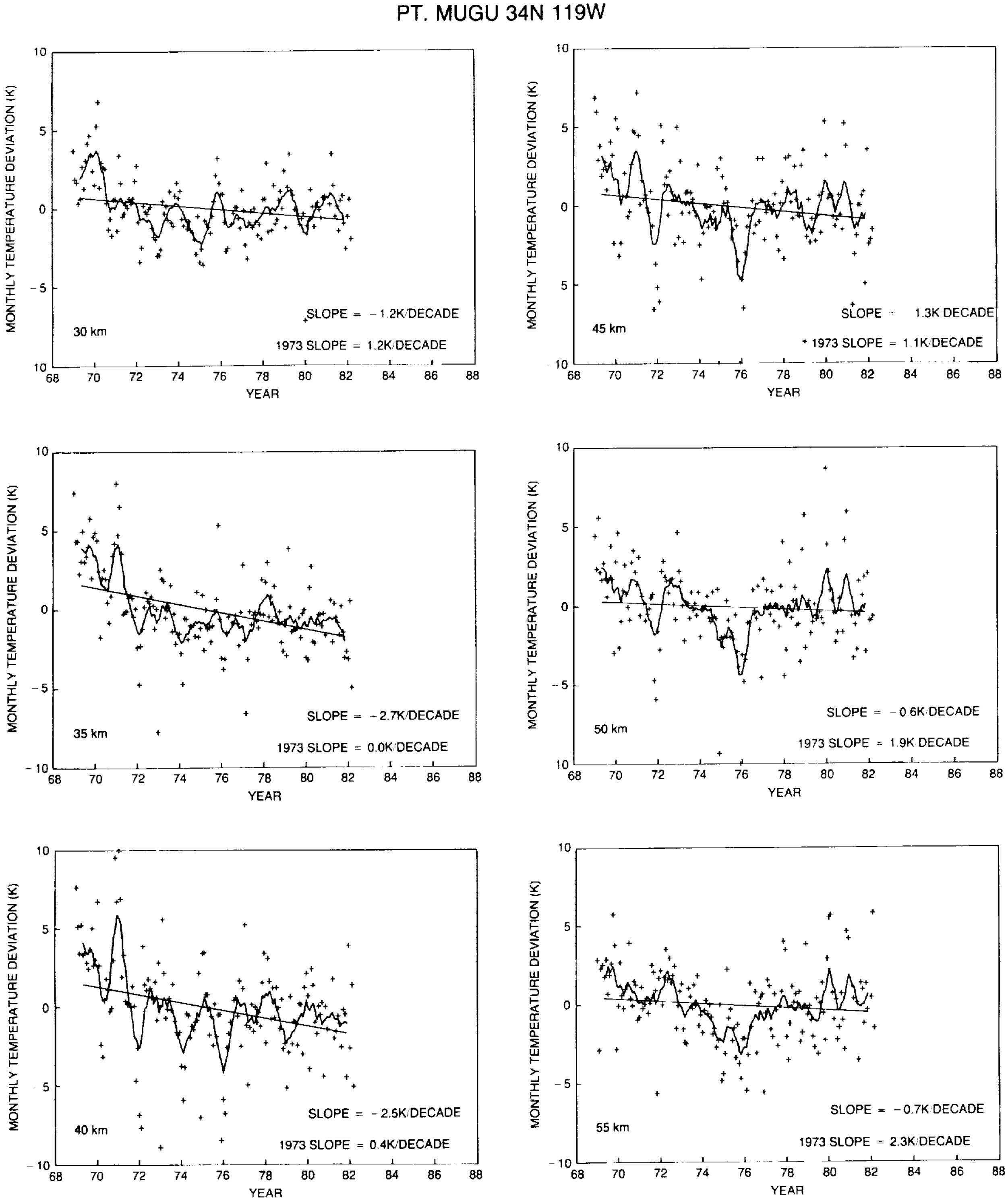

Figure 6.25 Same as 6.21 except for Pt. Mugu.

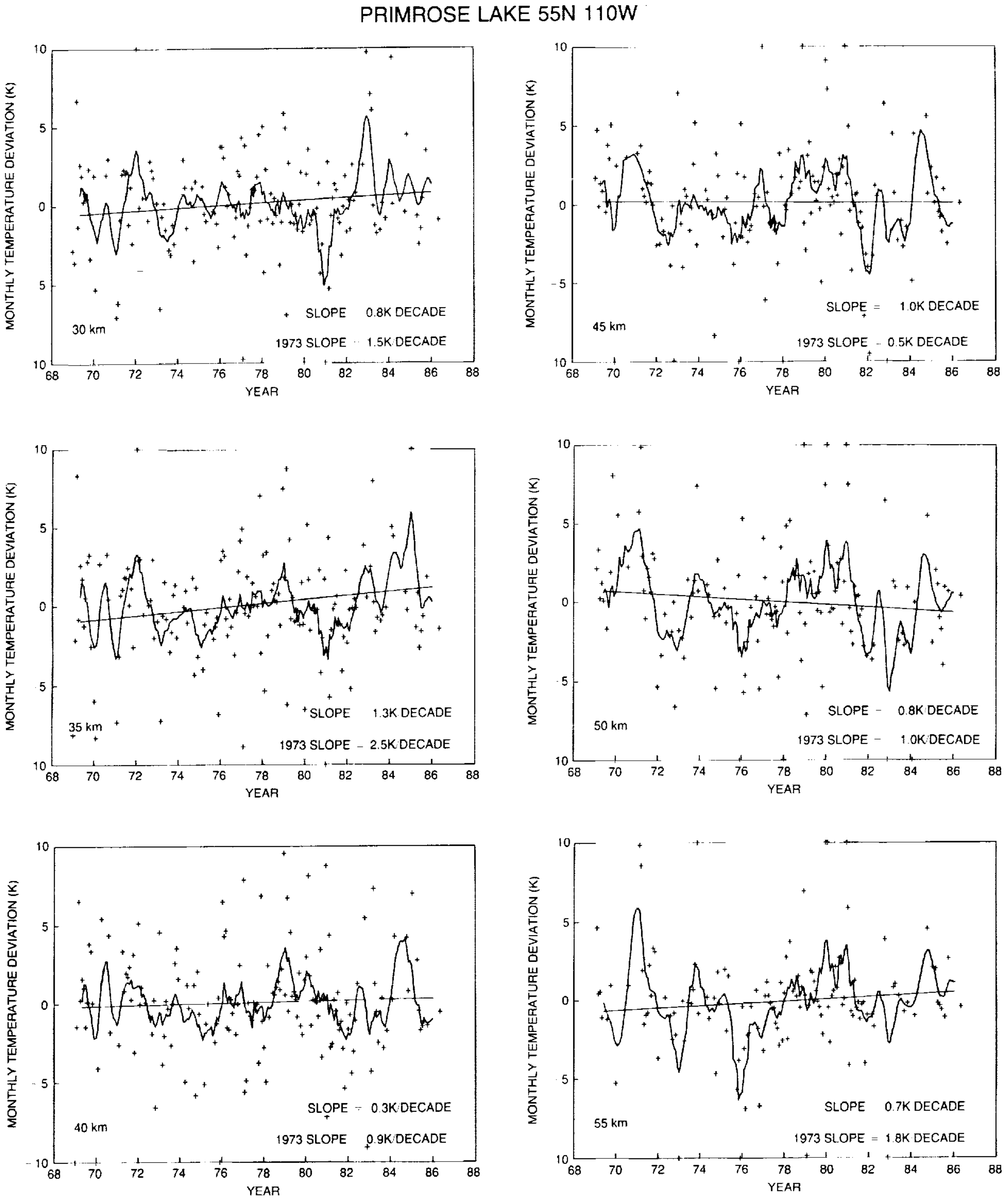

Figure 6.26 Same as 6.21 except for Primrose Lake.

6.4 MECHANISMS FOR ATMOSPHERIC TEMPERATURE TRENDS

In this section, the processes that could drive stratospheric temperature changes are discussed. Over the last 10 years during which satellite measurements have been available, the solar flux, the level of aerosol loading, and the concentrations of trace gases all have changed. Dynamical processes may also contribute to temperature changes. This section outlines the changes in temperature expected from these effects. If most of the processes contributing to the observed stratospheric temperature trends of the last decade can be quantitatively assessed, then it may be possible to infer the reliability of reported ozone changes (e.g., SBUV, SAGE, etc.), as well as model-computed ozone changes.

6.4.1 Global Ozone Changes

In this section, calculations that estimate temperature changes that would result from the global changes in ozone reported by the SBUV and SAGE data processing teams are summarized.

SBUV ozone-mixing ratios have been reported to be declining since 1979, with a maximum decrease of 20 percent at 1 mb from 1979 to 1986. Radiative equilibrium temperature calculations were made using 1979 and 1986 zonal mean SBUV ozone-mixing ratio profiles, at 80°N in June and 0° in March. These two cases were chosen because they represent situations in which dynamical effects should be minimal (Geller et al., 1983). Thus radiative equilibrium temperature computations may provide a reasonable assessment of temperature trends. Figure 6.27 shows SBUV ozone fractional decreases between 1979 and 1986.

The calculations are performed using three different radiative transfer models, as shown in Table 6.11. In Models 1 and 2, the tropospheric water vapor profiles are taken from the McClatchey (McClatchey et al., 1971) tropical and subarctic reference atmospheres for the equatorial and the polar calculations, respectively. Stratospheric water vapor is fixed at 5 ppmv, and the ground temperature is set equal to the air surface temperature. Model 3 has a simplified troposphere and specifies infrared fluxes and tropospheric albedos based on mean values that give approximately the correct upwelling flux at 100 mb. For the tropical equinox calculation, the solar declination angle is fixed at 0°, while for the summer polar calculation, the declination is fixed at 23.5. The surface albedo is set to 0.7 for the polar case and 0.07 for the tropical case, and no clouds are included. The temperatures are time-marched to radiative equilibrium using diurnally averaged solar heating.

Figure 6.28 shows the radiative equilibrium temperature changes resulting from the 1979 to 1986 SBUV ozone changes for the June polar case; Figure 6.29 shows the changes for the March equatorial case. The models are in remarkably close agreement. A maximum temperature decrease of 6.7–7.2K at about 0.5 mb occurs for the June polar case, while a decrease of 5.2–5.5K at 0.5 mb occurs for the March equatorial case. For both cases, the region of maximum cooling is fairly narrow, falling to zero by 2 mb. A temperature difference this sharply peaked may be difficult for satellites having broad instrument weighting functions (see Figure 6.2) to detect. When these temperature changes are convolved with the synthesized SSU–47X weighting function centered at 0.5 mb, the temperature changes that are predicted to be observed by satellite are reduced to −4.8K for the June polar and −3.8K for the March equatorial cases. The 2-year averaged SSU–47X differences (i.e., the 1985 through 1986 data differenced with the 1979 through 1980 data) shown in Table 6.10 show a global change of −1.75K, while SSU–36X (shown in Table 6.9) shows a global change of −1.4K.

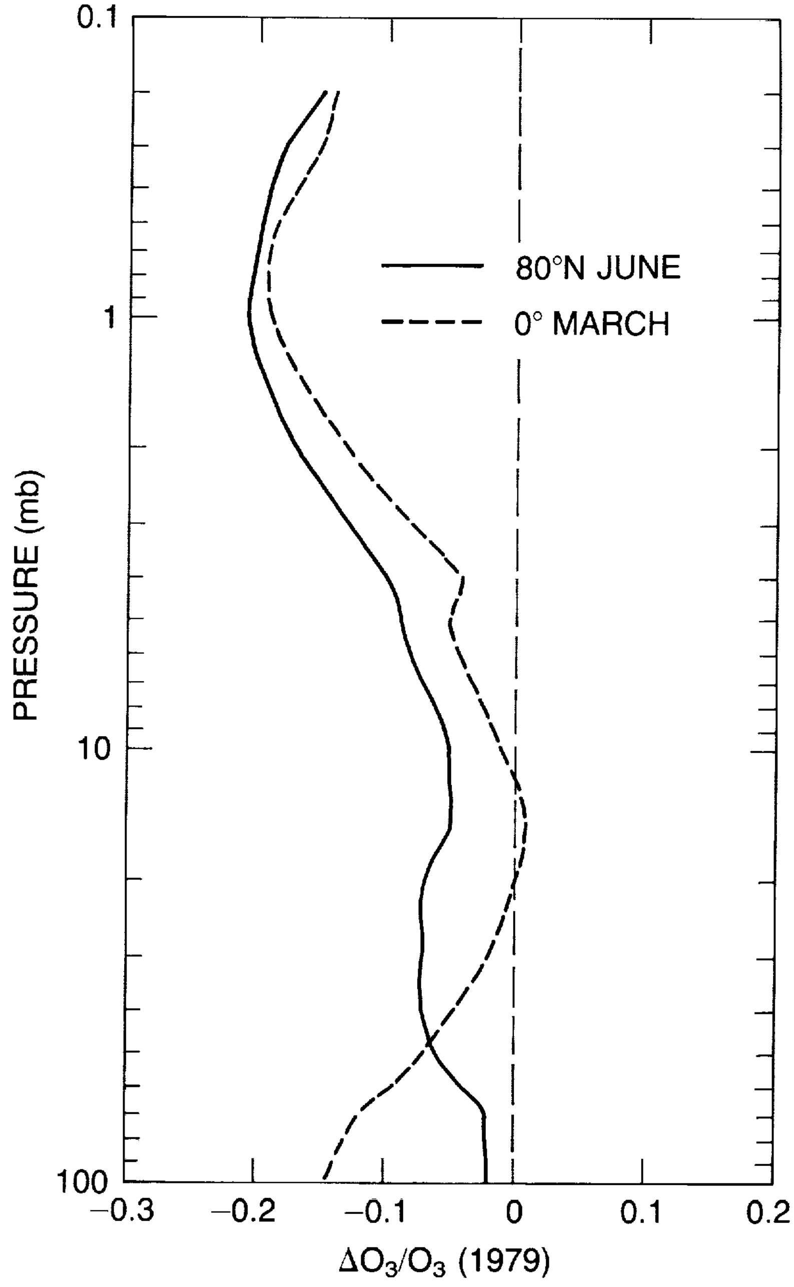

Figure 6.27 Fractional decrease between 1979 and 1986 SBUV zonal mean monthly mean ozone mixing ratios. The solid curve is for 80°N in June, and the dashed curve is for 0° at the Equator in March. Units are ppmv.

Table 6.11 Radiative Transfer Models Used in this Section

Model	Organization	Reference
1	NASA/GSFC	Rosenfield et al. (1988)
2	NOAA/GFDL	Schwarzkopf and Fels (1985), Fels and Schwarzkopf (1975), Lacis and Hansen (1974)
3	Univ. of Oxford	Shine (1987)

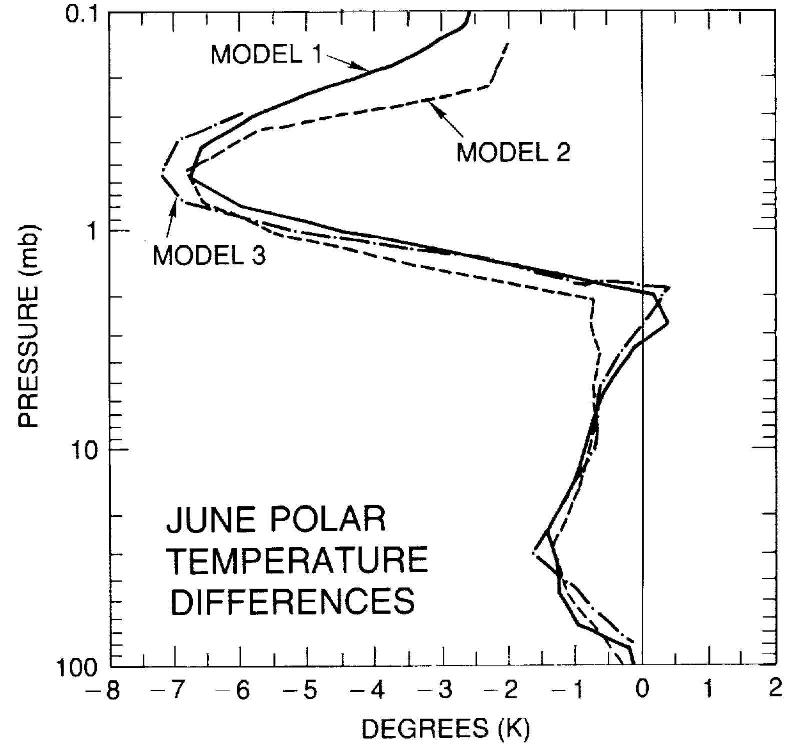

Figure 6.28 Radiative equilibrium temperature differences computed by the three models for the June summer polar case. The differences plotted are computed using 1986 and 1979 ozone data,

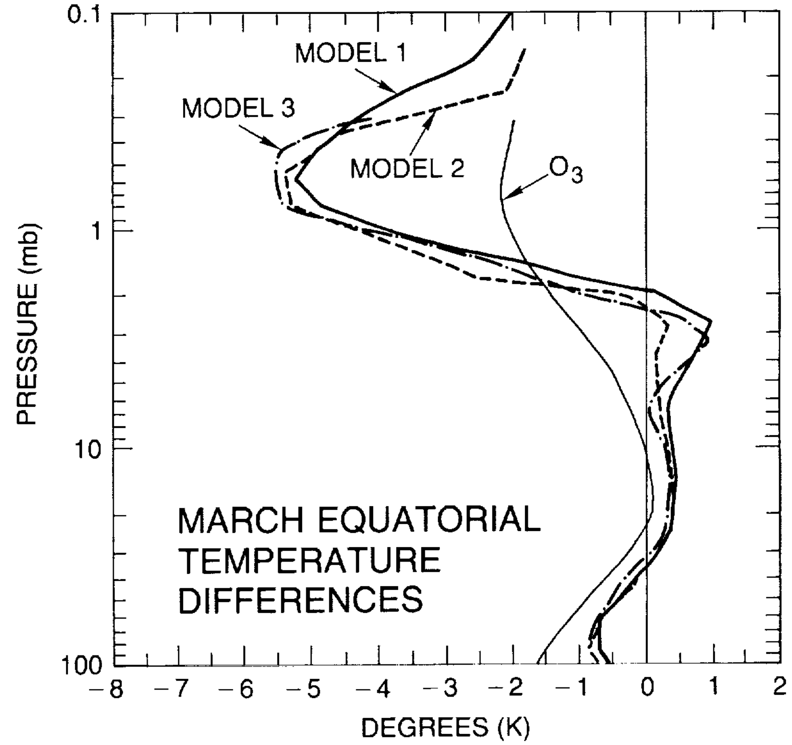

Figure 6.29 As in Figure 6.28 except for the March equatorial case.

The radiative temperature changes expected on the basis of the changes in ozone measured by the SAGE–I and SAGE–II instruments, which give an independent estimate for the period between 1980 and 1986 (cf. Chapter 5), are considered below. The SAGE data used are zonal mean profiles for a latitude band 15°S to 15°N and represent annual averages constructed from seven periods, during which both SAGE–I and SAGE–II sampled the Equator within roughly the same 30-day period of the year. It is important to realize that SAGE measures ozone only between 26 and 50 km. Because the predicted temperature is sensitive to the ozone change above 50 km, two cases have been considered: no ozone change outside 26 to 50 km, and −5 percent ozone change above 50 km and −2 percent below 26 km.

Figure 6.30 shows the ozone profiles, and the solar heating and radiatively induced temperature changes computed from Model 2 for the two cases. Notice that, at 47 km, both cases predict changes of about 1K, but above 50 km, the two cases disagree. It remains true, however, that both scenarios yield temperature changes much smaller than those predicted using the SBUV ozone discussed above.

When convolved with the appropriate SSU weighting functions 47X and 36X, the satellite-measured temperature changes are calculated to be:

SSU Channels	SAGE Case (a)	SAGE Case (b)	SBUV
47X	−0.4	−1.2	−3.6
36X	−0.2	−0.3	−1.8

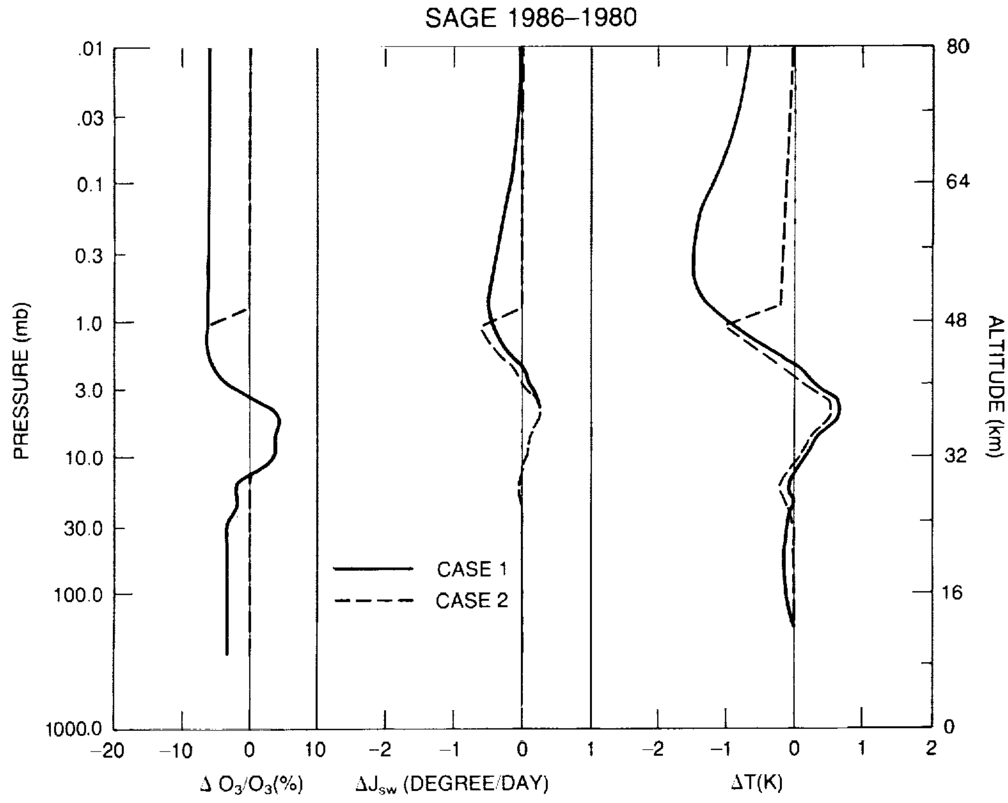

Figure 6.30 Radiative equilibrium computation for SAGE-observed ozone.

6.4.2 The Radiative Impact of Other Trace Gases

Significant changes are occurring in the middle atmosphere concentration of other radiatively active gases such as CO_2, CH_4, and N_2O. In the upper stratosphere, a near radiative balance exists between solar radiation absorbed by ozone and infrared radiation emitted by carbon dioxide, ozone, water vapor, and other trace gases. Higher levels of stratospheric trace gases increase infrared emittance and will produce a decrease in temperature. Fels (private communication, 1987) has computed that the increased cooling caused by CO_2 alone to yield a -0.2 to -0.3K change in temperature at 2 mb and a -0.15K change at 10 mb between 1979 and 1986. It is not likely that the expected changes in trace gases other than ozone could significantly modify the upper stratosphere temperature.

6.4.3 Solar Cycle

The solar UV flux that affects the 30 to 70 km region lies between wavelengths of 200 and 300 nm, where the Hartley absorption bands of ozone are located (see *WMO*, 1986). The radiation absorbed by ozone at these wavelengths gives rise to a strong heating, with a peak at 50 km.

During the course of the solar cycle from its maximum to its minimum, the incident UV flux at the top of the atmosphere decreases. This implies a decrease in the stratospheric heating rates, provided the ozone amounts remain unchanged (an assumption made throughout this section). The change in the UV flux (200 to 300 nm) is not uniform. While the flux at 205 nm changes by about 9 percent, that at 270 nm changes by about 1 percent. A one-dimensional radiative transfer model (Ramaswamy and Kiehl, 1985) is used to investigate the effects of the change in the Hartley band flux at the top of the atmosphere upon the heating rates during solar maximum and solar minimum. The wavelength-dependent reduction applied is based on the results of Heath and Schlesinger (1986) (see also Chapter 7). The resulting changes in the tropical stratospheric heating rates (Figure 6.31) are expressed as the difference between the values at the time of

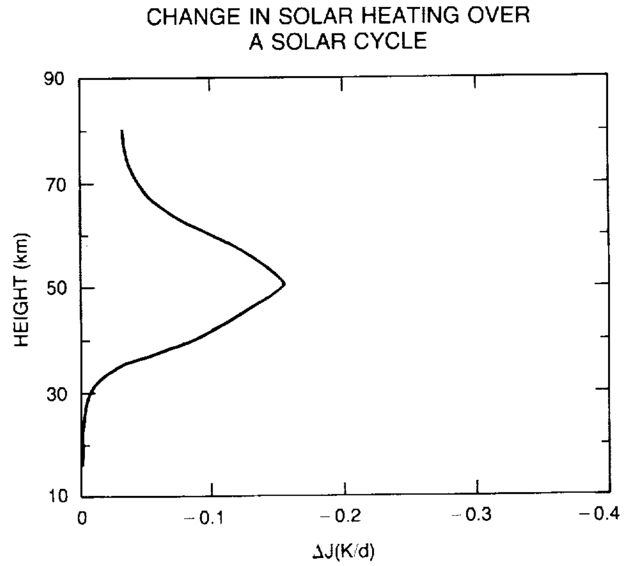

Figure 6.31 Changes in solar heating rates due to variations in the ultraviolet flux between solar minimum and solar maximum based on Heath and Schlesinger (1986) and Chapter 7 of this report. Units are degrees Kelvin per day.

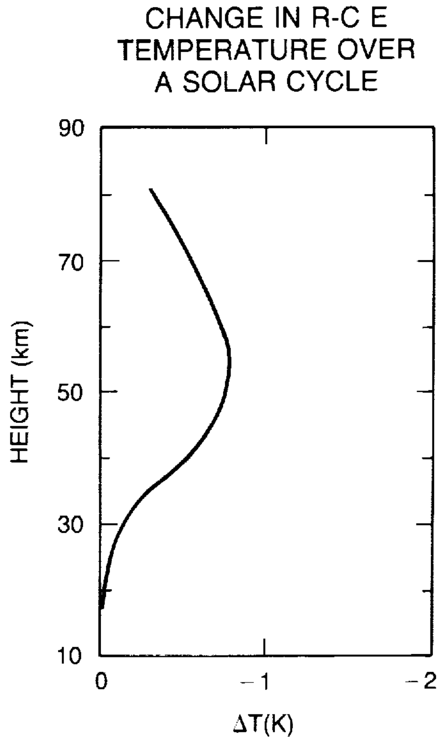

Figure 6.32 Changes in radiative–convective equilibrium temperature due to changes in the solar ultraviolet flux over a solar cycle.

solar minimum and those during the solar maximum. The maximum change, about 0.15K per day, occurs where the absolute values are peaked (50 km).

These heating perturbations are treated as a driving force in a radiative–convective equilibrium model (Fels et al., 1980) to investigate the resulting changes in the temperature structure (ozone amount is held fixed). As shown by the results in Figure 6.32, the profile of the temperature perturbations is similar to the profile of the heating rate perturbations. The change in the temperature between the solar minimum and the solar maximum at 50 km in the present calculation is about 0.8K.

6.4.4 Aerosols

Stratospheric aerosol loadings caused by volcanic emissions possess the potential to alter the transfer of radiation and perturb the energy balance of both the troposphere and the stratosphere. Radiative–convective model studies (Pollack et al., 1976; Hansen et al., 1978) have shown that the principal radiative effects of volcanic aerosols (composed typically of ash and sulfuric acid) are to reduce the solar flux in the troposphere and to cause a warming in the lower stratosphere. Part of this warming is a result of aerosol absorption in the solar spectrum, while the other part is caused by absorption of the longwave flux from the troposphere and the subsequent reemission at the colder stratospheric temperatures. As an example of the possible magnitude of this warming, Pollack and Ackerman (1983) estimate an increase in temperature of about 3.5K at 30 mb in the northern tropics due to the El Chichón volcanic cloud.

The magnitude of the warming in the lower stratosphere that results from volcanic emissions depends on the aerosol optical properties, their sizes, and the upwelling longwave flux from the troposphere, all of which exhibit considerable spatial and temporal variations. The nature of these dependencies is illustrated here for a diurnally averaged tropical atmospheric profile, using a one-dimensional radiative transfer and a radiative–convective model (Ramaswamy and Kiehl, 1985). For the purposes of the present sensitivity study, the aerosols are assumed to have a lognormal size distribution, with a constant number concentration between 16 and 25 km; it may be noted that this was a typical altitude for the El Chichón debris. The optical depth at a wavelength of 0.5 microns is assumed to be 0.08, unless stated otherwise.

The effects of the optical property and the size of the particulates are examined by considering three different cases: 1) a unimodal size distribution (mode radius of 0.08 micron) composed of spherical sulfate drops (optical properties from Palmer and Williams, 1975), 2) a bimodal distribution (two mode radii, 0.02 and 0.2 micron) containing larger particles, characteristic of the El Chichón debris at some locations, and 3) unimodal distribution of dust particles with the same size characteristics as in (1), but with different optical properties (Shettle and Fenn, 1979). The difference between (1) and (2) is due to the size distribution, while the difference between (1) and (3) is due to the optical properties.

The initial perturbations in the solar heating rates for each of the three cases are shown in Figure 6.33a; the perturbations in the longwave heating are shown in Figure 6.33b. Since sulfates absorb only in the near infrared, while dust absorption extends over the entire solar spectrum, the dust-induced solar heating exceeds that caused by the sulfates for similarly sized particles; the sulfates, however, are stronger absorbers than dust in the longwave spectrum. Larger sulfate particles result in increased longwave heating rates. The temperature perturbations are shown in Figure 6.33c. The vertical profile of the changes in the temperature is,

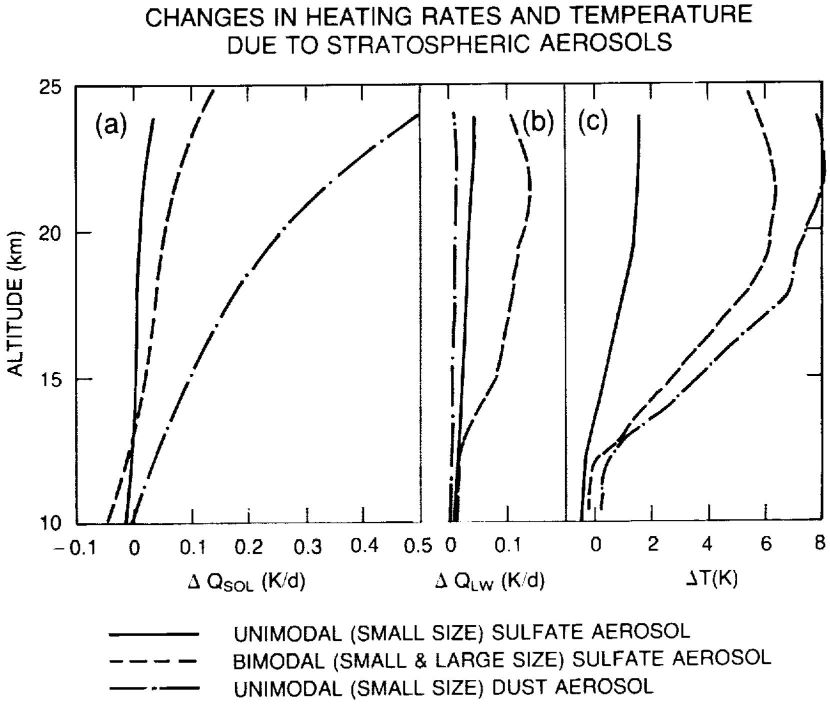

Figure 6.33 Effect of aerosols with an optical depth of 0.08 on a) the solar heating rate, b) the infrared heating rate, and c) the temperature, for a tropical profile. The solid curve is unimodal sulfate, the dashed curve bimodal sulfate, and the dot–dashed curve unimodal dust aerosol.

in each case, due to the influence of the net (solar and longwave) heating. Thus, the 8K change at 23 km for dust is primarily a consequence of the shortwave absorption, the change of 6K for the bimodal sulfate distribution is due to both solar and longwave perturbations, and the changes for the unimodal sulfate distribution are mostly a result of the longwave heating.

For typical volcanic injections (optical depths 0.1 to 0.3; Toon and Pollack, 1976), the stratospheric heating perturbations increase almost linearly with optical depth (Figure 6.34). The corresponding changes in the radiative–convective equilibrium temperature are shown in Figure 6.35. At 23 km, for example, the temperature perturbation can attain a value of 4K.

To examine the importance of the upwelling longwave flux from the troposphere for the lower stratospheric temperature perturbations, four numerical experiments are considered that involve the unimodal sulfate aerosols and upper tropospheric clouds (cloud stop altitude of 13 km). The aerosol optical depth in each case is assumed to be 0.2. All conditions remain the same unless otherwise specified below. In case 1, a clear sky is assumed. In case 2, nominal values for cloud properties (high cloud emissivity is 0.5) are assumed (Ramaswamy and Ramanathan, 1989); this is similar to the value for an optical depth of 0.2 in Figures 6.34–35. Cases 3 and 4 involve completely cloud-covered troposphere, with case 4 having a high cloud emissivity of 1. Cases 1–4 represent situations in which, successively, less of the upwelling longwave flux is available for absorption by the aerosol particles. Thus, the resulting temperature perturbation at 23 km (listed in Table 6.12) is greatest when this upwelling flux is at its maximum (Case 1; 3.5K), and least when the upwelling flux is at its minimum (Case 4; 1K).

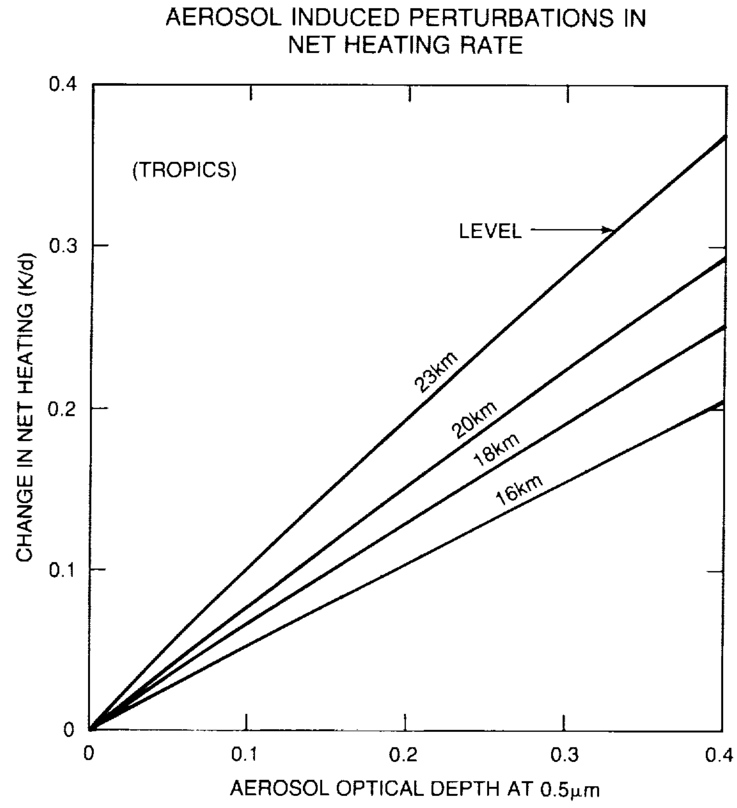

Figure 6.34 Changes in the net heating rate as a function of unimodal sulfate aerosol optical depth in a tropical atmosphere.

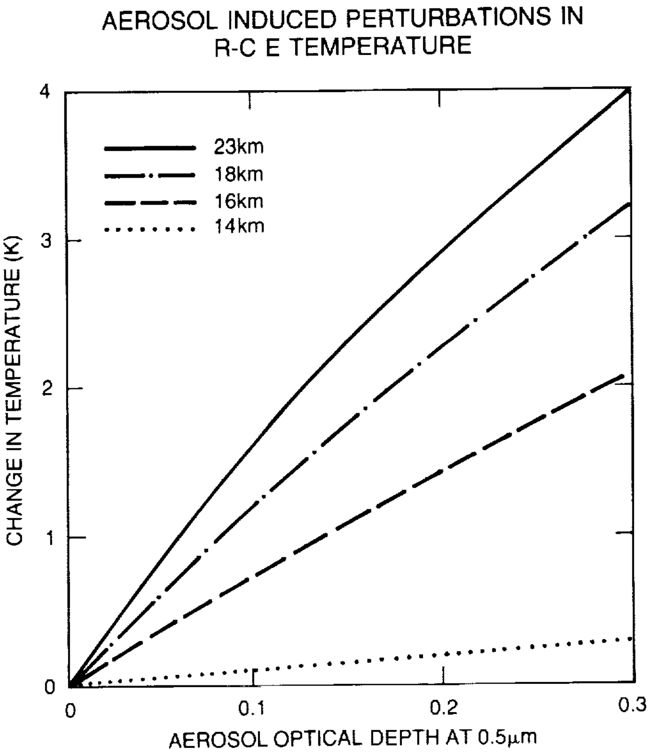

Figure 6.35 Aerosol-induced perturbations in radiative–convective equilibrium temperature as a function of unimodal sulfate aerosol optical depth.

It is tempting at this stage to associate the 1982 temperature deviation from the mean (shown in Section 6.3) with the El Chichón eruption. Pitari et al. (1987) have used a two-dimensional residual circulation model to consider the effects of the El Chichón eruption on temperatures and zonal circulation. Using observed aerosol properties, they estimated a 2–3K temperature increase in the tropical and midlatitudinal lower stratosphere, with negligible changes in the residual circulation. It can be concluded from the one- and two-dimensional model studies that, while a part of the deviation in the observed temperatures can be attributed to the volcanic emission, the issue cannot be resolved unambiguously because of uncertainties concerning the

Table 6.12 Dependence of Radiative Convective Equilibrium Temperatures on Cloud Properties

Aerosols Between 16 and 25 km
Low cloud (top 3.0 km; cloud cover = 0.31)
Middle cloud (top 5.6 km; cloud cover = 0.09)
(low and middle clouds assumed black)
High cloud (top 10.4 kms)

Experiment Description	Change in Temperature [δ T (K)] (23 km)
1. Clear	3.5
2. Nominal Clouds (High cloud cover = 0.23, Emissivity = 0.5)	2.8
3. Same as 2 except high cloud cover = 1.0	1.5
4. Same as 3 except emissivity of high cloud = 1.0	1.0

spatial and temporal variations in the aerosol optical properties. The problem of radiatively active species interacting simultaneously with the microphysical and large-scale dynamical processes must be addressed comprehensively before a definitive answer can be obtained from the models. Further, observations of both aerosol properties and temperatures also need to be accurate, since the lower stratosphere has a large radiative time constant.

6.4.5 Dynamics

The global circulation of the stratosphere is established largely through the interplay between the external tropospheric forcing and the radiative heating and cooling within the stratosphere. It has long been realized that trends in both temperature and ozone can result, in principle, from dynamical trends in the stratosphere. These changes can result from an alteration in the level of wave activity through tropospheric forcing or through changes in the wave propagation characteristics of the stratosphere itself. The latter changes can result from changes in winds and temperatures through a variation in the concentration of radiatively active gases, aerosols, or the solar flux. Since the concentrations of the radiatively active gases are, in turn, influenced by the transport properties of the stratosphere, which are partially determined by dynamical forcing, all of these processes are interdependent.

Eddy activity in the stratosphere tends to force the stratosphere away from a state of near-radiative equilibrium. In the absence of dynamical activity, long-wave cooling would balance short-wave heating everywhere except for small departures caused by thermal inertia and the seasonal cycle. Therefore, trends in both stratospheric temperatures and trace gases cannot be considered independent processes.

A number of authors have considered the feedbacks that might result from ozone depletions or solar cycle changes altering the insolation, the large-scale winter jet structure, and ultimately the propagation properties of large-scale waves (Schoeberl and Strobel, 1978; Fels et al., 1980; Callis et al., 1985b; Kiehl and Boville, 1988). These studies, which fixed the troposphere, found no significant change in the stratospheric dynamical activity except for scenarios of very sizable (>50 percent) ozone depletions. For example, using perpetual conditions from January, Kiehl and Boville (1988) concluded that the dynamical response to halving ozone uniformly was small. The dynamical response to a realistic ozone reduction scenario, with the largest ozone changes confined to high latitudes, was found to be not only quite different to that for uniform ozone reductions, but even smaller.

An estimate of the tropical stratopause temperature change caused by altered dynamics may be obtained by assuming that the globally averaged stratosphere at any level is in radiative equilibrium. If it is assumed that the largest temperature changes are likely to be in the polar night, and that these are, at most, on the order of 30K (Hamilton, 1982), then compensating changes on the order of several degrees in the tropics would be expected. This estimate is confirmed by Hamilton's analysis, which shows that even in years whose polar stratopause temperatures differ by 30K, the tropical temperatures at 1 mb are the same to within a few degrees. Thus, any dynamical process in the tropics cannot realistically be expected to mask the long-term temperature changes that would result from the SBUV-reported ozone changes in the upper stratosphere.

It is more difficult to assess how changes in the tropospheric forcing of the stratosphere might alter the lower stratospheric temperature structure. Current three-dimensional model simulations have difficulty even reproducing the observed stratosphere (Mahlman and Umscheid, 1984), although substantial improvements have been made by increasing the model resolution (Mahlman and Umscheid, 1987). A possible reason for a change in the tropospheric forcing is a change in the locations and intensity of convective regions. These regions can change in response to alterations in the fluxes of sensible and latent heat that result from a change in surface properties. While large-scale modification of the land surface has the potential to produce significant changes in the surface fluxes, a more likely candidate is a change in the distributions of sea surface temperatures and sea ice (e.g., Austin, private communication, 1987).

The sea surface temperature distribution is not independent of the atmospheric circulation. The major ocean current systems are primarily wind driven, so that the sea surface temperature distribution is intimately coupled with the atmospheric circulation on time scales ranging upwards from about a month. This coupling of atmosphere and ocean has the potential to introduce oscillations with time scales of years to millennia, which makes the definition and identification of truly external forcing processes difficult. An example of a fluctuation of the coupled ocean–atmosphere system is the El Niño–Southern Oscillation (ENSO), which has received a great deal of attention in recent years. Changes in the surface temperatures of the tropical Pacific Ocean have been shown to introduce changes in tropical convection and in planetary wave patterns in the extratropics of the Northern Hemisphere (see, e.g., Blackmon et al., 1983). There appears to be little doubt that variations in the tropical Pacific surface temperatures are a manifestation of the coupling with the atmosphere, and even though a considerable amount of work has been done on modeling the tropospheric response to sea surface temperatures, little information is available on the stratospheric response.

Figure 6.6 shows the long-term fluctuations in temperatures in the 30 to 100 mb layer at north temperature latitude. The amplitude of these fluctuations was less than 1K over decadal periods; since the source of these changes has not been identified radiatively, it can be hypothesized that they are dynamical in origin. Thus, a crude estimate of the magnitude of dynamical contributions to trends could be 1K per decade in the lower stratosphere.

Long-term changes in tropospheric dynamical activity could certainly produce midlatitude and polar stratospheric temperature trends as large as the observed year-to-year changes, and perhaps larger. These changes are as large as the predicted changes because of trends in the radiative source gases discussed earlier; therefore, they will add to the uncertainty in identifying trend mechanisms from temperature observations alone. However, tropical stratospheric responses to midlatitude dynamical changes are expected to be quite small, so that unambiguous trend detection may be possible in that region.

6.4.6 Radiative Photochemical Models

Radiative photochemical models predict a variation in stratospheric ozone and temperature during solar cycles and as the concentrations of ozone-catalyzing minor constituents increase with time (see Chapter 7). The calculation of the expected change in stratospheric temperature is complicated by feedbacks involving ozone photochemistry. For example, a decrease in temperature leads to some increase in ozone, which acts to offset the original temperature decline.

Table 6.13 summarizes the results from one-dimensional models at the altitude of peak cooling. All models listed are photochemical and include the effects of increased CO_2, CH_4, N_2O, and chlorofluorocarbons (and sometimes NO_x). The resultant decreases in ozone are also incorporated. The calculations are grouped into sets covering approximately the same period, and the trend in degrees Kelvin per decade is given for comparison. Since the periods shown are

Table 6.13 Comparison of Calculated Cooling From One-Dimensional Radiative–Photochemical Models Near to the Level of Peak Cooling

Paper	Period	Approximate Level of Peak Cooling	Temp Change	Approximate Change in temp/ decade
Brasseur and De Rudder	1960–80	45 km	−3.4K	−1.7K/decade
Bruhl	1960–85	1.5 mb (45 km)	−3.9K	−1.6K/decade
Vupputuri	1960–85	(at 42 km)	−3.8K	−1.5K/decade
Wuebbles	1960–83	42 km	−3.4K	−1.5K/decade
Brasseur and De Rudder	1940–80	45 km	−5.0K	−1.25K/decade
Bruhl	1935–85	1.5 mb (45 km)	−4.9K	−1.0K/decade
Owens et al.	1940–85	46 km	−3.8K	−0.84K/decade
Vupputuri	1940–85	(at 42 km)	−4.5K	−1.0K/decade
Wang et al.	1950–80	48 km	−1.9K	−0.6K/decade
Wuebbles	1950–80	42 km	−3.2K	−1.1K/decade
Bruhl	1860–1985	1.5 mb (45 km)	−6.0K	−0.48K/decade
Vupputuri	1850–1980	44 km	−5.5K	−0.42K/decade

roughly the length of an integral number of solar cycles, models that incorporate solar cycle changes can be compared with those that do not. Most of the model-computed temperature changes in Table 6.13 are caused by changes in the ozone. Bruhl (1987), for example, calculates a peak cooling of 1K between 1960 and 1985 for the CO_2 only, and the CO_2, CH_4, and N_2O only scenarios; this compares with a value of nearly 4K when the chlorofluorocarbons are included.

The agreement between different model calculations is good, particularly for the cooling over the past two or three decades. In the 40 to 50 km layer, these models predict a change of −1.5 to −1.7K over the last decade. The two-dimensional model computations presented in Chapter 7 give similar results.

Table 6.14 shows the cooling calculated at around 30 mb (24 km) for the same sets of calculations. The agreement between calculations is not as good as might be expected near a transition level. Bruhl's model, in particular, calculates a smaller cooling at 30 mb, since the height at which tropospheric warming changes to stratospheric cooling is several kilometers above the transition level found in other models. This level is particularly difficult to calculate and will depend on the particular convective scheme incorporated in the troposphere, as well as on other modeling details, such as vertical resolution. Thus trends estimated at the 30 mb level are likely to be subject to a greater uncertainty than those at lower pressures.

6.5 CONCLUSIONS

The stratospheric satellite, rocket, and radiosonde data sets analyzed in this chapter have been intercompared in detail. Temperature changes from 1979 to 1986 have been determined using radiosondes (Free University of Berlin and Angell and Korshover 1983a) and satellite radiances (United Kingdom Meteorological Office and NMC data). Radiosonde data above 30 mb were not considered reliable for trend determination. The rocket data used here have been edited extensively and improved so that the results are not comparable to previous studies. The rocket data and zonal mean satellite data were intercompared, and trends were determined over the longer rocket data period.

Table 6.14 Comparison of Calculated Cooling From One-Dimensional Radiative–Photochemical Models at About 30 mb (24 km)

Paper	Period	Approximate Level of Peak Cooling	Temp Change	Approximate Change in temp/ decade
Bruhl	1960–85	30 mb (24 km)	almost zero	
Labitzke et al.	1970–80	24 km	−0.2K	−0.2K/decade
Labitzke et al.	1960–85	24 km	−0.6K	−0.24K/decade
Vupputuri	1960–85	25 km	−0.8K	−0.32K/decade
Wuebbles	1960–83	24 km	−0.45K	−0.2K/decade
Owens et al.	1940–85	24 km	−0.6K	−0.13K/decade
Vupputuri	1940–85	25 km	−1.2K	−0.27K/decade
Wang et al.	1950–80	24 km	−0.2K	−0.07K/decade
Wuebbles	1950–83	24 km	−0.47K	−0.14K/decade
Bruhl	1860–1985	30 mb (24 km)	−0.3K	−0.02K/decade
Vupputuri	1850–1980	25 km	−1.6K	−0.12K/decade

This chapter also includes an investigation of the processes that could produce stratospheric temperature trends. These processes include global changes in ozone, solar flux, concentration of other trace constituents, and aerosol loading, as well as dynamical changes. The major conclusions are outlined below:

- The radiosonde and satellite data sets generally intercompare very well, although some periods of disagreement exist. Figure 6.17 shows the computed difference in global temperatures for 1985/86–1979/80. The largest global decline is in the upper stratosphere, with a computed change of −1.75K ±1.0K.

- The rocket data have insufficient spatial coverage to establish global trends and are subject to some uncertainties. Longer term trends from rocketsondes starting in 1969 indicate a cooling on the order of −1 to −2K per decade in the mid- to upper stratosphere. However, if the trends are calculated starting in 1973, they range from −1K per decade up to 2K per decade (warming). Hence, rocketsonde trends are subject to large uncertainties.

- Long-term trends in the lower stratosphere derived from radiosonde-based data sets show no significant cooling except in the Tropics and over Antarctica.

- There is a warming of the lower and middle stratosphere in the 1982–1983 period, which appears to be associated with, and is consistent with, radiative heating of the El Chichón aerosol cloud.

- Standard interactive photochemical and radiative transfer models estimate a cooling of the upper stratosphere of −1.2 to −1.7K per decade for 1970–1990 because of the ozone and trace gas changes. Since 1979, an additional cooling of −0.8K has occurred due to a decrease in the solar flux as part of the solar cycle.

- Using the reported SBUV ozone changes from 1979 to 1986, a radiative equilibrium tropical temperature decline of 5.5K can be computed. An additional 0.8K decline is expected as a result of the decrease in solar flux over that phase of the solar cycle. When this change is convolved with the SSU 47X weighting function centered at 0.5 mb, the detectable temperature change is −4.6K. This compares to the observed −1.3K ± 1K tropical change (Figure 6.18). Thus, the reported SBUV ozone changes in the upper stratosphere appear to be inconsistent with the observed temperature changes, while SAGE-reported ozone changes are not.

52-45
53450

#42

CHAPTER 7

N92-15459

Theory and Observations
Model Simulations of the Period 1955—1985

Panel Members

I. S. A. Isaksen, Chair ϕ2736708
R. Eckman
A. Lacis
M. Ko — A6525710
M. Prather - NC999967
J. Pyle — CE261061
H. Rodhe
F. Stordal —ϕ2736708
R. Stolarski - NC999967
R. P. Turco -
D. Wuebbles LH075075

Chapter 7

Theory and Observations
Model Simulations of the Period 1955–1985

Contents

7.0 INTRODUCTION 503

7.1 ATMOSPHERIC SCENARIOS FOR 1955–1990 503
- 7.1.1 Trace Gases 504
- 7.1.2 Solar Variability 506
- 7.1.3 Nuclear Test Series 507
- 7.1.4 Atmospheric Variations Not Modelled 508

7.2 THE MODELS 508
- 7.2.1 Model Descriptions 508
- 7.2.2 Basic Chemical Uncertainties 511
- 7.2.3 Uncertainties in Transport 512
- 7.2.4 Comparison of Models With the Contemporary Atmosphere 513
- 7.2.5 Stratospheric Temperature Feedbacks 521

7.3 MODEL SIMULATIONS OF OZONE CHANGE 521
- 7.3.1 Calculated Total Global Variations 522
- 7.3.2 Atmospheric Nuclear Tests 523
- 7.3.3 Column Ozone: Comparison With Observations 525
  - 7.3.3.1 Theoretical Fingerprints for the Solar Cycle and Trace Gases 525
  - 7.3.3.2 Thirty Years of Dobson Data 527
  - 7.3.3.3 Global Data From Satellite, 1979–1987 527
  - 7.3.3.4 Subtracting the Solar Cycle From Dobson Data 531
- 7.3.4 Profile Ozone: Comparison With Observations 532
  - 7.3.4.1 Fingerprints of the Solar Cycle and Trace Gases 532
  - 7.3.4.2 Trends in Vertical Structure, 1979–1985 535
- 7.3.5 Tropospheric Ozone 536
  - 7.3.5.1 Impact on Column Perturbations 536
  - 7.3.5.2 Uncertainties in the Estimates 537
- 7.3.6 Future Ozone Changes (1985–1990) 538
- 7.3.7 How Good Are the Models? 539

7.4 CONCLUSIONS 539

[illegible] 500 INTENTIONALLY [illegible]

PRECEDING PAGE BLANK NOT FILMED

7.0 INTRODUCTION

The main objective of the theoretical studies presented here is to apply models of stratospheric chemistry and transport in order to understand the processes that control stratospheric ozone and that are responsible for the observed variations. The model calculations are intended to simulate the observed behavior of atmospheric ozone over the past three decades (1955–1985), for which there exists a substantial record of both ground-based and (more recently) satellite measurements. Through comparisons of the modeled history of atmospheric ozone with these data, we hope to:

- Simulate the observed temporal and spatial variations of ozone.
- Focus on the specific patterns, or "fingerprints," of ozone change that, according to current understanding, can be uniquely associated with a specific cause.
- Identify the roles of human activity, solar cycle variations, and other undetermined natural variability in altering stratospheric ozone.
- Evaluate the reliability of models for stratospheric ozone and their ability to predict change.

The development of two-dimensional (2-D) models of stratospheric chemistry and transport has led to considerable improvement in our ability to describe the stratosphere, to predict ozone distributions, and to compare with observations of ozone and other trace compounds (see *WMO*, 1986). Two-dimensional calculations allow us to simulate both the latitudinal and seasonal variations in the stratosphere, a task beyond the scope of the 1-D models traditionally used for assessment. Results from the 2-D models may allow for identification of fingerprints in ozone: i.e., certain months and latitudes for which chlorofluorocarbon (CFC)-induced ozone effects are most pronounced. We have chosen to base our present study on results from 2-D models. We have included for historical perspective some results from parallel 1-D models (from the same research groups as for 2-D models), but find that 1-D models cannot be used to predict even the globally averaged perturbations to ozone.

Although many features in these atmospheric simulations are common to all models, significant differences exist. There are systematic discrepancies in all of the models with regard to the absolute concentrations of ozone at the stratopause and the source of odd nitrogen in the lower tropical stratosphere. These stratospheric models represent the most recent versions available from the research groups involved, and thus are not fully or, in some cases, partly documented in the published literature. A detailed intercomparison of the 2-D models has not yet been made, but is planned for 1988. For these reasons, we have incorporated a brief section on comparison with observations and an extended discussion on uncertainties pertinent to the model calculations in this study.

7.1 ATMOSPHERIC SCENARIOS FOR 1955–1990

The period of focus for this study was selected to be the last 30 years, because there is an extensive data base collected on total column ozone by the Dobson network for this period, starting with the International Geophysical Year, 1957. Factors that could have influenced atmospheric ozone during this period include slow increases in the concentration of biogenic/anthropogenic trace gases such as carbon dioxide (CO_2), methane (CH_4), and nitrous oxide

PAGE 502 INTENTIONALLY BLANK

PRECEDING PAGE BLANK NOT FILMED

(N_2O); a rapid rise in the concentration of stratospheric chlorine from the manmade gases $CFCl_3$, CF_2Cl_2, carbon tetrachloride (CCl_4), and methylchloroform (CH_3CCl_3); injection of nitrogen oxide (NO) by atmospheric nuclear tests; and variations in ultraviolet (UV) sunlight over the 11-year solar cycle. These terms have been included in the model scenarios selected here. Other geophysical factors that lead to noticeable changes include changes in tropospheric chemistry and climate, increases in brominated halocarbons, volcanos, heterogeneous chemistry in the polar stratosphere, and changes in circulation associated with the quasi-biennial oscillation (QBO) and the El Niño/Southern Oscillation (ENSO). The neglect of these latter terms is discussed with the uncertainties in the models. Table 7.1 indicates the combinations of factors that are incorporated in the different calculations.

In addition to the primary period, 1955–1985, we believe it is important to extend the calculations through 1991 in order to predict near-term global trends in ozone as we approach the next maximum in the solar cycle. A realistic assessment of the predictions of ozone change is needed since, according to current theory, increases in ozone caused by increasing solar intensity could fully or partially cancel the calculated ozone decreases caused by the effect of trace gases, as described below.

Table 7.1 Factors Included in Model Simulations

Case	CFC's	N_2O & CH_4	solar	nuclear	T & CO_2
1	yes	yes	no	no	(some)
2	yes	yes	yes	no	(some)
3	yes	yes	yes	yes	(some)

Case 1 illustrates the effects of changes in trace gases only. In case 2, the effects of the solar cycle are introduced through cyclic changes in the solar ultraviolet (UV) flux. In case 3, releases of NO from atmospheric nuclear tests during 1958–1962 are included. Changes in stratospheric temperature will be driven by changes in CO_2 and O_3; some of the models were able to include this feedback, others were not (see model description below).

7.1.1 Trace Gases

Emissions and atmospheric concentrations of important trace gases, such as CO_2, CH_4, N_2O, and several chlorocarbons, are known to have increased substantially over 1955–1985. Scenarios for the historical variations in these gases are based on observed increases in concentrations or on estimates of the emissions of these gases (Wuebbles et al., 1984), as outlined in Table 7.2. The scenarios employed here represent one possible reconstruction of the recent composition of the atmosphere. Nevertheless, the uncertainties in the trace gas composition of the atmosphere over

Table 7.2 Trace Gas Scenarios Adopted for 1950–1991

CO_2 (ppm)	$270 \times (1.00141)^{(t-1850)}$	$t < 1958.0$
	$270 + 44.4 \times (1.0192)^{(t-1958)}$	$t > 1958.0$
CH_4 (ppm)	$0.70 + 0.93 \times (1.018)^{(t-1980)}$	$t < 1980.0$
	$1.63 \times (1.010)^{(t-1980)}$	$t > 1980.0$
N_2O (ppb)	$285 + 14.0 \times (1.041)^{(t-1978)}$	all t

Concentrations refer to bulk tropospheric values; t is time in years. Based on fits supplied by D. Wuebbles (see Wuebbles et al., 1984).

the last three decades are bounded by measurements, and alternate scenarios that are consistent with observations would not produce significantly different results in these models.

Yearly release rates of chlorocarbons are given in Table 7.3 for each year between 1955 and 1985. Fluxes of chlorocarbons are assumed to be constant after 1985. Other trace gases, such as CO and NO_x ($=NO+NO_2$), which may have had important effects on tropospheric ozone, are kept at a constant level, partly due to major uncertainties about their emissions over this time period and partly due to the uncertainties connected to the treatment of tropospheric chemistry in the present models. For example, aircraft emissions of NO_x were not included; there are uncertainties in theoretical emission rates, in addition to uncertainties in how to model the tropospheric NO_x and ozone (O_3). Carbon monoxide (CO) increases are not considered, although there are indications that Northern Hemispheric levels have been increasing slowly (see Chapter 8). Halon (bromocarbon) scenarios were not included because the increase in

Table 7.3 Fluorocarbon Emission Fluxes (10^9g/yr) Used in Models for 1950–1991

Year	$CFCl_3$ (CFC–11)	CF_2Cl_2 (CFC–12)	$CHClF_2$ (CFC–22)	$C_2Cl_3F_3$ (CFC–113)	CCl_4	CH_3CCl_3
1955	21.5	46.9	0.6	0.0	91.0	3.4
1956	26.1	53.3	0.8	0.0	87.9	7.4
1957	31.3	60.5	1.1	0.0	84.8	16.4
1958	31.3	68.6	1.4	0.0	84.8	19.6
1959	31.3	77.9	1.9	0.0	84.8	23.3
1960	38.2	88.5	2.6	2.5	84.8	27.8
1961	47.3	100.5	3.5	3.0	84.8	33.0
1962	58.5	114.1	4.2	3.7	84.8	39.2
1963	72.4	129.5	5.1	4.4	88.7	46.6
1964	88.7	148.2	6.1	5.4	92.8	55.5
1965	100.8	167.6	7.3	6.5	97.0	65.9
1966	114.6	189.5	8.8	7.9	101.5	78.4
1967	130.2	214.3	10.6	9.6	106.1	93.2
1968	148.0	242.4	12.7	11.6	111.0	110.8
1969	168.2	274.1	15.3	14.0	116.1	131.7
1970	191.2	300.5	18.3	17.0	121.4	156.6
1971	217.3	327.9	22.0	20.6	127.0	186.2
1972	247.0	357.9	26.5	24.9	132.9	221.3
1973	280.7	390.6	31.8	30.2	139.0	263.1
1974	323.5	443.5	38.3	36.6	145.3	312.8
1975	323.5	434.6	46.0	44.3	131.2	371.9
1976	323.5	433.9	50.3	53.6	131.2	442.1
1977	325.5	418.0	55.0	65.0	131.2	454.5
1978	316.5	388.6	60.1	74.4	131.2	454.5
1979	307.8	388.6	65.7	85.1	131.2	454.5
1980	264.5	388.6	71.9	97.3	131.2	454.5
1981	264.5	412.2	71.9	97.3	131.2	454.5
1982	264.5	412.2	71.9	97.3	131.2	454.5
1983	264.5	412.2	71.9	97.3	131.2	454.5
1984	264.5	412.2	71.9	97.3	131.2	454.5
1985	264.5	412.2	71.9	97.3	131.2	454.5

stratospheric bromine from manmade halocarbons is expected to have had only a minor effect on ozone through 1985. (A notable exception may be the polar ozone reductions, which are not addressed in these calculations.)

7.1.2 Solar Variability

Variations in sunlight over the 11-year solar cycle are believed to manifest themselves as cyclic changes in the solar flux on the order of 10 percent or less in the far ultraviolet, with very small changes, if any, in the visible region of the spectrum. The far UV—wavelengths less than 220 nm—is responsible for photolysis of O_2 and, hence, primary production of ozone. (Destruction of ozone is driven, in general, by wavelengths longer than 240 nm.) The maximum in solar UV is associated with the maximum of the solar cycle (defined by sunspot number or $F_{10.7}$ flux) and is expected to produce an increase in stratospheric ozone. The magnitude of the solar-cycle effect on ozone will depend on the amplitude and spectrum of solar variations as well as their impact on the distribution of other trace gases in the stratosphere.

The large solar-cycle model used here for variations in solar UV, shown in Table 7.4, is based on SBUV data and the analyses of Heath and Schlesinger (1984; 1986). A fundamental assumption for this model is that the spectral pattern of variability observed over the solar rotation of active regions (27 days) is the same as that over the solar cycle (11 years). The magnitude of the solar cycle in UV irradiance is assumed to scale linearly with the ratio of the core-to-wing emissions of the Mg II line. An alternative case for solar variability is the small solar-cycle model, presented in *WMO* (1986) and based on Solar Mesospheric Explorer (SME) observations. Lean (1987) notes that the solar variability derived from SBUV data is significantly higher than that derived from SME satellite data. Some 2-D model calculations also were made with this pattern for the solar cycle.

Table 7.4 Assumed Peak-to-Peak Variation of UV Radiation During a Solar Cycle as a Function of Wavelength

Wavelength (nm)	Large* Model (%)	Small** Model (%)
175–190	12	2.0
190–210	10	3.0
210–240	4	2.6
240–260	3	0.5
260–300	1	0.5

*SBUV
**SME

In the present model studies, UV flux changes are represented by a simple sine curve through each solar cycle. This assumption ignores the asymmetry of the solar cycle observed in sunspots or $F_{10.7}$ flux, which exhibits a rapid rise to solar maximum and a slower decay to minimum. Variations in UV radiation that occur during a solar cycle are still highly uncertain. The magnitudes of individual solar cycles are based on solar radio emissions, $F_{10.7}$, assuming the magnitude of solar cycle 21 (1974–1985) to be unity. All solar cycles are assumed to have the same baseline flux at solar minimum. Table 7.5 shows the amplitude of each solar cycle. In these model studies, it is assumed that solar UV variation is the only external variation associated with the solar cycle.

Table 7.5 Relative Magnitude of Solar Cycles

Cycle No.	Year of Max.	Relative Magnitude
18	1946.5	0.89
19	1957.5	1.30
20	1968.5	0.86
21	1979.5	1.00
22	1990.5	1.00 (assumed)

Adopted from Heath & Schlesinger (1984), scaled to $F_{10.7}$ flux.

7.1.3 Nuclear Test Series

In estimating the changes in ozone during the 1960's, it is necessary to include the impact of NO produced by the U.S. and U.S.S.R. nuclear test series of the 1950's and 1960's. Past modeling studies (e.g., Chang et al., 1979; Wuebbles, 1983b) have predicted that these tests would have significantly perturbed stratospheric ozone.

For our calculations, we have selected a limited set of nuclear tests, based on the more complete list of Bauer (1979). This subset, shown in Table 7.6, includes all explosions greater than or equal to 10 megatons (MT) and accounts for about 70 percent of the total megatonnage during the primary testing period in 1961 and 1962. A comparison made with a more complete compilation of the test series shows that the limited set is a good approximation. The altitudes of the bottom and top of the stabilized cloud are taken from the empirically based analyses of Peterson (1970) and assume a uniform source of NO (molecules/cm^3) between cloud bottom and cloud top. The production of NO per megaton of explosion energy is still highly uncertain, with theoretical estimates ranging from 0.4–1.5 × 10^{32} (see discussion in Chang et al., 1979, or NRC, 1985). We assume here a value of 1.0 × 10^{32}. An exception to the above scenarios was the LLNL model which adopted a yield of 0.67 × 10^{32} NO per MT, and that used the altitude distribution of NO within the cloud from Peterson (1970).

The major uncertainties in simulating these nuclear tests are the yield of NO and the altitude range of the cloud, particularly for the high-latitude U.S.S.R. tests. The timing and yield (megatons) of the tests are well established.

Table 7.6 Limited Set of Nuclear Tests Used in Model Calculations

Date	Country	Latitude	Yield(MT)	Alt (km)+
May 12, 1958	USA	11°N	1.4*	13–19
July 28, 1958	USA	11°N	8.9*	18–29
Oct. 23, 1961	USSR	75°N	25	19–37
Oct. 30, 1961	USSR	75°N	58	20–42
June 27, 1962	USA	2°N	11	18–30
Aug. 5, 1962	USSR	75°N	38	20–41
Sep. 19, 1962	USSR	75°N	24	18–36
Sep. 25, 1962	USSR	75°N	27	18–36
Sep. 27, 1962	USSR	75°N	24	18–36
Oct. 30, 1962	USA	17°N	10	18–30
Dec. 23, 1962	USSR	75°N	20	19–35

+ Altitude range (km) of the injected NO
*Surface test

7.1.4 Atmospheric Variations Not Modeled

When comparing the model simulations discussed above with observed values of total ozone for the same period, it is important to bear in mind that the ozone concentrations are also influenced by factors that are not considered in the models.

The atmosphere is variable on all scales, many of which cannot be resolved by our current models. For example, some of the variability in total ozone appears to be correlated with the QBO, but this atmospheric cycle has not been included in these ozone trend studies. The more regular annual and semiannual cycles are generally included in these models through the seasonal variation in sunlight (included directly in the photochemistry and indirectly through imposed atmospheric temperatures or transports). The annual cycle is large at high latitudes, and most models would capture this variation producing a spring maximum and fall minimum in total ozone (see Figure 7.3). There is also a semiannual component that has been investigated in some models.

The QBO is quasi-periodic, which complicates attempts to model it with regular, periodic functions. In addition, major climatic events, such as ENSO, are likely to affect the stratosphere and induce temporary changes in ozone. Other irregular phenomena include solar proton events that are erratic, that tend to occur on the waning side of the solar cycle, and that can produce large amounts of NO_x in the middle and upper stratosphere (Crutzen et al., 1975; Jackman et al., 1980).

More important, the 2-D model studies presented here did not attempt to simulate the large ozone decreases observed in the Antarctic spring over the last 8–10 years, nor to study the possible consequences of proposed Antarctic chemistry at other latitudes. The model calculations also do not consider the possible effects on stratospheric ozone and temperatures of the volcanic eruptions of El Chichón in April 1982 and Agung in 1963. All of these studies require special research efforts, many of which are in progress. Neglect of these irregular geophysical phenomena probably represents an important source of error in simulating the recent ozone trends.

7.2 THE MODELS

7.2.1 Model Descriptions

The present work is based on experiments with four different 2-D models (described in Table 7.7) and with some parallel 1-D models. With the exception of the LLNL 2-D model, they were all used in the previous compilation of model results. (See *WMO* 1986, Chapters 12 and 13, for a more complete description of the types of 2-D stratospheric models and their performance.)

Three of the 2-D models (AER, LLNL, and Oslo) use a diabatic circulation, although their transport velocities can differ because the circulations are derived from different data sets. In the AER and Oslo models, the circulation is fixed in all computations. In the LLNL model, the temperatures are held fixed, while the radiative heating rates and the diabatic circulation are computed as ozone varies. The fourth 2-D model (Cambridge) uses a Eulerian circulation. The mean transport by waves in the Cambridge model is represented as momentum fluxes based on satellite observations and specified diffusion coefficients, and is held fixed while changes in the

Table 7.7 Characteristics of 2-D Models Used in Calculations of Chapter Seven

	AER	Cambridge	Oslo	LLNL	LLNL
Dimensions	**2-D**	**2-D**	**2-D**	**2-D**	**1-D**
Model Domain and Resolution	**Pole to Pole** **$\Delta \sim 9.5°$** **0–55km** **$\Delta Z = 3$km**	**Pole to Pole** **$\Delta \sim 10°$** **0–60km** **$\Delta Z \sim 3.5$km**	**Pole to Pole** **$\Delta = 10°$** **0–50km** **$\Delta Z = 2$km**	**Pole to Pole** **$\Delta = 10°$** **0–54km** **$\Delta Z = 3$km**	**0–56km** **$\Delta Z = 1$km**
Circulation	Diabatic circulation based on prescribed temperatures and diabatic heating rates	Eularian circulation derived from calculated momentum fluxes based on satellite obs.; latent heat release; radiative transfer (self-consistent); and prescribed diffusion coefficients	As AER	Diabatic circulation radiative heating rates calculated self-consistently both for shortwave heating and longwave cooling	
Diffusion	**Stratosphere**		**Stratosphere**	**Stratosphere**	
	Above 20mb: $K_{yy}=3.10^9$ Below 20mb: 30°S–30°N: 3.10^9 30°–Pole: 6.10^9 winter 2.10^{10} summer	Luther's (1973) monthly averaged K values	$K_{yy}=3.10^9$ cm^2s^{-1} $K_{zz}=1.10^3$ cm^2s^{-1}, increasing above 40km (gravity waves)	$K_{yy}=2.10^9$ cm^2s^{-1} $K_{zz}=1.10^3$ cm^2s^{-1}, increasing above 40km	K_z variable with altitude Wuebbles (1983b)
	$K_{zz}=1.10^3$ cm^2s^{-1}, increasing above 40km (gravity waves) Troposphere $K_{zz}=1.10^5$ cm^2s^{-1} $K_{yy}=2.10^{10} cm^2s^{-1}$		Troposphere: $K_{yy} \sim 4.10^{10}$ cm^2s^{-1} $K_{zz} \sim 1.10^5$ cm^2s^{-1}	Troposphere: $K_{yy} \sim 1.10^{11}$ cm^2s^{-1} $K_{zz} \sim 1.10^5$ cm^2s^{-1}	
Surface Boundary Condition O_3	Fixed mixing ratio	Dry deposition	Dry deposition	Dry deposition	As 2-D
Chemistry	Oxygen, hydrogen, methyl, nitrogen, chlorine species	Oxygen hydrogen, nitrogen, chlorine species, methyl chemistry parameterized	Oxygen, hydrogen, methyl, nitrogen, chlorine, bromine species	Oxygen, hydrogen, methyl, nitrogen, chlorine species	as 2-D + bromine
	Tropospheric H_2O specified by relative humidity	As AER	As AER	As AER	As AER
	Diurnal calculations performed 10 timesteps per day, 5 timesteps per night	Diurnal averaged	Diurnal calculations performed once every month $\Delta t = 15$ min.	Separate diurnal calculations are used to derive rate factors for diurnal-averaged model	As 2-D

Table 7.7 (Cont'd) Characteristics of 2-D Models Used in Calculations of Chapter Seven

	AER	**Cambridge**	**Oslo**	**LLNL**	**LLNL**
Dimensions	**2-D**	**2-D**	**2-D**	**2-D**	**1-D**
Model Domain and Resolution	**Pole to Pole** **$\Delta\varphi 9.5°$** **0–55km** **$\Delta Z = 3km$**	**Pole to Pole** **$\Delta\varphi 10°$** **0–60km** **$\Delta Z \sim 3.5km$**	**Pole to Pole** **$\Delta\varphi 10°$** **0–54km** **$\Delta Z = 2km$**	**Pole to Pole** **$\Delta\varphi 10°$** **0–54km** **$\Delta Z = 3km$**	**$\Delta\varphi 10°$** **0–56km** **$\Delta Z = 1km$**
Photolysis	Calculated ~every hour 93–405 nm $\Delta\lambda = 5$ nm or less. Two-stream approximation Rayleigh scattering Cloud albedo	Calculated 3 times per day 170–800 nm 171 intervals Parameterized Rayleigh scattering No clouds	Calculated every hour 180–800 nm 130 intervals Two-stream approximation Multiple Rayleigh scattering ($n = 3$) Cloud albedo	Calculated ~every 15 min. 133–735 nm 148 intervals Successive multiple Rayleigh scattering Cloud albedo	As 2-D
Temperature Calculations	Temperatures fixed	Solving the thermodynamic equation	Changes in temperatures in the stratosphere calculated as $\Delta T = \Delta T_{CO_2} + \tau . \Delta H$ where $\Delta^2 T_{CO_2}$ is a prescribed function of μ_{CO_2} (taken from the model of Lacis and Hansen (private comm.); the radiative damping time scale is prescribed and the change in the shortwave heating, ΔH, is calculated self-consistently with O_3 changes	Temperatures fixed	Radiative equilibrium temperatures in the stratosphere, calculated self-consistently
Solar Heating		O_3 and O_2 heating	O_3, O_2, and NO_2 heating	O_3, O_2, and NO_2 heating Near IR heating from H_2O, CO_2, and O_2	As 2-D
IR Cooling		15μm CO_2 Curtis matrix 9.6 μm O_3 cooling to space		Broadband model including CO_2, O_3, and H_2O	As 2-D
Literature References	Ko et al. (1985)	Harwood and Pyle (1975), Pyle (1980), Eckman, Haigh, & Pyle (1987)	Stordal et al. (1985), Isaksen and Stordal (1986b)	Wuebbles et al. (1987, in preparation)	Wuebbles et al. (1983a,b)

radiative transfer allow the circulation to change with ozone variations. The diffusion coefficients used for tracer mixing in the stratosphere are similar in the three diabatic circulation models, and generally larger in the Eulerian model.

All of the models are based on same chemistry (DeMore et al., 1985); however, the Oslo model is the only one to include bromine chemistry (held constant with time using background levels of CH_3Br). All the models assume the same values for the solar flux and compute photolysis rates at a number of different times during the day. Various techniques are used to include the effect of diurnal variations in the chemical constituents.

Temperatures are calculated *ab initio* only in the Cambridge model, which calculates the temperatures from the thermodynamic equation. The AER and LLNL models keep the temperatures fixed in all computations. In the Oslo model, the temperatures in the stratosphere are allowed to diverge from a reference value, thus allowing for a temperature feedback to the chemistry. The assumption made in the Oslo model is that temperature changes are a purely radiative adjustment in response to changes in solar heating, while the diabatic circulation remains unchanged. There is some evidence for this assumption from the 3-D GFDL model (Fels et al., 1980). The LLNL model has employed the other extreme approach, namely that changes in the heating rates are manifested purely as dynamical adjustment to circulation.

7.2.2 Basic Chemical Uncertainties

Uncertainties in perturbation calculations that are due to known measurement uncertainties in reaction rate coefficients have been estimated for pure chlorine perturbations and for at least one combined perturbation (Stolarski and Douglass, 1986; Grant et al., 1985). An important result from such studies of error propagation is that combinations of rate coefficients that lead to a very high sensitivity of ozone to chlorine give poorer results in matching observed atmospheric constituents than do the models (i.e., combination of rate coefficients) with lower sensitivity to chlorine (Douglass and Stolarski, 1987). The conclusion reached in that study was that a combination of chemical reaction rate coefficients that yields a sensitivity of ozone to chlorine more than twice that calculated with the currently recommended rate coefficients is unsatisfactory. The conclusion rests upon chlorine monoxide (ClO) being the rate-determining radical for chlorine chemistry. The study is based on comparison of modelled and measured trace species at midlatitudes and, further, does not include the heterogeneous chemistry believed to be important in forming the Antarctic ozone hole.

Perhaps the most important facet of the chemical uncertainty is the question of completeness of the chemical mechanism. Early information on the atmospheric chemical mechanism was derived from relatively high-pressure laboratory experiments in which many reactions were occurring simultaneously. The reactions believed to be important were then isolated one at a time, and their reaction rate coefficients were measured. This process occurred over several decades of careful laboratory experiments. Our present atmospheric chemical scheme is constructed from these individually measured fundamental reaction rate coefficients.

In the early 1970's, many of the basic catalytic reactions had significant uncertainties in their reaction rate coefficients. Progress in laboratory kinetics caused rapid changes in the evaluation of perturbations. An example was the 1976 measurement of the $NO + HO_2$ reaction, which found a rate coefficient more than an order of magnitude larger than previous values (Howard and Evenson, 1977). This led to model calculations of a lower stratosphere with significantly more hydroxyl radical (OH) in which chlorine-catalyzed loss of ozone becomes more important. It is now believed that uncertainties in most of the major catalytic reactions and radical–radical exchange reactions have been reduced to the order of 10–30 percent.

Another set of chemical uncertainties is associated with the major reservoir species such as chlorine nitrate ($ClONO_2$). Much of the present uncertainty in the calculated sensitivity of ozone to chlorine or total odd-nitrogen (NO_y) perturbations can be traced directly to the radical-reservoir balance, which is determined by the formation and destruction processes for the reservoirs. Many of the reservoir species are formed by three-body addition reactions, making their chemical impact greatest in the lower stratosphere and at high latitudes. These locations are shielded from UV radiation by ozone absorption, yielding significant reservoir molecule lifetimes, which in turn allow a buildup in their concentrations. The lower stratosphere and polar latitudes thus may be the regions of greatest chemical uncertainty.

More recently, the question has been raised as to whether there might be very slow reservoir–reservoir reactions that return two reservoir molecules to radicals, thus significantly enhancing radical chemistry and ozone destruction (*WMO*, 1986, Chapter 2). Laboratory experiments have shown that the homogeneous gas-phase rate coefficients for reservoir–reservoir reactions are insignificant, but the possibility remains of a significant heterogeneous contribution. This has, in fact, been suggested to be the mechanism for the rapid springtime change in Antarctic ozone (see, e.g., Solomon et al., 1986a; McElroy et al., 1986b; Isaksen and Stordal, 1986a; Crutzen and Arnold, 1986), where the surfaces for heterogeneous reactions are believed to be the polar stratospheric clouds (PSC's). New laboratory studies indicate that reservoir species containing chlorine are involved in this process. Observations of high ClO levels during periods with PSC's over Antarctica support this view (see the discussion in Chapter 11). The critical role of heterogeneous processes for Antarctic ozone chemistry is now emerging from a combination of atmospheric measurements, laboratory studies, and theoretical modeling efforts; but its importance for the rest of the stratosphere is still under debate. Of particular importance is understanding its role at high northern latitudes, where the meteorological patterns are quite different from those found over Antarctica, and also at all latitudes in the lower stratosphere after major volcanic eruptions.

As more and more laboratory studies are published, our confidence in the completeness of the chemical mechanism for stratospheric ozone has increased. Except for the effects of heterogeneous chemistry, the past 5 years have seen little change in the evaluation of specifically CFC perturbations.

7.2.3 Uncertainties in 2-D Model Transport

Significant advances have been made in the formulation of transport in 2-D models over the past few years. For instance, it has been shown that 3-D general-circulation models can be used to drive useful transport parameters for 2-D models (Plumb and Mahlman, 1987; Pitari and Visconti, 1985). Nevertheless, there are still many problems that could affect our ability to model changes in ozone: for example, only zonal mean processes can be explicitly described, and the transport changes slowly with season or with latitude. Unfortunately, we know that the atmosphere is highly variable on all scales. Data for trace gas distributions will reflect this variability; our models will not.

The rate of vertical advection coupled with the parameterization of eddy diffusion in the stratosphere determines much of the calculated distribution of the long-lived trace species. The estimated distribution of methane is of particular importance for the partitioning of the chlorine species. A slow transport leads to lower concentrations of methane in the upper stratosphere, favoring a more efficient Cl/ClO formation and thereby a more efficient ozone reduction by catalytic chlorine reactions. Therefore, if the transport is too slow in the models, the chlorine effect is overestimated in the upper stratosphere. Comparisons of the calculated methane distribution with observations in some of the model studies indicate that this might be the case. However, the comparisons are not conclusive since the observations are also uncertain. SAMS measurements of methane indicate large latitudinal gradients in the upper stratosphere such that lower concentrations occur at higher latitudes. Models that duplicate this behavior (e.g., Solomon and Garcia, 1984a) and extend it to the polar regions (for which we are lacking observations) show a high sensitivity of ozone to chlorine in this region because of the relative absence of methane. This may be particularly important in assessing the latitudinal dependence of perturbations.

Furthermore, some of the processes influencing ozone on short time scales are inherently difficult to model within a 2-D framework. This applies especially to the kind of dynamical regime believed to exist in the Antarctic. An isolated vortex whose breakdown may well depend on ozone concentration is very difficult to model in two dimensions. Much of the transport description in 2-D models is empirical and thus does not allow the kind of feedback processes that may well be important in studying trends in ozone.

7.2.4 Comparison of Models With the Contemporary Atmosphere

The credibility of stratospheric models in predicting future ozone change will depend on how well they reproduce current observations, particularly the distribution of key species directly involved in ozone chemistry. Such tests of the models allow for ready intercomparison of models and may help us understand any differences in the calculated scenarios for ozone, both past and future.

Because the chemistry of the stratosphere involves a nonlinear system of chemical reactions, one should expect the results of perturbation calculations to be sensitive to the initial chemical concentrations, in particular that of Cl_y (total inorganic chlorine = $Cl + ClO + HCl + HOCl + OClO + Cl_2 + (ClO)_2 + ClONO_2$). This is especially true for the NO_x-Cl_y system, where the reaction of ClO with NO and the reaction of ClO and NO_2 to form $ClONO_2$ provide rapid transition between regimes dominated by Cl_y- or NO_x-catalyzed loss of ozone. This set of chemical reactions has been shown to result in a rapid increase in ozone sensitivity to chlorine at the level where Cl_y is approximately equal to or greater than the total odd nitrogen concentration (e.g., Prather et al., 1984). For the current atmosphere, with Cl_y levels well below NO_y levels, the ozone depletion efficiency by chlorine reactions has been shown to increase with decreasing NO_y levels. A model with initial low NO_y levels tends to give greater ozone depletion from chlorine species than a model with high NO_y levels (Isaksen and Stordal, 1986b). Thus, our assessment of the effect of simultaneous changes in a number of species in the stratosphere depends not only on the relative changes in each of the species, but also on the absolute concentrations of many key species.

We have here selected a few key species to characterize the behavior of stratospheric chemistry in the different models. Some of the models (Oslo, AER, and a previous version of the Cambridge model) have been involved in a comparison study earlier (*WMO*, 1986). It is not the objective here to make an extensive comparison of the different models used, but rather to apply the most recent versions of the models and point out where significant differences occur. To validate or to test more thoroughly these 2-D models, a more complete intercomparison of 2-D models is planned as a separate task in the near future.

Ozone

All of the models show some of the main features common to the observed latitude–height distribution of ozone from the Limb Infrared Monitoring Spectrometer (LIMS) and the Solar Backscatter Ultraviolet (SBUV) (see Figure 7.1). Theoretical altitude profiles for the tropics are compared to a LIMS profile in Figure 7.2. The mixing ratio peaks above about 10 ppmv in the Tropics at about 34 km. The maximum calculated values range between 9 and 12 ppm in most models, (in reasonable agreement with the LIMS values). All models overpredict O_3 at 30 km and underpredict it above 40 km. In the lower stratosphere, where ozone is controlled more by dynamical transport, the mixing ratio surfaces slope poleward and downward due to the predominant Brewer–Dobson circulation. In the models with the weakest horizontal diffusion (Oslo and LLNL), the slopes are steeper. In general, the models used here overpredict the peak mixing ratio of ozone, and some of them place the maximum mixing ratios below those observed by several kilometers.

There is a systematic discrepancy between observed and calculated ozone above 40 km, as discussed in *WMO* (1986). In the upper stratosphere, ozone is controlled by photochemistry, and the discrepancy might indicate some important errors in modeling stratospheric chemistry.

The integrated column abundance of ozone (often called total ozone) is shown in Figure 7.3 as a function of latitude and time of year. Figure 7.3 shows TOMS observations along with results from all of the models. The main features in the observations are adequately described by the models: low total ozone in the Tropics with little seasonal variation; increasing ozone column with latitude; a maximum in the Northern Hemisphere at very high latitudes in late winter; large seasonal variation at high latitudes; and a maximum in the Southern Hemisphere spring that occurs in midlatitudes rather than over the pole. The seasonal variation is suppressed in some of the models (AER and Oslo), yielding too-high ozone columns in the summer and fall. In the Southern Hemisphere, the maximum columns are observed at about 60°S in spring. While this

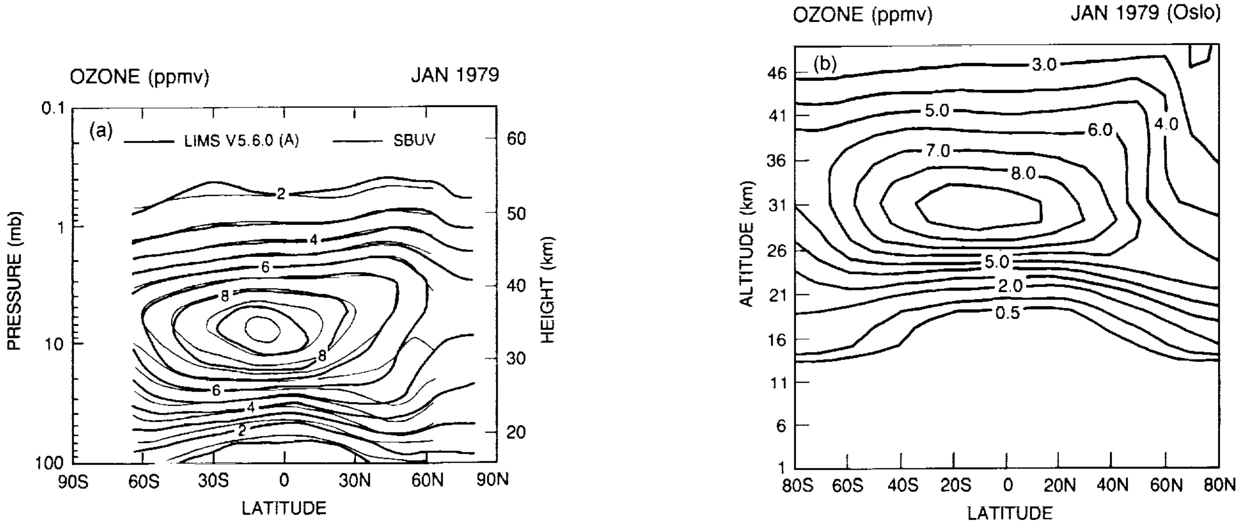

Figure 7.1 Ozone-mixing ratio (ppmv) as a function of latitude and altitude for January from (a) LIMS and SBUV observations for 1979, (b) Calculations using Oslo 2-D model.

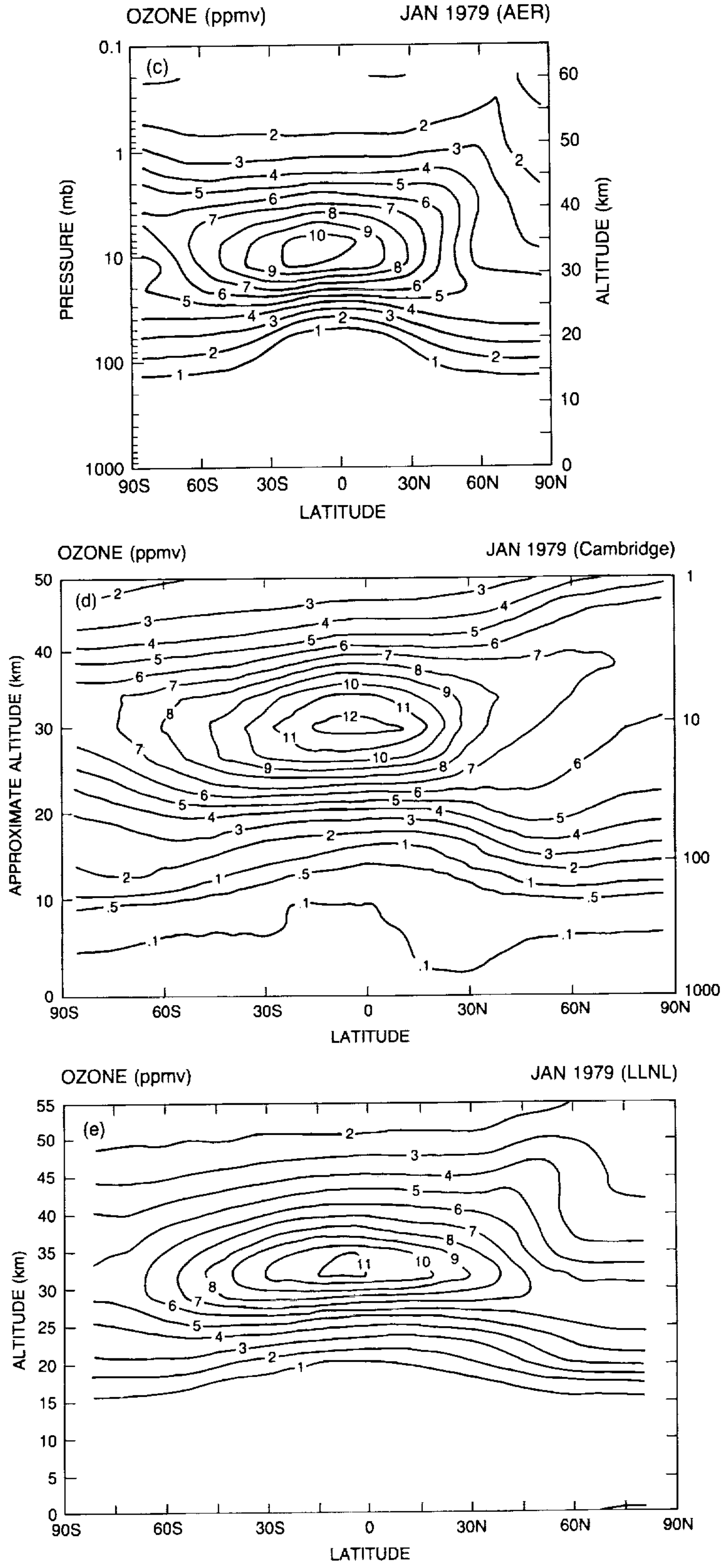

Figure 7.1 (Cont'd) Ozone-mixing ratio (ppmv) as a function of latitude and altitude for January from (c) Calculations using AER 2-D model, (d) Calculations using Cambridge 2-D model, (e) Calculations using LLNL 2-D model.

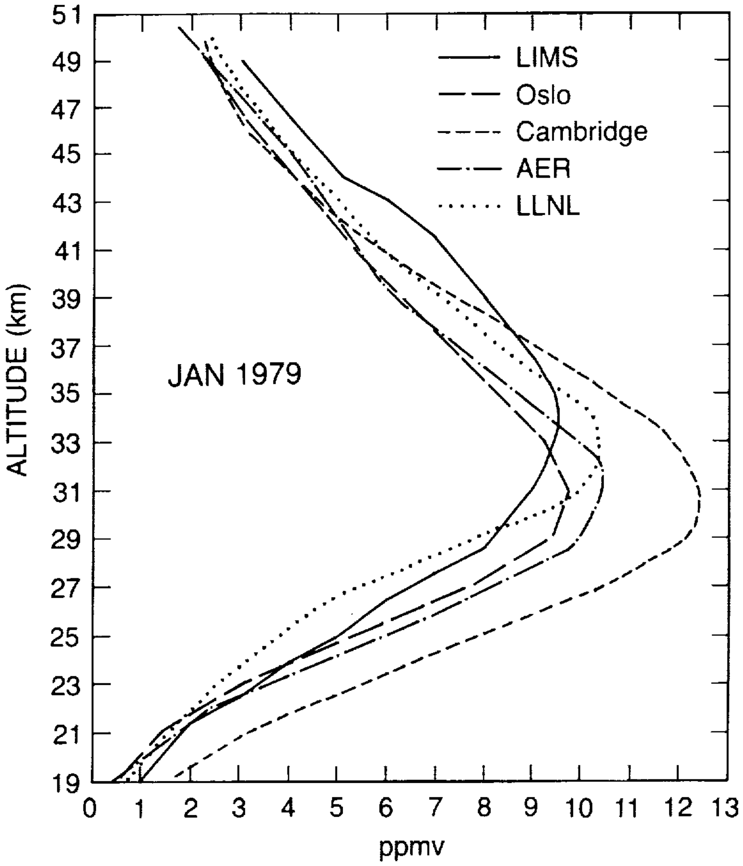

Figure 7.2 Altitude profile of ozone-mixing ratios for January in the Tropics from LIMS observations and the four 2-D models.

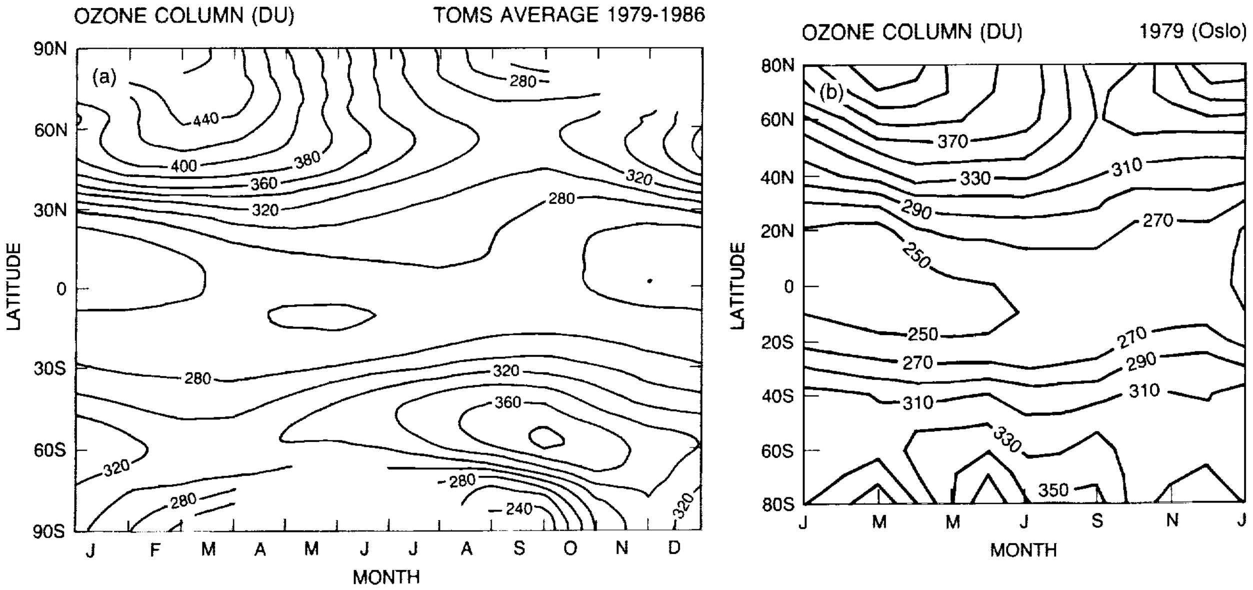

Figure 7.3 Total column ozone abundance (Dobson Units) as a function of latitude and season for (a) TOMS observations averaged 1979–1986, and (b) the Oslo models.

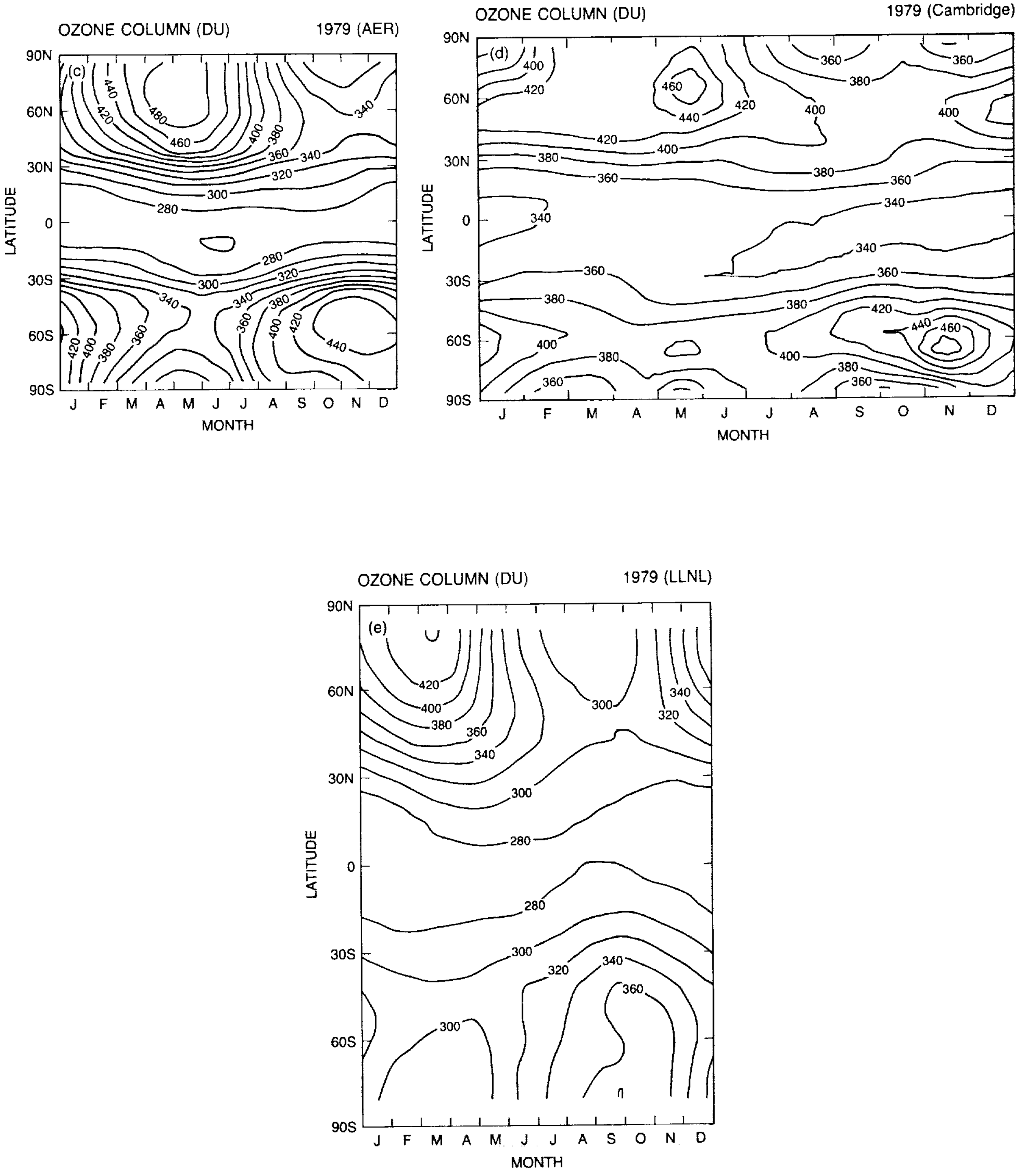

Figure 7.3 (Cont'd) Total column ozone abundance (Dobson Units) as a function of latitude and season for (c) AER, (d) Cambridge, and (e) LLNL models.

maximum is found somewhat further poleward and later in the AER model, it is missing in the Oslo model (see discussion in Stordal et al., 1985). The Cambridge model, on the other hand, calculates ozone columns too high in the Tropics, as is expected from the high ozone mixing ratios in the middle and lower tropical stratosphere (Figure 7.2). In the Northern Hemisphere, the Cambridge model predicts maximum ozone columns at high latitudes during early summer, later than observed. As already mentioned, none of the models describes the Antarctic ozone hole, which is apparent in the Total Ozone Mapping Spectrometer (TOMS) data covering 1979–1986.

Odd Nitrogen (NO_y)

One important issue brought up in previous 2-D model studies (*WMO*, 1986) was the apparent lack of agreement between models and observations of NO_x (LIMS observations of nighttime NO_2), particularly in the tropical lower stratosphere. Models tended to underestimate the NO_x present in this region. Large uncertainties in the NO_x distribution strongly limit the models' ability to predict ozone distribution, as ozone production from the CH_4–NO_x chemistry at these heights is very sensitive to NO_x levels. In the present diabatically driven 2-D models, additional NO_x is assumed to be produced by lightning, which is particularly efficient at high tropospheric altitudes. This source is shown to have a pronounced effect on NO_x levels in the upper troposphere and lower stratosphere in equatorial regions (Ko et al., 1986). Another possible mechanism that would increase NO_x levels in the lower tropical stratosphere is increased K_{yy} values, which would lead to increased transport of NO_x into the Tropics from midlatitudes.

Figure 7.4 is a latitudinal cross-section of NO_y at three different pressure levels—3 mb (~40 km), 16 mb (~30 km), and 30 mb (~25 km)—for July 1985. The figure shows that the present models (Cambridge model not shown) agree fairly well with the observed data. The modelled value for NO_y falls within the range of the data from LIMS and ATMOS (Russell et al., 1988). The NO_y maximum in the three models ranges from 21 to 23 ppb, which is within the uncertainty limits of the LIMS observations (Callis et al., 1985b).

The Oslo model has been used to study the impact of the lightning source of NO_x on ozone depletion. One scenario study has been performed both with and without the lightning source. In the case that involved changes in trace gases only, the depletion of globally averaged total ozone from 1960 to 1980 was reduced from -0.7 percent to -0.4 percent when a lightning source was introduced, as compared to a model without such a source; at the Equator, the ozone depletion changed from -0.7 percent to -0.3 percent. For the period 1960–1990, the calculated global decrease was reduced from - 1.4 percent to -1.0 percent. At high latitudes, ozone depletion is less sensitive to these NO_x sources, decreasing from -2.1 percent to -1.9 percent (March). The uncertainties connected with the magnitude of the lightning source in the upper troposphere (source strength, conversion to and removal of nitric acid (HNO_3) leads to additional uncertainties in these calculations.

In the present model simulations, one source of change in stratospheric odd nitrogen is included through the slow increase in the atmospheric concentration of nitrous oxide. Also included are the changes due to variations in UV radiation over the 11-year solar cycle. Several studies (e.g., Jackman et al., 1980; Garcia et al., 1984) have pointed out the potential for interannual as well as 11-year solar-cycle variations due to mesospheric and upper stratospheric production from energetic particles penetrating to these depths in the atmosphere. Callis and Natarajan (1986) claimed that a significant increase in odd nitrogen occurred as measured by SAGE–II in 1985 as compared to SAGE–I in 1979. Other observations so far have not confirmed the importance of such processes for variations in the ozone layer (see Chapter 9).

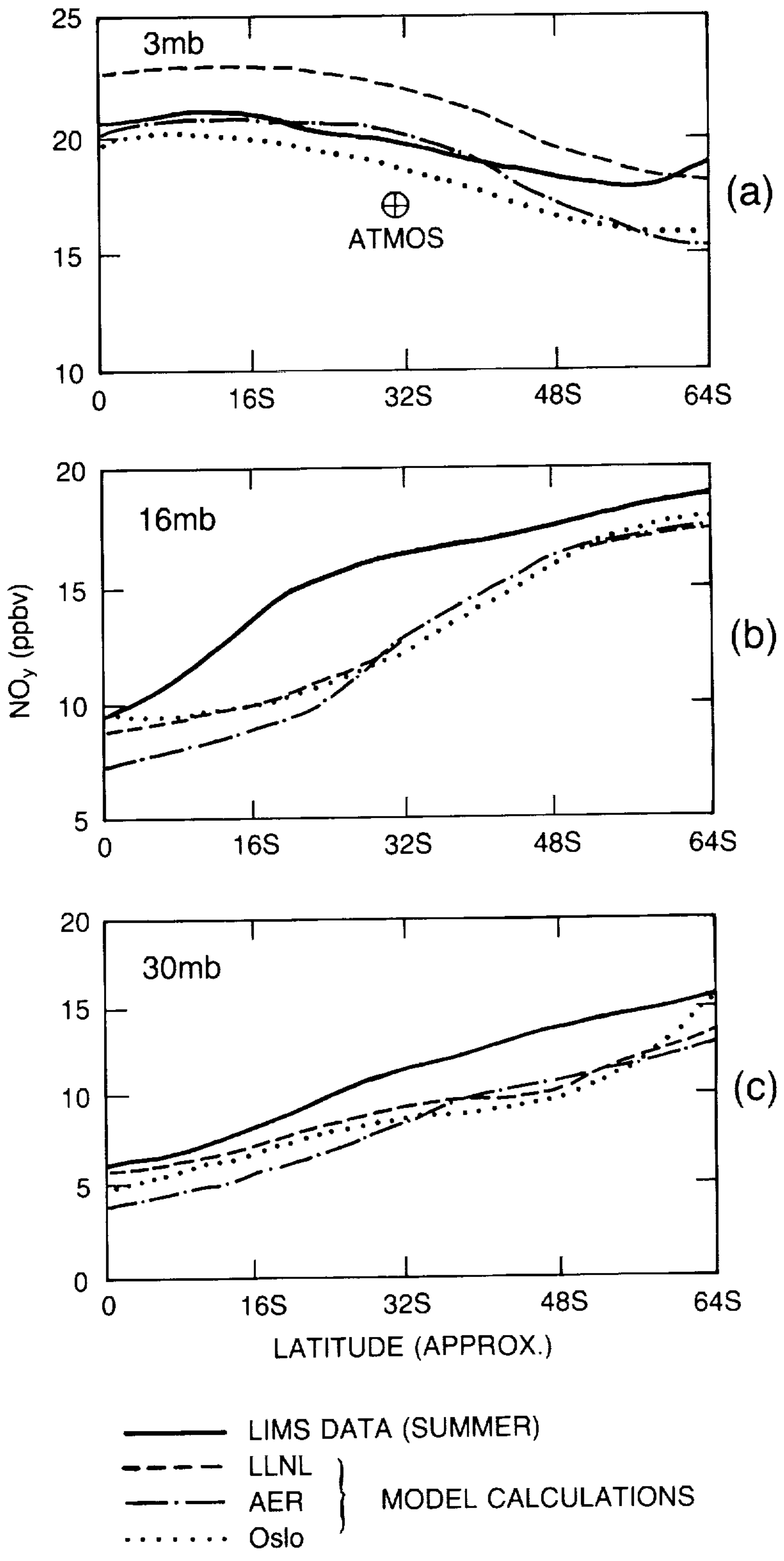

Figure 7.4 Total odd nitrogen (NO$_y$ in ppbv) as a function of latitude for summer from LIMS observations and from the four 2-D models for (a) 3 mb, (b) 16 mb, and (c) 30 mb. Also shown (crossed circle) are results from ATMOS.

ClO

ClO is directly linked to ozone loss through the catalytic chlorine loss cycle. The ability of models to give a realistic description of CFC-induced ozone loss depends critically on their ability to give a proper description of the atmospheric behavior of ClO and its future change. Consequently, any noticeable differences in ClO distribution among the models could result in a different potential for ozone depletion.

Table 7.8 shows the Cl_y values in the upper stratosphere in 1960 and 1985. A general feature is that the absolute chlorine level in the contemporary atmosphere is dominated by recent releases of anthropogenically produced halocarbons. The main differences in Cl_y between models are a reflection of the differences adopted for background levels in 1960.

Table 7.8 Total Chlorine Mixing Ratio (Cl_y in ppb) in the Upper Stratosphere at 30°N for July

	1960	1985	1985–1960
Oslo	0.9	2.4	1.5
AER	1.3	3.0	1.7
LLNL	0.9	2.6	1.7

Figure 7.5 shows the height profile of ClO (ppb) at 30°N during July 1985 for case 3, in which all effects are included. The vertical distributions of ClO at 30°N are similar in shape in all the models, but vary by more than a factor of two in concentration. As pointed out in *WMO* (1986), the model profiles are in reasonable agreement with the observations. Maximum ClO concentrations are predicted to occur around 40 km, with ClO levels between 0.5 and 1.0 ppb. The rapid decrease in mixing ratio below this altitude follows the observations quite well.

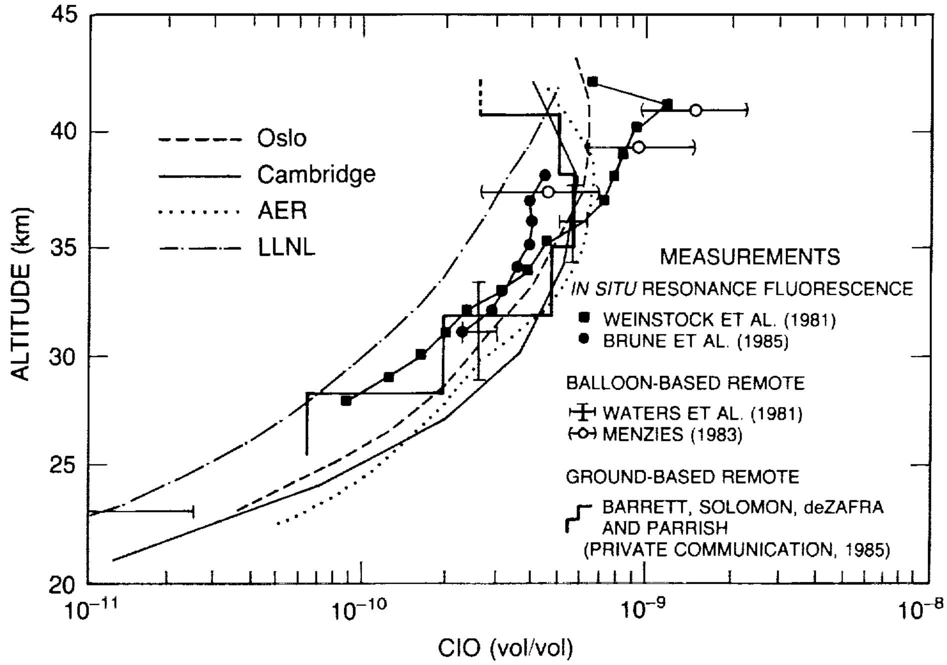

Figure 7.5 Altitude profiles of ClO mixing ratio for July, 30°N, from measurements and from four 2-D models.

7.2.5 Stratospheric Temperature Feedbacks

The temperature of the stratosphere is predicted to respond to changes in ozone, to increases in CO_2, and to volcanic aerosols, as well as to dynamical forcing through transport of heat. Over the study period, the past 30 years, model predictions indicate that stratospheric temperature changes associated with trace gases and the solar cycle are modest—a few degrees at most. These changes in temperature will feed back upon the chemical kinetics that control the concentration of ozone. The impact of including this feedback has been tested in the Oslo model. The 1979–1987 period corresponds to the most rapid decline predicted for ozone concentrations near 40 km. The estimated temperature decrease in the upper stratosphere is shown in Table 7.9 for the two solar-cycle cases over the 8 years. Inclusion of this decrease in temperature affects the predicted decline in O_3, reducing the depletion by approximately 20 percent (see also Table 7.10).

Table 7.9 Calculated Temperature Changes in 1985 vs. 1979 for Oslo Model, Case 3. Values Are Given for July at the Equator

Alt (km)	Large Solar Cycle Model	Small Solar Cycle Model
49	-2.40 K	-1.61 K
47	-2.86 K	-2.06 K
45	-2.94 K	-2.18 K
43	-2.84 K	-2.08 K
41	-2.15 K	-1.50 K
39	-1.44 K	-0.93 K
37	-1.30 K	-0.79 K
35	-1.10 K	-0.63 K

In the detailed comparison of the ozone simulations with observations, it may be important to include temperature changes caused by factors other than ozone. Temperature variations of a few degrees in the stratosphere due to year-to-year changes in dynamics or volcanic aerosols could have a significant effect on the modeled trend in ozone. The temperature record for this period is insufficient, however, and the model studies have not included this effect and its influence on ozone.

Estimated stratospheric temperature changes due to the increasing concentrations of CO_2 to date are small. Over longer time periods, however, looking into the next century, increases in CO_2 may have a more substantial impact on stratospheric temperatures. The effects of expected changes in tropospheric climate are not included in current stratospheric models and also may lead to uncertainties in the predicted temperatures of the stratosphere in the 21st century.

7.3 MODEL SIMULATIONS OF OZONE CHANGE

Calculations of the response of atmospheric ozone for the natural and anthropogenic variations described in Section 7.1 were made with the 2-D numerical models described in Section 7.2. The models were initialized with atmospheric conditions 1955 and integrated with time for the 30-year period of the study. One of the models (Oslo) continued calculations until 1991, the expected maximum of the upcoming solar cycle. The calculated history of ozone from the three cases defined in Table 7.1 is used to examine the relative contributions of the different geophysical forcings to changes in ozone over the study period.

All experiments have been examined two dimensionally both in space (ozone mixing ratios as a function of latitude and altitude) and space–time (ozone columns as a function of latitude and time). In 2-D calculations, the effects of CFC releases might be easier to separate from natural variations in specific regions of the atmosphere during certain seasons when the maximum effects are calculated to occur (the CFC "fingerprint"). Most 2-D models indicate that ozone depletion, as reflected in total ozone observations, is most pronounced at high latitudes during the winter and spring seasons. This analysis focusses on the period 1979–1985 because of the ability to compare these calculations with available satellite ozone observations.

To understand the impact of the atmospheric nuclear test series, the latitudinal and global distributions of ozone during the 1960's are examined. Because the tests occurred at widely varying geographical locations, the previous 1-D model investigations of the response of ozone to nuclear tests would not have been adequate to define the latitudinal variation of the calculated response. Of particular interest are the high-latitude tests, which would be expected to yield local perturbations not representative of a global-averaged response. The perturbations introduced by the atmospheric bomb tests are expected to be negligible a few years after the bomb tests are stopped; thus, changes after the late 1960's come from the response to solar UV variations and possible changes induced by man's releases of trace gases (e.g., CFC's).

7.3.1 Calculated Total Global Variations

As discussed in Section 7.1, four 2-D models were used to simulate expected ozone variations since 1960. Figure 7.6 shows the calculations from each of these models for the three cases given in Table 7.1. The model calculations are shown as percent deviations of the total column of ozone from the 1970 value. All four models show similar decreases for perturbation case 1 (trace gases only). The ozone change for this case is smooth, with a decrease of nearly 1 percent reached by 1985 as compared to 1970. The initial decay in the AER model from 1960 to 1965 is a transient, due to the start of the calculations in 1960 rather than 1955. The other models began their calculations prior to 1960, and no transients from the initial condition appear in 1960.

The superposed solar cycle in perturbation case 2 has an amplitude of 1.5–2.0 percent in each model, all of which used the large solar-cycle model (Heath and Schlesinger, 1984) defined in Table 7.4. Use of the small solar-cycle model deduced from the Solar Mesospheric Explorer (SME) measurements (also Table 7.4) leads to a solar-cycle-induced amplitude somewhat less than half of that shown in Figure 7.6 (0.7 percent for the Oslo model).

The atmospheric nuclear tests of the early 1960's are superposed in Figure 7.6 for perturbation case 3. These occurred at a time of minimum expected ozone during the solar cycle. The bomb effects are predicted to have disappeared by the late 1960's.

Also shown for comparison to these globally integrated 2-D models are results for perturbation case 1 (trace gases only) for the AER 1-D model. That model was run for exactly the same conditions as the 2-D counterpart. The 1-D model shows considerably less ozone depletion since 1970, -0.2 percent at most. Similar differences between 1D and 2-D models are observed in the LLNL models. Thus, we find that 1-D models *cannot* be used to calculate even the globally averaged change in stratospheric ozone.

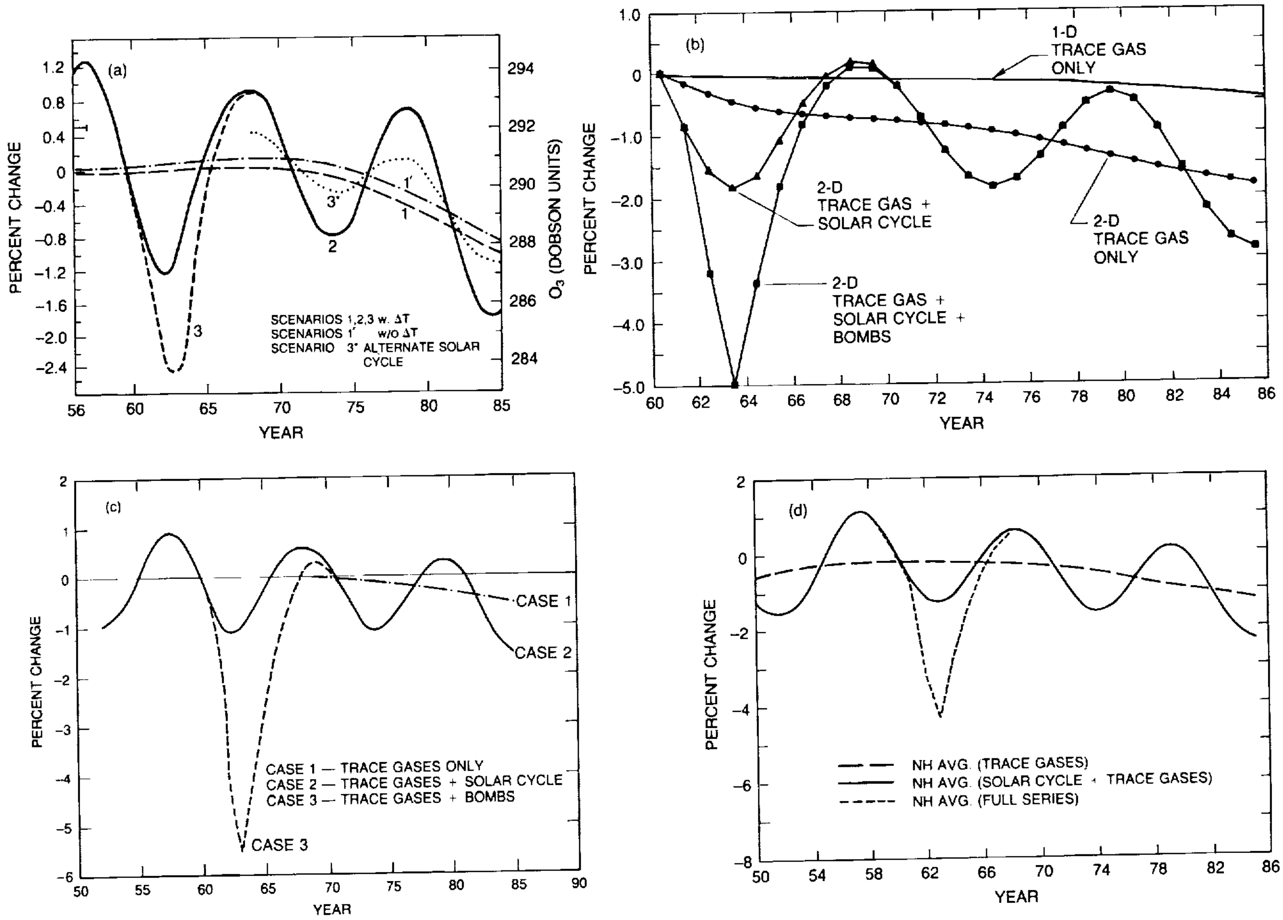

Figure 7.6 Timeline of percent change in globally averaged column ozone from model calculations for the three cases described in Table 7.1: (1) trace gas emissions only, (2) trace gases plus solar cycle, and (3) trace gases, solar cycle, and atmospheric nuclear tests for the (a) Oslo, (b) AER, (c) Cambridge, and (d) LLNL models.

7.3.2 Atmospheric Nuclear Tests

The nuclear bomb tests during the late 1950's and early 1960's, with their associated injection of large amounts of nitrogen oxides into the stratosphere, provide a possibility of testing some aspects of the chemistry/transport models of the stratosphere. The model simulations of this period are based on the emission scenarios given in Section 7.1.3. As seen in Figure 7.6, all four models show a substantial depletion of total ozone during the year following the large explosions in late 1962. The globally averaged decrease was substantially different in the four models, with maximum yearly decreases ranging from 1.3 percent (Oslo) to almost 4.5 percent (Cambridge). The probable cause of this difference is the transport formulation in the models, since the bomb tests are predominantly released at high northern latitudes. Figure 7.7 shows total ozone depletion following the bomb tests in 1962 with time and latitude as calculated by the LLNL model; the model estimates total ozone to have dropped by 56–68 DU (Dobson Units) at 70°N.

A depletion of similar magnitude has been reported for observations of total ozone from the Dobson network (Reinsel, 1981; Angell et al., 1985; Bojkov, 1987) (see Figure 7.10). However, the observed depletion tends to start well before the time predicted by the models. This discrepancy

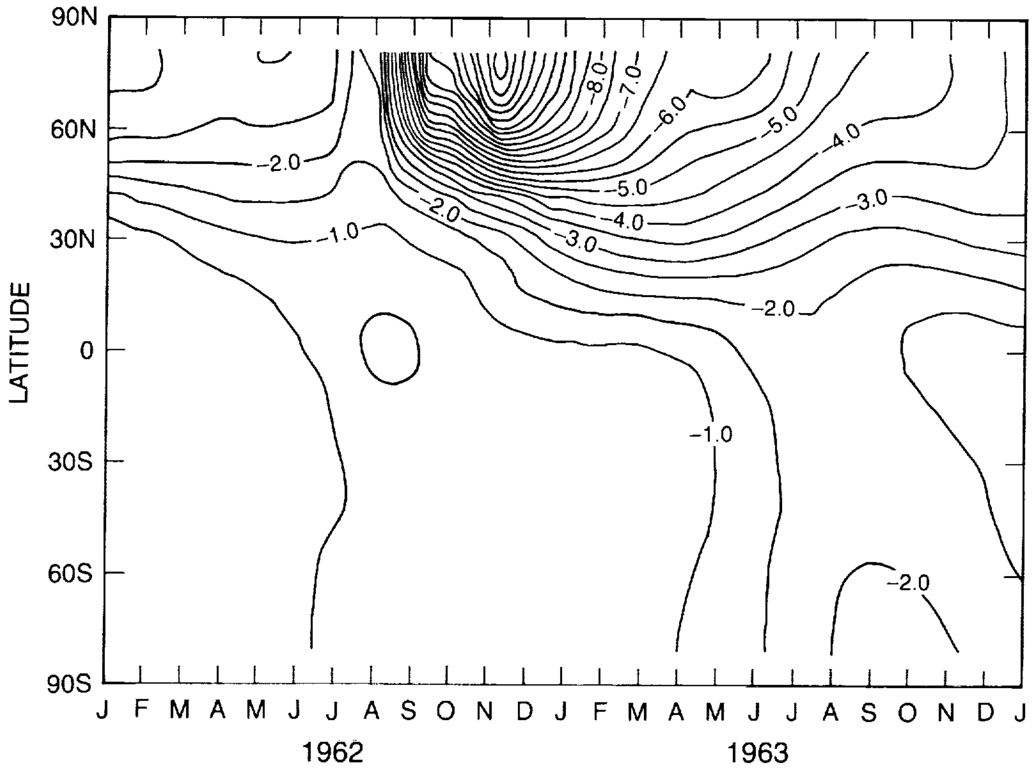

Figure 7.7 Calculated change (%) in column ozone changes as a function of time and latitude during the atmospheric nuclear tests. Results from the LLNL 2-D model are shown for 1962–1963.

could have many causes, including the limited geographic representativeness of the early Dobson network. Until the reasons for the discrepancy are better understood, it is difficult to draw conclusions from this comparison regarding the ability of the models to simulate the atmospheric test series.

We have studied the sensitivity of the above results to moderate differences in the scenario for NO generated by the atmospheric nuclear tests. The difference between a simulation using the reduced set of bomb tests (Table 7.6) and one using the full set, including the smaller bombs, is of the order of 10 percent for the Northern Hemisphere average, the full set giving the larger depletion (LLNL model). A similar comparison using the Oslo model yielded even smaller differences. Based on these considerations, we estimate that the bomb tests are likely to have produced an ozone depletion at high northerly latitudes in early 1963 of 25–75 DU. The corresponding range for the global average depletion is 3–15 DU. These estimates should be regarded as tentative, as there still are uncertainties connected to the models.

The absolute magnitudes of the calculated ozone depletion depends, among other things, on the adopted emission scenario for NO. The assumption of 1×10^{32} molecules of NO produced by each MT total yield of nuclear explosion, as used in the AER, Oslo, and Cambridge simulations, is probably uncertain by at least a factor of two (see discussion in Section 7.1.3).

As seen in Figures 7.6 and 7.7, the recovery time of the depletion following the major explosions is a few years. Five years after the major injection in late 1962, very little depletion remained. This is a feature common to all models.

7.3.3 Column Ozone: Comparison With Observations

The primary long-term data set that is available for comparison to model calculations is that for total ozone from the ground-based Dobson spectrophotometers. Approximately 30 years of data can be used for trend analysis. Satellite data give a better global coverage of ozone distribution but are available only from late 1978. In the following sections, ozone trends calculated with the four 2-D models will be compared with ozone trends deduced from the Dobson network. An example using data from the TOMS instrument on Nimbus–7 will also be used for comparison. The emphasis of these studies is to search for fingerprints from theoretical models that can use existing measurements to separate the changes due to solar cycle from those due to trace gases.

7.3.3.1 Theoretical Fingerprints for Solar Cycle and Trace Gases

We present two separate model calculations covering the period from solar maximum in 1979 to solar minimum in 1985: solar-cycle effects and concurrent changes in trace gases.

Calculated ozone changes due to solar-cycle effects alone are shown in Figure 7.8 for one model (Oslo), using the large solar-cycle case in Table 7.4. The main feature, which is the same for all four models, is the almost constant depletion of ozone with latitude and season ranging from 1.7 percent to 2.1 percent (Oslo model) going from solar maximum to solar minimum. For the small solar-cycle case, the Oslo model calculates ozone reductions of similar pattern, but smaller magnitude—about 0.7 percent.

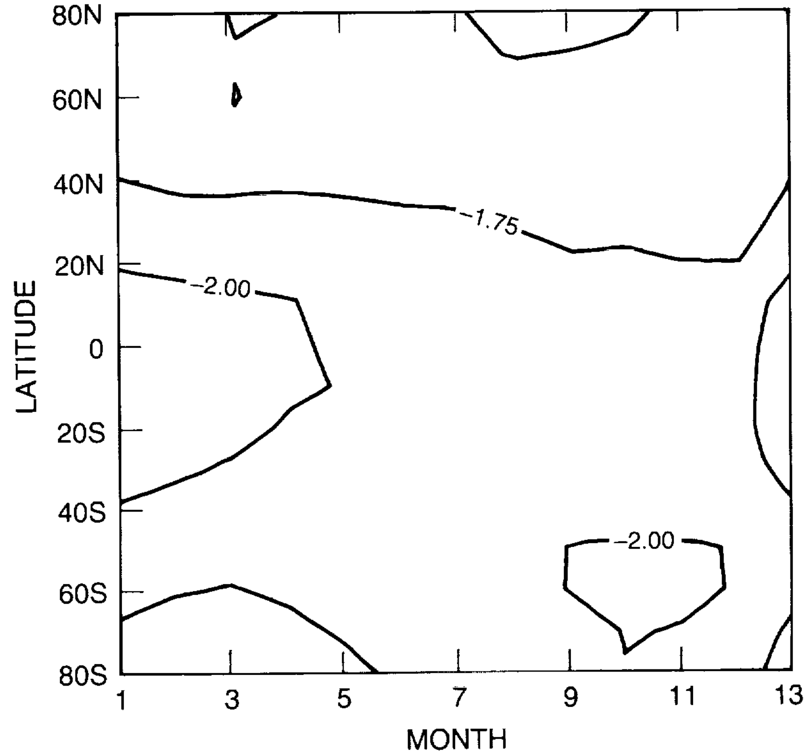

Figure 7.8 Calculated change (%) in column ozone from 1979–1985 as a function of latitude and month from the Oslo model. The results demonstrate the effect of solar cycle (maximum to minimum) alone, neglecting all other influences.

The calculation for the same period, but with only trace gas changes included (case 1), is shown in Figure 7.9. In contrast to the solar cycle case, all the models show distinct latitudinal and temporal patterns of ozone depletion, with the largest changes occurring at high latitudes during winter and spring (n.b., results from the Cambridge model were not available for this figure; the Cambridge model is known to produce a quite different pattern at high latitudes for trace-gas impacts on ozone). However, the magnitude of the depletion, a global average of order 0.3 to 0.6 percent over this period, is substantially less than that obtained for the solar-cycle

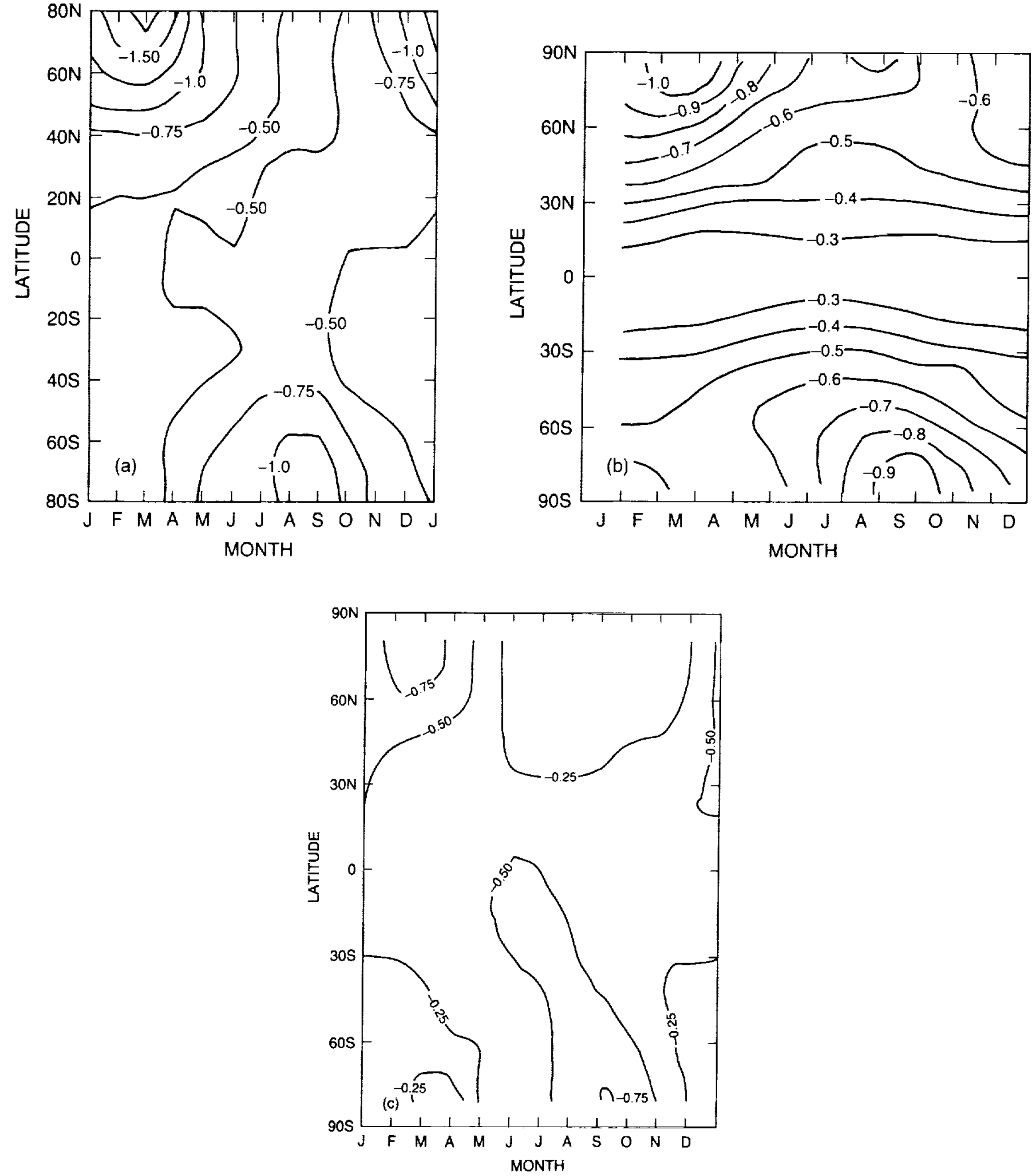

Figure 7.9 Calculated change (%) in column ozone from 1979–1985 as a function of latitude and month, considering trace gases only (case 1). Calculations are from the (a) Oslo, (b) AER, and (c) LLNL models.

effects in the large solar-cycle case. If we compare with the case for small solar-cycle variations, then trace gases become more significant, particularly at high latitudes.

The magnitude and phase of the solar cycle must be correctly taken into account in data analysis for comparison with the models. For example, results from the AER model showed that shifting the time period for comparison by 1 year (1978 to 1984) led to noticeable changes in the calculated solar-cycle impact. Our current model for the solar-cycle variations is simplistic (a sine curve), and future efforts will require a more realistic model scaled to solar activity, such as the 11-year pattern for sunspots or 10.7 cm flux.

7.3.3.2 Thirty Years of Dobson Data

Thirty years of total ozone observations have been reanalyzed by Bojkov (1987) and presented in Chapter 4 of this report. The data have been divided into latitude bands, based on station location. The three latitude bands for which there were sufficient data to construct a meaningful average are shown in Figure 7.10 (30–39°N, 40–52°N, 53–64°N). For each of these latitude bands, calculations from the four models are superposed.

The observations show a distinct biennial oscillation, which is particularly pronounced at high latitudes. This feature is not seen in the calculations for reasons that already have been discussed. Also, there is an apparent solar-cycle variation that is broadly in agreement with the calculated solar-cycle variation. However, any trends related to trace gas releases are difficult to deduce from Figure 7.10 due to the large variability of the observations.

7.3.3.3 Global Data From Satellite, 1979–1987

A characteristic of the Dobson data presented for latitude bands in Figure 7.10 is its variability on all time scales. Much of this variability is meteorological and can be removed by the more complete coverage of satellite data available from late 1978. Even when satellite data are used to integrate over large areas of the globe, however, significant variability remains. Figure 7.11 shows one example using data from the TOMS instrument on Nimbus–7. The dots are the daily values of the area-weighted integral of total ozone from 65°S to 65°N over the 9-year data record. The point values are relative to the 9-year average for that particular week; the line through the points is a 60-day running mean. Also shown by a heavy line is the annual average calculated by the Oslo model, including both solar cycle and trace gas effects. The TOMS result is similar to that previously presented by Heath (1988) for SBUV data, except in this case, the TOMS data have been corrected as a function of time over the 9-year period by adjusting to the Dobson record (i.e., using satellite overpasses and subtracting the mean difference between the two records). As can be seen in the figure, the long-term changes in total ozone calculated by the model are in general agreement with observations, but the data exhibit significant variability relative to the long-term changes. It is not clear whether we should regard this failure to reproduce the observed variability as a fundamental discrepancy between models and theory or, more likely, as an inherent limitation in the 2-D nature of the models.

Additional information can be obtained from the seasonal and latitudinal behavior of the change in total ozone, as shown in Figure 7.12 for TOMS data, where the difference between the mean of the years 1985 plus 1986 and the mean of the years 1979 plus 1980 is plotted. The data have been adjusted to account for the drift of TOMS with respect to Dobson overpasses. The springtime Antarctic ozone hole is clearly visible, with changes of greater than 30 percent (see

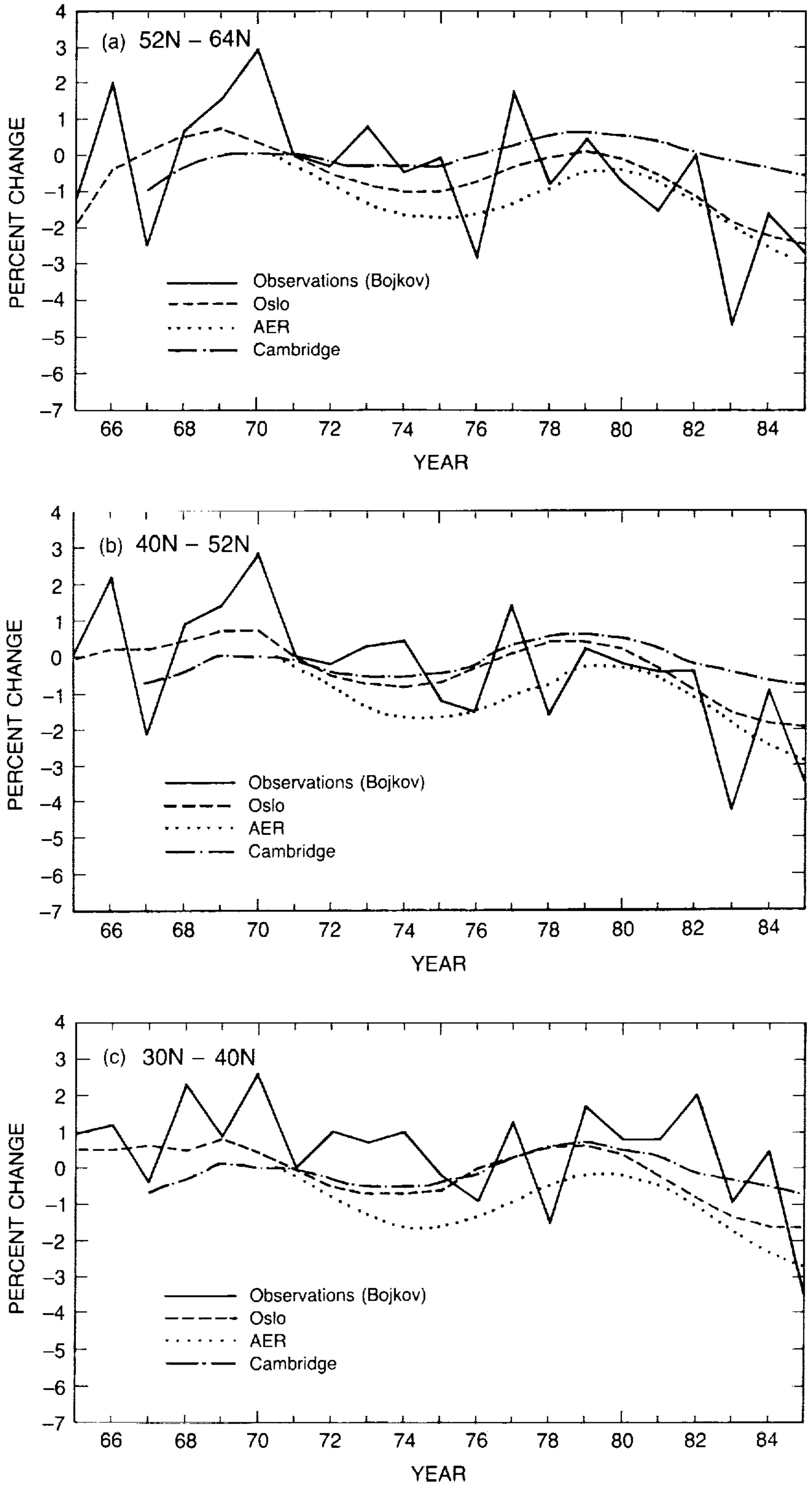

Figure 7.10 Timeline of percent change in column ozone from 1965 to 1985 for the latitude bands (a) 52–64°N, (b) 40–52°N, and (c) 30–40°N. Reevaluated data from the Dobson network (see Chapter 4) are shown by the thick line. Calculations from three models (Oslo, AER, and Cambridge) are also shown for comparison.

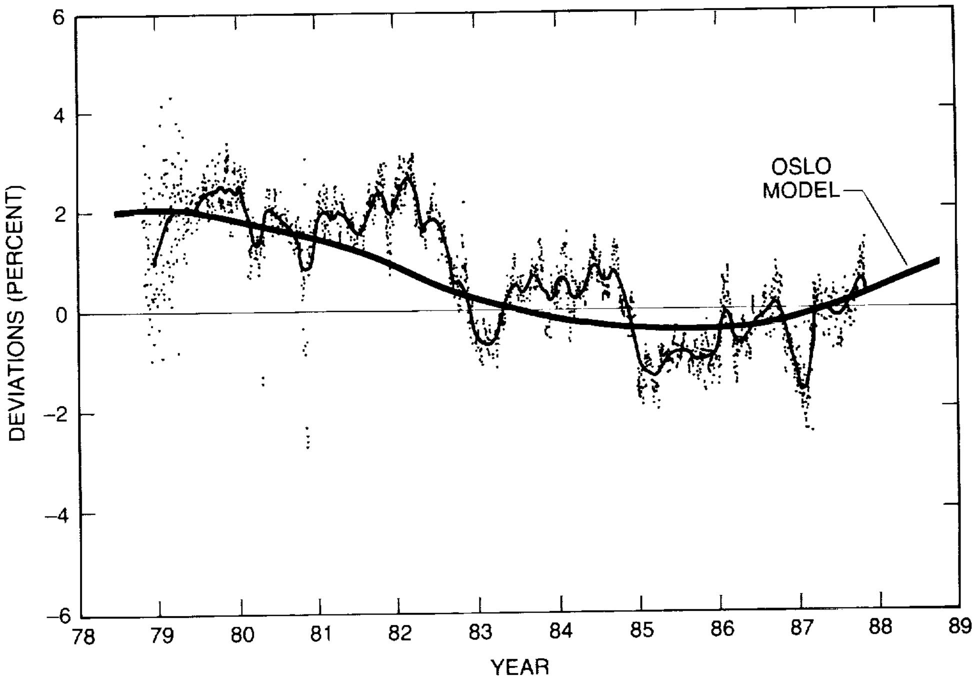

Figure 7.11 TOMS data for column ozone integrated from 65°S to 65°N are shown for 1978–1987. The TOMS satellite data have been normalized to the ground-based Dobson network. The points represent percent deviations of the daily average from the 9-year average for that particular week; the thin solid line is a 60-day running mean through the points. The thick solid line shows calculated total ozone (Oslo model) for this period.

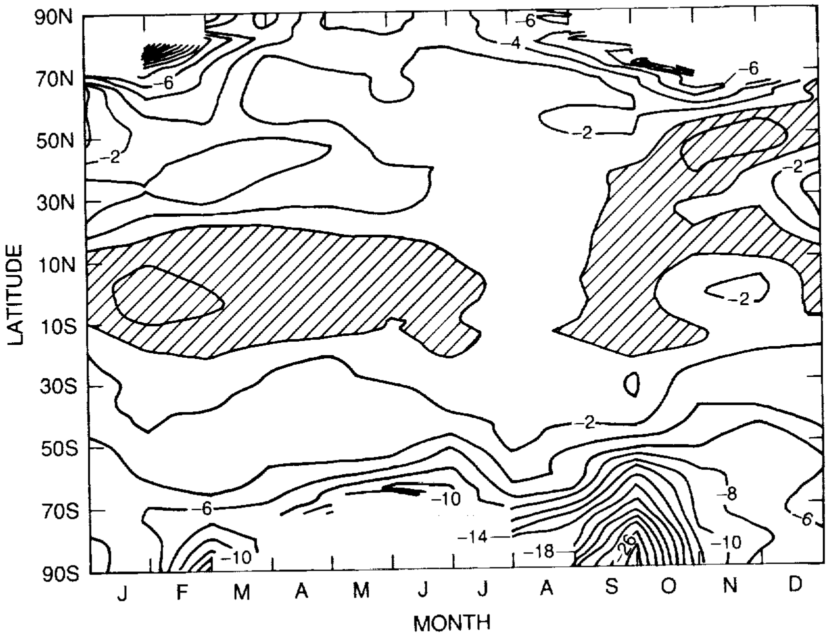

Figure 7.12 Observed change (%) in column ozone from TOMS data, the average of 1985–1986 minus the average of 1979–1980. The TOMS data have been recalibrated and do not reflect the currently archived data: TOMS data for 1985 and 1986 have been increased by approximately 4 percent to account for drift with respect to Dobson network.

Chapter 11). In addition to this primary signal, the data also show noticeable depletions at high latitudes in late fall, winter, and early spring. This pattern is closer to the calculated fingerprint for trace gases than it is to that for the solar cycle (see Figures 7.8 and 7.9). There is a possible indication from these TOMS data that the magnitude of the decrease in the winter at high latitudes may be more pronounced than that calculated in the models.

Calculations of the combined effects of trace gases and solar cycle from 1979 to 1985 are shown in Figure 7.13 as a function of latitude and season. The predominant change is a global net

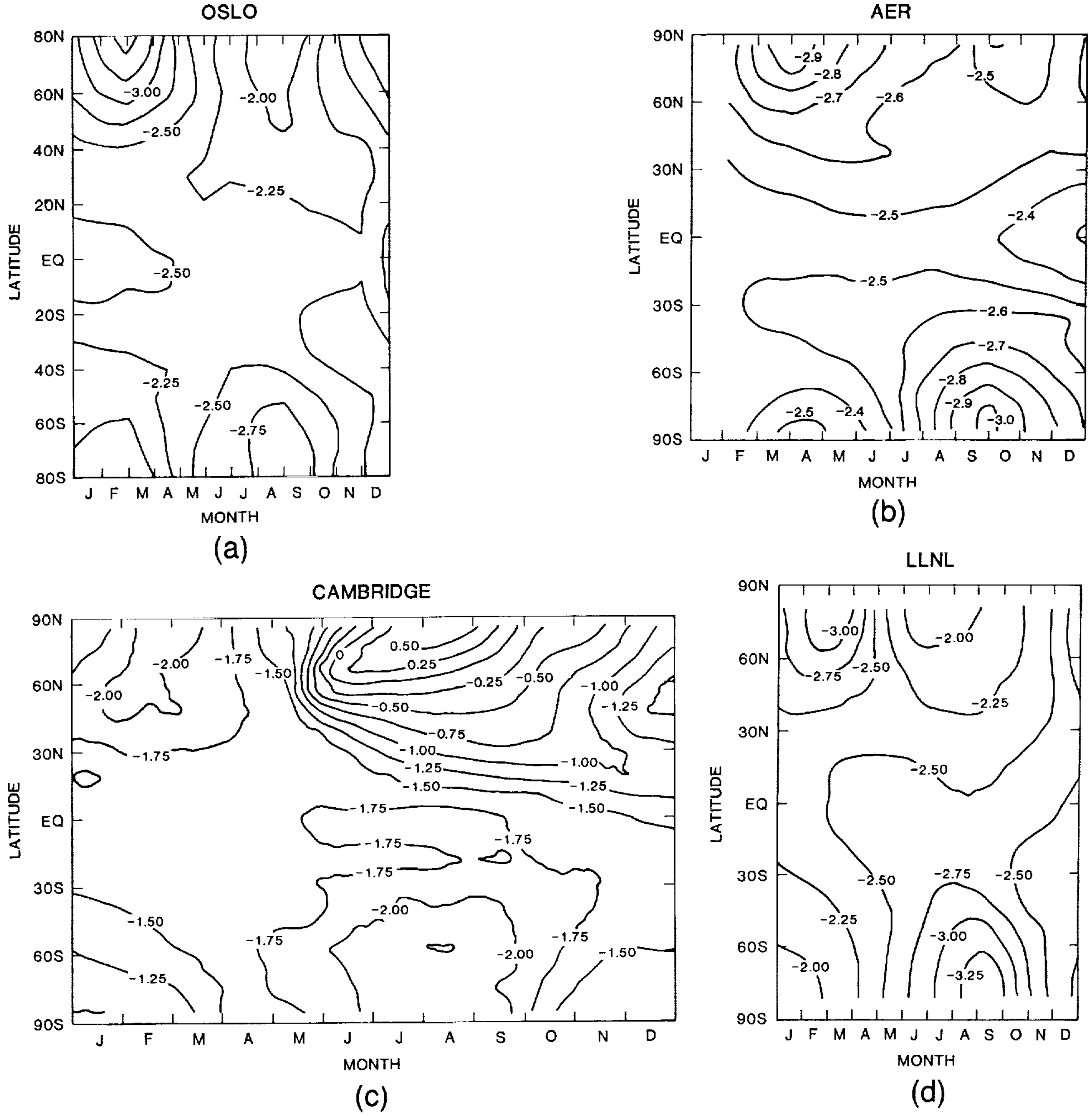

Figure 7.13 Calculated change (%) in column ozone as a function of latitude and season from 1979–1985, including effects of trace gases and solar cycle. Calculations are from the (a) Oslo, (b) AER, (c) Cambridge, and (d) LLNL models.

decrease of order 1.5 to 2.5 percent that is associated with the solar cycle, and a smaller influence of the trace gases that is superimposed. Three of the models show similar variations, with largest decreases at high latitudes during winter, but the Cambridge model gives a markedly different result with ozone increases as large as 0.5 percent at high latitude during summer. The cause of this difference is not yet understood.

7.3.3.4 Subtracting the Solar Cycle From Dobson Data

One way to separate the solar cycle and trace gas effects is to use the Dobson data over two complete 11-year solar cycles. Bojkov (1987) in Chapter 4 has done this by comparing the records during two different seasons for two 11-year averaging period: 1965–1975 and 1976–1986. Figure 7.14 shows the difference between these 11-year records for the summer season (May–August) and the winter season (December–March) from each of 36 stations that are plotted as a function of station latitude. The summer season differences are small and consistent with the two model calculations, also shown in Figure 7.14. Decreases during the winter season are pronounced, and generally much larger than the model predictions, particularly north of 30°N. Model calculations

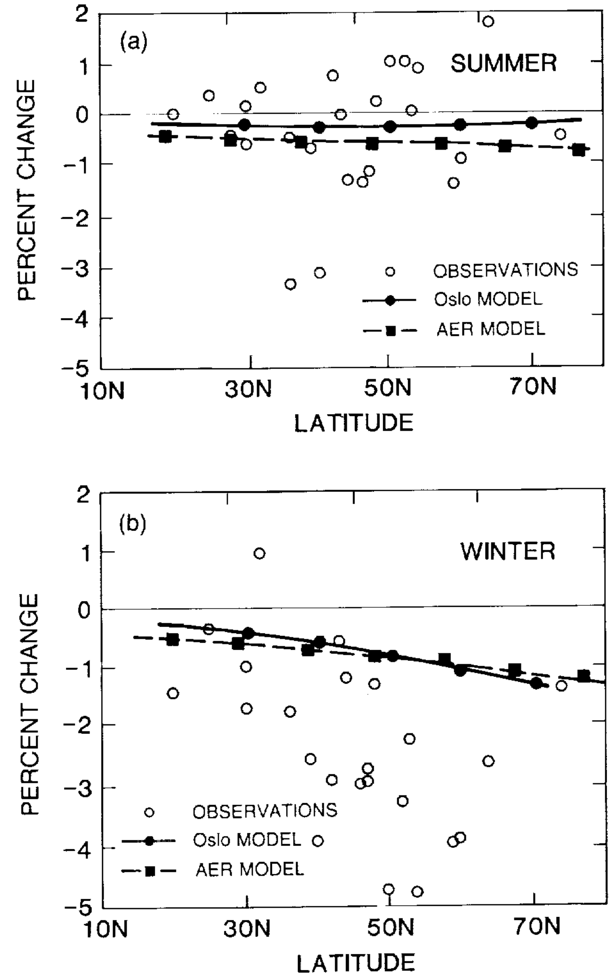

Figure 7.14 Observed change (%) in column ozone between the 11-year (solar-cycle) averages 1965–1975 and 1976–1986 for (a) summer season (May–June–July–August) and (b) winter season (December–January–February–March). Points representing values from single stations are plotted as a function of station latitude. Results from two 2-D models (Oslo and AER) are also shown.

(AER and Oslo) are in qualitative agreement with observations in that depletion increases toward higher latitudes, but the magnitude of the decrease predicted near 50°N (about -1 percent) is substantially less than that observed (about -1.5 to -4.5 percent).

If the similar feature seen in the TOMS data for 1979–1986 is robust (i.e., survives the current recalibration of the data set), then it is likely that current 2-D models underestimate the decreases in total ozone that have occurred at high northern latitudes over the last one to two decades. It is difficult at present to explain the cause of this discrepancy; however, it may be that the present 2-D models are missing some chemical processes, quite possibly heterogeneous chemistry that is particularly important at high northern latitudes, similar to that associated with the Antarctic ozone hole.

7.3.4 Profile Ozone: Comparison With Observations

We now examine the model-calculated changes in the local concentrations of O_3 as a function of latitude and altitude; we hope to associate different patterns of change with the geophysical forcing included in the models: trace gases, solar cycle, and atmospheric nuclear tests. This analysis will concentrate on the calculated differences between 1979 and 1985 (solar maximum to solar minimum). For this period, we have global data from satellites (SAGE–I and SAGE–II, SBUV) and limited coverage from ground-based observations (Umkehr). We focus on small percent changes in the vertical profile of ozone concentrations and look for latitudinal effects.

7.3.4.1 Fingerprints of the Solar Cycle and Trace Gases

Ozone perturbations induced by the solar cycle alone (1979–1985, maximum-to-minimum, no trace gas changes) as calculated by the models are shown in Figure 7.15a as a function of height and latitude. Solar flux changes for the large solar-cycle model are used in these calculations. The decrease in UV intensities leads to decreases in stratospheric ozone at all latitudes and altitudes. The models predict a broad maximum around 40 km, with ozone changes between -1.5 and -3.0 percent. Calculations with the small solar-cycle model give a similar pattern, but with substantially smaller ozone perturbations. A characteristic pattern for the solar-cycle-induced changes is that the latitudinal gradients are moderate at all altitudes.

The calculated changes in O_3 concentrations between July 1979 and July 1985 for case 2 (trace gases plus solar cycle) are shown in Figure 7.15b–e for all four models. Ozone changes in the upper stratosphere (1–3 mb, 48–40 km) are dominated by the effect of chlorine increases rather than solar cycle (compare Figure 7.15a with 7.15b). The effect of trace-gas changes has a pronounced latitudinal pattern and is approximately twice as large as that from the solar cycle. Maximum depletion of ozone occurs about 2 mb (43 km) and ranges from -7 ± 2 percent in the Tropics to -10 ± 2 percent at mid- and high latitudes. From 1979 to 1985, the models predict decreases in *stratospheric* ozone at almost all latitudes and altitudes, the one exception being the Cambridge model, which predicts increases in the high-latitude lower stratosphere during summer. The upper stratosphere is, therefore, an area where the impact of CFC's can be more readily detected, as the trace-gas effects dominate the solar cycle for the period 1979 to present.

Results from all models show similar morphology in the upper stratosphere, although there are some differences near the winter pole. These variations may indicate the different way in which models treat the chemistry near the polar night, or may reflect differences in stratospheric transport at high latitudes. The magnitude of the maximum calculated change is almost twice as large in polar regions relative to the Tropics in three of the four models, whereas the LLNL model

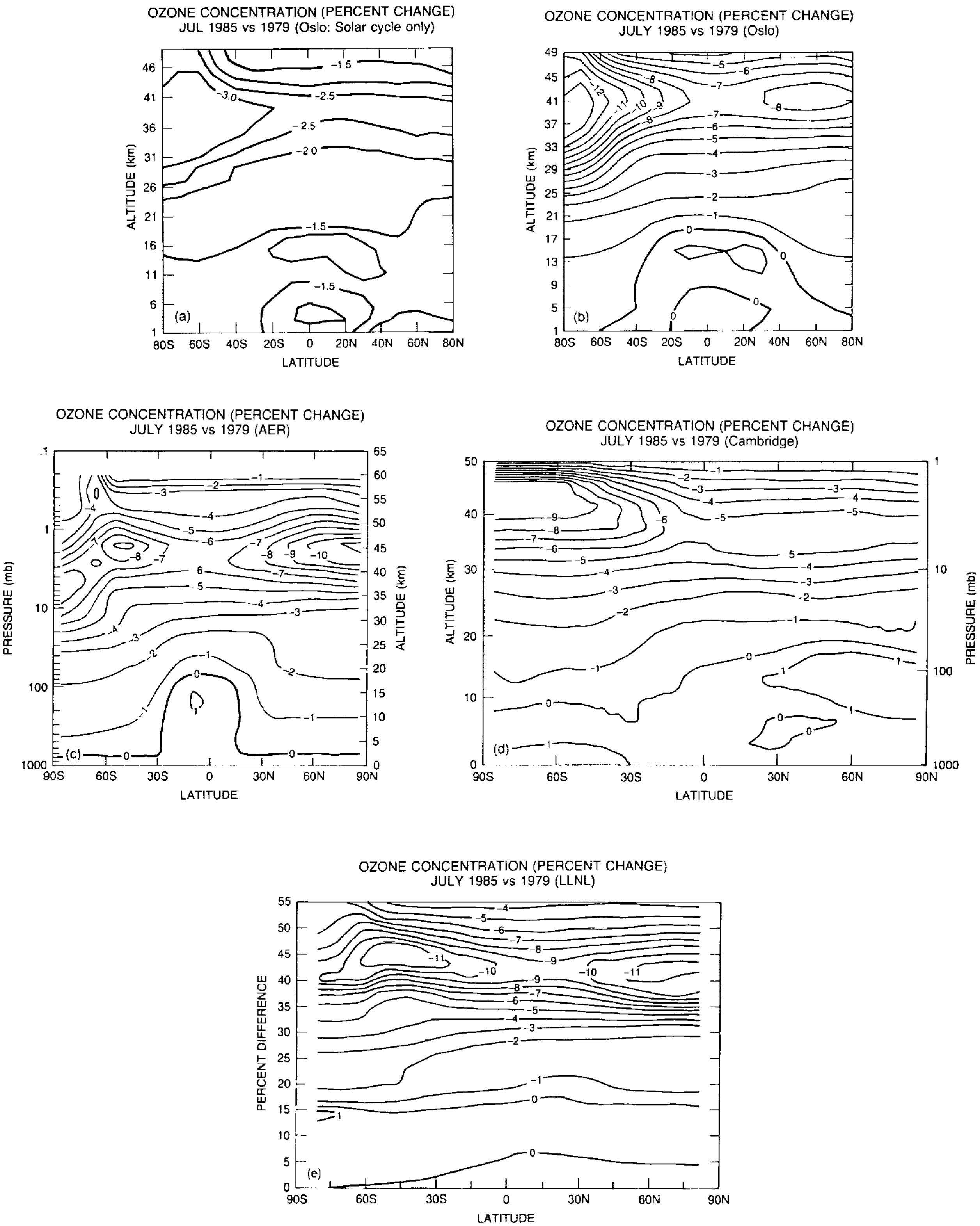

Figure 7.15 Calculated height–latitude changes (%) in ozone from July 1979 to July 1985 for solar cycle only from the Oslo model (a), and solar cycle plus trace gases (case 2) from the (b) Oslo, (c) AER, (d) Cambridge, and (e) LLNL models.

shows smaller latitudinal gradients at the altitude of maximum depletion (43 km). This latitudinal gradient in ozone depletion is, in part, a reflection of the relative distribution of ClO and CH_4. The ratio of ClO to CH_4 increases toward high latitudes in the upper stratosphere, making the chlorine-catalyzed destruction of ozone more efficient.

In the lower stratosphere and troposphere, calculated ozone changes are small and show different patterns among the four models. Changes to ozone in the lower stratosphere dominate the perturbations to the ozone column. Comparison of the model results with observations in the lower stratosphere are further complicated by the effects of annual, semiannual, and quasi-biennial oscillations, which are not included in any of the simulations.

In the troposphere, calculated ozone changes are small and also show significantly different patterns among the four models. In general, ozone concentrations increase in the troposphere, although the pattern is quite different among the models and the magnitude is much less than that reported from analysis of the limited data base of tropospheric measurements (see Section 7.3.5). The predicted changes to tropospheric ozone would have little influence on the changes in the ozone column, but increases as large as +10 percent over this period (as reported by some analyses) could alter the total column ozone by as much as +1 percent.

Systematic changes in stratospheric temperatures over 1979–1985 would affect the calculated change in ozone. For example, an increase in stratospheric temperatures tends to increase the efficiency of photochemical loss of ozone and thus reduce ozone concentrations. The temperature may change due to variations in solar heating (proportional to ozone concentrations), in the radiative cooling of other trace gases, or in the dynamical transport of heat. The primary change in temperature over this period as calculated by the current models is a major reduction throughout most of the upper stratosphere (30–50 km) in response to the reduced ozone concentrations and, hence, reduced solar heating. The reduction in temperature calculated by the Oslo model partially offsets the ozone depletion in the upper stratosphere, reducing the magnitude by approximately 20 percent (see Table 7.10).

Previous analyses of Umkehr data for the 1970's have reported statistically significant decreases in upper and middle stratospheric ozone during this period (Angell and Korshover, 1983b; Reinsel et al., 1984). Observations indicate a maximum ozone reduction of the order of 3–4 percent in Umkehr level 8; most of the Umkehr stations used in the data analysis are located between 30–50°N. Results from three models (Oslo, AER, and LLNL) for 1970–1981 are shown in Table 7.10 for comparison. The calculated values are from case 1 (trace gases only) for 40°N and Umkehr layers 5 through 9.

Table 7.10 Calculated Trends in Ozone at Umkehr Levels 5–9 for 1970–1981; Trace Gas Scenario Only

Umkehr Level	Oslo (T feedback)	Oslo (T fixed)	LLNL (T fixed)	AER (T fixed)
9	−6.5	−8.9	−9.3	−6.9
8	−6.8	−8.3	−11.0	−7.0
7	−3.7	−4.2	−4.9	−3.1
6	−1.5	−1.5	−1.5	−1.2
5	−0.5	−0.5	+0.2	−0.5

Results are for case 1 (trace gas only).

Results from the different models compare well in the lower layers, but there is a significant difference in layers 8 and 9, where the LLNL model gives the largest calculated change in ozone over 1970–1981. We are unable at present to explain these differences and await a more complete model intercomparison. Calculations with the University of Oslo model were done with fixed temperatures and with a parameterization for the change in temperature due to increased CO_2 and changes in O_3. As noted above, temperature feedback is important in calculating ozone change, particularly in the upper stratosphere, layers 7, 8, and 9. Although in qualitative agreement with observations, all models give calculated changes in ozone in Umkehr levels 8 and 9 that are substantially larger than those determined from analysis of Umkehr data; the comparison is better at the lower levels.

All models show that the upper stratosphere is the altitude region most sensitive to trace gas releases, and that the magnitude of the effect exceeds effects introduced by solar-cycle variations. The models also predict strong latitudinal gradients due to increases in trace gases, in contrast to the impact of the solar cycle. Therefore, the upper stratosphere is the region where it should be possible to identify the fingerprints of trace gases on ozone. Such identification, however, will depend critically on the quality and global representation of the observations.

7.3.4.2 Trends in Vertical Structure, 1979–1985

Figure 7.16 compares the changes in the altitude profile of ozone from SAGE–I (1979–1980) to SAGE–II (1984–1985, latitude belts 20–50°N and 20–50°S) and from the Umkehr network (stations

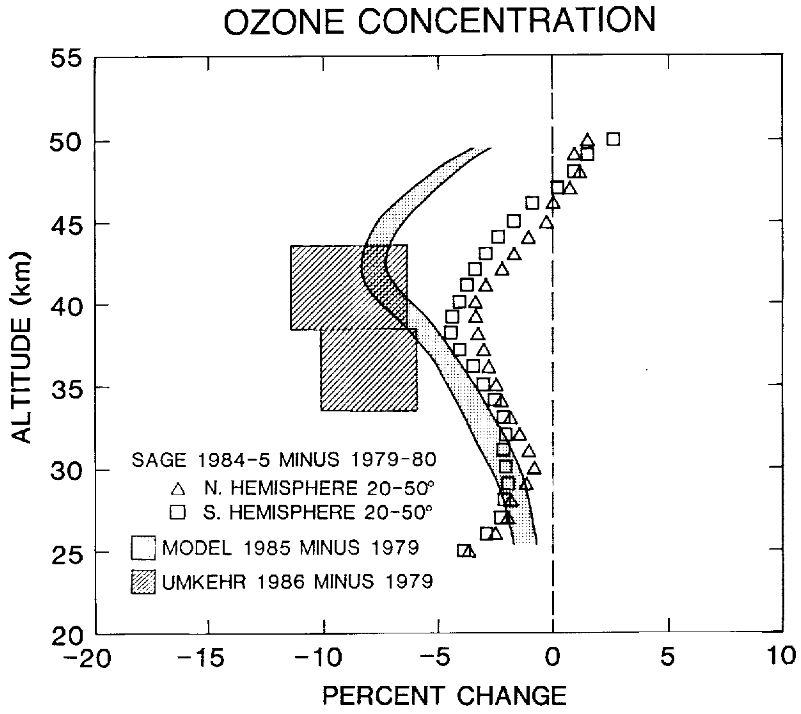

Figure 7.16 Observed changes (%) in stratospheric ozone profiles from different instruments over 1979–1986. Differences between SAGE–I (1979–1980) and SAGE–II (1984–1985) measurements are shown for northern and southern latitudes (20°–50°). Umkehr observations from 1979–1986 are limited to northern midlatitudes. The band shows the range of model calculations (1979–1985, midlatitude, Oslo model) for both large and small solar-cycle models.

C-2

between 36°N and 52°N) to the calculated change in ozone profile from the Oslo model (midlatitudes). Analysis of Umkehr data for trends during 1979–1986 is complicated by the strong interference of aerosols following the El Chichón eruption. One recent report, however, claims that it is possible to correct partially for this interference and, thus, to deduce upper stratospheric ozone changes over this period (see Chapter 5).

Both observations and models show ozone depletions that increase with altitude, peaking around 40–45 km. The calculated depletion in the upper stratosphere is larger than that reported from the SAGE observations, but slightly smaller than that from the Umkehr analysis. The discrepancy with the SAGE data is most pronounced around 50 km, where observations show a slight ozone increase. However, there is a possible systematic difference in derived ozone values between the two SAGE instruments that may be as large as ±4 percent (see Chapter 5). The scale on the SAGE curve in Figure 7.16 could be shifted by as much as 4 percent, bringing the observations into better agreement with the calculations between 30 and 45 km, but still not explaining the small change above 45 km or the significant depletion below 30 km. Similarly enhanced ozone depletion in the lower stratosphere is deduced from ozonesonde data for the last two decades over Germany (Bojkov and Attmanspacher, 1988); however, changes of this magnitude in the lower stratosphere should be clearly evident in the total ozone column—and this is not apparent from the ozone column data.

The currently archived SBUV data for the same period show ozone depletions that are substantially larger than the models or data shown in Figure 7.16 and that have a distinctly different profile: a maximum ozone depletion of approximately 20 percent is found at 50 km. It is believed that these data cannot be used to determine changes in the ozone profile (see Chapter 5).

7.3.5 Tropospheric Ozone

7.3.5.1 Impact on Column Perturbations

Although only about 10 percent or less of the total ozone column is located in the troposphere, increases in tropospheric ozone that have occurred over the last few decades might have produced a detectable change in the ozone column. Therefore, observed trends in total ozone must not be interpreted uncritically as reflecting stratosphere changes alone. Similarly, it is important for models to include tropospheric processes in a realistic way if they are to attempt to simulate changes in total ozone.

There are indications that the ozone levels in surface air are substantially higher in the present atmosphere over Europe and the U.S. than those found during the end of last century (Bojkov, 1986c; Kley et al., 1988), and that, during the last two decades, an increase of ~1 percent per year has taken place in the free troposphere over most of the observing sites in the Northern Hemisphere (Bojkov, 1988b). Measurements over the last 30 years show substantial increases, ~50 percent, during this period at surface levels over East Germany (Warmbt and Feister, 1984). The increases are not confined to the planetary boundary layer, but are observed also in the free troposphere. Ozone increases are observed to be largest northward of 40°N, with strong latitudinal dependence. Increases are particularly large over and around industrialized areas in Europe and North America (Logan, 1985). For example, ozonesonde observations over West

Germany (Bojkov and Attmanspacher, 1988) report increases much larger than 1 percent per year throughout the troposphere over the last 20 years.

Assuming that the reported increases in tropospheric ozone, ~1 percent per year, are representative of average conditions throughout the Northern Hemisphere for the last two decades, we can estimate the impact on the total ozone column. Tropospheric ozone should have produced an increase in column ozone of about 1 percent from 1970–1985 and about 0.5 percent from 1979–1985. Increases over industrialized areas would have been substantially greater, but these areas are a small fraction of the hemisphere. Therefore, the observed downward trend in total ozone at most northern sites might actually be larger than measured, being partially compensated for by increases in tropospheric ozone.

7.3.5.2 Uncertainties in the Estimates

The observed increase in tropospheric ozone is likely caused by anthropogenically induced increases in the concentration of precursor gases NO_x, CH_4, nonmethane hydrocarbons (NMHC), and CO, although quantitative estimates are connected with large uncertainties (e.g., Isaksen and Hov, 1987). A main uncertainty in modelling tropospheric ozone comes from our lack of knowledge of NO_x distribution in the troposphere. Due to short chemical lifetime (days or less) and uneven source distribution, NO_x shows strong temporal and spatial variations in the troposphere. The efficiency of the CH_4–NO_x chemistry for ozone production is strongly and nonlinearly dependent on NO_x levels, and the 2-D formulation of the current models is limited in representing the spatial variations in tropospheric NO_x. Additional uncertainties in ozone production and trends in the troposphere are introduced by our lack of knowledge of long-term trends in CO, NMHC, and NO_x.

The 2-D models used in this study all have a very crude representation of tropospheric processes. They do, in general, predict an increase in tropospheric ozone during the last two decades, but this increase is global and not limited to the northern midlatitudes, for which observations indicate substantially larger increases. Production of tropospheric ozone in the Northern Hemisphere may be underestimated because the models do not include any trends in short-lived anthropogenic species like CO, NO_x, and NMHC. According to model calculations with a 2-D tropospheric model by Isaksen and Hov (1987), these species may have a significant impact on the production of tropospheric ozone, particularly at high northern latitudes, and can yield ozone increases of approximately 1 percent per year.

Changes in the chemical composition of the troposphere may also influence stratospheric ozone indirectly through changes in the oxidation rate of trace species such as CH_4, CH_3CCl_3, CHF_2Cl, CH_3Cl, and CH_3Br. The atmospheric lifetimes of these species, and hence their concentrations, are determined by the tropospheric distribution of the hydroxyl radical, OH. It has long been known in tropospheric modelling that increases in CH_4 and CO can markedly reduce global OH (Sze, 1977) and that this may have occurred over the past few decades (Thompson and Cicerone, 1986). Increases in the NO_x levels, on the other hand, will increase OH levels through a more efficient conversion of HO_2 to OH through reaction with NO. In model calculations, Isaksen and Hov (1987) showed that the 1 percent per year growth in CH_4 coupled with a 3 percent per year growth in anthropogenic releases of CO, NMHC, and NO_x would produce little net change in tropospheric OH. Modelling of tropospheric chemistry is inherently more complex because of the greater range of heterogeneity in the troposphere; tropospheric results from the current 2-D stratospheric models must be regarded with caution.

7.3.6 Future Ozone Changes (1985–1990)

For the 7 years 1979–1985, trace gases and the solar cycle are calculated to act on ozone in the same direction. However, after 1985, trace gases and the solar cycle are expected to act on ozone in opposite directions as the increasing solar UV (ozone increases) is counteracted by the increase in stratospheric chlorine (ozone decreases). Figure 7.17 shows the calculated changes in globally averaged column ozone over one cycle from solar maximum to solar maximum, 1979–1990. Results from the Oslo model are shown for both the large and small solar-cycle cases. In the large solar-cycle case, the ozone changes from 1985 to 1990 are still dominated by solar-cycle effects, and ozone is predicted to increase by approximately 1.5 percent. In the small solar-cycle case, trace-gas effects are comparable, and total ozone increases are small, of the order 0.3 percent, from 1985 to 1990.

The picture is quite different when we look at predicted column ozone changes as a function of latitude where the trace gases have distinct fingerprints (i.e., largest depletions at high latitudes) and where the solar-cycle effects are uniform. Ozone increases from 1985 to 1990 in the large solar-cycle case are substantially smaller at high latitudes than for the global average. In the small solar-cycle case, trace gases dominate over solar cycle effects at mid- and high latitudes, leading to ozone decreases.

Over the next 5 years, detection and clear identification of the trace-gas signal in stratospheric ozone will require an accurate model for the solar cycle and its impact on ozone. Ozone trends in the near future depend critically on the magnitude of the solar UV variations. It is important to remember that, after 1991, when the solar cycle and trace gases again act in the same sense, total ozone is expected to decrease.

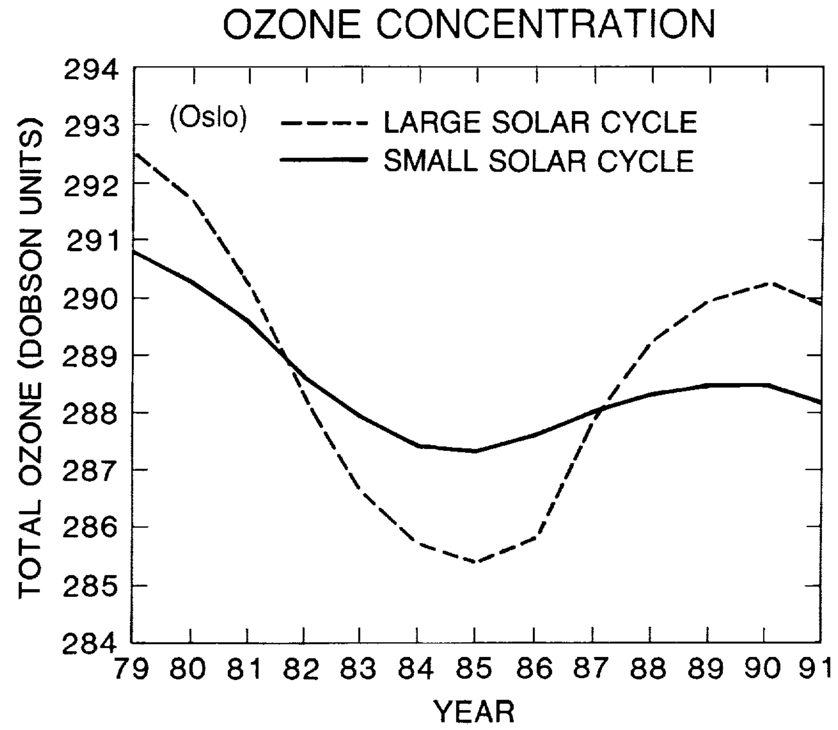

Figure 7.17 Model calculations (Oslo) of globally averaged column ozone (Dobson Units) from 1979 extended to 1991 for the large (dashed line) and small (solid line) solar-cycle variations.

7.3.7 How Good Are the Models?

The models participating in this study have a certain degree of realism in that they can predict absolute concentrations of ozone, including its latitudinal, altitudinal, and seasonal variations. This general success of the models regarding ozone does not, of course, imply that the models can correctly describe all the remaining chemical species of the stratosphere. Nor, for that matter, does it imply that perturbations to ozone can be predicted with great confidence.

In this study we have made several systematic comparisons among the four 2-D models. These intercomparisons show a good qualitative, and even quantitative, agreement between the models in most cases. Some of the disagreement can be understood from the differences in model structure. However, there are important differences in predictions for the lower stratosphere, which clearly underline the need for further comparisons both among models and between models and observations, especially in the lower stratosphere. The ultimate test of predicting trends with these models would be a comparison between calculated and observed variations on a time scale of decades, such as we have attempted here with only limited global data.

An obvious failing of all the stratospheric models used in assessing future perturbations to ozone was the Antarctic ozone hole. From intensive studies of the Antarctic ozone problem (see Chapter 11) we have found that PSC's play a major role in the gas-phase chemistry of the lower stratosphere, and even have identified an important new species in the laboratory, Cl_2O_2, with a new catalytic cycle for destruction of ozone. Furthermore, we have recognized the unique stratospheric circulation associated with the Southern Hemisphere, in particular the isolation of the springtime Antarctic vortex. We have found unusually low levels of long-lived trace gases (N_2O, CFC's) in the wintertime lower stratosphere over both poles. These recent findings have led to substantial revisions both to the chemistry and transport of stratospheric models, but the changes to the models will not fix all of the discrepancies with regard to observations. Most of these improvements have not yet been applied to the type of calculations described here, although in the next 2 years we should expect to see assessments of future ozone change, including the effects of heterogeneous chemistry, PSC's and precipitation, and winter polar vortices.

Future studies and assessments should attempt to improve our confidence in the stratospheric models by addressing the following questions:

- Which species should we measure to provide key tests of models?
- Can we design strategies to detect early changes in the ozone?
- How do we define a "good fit" between models and observations?

7.4 CONCLUSIONS

Ozone concentrations in the atmosphere vary on different time scales and for several different causes. The models described in this chapter are designed to simulate the effect on ozone of changes in the concentration of such trace gases as CFC, CH_4, N_2O, and CO_2. Changes from year to year in UV radiation associated with the solar cycle are also included in the models. A third source of variability explicitly considered is the sporadic introduction of large amounts of NO_x into the stratosphere during atmospheric nuclear tests.

On the other hand, the models are not designed to simulate variations associated with weekly meteorological variations, but should be able to calculate the average seasonal variation. Thus, the effects of the pronounced QBO in the wind systems of the lower stratosphere and of the ENSO on circulation of the tropical troposphere are not considered in the models. Another important limitation of the models is that they do not attempt to simulate effects of volcanic eruptions or of condensed-phase processes in general (i.e., heterogeneous chemistry and physics). This means that the Antarctic ozone hole does not show up in any of the model simulations discussed here.

The performance of the models has been tested by comparing the simulations against observations of ozone and some other key chemical compounds. The observations exhibit substantial variability in both space and time that is not reflected in the model simulation. Nevertheless the average seasonal variations of the ozone concentration as a function of height and latitude are simulated quite well. We have difficulty quantifying the uncertainty associated with the calculations of ozone changes due to systematic changes in forcing, such as increasing concentrations of CFC's. The ultimate test of the models in this context is a comparison between calculated and observed variations on time scales of years to decades.

A major source of uncertainty in 2-D models is the treatment of the troposphere: its chemistry, its zonal inhomogeneities, and the ability to predict changes in tropospheric ozone due to trace gas changes (CH_4, NO_x, NMHC's, CO). Over the time period considered here, increases in tropospheric CH_4, CO, and NO_x are likely to have led to significant increases in tropospheric ozone. Changes in tropospheric ozone may be large enough ($\sim$10 percent) to obscure small changes ($\sim$1 percent) in total column ozone resulting from changes in the stratosphere.

The series of atmospheric nuclear tests during the late 1950's to early 1960's represent an interesting test case. All four models show a substantial, though different, depletion of total ozone during the year following the large explosion in late 1962. A depletion of similar magnitude seems to be borne out by the observations of total ozone. However, the data are sparse and may not be representative of this period. Furthermore, the observed decrease in ozone appeared to start prior to the main bomb tests. No firm conclusions can be drawn from this simulation of the atmospheric nuclear tests.

Calculated changes in ozone due to increasing trace gas have specific patterns with latitude, altitude, and season (i.e., fingerprints) that differ from those resulting from solar-cycle variations. The primary impact of the trace-gas scenario is due to increasing levels of stratospheric chlorine. The fingerprint on column ozone of the trace gases for 1979–1985 shows a maximum variation at high latitude, with larger decreases occurring during late winter (0.75–1.5) percent and smaller decreases during summer (0.25–0.5) percent. A uniform decrease of 0.3–0.5 percent over the Tropics is estimated in the three models for which comparisons are available. The corresponding vertical profiles show depletion peaked at 40 km of the order of 7–10 percent at high latitudes and 3–5 percent in the Tropics.

As solar activity declines from maximum to minimum (1979 to 1985), the column ozone is predicted to decrease almost uniformly across all latitudes and seasons. The magnitude of this change in column ozone depends on the UV variations and ranges from about -2 percent for the large solar-cycle case to about -0.7 percent for the small solar-cycle case. The corresponding profiles decrease everywhere above 25 km with a broad extreme of about -3 percent near 40 km—a pattern that is less pronounced but similar to that from increases in CFC's.

Can we distinguish between solar-cycle changes in ozone and those induced by increases in CFC's and CH_4? The answer to this question requires the testing of all aspects of the fingerprints of the two perturbing influences. The first approach is to look at the long-term record from the Dobson network in a search for a cyclic change in column ozone that is correlated with solar activity over the solar cycle. The statistical uncertainty of the observed amplitude is large, and the solar cycle amplitude not well known. For this reason, the trace-gas signal cannot be clearly separated from the record by subtracting the solar effect.

Another approach used to remove the effects of the solar cycle and short-term variations is to average the Dobson record over two separate 11-year periods, assuming that different solar cycles have the same integrated impact on column ozone. Wintertime Dobson data for 1976–1986 are consistently lower than those from 1965–1975. The change was most pronounced at high- and midlatitudes (50–60°N), and about -3 percent at 60°N. This observed decrease in ozone over the period is substantially larger than that predicted by 2-D models on the basis of the adopted trace gas scenarios. The pattern is similar to the trace-gas fingerprint, indicating the possibility that the trace-gas effect is underpredicted. This is not sufficient reason, however, merely to scale the results for the trace-gas scenario without determining the source of error, such as the omission of certain physics and chemistry from the models.

The satellite data from TOMS/SBUV provide a more global picture of ozone, but only since late 1978. This period, 1979–1986, is one in which both the solar cycle and trace gases are expected to act in the same sense—that is, to reduce column ozone. The pattern of changes observed by TOMS corroborates the evidence from the 11-year average of the Dobson data: large decreases in ozone have occurred at high latitudes in both hemispheres in winter. To obtain a separation of the fingerprints of trace gases and solar cycle, global satellite data *must* be extended through the next solar maximum (circa 1991).

The observed changes in ozone concentration at different altitudes may also provide evidence of specific perturbations. The most reliable record for absolute changes in ozone profiles over the past decade is limited to satellite instruments, SAGE–I and SAGE–II, and to the recently analyzed Umkehr data (see Chapter 5). The difference between average ozone profiles from the SAGE instruments in 1979 and 1985 show a maximum change near 40 km of -4 ± 4 percent, and from the Umkehr observations -9 ± 5 percent between 1979 and 1986. This should be compared with a range of -6 percent to -10 percent predicted for the combined effects of increase in CFC's and decrease in solar UV. Although the decrease appears to be dominated by trace gases, the height profile is not sufficiently unique to make a definitive identification of fingerprints from trace gases.

The effect of the solar cycle on ozone after its passing through its minimum during 1985 is expected to be opposite that of the trace gases until the next solar maximum. Knowledge of the magnitude of the solar cycle impact is essential for predicting the change in total ozone during this period. The large solar-cycle case gives ozone changes that dominate over trace gas effects at all latitudes through 1990. Calculations using this model for solar variability predict an increase in globally averaged column ozone greater than 1 percent over this period. However, the small solar-cycle model with a less pronounced solar variation in UV flux gives ozone changes that are near zero over the next few years. Furthermore, the small solar-cycle model gives a distinct fingerprint over the next few years in which total ozone increases at low latitudes (solar-cycle effects dominate) and decreases at high latitudes (trace-gas effects dominate).

Obviously, our lack of knowledge of the magnitude of the solar-cycle variations in the UV limits our ability to identify fingerprints in the observed ozone changes over the next few years. Furthermore, the prediction of future ozone depletion from trace gases with the current 2-D models is uncertain because of the lack of heterogeneous chemistry in the models used here. We are still unsure whether the discrepancy between models and observations in the Northern Hemisphere over the past 20 years is statistically significant and, even if it is, we are unable to say how this error will propagate for future predictions of ozone.

S3-45

53440

CHAPTER 8

N92-15460

Trends in Source Gases

KP697650

Panel Members

CX510504

D. H. Ehhalt and P. J. Fraser, Co-Chairs
D. Albritton NJ920944
R. J. Cicerone
M. A. K. Khalil
M. Legrand
Y. Makide
F. S. Rowland
L. P. Steele
R. Zander

PRECEDING PAGE BLANK NOT FILMED

Chapter 8

Trends in Source Gases

Contents

8.1 INTRODUCTION 547

8.2 HALOCARBONS: CCl_3F, CCl_2F_2, CH_3CCl_3, CCl_4 548

8.3 OTHER CHLOROCARBONS 555

8.4 BROMOCARBON SPECIES 558

8.5 NITROUS OXIDE 559

8.6 METHANE 562

8.7 TRACE GASES INFLUENCING TROPOSPHERIC OZONE AND HYDROXYL RADICAL CONCENTRATIONS 565

8.8 CONCLUSIONS 568

PRECEDING PAGE BLANK NOT FILMED

PAGE 544 INTENTIONALLY BLANK

8.1 INTRODUCTION

Source gases are defined as those gases that, by their breakdown, introduce into the stratosphere halogen, hydrogen, and nitrogen compounds that are important in stratospheric ozone destruction. These source gases are emitted at the Earth's surface, either naturally or anthropogenically, and are long lived in the troposphere. Many show significant and well-documented increases in their tropospheric concentrations. The following chapter updates the existing concentration time series for chlorocarbons, nitrous oxide, and methane reported in the previous review (*WMO*, 1986). It also reviews the information accumulating on other halogen-containing species and investigates these data for possible trends. As far as it exists, evidence on trends in trace gases that influence tropospheric chemistry and thus the tropospheric lifetimes of source gases, such as carbon monoxide, carbon dioxide, or nitrogen oxides, is also reviewed. As an overview, the current trends and concentrations are summarized in Table 8.1. The implications of the observed trends in terms of global sources and sinks for these compounds are not discussed in detail in this chapter; the reader is referred to the previous review (*WMO*, 1986) for a comprehensive summary of these aspects of trace gas studies.

Table 8.1 Updated Global Trends and Tropospheric Concentrations of Source Gases for 1986. Where Appropriate and Available, Lifetimes Are Also Tabulated.

Source gas	Concentration 1986 pptv	Rate of increase 1986 pptv/yr	Rate of increase %/yr	Lifetime[a] yr
CCl_2F_2[a]	392	16.7	4.3	111^{+222}_{-44}
CCl_3F[a]	226	9.0	4.0	74^{+31}_{-17}
CH_3CCl_3[a]	139	6.2	4.5	7 ± 1
CCl_4[a,b]	129	1.8	1.4	≈ 40
CCl_2FCClF_2[b]	32	3.6	11.3	≈ 90
$CHClF_2$[b]	92	6.5(c)	7.1	≈ 20
CH_3Cl	≈ 600	—	—	≈ 1.5
$CBrF_3$[b]	2.0	0.3	15	≈ 110
$CBrClF_2$[b]	1.7	0.2	12	≈ 25
CH_3Br[b]	10–15	?		≈ 2
N_2O	$(306-309) \times 10^3$	$(0.65-0.8) \times 10^3$	0.2–0.3	≈ 150
CH_4[d]	1638×10^3	$(13-16) \times 10^3$	0.8–1.0	≈ 10
CO[b]	103×10^3	(see 8.7)		0.1–0.2
CO_2[d]	345×10^6	1.2×10^6	0.4	
Total Cl[e]	3185	104	3.3	
Total F[e]	1300	67.5	5.2	
Total Br[e]	14–19	0.5	3–4	

(a) The lifetimes of the first four species have been derived from observations (see 8.2). The others are adopted from *WMO* (1986).

(b) Calibration uncertain, see 8.3.

(c) Southern Hemisphere, see 8.3.

(d) 1985 data.

(e) The total amounts include all the appropriate compounds listed in this table, which are thought to be the major species of global importance. Because of its exceedingly long lifetime, CF_4 is not included in total F.

PAGE 546 INTENTIONALLY BLANK

PRECEDING PAGE BLANK NOT FILMED

8.2 HALOCARBONS: CCl_3F, CCl_2F_2, CH_3CCl_3, CCl_4

Measurements of the atmospheric halocarbons trichlorofluoromethane (CCl_3F, CFC–11), dichlorodifluoromethane (CCl_2F_2, CFC–12), methylchloroform (CH_3CCl_3), and carbon tetrachloride (CCl_4) have been made at a number of locations in both hemispheres. An important program in this context is the Global Atmospheric Gases Experiment (GAGE), which began in 1978 as the Atmospheric Lifetime Experiment (ALE) (Prinn et al., 1983a), and continues to the present. This program provides in situ measurements from five stations, three in the Northern and two in the Southern Hemisphere. Measurements of CCl_3F, CCl_2F_2, CH_3CCl_3, and CCl_4 have also been made on Hokkaido, Japan, since 1979, using air samples collected in stainless steel flasks (Makide et al., 1987a). Since 1977, the Geophysical Monitoring for Climatic Change laboratory (GMCC) of the National Oceanic and Atmospheric Administration (NOAA) has analysed air samples for CCl_3F and CCl_2F_2 collected in stainless steel flasks at Barrow, Alaska; Niwot Ridge, Colorado; Mauna Loa, Hawaii; Cape Matatula, Samoa; and the South Pole (GMCC, 1986a).

The GAGE data, up to mid-1984, were discussed in the previous report (*WMO*, 1986). Figures 8.1 to 8.4 extend the data to the end of June 1986 (Cunnold et al., 1983a,b, 1986; Prinn et al., 1983b, 1987; Simmonds et al., 1983, 1988). Average concentrations observed at each site in 1985 are shown in Table 8.2. The concentration of each gas is increasing with time. The growth rates, expressed as pptv per year (Table 8.3), averaged over the globe are 9.0(0.1) for CCl_3F, 16.7(0.1)

Table 8.2 Annual Mean Halocarbon Concentrations (pptv) Observed at the GAGE Sites in 1985. The Data Must Be Regarded as Preliminary. The Global Average Is the Mean of the Four GAGE Sites. CCl_3F Data Were Collected on a Porosil Column.

	CCl_3F	CCl_2F_2	CH_3CCl_3	CCl_4
Oregon	223.2	385.6	155.4	129.2
Barbados	221.8	381.7	141.4	129.2
Samoa	211.0	362.9	117.4	124.8
Cape Grim	210.2	361.7	116.6	124.3
Global Average	216.6	373.0	132.7	126.9

Table 8.3 Halocarbon Growth Rates (pptv/yr) Observed at the ALE–GAGE Sites Over the Period 1978 to June 1986. The Data Must Be Regarded as Preliminary. Adrigole Ceased Operation in 1984. Growth Rates Were Obtained by Least Squares Linear Regression; the Numbers in Parentheses Are Single Standard Deviations. The Global Average is the Mean of Growth Rates Observed at Oregon, Barbados, Samoa, and Cape Grim. CCl_3F Data Are From the Porosil Column.

	CCl_3F	CCl_2F_2	CH_3CCl_3	CCl_4
Adrigole	8.6(0.1)	16.9(0.2)	6.9(0.2)	0.6(0.2)
Oregon	8.5(0.1)	16.6(0.2)	6.2(0.2)	1.4(0.1)
Barbados	9.2(0.1)	16.8(0.1)	6.3(0.1)	2.0(0.1)
Samoa	8.9(0.1)	16.6(0.1)	6.1(0.1)	1.9(0.1)
Cape Grim	9.2(0.1)	16.8(0.1)	6.3(0.1)	1.7(0.1)
Global Average	9.0(0.1)	16.7(0.1)	6.2(0.1)	1.8(0.3)

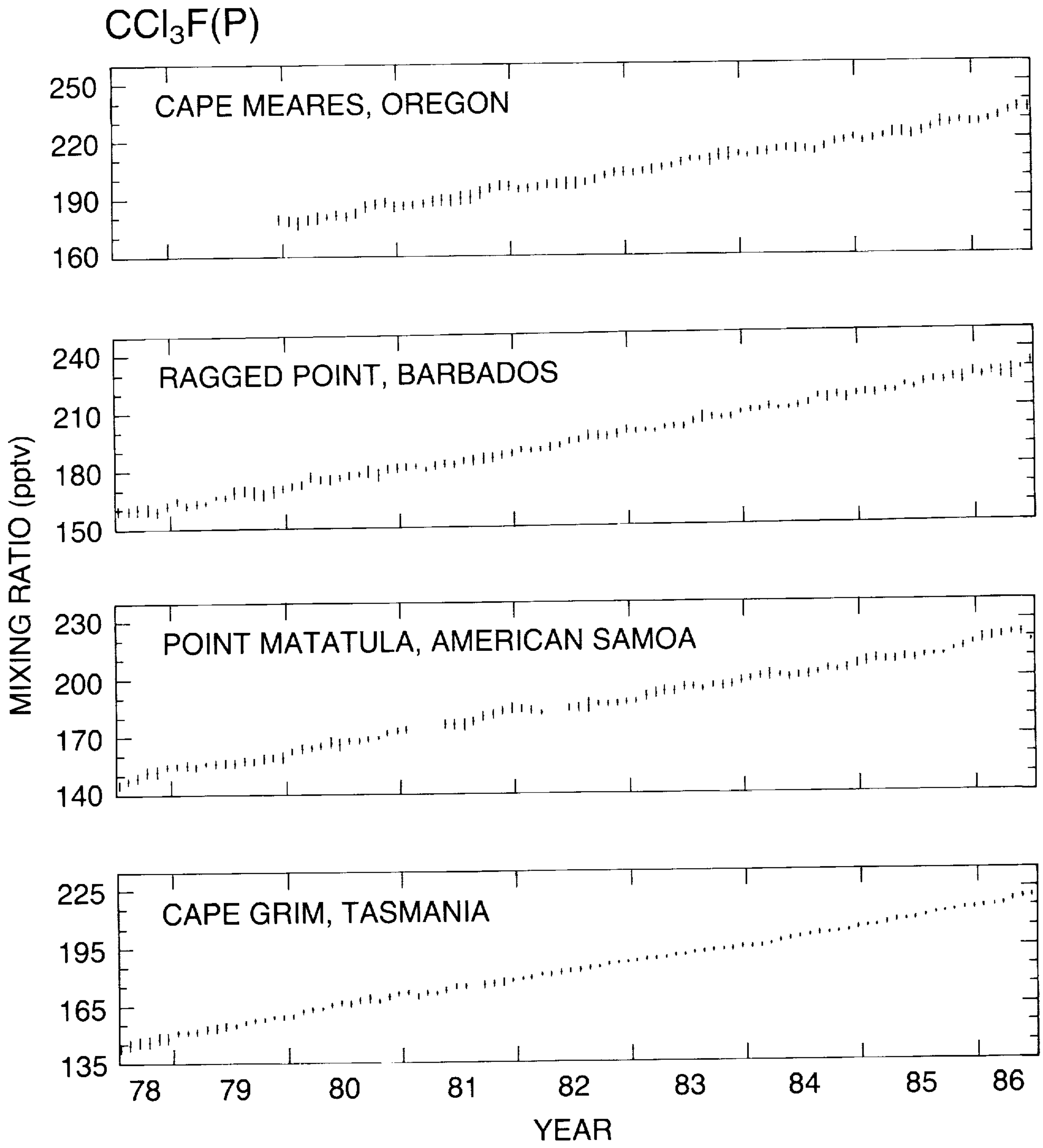

Figure 8.1 Monthly mean mixing ratios of CCl_3F measured with HP5840 and HP5880 gas chromatographs on porosil columns at the ALE–GAGE stations between July 1978 and June 1986 (see Prinn et al., 1983a; Rasmussen and Lovelock, 1983; Cunnold et al., 1983a; Cunnold et al., 1986, for further details). The data for 7/85 to 6/86 are preliminary (R. Prinn, R. Rasmussen, F. Alyea, D. Cunnold, A. Crawford, P. Fraser, P. Simmonds, and R. Rosen, private communication, 1987).

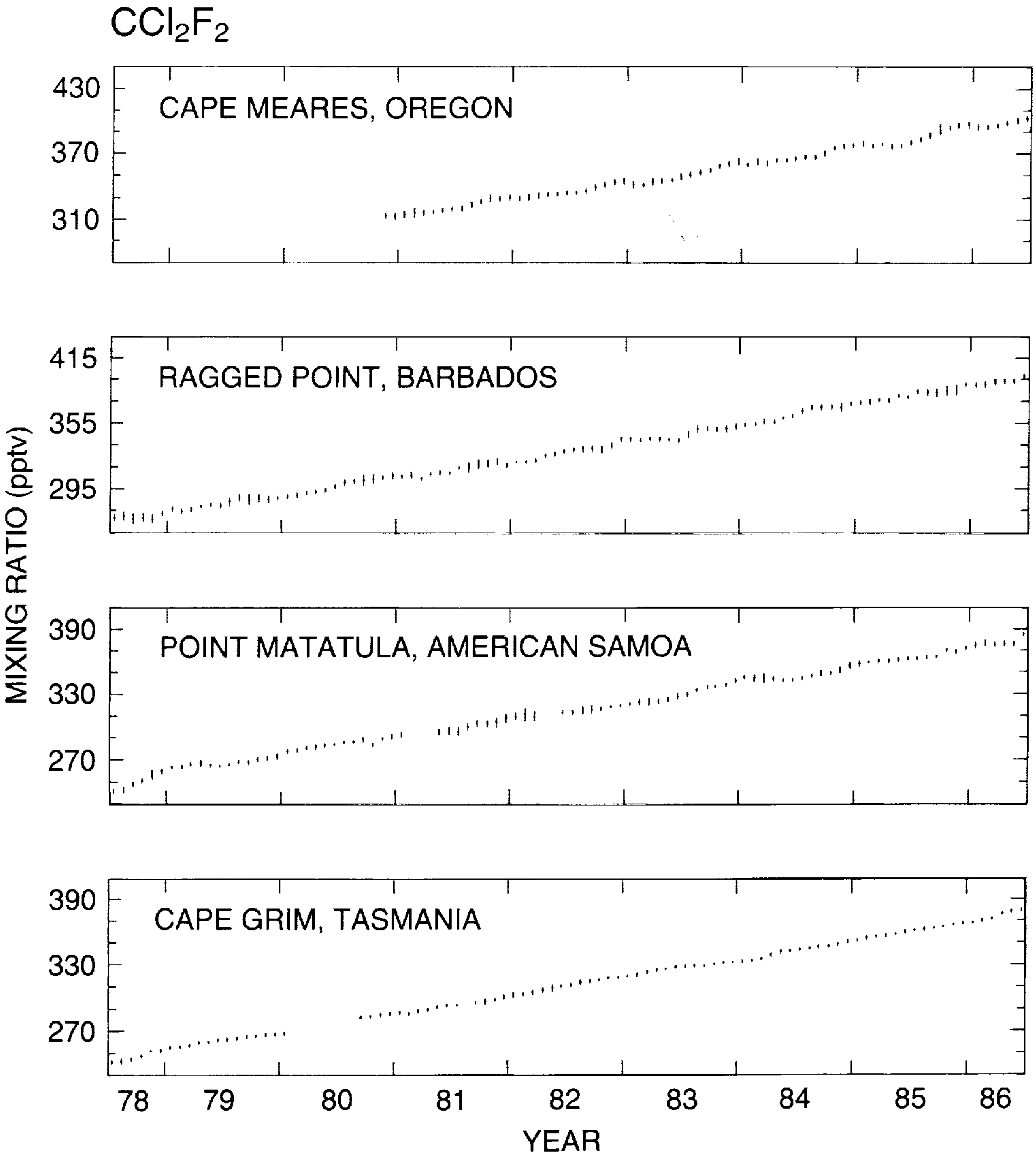

Figure 8.2 Monthly mean mixing ratios of CCl_2F_2 measured with HP5840 and HP5880 gas chromatographs on porosil columns at the ALE–GAGE stations between July 1978 and June 1986 (see Prinn et al., 1983a; Rasmussen and Lovelock, 1983; Cunnold et al., 1983b; Cunnold et al., 1986, for further details). The data for 7/85 to 6/86 are preliminary (R. Prinn, R. Rasmussen, F. Alyea, D. Cunnold, A. Crawford, P. Fraser, P. Simmonds, and R. Rosen, private communication, 1987).

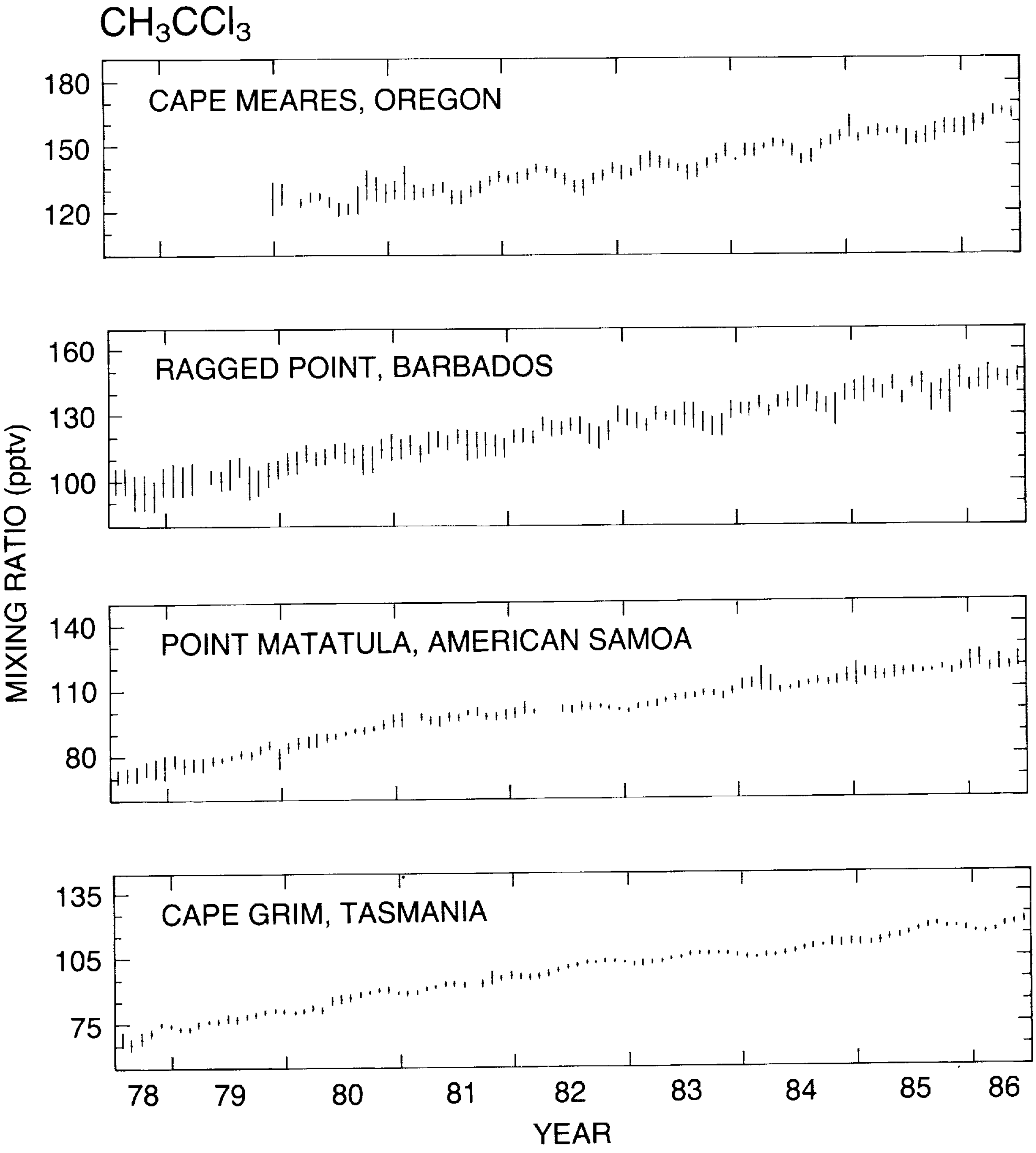

Figure 8.3 Monthly mean mixing ratios of CH_3CCl_3 measured with HP5840 and HP5880 gas chromatographs on silicone columns at the ALE–GAGE stations between July 1978 and June 1986 (see Prinn et al., 1983a; Rasmussen and Lovelock, 1983; Prinn et al., 1983b; Khalil and Rasmussen, 1984a; Prinn et al., 1987, for further details). The data for 7/85 to 6/86 are preliminary (R. Prinn, R. Rasmussen, F. Alyea, D. Cunnold, A. Crawford, P. Fraser, P. Simmonds, and R. Rosen, private communication, 1987).

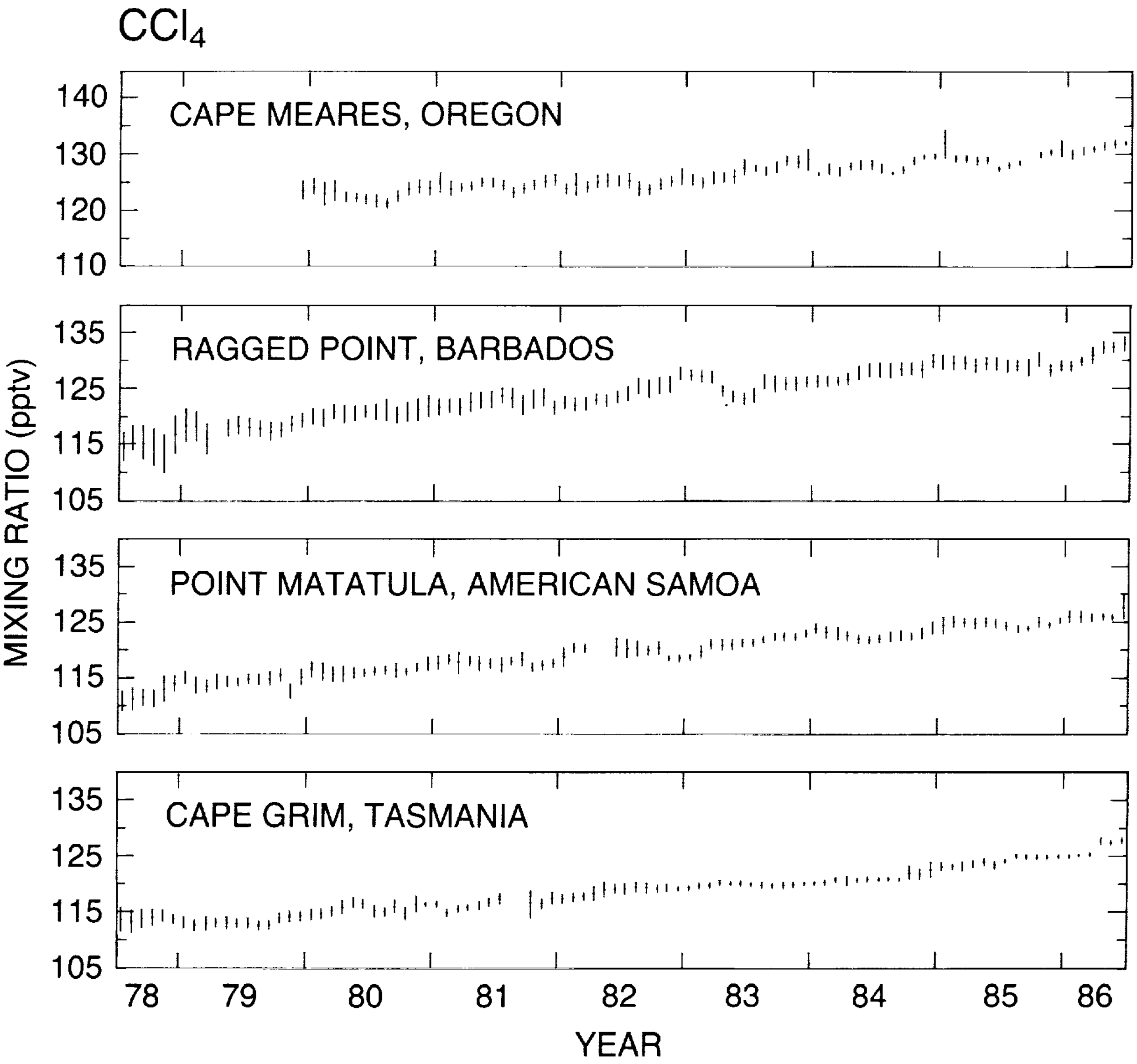

Figure 8.4 Monthly mean mixing ratios of CCl_4 measured with HP5840 and HP5880 gas chromatographs on silicone columns at the ALE–GAGE stations between July 1978 and June 1986 (see Prinn et al., 1983a; Rasmussen and Lovelock, 1983; Simmonds et al., 1983; Simmonds et al., 1986 for further details). The data for 7/85 to 6/86 are preliminary (R. Prinn, R. Rasmussen, F. Alyea, D. Cunnold, A. Crawford, P. Fraser, P. Simmonds, and R. Rosen, private communication, 1987).

for CCl_2F_2, 6.2(0.1) for CH_3CCl_3, and 1.8(0.3) for CCl_4. The numbers in parentheses are single standard deviations. Growth rates in 1985 averaged 4.2 percent per annum for CCl_3F, 4.5 percent for CCl_2F_2, 4.7 percent for CH_3CCl_3, and 1.4 percent for CCl_4 (Table 8.4).

One aim of ALE/GAGE is to determine the atmospheric lifetimes of these halocarbon gases, a key parameter controlling their ultimate impact on stratospheric chemistry and climate. The lifetimes are calculated by comparing independent estimates of release with the total amount or

Table 8.4 Halocarbon Growth Rates (%/yr) Observed at the GAGE Sites in 1985. Data Are Obtained From Tables 8.1 and 8.2.

	CCl_3F	CCl_2F_2	CH_3CCl_3	CCl_4
Oregon	3.8	4.3	4.0	1.1
Barbados	4.2	4.4	4.5	1.6
Samoa	4.2	4.6	5.2	1.5
Cape Grim	4.4	4.6	5.4	1.4
Global Average	4.2	4.5	4.7	1.4

rate of increase of these species in the atmospheres. Conversely, if independent lifetime calculations can be made, then the data can be inverted to derive releases. Since there are no new emission estimates of CCl_3F and CCl_2F_2 from industry, the measured global atmospheric increases of these species are an important way in the immediate future of monitoring the global release of these species. Results from the extended ALE–GAGE data set can be summarized as follows:

CCl_3F and CCl_2F_2

The lifetimes of CCl_3F and CCl_2F_2 are 74^{+31}_{-17} and 111^{+222}_{-44} years, respectively, from trend analysis of 5 years of data (1978 to 1983) (Cunnold et al., 1986). Both lifetimes are consistent with estimates of removal rates in the stratosphere. The uncertainties in the trend lifetime estimates are dominated by release uncertainties. Inverting the analysis, assuming stratospheric photodissociation to be the only atmospheric sink for CCl_3F and CCl_2F_2, yields annual release estimates with an accuracy that, based on the precision of the measurement system only, is claimed to be approximately 8 percent (Cunnold et al., 1986). The release estimate for CCl_3F derived from observations agrees with the Chemical Manufacturers Association estimate based on production (CMA, 1985); for CCl_2F_2, the estimate, although exhibiting variability from year to year, suggests that the emissions in the USSR and Eastern Europe have remained roughly constant over 1979 to 1982 at about 10 percent of global emissions (Cunnold et al., 1986).

CH_3CCl_3

Methylchloroform (CH_3CCl_3) is released to the atmosphere in larger amounts (500 to 550 × 10^6 kg per year) than any other anthropogenic chlorine-containing gas. Because it is susceptible to chemical attack by OH radicals.

$$CH_3CCl_3 + OH \rightarrow CH_2CCl_3 + H_2O,$$

a larger fraction of CH_3CCl_3 molecules is removed in the troposphere, and its potential threat to stratospheric ozone depletion is correspondingly reduced.

The lifetime of CH_3CCl_3 was calculated to be $6.9^{+1.2}_{-0.9}$ years from trend analysis of 7 years of observations (1978 to 1985). A lifetime of $6.0^{+1.1}_{-0.8}$ years was obtained by comparing the total atmospheric content with the release data, and a third method, comparing observed and calculated latitudinal gradients, gave a lifetime of $6.0^{+1.4}_{-1.0}$ years. Combining all three ways of analysing the CH_3CCl_3 data, the best estimate of the atmospheric lifetime of CH_3CCl_3 is $6.3^{+1.2}_{-0.9}$ years (Prinn et al., 1987). If 6.3 years is assumed to be the lifetime of CH_3CCl_3, then, by inverting the data, emissions can be calculated that generally agree with those deduced from industry data. The best estimate of a lifetime of 6.3 years corresponds to a globally averaged tropospheric OH concentration of $(7.7 \pm 1.4) \times 10^5 cm^{-3}$. This estimate is more accurate than that derived previously (Singh, 1977; Lovelock, 1977; Makide and Rowland, 1981; Prinn et al., 1983b; Khalil and Rasmussen, 1984a; Fraser et al., 1986a).

CCl_4

The observed trend and latitudinal gradient of CCl_4 are consistent with an atmospheric lifetime of about 40 years, and with releases of CCl_4 averaging $(9.0 \pm 0.9) \times 10^7$kg/year over the period 1978 to 1985. Consistency between release estimates and observations was obtained by assuming a CCl_4 calibration based on a comparison of ALE–GAGE data and the data collected by Makide et al. (1987a) on Hokkaido. The global release estimates suggest that the majority of CCl_4 is derived from chlorofluorocarbon production (Simmonds et al., 1986). However, on a regional scale, the observations at Adrigole, Ireland, imply that there is a significant contribution to European emissions from Eastern Europe, adding to the industrial losses and solvent use reported in Western Europe (Prather, 1985, 1988).

The data from Hokkaido obtained during 1985 are summarized in Table 8.5 and compared to similar GAGE data obtained at Cape Meares, Oregon. Concentrations of CCl_3F, CCl_2F_2, CH_3CCl_3, and CCl_4 on Hokkaido are 2 percent lower, 5 percent higher, 19 percent lower, and 18 percent lower, respectively, than those observed at Cape Meares. The concentration increases are similar at both locations for CCl_3F and CCl_2F_2 (4 to 5 percent per year), but significantly different for CH_3CCl_3, where a higher rate is observed in Oregon, and for CCl_4, where a higher rate is observed on Hokkaido. The differences in concentration for all species at both sites could be due largely to calibration differences. However, other factors such as the strength and location of regional sources and the different observation methodologies could contribute to the observed differences. The lower concentration of CCl_4 observed at Hokkaido has been used to support a lowering of the GAGE absolute calibration standard (Simmonds et al., 1986).

Table 8.5 Annual Mean Halocarbon Concentrations and Trends Observed at (a) Hokkaido, Japan (42° to 45°N) (Makide et al., 1987a), and (b) Oregon, USA (45°N) (GAGE data), in 1985. Concentrations Are in pptv, Annual Increases (pptv/yr) Were Obtained by Linear Regression, and the Number in Parentheses Is One Standard Deviation. Data at Both Sites Were Collected From 1979 to 1986.

	CCl_3F		CCl_2F_2		CH_3CCl_3		CCl_4	
	a	b	a	b	a	b	a	b
1985 Concentration	218.7	223.2	404.8	385.6	126.4	155.4	105.3	129.2
Increase (pptv/yr)	8.9 (0.3)	8.5 (0.1)	18.5 (0.6)	16.6 (0.2)	3.7 (0.4)	6.2 (0.2)	1.6 (0.5)	1.4 (0.1)
1985 Increase (%/yr)	4.1	3.8	4.6	4.3	2.9	4.0	1.5	1.1

Table 8.6 Annual Mean CCl_3F and CCl_2F_2 Concentrations (pptv) and Increases (pptv/yr, %/yr) Observed at the Five Geophysical Monitoring for Climatic Change Stations (GMCC, 1986a).

	CCl_3F	Increase		CCl_2F_2	Increase	
		pptv/yr	%/yr		pptv/yr	%/yr
Barrow	227.4	9.1(1.0)	4.0	390.7	15.8(0.1)	4.0
Niwot Ridge	223.7	9.1(1.0)	4.1	384.5	15.1(0.2)	3.9
Mauna Loa	220.5	9.4(0.1)	4.3	381.7	15.0(0.2)	3.9
Samoa	213.1	9.7(0.1)	4.6	374.3	16.9(0.1)	4.5
South Pole	216.3	9.6(0.4)	4.4	366.4	16.8(0.3)	4.6
Global Average	220.2	9.4	4.3	379.5	15.9	4.2

The GMCC data obtained in 1985 are summarized in Table 8.6. Globally averaged CCl_3F and CCl_2F_2 concentrations were both 1.7 percent higher than those observed in the GAGE program. At Samoa, where both programs share a common site, CCl_3F and CCl_2F_2 concentrations in 1985 were 1.0 and 3.1 percent higher, respectively. These differences could be due to calibration, but differences in sampling strategies and data rejection criteria to remove local pollution episodes might also contribute to a bias. The concentration increases observed globally are similar for both programs, 4.2 and 4.3 percent per year for CCl_3F from ALE–GAGE and GMCC programs, respectively, and, for CCl_2F_2, 4.2 percent per year by GMCC compared to 4.5 percent per year by GAGE.

8.3 OTHER CHLOROCARBONS

CCl_2FCClF_2 (CFC–113)

Observations of background concentrations of CCl_2FCClF_2 have been reviewed (*WMO*, 1986), but the data were not extensive enough to quantify global trends. Long time series of CCl_2FCClF_2 measurements have been made available based on the analysis of flask air samples collected in Alaska, Oregon, Hawaii, American Samoa, Tasmania, and at the South Pole (M.A.K. Khalil and R.A. Rasmussen, unpublished data), and in Hokkaido (Makide et al., 1987b).

The observed trends of CCl_2FCClF_2 are shown in Figure 8.5 as a global average of the six Khalil and Rasmussen sampling sites and for Hokkaido. For 1985, the average global concentration reported by Khalil and Rasmussen is approximately 31 pptv, whereas Makide et al. (1987b) deduce a 1985 average value on Hokkaido of 46 pptv. A large component of this discrepancy appears to be due to calibration differences; this needs to be resolved.

The annual increase in CCl_2FCClF_2 concentration based on linear regression is 3.6(±0.1) pptv/yr or 11.6%/yr (1985) from the global average data (Khalil and Rasmussen), and 4.8(±0.2) pptv/yr or 10.5%/yr (1985) from the Hokkaido data. The rate of increase could itself be increasing, since the last 4 years at Hokkaido show an increase of 11.6%/yr in 1985. The reasonable agreement between the two data sets for the %/yr increase (11 to 12 percent in 1985) supports the conclusion that the difference between the two data sets in absolute concentration is caused by a calibration problem.

The latitudinal distribution in 1985 for the six sampling sites of Khalil and Rasmussen is shown in Figure 8.6. The average concentration in the Southern Hemisphere is about 17 percent

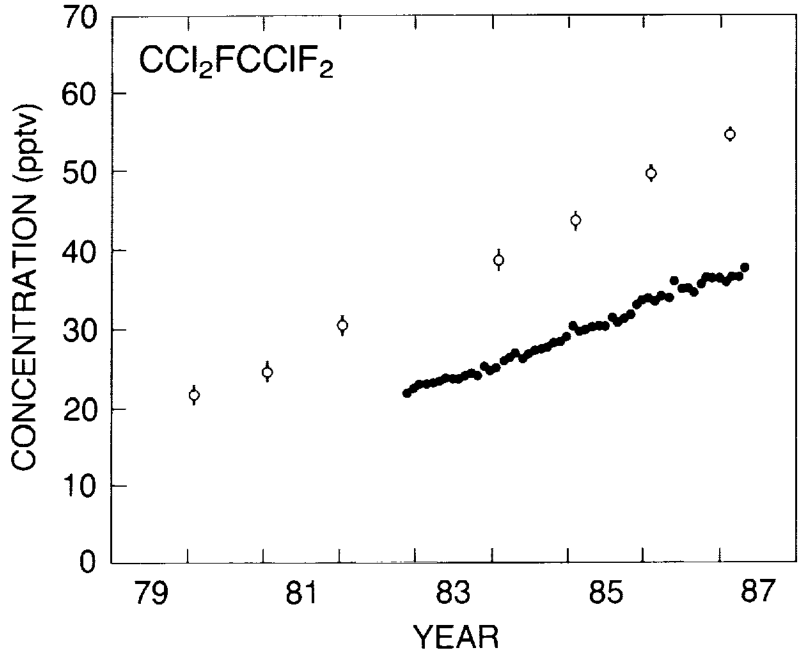

Figure 8.5 Trends of atmospheric concentrations of CCl_2FCClF_2 (CFC–113) observed in Hokkaido, Japan (43°–45°N; ○ Makide et al., 1987b), and as a global average of six sampling sites (76°N–90°S; ● M.A.K. Khalil and R.A. Rasmussen, unpublished data). Error bars are single standard deviations.

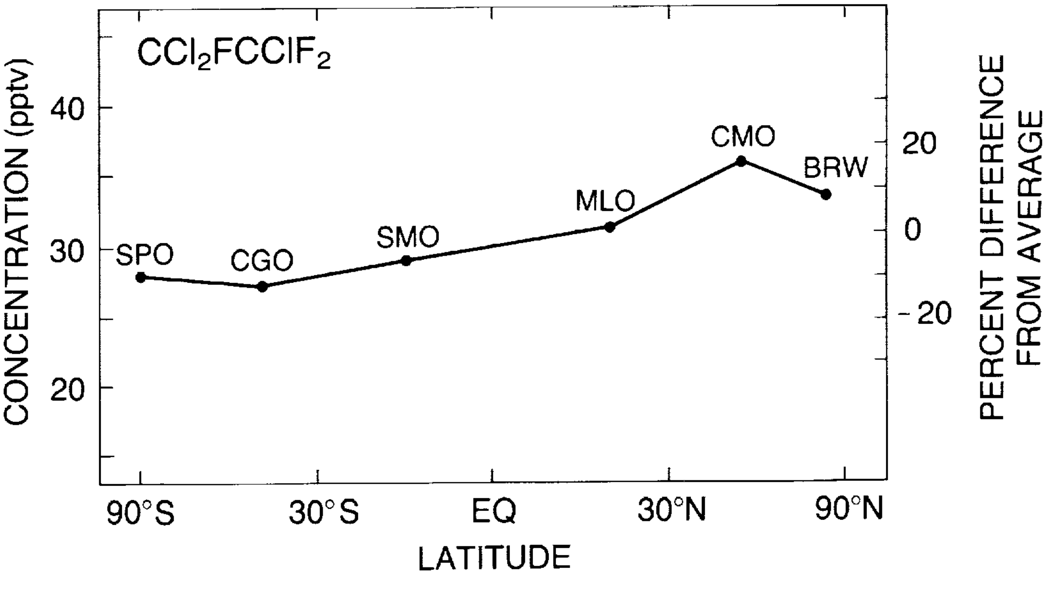

Figure 8.6 The global distribution of CCl_2FCClF_2 in 1985 from six sampling sites (BRW, Barrow, Alaska; CMO, Cape Meares, Oregon; MLO, Mauna Loa, Hawaii; SMO, Cape Matatula, American Samoa; CGO, Cape Grim, Tasmania; SPO, South Pole) (M.A.K. Khalil and R.A. Rasmussen, unpublished data).

lower than in the Northern Hemisphere, reflecting its dominant release in the Northern Hemisphere and rapid increase of atmospheric concentration.

$CHClF_2$ (CFC-22)

In the previous report (*WMO*, 1986) the only information available on the atmospheric trend of $CHClF_2$ was from an early paper of Khalil and Rasmussen (1981), which showed an increase of about 12%/yr. Unfortunately, very little further data are available. However, observations of $CHClF_2$ have been reported from Cape Grim, Tasmania (Khalil and Rasmussen, 1987a; Fraser et al., 1987a), which show an average 1985 concentration of 77 pptv increasing at 6.5 pptv/yr or 8.4%/yr. The data are shown in Figure 8.7. The global average concentration of $CHClF_2$, 92 pptv, given in Table 8.1, is based on the Cape Grim value and an interhemispheric concentration ratio of 1.16 (*WMO*, 1986).

CH_3Cl

Very little new information has appeared on CH_3Cl since the last report (*WMO*, 1986). Three years of observations at Cape Grim (Khalil and Rasmussen, 1987a; Fraser et al., 1987a) do not show any obvious change with time, apart from a clear annual cycle, which is presumably related to the removal of CH_3Cl from the atmosphere by hydroxyl radicals (Figure 8.8). A number of trace gases such as CH_3CCl_3, methane, and carbon monoxide at Cape Grim show annual cycles of phases similar to those observed for CH_3Cl, and they have been attributed to the seasonal variations in the magnitude of the hydroxyl radical sink (Fraser et al., 1986a). The global average concentration is approximately 600 pptv (see *WMO*, 1986).

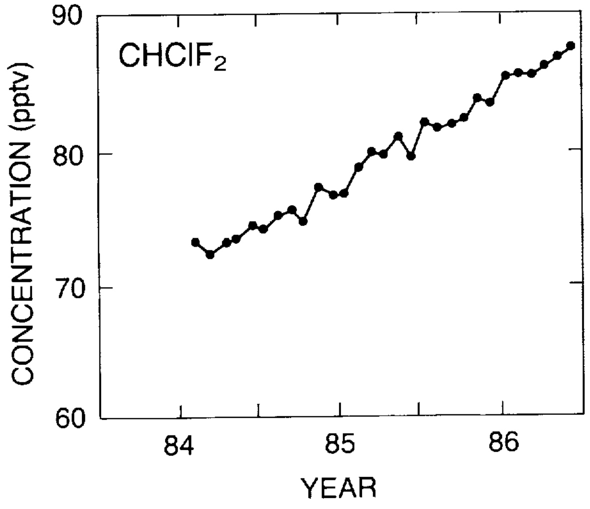

Figure 8.7 Monthly mean $CHClF_2$ observations (pptv) at Cape Grim, Tasmania, from the Oregon Graduate Center flask sampling program (Khalil and Rasmussen, 1987a; Fraser et al., 1987a).

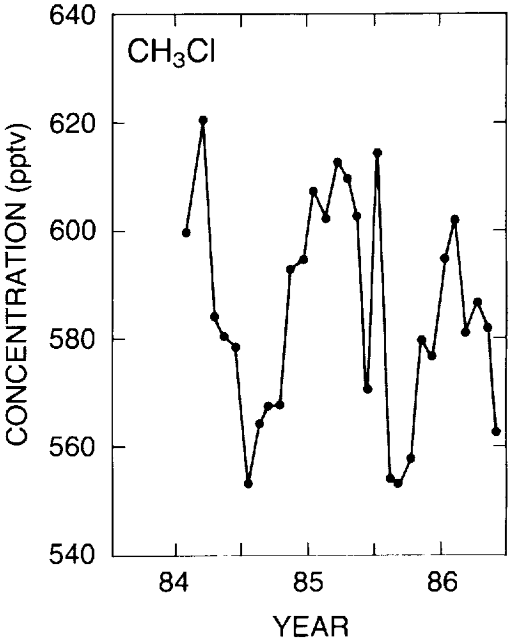

Figure 8.8 Monthly mean CH_3Cl observations (pptv) at Cape Grim, Tasmania, from the Oregon Graduate Center flask sampling program (Khalil and Rasmussen, 1987a; Fraser et al., 1987a).

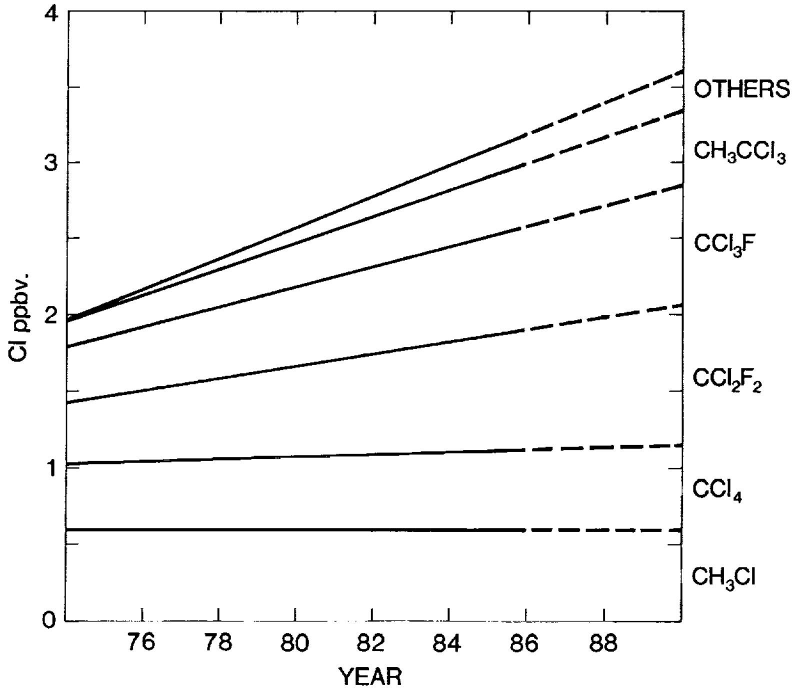

Figure 8.9 Measured and predicted cumulative increases of chlorinated source gases in the troposphere over the past decade and up to 1990. The concentrations are given as chlorine atom equivalents. Future increases are indicated by dashed lines, based on constant emission rates at current levels. CCl_3F, CCl_2F_2, CH_3CCL_3, CCl_4, and CCl_2FCClF_2 data are from the ALE–GAGE program (see Sections 8.2 and 8.3). $CHClF_2$ data are derived from Cape Grim data (see Section 8.3).

The largest perturbation in stratospheric ozone is expected from the observed increases in chlorinated source gases, which determine the growth of reactive chlorine species in the stratosphere. It is, therefore, instructive to look at the temporal increase of the total gaseous chlorine in the troposphere (Figure 8.9). The current rate of increase (1986) in total chlorine is 3.3 percent per year.

8.4 BROMOCARBON SPECIES

Interest in atmospheric bromine compounds has increased because of the possible role of bromine radicals in the loss of Antarctic ozone (McElroy et al., 1986a; Crutzen and Arnold, 1986; Isaksen and Stordal, 1986a). Relatively few studies have been made, however, and bromine compounds were considered only briefly in the previous report (*WMO*, 1986).

The last decade has seen the emergence of a new class of perhalogenated bromine gases, bromotrifluoromethane ($CBrF_3$, Halon–1301) and bromochlorodifluoromethane ($CBrClF_2$, Halon–1211). These chemicals are long lived in the atmosphere, and their use has been growing rapidly, particularly for fire suppression in military and high-technology environments. Concentrations in the upper troposphere and lower stratosphere were about 1 pptv for $CBrF_3$ in 1980 and 1.5 pptv for $CBrClF_2$ in 1984 (Fabian et al., 1981; Lal et al., 1985). Concentrations of both species appear to be increasing between 10 percent and 20 percent per year (Lal et al., 1985; Khalil and Rasmussen, 1985), and the total halon content in the Northern Hemisphere is now about 4.5

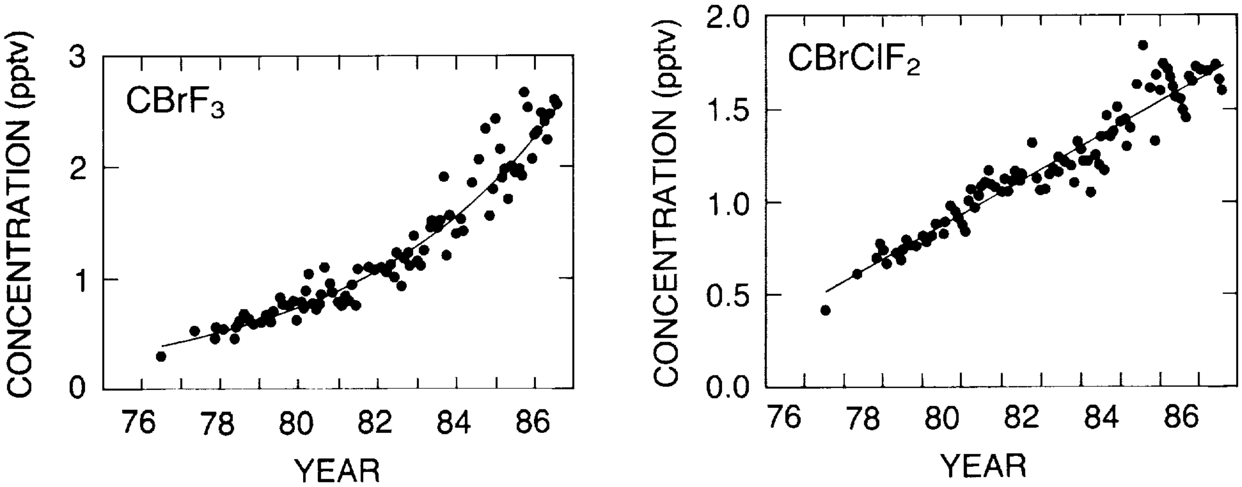

Figure 8.10 Monthly mean concentrations of $CBrF_3$ and $CBrClF_2$ at Cape Meares, Oregon, over the last decade. Concentrations of $CBrF_3$ have increased exponentially at 18(±1) percent/yr and linearly for $CBrClF_2$ at 0.12(±0.01) pptv/yr (Khalil et al., 1986; R.A. Rasmussen, R. Gunawardena, and M.A.K. Khalil, unpublished data).

pptv (see Figure 8.10). The 1985 concentration of $CBrClF_2$ was 1.5 to 1.6 pptv at Cape Meares and about 1.3 to 1.5 at Cape Grim (see Figure 8.11). Although these results are based on data from only two stations, they should also apply globally, because the atmospheric lifetimes of the halons are quite long (see Table 8.1), so that these halons are well mixed globally. The rate of increase has accelerated dramatically since 1978, when concentrations were less than 0.5 pptv for each halon. The rate of increase of $CBrClF_2$ seems to be about 0.2 pptv/yr in both hemispheres. Stratospheric profiles indicate rapid decline with altitude above the tropopause, reflecting photolytic decomposition. The concentration at 20 km is less than 20 percent of the value at the tropopause (Fabian et al., 1981; Lal et al., 1985). Hence, there is little doubt that these compounds add significant quantities of bromine to the stratosphere.

New data and interpretations have emerged on organobromine gases of stratospheric importance, in addition to those for $CBrF_3$ and $CBrClF_2$. Salawitch et al. (1988a) have reviewed data on gaseous organic bromine from several investigators from the 1970's and 1980's. They note that major uncertainties, such as differences in experimental techniques, are involved, but they conclude that atmospheric CH_3Br has probably increased significantly, perhaps by a factor of two, in the past 10 years. Cicerone et al. (1988) have measured CH_3Br in almost 1,000 samples of air from five background sites, three in the Northern Hemisphere and two in the Southern Hemisphere, from January 1985 through September 1987. At all five sites, there were CH_3Br variations during this period, but trends are not yet clear. It appears that the current global background levels of CH_3Br are between 10 and 15 pptv (Salawitch et al., 1988a; Cicerone et al., 1988).

8.5 NITROUS OXIDE

Atmospheric nitrous oxide (N_2O) concentrations have continued to increase. R.F. Weiss (Scripps Institute of Oceanography) has extended the measurement program of Weiss (1981) into 1987. The results may be summarized as follows. Samples from over 1,100 flasks for the

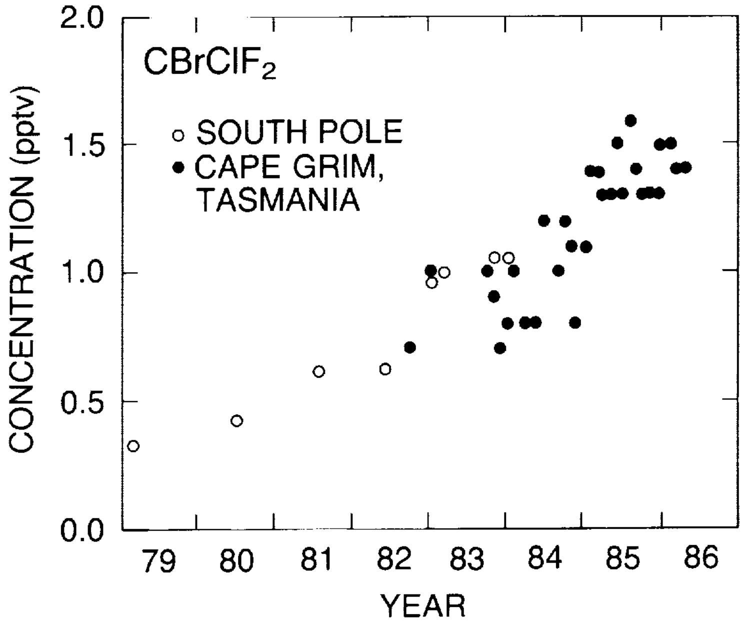

Figure 8.11 Observations of $CBrClF_2$ (pptv) in the Southern Hemisphere at Cape Grim, Tasmania (●), and at the South Pole (○) (Khalil and Rasmussen, 1985; Khalil et al., 1986; R.A. Rasmussen and R. Gunawardena, unpublished data).

period 1976 to early 1987 show very similar rates of N_2O increase. The January 1986 rates of increase are 0.65(±.02), 0.66(±.04), 0.67(±.04), and 0.61(±.04) ppbv/yr for all data, Barrow, Mauna Loa, and South Pole, respectively. The mean N_2O concentration in January 1986 was 304.8 ppbv. The complete data set, which includes flask samples from several ship tracks, displays a north–south gradient of 0.76(±.09) ppbv.

N_2O measurements have been made at the ALE–GAGE sites since July 1978 (Prinn et al., 1983a, 1988; *WMO*, 1986). Khalil (Oregon Graduate Center) has combined these data (about 60,000 real-time measurements) with flask measurements from Barrow and Mauna Loa (Khalil and Rasmussen, 1983a) to produce the global average shown in Figure 8.12. The average rate of increase of N_2O over the 7-year period 1979 to 1985 is 0.8(±0.05) ppbv/yr. The global average concentration in 1985 was 308.2 ppbv, with Northern Hemispheric concentrations being higher than Southern Hemispheric by 0.6(±0.1) ppbv.

N_2O measurements have been made on flasks collected at the GMCC sites since mid-1977 (GMCC, 1986a). J. Elkins (NOAA/GMCC) has analysed these data from 1978 through 1986; the rates of increase obtained by linear regression are 0.54(±0.06), 0.63(±0.09), 0.79(±0.07), 1.04(±0.08), and 0.57(±0.15) ppbv per year for Barrow, Niwot Ridge, Mauna Loa, Samoa, and the South Pole, respectively, the average rate being 0.7(±0.1) ppbv per year. The global average concentration in 1985 was 306.1 ppbv, with the three Northern Hemisphere stations being 2 ppbv higher than the South Pole. However, the GMCC observations at Samoa are approximately 6 ppbv higher than at the South Pole.

In summary, from three independent networks, the global rate of increase in N_2O ranges from 0.65 to 0.8 ppbv/yr, and the global average concentration ranges from approximately 305 to 308 ppbv, with the small differences probably due to differences in calibration.

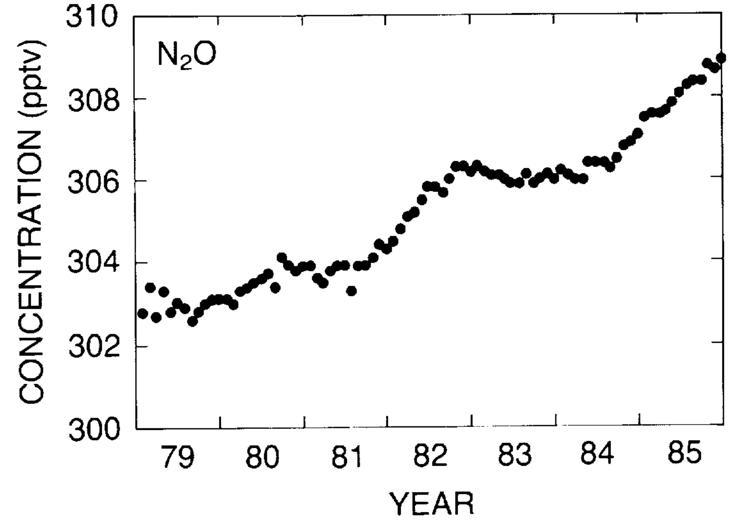

Figure 8.12 The monthly and globally averaged concentrations of N_2O based on ALE–GAGE data collected using in situ gas chromatographs at Adrigole, Cape Meares, Barbados, Samoa, and Cape Grim, and flask data from Barrow and Mauna Loa (Prinn et al., 1983a; Khalil and Rasmussen, 1983a; *WMO*, 1986; Prinn et al., 1988; M.A.K. Khalil and R.A. Rasmussen, unpublished data).

Evidence for a long-term trend in N_2O has been obtained from analysis of ice cores. Results from two recent studies are summarized in Figure 8.13 (Pearman et al., 1986; Khalil and Rasmussen, 1987b; Etheridge et al., 1987). The ice core data are noisy, but they do suggest that concentrations prior to 1800 were in the range of 280 to 290 ppbv. Measurements on modern ice (after 1960) are in reasonable agreement with current atmospheric observations.

Three possible sources of N_2O could account for the observed increases: (1) nitrification and denitrification of nitrogen from industrially produced nitrogenous fertilizers and wastes that are

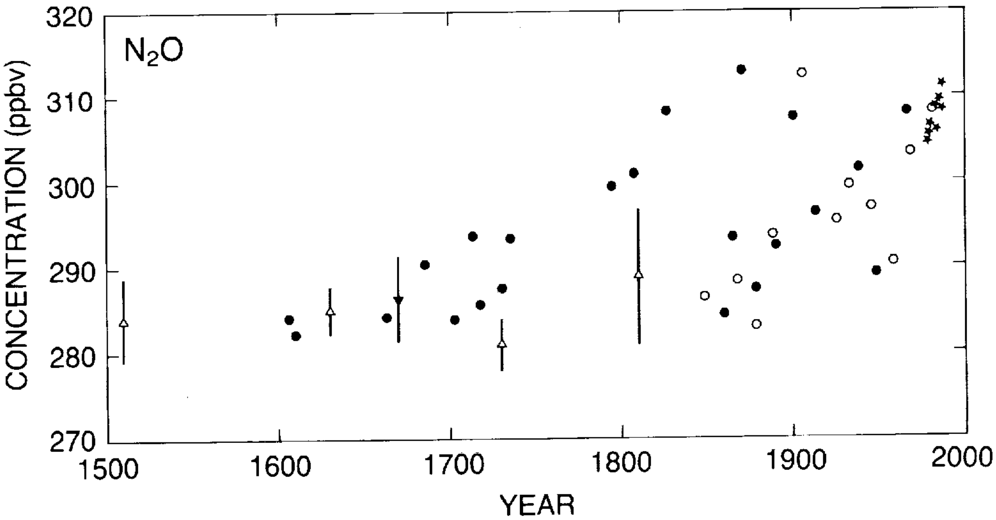

Figure 8.13 N_2O measurements obtained from ice cores. Data labeled ● and ○ are two different cores from Law Dome, Antarctica (Pearman et al., 1986; Etheridge et al., 1987; G.I. Pearman, D. Etheridge, F. de Silva, and P.J. Fraser, unpublished data); ▼ South Pole (Khalil and Rasmussen, 1987b) and Δ Greenland (Khalil and Rasmussen, 1987b) with 90 percent confidence intervals. Data labeled ★ are in situ ALE–GAGE measurements from Cape Grim, Tasmania (Fraser et al., 1986b; Fraser and Derek, 1987).

attributable to this fertilizer, (2) biomass burning, and (3) high-temperature combustion (*WMO*, 1986). Evidence from Hao et al., 1987 shows that N_2O production in combustion is due largely to pre-existing nitrogen content of fuels (e.g., organic nitrogen in coals), and that this N_2O source can probably account for most of the observed N_2O increase. The reaction most likely to produce N_2O in this way is:

$$NO + NCO \rightarrow N_2O + CO$$ (Perry, 1985).

Very recent experiments by Muzio and Kramlich (1988) have demonstrated that the high-temperature combustion source of N_2O has been overestimated due to an unrecognized artifact in previous measurements. Thus, at present, our understanding of the causes of the contemporary N_2O increase is far from satisfactory.

8.6 METHANE

There are now four extensive data sets based upon direct measurements of atmospheric methane by gas chromatography with a flame ionization detector. These data sets have been generated by the Commonwealth Scientific and Industrial Research Organisation, Australia (CSIRO); the Geophysical Monitoring for Climatic Change (GMCC) program of the National Oceanic and Atmospheric Administration (NOAA); the Oregon Graduate Center, Beaverton, Oregon (OGC); and the University of California at Irvine (UC). The CSIRO program makes measurements at a number of sites, with the longest record being at Cape Grim. CSIRO also has made unique time series of measurements in the mid- and upper troposphere over the southeastern Australian region by flask sampling from aircraft (Fraser et al., 1986a). The NOAA results are presented here as global average concentrations estimated from weekly flask sampling at over 20 sites in a globally distributed network (Steele et al., 1987). The OGC results are also global average values calculated as a weighted average of monthly mean concentrations from the six sites of Barrow, Cape Meares, Mauna Loa, Samoa, Cape Grim, and Antarctica (Khalil and Rasmussen, 1983b). The weighting factors for each site are determined according to the fraction of global surface area represented by each site (M.A.K. Khalil and R.A. Rasmussen, unpublished data). The UC data are also estimates of the global mean concentration based upon "snapshots" of the latitudinal profile from the Arctic to the mid-latitudes of the Southern Hemisphere, with appropriate weighting for latitude (Blake and Rowland, 1986 and 1988).

The CSIRO Cape Grim data, as well as the NOAA, OGC, and UC measurements, are shown in Figure 8.14, while the CSIRO mid-tropospheric data are shown in Figure 8.15. All methane concentrations are expressed in units of parts per billion by volume in dry air (ppbv). The CSIRO, NOAA, and OGC data are all based upon the same calibration scale (see Rasmussen and Khalil, 1981). The long-term increase is clearly evident in all data sets. Growth rates have been calculated as the slopes of least squares linear fits to the actual UC data, and to the 12-month running mean methane concentrations found from the other four data sets. To enable ready comparison of the growth rates from the different data records, the time period was restricted to be identical, or as close as possible, to that of the shortest record, namely, that of NOAA. These growth rates are given in Table 8.7. Over the 4-year period from April 1983 to May 1987, it is clear that the methane growth rate is less than 1 percent per year in all five data records. It is particularly significant that the CSIRO mid-tropospheric results give a growth rate identical to that found from the Cape Grim data, indicating that the long-term increase is indeed occurring throughout the atmosphere, and not just at surface locations. Contrary to previous reports, the long-term data (*WMO* 1986; Khalil and Rasmussen, 1986) do not show any significant effect due to the El Niño-Southern Oscillation.

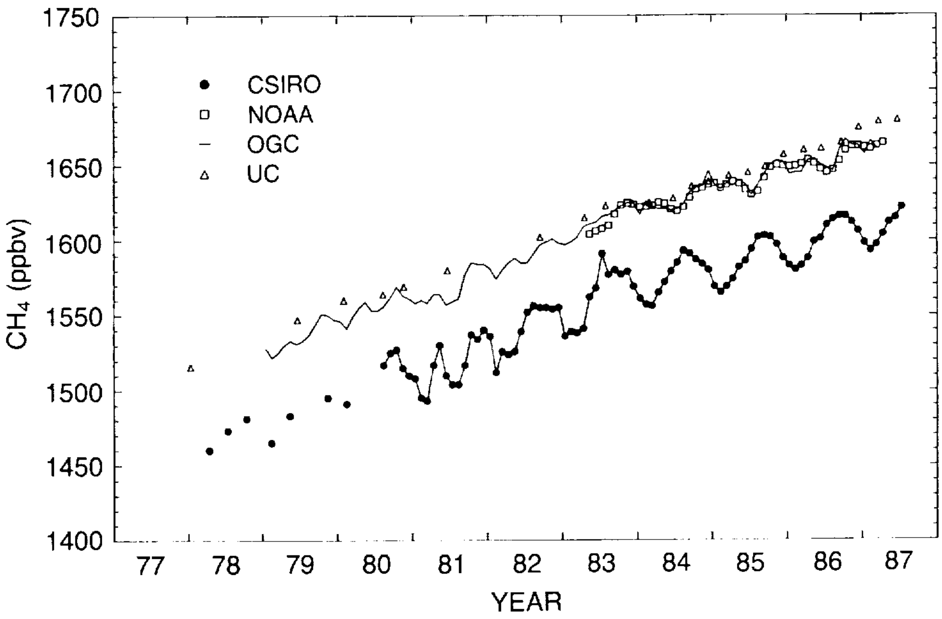

Figure 8.14 Results from four long-term, methane measurement programs based upon gas chromatography and flame ionization detection: (a) the Commonwealth Scientific and Industrial Research Organisation, Australia (CSIRO); (b) the Geophysical Monitoring for Climate Change program of the National Oceanic and Atmospheric Administration (NOAA); (c) the Institute of Atmospheric Sciences, Oregon Graduate Center (OGC); and (d) the University of California at Irvine (UC).

Data shown are monthly mean values except for UC (see text). For clarity, the monthly data of OGC are plotted as a solid line rather than as individual points. All values are estimates of the global average concentration except for those of CSIRO, which are for Cape Grim, Tasmania. The lower values for the CSIRO data set reflect the observed latitudinal gradient in methane concentrations.

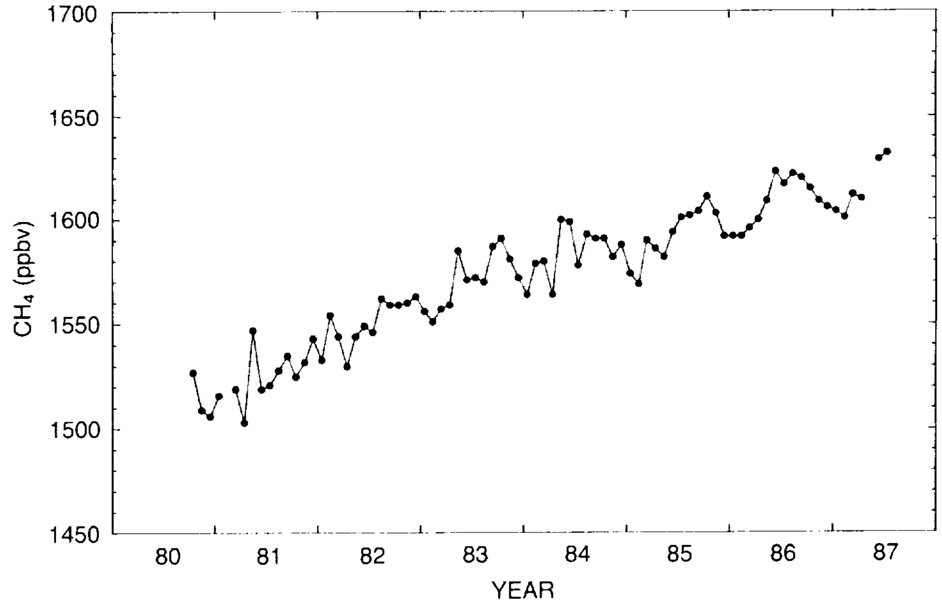

Figure 8.15 Time series of monthly mean methane concentrations measured by flask sampling from aircraft in the mid-troposphere (3.5 to 5.5 km altitude) over the southeastern Australian region (Fraser et al., 1986a, and unpublished data of P.J. Fraser et al.).

Table 8.7 Comparison of Growth Rates of Atmospheric Methane. For All Data Sets Except UC the Growth Rates Are Given by the Slope of a Least Squares Linear Fit to 12-Month Running Mean Methane Values Calculated From the Monthly Data. The Values in Parentheses Are the Standard Errors of These Slopes. The Growth Rate for the UC Data Was Found by a Least Squares Linear Fit to the Actual Data Over the Period Specified.

Program	CH_4 Growth Rate (ppbv/yr)	Period Covered
CSIRO, Cape Grim	11.9(0.2)	May 83 – Apr 87
NOAA/GMCC (global)	12.92(0.04)	May 83 – Apr 87
OGC (global)	13.1(0.1)	May 83 – Mar 87
UC (global)	15.8(0.6)	Apr 83 – Mar 87
CSIRO, mid-troposphere (Southern Hemisphere)	11.9(0.9)	May 83 – Apr 87

Recently, the solar infrared spectra taken from Jungfraujoch in 1951 were evaluated, and an annual average column density of methane was obtained (Zander et al., 1989). In addition, new measurements at Jungfraujoch in 1985 and 1986 show a well-defined seasonal variation in the total methane column density. Comparison of these annual average column densities for 1951 and 1985 to 1986 indicates an average increase of .72 (±.15)%/yr over this period (Zander et al., 1989; cf. Ehhalt et al., 1983). This rate of increase is significantly lower than the value of 1.1(±0.2)%/yr reported by Rinsland et al. (1985), who used a less complete set of the 1951 solar infrared spectra from Jungfraujoch.

The zonally averaged distribution of methane in the remote marine boundary layer is shown in Figure 8.16. This figure shows 4 years of results from the NOAA/GMCC cooperative flask

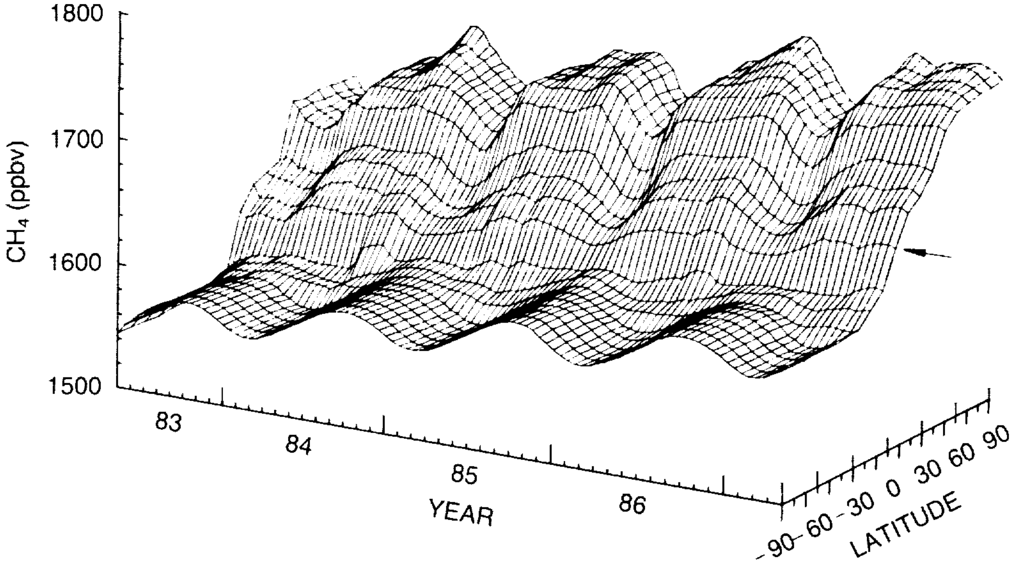

Figure 8.16 Zonally averaged representation of the variations in atmospheric methane concentrations in the remote marine boundary layer for the 4-year period May 1983 to April 1987. Grid spacing is 10° in latitude, and 0.5 month in time. The arrow indicates the position of the Equator. Data used to construct this figure are drawn from the globally distributed cooperative flask sampling network of NOAA/GMCC (Steele et al., 1987, and unpublished data of L.P. Steele).

sampling network, which now comprises 26 globally distributed sites (Steele et al., 1987, and unpublished results of L.P. Steele et al.). The seasonality in the Southern Hemisphere is quite repeatable from one year to the next, but less so in the Northern Hemisphere. Nevertheless, over this period the annually averaged latitudinal gradient of methane has not changed.

Many studies have reported the measurement of methane concentrations in air bubbles trapped in ice from both Antarctica and Greenland (Robbins et al., 1973; Craig and Chou, 1982; Khalil and Rasmussen, 1982; Rasmussen and Khalil, 1984; Stauffer et al., 1985; Pearman et al., 1986; Etheridge et al., 1987). If these air bubbles are truly indicative of atmospheric methane levels at the time that they were trapped in the ice, then the results from all of these studies (see Figure 8.17) are broadly consistent and show that, over the past 300 years, there has been more than a doubling of methane concentrations.

8.7 TRACE GASES INFLUENCING TROPOSPHERIC OZONE AND HYDROXYL RADICAL CONCENTRATIONS

A number of reactive trace gases play an important role in tropospheric chemistry because they influence the tropospheric distribution of ozone and hydroxyl radicals. Methane, carbon monoxide, and the nitrogen oxides are examples. All of these have strong anthropogenic sources and thus are expected to increase on a global or at least on a hemispheric scale. The trend in troposphere CH_4 was discussed above. Evidence for possible increases in CO and NO_x is described in the following paragraphs.

Carbon Monoxide

Since about half of the atmospheric CO is estimated to come from anthropogenic activities, primarily from combustion sources and from the oxidation of methane, it is expected that the

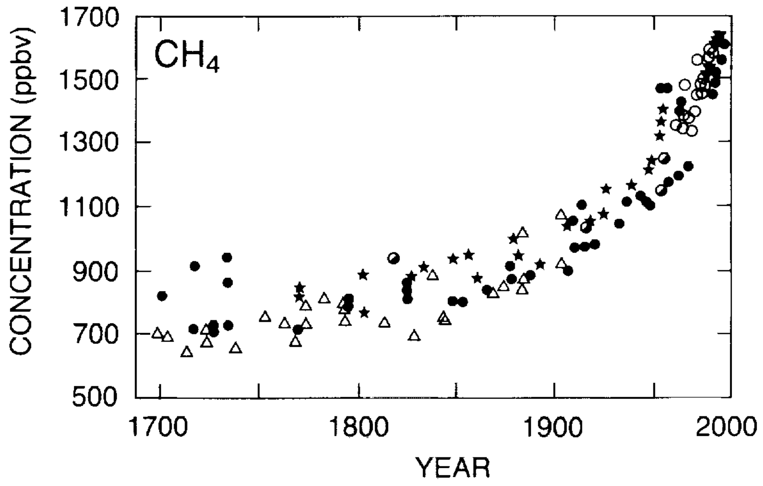

Figure 8.17 Summary of methane concentrations measured in air bubbles extracted from ice cores in both Greenland and Antarctica. Data are from several investigations, and differing methods of extracting the air from the ice have been used. References: ★, Stauffer et al. (1985); ∆, Khalil and Rasmussen (1982), Rasmussen and Khalil (1984); ○, Craig and Chou (1982); ●, Pearman et al. (1986), Etheridge et al. (1987), G.I. Pearman, D. Etheridge, F. de Silva, and P.J. Fraser, unpublished data. ▼ and ○ are globally averaged methane concentrations obtained from recent (Rasmussen and Khalil, 1986) and early (Khalil and Rasmussen, 1987c) gas chromatographic measurements of ambient air, respectively.

concentration of CO should increase as these sources continue to grow. However, because of short residence time (2 to 3 months), the determination of a secular trend in CO concentrations is very difficult.

The evidence for a global increase of CO has been controversial. A number of studies have estimated local CO trends ranging from 0 to 6 percent per year (Graedel and McRae, 1980; Dianov-Klokov and Yurganov, 1981; Dvoryashina et al., 1984; Seiler et al., 1984; Khalil and Rasmussen, 1984b; Rinsland and Levine, 1985; Fraser et al., 1986a,c). From these data, it would appear that CO concentrations in the Northern Hemisphere have increased in the past 15 to 30 years, but there is no convincing evidence of a Southern Hemisphere trend (Cicerone, 1988).

Recent analyses of measurements spanning 6 to 8 years suggest a global trend of about 1.0(±0.4)%/yr (Khalil and Rasmussen, 1988). The measurement sites are those of the Oregon Graduate Center flask sampling network, as well as the Cape Meares station, which incorporates in situ measurements, and Barrow, Mauna Loa and Cape Kumukahi (Hawaii), Samoa, Tasmania, and the South Pole. In Figure 8.18, the Northern Hemispheric, Southern Hemispheric, and global average concentrations are shown as monthly averages. The trends are claimed to be significant at the 95 percent level. At most individual sites, the trends are positive, but significantly greater than 0 only at the 90 percent level. At Cape Grim, the trend is very small and not statistically significant. It should be noted, however, that the estimation of a secular trend for CO is particularly difficult, because the species is short lived and shows a strong seasonal and spatial variation. Overcoming these problems requires long data records at a sufficiently large number of stations and a careful deseasonalization of the data. It is not clear that all these requirements are met by the available data sets.

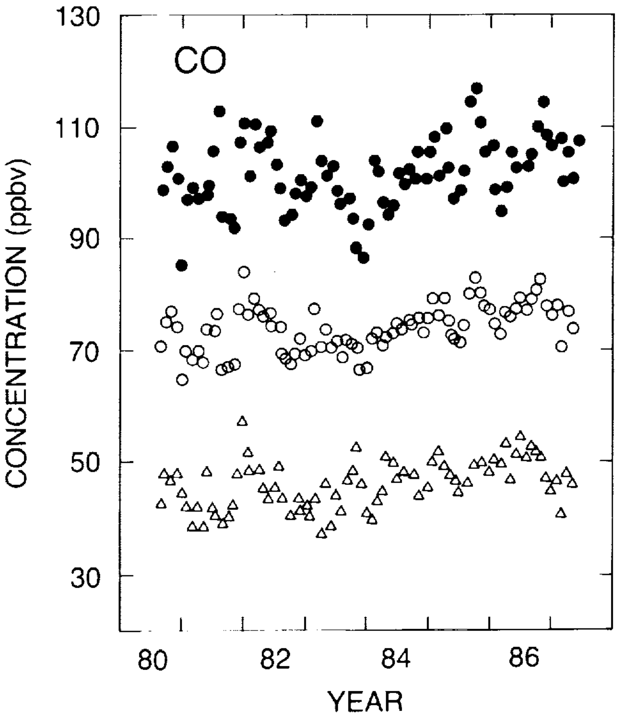

Figure 8.18 Hemispheric (●, Northern Hemisphere; Δ, Southern Hemisphere) and global (○) averages of deseasonalized CO concentrations (M.A.K. Khalil and R.A. Rasmussen, unpublished data).

Data from another flask sampling network in the Southern Hemisphere (Samoa; Cape Grim, Tasmania; Mawson, Antarctica; the South Pole; and the middle and upper troposphere over southeast Australia) do not show evidence for increasing concentrations of CO (Fraser et al., 1986a,c; Fraser et al., 1987b). The surface data are summarized in Figure 8.19.

In summary, it would appear that atmospheric CO concentrations have increased in the Northern Hemisphere, but, if they have increased in the Southern Hemisphere, the trend is probably smaller than the limit of detection of the current observational networks.

Nitrogen Oxides

Atmospheric nitrogen oxides (NO_x) are eventually converted to nitric acid, HNO_3, or aerosol nitrate, NO_3^-, and deposited at the Earth's surface. It has been proposed to use the measurement of NO_3^- in ice cores as an indicator of NO_x concentrations in the past atmosphere. Under present climatic conditions, nitrate is present in polar ice mainly as nitric acid (Legrand and Delmas, 1984). From measurements along an ice core collected in Greenland covering the last 100 years (Figure 8.20, curve A), Neftel et al. (1985) found a significant increase in NO_3^- that suggested that the NO_x budget of the high latitudes in the Northern Hemisphere has been significantly modified by human activities. In contrast, the nitrate profile observed in Antarctica over the same time period (Figure 8.20, curve B) exhibits no such trend, suggesting that the influence of anthropogenic NO_x was limited to the Northern Hemisphere. However, it currently is not possible to translate the observed NO_3^- increase in Greenland ice into a more quantitative statement about the NO_x budget of the Northern Hemisphere. The nitrate profiles from the South Pole do not support an earlier suggestion by Laird (1983) and Dreschhoff et al. (1983) of a modulation in NO_3^- deposition by solar activity (Herron, 1982; Legrand and Delmas, 1986).

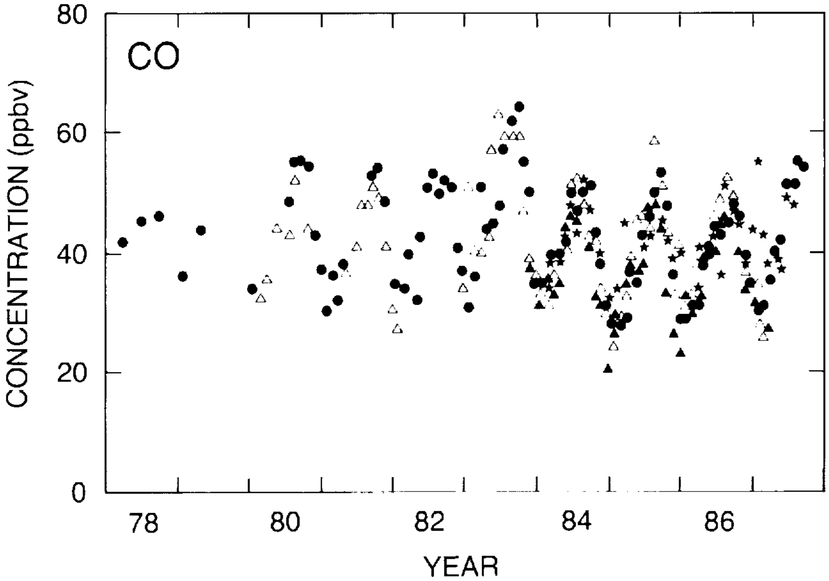

Figure 8.19 Monthly mean CO observations in the Southern Hemisphere from Samoa (★), Cape Grim (●), Mawson (Δ), and the South Pole (▲) (Fraser et al., 1986a,c; Fraser et al., 1987b; P.J. Fraser, unpublished data).

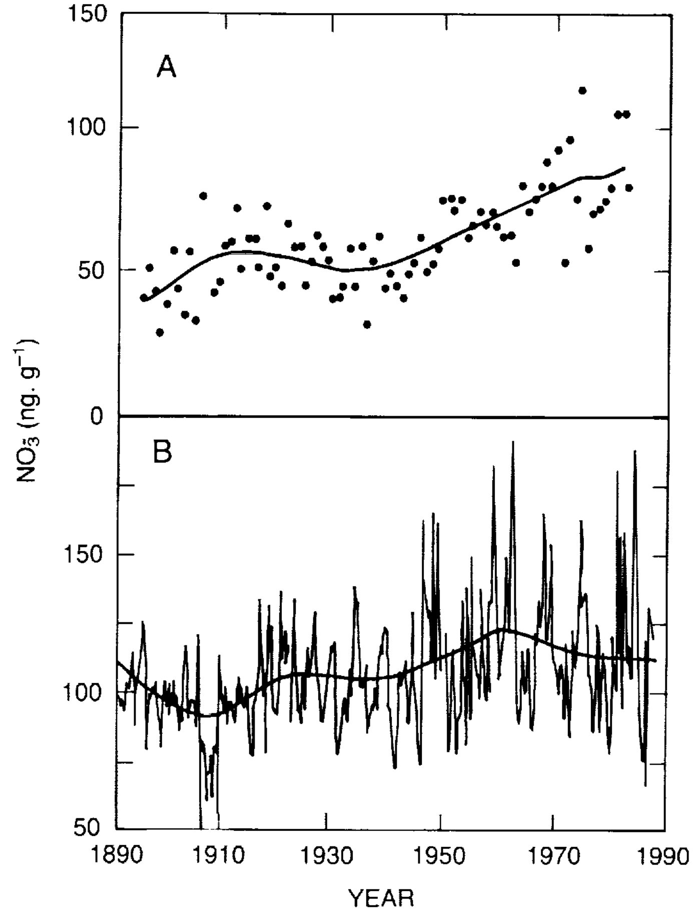

Figure 8.20 Nitrate (NO_3^-) trends over the last 100 years: (a) Dye 3, South Queensland (Neftel et al., 1985). (b) South Pole, Antarctica (S. Kircher, personal communication).

Carbon Dioxide

Carbon dioxide is not a photochemically active species in either the troposphere or the stratosphere. However, it is included in a discussion of source gases because it has a strong influence on the temperature-dependent photochemistry of the stratosphere, and, for example, it can thus influence levels and trends of stratospheric ozone.

While the long-term global rate of increase is about 1.5 ppmv per year (Fraser et al., 1983), the growth rate during 1981 to 1985 has been significantly lower, at approximately 1.2 ppmv per year. This lower growth rate is due, at least in part, to the effect of the intense ENSO event during 1982 to 1983 (see Conway et al., 1988; GMCC, 1986b).

8.8 CONCLUSIONS

Many of the source gases show a significant and well-documented increase in tropospheric concentration. The current rates of increase, along with the current concentrations and estimates of tropospheric lifetimes, are summarized in Table 8.1.

Available evidence indicates that increases in the atmospheric levels of CH_4, CO_2, and N_2O have been sustaining for long periods and that the increases derive from large-scale human activities, mainly food and energy production. From this viewpoint, it would be expected that possible trends in CO and NO_x may also have been sustained for a long time. It also seems improbable that the present trends of these gases will be arrested or reversed in the near future.

The highest relative rates of increase are observed for the exclusively manmade source gases (all gases in Table 8.1 except CH_3Cl, CH_3Br, N_2O, CH_4, and CO_2), because their lifetimes are long compared to the time since the beginning of release and they have not reached steady state. The two exceptions are CCl_4 and CH_3CCl_3, which are approaching steady state. The manmade halogen-containing gases are expected to continue their increase in the immediate future.

Evidence for increasing concentrations of $CBrClF_2$ and $CBrF_3$, often referred to as halons, is only just beginning to become available. Together with CH_3Br, they cause the total concentration of bromine to increase in the troposphere.

It is noted that the absolute accuracy of the concentration measurement is still unsatisfactory for some source gases, e.g., CCl_4, CH_3Br, $CBrClF_2$, $CBrF_3$, CCL_2FCClF_2, $CHClF_2$, and CO—mainly because calibration standards of suitable concentrations and integrity are not available. In addition, the global rates of increase for most of these gases are uncertain: for $CHClF_2$, $CBrClF_2$, and $CBrF_3$ because their increase has been monitored at only a few stations. Nevertheless, for the latter gases, the lifetimes are sufficiently long such that local increases are indicative of a global trend. The existence of a global trend in atmospheric CO levels remains uncertain.

54-45
53441
P20

CHAPTER 9

N92-15461

Trends in Stratospheric Minor Constituents

Panel Members

R. S. Stolarski, Chair - NC999967
W. P. Chu ND210491
M. T. Coffey
W. S. Heaps
J. A. Kaye
M. P. McCormick
R. Zander

PRECEDING PAGE BLANK NOT FILMED

PAGE 510 INTENTIONALLY BLANK

Chapter 9

Trends in Stratospheric Minor Constituents

Contents

9.1 INTRODUCTION 575

9.2 ODD NITROGEN 575

9.2.1 Nitrogen Dioxide—NO_2 576
9.2.2 Nitric Oxide—NO 578
9.2.3 Nitric Acid—HNO_3 580
9.2.4 Other Odd Nitrogen Compounds 582
9.2.5 Trends in Total Odd Nitrogen 582

9.3 HALOGENS—CHLORINE, FLUORINE, BROMINE (Cl, F, Br) 582

9.3.1 Hydrogen Chloride—HCl 583
9.3.2 Hydrogen Fluoride—HF 586
9.3.3 Chlorine Monoxide—ClO 587
9.3.4 Inorganic Bromine—Brx 588

9.4 H_2O/HO_x 589

9.4.1 Water—H_2O 589
9.4.2 Hydroxyl—OH 592

9.5 SUMMARY 592

PAGE 572 INTENTIONALLY BLANK

PRECEDING PAGE BLANK NOT FILMED

9.1 INTRODUCTION

The evidence for increasing concentrations of the source gases (CFC's for Cl and F, N_2O for N, and CH_4 for H, among others) has been summarized in Chapter 8 of this report. Photochemical models predict that increasing source gas concentrations are also expected to lead to changes in the concentrations of both catalytically active radical species (such as NO_2, ClO, and OH) and inactive reservoir species (such as HNO_3, HCl, and H_2O). For simplicity, we will refer to all these as trace species. This chapter addresses the question of long-term trends in these trace species.

In particular, we consider two questions associated with trace species concentrations. First, are those species whose concentrations are expected to be increasing actually doing so? Second, are there observed changes in any trace species not expected on the basis of the measured increase in source gases?

The consideration of these questions is difficult because of the limited data base of measurements of stratospheric trace species. In situ measurements are made only infrequently, and there are few satelliteborne measurements, most over a short time span insufficient for trend determination. Instead, ground-based measurements of column content must be used for many species, and interpretation is complicated by contributions from the troposphere or mesosphere or both. In this chapter, we examine existing measurements as published or tabulated; they have not been subjected to the rigorous review that has been applied to the ozone data examined in the bulk of this report.

9.2 ODD NITROGEN

The odd nitrogen compounds (N, NO, NO_2, HNO_3, N_2O_5, $ClONO_2$, and HO_2NO_2) are important to the chemical balance that determines stratospheric ozone concentrations. They participate in catalytic reactions and can interfere with catalysis by chlorine, hydrogen, and bromine compounds. Because their principal source is nitrous oxide—N_2O—which is known to be increasing at about 0.2 percent per year (see Chapter 8 of this report), a slow increase in the concentration of odd nitrogen compounds should be expected. This increase is sufficiently slow that no currently measurable changes in stratospheric odd nitrogen compounds are expected to result from it. Superimposed on this should be variations caused by interannual variability of the dynamics that transport odd nitrogen from its source in the middle stratosphere to its sinks, either in the mesosphere or troposphere.

Larger changes or long-term cyclical variations, if they are to occur, would likely have to arise from changes in the amount of odd nitrogen generated elsewhere in the atmosphere. In the upper mesosphere and lower thermosphere, processes involving ions and electrons lead to production of NO, which is then transported down to the stratosphere. This problem has been discussed extensively by Solomon and Garcia (1984b), Jackman et al. (1980), and Callis and Natarajan (1986). It has also been suggested (Ko et al., 1986, and references therein) that lightning may be an important source of odd nitrogen production, especially in the tropical upper troposphere. This odd nitrogen might then be transported into the stratosphere. Thus, changes in the rate of troposphere–stratosphere transport in the Tropics might also lead to changes in stratospheric odd nitrogen content. The rest of this section reviews the measurement evidence for changes in the odd nitrogen compounds.

PRECEDING PAGE BLANK NOT FILMED

PAGE 574 INTENTIONALLY BLANK

9.2.1 Nitrogen Dioxide—NO_2

Callis and Natarajan (1986) used differences between data from the Stratospheric Aerosol and Gas Experiment (SAGE–I and SAGE–II) experiments to deduce a dramatic change in odd nitrogen species between 1979 and 1984. They found 60 to 70 percent larger stratospheric NO_2 concentrations at midlatitudes in 1984 as compared to 1979. Data taken in 1979 by the Limb Infrared Monitor of the Stratosphere (LIMS) instrument on Nimbus–7 indicate low NO_2 values consistent with SAGE–I, while data taken in 1982 by the Solar Mesosphere Explorer (SME) satellite are consistent with the higher values measured by SAGE–II in 1984. Figure 9.1 from Callis and Natarajan (1986), shows 1 day of data from each of the SAGE instruments. Figure 9.1a shows SAGE–I data for November 25, 1979, at approximately 66°S latitude, as a function of altitude and longitude. Peak values of slightly over 6 ppbv occur between 30 and 35 km altitude. Figure 9.1b shows the same type of plot from SAGE–II for December 4, 1984. Peak mixing ratios are greater than 10 ppbv. Although the figure shows data from 2 particular days, Callis and Natarajan state that these are consistent with the results obtained over larger periods. They showed data averaged over several days (3 days of SAGE–I data, 7 days of SAGE–II data), indicating that the SAGE–II-determined profile was greater than that of SAGE–I by an amount in excess of the maximum difference attributed to the error bars in the measurements.

The detailed comparison of SAGE–I and –II data is complicated by the fact that different wavelength channels were used in the measurements of NO_2 by the two instruments. In SAGE–I, NO_2 amounts were obtained largely by consideration of the difference in absorption strength of NO_2 between two relatively broad-band channels at 385 and 450 nm, with bandwidths of 30 and 20 nm, respectively (Chu and McCormick, 1986). In SAGE–II, two narrow-band channels at 452.4 and 447.5 nm, with bandwidths of 1.9 and 3.2 nm, respectively, were used (McMaster, 1986; Chu, 1986).

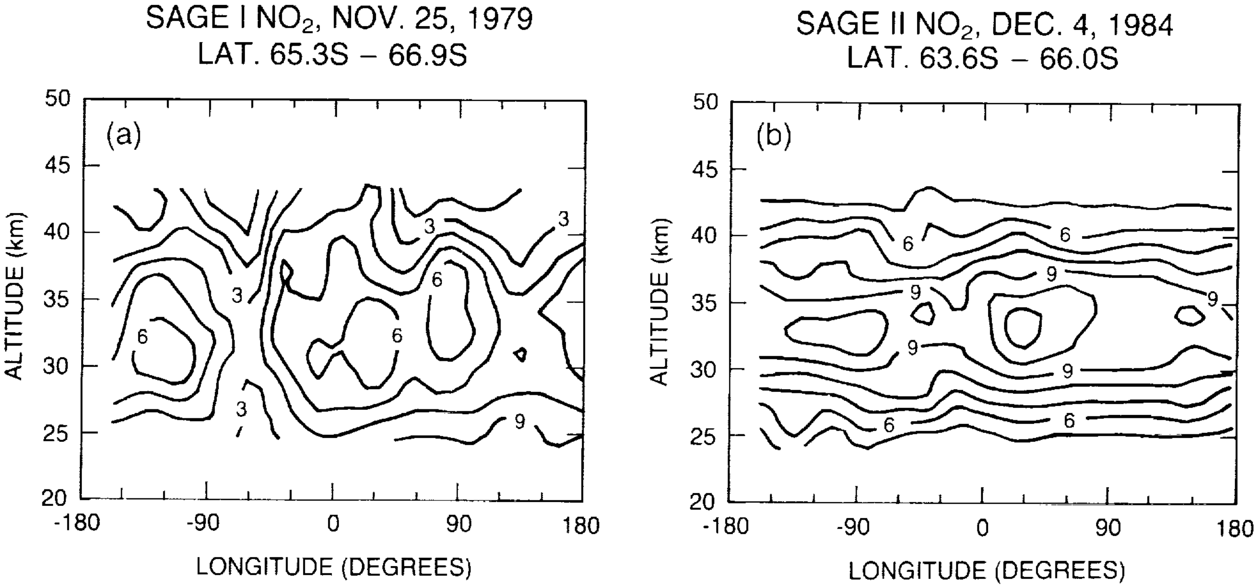

Figure 9.1. Solar occultation measurements of daytime mixing ratios of NO_2 in ppbv by the SAGE and SAGE–II (preliminary data) instruments. Positive longitudes are those east of Greenwich. (a) Longitude–altitude plot of 1979 SAGE data for November 25, 1979, using data over a latitude range from 65.3°S to 66.9°S. (b) Similar plot for SAGE–II data for December 4, 1984, for the latitude range 63.6°S to 66.0°S. Contour interval for both plots is 1 ppbv. Figure taken from Callis and Natarajan (1986).

The reality of these changes is critically dependent upon the absolute calibration of each satellite instrument. In particular, the SAGE–II information was based on a preliminary calibration obtained as a personal communication from McCormick and Chu. The SAGE–II data are being validated by the SAGE–II Science Team for release. Thus, any final statements concerning NO_2 changes cannot be made as of this writing.

Another way to test the relative calibration of satellite measurements is to compare them to ground-based measurements that can be continually checked for the maintenance of their calibration. For NO_2, the principal available ground-based measurements are of the column amount during the daytime. These are made by visible absorption spectroscopy (Noxon et al., 1979; McKenzie and Johnston, 1984; Elansky et al., 1985; Shibasaki et al., 1986, and references therein). The ground-based measurements have been discussed in detail in *WMO* (1986). These measurements have been made sporadically since the mid-1970's. Figure 9.2, from Coffey (1988), shows sunset measurements of the total column of NO_2 by various experimenters plotted as a function of time from 1975 through 1986. The figure is broken into four panels based on the latitude of the measurements. Figure 9.2a shows the high northern latitude measurements (60°N to 80°N). The solid curve is a sinusoid with a frequency of one per year and a minimum on January 1 chosen to represent the expected seasonal variation of stratospheric NO_2 (annual cycle, winter minimum). The amplitude of the sinusoid is chosen to include approximately the full range of the values measured. The high northern latitude data clearly are too sparse to draw any significant conclusions concerning trends in NO_2.

Figure 9.2b shows the northern midlatitude (35°N to 45°N) measurements with a sinusoidal curve determined as above. Although a number of interpretations are possible for the data shown, it is clear that there is no large trend in the data. The minimum in the winter of 1979 to 1980 seems to be a bit lower than those of the early 1980's by some 20 percent, but there is no obvious upward trend in the maxima. The data during the rapid spring increase and fall decrease are very difficult to evaluate in terms of trend because of the possibility of small shifts in the seasonal phase. Figures 9.2c and 9.2d show the data for NO_2 column amount for the mid-southern latitudes and high-southern latitudes, respectively. In both cases, insufficient data exist to make any statements about trends.

Coffey (1988) has performed a similar comparison with satellite data for NO_2 from the LIMS, SAGE–I, SAGE–II, and SME instruments. Because the satellite measurements are not made below about 24 km, the integrals shown are above 24 to 25 km altitude for each instrument, and only sunset data are used for the SAGE instruments. About half of the NO_2 column is included in an integral above 24 km. Figure 9.3 shows the comparisons in the same format as in Figure 9.2. Figure 9.3a is for 60°N to 80°N with LIMS, SAGE–I, SME, and SAGE–II data. The peak values seen in 1979 are certainly lower than in 1983 to 1985, but it is not entirely clear from the data in the figure that this is representative of any long-term change. It is clear that careful examination of an entire seasonal cycle is important in assessing the meaning of any observed changes. Figure 9.3b shows the same comparison for 35°N to 45°N. Again, no clear picture of long-term change emerges. The data for 35°S to 45°S and for 60°S to 80°S are shown in Figures 9.3c and 9.3d, respectively. Here the seasonal peak is clearly defined, indicating a somewhat lower concentration of NO_2 in 1979 than in the mid-1980's. The difference is about 20 percent. Figure 9.4, from Johnston and McKenzie (1989), shows an update through early 1988 of the monthly average NO_2 slant column amounts measured at Lauder, New Zealand. The record is dominated by a seasonal cycle, shows some interannual variability, but contains no large trend.

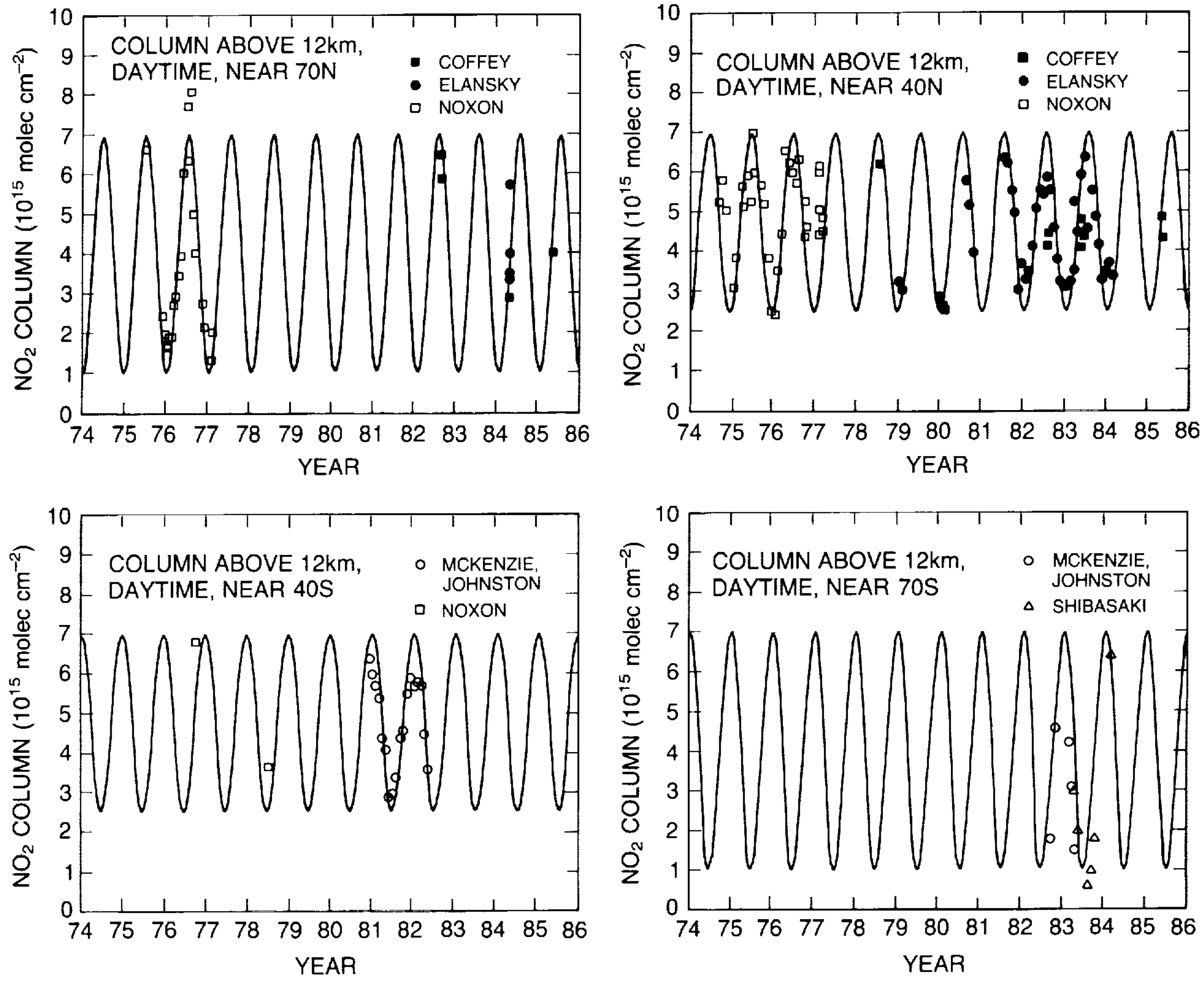

Figure 9.2. NO_2 column amounts above 12 km from a number of ground- and aircraft-based measurements. The curve is a sinusoid chosen as described in the text; maximum in summer and a minimum in winter; data are taken from the groups shown. (a) 70°N (top left), (b) 40°N (top right), (c) 40°S (bottom left), (d) 70°S (bottom right). Altitude ranges are approximate. Figure taken from Coffey (1988).

The problem of changes in NO_2 remains interesting and largely unsolved. More definitive statements await the formal release of the SAGE–II data. The data shown indicate the possibility of some relatively large changes and cannot rule out an increase of 10 to 20 percent in the Southern Hemisphere from 1979 to 1986. They do not appear to support the 60 to 70 percent changes reported by Callis and Natarajan (1986), however. The smaller changes of order 10 to 20 percent would still give rise to significant variations in the balance of the stratospheric ozone photochemistry. The data record is still insufficient to determine whether any observed changes are long-term trends, solar cycle variations, or just dynamically induced interannual variability.

9.2.2 Nitric Oxide—NO

There are not nearly as many measurements of NO as there are of NO_2. A number of in situ altitude profile measurements have been made from balloons and some latitude surveys have

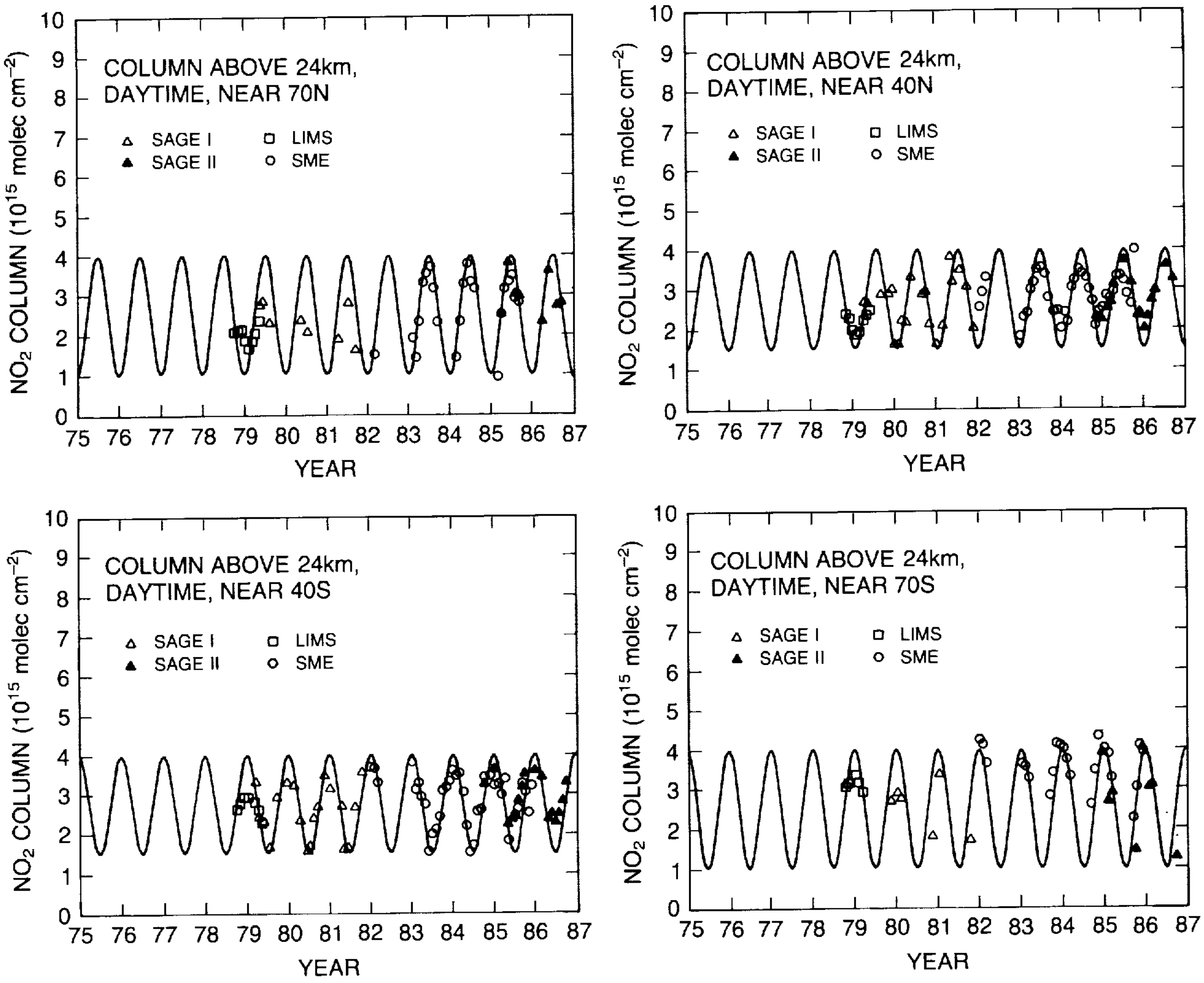

Figure 9.3. NO_2 column amounts above 24 km from indicated satelliteborne experiments. Curve is a sine function as in Figure 9.2. Arrangement and labeling of panels is as in Figure 9.2. Figure taken from Coffey (1988).

been made from aircraft. These measurements are described in *WMO* (1986) in some detail. While they are very important in examining the stratospheric chemical mechanism and in testing some ideas about transport, they do not form a long-term data base suitable for determining stratospheric odd nitrogen trends.

McPeters (1989) has deduced NO concentrations near and above 1 mb from the 255.5-nm albedos measured by the SBUV instrument. This is a wavelength that was originally used to measure ozone near the stratopause but was found to be contaminated by the nitric oxide gamma bands resulting from resonant-fluorescent scattering of sunlight by NO. The region at or above 1 mb is one in which the NO concentration might be expected to be quite variable because of the influence of mesospheric and lower thermospheric sources of odd nitrogen from particle precipitation.

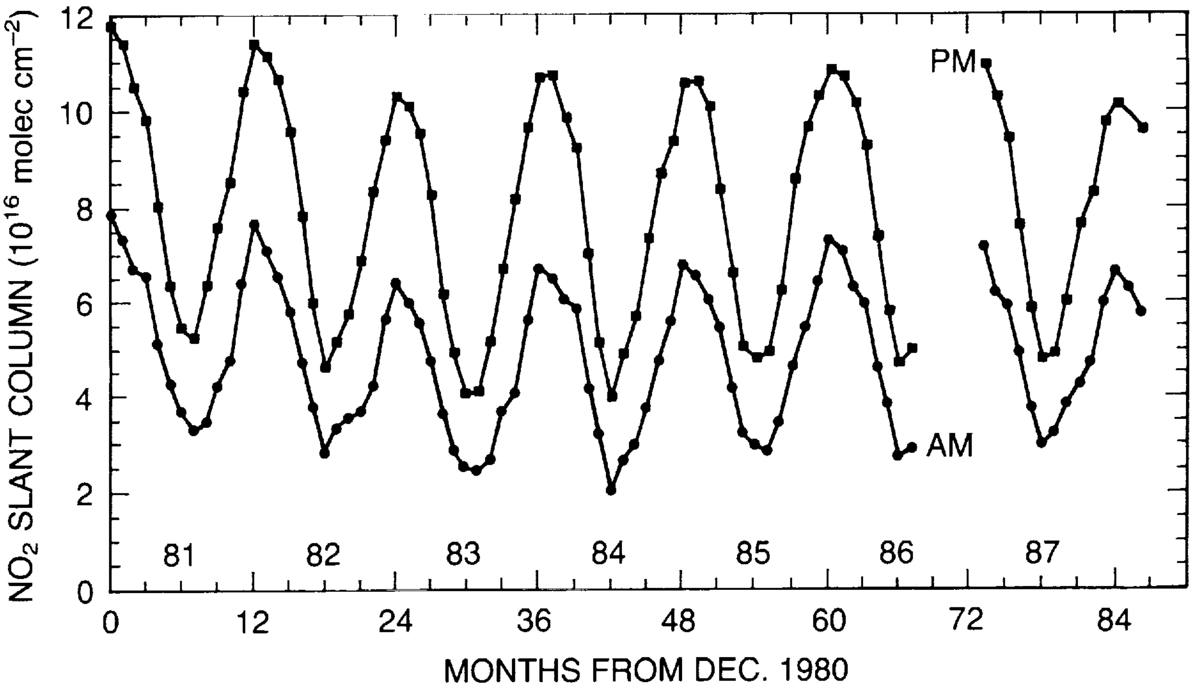

Figure 9.4. Monthly averaged NO_2 slant column amounts at Lauder, New Zealand (45°S, 170°E). Figure taken from Johnston and McKenzie (1989).

Figure 9.5 shows the variation of cumulative NO above 1 mb (48 km) between 1979 and 1986 for five latitude zones. A clear decreasing trend of about a factor of 2 is seen at equatorial latitudes. This decrease occurs during a period of decreasing solar activity (Lean, 1987), but without a longer data period it is impossible to determine whether there is any connection to solar activity. The measurement of cumulative NO above 1 mb includes a large contribution from NO in the upper mesosphere and thermosphere; much of the variation may be due to changes in these regions. Because the NO measurement depends on the relative strengths of individual NO gamma bands, it is little affected by possible changes in instrument calibration (McPeters, 1989). The annual variation of NO at high latitudes is of much larger amplitude than in the Tropics, making long-term changes more difficult to detect. There is not any clear trend in NO above 1 mb outside of the Tropics. There is, however, a large degree of interannual variability at high latitudes. For example, the large increase in NO from 60°S to 80°S in July 1982 is known to be related to the solar proton event of July 13, 1982 (McPeters, 1986).

9.2.3 Nitric Acid—HNO_3

There are not enough column or in situ measurements of HNO_3 to deduce any significant changes. The only satellite-based data—those from the LIMS experiment on Nimbus–7—cover only a short (7 month) time period and, thus, are not useful in trend determination. One pair of relevant measurements is that recently reported by Murcray et al. (1987) for HNO_3 column measurements made at the South Pole on December 5, 1980, and November 26, 1986. Within their respective error bars, the two amounts were equal—$(1.6 \pm 0.3) \times 10^{16}$ molecules per cm^2 in 1980, $(1.4 \pm 0.4) \times 10^{16}$ in 1986.

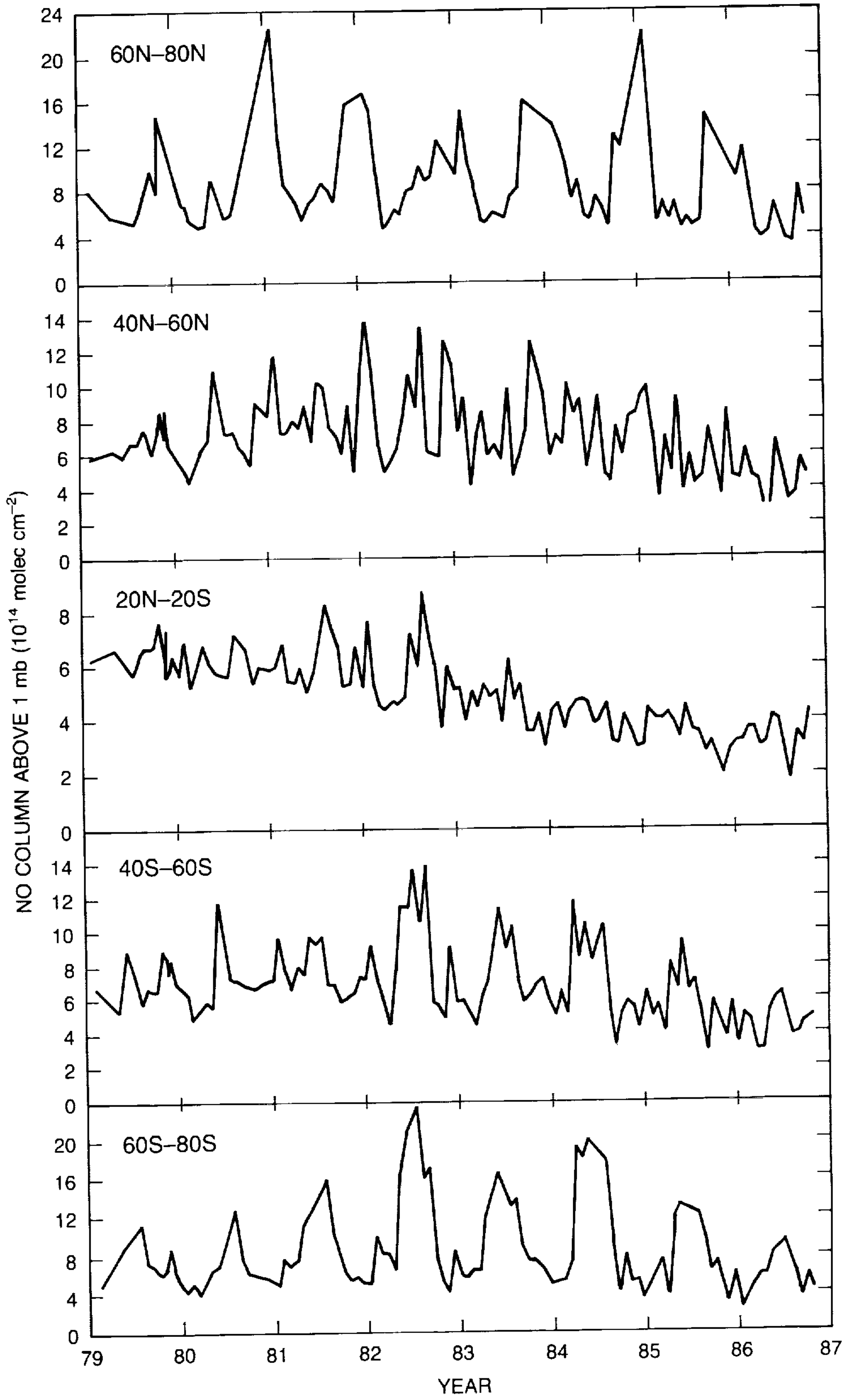

Figure 9.5. SBUV NO data showing column amount of NO above 1 mb in molecules per cm^2 as a function of time for the period 1979 to 1986 in the indicated latitude ranges. Figure obtained from McPeters (1989).

9.2.4 Other Odd Nitrogen Compounds

Only recently have unambiguous measurements of the remaining stratospheric odd nitrogen compounds N_2O_5, $ClONO_2$, and HO_2NO_2 become available. All were observed by the shuttleborne Atmospheric Trace Molecule Spectroscopy (ATMOS) instrument, which flew as part of Spacelab 3 in 1985 (Russell et al., 1988). Measurements of $ClONO_2$ have also been made using the balloonborne Stratospheric Infrared Interferometer Spectrometer (SIRIS) instrument (Massie et al., 1987), as well as from the ground by Zander and De Moulin, 1988. These data, together with what little data existed before (*WMO*, 1986), are inadequate for trend determination.

9.2.5 Trends in Total Odd Nitrogen

Each of the above species can show trends with time either because of a variation in the total odd nitrogen or because of a change in the balance of the chemistry within the nitrogen family. The two effects could also counteract one another somewhat by being of opposite sign for the particular constituent. The only way to uniquely separate the effects is to measure the total odd nitrogen concentration. This is an especially important quantity, as the efficiency with which chlorine catalyzes ozone destruction is nonlinearly dependent on the total amount of stratospheric odd nitrogen.

Determination of total odd nitrogen has been done only once, using measurements of all important odd nitrogen constituents (NO, NO_2, HNO_3, HNO_4, N_2O_5, and $ClONO_2$) made with the ATMOS spectrometer. Measurements were made for two latitudes (30°N, 48°S) on May 1, 1985. Maximum values of approximately 17 ppbv were obtained at approximately 43 km (2 mb) (Russell et al., 1988).

Estimates of total odd nitrogen were also inferred previously from LIMS measurements of nighttime NO_2 and HNO_3. These two constituents make up most of the total odd nitrogen at night, the remainder being in the form of N_2O_5, $ClONO_2$, and HNO_4. Maximum values of 24.4 to 27.7 ppbv were inferred, with maximum zonal and meridional monthly averages ranging between 22.8 and 23.8 ppbv in the 35 to 37 km range (Callis et al., 1986). Substantially smaller values (maximum of 21 ppbv) were calculated by Solomon et al., as described in *WMO* (1986), using LIMS daytime measurements and a photochemical model. The difference in these two inferred values emphasizes the uncertainties in the precise interpretation of total odd nitrogen from limited data.

A comparison of the total odd nitrogen inferred from the LIMS data and that directly measured by ATMOS for May 1 at 30°N is shown in Figure 9.6. The two results are in agreement within their respective error bars below 42 km, differing by a maximum of about 15 percent, with larger differences above that altitude. The differences are within the extremes of the error limits of the two instruments, but also may be related to real atmospheric variability. Thus, the data are insufficient to discriminate among models that predict different total odd nitrogen amounts. Additional measurements using the surface-catalyzed reduction technique (Fahey et al., 1985), which was used most recently as part of the Airborne Antarctic Ozone Experiment, should make in situ measurement of total odd nitrogen easier in the near future.

9.3 HALOGENS—CHLORINE, FLUORINE, BROMINE (Cl, F, Br)

The major source molecules for halogens are known to be increasing by amounts corresponding to 5.4 percent per year for fluorine, 3.4 percent per year for chlorine, and 2 to 4 percent per

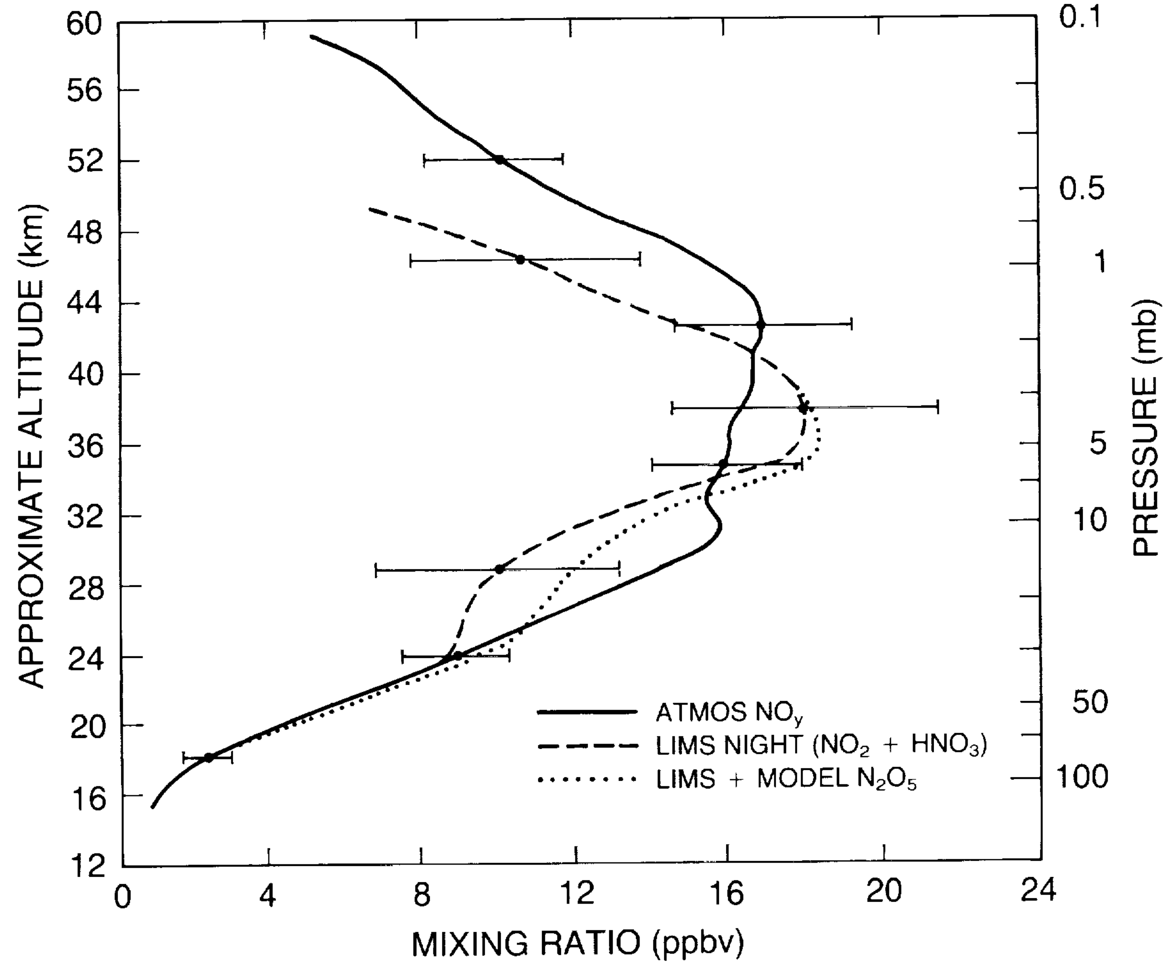

Figure 9.6. Plot of total odd nitrogen measured by ATMOS on May 1, 1985, at 30°N (solid line), LIMS descending node $NO_2 + HNO_3$ (dashed line), and LIMS descending node $NO_2 + HNO_3$ plus twice the N_2O_5 inferred from a photochemical model (dotted line), from Russell et al. (1988).

year for bromine, based on measurements of halogenated organics in the troposphere (see Chapter 8, Table 8.1). The rate of increase for bromine is caused entirely by growth in halons and does not include possible growth in CH_3Br. It is considered an inevitable consequence of these increases that the concentrations of the resulting stratospheric gases (Cl, ClO, HCl, $ClONO_2$, HOCl, HF, etc.) should increase. The evidence for actual increases in these gases is unclear with the exception of HF and, to a lesser extent, HCl.

9.3.1 Hydrogen Chloride—HCl

Two sets of long-term column measurements of HCl seem to show contrasting results. In a series of aircraft-based measurements, Mankin and Coffey (1983) found evidence for an annual increase of the HCl column above 12 km of 5 percent per year from 1978 to 1982. This estimate was obtained by considering all data taken between the latitudes of 35°N and 55°N, and converting them to 45°N based on the observed latitude dependence, and then fitting a linear temporal trend to the converted data. Data of Mankin and Coffey (1983) taken between 35°N and 55°N and normalized to 45° are shown in Figure 9.7. This increase has been confirmed with

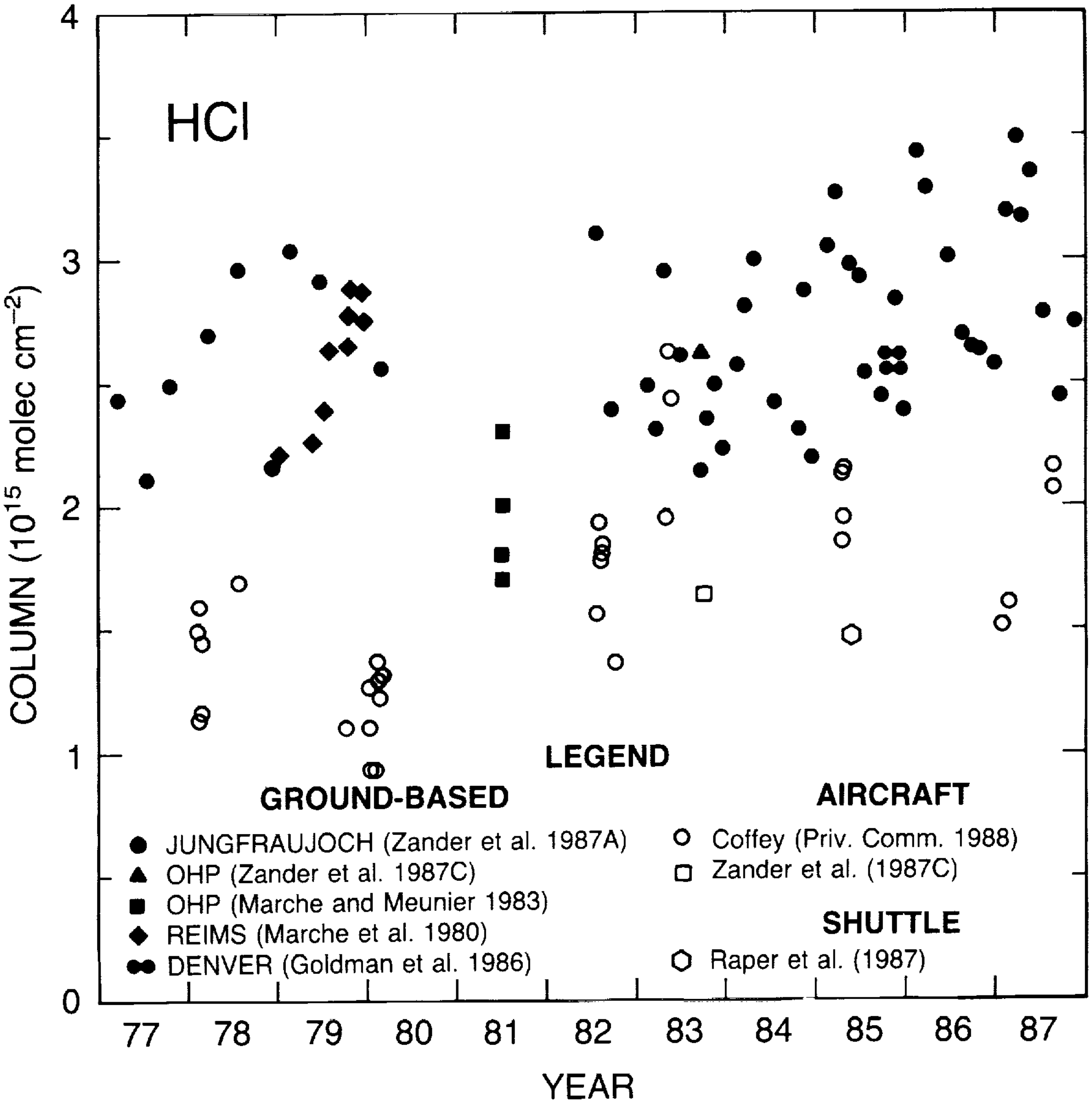

Figure 9.7. Time series plot of column amount of hydrogen chloride (HCl) measured from the ground, aircraft, or shuttle during the period 1976 to 1987. Symbols correspond to data taken by various experimenters as indicated on the figure.

additional measurements made through 1987 (Coffey, personal communication, 1988), also normalized to 45°; these also are shown in Figure 9.7.

In a series of ground-based measurements from the Jungfraujoch Observatory in Switzerland (3.58 km, 46.55°N) since 1977, also shown in Figure 9.7, Zander et al. (1987a) found evidence of an apparent small increase in the total HCl column. A trend of 0.75 ±0.2 percent per year or about 2 × 10^{13} molecules per cm^2 per year increase in HCl was deduced by Zander et al. (1987a). This trend was calculated by determining the mean of the 1977 to 1980 observations and that of the 1983 to 1986 observations and assuming a constant rate of increase between these mean points. The weak linear trend is superimposed on significant short-term variability, which may be partially a result of variability in the tropospheric HCl column (see below), although analysis of the line shape indicates that much of this variability is caused by changes in the HCl amount above 8 km (Zander et al., 1987a). There is also a seasonal variation, in which the HCl column maximizes in the spring and minimizes in late summer to early winter. The amplitude of the seasonal variation is approximately 10 percent (Zander et al., 1987a).

A trend analysis of these data shows that the total HCl column has been increasing at about two to three times the rate deduced by Zander et al. (1987a) over the time of the measurements. There are two major reasons for this difference: the extension of the data through 1987 and the deseasonalization of the pre-1982 data, which are biased in favor of high HCl months. The large seasonal variation and the uneven sampling in the 1977 to 1981 data cause the mean value to be above what it would be if the seasonal variation had been removed before taking the mean. A simple deseasonalized recalculation of the means of 1977 to 1980 and 1983 to 1986 data using the seasonal cycle as given in Zander et al. (1987a) more than doubled the derived slope in the HCl data (4.5×10^{13} molecules HCl per year). In a more detailed analysis (Wofsy, personal communication), the data were deseasonalized by separately averaging for each year the months of seasonal high (February to June) and seasonal low (July to November) values, omitting the December values, which are frequently lower than the other fall month values. The values for the seasonal high group were corrected to those of the seasonal lows by subtracting an amount of 4.5×10^{14} molecules per cm^2. A plot of these 17 deseasonalized values vs. time is well fit, with the exception of one value, by a straight line with a slope equivalent to an annual increase of $(6.0 \pm 1.3) \times 10^{13}$ molecules cm^{-2} yr^{-1}, which corresponds to an annual increase of between 2 and 3 percent per year over the 1976 to 1987 time period. The scatter of the pre-1982 data about this line is substantially greater than for the post-1982 data.

There is also an unexplained difference between the rate of increase in the post-1982 seasonal high (February to March) and seasonal low values. The annual rate of increase in the former appears to be at least a factor of 2 larger than in the latter. Further data over the next few years will be necessary to quantify any changes in the seasonal cycle. One should interpret annual rates of increase that are seasonally dependent with some caution.

Several additional measurements of the HCl column are also presented in Figure 9.7. These include the ground-based measurements of Marche et al. (1980) made from Reims, France (83 m altitude, 49°N) in 1979, and of Marche and Meunier (1983) and Zander et al. (1987c) from the Observatoire de Haute-Provence (OHP) Mt. Chiran station (1.905 km altitude, 43.88°N) in June 1981 and September 1983, respectively. Also plotted are an aircraft-based measurement made from 11.9 km altitude at 45°N in September 1983 (Zander et al., 1987c) and a shuttle-based measurement made with the ATMOS instrument in May 1985 covering the altitude range of 15 to 55 km (Raper et al., 1987). Finally, two measurements of the total HCl column above Denver made in October 1985 by Goldman et al. (1986) are also shown. These additional data shed no direct light on trends, but do support the magnitude of the total HCl column $(2\text{–}3) \times 10^{15}$ molecules per cm^2, the important contribution of tropospheric HCl, and the existence of important short-term variability in the HCl column (the data of Marche and Meunier, 1983, showed a 25-percent change in the HCl column over a period of 1 week).

The difference in magnitude between the aircraft results of Mankin and Coffey (1983) and the ground-based results of Zander et al. (1987a) should be related to the tropospheric HCl content. This is known to be highly variable, both in total amount and in vertical dependence (Vierkorn–Rudolph et al., 1984). In an aircraft flight made off Tromso, Norway, on September 8, 1981, under conditions of heavy clouds and rain, during which HCl is expected to be efficiently scavenged, a well-mixed profile with a mixing ratio of approximately 70 pptv was obtained from 0.5 to 7 km. This suggests that 70 pptv is a reasonable value for the "clean" troposphere. Such a mixing ratio would lead to an expected HCl column from 3.5 to 12 km (the approximate altitudes of the Jungfraujoch and aircraft observations, respectively) of 0.7×10^{15} molecule per cm^2. Larger tropospheric columns were obtained in other measurements, but in most of these the highly elevated HCl values observed (as large as nearly 500 pptv) were confined to altitudes near and below 1 km, and thus may not strongly influence the Jungfraujoch data, which are obtained at 3.58 km altitude; they will be more important for lower altitude stations, such as OHP.

The differences between HCl columns measured from the ground on September 8, 1983, at Jungfraujoch (2.43×10^{15} molecules per cm^2) and OHP (2.67×10^{15} molecules per cm^2) and that measured on the same day from an aircraft (1.65×10^{15} molecules per cm^2) at 11.9 km (Zander et al., 1987c) are somewhat larger than the expected tropospheric values based on a mixing ratio of 70 pptv, but the differences are within the uncertainties of the measurements plus meteorological variability.

There is also evidence that stratospheric HCl amounts may be strongly affected by large volcanic eruptions, such as those of El Chichón in March and April 1982 (Mankin and Coffey, 1984); this has been discussed in *WMO* (1986). No additional evidence has become available since publication of that report. Given the apparent increase in the column HCl amounts in the post-1982 measurements of Zander et al. (1987a), it is important that the effects of volcanic eruptions on stratospheric HCl amounts be better understood.

9.3.2 Hydrogen Fluoride—HF

Measurements of a substantial increase in the HF column have been made from both ground-based (Zander et al., 1987b) and aircraft-based (Mankin and Coffey, 1983) techniques. Zander et al. (1987b) reported evidence of a cumulative annual increase since 1976 of 8.5 ± 1 percent in the total HF column above the Jungfraujoch station (see Figure 9.8). Mankin and Coffey (1983) found evidence for an annual increase of 12 percent in the HF column above the 12-km cruising altitude of their aircraft for the period 1978 to 1982. Zander et al. (1987b) also found a strong seasonal variation in the total HF column, very similar in amplitude and phase to that of HCl described above. Since the chemistries of stratospheric HCl and HF are quite different (HCl is converted to ClO and, thus, the other chlorine-containing species by reaction with OH, while HF is nearly completely unreactive), this suggests that much of this seasonal variation is dynamical in origin.

A statistical analysis of the Zander et al. (1987b) HF data, similar to the one for HCl, yielded a trend line with a slope of $(3.62 \pm 0.24) \times 10^{13}$ molecules $cm^{-2}\ yr^{-1}$, corresponding to an increase of between 5 and 10 percent per year over the 11 years of data.

The ratio of HF to HCl given by the total column measurements provides an indication of the contribution of chlorofluorocarbon decomposition to the total stratospheric chlorine burden, as naturally occurring sources of stratospheric chlorine do not contain fluorine. The measurements of Zander et al. (1987b) show that this ratio has increased substantially from the 1977 to 1979 time period, when it was 0.15, to the 1983 to 1985 time period, when it was 0.24.

Mankin and Coffey (1983) similarly found a ratio of 0.19 for 1978 to 1979 and 0.23 for 1983 to 1985 (Mankin and Coffey, personal communication). The ATMOS value obtained in May 1985 was 0.25 (Raper et al., 1987). The large increase in the HF–HCl ratio provides important

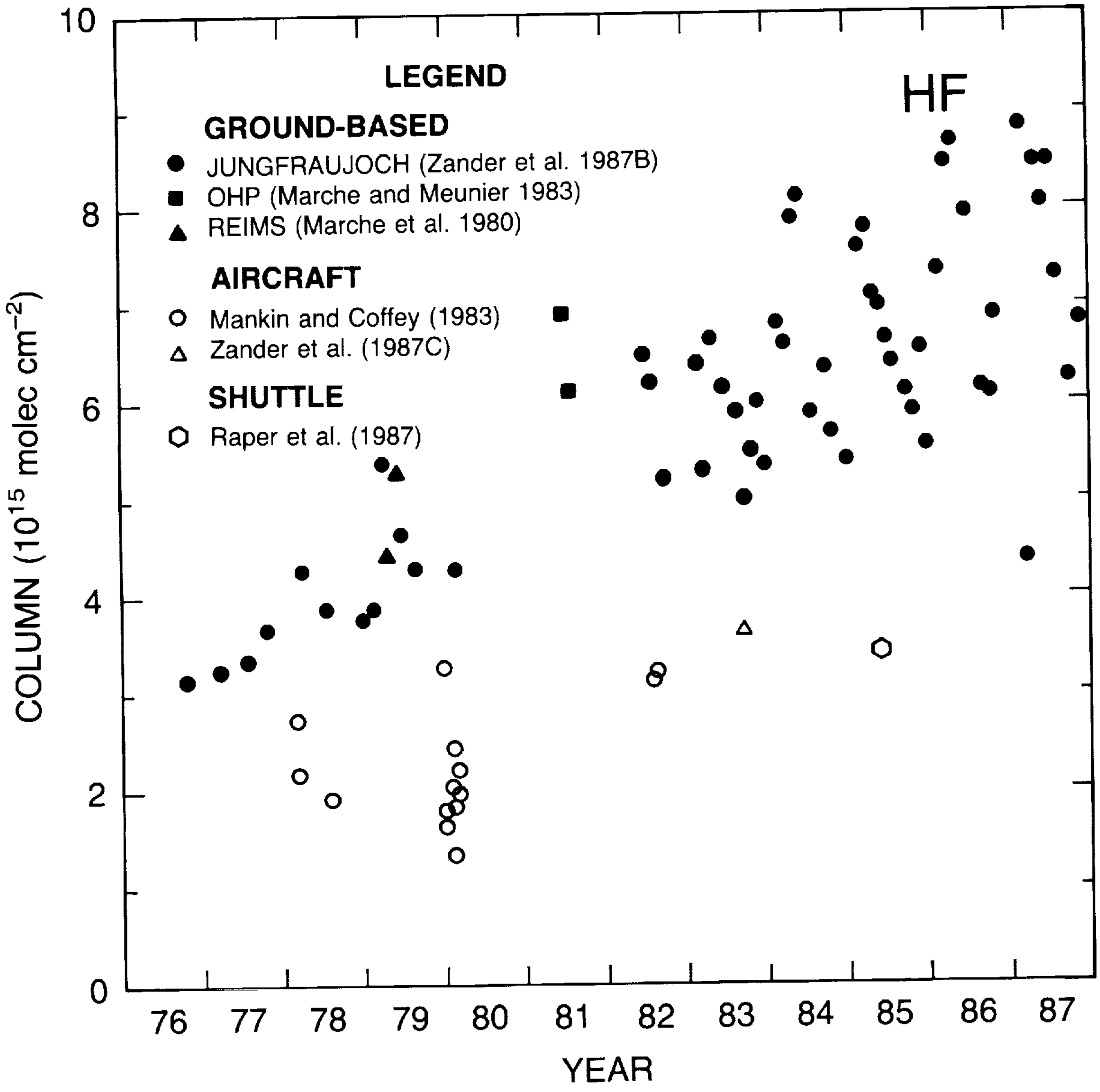

Figure 9.8. Time series plots of column amount of hydrogen fluoride (HF) measured from the ground, aircraft, or space during the period 1976 to 1987. Symbols correspond to data obtained by various experimenters as indicated in the figure.

confirmation of the breakdown of fluorocarbons in the stratosphere. In Wofsy's analysis, the annual increase in the HCl column is 1.7 times that of the HF column, which is consistent with that based on industrial emissions.

9.3.3 Chlorine Monoxide—ClO

While there are a number of in situ measurements of stratospheric ClO content, made primarily by Anderson and coworkers (see *WMO*, 1986), the large variation obtained in these measurements and their limited number precludes their use in determination of long-term trends of stratospheric ClO. There are, however, 5 years of ground-based microwave column measurements taken over Hawaii (deZafra et al., 1985; P.M. Solomon, personal communication), as well as several data points taken earlier elsewhere. These measurements determine the total ClO column density above a pressure level corresponding to approximately 30 km altitude. The results of this period of measurement, summarized in Figure 9.9, do not yet show any clear indication of an increase in upper stratospheric ClO. Accurate trend determination will require substantially increased sampling frequency and a longer data record.

9.3.4 Inorganic Bromine—Brx

Increasing concentrations of bromine-containing molecules in the stratosphere, primarily BrO, are expected based on the 3 percent per year observed increase in the concentrations of several brominated source gases (see source gas chapter of this report), especially $CBrClF_2$ and $CBrF_3$. Only very limited data of stratospheric Brx compounds exist, however, and these data are not sufficient for trend determination.

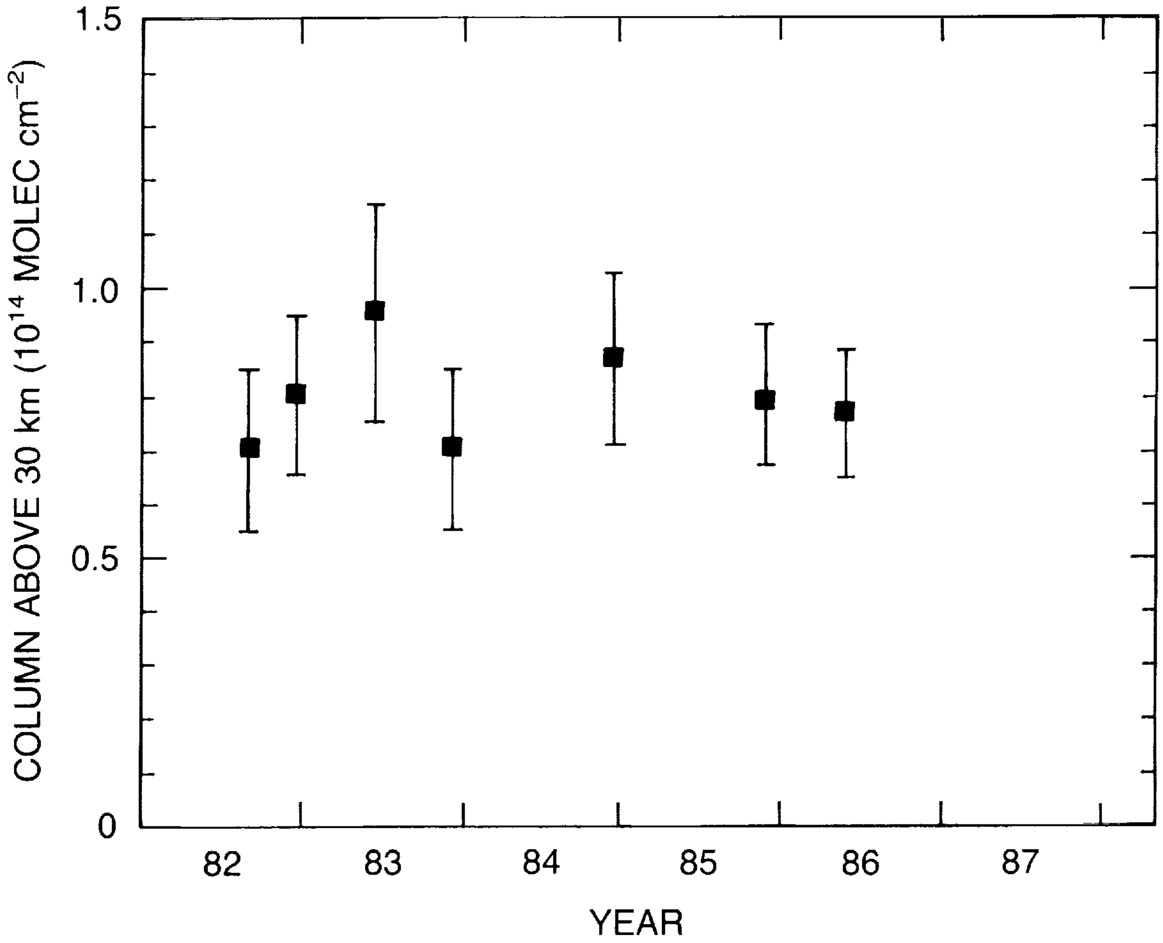

Figure 9.9. Time series of midday ClO column abundances above 30 km measured by ground-based millimeter wave spectrometry taken from Hawaii (from deZafra et al., 1985, with data since 1984 provided by P. Solomon, personal communication, 1987).

9.4 H_2O/HO_x

9.4.1 Water—H_2O

Upper stratospheric water vapor should be changing as a result of its production from oxidation of methane (CH_4), which in the troposphere is known to be increasing at the rate of approximately 1 percent per year (see Chapter 8 of this report). The data on upper stratospheric water vapor are too sparse and variable to discern any trend.

Substantially more data exist on the water content of the lower stratosphere, however, where methane oxidation is not expected to be a significant source of water. Most of these have been made with a balloonborne frost-point hygrometer. Lower stratospheric water vapor is thought to most strongly reflect temperatures near the tropopause and may thus be a better diagnostic of changing tropopause meteorology and of troposphere–stratosphere exchange than of changing methane oxidation amounts.

In a series of balloon flights from Washington, D.C. (1963 to 1980), and Boulder, Colorado (since 1980), Mastenbrook and Oltmans (1983) have shown evidence for both a quasi-biennial oscillation and a nonlinear long-term trend in the H_2O mass-mixing ratio at 60 mb. This may be seen in Figure 9.10a (Oltmans, personal communication, 1987), which shows that H_2O amounts tended to increase over the first third of the data set, to decrease over the middle third, and to be relatively constant over the final third. Trend determination from these measurements is difficult because of the shorter term variability. This is removed in the calculation of a 12-month running mean, which is the solid line shown in Figure 9.10a. Some differences between the Washington, D.C., data and the Boulder data are also possible, as the balloons launched from Washington, D.C., ascended through the relatively humid boundary layer, while those launched from Boulder encountered much drier air during the early portion of their ascent.

Examination of measurements made at higher altitudes (up to 20 mb, or approximately 27 km) over Boulder from 1980 to 1987 shows no clear evidence of any long-term trend (Oltmans, 1986; Oltmans, private communication, 1987). All time series (plots of mixing ratio vs. measurement time) in the 20 to 60 mb range are well represented by lines of zero slope with small scatter. Data down to lower altitudes (120 mb, or approximately 15 km) are also well represented by lines of zero slope, but the scatter of the points increases substantially with increasing pressure.

Additional measurements of lower stratospheric water vapor were made with an aircraftborne frost-point hygrometer over southern England during 1972 to 1980. These data, plotted in the form of representative stratospheric humidity (r.s.h), defined as the average of the humidity mixing ratios at 180, 160, and 147 mb when they were within 20 percent of each other, show an apparent decrease in H_2O mixing ratio from 1972 to 1976 and an increase from 1977 to 1980. Trend determination from these data, taken from Foot (1984) and shown in Figure 9.10b, is clearly complicated by their large variability. Because these data were taken so low in the stratosphere, the air masses sampled may contain a nonnegligible tropospheric component.

Several years of measurements of stratospheric water vapor over Mildura and Alice Springs, Australia, have also been reported (Hyson, 1983). These data, made by an aircraftborne far infrared radiometer, give mean-mixing ratios over 1-km altitude increments up to 21 km. The mean 15 to 21 km mass-mixing ratios, shown in Figure 9.10c for the period 1973 to 1979, show clear evidence of a quasi-biennial oscillation and some indication of a decrease from approximately 3.0

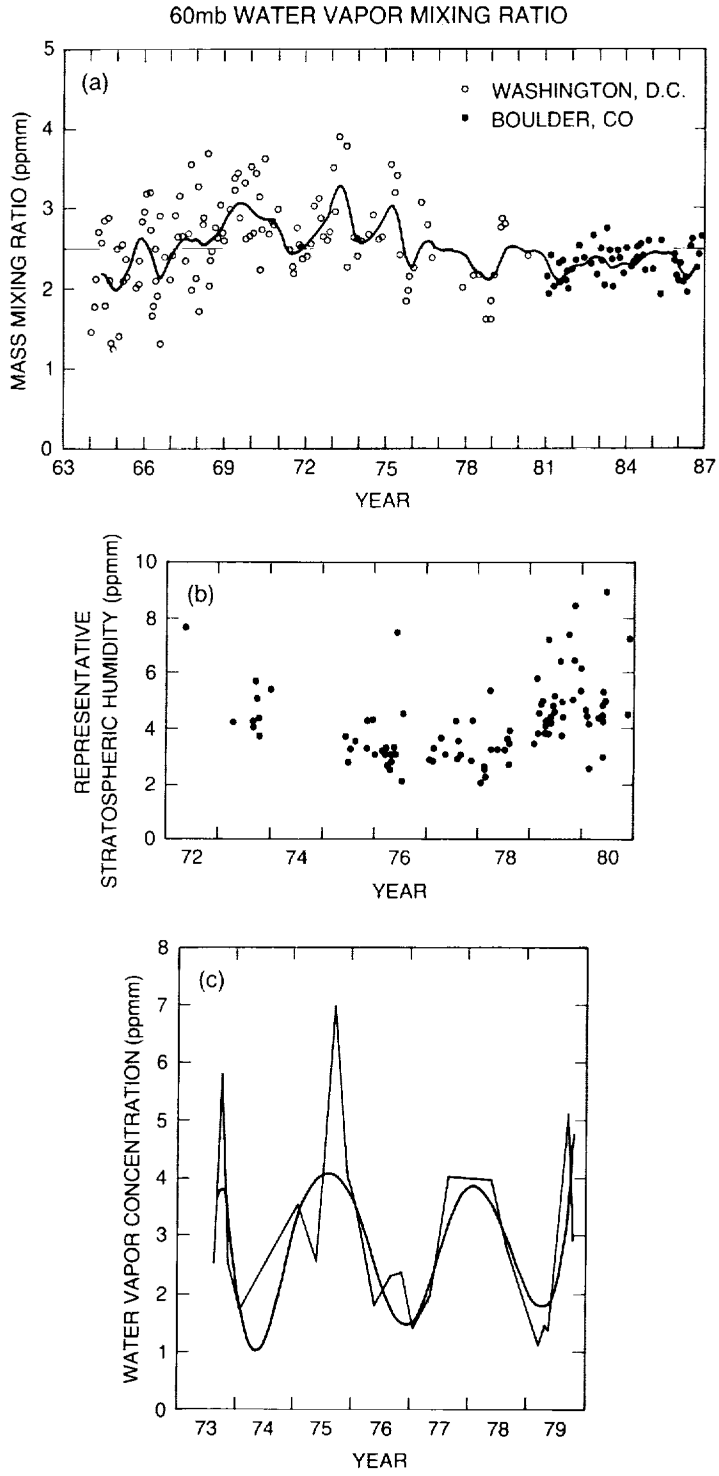

Figure 9.10. Time series of stratospheric H_2O vapor measurements made by frost-point hygrometer measurements. (a) 60 mb mixing ratios obtained from balloon flights launched at Washington, D.C. (1963 to 1980), and Boulder, Colorado (since 1980). Solid line is 12-month running mean through the data. Figure obtained from S. Oltmans (private communication, 1987). (b) Representative stratospheric humidity measured on aircraft flights over southern England near 50°N from 1972 to 1980. Figure taken from Foot (1984). (c) Mean 15 to 21 km water vapor mixing ratio (ppmm) over Mildura and Alice Springs, Australia, from 1973 to 1979. Curve is cubic spline fit to data. Figure taken from Hyson (1983).

ppmm during 1973 to 1976 to 2.3 ppmm during 1976 to 1979. The limited number of data and the large quasi-biennial oscillation make quantitative trend determination difficult, however.

Evidence against very large changes in stratospheric H_2O amounts was obtained by comparison of monthly zonal means in the lower stratosphere of LIMS (November 1978) and SAGE–II (November 1985) data. The two satellite instruments, using very different techniques, obtained H_2O amounts within 20 percent at all latitudes studied outside of the hygropause region (Larsen et al., 1986). Because of the preliminary nature of the SAGE–II analysis, it is impossible at this time to offer a more definitive conclusion about any change in stratospheric water vapor.

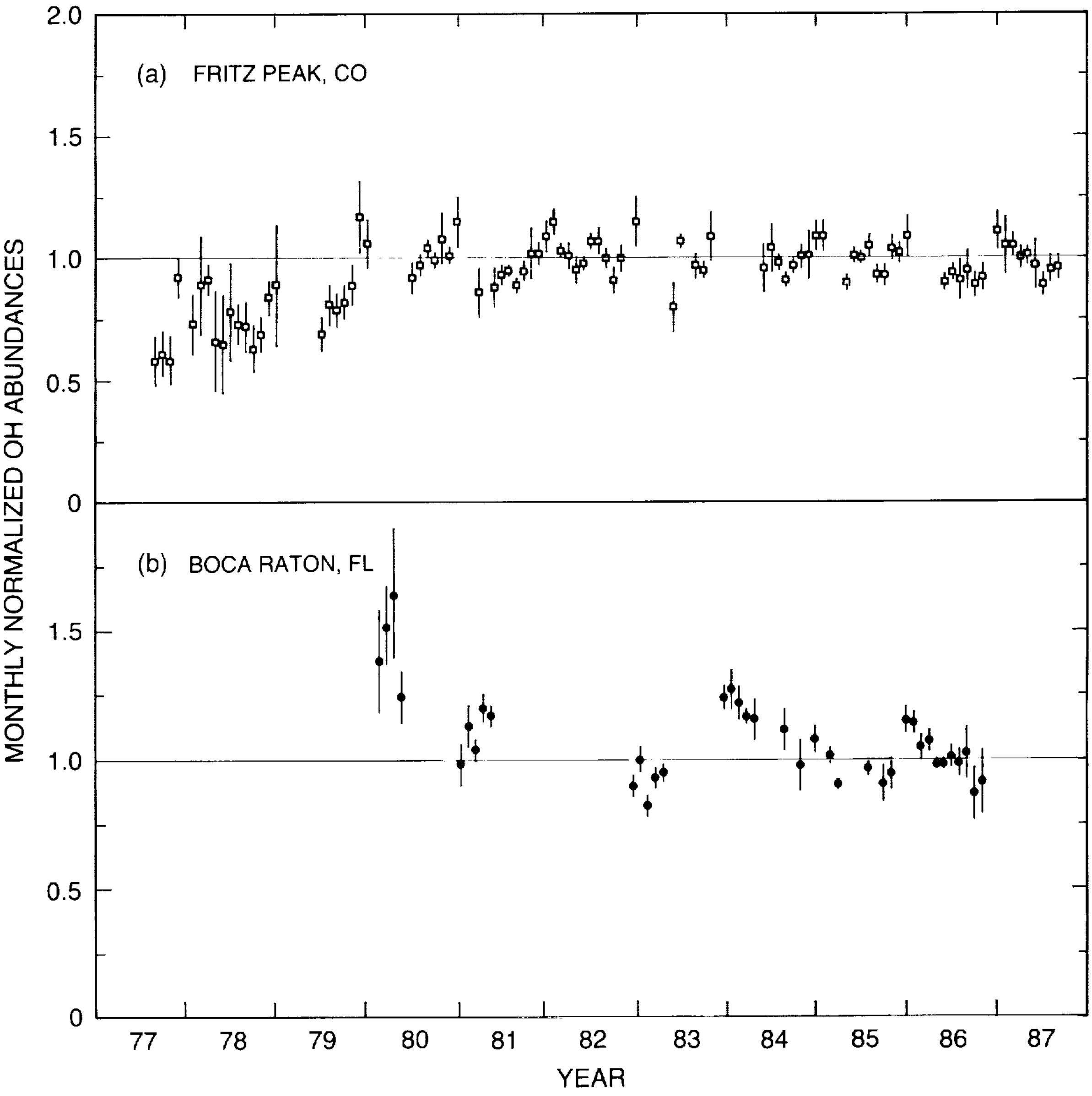

Figure 9.11. Time series of normalized monthly OH column amounts from indicated groundstations. Normalization procedure is described in Burnett et al. (1988). (a) Fritz Peak, Colorado. Figure obtained from E. Burnett (private communication, 1987). (b) Boca Raton, Florida. Figure obtained from Burnett et al. (1988).

9.4.2 Hydroxyl—OH

The only data set of upper atmospheric OH amounts potentially suitable for determining long-term trends is the total column measurements made by Burnett and coworkers with a Pepsios spectrometer. The longest running data set is that taken from the NOAA Fritz Peak Observatory, dating back to 1977 (Figure 9.11a). Additional data recently have become available from Boca Raton, Florida (Figure 9.11b), and Poker Flat, Alaska (Burnett et al., 1988). Interpretation of these measurements is complicated because they are of the total OH column, which includes a small tropospheric and a large mesospheric contribution, so that stratospheric OH may make up only some 40 percent of the observed amount. Also, the measured OH column reflects the strong diurnal variation of OH, which needs to be accounted for in any comparison of data. Finally, OH is expected to have a strong seasonal variation, associated mainly with the seasonal variation in the solar zenith angle.

The data from the Fritz Peak and Boca Raton stations are summarized in Figure 9.11 (Burnett et al., 1988; Burnett, personal communication, 1987). These data have been normalized to remove the dependence that can be directly related to solar zenith angle, thus removing diurnal and some seasonal dependence. Variation remaining reflects other seasonal processes (those not directly related to solar zenith angle) and any long-term variation. The Fritz Peak data show a substantial increase from 1977 to 1980, which has been suggested but not demonstrated to be associated with the solar cycle (*WMO*, 1986), but little or no evidence for long-term changes since that time. The Boca Raton data might be interpreted as showing a net decrease over the 1980 to 1982 period, with evidence for strong variability after 1984. The limited number of data, the large error bars, and the complicating seasonal variations make it impossible to determine whether there is any long-term variation in these measurements.

9.5 SUMMARY

An unambiguous long-term increase of between 5 and 10 percent per year in the total column amount of atmospheric HF has been observed over the last decade in measurements from the ground and from aircraft. This is consistent, within error bars, with predictions based on the measured increase of organic fluorine in the troposphere. An increase of the column amount of atmospheric HCl has now also been observed. Aircraft data that measure the column amount in the stratosphere show a large increase (5 percent per year). Ground-based data from the observatory at Jungfraujoch of the total column above the station, which includes both tropospheric and stratospheric components, indicate a smaller change (2 to 3 percent per year). These data now extend into 1987, and have been reanalyzed to account for seasonal variations in the trend estimates. Trend measurements of HCl are especially difficult to make because a large and variable contribution of tropospheric HCl to the total column, a large seasonal variation, and a possible interference from volcanically injected HCl all are superimposed on the small annual increase expected. It should be noted that any differences between the absolute values or trends determined from ground-based and aircraft measurements should, in general, be attributable to a tropospheric column contribution in the former. In the present case, this comparison leads to a tropospheric HCl column above Jungfraujoch that is somewhat larger than reported in a limited set of independently measured tropospheric HCl concentrations, but the differences are within the uncertainties of the measurements plus meteorological variability.

There is not yet a clear indication of an increase in the column amount of upper stratospheric ClO (also expected to be increasing at the same rate as HCl). There are insufficient data to study the long-term trends of stratospheric bromine compounds.

Satellite-based measurements of NO_2 have been interpreted as showing large (60 to 70 percent) increases during 1979 to 1984, but such increases are not supported by ground-based and aircraft measurements over that time. Subsequent analyses of SAGE data also do not support the large increases originally suggested, but do not rule out the possibility of smaller changes (10 to 20 percent) during the 1979 to 1984 period, especially in the Southern Hemisphere. Such increases, if real, must be due to changing inputs of odd nitrogen from either the mesosphere (NO produced from ionic processes in the thermosphere) or troposphere (NO produced in lightning discharges), as they are much larger than the very small (1 percent) increases expected over that time from increasing concentrations of stratospheric N_2O. SBUV data of NO at and above the stratopause region seem to imply some long-term decrease in the Tropics over 1979 to 1986, but no clear trends were seen at high latitudes. No definitive changes in the total amount of stratospheric odd nitrogen, which includes NO, NO_2, HNO_3, N_2O_5, $ClONO_2$, and HNO_4, can be deduced at this time.

Balloonborne frost-point hygrometer measurements of water vapor made over Boulder 1980 show no evidence of a trend in middle and lower stratospheric (20 to 120 mb) water vapor. Analysis of data obtained previously over Washington, D.C., appeared to show some unexplained cyclical variation over 1963 to 1980, but these data are complicated by substantial short-term variability and a quasi-biennial oscillation. There is also no evidence of a trend in the total OH column over Fritz Peak over 1980 to 1987, although some unexplained variation prior to 1980 was obtained. Neither of these unexplained variations is related to the expected increase in stratospheric hydrogen species associated with the oxidation of the increasing amounts of stratospheric methane.

In order to determine unambiguously what the long-term trends of these species are, a campaign of frequent measurements of these constituents must be carried out. In the long term, the Network for the Detection of Stratospheric Change (NDSC) will be very useful for trend determination. Plans have already begun for setting up stations in both the United States and Europe. This network must evolve into a set of worldwide stations that measure the concentrations of key atmospheric molecules on a continuing basis. In the short term, measurements need to be made on a continuing basis by existing instruments at their current locations (e.g., HCl and HF from Jungfraujoch, ClO from Hawaii, OH from Fritz Peak, H_2O from balloon measurements in Boulder, etc.). In addition, the SAGE–I and –II NO_2 and H_2O data should be fully exploited after release by their science team. Periodic measurements of trace constituent concentrations by aircraft instruments and the shuttleborne ATMOS instrument could also play an important role in determining their long-term trends. When the UARS satellite is launched, additional information concerning trends should be available from several instruments on that satellite. A coordinated plan for determining trends in the species considered here has been presented in the U.S. National Plan for Stratospheric Monitoring 1987 to 1997 (Federal Coordinator, 1988).

S5-45
53442
p.69

CHAPTER 10

N92-15462

Trends in Aerosol Abundances and Distributions

Panel Members

ND210491

R. P. Turco and M. P. McCormick, Co-Chairs

R. T. Clancy
R. Curran
J. DeLuisi — NJ920944
P. Hamill
G. Kent
J. M. Rosen
O. B. Toon
G. Yue

PAGE 594 INTENTIONALLY BLANK

PRECEDING PAGE BLANK NOT FILMED

Chapter 10

Trends in Aerosol Abundances and Distributions

Contents

10.1 INTRODUCTION 599

10.2 AEROSOLS IN THE MIDDLE AND LOWER ATMOSPHERE 599

- 10.2.1 Aerosol Species 599
- 10.2.2 Optical Properties of Aerosols 602
- 10.2.3 Aerosol Radiative Transfer 604
- 10.2.4 Measured Properties of Aerosols 606
- 10.2.5 Aerosol Microphysical Parameters 607

10.3 LONG-TERM AEROSOL DATA BASES 609

- 10.3.1 Mauna Loa Observations 609
- 10.3.2 University of Wyoming Dustsonde 611
- 10.3.3 Satellite Systems: SAM, SAGE, SME 615
  - 10.3.3.1 SAM and SAGE 615
  - 10.3.3.2 SME 618
  - 10.3.3.3 SAGE/SME Intercomparisons 622

10.4 AEROSOL PERTURBATIONS: EL CHICHÓN AND OTHER EVENTS 622

- 10.4.1 El Chichón 623
  - 10.4.1.1 Cloud Characteristics and Behavior, April–December 1982 625
  - 10.4.1.2 Cloud Characteristics and Behavior, 1983–1986 628
- 10.4.2 Mount St. Helens and Other Volcanic Eruptions 629

10.5 AEROSOL IMPACT ON OZONE OBSERVATIONS 632

- 10.5.1 Umkehr 632
  - 10.5.1.1 Description of the Aerosol Error 632
  - 10.5.1.2 Calculation of Umkehr/Aerosol Errors 636
- 10.5.2 Solar Backscatter Ultraviolet (SUBV) 639
  - 10.5.2.1 Description of the Aerosol Error 639
  - 10.5.2.2 Implications of SME Data for SBUV Ozone Trends 640
- 10.5.3 Aerosol Data Requirements for Ozone Observing Systems 640

10.6 POLAR STRATOSPHERIC CLOUDS AND THE OZONE HOLE 641

- 10.6.1 Observations and Morphology of PSC's 642
  - 10.6.1.1 The SAM–II Satellite System 642
  - 10.6.1.2 PSC Properties 643
  - 10.6.1.3 PSC's in the Northern Polar Vortex 650
  - 10.6.1.4 Long-Term Trends in PSC Properties 651

PRECEDING PAGE BLANK NOT FILMED

PAGE 596 INTENTIONALLY BLANK

10.6.2 Physical Chemistry and Microphysics of PSC's 651
    10.6.2.1 Sulfuric Acid Ice Clouds 652
    10.6.2.2 Nitric Acid Ice Clouds 655
    10.6.2.3 Hydrochloric Acid Ice 659
    10.6.2.4 Ice Clouds 660
10.6.3 Radiative Properties of PSC's 660
    10.6.3.1 PSC Lidar Backscatter and Polarization Characteristics 660
    10.6.3.2 Radiative Heating of PSC's 661

10.7 CONCLUSIONS 662

10.1 INTRODUCTION

In this chapter, the properties of aerosols that reside in the upper atmosphere are described, with special emphasis on the influence these aerosols may have on ozone observation systems, mainly through radiative effects, and on ambient ozone concentrations, mainly through chemical effects. It has long been appreciated that stratospheric particles can interfere with the remote sensing of ozone distribution. Here, the mechanism and magnitude of this interference, and potential spatial and temporal trends in the interference, are evaluated. Separate sections deal with the optical properties of upper atmospheric aerosols, long-term trends in stratospheric aerosols, perturbations of the stratospheric aerosol layer by volcanic eruptions, and estimates of the impacts that such particles have on remotely measured ozone concentrations.

Another section is devoted to a discussion of the polar stratospheric clouds (PSC's). These unique clouds, recently discovered by satellite observation, are now thought to be intimately connected with the Antarctic ozone hole (see Chapter 11). Accordingly, interest in PSC's has grown considerably in recent years. This chapter describes what we know about the morphology, physical chemistry, and microphysics of PSC's.

10.2 AEROSOLS IN THE MIDDLE AND LOWER ATMOSPHERE

The global measurement of ozone from orbiting satellites using the spectral signature of Earth's albedo is complicated by the presence of fine light-scattering (and absorbing) particles in the upper atmosphere. If the spatial distribution, size distribution, composition, and morphology of these particles are known, their optical properties can be determined and employed in the calculation of ozone abundances from the raw satellite radiance data. Most ozone-sensing systems are not designed to measure independently the aerosol properties that are required. Accordingly, in cases where aerosol interference is identified as a problem, corrections to the ozone observations may be estimated by using either a standard aerosol model, or coincident aerosol data from other sensors, or reanalysis of the onboard data (through a modified inversion scheme) to deduce the aerosol fields. Thus, several alternatives may be available to correct for the effects of aerosols in data retrieval procedures.

Two principal concerns regarding aerosol effects are noted:

1. Research teams working with the satellite radiance data and inversion schemes should be aware of the types and variations of particles in the upper atmosphere and their general optical properties.

2. Past measurements of ozone, both satellite and ground based, which may have been inadvertently contaminated by aerosol scattering effects, might be recalibrated (if this is possible) to allow more accurate ozone trend analyses.

10.2.1 Aerosol Species

Table 10.1 summarizes and compares information on the most prominent atmospheric particulates, including water clouds. Specific types of aerosols may not significantly affect a particular system, or may have been taken into account in designing the system. The general optical properties of aerosol particles are discussed in Section 10.2.2.

Table 10.1 Properties of Atmospheric Aerosols* and Clouds

Type of particulate	Altitude (km)	Horizontal scale (km)	Occurrence frequency	Composition	Mass loading (mg/m^3)	Vertical optical depth (at 550 nm)	Mean particle number radius (μm)	Principal size range (μm)
Stratus, cumulus, nimbus clouds	1–18	10–1,000	0.5	Water, ice	1,000–10,000	~1–100	10–1,000	Variable
Cirrus clouds	7–16	10–1,000	0.3	Ice	10–100	~1	~10–100	Variable
Fog	0–1	10–100	Sporadic	Water	10–100	1–10	~10	10–50
Tropospheric aerosols	0–10	1,000–10,000 (ubiquitous)	1	Sulfate, nitrate, minerals	0.01–0.1	~0.1	0.1–1	~0.3
Ocean haze	0–1	100–1,000	0.3	Sea salt sulfate	0.1–1	0.1–1	0.5	~0.3
Dust storms	0–3	10–1,000	Sporadic	Silicates, clays	<1–>100	1–10	1–10	10–100
Volcanic clouds	5–35	100–10,000	Sporadic	Mineral ash, sulfates	<1–>1,000	0.1–10	0.1–10	1–10
Smoke	0–10	1–100	Sporadic (from fires)	Soot, ash, tars	0.1–1	~0.1–10	0.1–1	~0.3
Stratospheric aerosols	10–30	1,000–10,000 (ubiquitous)	1	Sulfate	0.001–0.01	~0.01	0.1	~0.1
Polar stratospheric clouds	15–25	10–1,000	0.1 (winter only)	HNO_3/H_2O ice	0.001–0.01	~0.01–1	1–10	~1
Polar mesospheric clouds	80–85	~200 (polar regions above 50°)	0.1 (summer only)	Ice	~0.0001	~0.0001–0.01	~0.05	~0.02
Meteoric dust	50–90	10–1,000	0.5–1	Minerals, carbon	~0.00001	~0.00001	≤0.01	Wide range incl. micrometeors

*All particles that can be nucleated into cloud (water) droplets at supersaturations of $\gtrsim$10% are referred to as "condensation nuclei," or cn. Those particles that can be nucleated at low supersaturations of $\lesssim$1% are referred to as "cloud condensation nuclei," or ccn.

The aerosols of primary interest include:

Volcanic Eruption Clouds

Large volcanic eruptions deposit ash and sulfurous gases in the stratosphere between 10 and 35 kilometers altitude. While the larger ash debris falls out of the atmosphere within a fairly short time (a few weeks or months) and locally near the explosion site, the sulfuric acid aerosol generated from the gaseous sulfur emissions can remain suspended for several years; the particle density and global distribution evolve over this period. The sulfuric acid particles typically have a radius <1 micrometer (or micron, μm), and thus are very efficient at light scattering. The vertical stratospheric extinction optical depth in major volcanic eruption plumes will vary from very high values at early times to values of ~0.1 to 0.5 over global scales at longer times. The occurrence of eruptions large enough to affect the stratosphere is unpredictable, with major events occurring on a time scale of decades, and smaller but significant events occurring perhaps every few years.

The optical properties of aged volcanic aerosols (at least several months old) are relatively uniform over hemispheric scales. Accordingly, the interfering aerosol radiances may be more readily characterized and corrected in the ozone algorithms. Nevertheless, the distribution of aerosol light scattering exhibits large- and small-scale inhomogeneities that could still be significant. Moreover, the spectral signature of the aerosols depends on their size distribution, which can vary with time, location, and altitude. For a rough first-order optical analysis of solar transmission through background aerosols, it is probably adequate to assume a λ^{-1} dependence for light extinction (see Section 10.2.2).

The aerosol contribution to the radiance may be determined directly from the observations by including a factor in the inversion equation to account for aerosol effects. One or more of the sensor wavelengths may be used to characterize the aerosol properties. Alternatively, independent measurements of the aerosol properties from other satellites, aircraft surveys, or ground-based lidar soundings could be employed to develop a time-dependent model for the particulate radiances to be treated in the data retrieval scheme. At a simpler level, a standard volcanic-aerosol radiance model could be formulated and applied to correct the satellite data, after the absolute radiances in the model had been calibrated at a reference frequency.

Nacreous Clouds and Polar Stratospheric Clouds (PSC's)

These clouds are largely a manifestation of water vapor condensation (likely in combination with nitric acid vapor) in regions of extremely low stratospheric temperatures. The classical nacreous, or "mother of pearl," clouds often occur in the lee waves of orographic features, in the ascending, cooling region of the waves. Nacreous clouds are a relatively rare phenomenon and reside primarily in the lower stratosphere. They apparently consist of supercooled liquid droplets of about 1 micron radius with a very narrow size dispersion (which is responsible for the strong wavelength dependence of light scattering leading to the distinctive coloration of these clouds). PSC's are observed in the polar regions mainly in winter. Most of our knowledge of PSC's is derived from remote observations by the SAM–II satellite instrument. The clouds extend between roughly 10 and 25 kilometers in altitude, and are found at latitudes above about 65°. While the sizes and composition of PSC particles are not yet known precisely, a substantial amount of information is available to define their general physical and morphological properties (see Section 10.6). Measured extinction coefficients at 1 micron wavelength averaged over path lengths of ~100 km are typically of the order of 10^{-3}/km, although higher and lower values are frequently observed. Hence, vertical cloud extinction optical depths of the order of 10^{-2} are expected, although much higher values could be found in fully developed clouds.

PSC's can have considerable spatial structure, as is revealed by lidar surveys. However, the clouds are largely confined to the polar regions in winter. Ozone data should be carefully analyzed for PSC effects under these observational conditions. The clouds are likely to be most prominent in the perpetual nighttime zone of the polar winter stratosphere when air temperatures are coldest; satellite sensors that use the Sun as a light source are quiescent in this situation (although other bright astronomical objects have been used as alternate light sources under special circumstances).

Noctilucent Clouds

These clouds are most likely water ice clouds formed near the mesopause (~80 km) in the summer at high latitudes. Noctilucent clouds have been studied extensively using ground-based observations, with occasional in situ measurements. However, even under optimal conditions, ground sitings of the clouds are quite rare. On the other hand, the SME satellite has cataloged a more pronounced circumpolar cloud layer at the summer mesopause extending poleward from about 70°. The layer is only a few kilometers thick and seems to consist of ice crystals (of unknown morphology) of about 0.05 micron radius. The vertical optical thickness of the clouds is only $\sim 10^{-4}$. Reviews of noctilucent cloud properties based on past observations are provided by Fogle and Haurwitz (1966), Avaste et al. (1980), and Thomas (1984).

Because the noctilucent cloud particles are so small, their optical properties may be adequately described by Rayleigh scattering theory (see Section 10.2.2). In this case, the wavelength dependence of the light extinction (or scattering) would be given by λ^{-4}. This strong wavelength variation is in contrast to the much weaker wavelength dependence of scattering in suspensions of larger particles such as volcanic acid aerosols.

Tropospheric Aerosols

The particulates discussed so far reside in the stratosphere and mesosphere. Because they are coincident with the ozone layer, particles in the middle atmosphere can have a direct impact on the radiance fields that must be analyzed to obtain ozone profiles. Fortunately, the aerosols that might cause problems have, in general, small optical depths. By contrast, tropospheric clouds, hazes, and fogs can have large optical depths and substantial effects on Earth radiances (see Table 10.1). Because tropospheric clouds lie below the ozone layer, they introduce difficulties mainly in the following circumstances:

- When underlying the satellite field of view, they enhance the upwelling shortwave radiation and block the direct observation of the tropospheric component of the total ozone column concentration.

- When overlying ground-based instruments, they create a diffuse radiation field that dominates the radiance at the sensor.

Because of their more obvious manifestations, tropospheric clouds have been extensively treated in ozone observing systems, such as the Dobson network (see Chapter 3, which discusses ozone retrieval algorithms).

10.2.2 Optical Properties of Aerosols

The fundamental aerosol optical properties of importance here are the extinction coefficient and scattering phase function. The extinction cross-section of a single spherical particle at a specific wavelength can be written:

$$\sigma_e(\lambda) = \pi r^2 Q_e(r,\lambda,\eta),$$

where σ_e = cross section (cm^2)
r = particle radius (cm)
λ = wavelength (cm)
η = index of refraction $= \eta_r - i\eta_i$.

Q_e is the Mie extinction efficiency, which can be expressed as a function of the Mie parameter **x**:

$$x = 2\pi r/\lambda,$$

or,

$$Q_e = Q_e(x,\eta).$$

Extinction is the sum of light scattering by a particle plus light absorption in the particle. Thus,

$$Q_e = Q_s + Q_a,$$

$$\sigma_e = \sigma_s + \sigma_a,$$

where Q_s and Q_a are the Mie scattering and absorption efficiencies, respectively, and σ_s and σ_a are the scattering and absorption cross sections, respectively.

The single-scatter albedo is defined as

$$\omega_o = \sigma_s / \sigma_e = Q_s / Q_e.$$

The detailed distribution of the scattered energy is described by the phase function, $P(\theta)$, such that the fraction of the total energy scattered into a small angular width $d\theta$ about the scattering angle θ is

$$\sigma_s(\theta,\lambda) = \sigma_s(\lambda)\, P(\theta) \sin(\theta) / 2d\theta$$

where P is then normalized as

$$\tfrac{1}{2}\int_0^{\pi} P(\theta) \sin(\theta)\, d\theta = 1.$$

Here, θ is the scattering angle measured from the forward direction of the light ray ($\theta = 0$) toward the backward direction ($\theta = \pi$), and azimuthal symmetry is assumed for the scattered field.

It is also convenient to define the asymmetry factor for particle scattering as

$$g = \tfrac{1}{2}\int_0^{\pi} P(\theta) \cos(\theta) \sin(\theta)\, d\theta.$$

Aerosols tend to scatter light preferentially in the forward direction, with $g{\sim}0.7$. Cloud droplets exhibit stronger forward scattering, with $g{\sim}0.9$. For molecular (Rayleigh) scattering, $g=0$; that is, there is equal forward and backward scattering.

Individual aerosol particles have phase functions that exhibit a complex structure of scattering intensity lobes; the number of such lobes is generally equal to the Mie parameter x. However, in a typical collection of atmospheric particles of different sizes, the "lobe" structures in the scattered radiation field are averaged out. Accordingly, it is often possible to employ a simplified composite scattering pattern such as the Henyey–Greenstein phase function (which, however, neglects the backscatter peak):

$$P(\theta) = (1-g^2)/[1+g^2-2g \cos(\theta)]^{3/2},$$

where g is the average asymmetry factor for the aerosols.

A collection of spherical particles of a given type can usually be accurately described by a size distribution function $n_p(r)$, where $n_p(r)dr$ is the number of particles per cubic centimeter of air with sizes between $r \rightarrow r + dr$. The volume extinction (scattering, absorption) coefficient is defined as

$$\beta_{e\lambda}(\overline{y}) = \int_0^{\infty} \pi r^2 Q_e(r,\lambda,\eta) n_p(r,\overline{y}) dr \quad (\mathrm{cm}^{-1}),$$

where the spatial variation has been included through the vector location $\overline{y}$, and η is assumed to be independent of particle size and location. The total concentration of particles is given by

$$N_p(\overline{y}) = \int_0^{\infty} n_p(r,\overline{y})\, dr \quad (\mathrm{particles/cm^3}).$$

The extinction (scattering, absorption) *optical depth* along a specific ray through the atmosphere is defined in terms of the extinction coefficient as:

$$\tau_{e\lambda} = \int_{\mathrm{ray}\ \overline{s}} \beta_{e\lambda}(\overline{y})\, ds.$$

where ds is the length increment along the ray $\overline{s}$.

In lidar observations, the radiation received at the instrument originates in the backscattering of the emitted laser beam. The backscatter cross-section is given by $\sigma_s(\pi, \lambda)$, and can be integrated over the particle size distribution in analogy to the extinction cross-section to yield the backscatter coefficient, $\beta_{b\lambda}(\overline{y})$. Occasionally lidar data are reported as integrated backscatter coefficients, in which $\beta_{b\lambda}(\overline{y})$ is integrated along the lidar path through the aerosol layer, by analogy with the extinction optical depth. The radiance seen by a lidar instrument also contains a Rayleigh scattering component from the air molecules in which the observed aerosols are embedded. The analysis for the aerosol component of the scattered radiance is usually based on a background atmospheric model for the air scattering, or normalization of the return signal in regions where aerosols are not expected to be present.

When an ensemble of different particle and gas species that scatter and absorb radiation is considered, all of the above optical parameters must be summed over the ensemble (for the scattered radiation, contributions from individual scattering centers are treated as incoherent sources).

10.2.3 Aerosol Radiative Transfer

The basic problem in radiative transfer as applied to remote sensing in general, and thus to ozone detection, is to solve the monochromatic transfer equation

$$dI_\lambda / d\tau_\lambda = -I_\lambda + S_\lambda,$$

for the appropriate wavelengths (or wavelength bands), geometries and boundary conditions. In this equation, I_λ is the radiance (energy/area-time-steradian-wavelength), $d\tau_\lambda$ is the differential optical depth (including all optically active species) along the ray path, and S_λ is the source function, which at visible and near-ultraviolet wavelengths can have a direct and single-scatter solar component, a multiple-scatter skylight component, and possible contributions from fluorescence and chemiluminescence.

Solution of the general radiative transfer equations in practical situations usually involves a number of simplifications. For example, light scattering by air molecules and very small particles may be described by the Rayleigh cross-section and phase function, for which

$$Q_s(x,\eta) = \tfrac{8}{3}\, x^4 \left| (\eta^2-1)/(\eta^2+2)\right|^2,$$

and

$$P_R(\theta) = \tfrac{3}{4}\,[1+\cos^2(\theta)].$$

For air, the Rayleigh extinction coefficient can be accurately expressed in the form

$$\beta_{e\lambda}(\bar{y}) = c\,\rho(\bar{y})/\lambda^4,$$

where $\rho(\bar{y})$ is the density of air (g/cm^3) and c is a constant.

The single-scattered radiance reaching a satellite sensor from an atmosphere containing particles may be expressed as follows:

$$I_s\lambda = \int_{\substack{\text{obs.path}\\ \bar{s}}} \left[P_R(\theta)\beta_{gs\lambda}(\bar{y}) + P_p(\theta)\beta_{ps\lambda}(\bar{y})\right]F_{o\lambda}\exp[-\tau_{eo\lambda}(\bar{y})]\exp[-\tau_{e\lambda}(\bar{y})]\,ds$$

where $F_{o\lambda}$ = incident solar irradiance
$\beta_{gs\lambda}$ = volume scattering coefficient for the gases
$\beta_{ps\lambda}$ = volume scattering coefficient for larger particles
P_R = Rayleigh scattering phase function
P_p = average aerosol phase function, which may vary along the ray path
$\tau_{eo\lambda}$ = total extinction optical depth for solar rays to the point $\bar{y}$, equal to $\tau_{geo\lambda} + \tau_{peo\lambda}$,
$\tau_{e\lambda}$ = total extinction optical depth for the observation ray to the point $\bar{y}$, equal to $\tau_{ge\lambda} + \tau_{pe\lambda}$.

The total extinction and scattering terms have components associated with molecular Rayleigh scatter, ozone absorption, other gaseous absorption depending on wavelength, and particle scattering and absorption. Additional contributions to the radiance should be included for surface and cloud reflection, multiple-scattered light, and fluorescence.

Figure 10.1 illustrates some of the possible geometries for passive remote sensing of the lower atmosphere and ozone layer from space and from the ground.

As an example of the application of the general radiative transfer equation displayed above to a nadir-viewing satelliteborne sensor, the angle θ would be equated to the solar zenith angle, and the optical depths $\tau_{eo\lambda}$ and $\tau_{e\lambda}$ would be related by $\tau_{eo\lambda} = \sec(\theta)\tau_{e\lambda}$. Inasmuch as $P_p(\theta)$ is generally much smaller than $P_R(\theta)$ in the stratosphere for typical geometries because particles are more strongly forward scattering, the aerosol contribution to the total radiance is relatively less important. However, since $\beta_{gs\lambda} \propto \lambda^{-4}$ while $\beta_{gs\lambda} \propto \lambda^{-1}$, aerosol scattering is relatively more important at longer wavelengths. Aerosol scattering is also greatly enhanced after volcanic eruptions, in the presence of stratospheric clouds, or in the troposphere where very large particulate optical depths can occur.

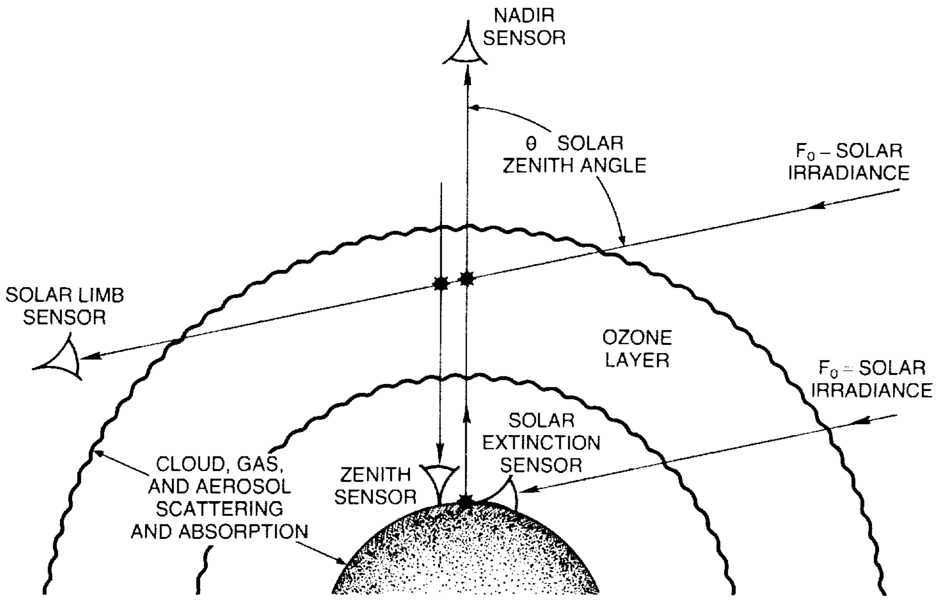

Figure 10.1 Geometries for ozone passive remote sensing. Configurations for both space-based and ground-based sensors are indicated.

It should be noted that multiple scattering is often ignored (at least in its details) in the analysis of stratospheric remote sensing data. A discussion of the analytical approaches employed in ozone remote sensing is given in Chapters 2 and 3. In full generality, the solution for remote sensing involves multiple-nested integrations over particle sizes, ray paths, and diffuse radiation fields, and may involve a further integration over wavelength and instrument bandpass function.

Most atmospheric aerosols exhibit only weak absorption at visible wavelengths (i.e., $\eta_i \sim 0$ and $\omega_0 \sim 1$). Moreover, the normal particle-size dispersions encountered in atmospheric settings yield extinction coefficients that vary with wavelength approximately as λ^{-1}. From the previous exposition, and the known properties of atmospheric aerosols including dependencies on wavelength, the simple λ^{-1} rule should be used only as a rough representation.

Complications to the above analysis arise from anisotropic scattering by particles, polarization effects, and the presence of nonspherical particles. Because large particles (exceeding a few tenths of a micron in size) have restricted sources and very short residence times in the upper atmosphere, their concentrations are typically quite low. On the other hand, the optical properties of very small nonspherical particles may still be adequately described using the Rayleigh theory. Corrections for anisotropy also can be made empirically. Hence, these complications may be treated in data retrieval algorithms.

10.2.4 Measured Properties of Aerosols

Measurements of atmospheric aerosols generally yield a specific property or subset of properties of the particles under observation. However, the analysis of satellite radiances may call for other properties that must be inferred from the measurements. For example, a lidar can measure the light backscatter efficiency for an aerosol, but a satellite sensor may detect the light scattered at some other, arbitrary angle. Or an aerosol size distribution may be measured in situ at a few discrete points, and the entire size range fit to a standard distribution from which optical coefficients are then calculated.

Some of the commonly measured parameters are:

- Total extinction optical depth of the atmosphere, $\tau_{e\lambda}$, by observation of solar attenuation; typically, $\tau_{e\lambda}$ is referred to the zenith even when slant observation paths are used. The extinction optical depth is thus the height integral of the extinction coefficient (or extinction profile).
- Integrated lidar backscatter coefficient, with units of sr^{-1}, defined as the altitude integral of the measured backscatter coefficient, $\beta_{b\lambda}$. Because the backscatter coefficient involves an integral over the aerosol size distribution (see Section 10.2.3), the backscatter coefficient may be related to the total aerosol mass if the particle size distribution parameters can be determined independently.
- Lidar backscatter ratio, at each point along the observation path, is the ratio of the measured total aerosol plus molecular Rayleigh backscatter intensity (for light scattered from the lidar beam) to the modeled (or otherwise determined) Rayleigh (clear air) backscatter intensity alone.
- Volume scattering ratio, which is the quotient of the total light scattering from a unit volume of air (integrated over all angles, for all particles and gases), to the scattering caused by air molecules alone. For nonabsorbing aerosols, the volume scattering ratio is equivalent to the extinction ratio, defined in an analogous manner for a unit length of the observation path.
- Particle size ratio, defined as the quotient of the number of particles that are larger than two specific radii (usually 0.15 and 0.25 μm).
- Aerosol mass mixing ratio, defined as the mass mixing fraction of particles, either measured directly using aerosol filter collection techniques or deduced from size distribution measurements as

$$M_p = \int_0^\infty \tfrac{4}{3}\pi r^3 \rho_p n_p(r)\, dr,$$

where ρ_p is the particle density (g/cm^3).

- Lidar depolarization ratio, defined as the intensity of the backscattered light, after filtering by a polarizer set 90° to the polarization of the incident lidar beam, divided by the intensity of the incident linearly polarized beam; generally speaking, more irregular particles will produce larger depolarizations than more spherical particles, thus allowing some discrimination between liquid and solid aerosols.

10.2.5 Aerosol Microphysical Parameters

In dealing with atmospheric aerosols and their differences from gaseous species, several key microphysical processes must be defined. Detailed descriptions of these microphysical processes are available (Twomey, 1977; Pruppacher and Klett, 1978). Among the more important processes (see Table 10.2 and Turco et al., 1982) are:

Gravitational Sedimentation

Particles will fall relative to the surrounding atmosphere under the influence of gravity. For particles in the submicron size range at stratospheric altitudes, the fallspeed is roughly proportional to the particle radius. With a particle density of 1 g/cm^3, the fall velocity of a 0.1 μm radius spherical aerosol at 20 km is about 3×10^{-3} cm per second, or about 1 km per year. In this particle size regime, the fall velocity is proportional to the particle density and inversely proportional to the air density (see Table 10.2).

For particles greater in radius than a few microns, the fall velocity is roughly proportional to the particle radius squared. Thus, a 10 μm radius particle of unit density at 20 km would fall at about 2.5 cm per second, or about 2 km per day. The fallspeed is proportional to the particle density and is approximately independent of the air density (and thus height) in this size regime.

Coagulation

The collision and adhesion of small particles undergoing Brownian diffusion is the primary coagulation mechanism for stratospheric aerosols. For the purpose of estimating stratospheric time scales, a coagulation coefficient, K_c, of 1×10^{-9} cm^3 per second is appropriate, and the time constant for coagulation is

$$t_c = (K_c\, n_o)^{-1},$$

Table 10.2 Time Constants* for Aerosol Processes

Process	Time constant	Conditions
1. Sedimentation** $\tau \simeq \Delta z / v_f(r)$	$\approx 4 \times 10^7$ sec	0.1 μm radius unit density ($\rho = 1$ g/cm^3) ice sphere falling 1 km at 20 km altitude ($p = 50$ mb)
	$\approx 3 \times 10^6$ sec	1 μm particle
$v_f(r) \propto \rho r^{\alpha} / p^{\beta}$	$\approx 7 \times 10^4$ sec	10 μm particle
$1 \leqslant \alpha \leqslant 2$ $1 \geqslant \beta \geqslant 0$	$\approx 10^3$ sec	100 μm particle
2. Coagulation $\tau \simeq 1/[n_o K_c(r)]$	$\approx 10^8$ sec	1 μm radius particle with $n_o = 10/\text{cm}^3$ $K_c = 10^{-9}$ cm^3/sec
3. Condensation/ evaporation $\tau \simeq c\, \dfrac{r(S+1)}{p\xi S}$ $S = \left\| \dfrac{n}{n_v} - 1 \right\|$	$\approx 10^5$ sec	1 μm radius particle at 10% supersaturation (S = 0.1) at 20 km (p = 50 mb) for 1 ppbv of condensing vapor ($\xi = 1 \times 10^{-9}$). A unit accommodation coefficient is assumed.

*Time constants may be estimated for other conditions by scaling according to the parameter relationships given (from Hamill et al., 1988).

**For submicron particles, $\alpha \simeq 1$ and $\beta \simeq 1$; for supermicron particles, $\alpha \simeq 2$ and $\beta \simeq 0$.

where n_0 is the background particle concentration (number/cm^3). For a typical stratospheric aerosol abundance of about 10/cm^3, the coagulation time constant is ~3 years. Hence, coagulation is important primarily with enhanced particle concentrations, as may occur following major volcanic eruptions.

Condensational Growth

The growth of aerosols by the condensation of a vapor depends on the concentration of the vapor in the vicinity of the particle, the supersaturation of the vapor (i.e., the ratio of its concentration to its equilibrium vapor pressure at the ambient temperature, minus unity—or $S = n/n_v - 1$), and the particle radius. Because of the complexity of these dependencies, growth rates are more difficult to estimate than settling and coagulation rates. To grow a spherical droplet of 1 micron radius at 20 km in a vapor with a concentration of 1 ppbv and a supersaturation of 10 percent would take about 1 day. Table 10.2 gives an approximate relation for scaling this growth rate to other conditions.

The evaporation of volatile aerosols can occur on even shorter time scales when the air mass holding the aerosols is heated, because the vapor pressures of the volatile components usually increase exponentially with increasing temperature.

10.3 LONG-TERM AEROSOL DATA BASES

In order to understand the effects of aerosols on ozone trend analyses, the long-term behavior of upper atmospheric aerosols must be known. Although long-term data sets have been obtained at a few fixed observational sites during the last 10 to 30 years, these data pertain to specific aerosol characteristics such as broadband spectral transmissions, laser radar (lidar) backscatter at fixed wavelengths, or particle size distributions above certain threshold sizes. Some systematic information is also available from in situ aircraft and balloon sampling and airborne remote sensing, but these data sets generally correspond to shorter time intervals. Of the types of measurements noted, the lidar observations provide the longest data base at multiple sites, although all of the data sets extending over several years or more were taken in the Northern Hemisphere above about 19°N. For example, lidar data are available from the NASA Langley Research Center (37°N, Hampton, Virginia) from 1974. The University of Wyoming (41°N) balloon sampling program offers a 15-year data base for specific aerosol properties obtained through a consistent series of measurements. A global data base has evolved from satellite observations by the SAM–II, SAGE–I, SAGE–II, and SME systems beginning in 1978; thus, archived satellite data now span a period of about 5 years.

10.3.1 Mauna Loa Observations

Figure 10.2 shows the longest continuous aerosol data base known. The observations have been recorded at Mauna Loa, Hawaii (19°N), since 1958 using an Eppley normal-incidence pyrheliometer to measure the broadband (290–2,500 nm) solar transmission of the atmosphere. Figure 10.2 gives the difference between the measured total transmission and a transmission calculated for a Rayleigh-scattering atmosphere without aerosols. Water vapor effects, which are not considered significant for the broadband transmission, are not included in the analysis. The largest features in the plotted residual transmission deficits are associated with perturbations (actually decreases in transmission) caused by the volcanic eruptions of Agung in 1963 and El Chichón in 1982. There also appear to be seasonal variations in the residual (aerosol) transmissivity, although the signals are quite small.

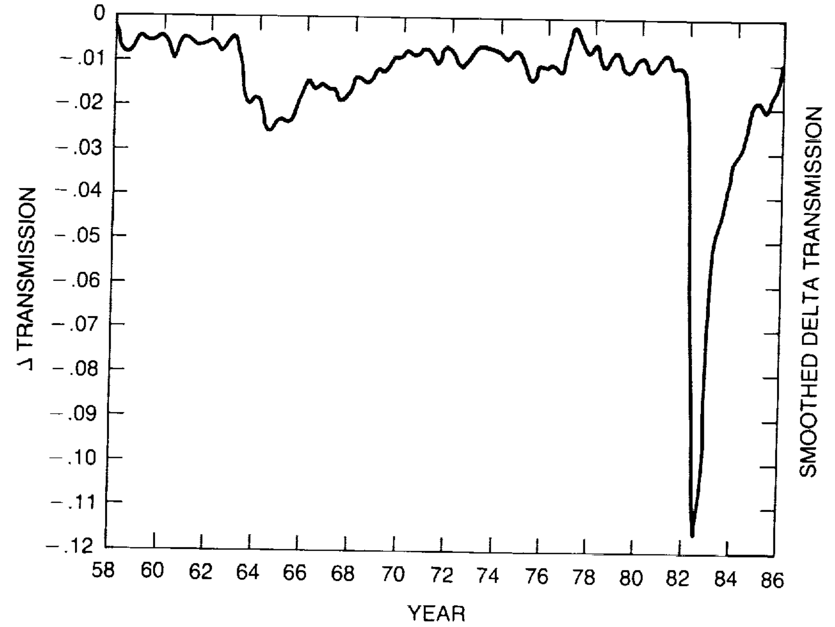

Figure 10.2 Decrease in direct solar transmission due to aerosol turbidity (extinction) at Mauna Loa, Hawaii, from 1958 to 1986, based on broad-band solar pyrheliometer measurements (J. DeLuisi, private communication, 1987).

As mentioned in the introductory comments, lidar systems have contributed significantly to the knowledge of the long-term behavior of stratospheric aerosols, at Mauna Loa and elsewhere. Lidar systems project a pulse of coherent laser radiation into the atmosphere and collect with a telescope the radiation that is backscattered toward the transmitter (Fiocco and Grams, 1964; Fox et al., 1973). In modern systems, the laser pulse at a fixed wavelength is about 10 meters in length. The delay between pulse transmission and backscatter collection provides a means of determining the distance of individual scattering elements from the instrument. The range-resolved backscatter intensity yields a profile of the scattering elements along the beam path. The background molecular scattering component is removed by normalizing the scattered intensity in a region where few aerosols are believed to exist (e.g., near the tropopause, or at ~30 km). The integrated differential backscatter along the beam path is a measure of the total aerosol mass or optical depth along the path, after assumptions are made about the particle size distribution, composition, and shape.

Because of the vertical profiling capability of lidars, and the relatively high mixing ratios of particles in the lower stratosphere, lidars have found extensive use as remote stratospheric aerosol sounders. Table 10.3 summarizes the lidar sites worldwide that have long-term (more than 3-year) operations.

Figures 10.3a and 10.3b show integrated aerosol backscatter versus time from 1974 to the present for the lidar systems located at Mauna Loa and Hampton, respectively. On the abscissa are indicated the volcanic eruptions that could have perturbed the stratospheric aerosol significantly. A comparison of the lidar records in Figures 10.3a and 10.3b show differences that reflect the widely separated geographical locations of the instruments, the frequency of sampling, and the variation in temporal and spatial responses of the aerosol layer to volcanic influences. Following the El Chichón eruption in 1982, the lidar signals have been dominated by a steady decay of the stratospheric aerosol layer (see Section 10.4 for a complete discussion).

Table 10.3 Sites of Long-Term Aerosol Lidar Observations

Location	Latitude	Longitude	Dates
Mauna Loa, Hawaii; National Oceanic and Atmospheric Administration	19.5°N	156.6°W	1974 to Present
Hampton, Virginia; NASA Langley Research Center	37.1°N	76.3°W	1974 to Present
Garmisch-Partenkirchen, West Germany; Fraunhofer Institute for Atmospheric Environmental Research	47.5°N	11.0°E	1976 to Present
Tsukuba/Yatabe, Japan; National Institute for Environmental Studies	36.0°N	140.0°E	1983 to Present
Verrieres le Buisson, France; Observatoire de Haute Provence	43.9°N	5.7°E	1981 to Present
Aberystwyth, Wales; University College of Wales	52.4°N	4.1°W	1985 to Present
Fukuoka, Japan; Kyushu University	33.7°N	130.4°E	1983 to Present

10.3.2 University of Wyoming Dustsonde

The basic dustsonde instrument flown by the University of Wyoming research group is a balloonborne light-scattering photoelectric-detector particle counter. Basically, the instrument measures the number of particles in air drawn through the detector, from which the ambient particle concentrations are deduced. The system employs a coincidence sensor to eliminate spurious counting caused by cosmic rays at high altitude and to reduce Rayleigh-scattering background at low altitudes. The development of the instrument began in 1961, and the first flight occurred in August 1963, just after the Agung volcanic eruption (Rosen, 1964). Systematic measurements were not begun until October 1971 from Laramie, Wyoming (41°N). The pre-1971 soundings lacked a reliable calibration scheme, and cannot easily be compared quantitatively to later measurements.

It is usually assumed—based on observational evidence—that the background stratospheric aerosols (as well as aged volcanic aerosols) are supercooled liquid droplets and, hence, also spherical (Rosen, 1971). This allows reliable theoretical (Mie scattering) calculations of the aerosol optical properties, as well as confident analytical interpretation of data obtained with light-scattering instruments such as the dustsonde. The response of the dustsonde to spherical nonabsorbing particles of varying size and index of refraction has been studied in considerable detail (Pinnick et al., 1973; Pinnick and Hofmann, 1973). These investigations show that for particle sizes below about 0.25 μm radius, the response of the instrument is strictly single valued and not very sensitive to index of refraction. Further, because the response is proportional to a high power of the particle size, small errors in the signal discrimination level do not lead to significant errors in the deduced particle size.

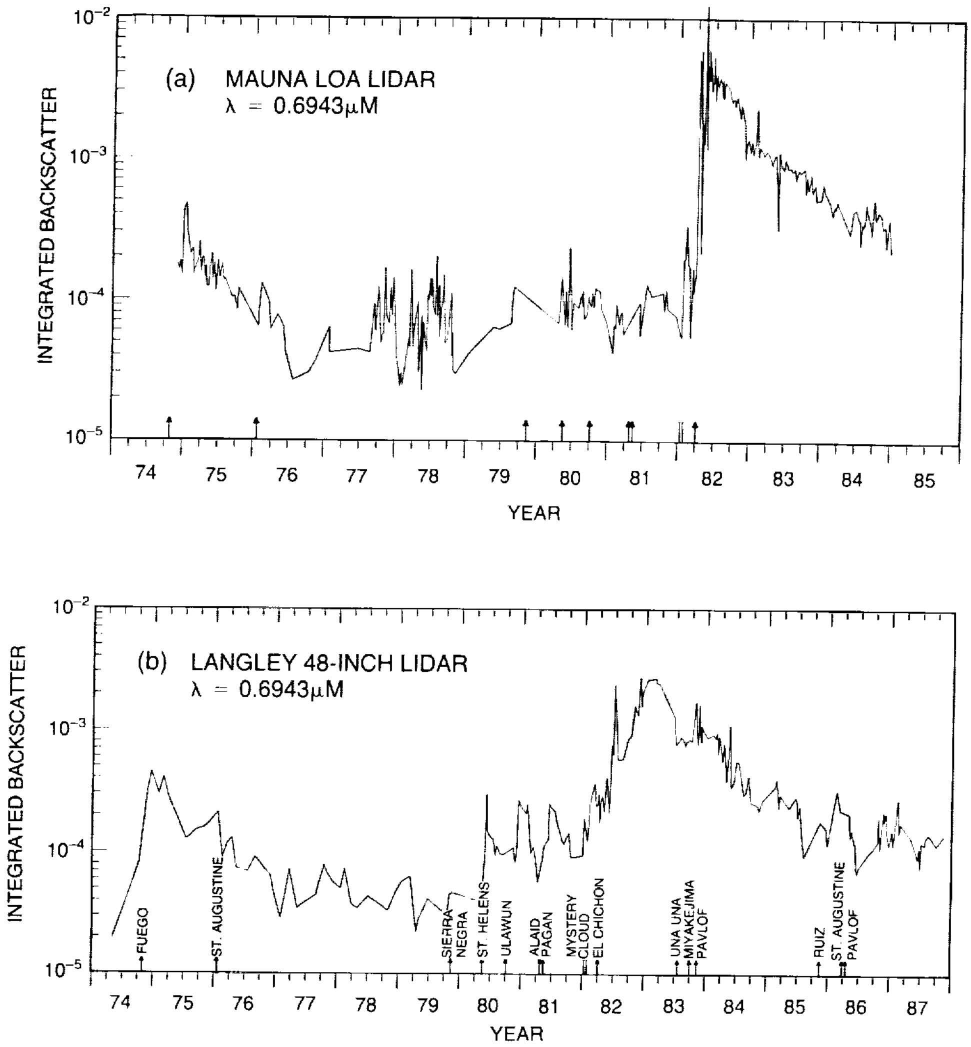

Figure 10.3 Integrated lidar backscatter intensities over the decade 1974 to 1985 for a wavelength 0.6943 μm at two sites: (a) Mauna Loa (DeLuisi et al., 1982; J. DeLuisi, private communication, 1987); (b) Hampton, Virginia (M.P. McCormick, private communication, 1987). The backscatter radiance includes contributions from air molecules and aerosols. The data correspond to the stratospheric component of the scattering.

Since about 1970, the basic dustsonde has been adjusted to detect particles with radii >0.15 μm and >0.25 μm. These are the two operational channels most commonly used, although the instrument can be set to operate over a much wider range of sizes. The cosmic ray interference (from scintillation in the glass of the photodetectors) effectively limits the aerosol detection threshold to about 10^{-2} particles/cm^3 in the 0.15 μm channel and to about 10^{-4} to 10^{-3} particles/cm^3 in the 0.25 μm channel.

The standard two-channel dustsonde measurement is subject to uncertainties associated with the sample flow rate, sharpness of the size discrimination, statistical fluctuations in the counting rate, calibration accuracy, and particle index of refraction (Russell et al., 1981). The net uncertainty in measured stratospheric aerosol concentrations is estimated to be about 10 percent. The reproducibility of measurements is considerably better than 10 percent, however; identical instruments flown in parallel typically agree to within a few percent (Hofmann et al., 1975).

The standard dustsonde has been applied in other configurations to measure the "total" aerosol concentration (>0.01 μm, often referred to as "condensation nuclei" or cn), or the concentration of very large particles (>1 μm) in the atmosphere (Rosen and Hofmann, 1986). In practice, the lowest particle concentration that can be observed with the modified dustsonde is $\sim 10^{-6}/\text{cm}^3$.

Although the concentration of the largest particles may be measured only to within an order of magnitude, the total aerosol mass determined by integrating the measured size distribution may have as little as ~10 percent uncertainty. Comparisons between direct measurements of stratospheric aerosol mass (and optical properties) and values calculated from dustsonde data generally agree to within 10 percent (Russell et al., 1981; Rosen and Hofmann, 1986).

Dustsondes also have been used to examine the correlation between the structures in aerosol and ozone profiles (Rosen, 1966 and 1968). Figure 10.4 illustrates a very distinct ozone/aerosol layer at 11 km transported from more northerly latitudes; the layer has descended several kilometers over the horizontal range, bringing ozone- and aerosol-rich air to low altitudes. Such circumstances are frequently observed at midlatitudes, emphasizing the role of ozone transport compared to chemical processes at these altitudes. The correlation of aerosol and ozone profiles in polar regions may, therefore, represent an important diagnostic for high-latitude dynamics and chemistry, including the seasonal formation of the "ozone hole."

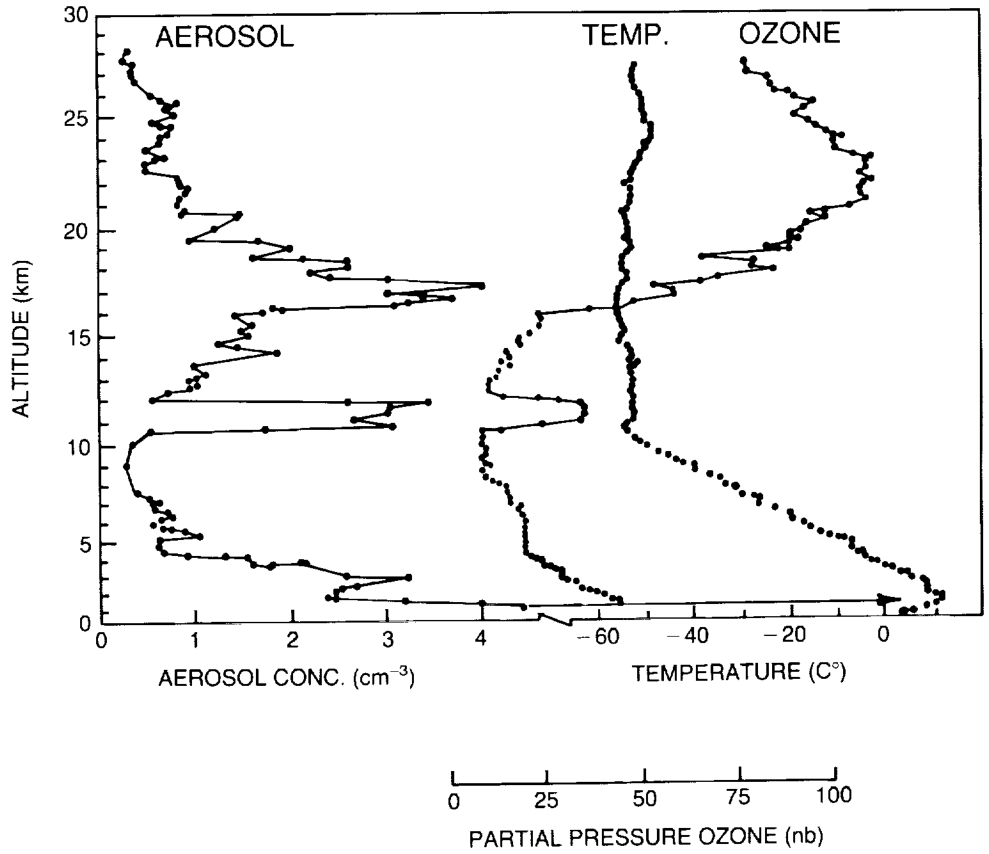

Figure 10.4 Simultaneously measured aerosol and ozone profiles over Minneapolis, Minnesota, on December 22, 1965. The aerosol concentration corresponds to particles with sizes greater than about 0.15 μm radius (Rosen, 1966).

Figure 10.5 illustrates results obtained with the dustsonde expanded to six size channels during a volcanically disturbed period. First, as is usually the case even under background conditions, the total aerosol population (r>0.01 μm) exhibits a fundamentally different profile than the concentration of larger particles, with no relative maximum of the former at the level of the classical "Junge" layer. Also note, however, the unusual circumstance that a cirrus cloud can be identified in the sounding by the fact that the two largest particle channels show exactly the same counting rate, indicating that the particles are larger than the size thresholds for these channels and have a low concentration. The cirrus cloud does not appear to have affected the concentrations of the smaller aerosols.

Long-term observation of the stratospheric aerosol layer using the dustsonde (and lidar) clearly shows that volcanic eruptions cause the most prominent changes in the layer. Figure 10.6 gives the peak mass mixing ratio of the aerosols deduced from dustsonde measurements of the aerosol size distribution since about 1972. The eruption of El Chichón in 1982 obviously caused the largest perturbation since the beginning of the dustsonde measurements. Moreover, El Chichón was apparently the only eruption in the last 15 years to produce a large and persistent increase in the average particle size. Even as late as May 1987, the stratosphere had not completely recovered from the El Chichón event. Smaller eruptions such as Nevado del Ruiz (5°N, November 1985) may have delayed somewhat the recovery of the upper atmosphere from El Chichón.

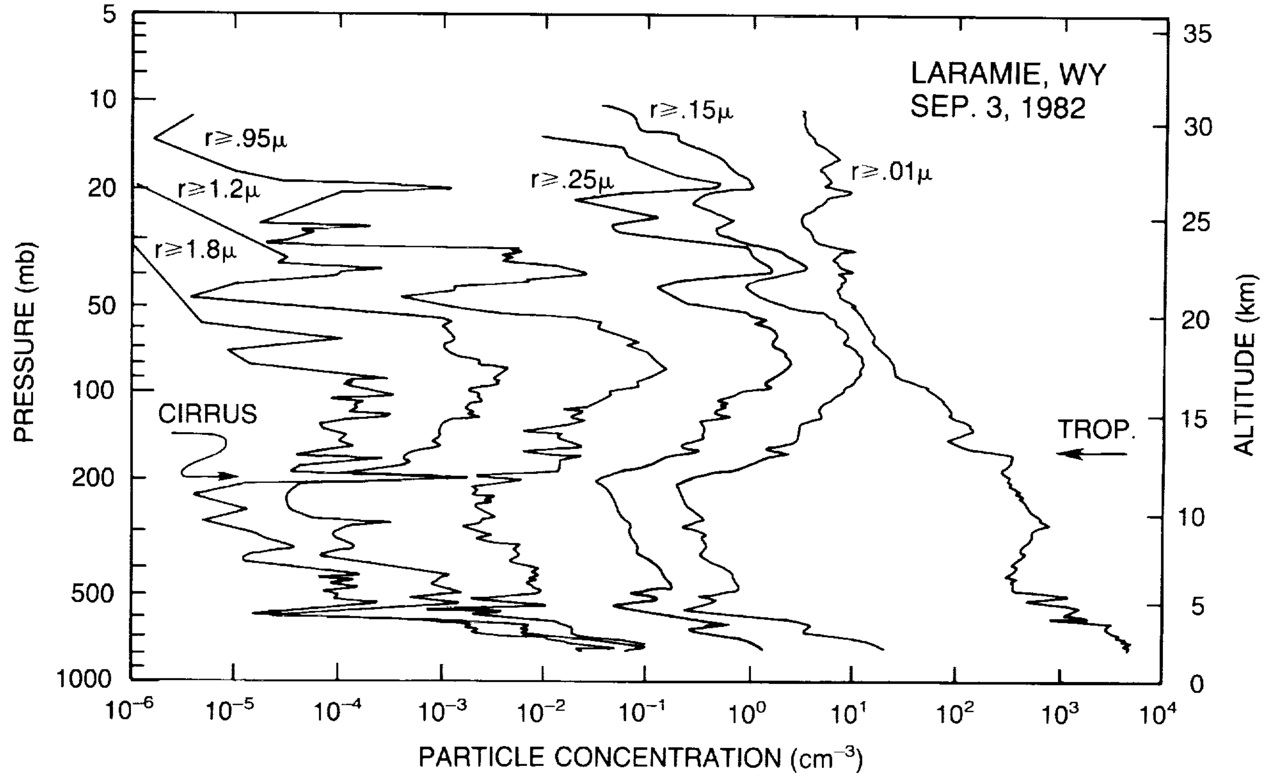

Figure 10.5 Aerosol vertical profiles obtained with the six-channel dustsonde. The concentrations range over 10 orders of magnitude. A subtle anomaly in the profiles associated with a cirrus cloud layer is indicated; although the cirrus cloud could be seen in the sky on the day of the sounding, it is nevertheless difficult to detect in the measured aerosol profiles (Rosen and Hofmann, 1977).

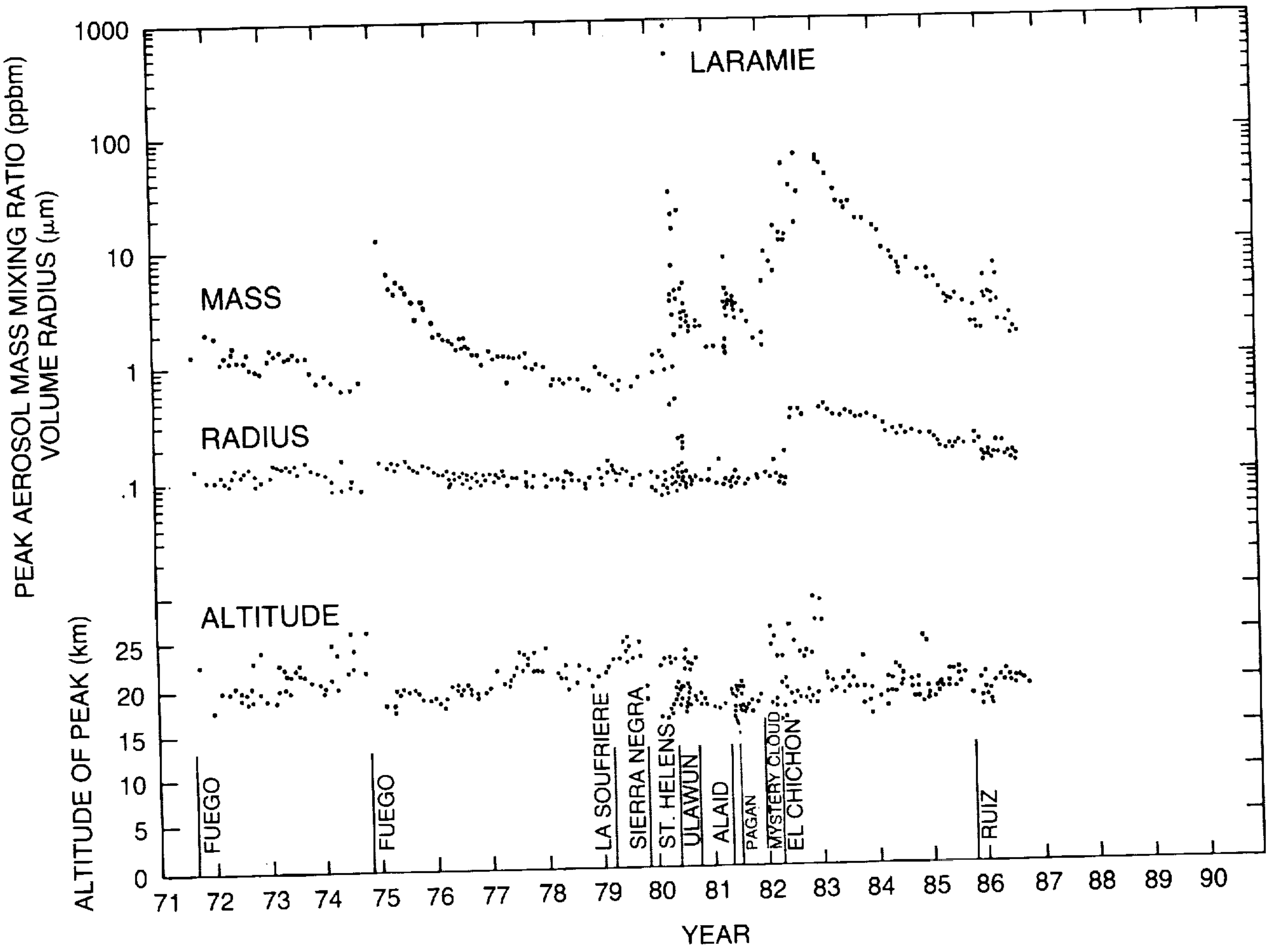

Figure 10.6 Time development of the peak mass mixing ratio of the stratospheric aerosol layer over Laramie, Wyoming, during the entire period of regular dustsonde operations at that site. Also shown are the altitude of the mass peak and the average volume-weighted particle radius at that height. The abrupt change in the particle radius in 1982 is associated with the eruption of El Chichón. The calculations of aerosol mass from the measured aerosol size data are described by Rosen and Hofmann (1986).

10.3.3 Satellite Systems: SAM, SAGE, SME

10.3.3.1 SAM and SAGE

Table 10.4 lists satellite instruments that have collected data bearing on the long-term behavior of stratospheric aerosols. The SAM-II (Stratospheric Aerosol Measurement II) and SAGE (Stratospheric Aerosol and Gas Experiment) systems were developed specifically for performing stratospheric aerosol measurements by the technique of solar limb extinction (McCormick et al., 1979; also see Chapters 2 and 3). During each spacecraft sunrise or sunset, the instrument locks onto the centroid of the Sun's disc in azimuth (yaw) and scans vertically across the disc with an optics field of view of about 0.5 arc minutes. The instrument continues to track the Sun as it rises or sets with respect to the spacecraft. The small field of view provides roughly a 1 km vertical resolution for the observations. In obtaining data well above the limb (atmosphere) during each sunrise or sunset event, the measurements are self-calibrated relative to the absolute solar irradiance.

Table 10.4 Long-Term Aerosol Measurements From Satellites

Satellite Instrument*	Period of Operation	Aerosol Channel(s) (μm)	Lower Altitude Limit	Latitude Coverage
Solar limb extinction				
SAM–II	October 1978 to Present	1.00	Surface	64°–80°N 64°–80°S
SAGE–I	February 1979 to November 1981	1.02 0.45	Surface 10 km	75°S–75°N
SAGE–II	October 1984 to Present	1.02 0.53 0.45 0.38	Surface 6.5 km 10.5 km 14.5 km	80°S–80°N
Solar limb scattering				
SME	October 1981 to October 1986	0.44	30–50 km	Sunlit latitudes; 3–5 longitudes per day

*For additional specifications on these satellite systems, see Chapter 2.

For aerosol observations, SAM–II, SAGE–I, and SAGE–II all use a primary spectral channel at 1.0 μm wavelength. Both SAGE instruments also use a second channel at a shorter wavelength to obtain information on the wavelength dependence of the aerosol extinction. In the case of SAGE–I, measurements are made simultaneously for ozone and nitrogen dioxide absorption; in the case of SAGE–II, water vapor near-infrared absorption is also measured. These additional data are used to make small corrections to the aerosol measurements (and to deduce the ozone, NO_2, and water vapor profiles, as discussed in Chapter 3). Forward scattering of light by the aerosols does not introduce a significant error in these systems.

The basic aerosol property measured by the SAM and SAGE instruments is the path-integrated aerosol extinction at one wavelength (1 μm) versus the tangent altitude of the solar ray. The path extinctions for various tangent heights are converted to a vertical extinction profile using a homogeneous atmospheric shell model. The height integral of this extinction profile yields the vertical optical depth at 1 μm of the aerosols between the lowest and highest altitudes of the observations. In Figure 10.7 this optical depth is plotted for the altitude interval from 2 km above the tropopause to about 30 km; weekly averaged optical depths are given for SAM–II sunrise measurements, which occur over the Antarctic, and for SAM–II sunset measurements, which occur over the Arctic. Optical depths are calculated only for heights well above the tropopause to exclude the effects of high-altitude tropospheric clouds. For each SAM–II measurement, the altitude of the local tropopause is determined from the National Weather Service gridded analysis.

In Figure 10.7, strong effects are seen from volcanic eruptions that were powerful enough to inject into the stratosphere a large quantity of debris, some of which was subsequently transported to the polar region. The Arctic aerosols show strong effects of eruptions such as Mount St.

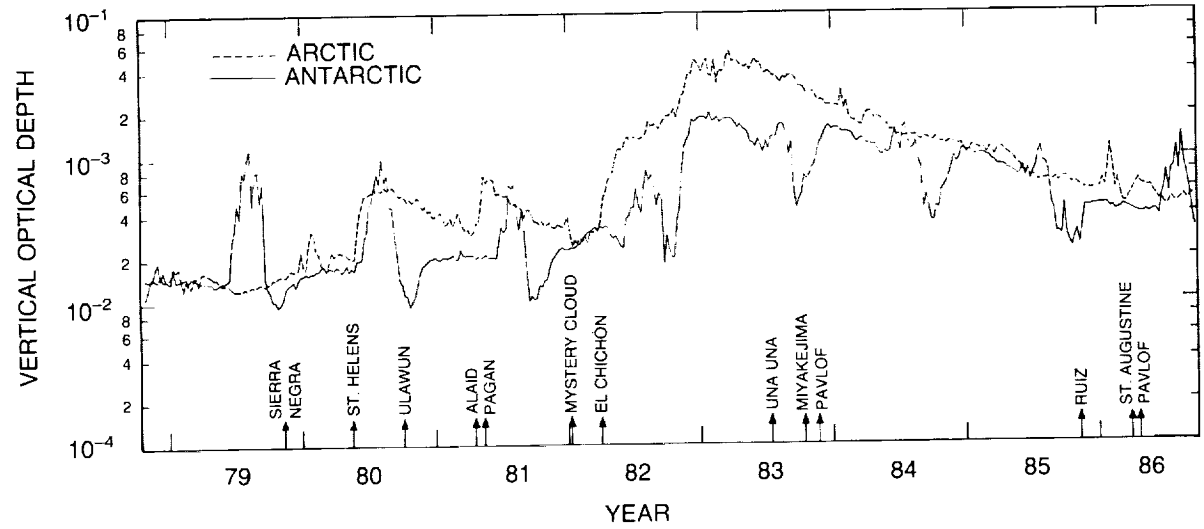

Figure 10.7 Optical depth of aerosols in the polar stratosphere at a wavelength of 1 micron measured by the SAM–II satellite from October 1978 through September 1986. Optical depths are given separately for the Arctic and Antarctic regions. The optical depths represent vertical projections of particle extinctions measured along satellite slant observation paths. A distinct seasonal variation is seen in the optical depth because of the formation of polar stratospheric clouds in the winter season; this variation is particularly noticeable in the Southern Hemisphere. The El Chichón aerosols also have an obvious effect on the polar optical depths in both hemispheres (McCormick and Trepte, 1987).

Helens (1980) and El Chichón (1982). The El Chichón eruption is also obvious in the Antarctic record, although most other eruptions (during the period of the SAM observations) are not. Notably, most of these eruptions were smaller, Northern Hemisphere events.

Clearly evident in the Antarctic aerosol record are the order of magnitude optical depth enhancements caused each austral winter by PSC's. These clouds are composed of ice and nitric acid condensed at temperatures below about 195 K (see Section 10.6). Interestingly, minimum optical depths are seen each austral spring in October, after stratospheric temperatures have warmed and the PSC's have evaporated, suggesting a cleansing of the upper atmosphere. However, by the first week of November, the winter polar vortex has weakened or moved off the pole; aerosols are thus advected from lower latitudes into the polar regions, increasing the optical depths there. Although PSC's are also evident in the Arctic aerosol record from December to February, they are much less frequent on a weekly average basis.

Volcanic aerosol injections can change the character of the seasonal variation in the polar aerosol optical depth. For example, particles generated by El Chichón partially masked the Antarctic winter PSC peak for several years, although the spring (October) aerosol minimum remained apparent.

The SAGE–I and –II instruments provide aerosol data for latitudes up to about 70°. The highly precessing orbits of these spacecraft (about 56° inclination) cause satellite sunrises and sunsets to vary over a wide range of latitudes each month. In Figure 10.8, a month of SAGE–I extinction profiles have been used to construct an average optical depth map for the Mount St. Helens eruption cloud in summer 1980. These data show a clear tendency for the aerosol to drift toward high latitudes and the persistence of inhomogeneities in the aerosol clouds. Both effects are relevant to the observation of ozone using techniques that are sensitive to the presence of aerosols.

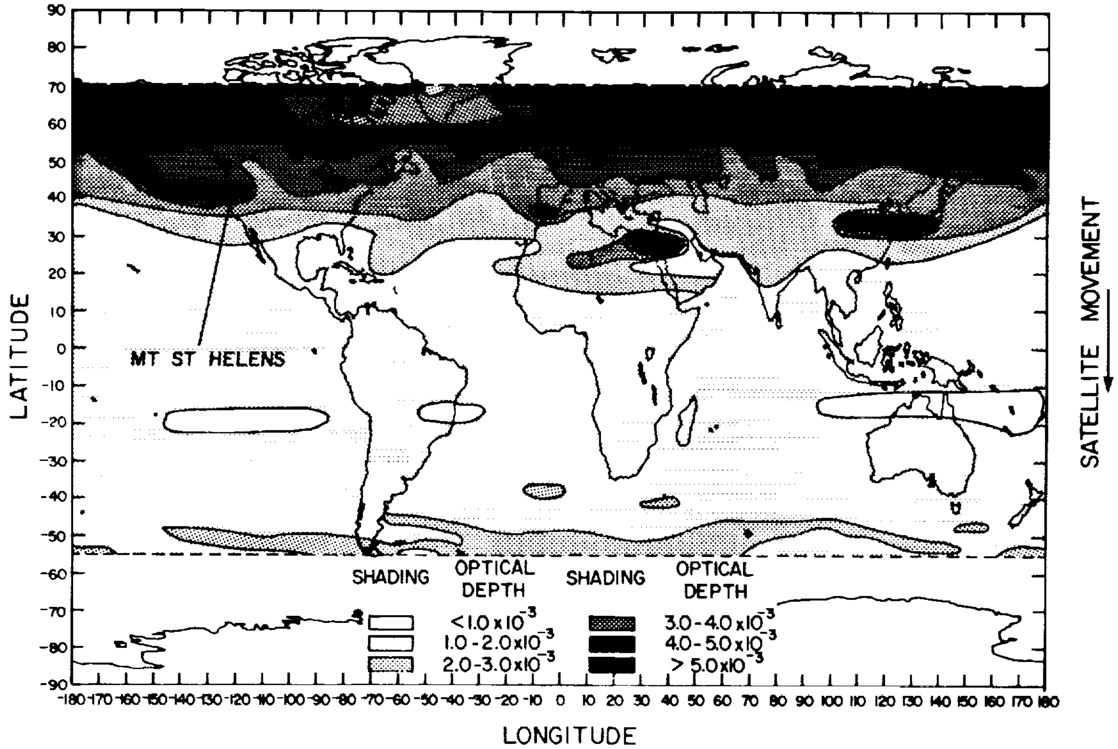
LATITUDE
90
80
70
60
50
40
30
20
10
0
-10
-20
-30
-40
-50
-60
-70
-80
-90
MT ST HELENS
SATELLITE MOVEMENT
SHADING
OPTICAL DEPTH
SHADING
OPTICAL DEPTH
<1.0x10^{-3}
1.0-2.0x10^{-3}
2.0-3.0x10^{-3}
3.0-4.0x10^{-3}
4.0-5.0x10^{-3}
>5.0x10^{-3}
-180 -170 -160 -150 -140 -130 -120 -110 -100 -90 -80 -70 -60 -50 -40 -30 -20 -10 0 10 20 30 40 50 60 70 80 90 100 110 120 130 140 150 160 170 180
LONGITUDE

Figure 10.8 Global distribution of the aerosol optical depth (measured at a wavelength of 1 μm) roughly 2.5 months after the eruption of Mount St. Helens in May 1980. The map was constructed using approximately 450 SAGE satellite observations for the period July 21 to August 26, 1980. Particularly noteworthy is the heavy concentration of volcanic aerosol at high northern latitudes (the eruption occurred at 46°N) (Kent and McCormick, 1984).

10.3.3.2 SME

The Solar Mesosphere Explorer (SME) satellite was launched on October 6, 1981, into a near-polar Sun-synchronous orbit. The mission was designed to provide stratospheric and mesospheric limb sounding profiles at ~5° latitude and 3.5 km altitude resolution for 3 to 5 longitudes per day for all sunlit latitudes. The SME complement of ultraviolet, visible, and thermal infrared spectrometers has operated continuously from the end of 1981 through the end of 1986. The extensive observations of stratospheric aerosols include data covering the El Chichón eruption of April 1982 (Barth et al., 1983).

The SME aerosol observations consist of two distinct remote-sensing techniques. The infrared observations, at 6.8 μm and 9.6 μm, are sensitive to thermal emission from H_2SO_4 aerosol. Sulfuric acid has a very large imaginary index of refraction at these wavelengths ($>10^{-2}$), such that H_2SO_4 aerosols emit in the infrared with an intensity proportional to the total aerosol mass. The SME 6.8 μm radiances were inverted to obtain stratospheric sulfate aerosol mass loading for 1982 to 1983, including the period of initial injection, peak mass loading, and initial decay of the aerosol perturbation (Thomas et al., 1983; see Figure 10.9, and note that the extinction at 6.8 μm is normally much smaller than the extinction at visible wavelengths). The infrared analysis is relevant primarily for sulfate aerosols between 20 km and 30 km altitude, where the infrared aerosol emission was several times the expected emission from stratospheric water vapor (for which the SME 6.8 μm channel was designed).

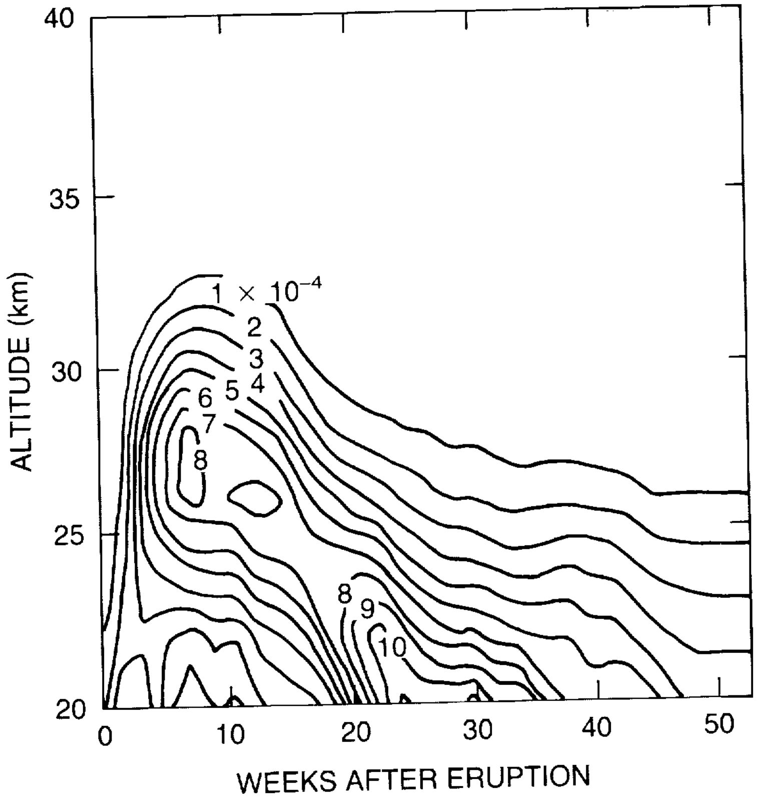

Figure 10.9 Contours of inferred vertical and temporal variations in the aerosol extinction at a wavelength of 6.8 μm (given in units of 10^{-4} km^{-1}, with values indicated on the contours) from SME infrared radiometer data for the first year following the El Chichón eruption of April 4, 1982 (Thomas et al., 1983).

A second independent set of aerosol observations was derived from limb profiles of visible sunlight scattered by the neutral atmosphere and aerosols in the middle and upper stratosphere (30 km to 50 km). These profiles indicate distinctly non-Rayleigh (nonmolecular) scale heights. The data were converted to volume-scattering ratios for 1982 to 1984 (Clancy, 1986). Inherent in the analysis scheme is the removal of any component of particle scattering that may be due to vertically well-mixed aerosol, as this radiance component would be interpreted as molecular scattering. Hence, the derived residual aerosol scattering may be a lower limit, although other factors contribute to uncertainties in the interpretation of the observed excess limb radiances.

The SME limb analysis has recently been extended through the middle of 1986 with significant improvements in the data processing and inversion schemes. Figures 10.10 and 10.11 display the latitudinal, vertical, and temporal behavior of the aerosol volume-scattering ratio derived from the SME visible-light (440 nm) limb profiles. Because the SME scattered-light observations are constrained to scattering angles between 40° and 130°, the volume-scattering ratios in Figures 10.10 and 10.11 depend on the assumed aerosol size distribution. A standard gamma distribution (mean radius = 0.1 μm, variance = 0.05 μm) was used in the data analysis. The uncertainty in the size distribution of the aerosol introduces a substantial uncertainty into the derived aerosol concentrations (see Section 10.2.3.3).

The SME observations suggest significant aerosol radiance effects above 30 km. For example, the data indicate that (1) the El Chichón eruption cloud had risen to an altitude of 30 km within 1 to 2 weeks after the eruption, then took 1 to 2 months longer to penetrate to 40 km, (2) a topside

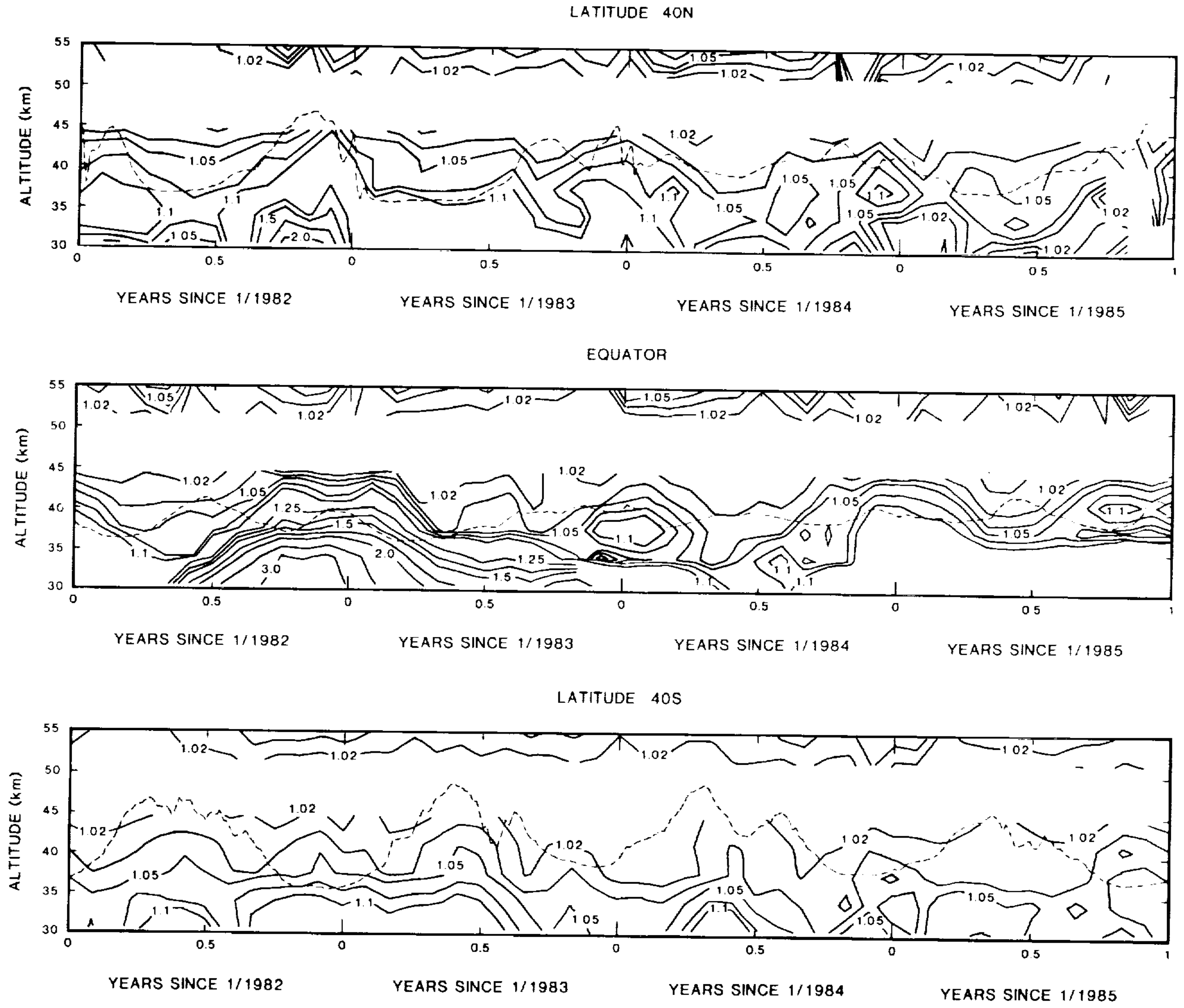

Figure 10.10 Contours of volume-scattering ratios at a wavelength of 440 nm from the SME visible spectrometer for observations at 40°N, the Equator, and 40°S, covering the period 1982 through mid-1986. The dashed line indicates the altitude at which an H_2SO_4 mass mixing ratio of 4×10^{-10} would be saturated, assuming NMC temperature and pressure profiles and a 75 percent sulfuric acid aqueous solution (R.T. Clancy, private communication, 1987).

boundary to the aerosol layer appeared to form near 40 km (possibly reflecting sulfuric acid vapor supersaturation only below this level, assuming a global average H_2SO_4 mixing ratio of about 4×10^{-10}; see the dashed lines in Figure 10.10), (3) there may be a seasonal variation in the altitude of this topside boundary due to seasonal changes in stratospheric temperatures, (4) a 1-year lifetime may be deduced for the principal injection of El Chichón, with a much longer lifetime for the residual aerosol loading, and (5) a new enhancement of the upper aerosol layer in late 1985 may be partly associated with the Nevada del Ruiz eruption.

The overall uncertainty inherent in the SME visible-light scattering analysis for aerosols could be reduced through corroborative analyses using the SME 6.8 μm radiance data above 30 km. A

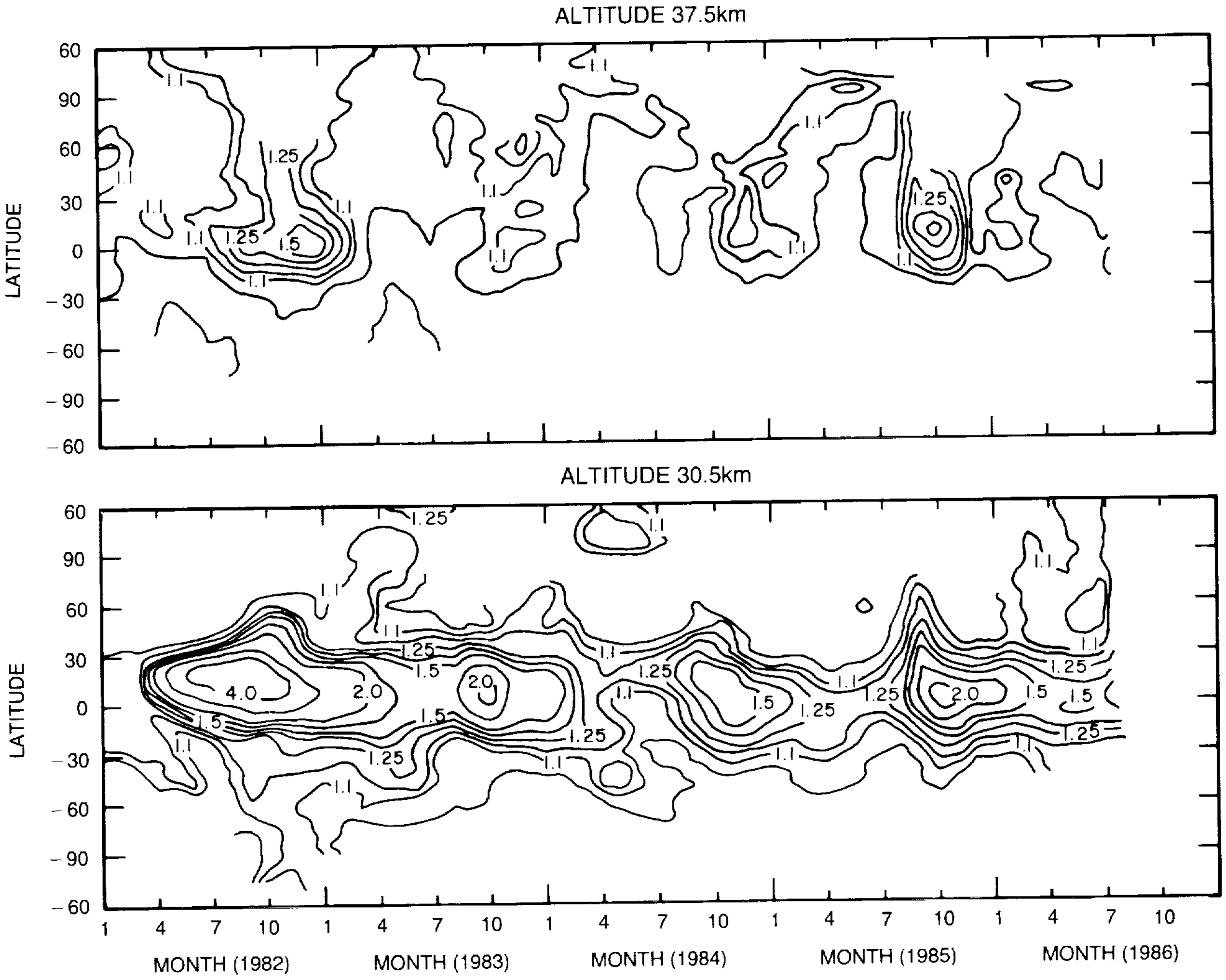

Figure 10.11 Time–longitude contours of SME visible-wavelength (440nm) volume-scattering ratios at equatorial latitudes, for altitudes of 37.5 km and 30.5 km (R.T. Clancy, private communication, 1987).

recent study of these radiances by Jakosky et al. (1988) also indicates substantial pre-El Chichón aerosol loading above 30 km from January–March 1982. Very preliminary results of visible–infrared comparisons in March 1982 and 1985 suggest that agreement between the two sets of SME data can be achieved if it is assumed that the aerosol between 30 km and 40 km consists of ~0.1 μm radius sulfate particles with a peak concentration of ~$15/\mathrm{cm}^3$ (mass mixing ratio of 2×10^{-9}).

The deduced particle number *concentration* is roughly consistent with values measured in situ by Hofmann and Rosen during February to March 1985 (i.e., ~10–$15/\mathrm{cm}^3$ at ~30 km; J. Rosen, private communication, 1987). However, the particle size limits for these balloon observations are 0.01 μm $<r<$ 0.15 μm, with actual particle sizes probably lying closer to the smaller end (e.g., Rosen and Hofmann, 1983). Accordingly, the aerosol *mass* concentrations inferred from the Hofmann and Rosen data seem to be much smaller than those inferred above from the SME observations.

10.3.3.3 SAGE/SME Intercomparisons

On occasion, the SAM–II, SAGE–I and –II, and SME satellites obtain paired measurements that are nearly coincident in time and space. Hence, opportunities exist for intercomparing the aerosol properties obtained by these related sensors. Comparisons of the aerosol extinction profiles obtained with the SAM–II and SAGE–I (Yue et al., 1984) and with SAM–II and SAGE–II (Yue et al., 1989) show excellent agreement. The paired data sets, obtained using similar solar extinction techniques, appear to be self-consistent.

The SME satellite measures the scattering of solar rays at a specific scattering angle determined by the viewing geometry at the time of the observation. The SME data can be converted to equivalent volume-scattering coefficients (or extinction coefficients, since the two parameters are analogous for nonabsorbing aerosols) by assuming a particle size distribution, calculating a scattering phase function, and normalizing the observed scattering to the predicted phase function. Typically, the measurements are expressed in terms of the volume-scattering ratio (see Section 10.2.4). The conversion of raw observational data on scattered light to volume-scattering coefficients is very sensitive to the assumed particle size distribution used in the conversion calculation.

The SAM and SAGE systems measure the aerosol extinction directly (albeit along an oblique path). Measurements of extinction do not depend on the viewing angle, unlike measurements of scattering. Thus, extinction is a more easily defined property of aerosols. Because the size distributions of particles above ~30 km are highly uncertain, the conversion of scattering measurements to equivalent extinction profiles, or vice versa, is subject to significant error. An illustration of this problem is given in Figure 10.12, in which extinction ratios measured by SAGE are compared with equivalent volume-scattering ratios deduced from coincident SME scattering data using two particle size distributions. To achieve reasonable agreement near 30 km, the assumed SME particles must be of the order of 0.1 μm in radius; if the particles are assumed to have a radius of 0.045 μm, the agreement is very poor. However, the implied aerosol mass with $r \sim 0.1$ μm exceeds the direct measurements of aerosol mass that are available (see the discussion in the previous section). The SAGE instrument, which provides a direct measurement of extinction, has not detected significant aerosol effects above approximately 35 km. SME also shows small extinction ratios at altitudes above ~35 to 40 km, except during a short period following the El Chichón eruption.

It might be concluded that the inversion scheme applied to SME radiance measurements, which depends on knowledge of the aerosol-scattering phase function, requires more precise calibration. Such a calibration could be based on the SAGE extinction data, if these were more reliable at the higher altitudes. Tentatively, it is fair to conclude from the preliminary SAGE/SME intercomparison that there is little direct evidence for the presence of optically significant, widespread aerosol layers in the region above about 35 km.

10.4 AEROSOL PERTURBATIONS: EL CHICHÓN AND OTHER EVENTS

In previous sections, the observational basis for understanding upper atmospheric aerosols was established. In certain places, reference was made to perturbations of the aerosols, particularly those caused by major volcanic eruptions that directly inject huge quantities of dust and gas into the upper atmosphere. In this section, a more detailed account is given of knowledge of the most recent aerosol perturbations that might be expected to influence atmospheric radiances and, hence, the remote sensing of ozone concentrations and distributions.

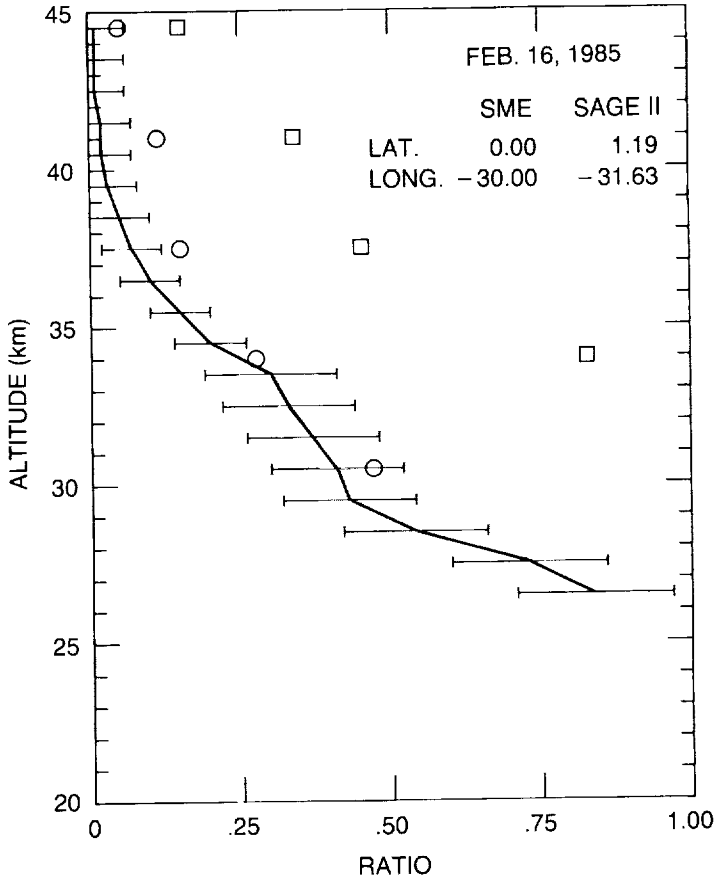

Figure 10.12 Comparison of extinction ratios (here, the ratio of aerosol extinction to molecular Rayleigh extinction, at a wavelength of 450 nm) from SAGE–II limb extinction measurements and from SME light-scattering measurements converted to extinction (volume scattering) using two distinct aerosol size distributions. The solid line with error bars shows the SAGE–II profile. Circles show SME data calculated by assuming a standard gamma distribution, with $r_g = 0.1$ μm and variance = 0.0025 μm^2 (the total number of particles is ~15/cm^3, and the mass mixing ratio is 2 ppbm). Squares show SME data calculated for another standard gamma size distribution, with $r_g = 0.14$ μm (number ~3/cm^3 and mass mixing ratio 1 ppbm). In the latter case, one would obtain the same result using a log-normal size distribution, with $r_g = 0.045$ μm, sigma = 2.5, and n = 1/cm^3 (G. Yue and R.T. Clancy, private communication, 1988).

10.4.1 El Chichón

The El Chichón volcano is situated in Mexico at 17.3°N latitude and 93.2°W longitude. Four major eruptions took place between March 28 and April 4, 1982, when the final and largest explosion occurred. The GOES and NOAA–6 satellites observed the clouds from these eruptions, indicating that at least two had penetrated the tropopause (Bandeen and Fraser, 1982). The cloud quickly spread westward over the Pacific Ocean. Lidar observations made at the Mauna Loa Observatory on April 9 showed a scattering layer at an altitude of 26 km; the scattering ratios were the greatest ever observed at Mauna Loa (DeLuisi et al., 1983). Subsequent lidar measurements (McCormick et al., 1984b) and in situ dustsonde observations (Hofmann and Rosen, 1983a) showed that the bulk of the injected material had dispersed up to 30 km, and two distinct stratospheric layers had formed with a demarcation at about 21 km marked by minimum aerosol concentrations. These layers appeared to be controlled by upper level wind systems.

The development of the eruption clouds was monitored by the Nimbus–7 Total Ozone Mapping Spectrometer—TOMS (Krueger, 1983), SME (Barth et al., 1983)—and the AVHRR sea surface temperature sensor (Strong, 1984). The stratospheric aerosols have been studied extensively, often by coordinated missions. Table 10.5 summarizes the principal observational studies. The early period just following the eruption was the most intensively investigated. However, routine measurements of the aerosol cloud, both by remote and in situ techniques, have continued to the present.

Table 10.5 Observational Methods Used To Study the Stratospheric Effects of the El Chichón Volcanic Eruption

Technique	Notes	References
Ground-Based		
Lidar backscatter	Numerous stations, mainly in the Northern Hemisphere.	McCormick, 1985; Jager et al., 1984; DeLuisi et al., 1983; Reiter et al., 1983; Adriani et al., 1983; Post, 1985; Uchino, 1985; Clemesha & Simonich, 1983; Shibata et al., 1984; Iwasaka et al., 1985a.
Solar and stellar photometer optical depth	Part of long-term data sets from Mauna Loa, Hawaii, and Flagstaff, Arizona.	DeLuisi et al., 1983; Lockwood et al., 1984.
Spectrophotometer		Evans and Kerr, 1983.
SO_2 Measurements	Used to estimate total SO_2 injection.	
Airborne and Balloon		
Lidar backscatter	Numerous flights by NASA–LaRC.	McCormick & Swissler, 1983; McCormick et al., 1984.
In situ sampling of aerosol size and composition	Aircraft flight altitude limits sampling to lower part of aerosol cloud.	Oberbeck et al., 1983; Knollenberg & Huffman, 1983; Gooding et al., 1983; Gandrud et al., 1983; Woods & Chuan, 1983; Mroz et al., 1983.
In situ gaseous sampling or overburden measurement	Aircraft flight altitude limits sampling to lower part of aerosol cloud.	Vedder et al., 1983; Evans & Kerr, 1983.
Balloon-based particle counter	Numerous flights to 30 km by U. of Wyoming.	Hofmann & Rosen, 1983a,b; Hofmann & Rosen, 1984, 1985.
Infrared transmission	Additional absorption features due to El Chichón effluents measured.	Whitteborn et al., 1983.

Table 10.5 (continued)

Multiwavelength Sun photometer	Measures wavelength dependence of optical depths.	Dutton & DeLuisi, 1983; Swissler et al., 1983; Spinhirne, 1983; Shah and Evans, 1985.
Satellite		
Nimbus–7 TOMS	Shorter wavelengths used to map SO_2 cloud.	Krueger, 1983.
NOAA 7 & GOES	Mapped spreading of dust cloud.	Robock & Matson, 1983.
SME thermal emission	Mapped initial distribution of aerosol cloud.	Barth et al., 1983; Thomas et al., 1983.
AVHRR	Negative bias on sea surface temperature indicated locations of aerosol cloud.	Strong, 1984.
SAM–II	1 μm optical depth, in polar regions only.	McCormick, 1985.
SAGE–II	Since October 1984 only.	Mauldin et al., 1985a,b.

10.4.1.1 Cloud Characteristics and Behavior, April–December 1982

Global Dispersion

The early dispersal of the stratospheric eruption clouds is most clearly delineated on satellite images from NOAA-7, GOES-E, and GOES-W (Robock and Matson, 1983). The cloud spread westward from Mexico in a restricted longitudinal band, circumnavigating the globe by April 25, about 3 weeks after the major eruption. The cloud passed over Mauna Loa, where lidar backscatter ratios exceeded 300; the densest part of the cloud was at 26 km, with an upper boundary at about 35 km (DeLuisi et al., 1983). Local optical depths at a wavelength of 425 nm reached 0.7 that April, compared with normal background values of ~0.02.

Meridional spreading of the cloud was recorded by lidar probes at middle and high latitudes. At Tsukuba, Japan (30°N, 140°E), a dense aerosol layer was detected at 15 km on April 25 (Uchino, 1985). At the NASA Langley Research Center (37°N, 76°W), a particle layer was seen at a similar altitude on April 29 (McCormick et al., 1984b). This low-altitude cloud (lying below about 21 km) reached European lidar stations soon afterward. It was observed over Garmisch-Partenkirchen (47°N, 11°E) on May 3, 1982 (Reiter et al., 1983), and over Frascati, Italy (42°N, 23°E), on May 13 (Adriani et al., 1983). Movement of the cloud into the Southern Hemisphere proceeded more slowly. Lidar observations at San Jose dos Campos (23°S, 40°W) showed the first major enhancement in July 1982; as in the Northern Hemisphere midlatitudes, the peak scattering intensity originated below 20 km (Clemesha and Simonich, 1983).

These lidar observations are supported by concurrent satellite measurements. Data from SME at a wavelength of 6.8 μm taken on May 21 placed the bulk of the injected aerosol between the Equator and 30°N; a less dense layer at lower altitudes extended to about 60°N (Barth et al., 1983). Traces of volcanic aerosol had reached higher northern latitudes by this time. Close examination of SAM–II satellite profiles reveal particle layers below 20 km arriving at latitudes of 65°–80°N by May 1982.

An accurate description of the longer term meridional and vertical distribution of the El Chichón cloud was obtained using the NASA Langley Research Center airborne ruby lidar system on a flight between NASA Wallops Flight Center and the Caribbean between July 9–12, 1982. Individual vertical profiles showed a layer peak at an altitude of about 26 km with maximum scattering ratios of about 50. The main layer above 21 km remained essentially confined to the latitude band between about 27°N and 5°–10°S, although the aerosol below 20 km had spread much farther north. A second lidar expedition in October 1982, covering the latitude range 46°N to 46°S, showed aerosol distributed over this entire span. However, maximum concentrations in the upper layer were still limited to a band from about 10°S to 30°N (McCormick et al., 1984b; McCormick and Swissler, 1983). By the end of 1982, the distinction between the upper and lower layers had largely disappeared.

SAM–II data for the Antarctic region obtained in December 1982 revealed that, by this time, the aerosol had reached high southern latitudes (60°–65°S). Simultaneously, in the Arctic region, the optical depths at a wavelength of 1 μm were close to their peak values of approximately 0.1 (weekly averaged).

Gas and Aerosol Properties

Estimates of SO_2 concentrations in the El Chichón eruption plume were made using satellite data (Krueger, 1983), in situ aircraft measurements (Vedder et al., 1983), and ground-based observations (Evans and Kerr, 1983). The SO_2 cloud spread westward from Mexico with the aerosol cloud. Satellite measurements suggest that approximately 3×10^6 tons of SO_2 were injected into the stratosphere. In situ measurements in the lower part of the cloud during 1982 yielded SO_2 mixing ratios of 8 to 132 pptv. Ground-based observations of the SO_2 column content over Mauna Loa, in combination with airborne measurements of the vertical and horizontal distributions of the volcanic clouds, suggest a substantially larger SO_2 injection of up to 13.4×10^6 tons (Evans and Kerr, 1983).

Size-specific composition measurements of the aerosols in the lower part of the cloud using a quartz crystal microbalance (Woods and Chuan, 1983) revealed a complex aerosol evolution. During the first months after the eruption, the aerosol mass was dominated by solid micron-sized particles, some having the appearance and composition of halite crystals. Submicron particles composed of sulfuric acid were also present. By November and December 1982, few of the large solid particles were evident, presumably depleted by sedimentation. Gooding et al. (1983) obtained similar results for aircraft samples collected at altitudes up to 19 km between 10°S and 75°N.

Balloonborne measurements in the El Chichón clouds have shown in detail the variation of particle concentration, size distribution, and mass-mixing ratio to altitudes of about 30 km (Hofmann and Rosen, 1983a,b, 1984). The measurements confirm the formation of two major layers differentiated at an altitude of 21 km. The mean radius of the particles in both layers increased with time. In the upper layer (above about 20 km), the radius peaked at ~0.3 μm about 4 months after the eruption; in the lower layer, the size increased more slowly to ~0.2 μm within 1 year. Figure 10.13 shows a balloon sounding made on December 9, 1982, when the highest

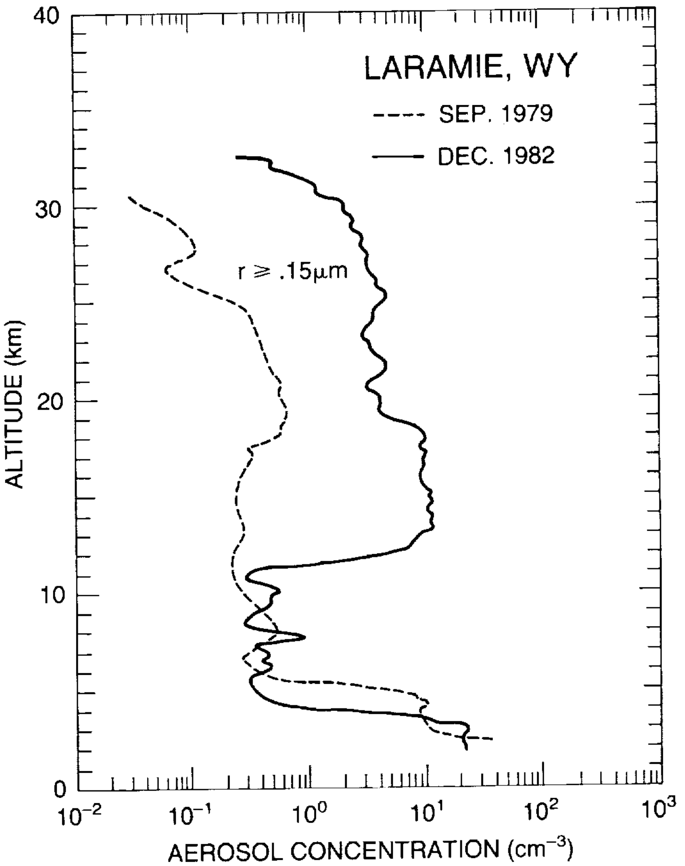

Figure 10.13 Balloonborne dustsonde measurements of the vertical concentration profile of particles with radii greater than 0.15 μm over Laramie, Wyoming. The dashed curve represents a typical background prevolcanic aerosol layer. The large enhancement in aerosols is due to the El Chichón eruption (J. Rosen, private communication, 1987).

stratospheric aerosol concentrations were observed over Laramie. These are the greatest values seen in the last 25 years.

In the upper layer, the early-time particle size distributions also exhibited a small particle mode with radii near 0.02 μm, which is consistent with the formation of new particles by nucleation of H_2SO_4 vapor.

Mass Loading

Estimates of the aerosol mass produced by El Chichón range from roughly 7×10^6 tons by Krueger (1983), to $8\text{-}20 \times 10^6$ tons by Hofmann and Rosen (1983a,b), to 27×10^6 tons by Evans and Kerr (1983) (where measurements of SO_2 emission have been converted to an equivalent 75-percent-H_2SO_4/25-percent-H_2O aerosol mass using a multiplicative factor of 2, although the conversion factor would vary according to the actual aerosol composition). The highest figures are probably overestimates of the El Chichón emissions. Nevertheless, the total stratospheric aerosol mass generated by El Chichón may be comparable to that of the Agung eruption of 1962. In Figure 10.2, for example, the El Chichón eruption (17.3°N, April 1982) caused a much larger transmission anomaly at Mauna Loa (19.5°N) than did the Agung eruption (8.3°S, March 1963).

The time delay to the apparent maximum in the aerosol mass loading following El Chichón varied with latitude from about 3 months at latitudes near that of the eruption to about 1 year at high northern latitudes. Viewed globally, the total aerosol mass may have peaked in about 5 to 6 months (between August and September 1982; McCormick, 1984). The latitude distribution of the mass loading, roughly 7 months after the eruption, is illustrated in Figure 10.14 (McCormick and Swissler, 1983). Globally averaged stratospheric aerosol optical depths during the period of maximum loading varied from 0.03 to 0.15 at visible wavelengths, with the highest values observed at about 20°N (Spinhirne, 1983; Shah and Evans, 1985). Minimum optical depths were also observed in the vicinity of 35°N.

10.4.1.2 Cloud Characteristics and Behavior, 1983–1986

During 1983 to 1986, the aerosol generated by the El Chichón eruption steadily decayed. The decline was interrupted only briefly in late 1985 by the eruption of Ruiz in Colombia. The El Chichón particulate spread relatively uniformly over the globe during this period. Balloonborne particle detectors flown over Antarctica in October 1983 showed a substantial aerosol layer within the south polar vortex at 78°S (Hofmann and Rosen, 1985). Figure 10.15 indicates the complex structure in the geographical distribution of the residual aerosols of El Chichón; such variability has been detected in other volcanic clouds as well (Kent and McCormick, 1984).

M.P. McCormick and T. Swissler (private communication, 1987) employed lidar and satellite extinction data to estimate the decay rate of the El Chichón aerosol mass. The decay rates were

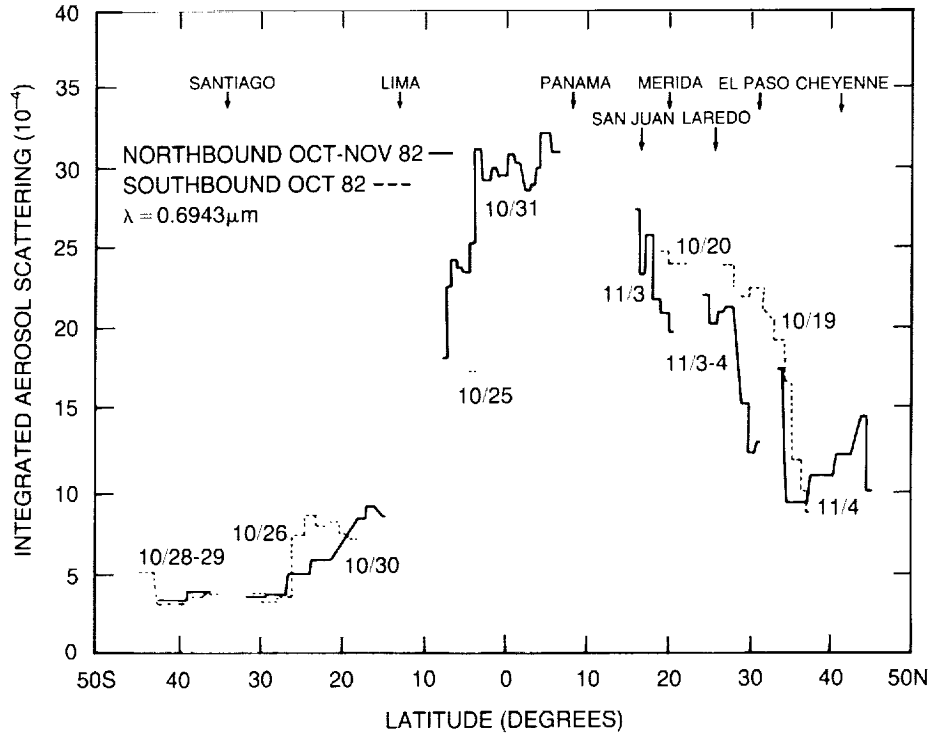

Figure 10.14 Integrated lidar aerosol backscatter intensity (in units of 10^{-4} sr^{-1}) for the stratosphere (i.e., from the tropopause upward) versus latitude from an aircraft survey (McCormick and Swissler, 1983). The integrated backscatter can be related to the aerosol mass if the size distribution and composition of the particles are known (see Section 10.2).

found to depend on latitude and the period of observation. The average e-folding time in the Northern Hemisphere for periods extending over a year or more was roughly 10 to 11 months. Similar stratospheric decay lifetimes were deduced for other volcanic events.

While the El Chichón aerosol mass decayed, the mean particle radius in the upper cloud layer decreased (Hofmann and Rosen, 1984), and the altitude of the layer dropped from about 26 km in August 1982 to about 21 km in August 1983 (McCormick, 1984). Lidar backscatter measurements at 10.6μm—a wavelength sensitive to the larger particles in the cloud—and at 40°N showed similar decreases in the peak scattering intensity and layer height (Post, 1985). Post estimated that the time constant for the aerosol backscatter decay was about 7 months. A research flight to the Arctic in March 1983 yielded evidence of downward transport of the volcanic aerosol in a tropopause fold on the flank of the polar vortex (Shapiro et al., 1984). A similar stratosphere–troposphere exchange of volcanic particles was observed following the eruption of Mount St. Helens in 1980 (Kent et al., 1985a).

10.4.2 Mount St. Helens and Other Volcanic Eruptions

In addition to the eruption of El Chichón, which produced an order-of-magnitude increase in the stratospheric aerosol loading, several other recent smaller eruptions led to measurable stratospheric perturbations. Table 10.6 lists three of the most massive historical eruptions as well as the more recent events that have affected the stratosphere. There is no reason to believe that the frequency of occurrence of such perturbing eruptions recorded in Table 10.6 is unique to the last decade of intensive monitoring. Accordingly, relatively frequent volcanic disturbances at irregular intervals must be anticipated for the future. On the other hand, eruptions of the magnitude of El Chichón (in atmospheric effects) would be expected only once every few decades statistically (Self et al., 1981; Simkin et al., 1981). Although it is difficult to estimate accurately the frequency of volcanic eruptions as a function of eruption size (measured by the mass of the aerosol injection at high altitudes), it appears that stratospheric injections of $\sim 10^5$ tons or more can occur, on average, about once every year.

The background stratospheric aerosol mass loading reached its lowest recorded global level, about 0.5×10^6 tons, in 1979. The eruption of El Chichón increased the total loading above background by a factor of about 20. As a result, during the period from April 1982 through 1984, eruptions even the size of Mount St. Helens would have been difficult to detect, except in the first few days when the clouds would be localized and very dense.

Following the volcanic injection of gases and ash, the globally integrated optical extinction typically rises to a maximum in roughly 3 months (Turco et al., 1982). This is followed by a decay in the aerosol optical effects with a time constant of about 6 to 12 months. The early rise in the perceived average particle extinction is caused by the spreading of the dense emission cloud and the conversion of sulfur gases to sulfuric acid aerosols. The larger ash particles generally fall out during this period. The decay in extinction following the maximum is associated with the global dispersal and thinning of the clouds and with the removal of sulfuric acid aerosols from the stratosphere. The variation in recovery time from eruption to eruption does not appear to be large. Figure 10.16 shows the changes in mean global aerosol optical depths between February 1979 and November 1981. Over this period, five eruptions caused significant stratospheric effects. The data illustrate the rise to a maximum optical depth (extinction) about 3 months after each eruption, followed by a slower decay. Because there have not been any recent large volcanic events, it is not possible to say if this regular temporal pattern of growth and decay would also occur in such cases.

Table 10.6 Volcanic Eruptions Known To Have Injected Material Into the Stratosphere

(a) *Massive Eruptions Prior to 1974*

Date	Volcano	Location	Total Global Injection* (10^6 metric tons)	Source
August 1883	Krakatoa	6.1°S, 105.4°E	50	Deirmendjian (1973)
June 1912	Katmai	58.3°N, 155.0°W	20	Deirmendjian (1973)
March 1963	Agung	8.3°S, 115.5°E	16	Deirmendjian (1973)
			30	Cadle et al. (1976, 1977)

(b) *Eruptions Since 1974*

Date	Volcano	Location	Total Global Injection* (10^6 metric tons)	Source
October 1974	Fuego	14.5°N, 90.9°W	6	Cadle et al. (1976, 1977)
			3	Lazrus et al. (1979)
January 1976	Augustine	59.4°N, 153°W	0.6	Cadle et al. (1977)
February 1979	Soufriere	13.3°N, 61.2°W	0.002	McCormick et al. (1981)
November 1979	Sierra Negra	0.8°S, 91.2°W	0.16	Kent & McCormick (1984)
May 1980	St. Helens	46.2°N, 122.2°W	0.55	Kent & McCormick (1984)
October 1984	Ulawun	5.0°S, 151.3°E	0.18	Kent & McCormick (1984)
April 1981	Alaid	50.8°N, 155.5°E	0.50	Kent & McCormick (1984)
May 1981	Pagan	18.1°N, 145.8°E		
January 1982	Mystery Volcano		0.85	Mroz et al. (1983)
April 1982	El Chichón	17.3°N, 93.2°W	12.0	McCormick (1984)
November 1985	Ruiz	4.9°N, 75.4°W		

*Mass of stratospheric aerosol

The dispersal of volcanic debris clouds is initially zonal in character (e.g., Robock and Matson, 1983). The rate and detailed nature of the dispersion depend on the latitude and season of the eruption and on the heights of debris injection. Wind shears tend to distort the clouds, creating large geographical inhomogeneities, and local fluctuations in the zenithal extinction. Over the course of several weeks or months, the clouds become more uniform in their zonal distribution. Meridional mixing also occurs with the following general behavior (Kent, 1986):

- The majority of the material injected by high-latitude eruptions remains within the same hemisphere.
- The material injected by low-latitude eruptions disperses into both hemispheres, with the transport rate being seasonally modulated and most rapid into the winter hemisphere.
- The volcanic debris tends to collect into three latitude bands—20°S to 20°N, >40°N, and >40°S.

For example, the aerosol injected by Mount St. Helens (46°N) remained almost entirely within the Northern Hemisphere (see Figure 10.8), while that from Sierra Negra (1°S) dispersed over several months into both hemispheres. Material injected by El Chichón (17°N) at somewhat higher latitudes than Sierra Negra remained largely in the Northern Hemisphere, although an appreciable fraction drifted into the equatorial regions and thence into the Southern Hemisphere (see Figure 10.15).

As the aerosols move poleward from the latitude of injection, the altitude of the cloud decreases. This is the same tendency seen in the meridional distributions of trace gases, and reflects the downward slope of isentropic surfaces toward the poles. The removal of the aerosols from the stratosphere probably occurs at midlatitudes as well as in the winter polar vortex. However, the details of the removal mechanisms are not well characterized. The initial height of injection, particle sedimentation, stratosphere–troposphere exchange, and polar subsidence all may have roles in purging the stratosphere of volcanic debris (Post, 1985; Kent et al., 1985a,b).

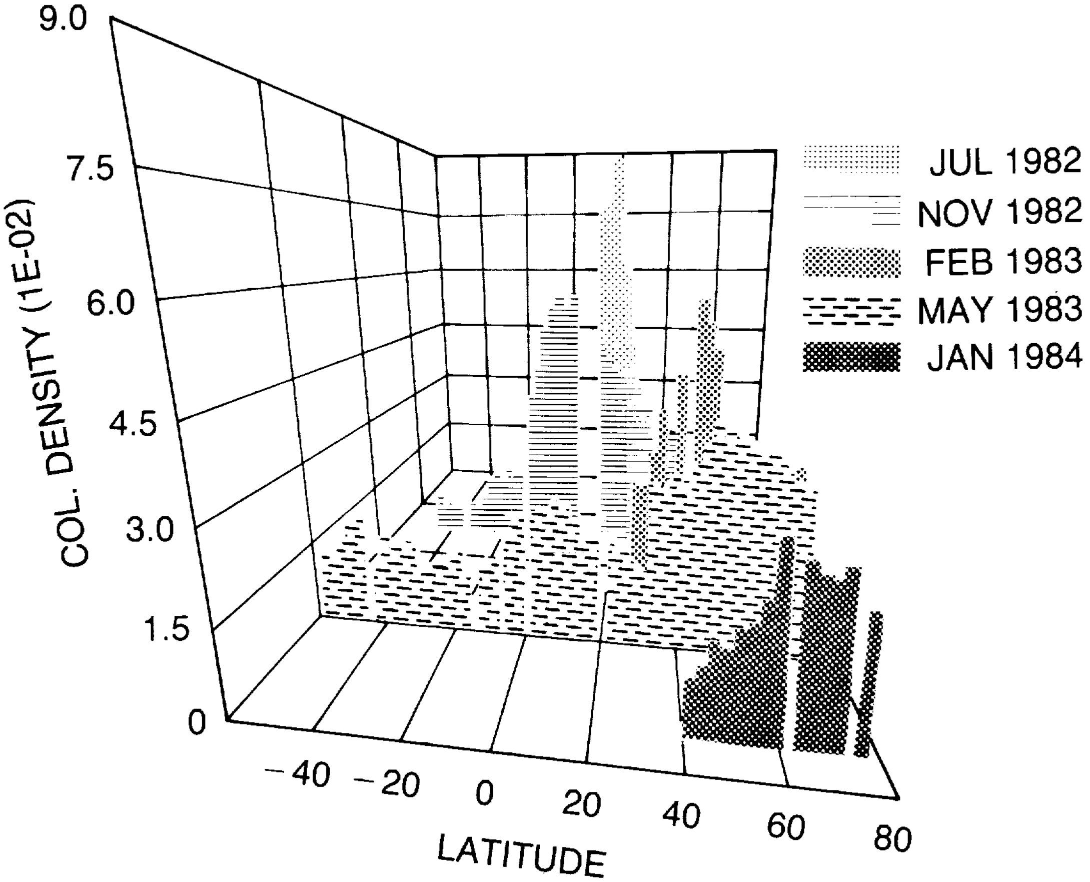

Figure 10.15 Perspective plot of the integrated stratospheric lidar backscatter intensity versus latitude for different times after the El Chichón eruption. The backscatter data have been converted to a vertically integrated aerosol column mass density (g/m^2) using an appropriate aerosol size distribution/composition model (McCormick et al., 1984). The data were collected by aircraft survey at the times indicated in the legend.

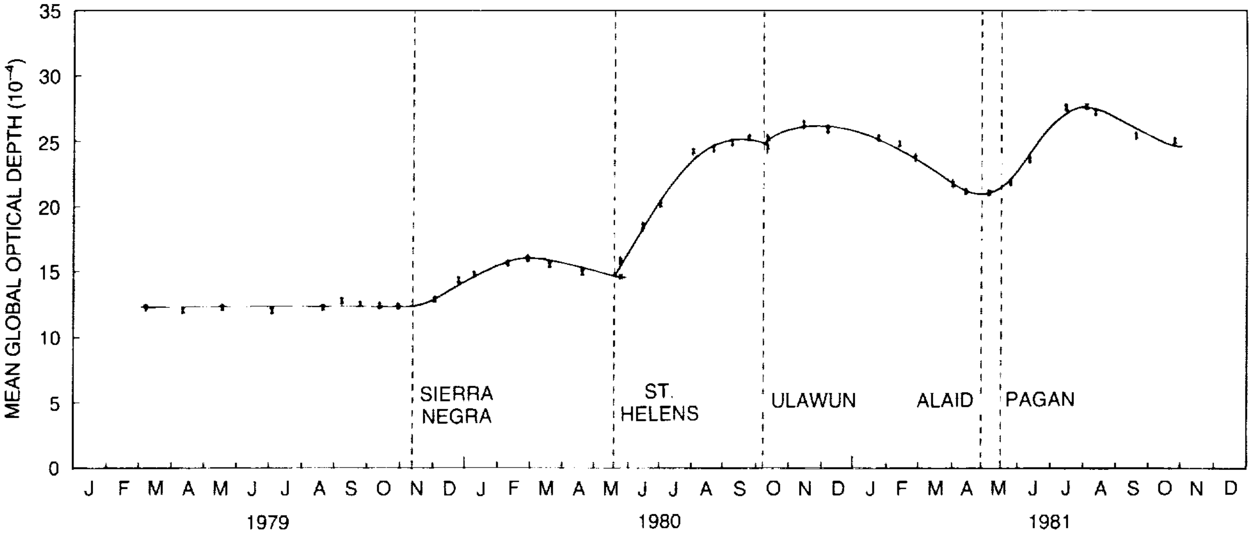

Figure 10.16 Time development of the global-average stratospheric aerosol optical depth, referred to the zenith, at a wavelength of 1 μm. Data were obtained from the SAGE and SAM–II satellite systems. The points correspond to derived observational values, while the solid curve is an empirical fit to the data (G.S. Kent, private communication, 1987).

10.5 AEROSOL IMPACT ON OZONE OBSERVATIONS

Passive remote-sensing techniques not specifically concerned with the detection of aerosol properties generally assume an atmosphere containing molecular Rayleigh scatterers and gaseous absorbers or emitters. Limited attention has been given to the possible effects of aerosols on remote ozone observations. In the near and thermal infrared wavelength regions, including the 8μm to 12μm window, molecular scattering is negligible. Typically, aerosols will have an effect only if a substantial concentration of micrometer-size particles is present. Nevertheless, tropospheric aerosols can produce substantial radiance signals in systems that use near-infrared bands to measure surface properties, and in certain wavelength channels of atmosphere-observing systems such as the AVHRR.

Much of the attention focused on the remote-sensing impacts of aerosols has emphasized the errors generated in ozone measurements at visible and near-ultraviolet wavelengths. In this section, aerosol interference in the ground-based Umkehr and space-based Solar Backscatter Ultraviolet (SBUV) methods of determining the vertical ozone profile are described, and problems encountered in correcting for the aerosol interference are discussed. The Umkehr and SBUV errors exhibit different sensitivity to the vertical ozone distribution and the optical properties of the particles. Hence, different approaches to analysis must be taken in each case.

10.5.1 Umkehr

10.5.1.1 Description of the Aerosol Error

The standard C-wavelength-pair (311.4 nm and 332.4 nm) Umkehr device measures the ratio of the cloud-free zenith sky intensities (skylight) at these wavelengths as the solar elevation angle changes from 0° to 30° (solar zenith angle changes from 90° to 60°) during sunrise or sunset. Measurements normally are taken at 12 to 14 solar elevations, although only 12 observations are used to determine the ozone profile. The Umkehr algorithm for deriving the ozone profile is based upon a mathematical model of radiative transfer in a molecular scattering and absorbing atmosphere (Bojkov, 1969a). Particle effects are neglected in the standard algorithm for several reasons: the perturbations caused by the presence of background stratospheric aerosols are estimated to be quite small; accurate quantitative information on the distribution and properties of aerosols over Umkehr sites is not generally available; and inversion algorithms including aerosols are considerably more complex.

The Umkehr method yields ozone profile information at large solar zenith angles—essentially approaching twilight conditions. Hence, the direct rays of the Sun (particularly at the longer of the two Umkehr wavelengths) must traverse a long optical path through the stratospheric aerosols before being scattered vertically downward to the instrument (see Figure 10.17). The solar rays that produce the zenithal scattered light at the shorter of the wavelength pair have passed through air layers at higher altitudes, where the ozone absorption is small enough to allow penetration of the solar beam. Accordingly, the short wavelength radiation should be much less affected by aerosols than the long wavelength radiation, because the aerosol concentrations are smaller at higher altitudes; nevertheless, the zenithal scattered light is modified in traversing the underlying aerosol (and ozone) layer (Figure 10.17). The difference in the effect

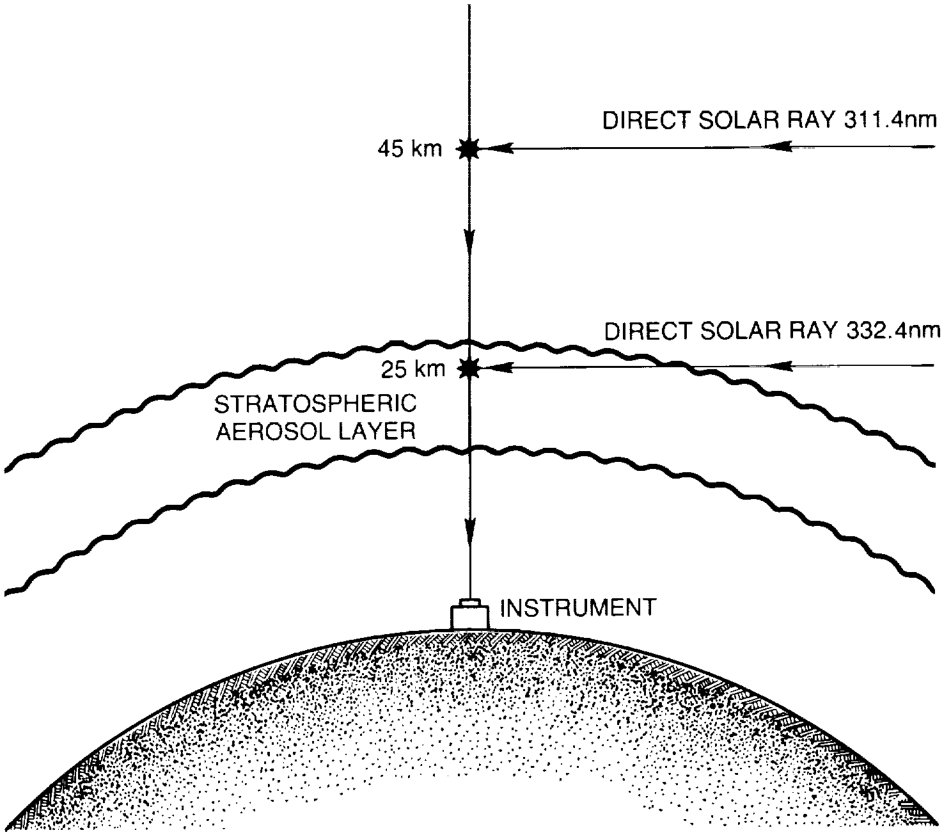

Figure 10.17 Illustration of the geometry for zenith Umkehr observations of scattered solar radiation, with the Sun at an elevation of 0°. In the near-ultraviolet spectrum, different wavelengths of light penetrate to different depths in the atmosphere and are scattered by air molecules with different efficiencies (see Figure 10.18). The optimum tangent rays corresponding to the Umkehr C-pair of wavelengths are shown. The 332.4 nm ray is scattered mainly in the region of the stratospheric aerosol layer.

of aerosol extinction between the long and short wavelengths leads to an ozone error in the Umkehr inversion, because the aerosol signal is misinterpreted as a *deficit* of ozone above the ozone maximum and as an *excess* of ozone below the maximum. The aerosol extinction optical depth is, therefore, of first-order importance in this error-generating process.

The location of the aerosol layer in relation to the ozone maximum is also important (DeLuisi, 1969). The altitude distribution of aerosols affects the severity of the error because it modulates the differential impact of aerosols between the two independent scattering regions (Figure 10.18). The scattered radiation at the longer wavelength, for example, originates at about 20 km to 25 km near twilight, while the radiation at the shorter wavelength originates much higher. As

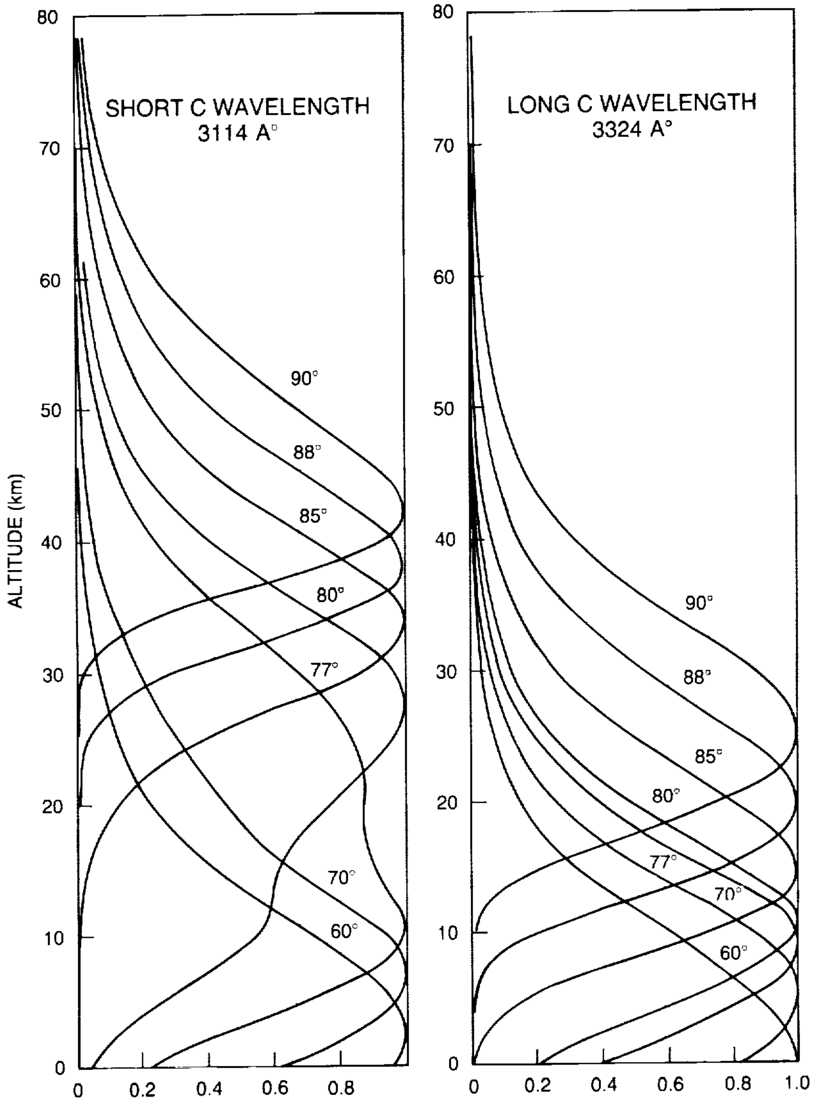

Figure 10.18 Normalized contribution functions (i.e., the relative vertical intensity profiles for primary scattered radiation, which are related to the weighting functions of Chapter 3) for the Umkehr C (311.4 and 332.4 nm) wavelength pair at several solar zenith angles. The profiles illustrate the strong overlap between the region of long wavelength scattering and the stratospheric aerosol layer. The contribution functions move downward as the solar zenith angle decreases from 90° (Mateer, 1964).

a result, a small aerosol-induced Umkehr "N-value" (see Section 3.3.4) is superimposed on the normal Umkehr N-value for a pure molecular atmosphere (or at least a relatively particle-free stratosphere). The normal N-value ranges from about 50 at a solar zenith angle of ~60°, to a peak value of about 130 at a solar zenith angle of ~85°. The magnitude of the anomalous aerosol contribution is illustrated in Figure 10.19 as a function of the solar zenith angle for the aerosol profiles given in Figure 10.20.

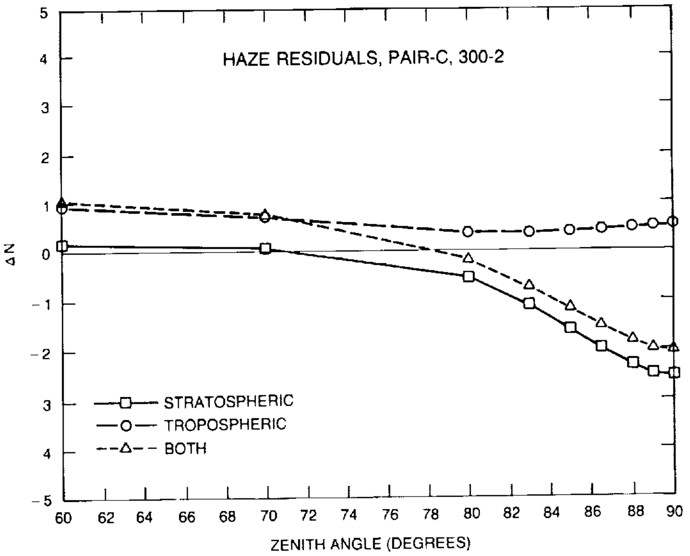

Figure 10.19 Residual, or aerosol-induced, Δ N-values in the Umkehr C-pair measurement versus solar zenith angle for three aerosol fields: tropospheric aerosols only, optical depth = 0.188, Haze L aerosol model; stratospheric aerosol only, optical depth = 0.0147, Haze H; both tropospheric and stratospheric aerosols (Haze L and H are standard aerosol size distribution models; the particle index of refraction is 1.5 - 0.03i). The vertical aerosol distributions are presented as profiles 1 and 3 in Figure 10.20. Effects of multiple scattering are included (J. DeLuisi, private communication, 1987).

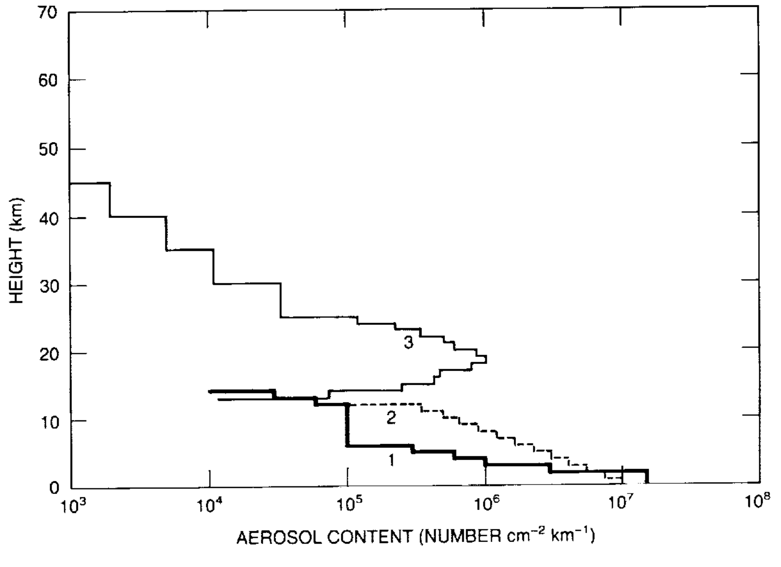

Figure 10.20 Model profiles for aerosol concentration that have been used in ozone/aerosol Umkehr error calculations. Profiles 1 and 2 correspond to the background tropospheric aerosols; profile 3 corresponds to a moderately (volcanically) perturbed stratospheric aerosol (Dave et al., 1979).

The aerosol "residual" contribution varies with solar elevation because the two scattering levels (Figure 10.18) move in relation to the ozone and aerosol layers in different ways as the solar zenith angle varies. Conversely, for a fixed solar zenith angle, the aerosol Umkehr term varies according to the relative position of the aerosol profile with respect to the ozone profile. Since the vertical distributions of stratospheric aerosols are somewhat constrained by physical processes, the impact of uncertainty in the aerosol profile on Umkehr ozone measurement accuracy is expected to be of second order.

Variable particle scattering and absorption properties (particularly the phase function) produce a small perturbation in the scattered radiance field (see Section 10.2). Again, the optical properties of the stratospheric aerosols are sufficiently constrained that uncertainty in the phase function should not seriously degrade the Umkehr data analysis. The stratospheric aerosols are, moreover, not usually highly absorbing, and single-scatter albedos ~1 can be assumed with little error.

Table 10.7 summarizes the sensitivity of the Umkehr technique to variations in several aerosol properties, as discussed above. Umkehr ozone retrievals are most sensitive to the total aerosol optical depth (or equivalently, the integrated extinction).

Table 10.7 Aerosol Impact on Umkehr and SBUV Measurement Systems, in Order of Importance of Aerosol Properties to Each System

Umkehr	SBUV
1. Optical depth	1. Profile and phase function
2. Profile	2. Optical depth
3. Phase function and refractive index	3. Refractive index

Note: The specification of both the aerosol profile and optical depth as parameters may appear to be redundant. However, a specific observational system may derive one parameter independently of the other at a particular wavelength. For example, a sunphotometer measurement from the surface may provide only optical depth information. (J. DeLuisi, private communication, 1987).

10.5.1.2 Calculation of Umkehr/Aerosol Errors

If the aerosol size distribution, refractive indices at the relevant wavelengths, and vertical distribution are known, the resulting error in the Umkehr measurement can be calculated theoretically (e.g., Dave et al., 1979). An intensive study of the Umkehr errors introduced by the El Chichón eruption is being conducted by J. DeLuisi and coworkers (private communication, 1987). Results from these error calculations are consistent with empirically deduced errors, such as those reported by Reinsel et al. (1984) (additional analyses of Umkehr and lidar observations at Mauna Loa during the El Chichón period provide further support for these error correction schemes; DeLuisi, 1979, and private communication, 1987).

Figure 10.21 shows the potential errors in ozone measurements at each Umkehr level due to stratospheric aerosols. The error is defined as the difference between the Umkehr ozone inversion values with and without stratospheric aerosols present, for a total aerosol optical depth of 0.01. The errors for other aerosol optical depths would be estimated by simple linear scaling of the errors in Figure 10.21, which correspond to an aerosol optical depth of 0.01. The actual error would be somewhat different, depending on the specific vertical distributions of ozone and aerosols, the true optical properties of the aerosols, and geometric factors.

C-3

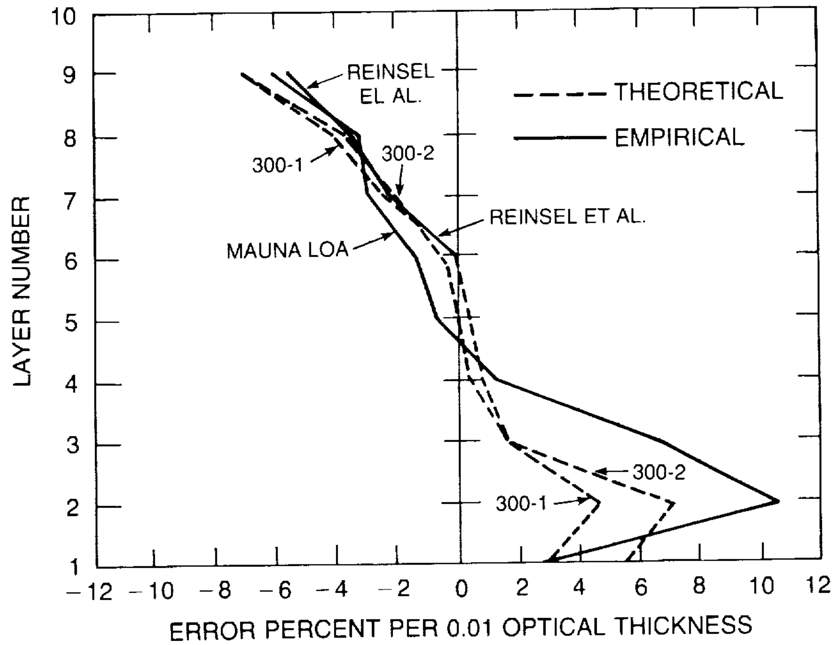

Figure 10.21 Errors in Umkehr ozone measurements resulting from stratospheric aerosol interference. The errors are given at each Umkehr level assuming a total aerosol optical depth of 0.01; that is, the ozone errors are normalized to a stratospheric optical thickness of 0.01. The theoretical errors were calculated by Dave et al. (1979) as described in the text, for two initial ozone profiles (300-1 and 300-2). The empirical errors were derived from combined Umkehr and lidar measurements at Mauna Loa from 1983 to 1986 (J. DeLuisi, unpublished data) and elsewhere (Reinsel et al., 1984; J. DeLuisi, private communication, 1987).

In Figure 10.21, the errors were determined by two independent procedures, with fairly consistent results. The "empirical" error estimate was derived from direct simultaneous measurements of ozone and aerosols. In one case, the Mauna Loa lidar and Umkehr data records for 1983 to 1986 were used to study the statistical correlations between changes in the stratospheric optical depth as sensed by lidar, and the (apparent) changes in ozone as deduced by Umkehr. The resulting correlation at each Umkehr level could then be expressed as a statistical error in the apparent ozone concentration at that level for a standard optical depth of 0.01, assuming that the errors at other aerosol optical depths could be estimated using a linear relationship between optical depth and error over the range of interest.

The "theoretical" errors in Figure 10.21 were calculated in accordance with a procedure described by Dave et al. (1979). In this case, a radiative transfer code was used with an observed ozone profile and a measurement-based aerosol model to calculate explicitly the aerosol interference (or apparent ozone error). Two examples of such a computation are shown in Figure 10.21. The aerosols are characterized by their total optical depth, vertical distribution, and physical parameters (i.e., size distribution and index of refraction, assuming homogeneous composition and spherical shape). Figure 10.22 illustrates a midlatitude stratospheric aerosol optical depth model constructed from lidar data and applied to analyze northern midlatitude Umkehr station observations during the El Chichón epoch (J. DeLuisi and D. Longenecker, private communication, 1987). The aerosol vertical profile and physical properties are based on in situ measurements (e.g., Dave et al., 1979). Typically, climatological ozonesonde data are used to initialize the ozone profile for estimating the Umkehr errors; iterative schemes using derived ozone profiles to improve the error estimate are also available.

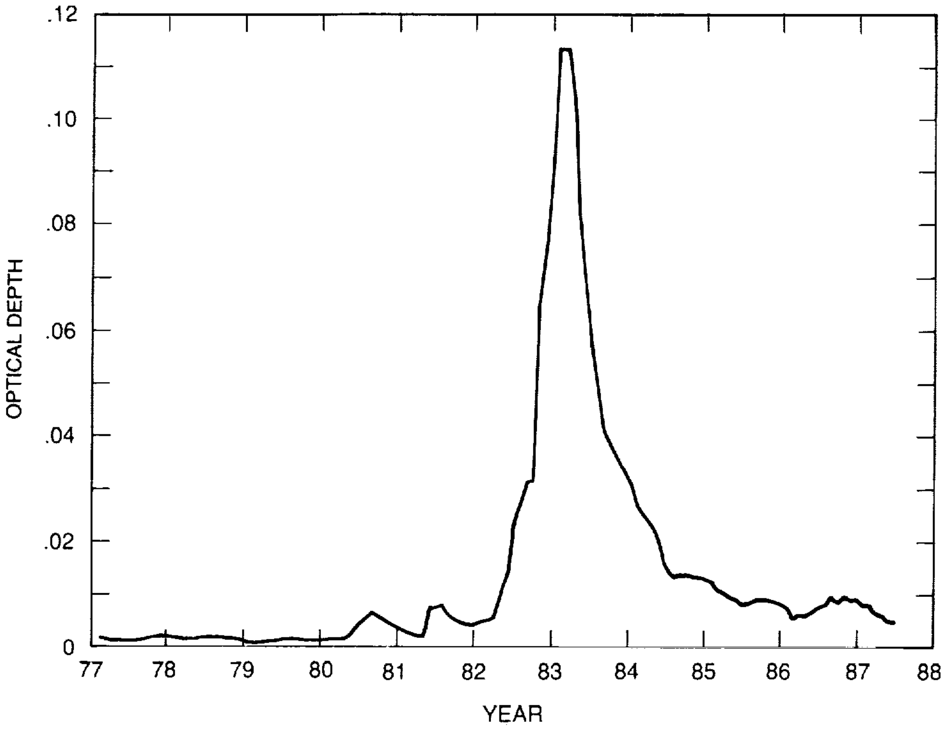

Figure 10.22 Monthly averaged midlatitude stratospheric aerosol optical depth (above 15 km) versus time, as compiled from lidar measurements at four sites in the United States, Wales, Germany, and France (J. DeLuisi and D. Longenecker, private communication, 1987).

The data in Figure 10.21 indicate that aerosols can have a major impact on Umkehr observations. In the lower Umkehr layers (1 to 3), the error in apparent ozone concentrations for a particle optical thickness of 0.01 can range up to 10 percent, and is at least a few percent. During volcanically disturbed periods, stratospheric aerosol optical depths of ~0.1 to 0.2 may exist for a year or more, leading to potential Umkehr errors of tens of percent. These errors can be corrected by the procedures discussed above (DeLuisi, 1979; Dave et al., 1979; Reinsel et al., 1984; J. DeLuisi, private communication, 1987).

Nevertheless, the residual error associated with uncertainties in the properties of the aerosols that are affecting the Umkehr system is not well defined. Lidar backscatter measurements are rarely made concurrently with Umkehr observations. Moreover, although lidar data provide information on the vertical distribution of particles, independent measurements are needed to define the other aerosol properties that are relevant to the Umkehr system. The use of average aerosol models or climatological data in correcting the Umkehr measurements leaves open the possibility of significant residual errors during volcanically perturbed times, particularly when observations from dispersed Umkehr sites are treated as a uniform data set.

J. DeLuisi (private communication, 1987) has made a preliminary detailed analysis of Umkehr errors and corrections following the El Chichón eruption. He concludes that the aerosol-induced Umkehr error can be reduced to a magnitude that is less than the standard Umkehr error (see Chapter 3), *if* adequate accurate aerosol data are available for the correction process. Considering past Umkehr observations, the quality and quantity of the aerosol data available for accurate correction are questionable. Accordingly, historical Umkehr data collected during volcanic epochs, even after correction, should be treated cautiously in ozone trend analysis. Based on the error estimates in Figure 10.21, aerosol problems would seem to be most manageable in the middle Umkehr levels (4 to 7), but potentially serious in the lowest and highest levels.

The aerosol error could be minimized in future Umkehr measurements through careful monitoring of the stratospheric aerosols over key Umkehr sites by local lidar and remote satellite observations (also see Section 10.5.3 below).

10.5.2 Solar Backscatter Ultraviolet (SBUV)

10.5.2.1 Description of the Aerosol Error

The SBUV measures solar ultraviolet radiation that is scattered back to space by the atmosphere; the geometry is illustrated in Figure 10.23. Atmospheric layers that contain aerosols can affect the scattered radiance detected at the satellite, thus affecting the ozone retrieval process. In general, the resulting ozone concentrations are underestimated in the region of the aerosol

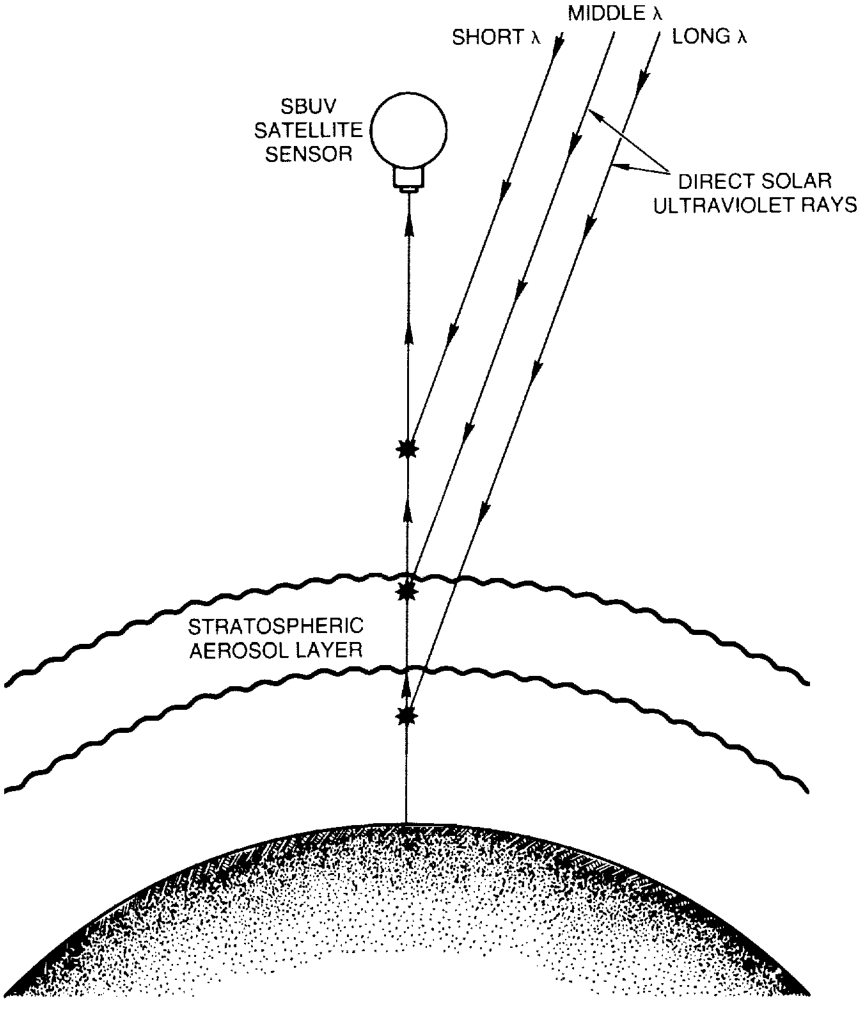

Figure 10.23 Illustration of the geometry for SBUV nadir observations of scattered solar radiation. The longer wavelength radiation reaching the sensor may be scattered from, or traverse, the region occupied by stratospheric aerosols.

layers. In contrast to Umkehr, the aerosol light-scattering phase function is an important factor in the SBUV error signal, because the SBUV normally operates over a much wider range of scattering angles. The aerosol optical depth is also important. For retrieval heights above the stratospheric aerosol layer, the SBUV-derived ozone profile is not affected by aerosol scattering. By contrast, in the Umkehr technique, all ultraviolet radiation reaching the instrument must pass through the ozone and aerosol layers, affecting the retrieval at all heights.

Current theoretical calculations of aerosol effects on SBUV ozone measurements are concerned primarily with perturbations connected with the El Chichón eruption (R.D. Hudson, private communication, 1987). While the ozone error may be especially sensitive to volcanic aerosols residing above 30 km, the SBUV system overall is much less sensitive to aerosol interference than Umkehr. Moreover, independent measurements of aerosols in the region above 30 km by the SAGE and SME satellite sensors are not completely consistent and remain uncertain (see Section 10.3.3). Accordingly, only a limited research effort has been directed toward defining the magnitude of the aerosol-induced error in SBUV ozone data. A qualitative assessment of the sensitivity of SBUV ozone measurements to aerosol interference is summarized in Table 10.7.

10.5.2.2 Implications of SME Data for SBUV Ozone Trends

Analysis of SME solar-scattering observations (Section 10.3.3.2) suggests that considerable particulate matter may have existed between 30 km and 40 km following the eruption of El Chichón. The effect of such aerosols on the SBUV ozone retrievals during this period is not clear. A substantial uncertainty in the properties of the aerosols above 30 km seems to preclude a definitive assessment at this time. Nevertheless, a preliminary analysis carried out for this report indicates that aerosol-scattering effects probably cannot explain any significant part of the long-term drift in the SBUV ozone observations at altitudes above about 30 km (R.T. Clancy, private communication, 1987).

10.5.3 Aerosol Data Requirements for Ozone Observing Systems

Measurements of the stratospheric ozone profile, and thus ozone concentrations at specific altitudes as well as trends in those concentrations, are routinely made by the Umkehr, SBUV, and SAGE systems. Both the Umkehr and SBUV observational systems are susceptible to error when stratospheric aerosols are enhanced by major volcanic eruptions. Umkehr is more sensitive than SBUV in the high-altitude region from 30 km to 50 km.

Continuous Umkehr and SBUV data records are available since 1958 and 1978, respectively. Interpretations of these data indicate significant trends in ozone concentrations near 40 km (see Chapter 6). Over the same periods of observation, however, volcanic eruptions have injected substantial quantities of particles into the stratosphere on several occasions. Umkehr measurements can be corrected for such aerosol enhancements through the procedures outlined in Section 10.5.1. In a few cases, extensive Umkehr corrections have been calculated and published (Section 10.5.1.2). On the other hand, SBUV observations have not been systematically adjusted for aerosol effects. If the accuracy of archived ozone observations is to be improved, and if maximum information is to be gained from future observations, then appropriate correction algorithms must be designed and the necessary aerosol data base developed.

Stratospheric aerosol data that are most relevant for correcting Umkehr and SBUV observations are not routinely monitored. Although aerosol measurements are frequently made by lidars as well as aircraft, balloon, and satellite sensors, the quantity and quality of the optical data obtained are insufficient. Moreover, some fundamental information on aerosol composition and scattering properties is very limited. For example, aerosol-scattering intensities over a wide range of scattering angles are needed for SBUV analysis (Table 10.7), but such data are rarely collected. The scattering phase function could be calculated using Mie theory if adequate particle size distribution and composition data were available. Typically, such aerosol data, even when available, are not highly accurate for particles in the most optically active size range.

Most observations of stratospheric aerosols are carried out at visible and near-infrared wavelengths. Yet, for application to ozone-observing systems, it is necessary to obtain aerosol properties at wavelengths in the near-ultraviolet spectrum. Further uncertainties can, therefore, be introduced when aerosol properties are extrapolated to shorter wavelengths.

A complete set of aerosol measurements that could be used in the ozone correction algorithms described earlier (and likely in algorithms yet to be designed for this purpose) to improve the accuracy of Umkehr and SBUV ozone profiles includes:

- The vertical profile of aerosols at several latitudes covering the observational zone—these data could be collected on a continuous basis by lidar and satellite instruments.
- The spectral extinction of the aerosols across the visible spectrum—these data might be obtained by continuous solar photometry or satellite limb extinction measurements.
- The size distribution of the aerosols and its variation with altitude—these data could be taken by occasional in situ sampling or remote-sensing techniques from the ground or space.
- The mass, composition, and morphology of the aerosols—these data might be obtained periodically by in situ analysis from balloon or aircraft platforms.

The time series, global coverage, and vertical resolution for such a data acquisition program would depend on planned uses of the data, the accuracy desired in the ozone/aerosol correction scheme, and the availability of resources. A minimum data collection plan for the Umkehr network would include lidar aerosol sounders at key Umkehr sites.

10.6 POLAR STRATOSPHERIC CLOUDS AND THE OZONE HOLE

Accumulating evidence now suggests that the polar stratospheric clouds that appear over Antarctica in the winter season may play an important role in the formation of the recently discovered "ozone hole" (see Chapter 11). This idea is strengthened by the correlation in time and space between PSC's and the ozone hole. New physical and kinetic chemical data, as well as direct measurements within the ozone hole (Chapter 11), allow a consistent physical theory for ozone hole formation to be structured around the properties of PSC's. Accordingly, it is essential to define as completely as possible the distribution, morphology, and physical chemistry of PSC's. In this section, the characteristics of polar stratospheric clouds deduced from SAM–II satellite measurements and other observations are outlined in some detail. The microphysical processes by which PSC's may form and evolve are described in view of the present, limited, knowledge. The optical and chemical properties of polar stratospheric clouds that may affect polar ozone concentrations are also discussed.

10.6.1 Observations and Morphology of PSC's

10.6.1.1 The SAM–II Satellite System

The SAM–II satellite sensor is a single-channel Sun photometer designed to measure solar intensity at a wavelength of 1.0 μm with a 20 nm bandpass.

The instrument is mounted on the Nimbus–7 satellite and is activated each time the satellite enters into or emerges from the shadow of Earth. Because Nimbus–7 is in a Sun-synchronous orbit, the measurement opportunities for SAM–II occur at high latitudes (64° to 84°, depending on the season). During each measurement, the instrument scans the solar disc, recording the intensity as a function of time. A complete discussion of the sensor operation is given by McCormick et al. (1979) (also see Section 10.3.3.1).

The data obtained in each measurement event are used to construct atmospheric limb transmission profiles; the shape of the refracted solar disc and the ephemeris are employed to evaluate the altitudes of the ray paths. The limb transmission profiles are then inverted using the techniques described by Chu and McCormick (1979) to yield a vertical profile of the average 1-μm extinction in each atmospheric layer. An extinction profile is obtained for each sunrise and sunset event with 1-km resolution.

The SAM–II sunset measurements are made at latitudes between about 64° and 84° in the Northern Hemisphere, and the sunrise measurements at latitudes between 64° and 81° in the Southern Hemisphere. The orbital period is 104 minutes, so there can be 14 sunrise and sunset events each day separated by 26° in longitude and by about 0.01° to 0.02° in latitude. Thus, the latitude of the measurement changes very slowly with time (by about 1° per week), varying from the lowest latitude at the solstice to the highest latitude at the equinox.

The SAM–II system originally was intended to determine the climatology of the high-latitude aerosol. A routine analysis of the SAM–II measurements made in the Northern Hemisphere in January 1979 revealed 11 extinction profiles with unusually large aerosol optical depths. One of these profiles is illustrated in Figure 10.24, and should be compared with a "normal" extinction

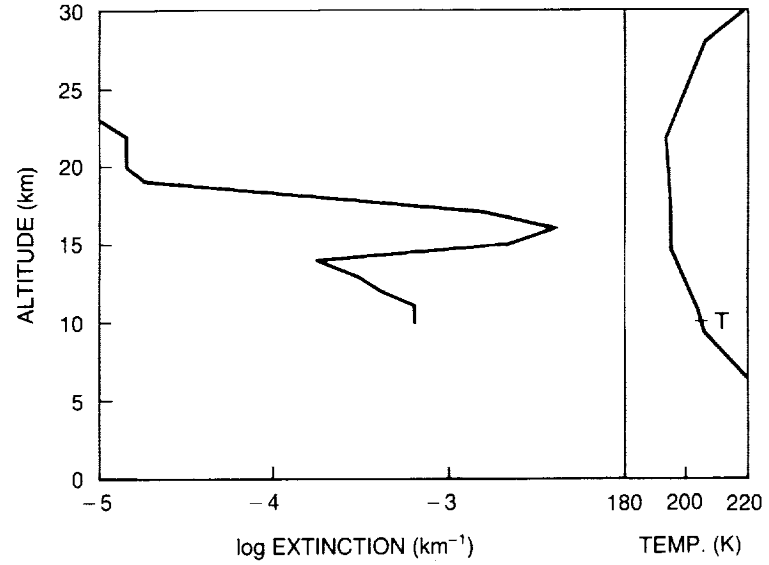

Figure 10.24 A polar stratospheric cloud extinction profile obtained from SAM–II data for January 23, 1979, at 68.7°N and 27°W (McCormick et al., 1982). The right panel shows the corresponding temperature profile.

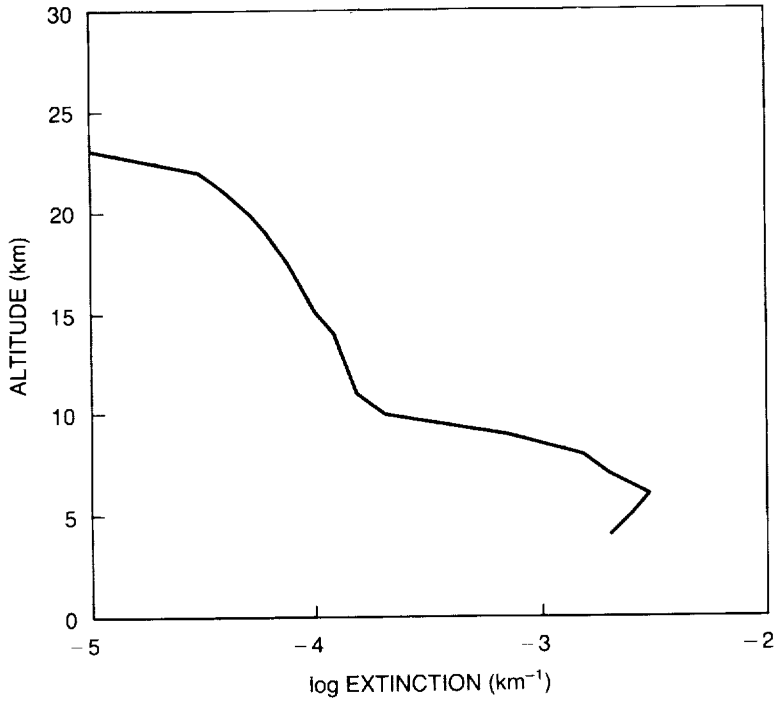

Figure 10.25 Average aerosol extinction profile for January 1979 in the Northern Hemisphere. The data correspond to all of the SAM–II observations for that month (McCormick et al., 1982).

profile, illustrated in Figure 10.25. The large anomalous extinction at about 15 km in Figure 10.24 suggested the presence of an optically dense aerosol layer at this height and location; these unusual aerosol manifestations were named polar stratospheric clouds by McCormick et al. (1982). Note from the accompanying temperature profile in Figure 10.24 the very low temperatures associated with the PSC.

The previously known nacreous or mother-of-pearl clouds are less frequent, lower latitude stratospheric clouds usually formed in the lee of mountain ranges. The relationship of high-latitude PSC's to nacreous clouds is not yet understood; the mother-of-pearl clouds, formed in regions strongly influenced by local dynamics, may be considered a subset of the more frequent PSC's.

An early workshop on the newly discovered polar stratospheric clouds described the initial understanding of this complex phenomenon (Hamill and McMaster, 1984). Considerable knowledge has accumulated since that time, as is summarized below.

10.6.1.2 PSC Properties

PSC's were first discovered in the Northern Hemisphere in January 1979 by the SAM–II satellite. At that time, 11 clouds were recorded. However, the SAM–II instrument samples only a limited part of the polar stratosphere, while PSC's can exist throughout the stratosphere. Indeed, when the south polar data for June to September 1979 were analyzed, hundreds of cloud events were detected, which is now understood to be related to the colder temperatures that exist in the southern winter stratosphere. Typically, the SAM analysis assumes that any observation of an extinction greater than 8×10^{-4}/km at an altitude 3 km or more above the local tropopause constitutes a PSC sighting (McCormick et al., 1982). Although this definition is somewhat arbitrary, it does allow a clear distinction between PSC's and the background stratospheric aerosols. Such a distinction could also have been made spectrally if SAM–II had had several wavelength channels for discrimination.

The vertical extinction profile derived from the SAM–II observations is an average value for the slant observation path of the instrument. The cloud actually may be localized along the observation path and within the SAM–II field of view. That field of view extends about 0.5 km vertically and 200 km horizontally at the minimum ray altitude. Thus, a dense (high optical depth) cloud that partially fills the field of view can be indistinguishable from a thinner cloud that completely fills the field of view. Moreover, the distribution of extinction along the observation ray cannot be finely resolved and may be highly localized. Nonetheless, extensive observations of PSC's now suggest that the aerosols are largely distributed as an extended haze, in which case the SAM–II data accurately represent average local extinction values.

Following the eruption of El Chichón, the threshold extinction for PSC detection had to be increased because of the volcanically enhanced background aerosol opacities. Accordingly, there is some ambiguity in the definition of PSC's and in the statistics of PSC's derived from the SAM–II observations, although such ambiguities are easily resolved in the long-term optical depth record from SAM–II (see Figure 10.7, for example).

In describing the general properties of PSC's, data are taken from observations in the pre-El Chichón years of 1979 to 1981, and in 1986. Following the eruption of El Chichón in the spring of 1982, the stratospheric aerosols, including those in the polar regions, were highly disturbed. In taking a conservative approach here, the satellite observations from 1982 through 1985 are not considered in any statistical or morphological analyses.

In 1979, 387 clouds were detected in the Southern Hemisphere in the winter season (June to September). The average cloud thickness was about 4.2 km (note, however, that for individual measurements SAM–II can resolve the vertical thickness only to the nearest kilometer). The average altitude of the peak extinction was ~15 km, and the average extinction (averaged over slant path for the layer of observation) was about 1.4×10^{-3}/km. The observed clouds were clustered around the longitude of Greenwich, with about 50 percent of the clouds appearing between 40°E and 40°W (see Table 10.8 for additional statistics).

In 1980, 433 clouds were recorded with an average thickness of ~5.8 km and an average peak extinction of about 1.4×10^{-3}/km. The average altitude of the clouds was near 15.6 km. Once again, the clouds were clustered around Greenwich with about 40 percent lying within 40 degrees of that parallel.

Table 10.8 Observed PSC Properties: 1979 to 1981

Year	Number of Cloud Observations	Average Cloud Thickness (km)	Maximum Extinction (km^{-1}) (km)	Altitude of Maximum Extinction (km)	Minimum Temperature (K)	Altitude of Minimum Temperature (km)
1979	387	4.2	0.00142	14.9	190	17.9
1980	433	5.8	0.00144	15.6	189	19.7
1981	449	4.2	0.00129	14.6	190	18.5

(P. Hamill, private communication, 1987)

In 1981, 449 clouds were seen with an average thickness of about 4.2 km, maximum extinction of about 1.3×10^{-3}/km, and average height of 14.6 km. Moreover, 42 percent lay within 40 degrees of Greenwich.

The average longitudinal distribution of the cloud sightings for 1979 to 1981 is illustrated in Figure 10.26. This preference for the clouds to lie near Greenwich is probably associated with the strong stationary wave-number-one feature in the Antarctic circumpolar flow, which is reflected in the temperature structure of the lower polar stratosphere in winter.

There is observational evidence that the heights of the PSC's decrease as the winter progresses. In Figure 10.27, measured cloud heights are plotted over a 13-week period of the Antarctic winter. It appears that the clouds have descended several kilometers over this time. The descent may be explained by the sedimentation of cloud particles or the slow subsidence of air in the winter polar vortex. The actual cause remains unresolved, although recent theories on PSC formation suggest that sedimentation may be sufficient to account for at least part of the decrease in elevation.

The frequency of cloud occurrence as a function of the minimum stratospheric temperature in the vicinity of the cloud (as deduced from NMC temperature fields) is illustrated in Figure 10.28 for the austral winter of 1981. In this year, no clouds were seen when temperatures exceeded about 200 K. Cloud formation seems to have a fairly high probability (~30–50 percent) once the temperatures fall into the range of ~189 K to 195 K. At temperatures below ~185 K, the probability of PSC's approaches 100 percent. Interestingly, that temperature (185 K) roughly corresponds to the frost point of water at typical stratospheric mixing ratios. Thus, on observational evidence, there seem to be at least two distinct cloud types or growth stages: Type I, which

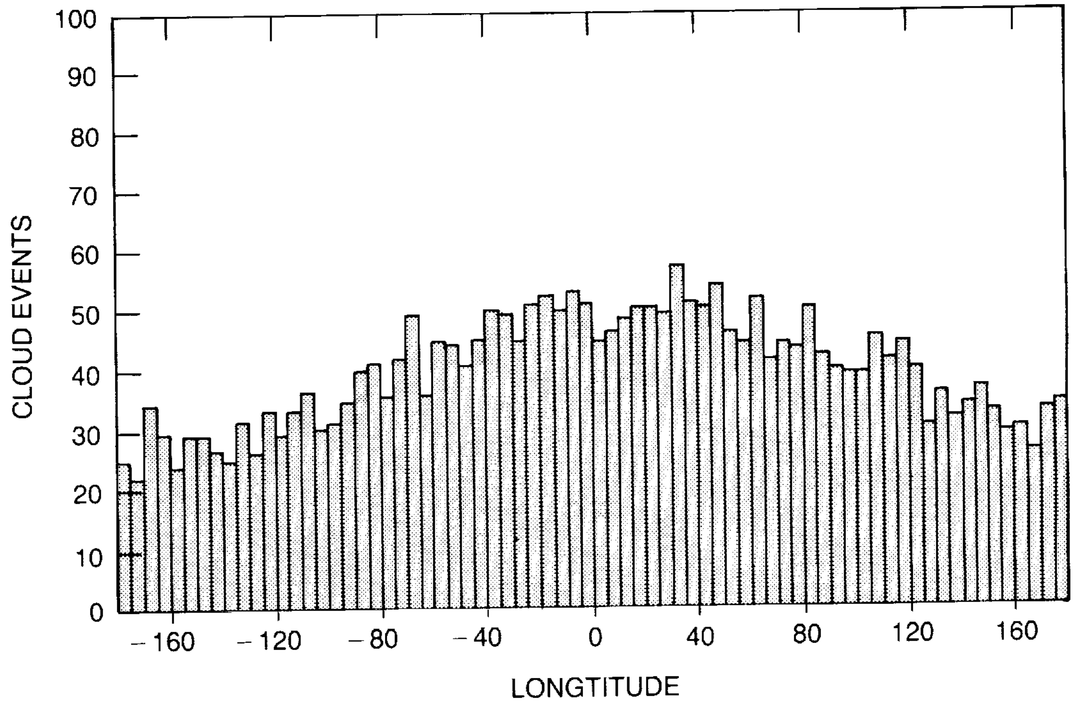

Figure 10.26 Histogram showing the longitudinal distribution of PSC events in the Southern Hemisphere for the winters of 1979–1981 based on SAM–II observations (P. Hamill, private communication, 1987).

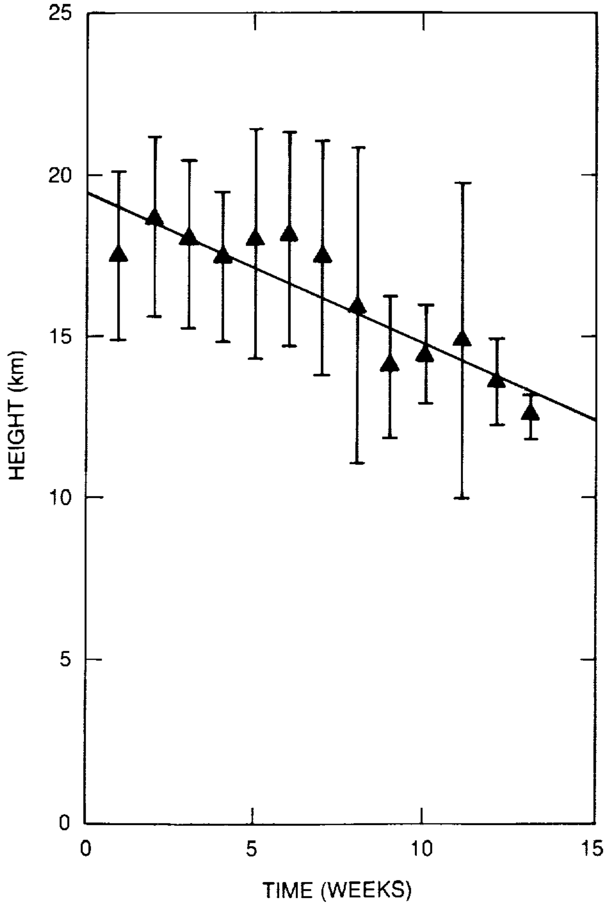

Figure 10.27 Average altitude of the maximum aerosol (PSC) extinction (on the vertical profile of extinction) for SAM–II satellite measurements over Antarctica during 13 weeks of a winter season (P. Hamill, private communication, 1987).

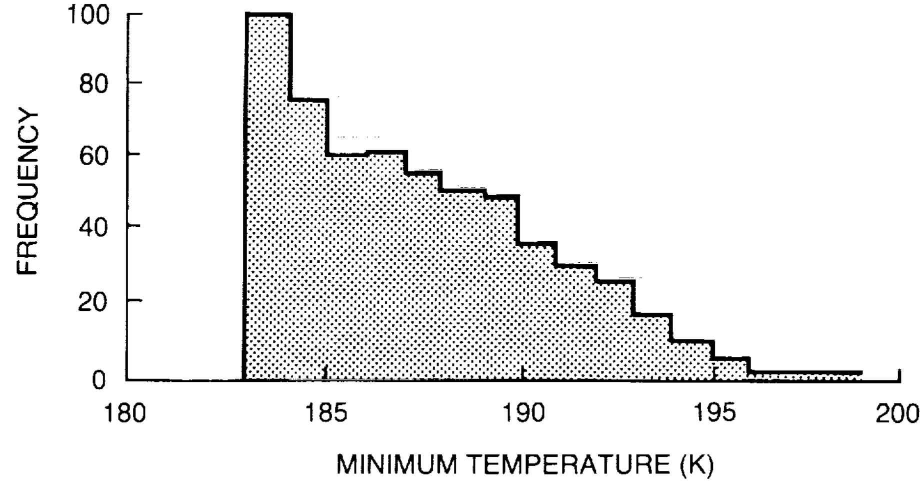

Figure 10.28 Frequency of cloud sightings by the SAM–II detector as a function of the minimum stratospheric temperature in the vicinity of the clouds, during the austral winter of 1981 (P. Hamill, private communication, 1987).

occurs at temperatures from about 195 K to temperatures as low as ~185–189 K, and Type II, which occurs below ~185–189 K. The Type II clouds are thought to be water ice clouds. As is discussed below, the Type I clouds are inferred to be composite nitric acid–hydrochloric acid–water ice aerosols (Toon et al., 1986; Crutzen and Arnold, 1986; Poole and McCormick, 1988; Hamill et al., 1988; Wofsy et al., 1988). Other evidence for these distinct cloud types is discussed in Section 10.6.2.4.

The variability in PSC properties can be illustrated by considering the measured cloud extinctions at a fixed pressure level without temporal and spatial averaging. Such a data record is provided in Figure 10.29 at 50 mb for the winter of 1981. The data clearly show that the clouds are highly variable from measurement to measurement, probably reflecting spatial inhomogeneity. Nevertheless, there is a clear trend for the extinction (at 50 mb) to increase during the winter and then decrease in the spring, leaving the stratosphere relatively clean. This observation is also consistent with the data in Figure 10.7, as discussed in Section 10.2.3.

An expanded view of the cloudiest period in Figure 10.29 is given in Figure 10.30. To interpret these data, recall that the satellite orbit precesses in longitude roughly 360° per day. Figure 10.30 shows an apparent periodicity in the extinction corresponding roughly to 24 hours in time or 360 degrees in longitude. This implies that PSC's are preferentially formed in the specific regions of the stratosphere that are the coldest. Support for this idea can be found in the corresponding 50 mb temperatures plotted in Figure 10.31. By comparing Figures 10.30 and 10.31, a close correlation can be seen between low temperature and high extinction with a repetition rate approximately each 360 degrees of scan in longitude. One interpretation of this behavior is that

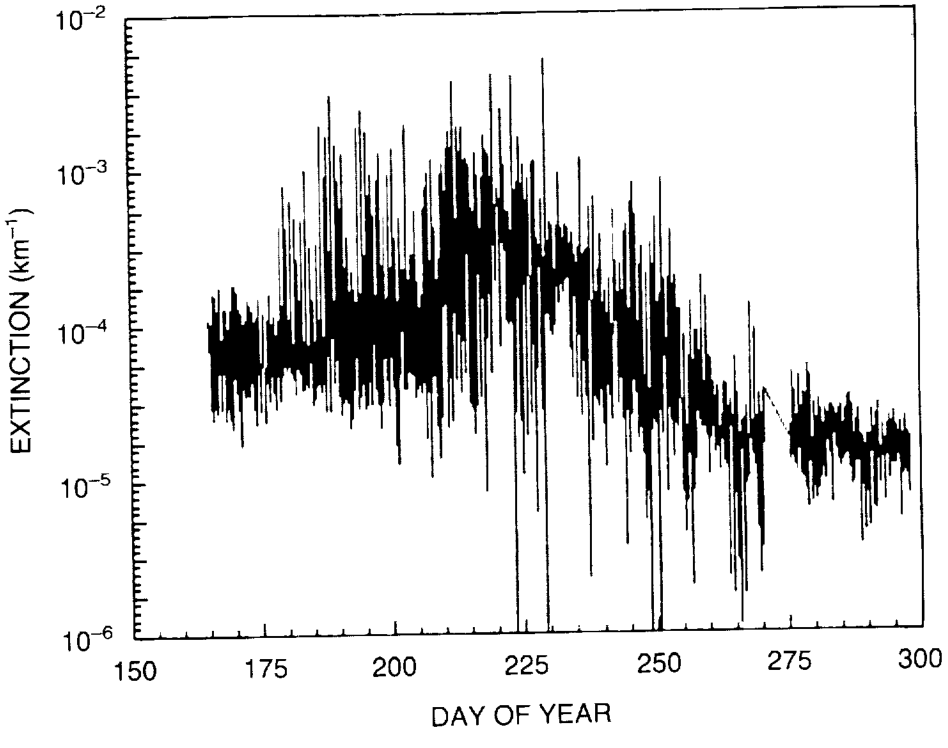

Figure 10.29 Detailed SAM–II extinction measurements at 50 mb over a 130-day period during the austral winter and spring of 1981. The data reflect the actual variability detected by the SAM–II sensor (P. Hamill, private communication, 1987).

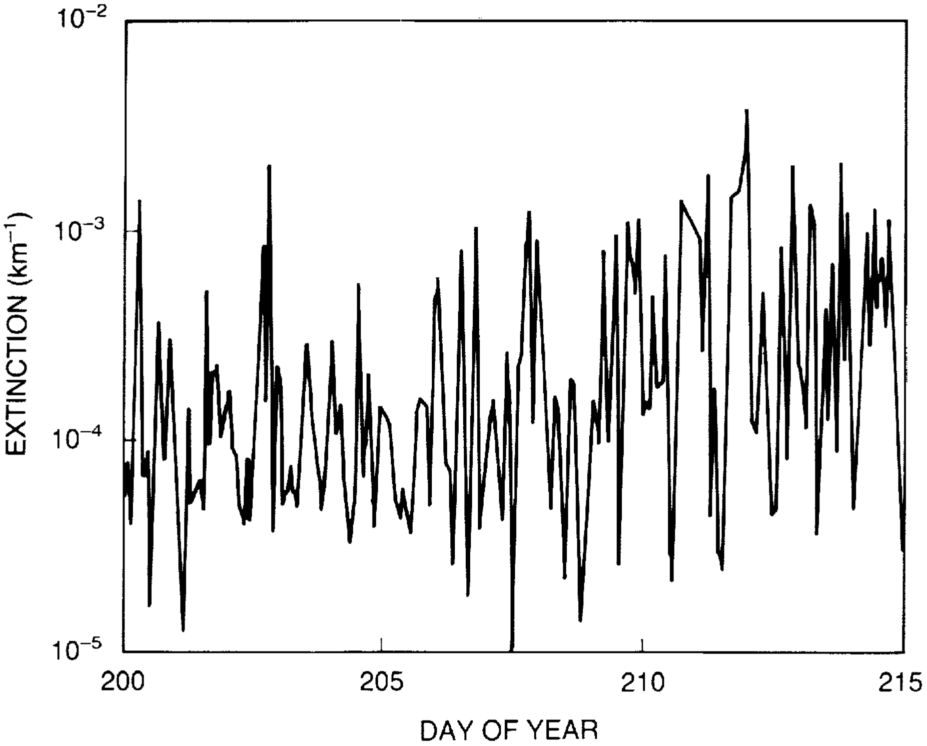

Figure 10.30 An expanded plot of a segment of the data in Figure 10.29 (P. Hamill, private communication, 1987).

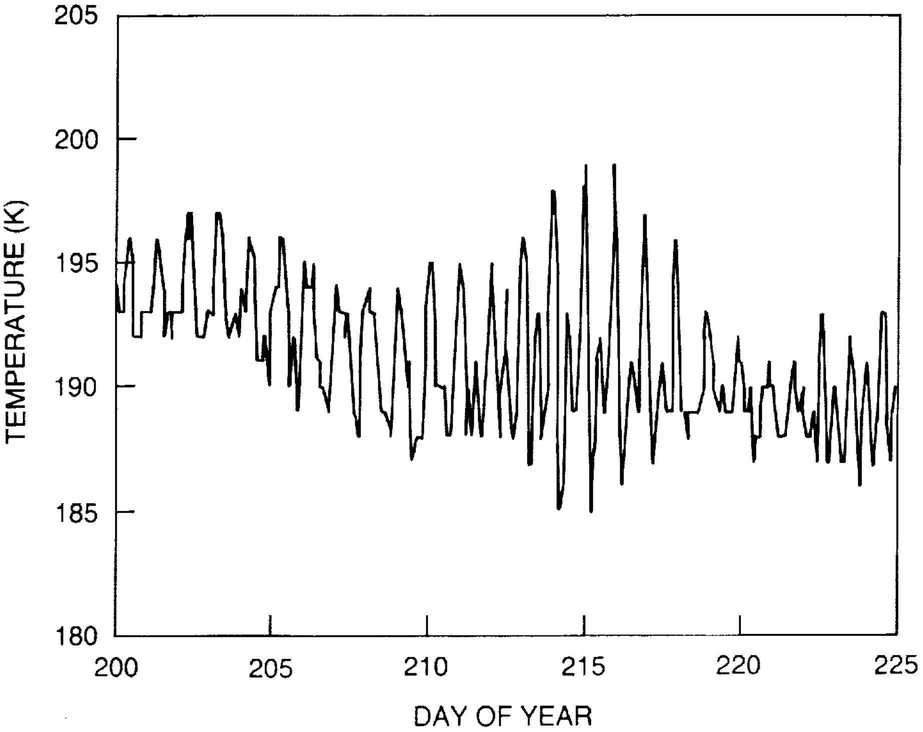

Figure 10.31 Temperature variations at 50 mb for the same period and geographical locations as in Figure 10.30 (P. Hamill, private communication, 1987).

approximately each 360 degrees of scan in longitude. One interpretation of this behavior is that the point of measurement is moving in and out of the cold polar vortex as the satellite precesses in longitude (McCormick et al., 1983). Another explanation is that air is being lifted and cooled locally, with the clouds appearing in the air parcels circulating through these cold regions.

The 1986 SAM–II data are of interest because the upper cutoff for extinction measurements (10^{-2}/km) was relaxed, and events of greater extinction were recorded and analyzed for the presence of polar stratospheric clouds. In that year, the total number of observations of clouds with extinctions greater than 0.8×10^{-3}/km was about 920, with 82 observations of clouds with extinctions exceeding 1×10^{-2}/km. To limit the data set, P. Hamill (private communication, 1987) has compiled information on the subset of clouds with observed extinctions greater than 2×10^{-3}/km, of which about 290 were sighted during 1986. In Figure 10.32, the statistical characteristics of these Southern Hemisphere PSC's are summarized. The data show clearly that the PSC's began to appear frequently at temperatures below about 195 K, and increased in frequency as the winter season progressed (presumably, as the polar stratosphere continued to cool). Most of the clouds appear to reside between about 14 km and 20 km, but with a significant number of clouds up to about 24 km.

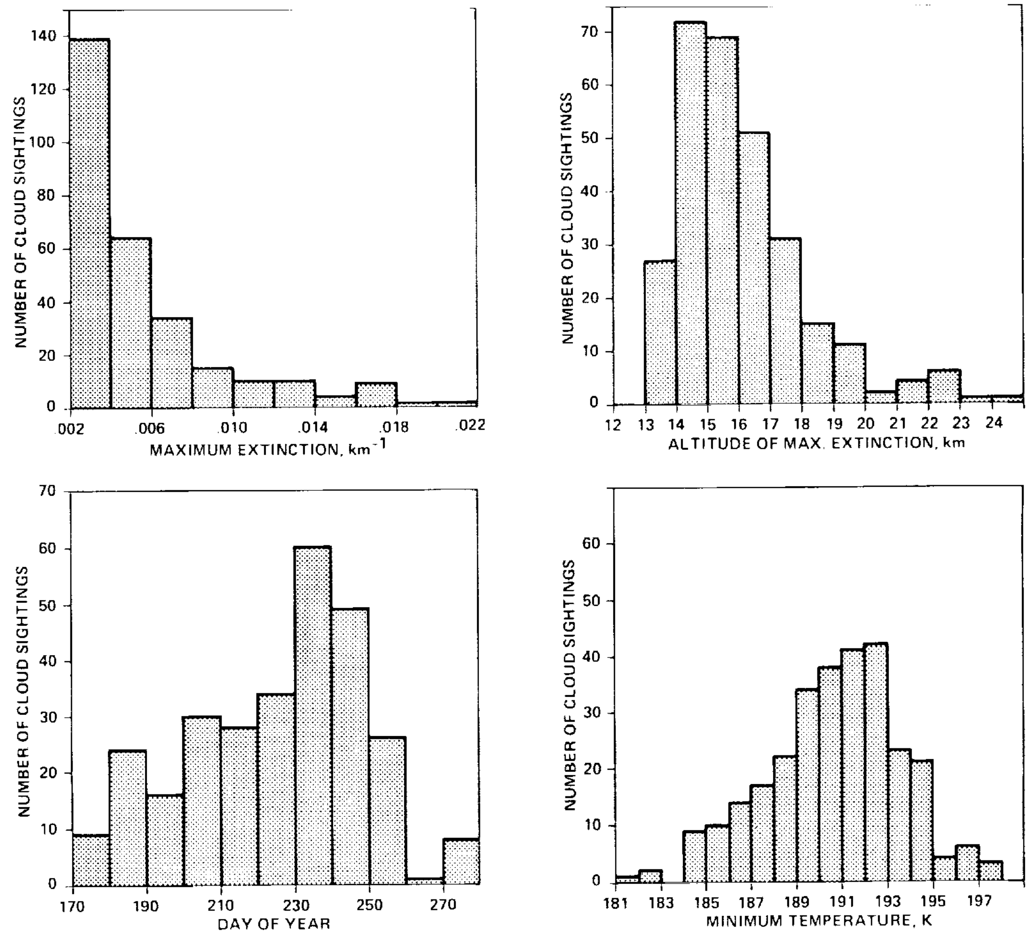

Figure 10.32 Histograms of the statistical characteristics of the total ensemble of Southern Hemisphere PSC's having extinctions greater than 2×10^{-3} detected by the SAM–II satellite in 1986. The number of clouds indicated corresponds to the range of the parameter delimited by the bar (P. Hamill, private communication, 1987).

10.6.1.3 PSC's in the Northern Polar Vortex

Although considerable attention has been focused on the ozone hole over Antarctica, relatively little attention has been given to the possibility of a similar phenomenon over the North Pole. This neglect is due in part to satellite observations indicating that the total ozone column content does not show a significant depletion in the Arctic spring. However, Evans (1987) has described a series of ozone profiles taken at Alert, Canada (82.5°N), during the breakup of the Arctic winter vortex; the individual profiles are very similar in character to profiles obtained by Hofmann et al. (1987a) from McMurdo during the breakup of the Antarctic vortex, displaying a "notching" effect or ozone depletion occurring in layers throughout the 12 km to 20 km altitude range. This may imply that analogous ozone depletion mechanisms are operating at both poles in the winter season.

Conditions in the core of the Arctic polar vortex may resemble those in the Antarctic, especially during those winters when the vortex is least disturbed and persists longest into the spring. Under these circumstances, some or all of the chemical processes believed to be occurring in the Antarctic stratosphere might be detected in the Arctic stratosphere as well.

Figure 10.33 summarizes the statistical characteristics of the PSC's observed by the SAM–II satellite in the northern polar region in 1986. There are significant differences in comparison to

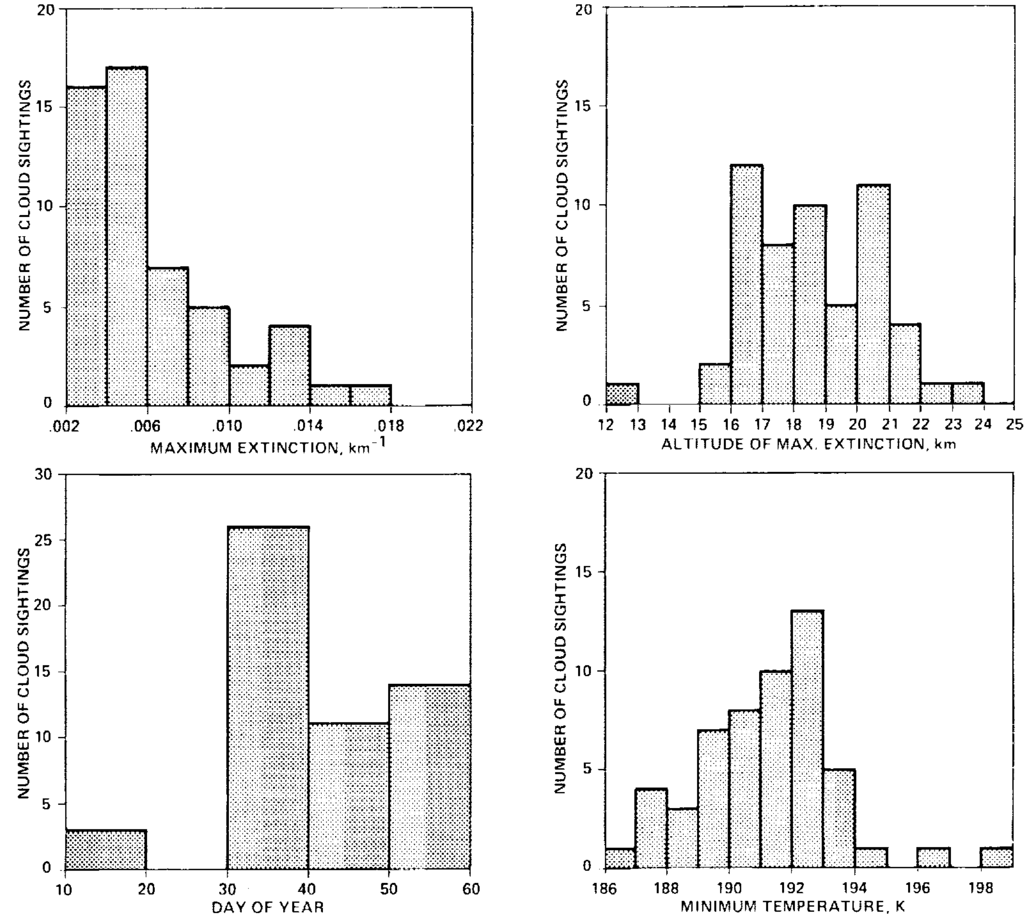

Figure 10.33 As in Figure 10.32, except for the PSC's observed in the Northern Hemisphere in 1986 (P. Hamill, private communication, 1987).

the southern polar data (Figure 10.32). The northern clouds tend to be much less frequent and reside at higher altitudes. However, the optical densities and seasonal behavior are roughly equivalent. Moreover, the frequency of appearance versus temperature is very similar in both hemispheres, suggesting a common microphysics (which is discussed in the next section).

10.6.1.4 Long-Term Trends in PSC Properties

The period of comprehensive observations of PSC's is relatively short, beginning in 1979 and extending to the present. Moreover, from 1982 to 1985, the El Chichón volcanic eruption filled the polar stratospheric regions with aerosols that masked to some extent the direct observations of PSC's (see Figure 10.7). Because of these constraints, it is not yet possible to make a definitive statement about possible long-term trends in PSC properties. Nevertheless, the most recent SAM–II satellite measurements indicate a marked increase in Antarctic PSC occurrence in 1987 as compared to previous years.

Figures 10.34a–d show the individual SAM–II measurements of aerosol extinction in the southern polar region for 1979, 1985, 1986, and 1987. The data are presented in terms of the equivalent local aerosol extinction at 18 km, which is representative of the PSC formation region. The plots clearly show the onset of PSC's in mid-June, with dissipation of the clouds in September. The influence of volcanic aerosols is seen as elevated background extinctions in these figures. There is a noticeable increase in cloud sightings between 1979 and 1985–87; however, keep in mind that the nominal upper extinction cutoff of 10^{-2}/km for PSC's was relaxed in 1986, and more cloud events were subsequently recorded—see Section 10.6.1.2. It appears that the onset of PSC formation is occurring earlier in the winter in recent years, and that the PSC's are persisting longer into the spring, particularly in 1987 (Figure 10.34d). An analysis of the SAM–II data for September 10 to 20 and September 20 to 30 is provided in Figures 10.35a and b, respectively, for each year represented in Figure 10.34. These data indicate that the frequency of cloud events with high extinctions is substantially greater in 1987 later in the spring season than in earlier years (of SAM–II observations). Indeed, PSC events were recorded into October 1987 for the first time. Statistically, the years 1979, 1985, and 1986 are not distinguishable in this regard (allowing for interannual variability seen throughout the SAM–II record).

The earlier onset of PSC's, their greater frequency over the winter, and their persistence into the spring may be associated with a general cooling of the late winter–early spring polar vortex in recent years, with a significant quasi-biennial signal (see Section 11.2.3). The largest Antarctic ozone reductions to date were also measured in 1987, suggesting a possible mechanistic relationship between PSC formation, ozone depletion, and stratospheric cooling (see Sections 6.4.4 and 11.3.3). A trend in the occurrence of PSC's could also be caused by changes in stratospheric composition, including trends in the abundances of water vapor and nitrogen oxides, which condense to form cloud particles (as described in the following section). However, no clear trends in either H_2O or NO_x over the period of PSC observation have been unambiguously identified (see Chapter 8). Because reliable measurements of these trace species are very limited, the possibility of trends in their concentrations cannot be ruled out.

10.6.2 Physical Chemistry and Microphysics of PSC's

Polar stratospheric clouds may influence the formation of the Antarctic ozone hole (Solomon et al., 1986a; Crutzen and Arnold, 1986; McElroy et al., 1986a; Hamill et al., 1986). Recent laboratory studies (e.g., Molina et al., 1987) and field measurements (see Chapter 11) strongly

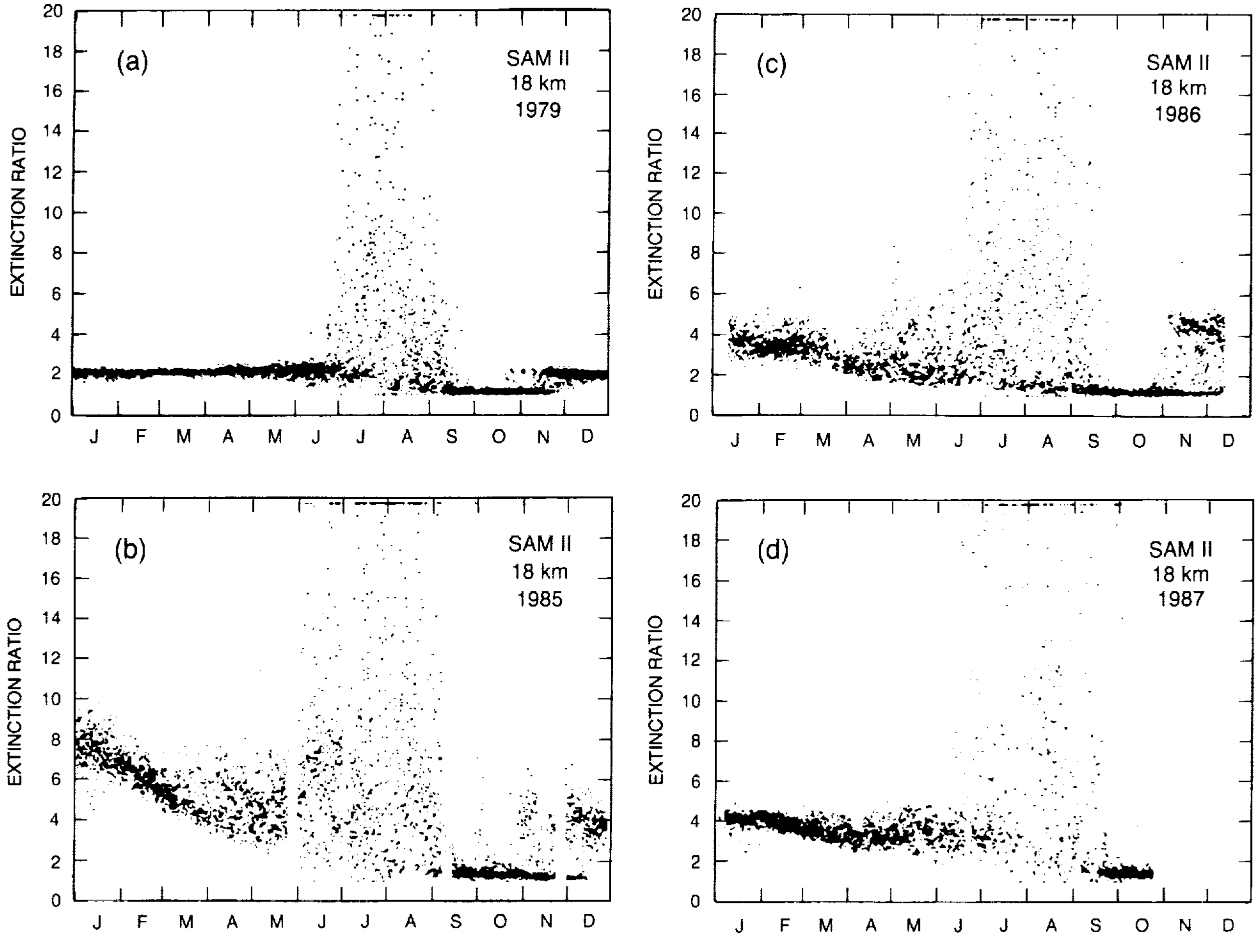

Figure 10.34 Extinction ratios at 18 km versus time as measured by the SAM–II system in the Southern Hemisphere (i.e., the total extinction including aerosol effects obtained by the satellite limb sensor, divided by the extinction caused by molecular Rayleigh scattering obtained from an atmospheric model; ratios that exceed unity are associated with aerosol extinction). The data are presented as scatter plots for a) 1979, b) 1985, c) 1986, and d) 1987. Extinction ratios greater than ~20 are aggregated at the top of the plots. The differences between the background levels for each year reflect the presence of volcanic aerosols from the eruptions of El Chichón in April 1982 and Ruiz in November 1985; the volcanic anomaly is seen to decay from 1985 through 1987 (M.P. McCormick, private communication, 1988).

support this idea. The statistical characteristics of PSC's (as described in previous sections) are also consistent with the appearance and behavior of the ozone hole. To evaluate properly the role of PSC's, and to develop a realistic model for cloud–chemistry interactions, it is necessary to understand the microphysics of the cloud particles. The polar stratospheric clouds may be composed of ice crystals condensed on a core of sulfuric acid, or may be frozen nitric acid, or may be a combination of these including condensed hydrochloric acid. Some of these possibilities are discussed below. The microphysical time constants relevant to PSC evolution can be derived from the data in Table 10.2.

10.6.2.1 Sulfuric Acid Ice Clouds

Steele et al. (1983) originally proposed that PSC's were formed on the background stratospheric sulfate particles. If these particles were supercooled droplets, their composition (i.e., the

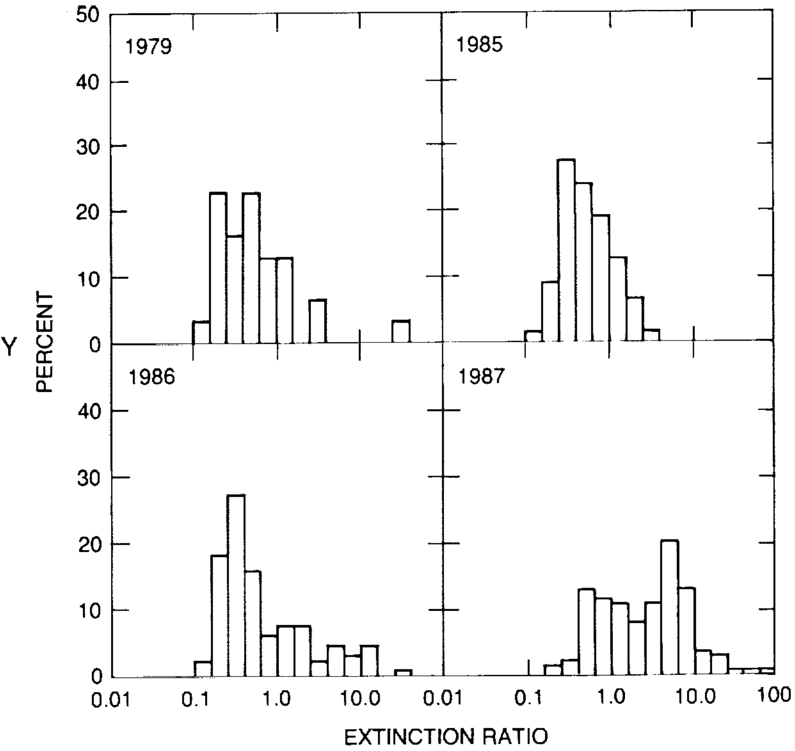

(a)

SAM II EXTINCTION RATIO FREQUENCY
SEP. 10—SEP. 20 AT 18 km

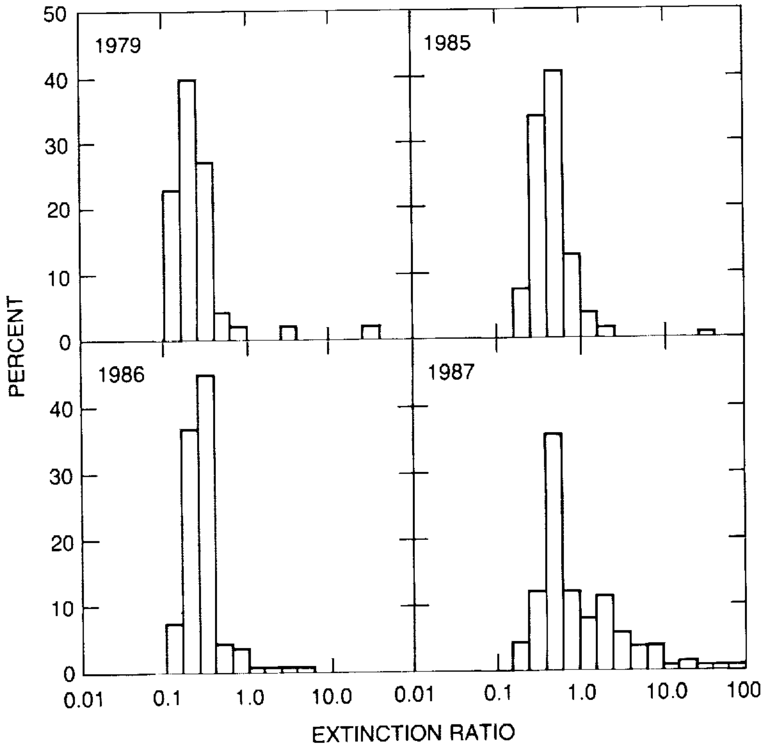

(b)

SAM II EXTINCTION RATIO FREQUENCY
SEP. 20—SEP. 30 AT 18km

Figure 10.35 Relative frequency (in percent) of observed aerosol extinction ratios at 18 km for 1979 and 1985 through 1987 (as in Figures 10.34a–d) for two specific intervals: (a) September 10 to 20 and (b) September 20 to 30 (M.P. McCormick, private communication, 1988).

weight fractions of water and sulfuric acid in solution) would maintain close equilibrium with the ambient water vapor concentration at all altitudes, because the water vapor concentration exceeds the sulfuric acid concentration by several orders of magnitude. Hence, as the environmental temperature decreased (for example), the equilibrium H_2O vapor pressure of the solution would decrease, allowing the droplets to absorb additional water and grow larger and more dilute—through the process of heteromolecular condensation (Hamill, 1975). In the later stages of growth, at even lower temperatures, the droplet would be essentially pure water (which might be frozen). At this stage, further growth could not be maintained by continuing dilution, and growth would cease until the temperature had fallen below the local frost point (of water vapor).

Steele and Hamill (1981) first delineated this aerosol growth mechanism for stratospheric aerosols. Steele et al. (1983) showed that the theoretical relationship between aerosol extinction and temperature is in reasonable agreement with the 1979 SAM–II data at the 50-mb and 100-mb pressure levels.

Although the stratospheric aerosols were assumed to be highly supercooled, logically they would eventually freeze. Then, if temperatures fell below the local frost point, water vapor could deposit on the particle surfaces to form a water ice crystal with a dilute sulfuric acid core. If a large fraction of the sulfate particles were thus activated as water ice nuclei, a high concentration of relatively small (~ 10 μm) ice particles would result. In this case, very large optical depths would occur when temperatures fell below about 185 K. On the other hand, if only a small fraction of the stratospheric aerosols were activated as ice nuclei, fewer larger ice crystals would be formed, with a lower optical depth.

Based on satellite observations, the amount of water vapor in the polar stratosphere is in the range of 3 to 5 ppmv. At a pressure level of 50 mb (about 20 km), the H_2O partial pressure is therefore about $1.5–2.5 \times 10^{-4}$ mb. The saturation vapor pressure over ice exceeds 2.5×10^{-4} mb for all temperatures greater than 188.6 K (List, 1951). Consequently, pure ice crystals would not form until the air at 50 mb had fallen below this extremely cold temperature. At 100 mb (about 14 km), pure ice crystals could not form until temperatures had dropped below about 192 K. Furthermore, if the air is desiccated, as recent observations indicate (Chapter 11), the formation of pure water ice clouds would require an even larger temperature depression. For example, if the water vapor mixing ratio were 1 ppmv, the temperature required to condense pure ice clouds at 50 mb would be 179 K, and, at 100 mb, 183.4 K.

Extremely low temperatures have been observed in the Antarctic stratosphere, particularly near the pole. However, the SAM–II instrument is restricted to make observations at latitudes below about 83°, while the coldest air masses are generally found at higher latitudes. Even so, temperatures below 190 K are frequently observed at latitudes within the SAM–II field of view (for example, see Figure 10.28). Moreover, individual air parcels within the polar vortex at lower latitudes can be exposed to colder temperatures as the air circulates around the pole and is vertically displaced.

It is possible that ice clouds form during the early part of winter and that sedimentation of the crystals transports water out of the stratosphere. The remaining air would then be drier, which is consistent with observations (Chapter 11). Sanford (1977) rejected this mechanism because the fall velocities of particles about 1 micron in radius (the particle size deduced from the optical manifestations of mother-of-pearl clouds) are too low (see Table 10.2). However, it is possible that a smaller number of larger ice crystals are nucleated from the stratospheric aerosols within the winter polar vortex, as noted above (Hamill et al., 1988), and that these particles rapidly fall to lower altitudes. Rosen et al. (1988) have suggested that the formation of such polar stratospheric cirrus clouds (Type II PSC's) is more consistent with lidar backscatter and satellite extinction measurements than is the exclusive formation of extended aerosol hazes (Type I PSC's).

10.6.2.2 Nitric Acid Ice Clouds

Recently, Toon et al. (1986) and Crutzen and Arnold (1986) independently suggested that polar stratospheric cloud particles might be formed of frozen nitric acid. Toon et al. proposed that hydrochloric acid ice might condense as well. Figure 10.36 gives the freezing point temperature of aqueous solutions of nitric acid (Pickering, 1893). Nitric acid solutions of any composition should be frozen at the normal temperatures of the lower stratosphere ($\leq$220 K), since the minimum freezing point is 229 K (corresponding to the eutectic near 70 percent weight fraction of HNO_3). Likewise, the condensation of nitric acid vapor on pre-existing surfaces should occur in the form of various HNO_3/H_2O crystalline phases.

Toon et al. pointed out that the vapor pressures of both H_2O and HNO_3 over supercooled or frozen nitric acid mixtures at normal stratospheric temperatures are much greater than the respective partial pressures of these species in ambient stratospheric air. Hence, nitric acid particles cannot form in the stratosphere for typical background conditions. Moreover, extrapolations of the vapor pressures of supercooled HNO_3/H_2O solutions indicate that such solutions are unlikely to exist even at the colder temperatures of the polar winter stratosphere.

Rough estimates of the HNO_3 and H_2O vapor pressures over HNO_3/H_2O ice crystals as a function of temperature are presented in Figures 10.37a and b and 10.38 (Clavelin and Mirabel,

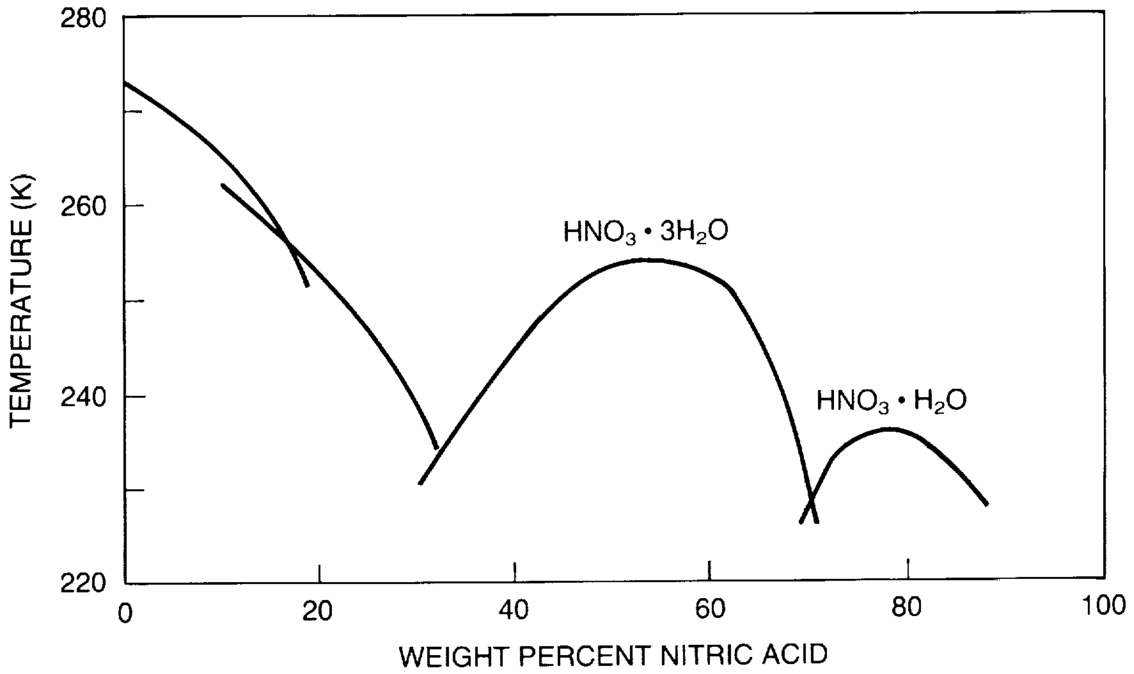

Figure 10.36 Freezing-point curves for nitric acid aqueous solutions as a function of the nitric acid weight percent of the solution at a pressure of 1 atmosphere (Pickering, 1893).

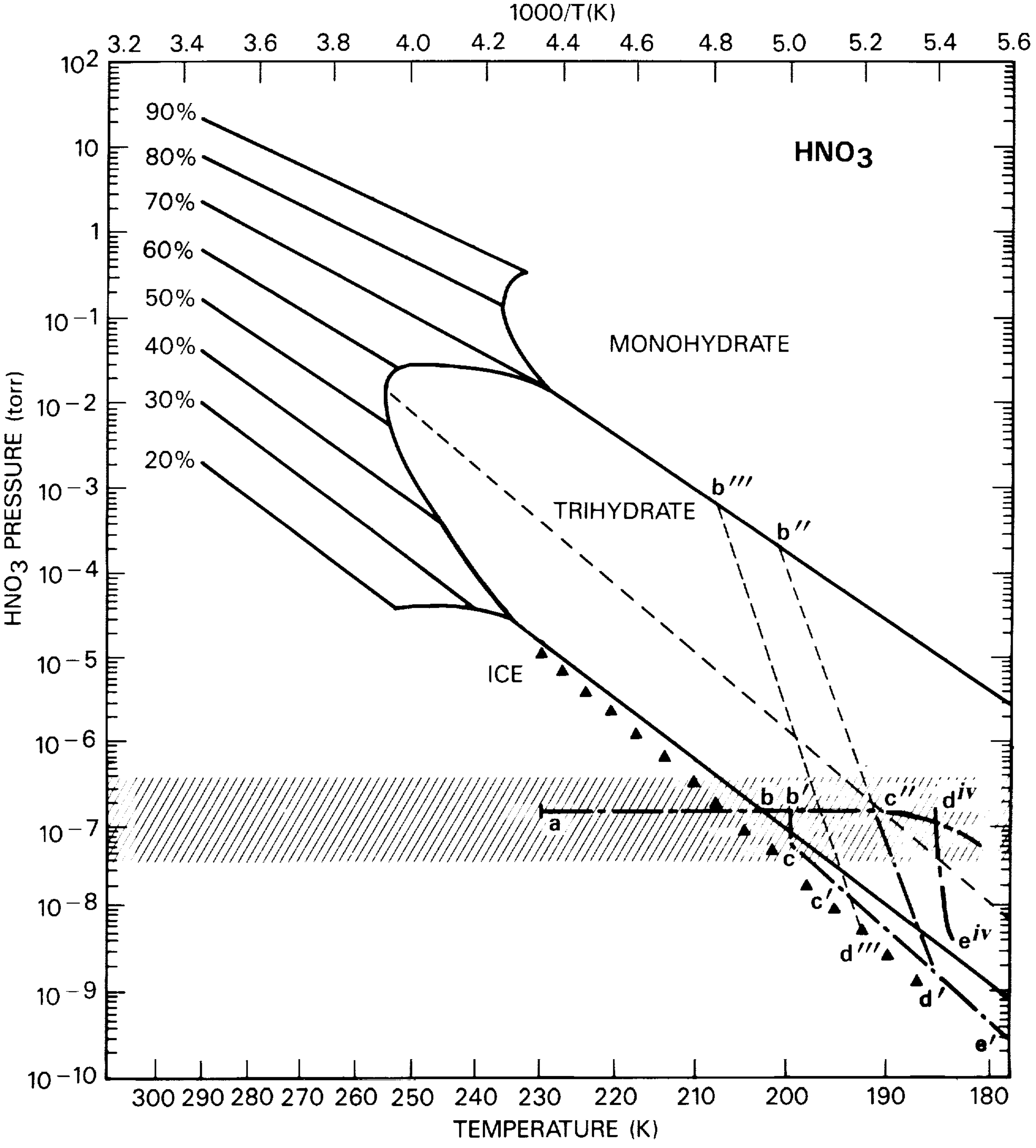

Figure 10.37a Vapor pressures of HNO_3 over aqueous solutions and ices of various compositions as a function of temperature (1000/T). The vapor pressures for the liquid-phase mixtures are based on laboratory data (see Toon et al., 1986). The vapor pressures for the solid phases have been estimated using thermodynamic arguments. Two extrapolations are shown. The solid lines originating at the quadruple points define the phase boundaries between distinct crystalline forms of HNO_3/H_2O ices, and are based on estimates of the partial molar enthalpies of HNO_3 and H_2O in each pure crystalline phase. The dashed lines correspond to the vapor pressure of trihydrate ice that is likely to condense from the vapor phase under stratospheric conditions (Hamill et al., 1988; Turco et al., 1989).

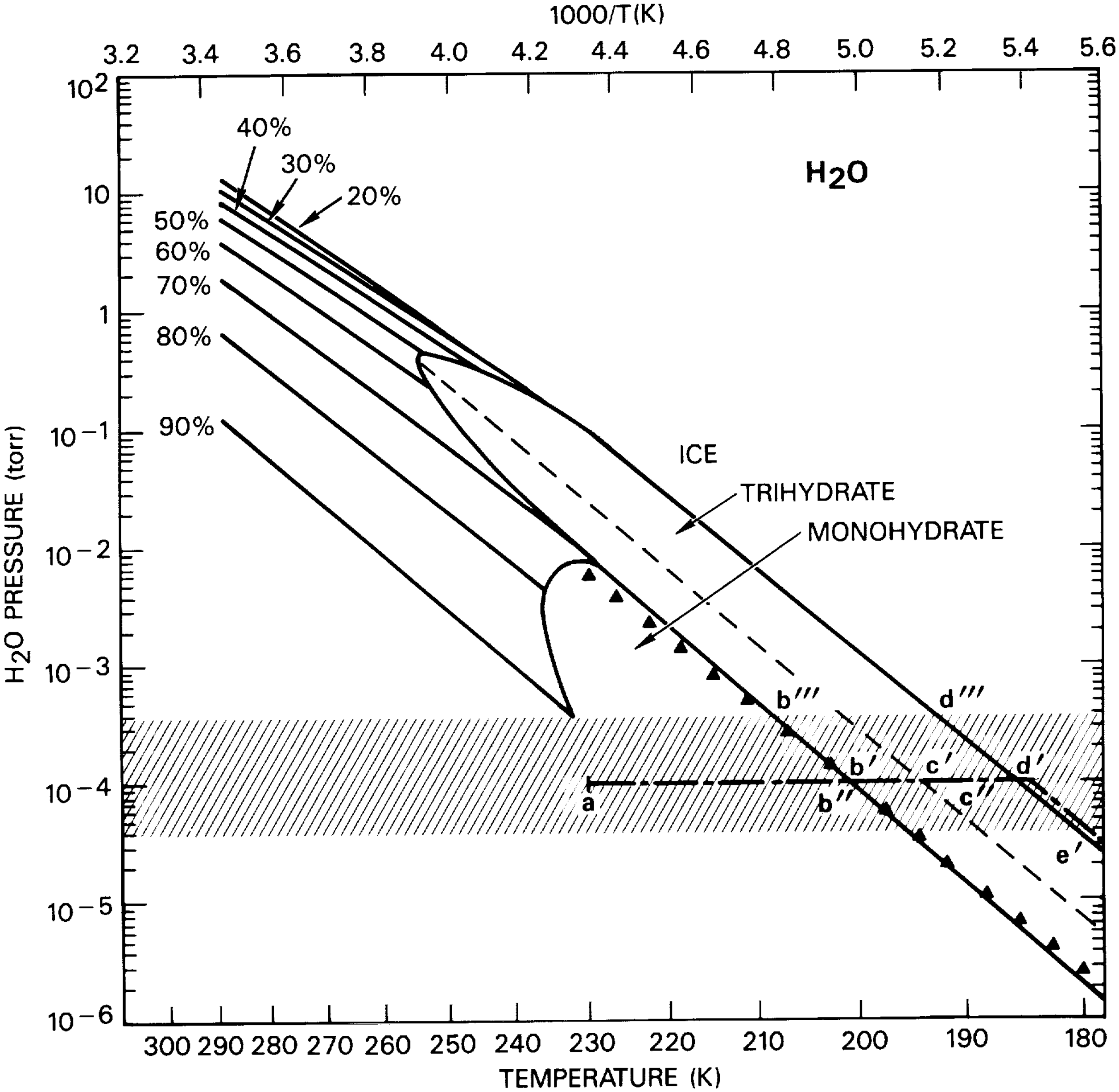

Figure 10.37b Same as Figure 10.37a, except for the H_2O vapor pressures (Hamill et al., 1988; Turco et al., 1989).

1979; Toon et al., 1986; Crutzen and Arnold, 1986; McElroy et al., 1986; Hamill et al., 1988). These vapor pressures are uncertain because measurements corresponding to the extreme conditions of the polar winter stratosphere are lacking. Representative ambient partial pressures of HNO_3 and H_2O in the lower stratosphere are indicated by the hatched bars in Figures 10.37a and b. It is apparent that the partial pressures fall below the vapor pressures of the principal hydrate ice

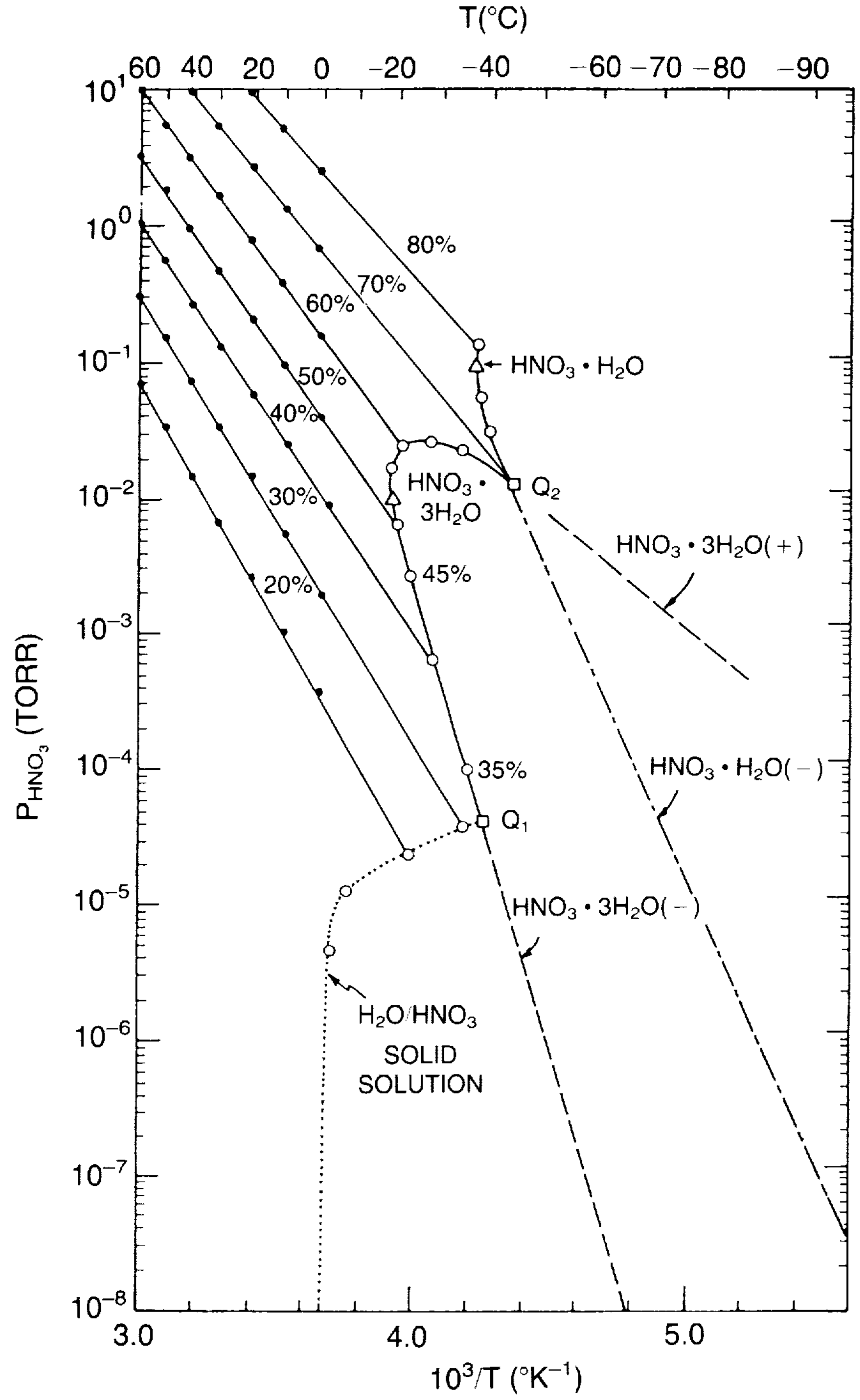

Figure 10.38 HNO_3 vapor pressures over aqueous HNO_3 solutions and solid phases. Closed circles represent HNO_3 fugacities reported by Clavelin and Mirabel (1979), and the open circles represent the freezing points of Pickering (1893) placed on the fugacity lines to define the phase transition. The liquid solution compositions are labeled by HNO_3 weight percentage. The locus of open circles defines the solid–liquid phase boundary. The dotted line denotes the phase boundary between liquid solution and solid solution. The dashed lines depict estimates of the vapor pressures over the crystalline hydrate phases. Imperfect crystal phases depleted in HNO_3 are labeled with (–); phases enriched in HNO_3 are labeled (+) (From McElroy et al., 1986, with modifications).

forms at temperatures above about 200 K. At lower temperatures, however, crystals with the composition of the trihydrate (~54 percent HNO_3 by weight) appear to be thermodynamically stable (Toon et al., 1986; Crutzen and Arnold, 1986; also, Hamill et al., 1988, provide a detailed discussion of the likely composition and morphology of the condensate). An alternative extrapolation of the hydrate vapor pressures is presented in Figure 10.38, from which McElroy et al. (1986a) concluded that crystals nearer to the composition of the monohydrate (~78 percent HNO_3 by weight) are preferred thermodynamically.

If the gas phase partial pressures of HNO_3 and H_2O both lie within the vapor pressure stability regimes for a specific hydrate (e.g., as indicated by point c in Figures 10.37a and b), then gas-phase molecules can deposit on pre-existing surfaces as crystals of that hydrate. If either of the partial pressures lies outside of its respective stability regime for that hydrate, or moves outside of the stability regime (for example, because of a change in temperature), then the hydrate is unstable and either will not form or will evaporate. It is unlikely that pure crystal hydrates will precipitate in the stratosphere, however. The expected ice forms would consist of impure crystals, amorphous ices, and solid solutions of HNO_3 in water ice (Hamill et al., 1988).

The germination of polar stratospheric clouds may involve ternary mixtures of H_2SO_4–HNO_3–H_2O. The vapor pressures and other properties of such mixtures at low temperatures are unknown. However, the properties may not be too different from those of H_2SO_4–H_2O and HNO_3–H_2O binary systems (Kiang and Hamill, 1974).

While it is not possible to deduce precisely the mechanisms by which nitric acid clouds form, it is reasonable to assume that, as the temperature of the stratosphere decreases, crystals of nitric acid ice will condense on frozen sulfuric acid particles.

These frozen HNO_3/H_2O aerosols would initially constitute a haze of micron-sized particles (Type I PSC). The ice aerosols would grow and evaporate as the temperature fluctuated around the condensation temperature. Although the composition of the solid phase is uncertain, it may consist of various impure crystals approaching the composition of nitric acid trihydrate ice (roughly 50 percent HNO_3 by weight). If it is assumed that all of the stratospheric sulfate aerosols are nucleated into nitric acid particles in this way, Type I PSC's would contain about 1 to 10 particles per cubic centimeter. Then, if all of the available nitric acid were condensed onto these particles, the average particle radius would be roughly 0.3 μm to 0.5 μm. The smaller the fraction of sulfate aerosols initially converted into nitric acid particles, the greater the average size of the haze particles in Type I PSC's. Moreover, as time progresses, the haze particle size distribution would tend to evolve, under the influence of the Kelvin vapor pressure effect, toward one with a smaller number of much larger particles (Pruppacher and Klett, 1978).

10.6.2.3 Hydrochloric Acid Ice

Toon et al. (1986) suggested that, under the environmental conditions of the polar winter stratosphere, HCl vapor might condense as ice with water vapor. Extrapolating measured vapor pressures of HCl and H_2O for liquid solutions, Toon et al. concluded that the HCl composition of the ice would be less than 20 percent. In other words, the common HCl/H_2O hydrates (dihydrate and trihydrate) could not form (McElroy et al., 1986a), and only amorphous ices or solid solutions of HCl in ice could condense. Recently, Molina et al. (1987) and Wofsy et al. (1988) measured the composition and vapor pressures of HCl solid solutions and confirmed that, under polar winter stratospheric conditions, such condensates are stable (with HCl weight fractions in the range of 1 to 5 percent). It is also expected that HCl would be absorbed into nitric acid ices.

The presence of HCl in solid solution leads to the possibility of rapid "heterogeneous" reactions involving PSC particles; studies of potentially important heterogeneous chemical processes are discussed in Chapter 11.

10.6.2.4 Ice Clouds

The discussion of water ice condensation on sulfuric acid aerosols in Section 10.6.2.1 applies as well to water ice condensation on nitric acid aerosols below the frost point of water. In this case, a few of the nitric acid crystals would grow rapidly into large ice crystals (Heymsfield, 1986; Rosen et al., 1988; Hamill et al., 1988). Heymsfield (1986) has, in fact, proposed that the PSC's should be more like cirrus clouds than activated aerosol hazes. However, considerable evidence now is available pointing to the existence of two distinct cloud morphologies (Type I and II PSC's) (also see below).

10.6.3 Radiative Properties of PSC's

10.6.3.1 PSC Lidar Backscatter and Polarization Characteristics

In Figure 10.39, a lidar return signal is shown for a PSC at 86°N observed with the NASA/Langley airborne lidar system. Although obtained in the Northern Hemisphere, the enhanced signal is similar to cloud returns measured by Iwasaka (1986) at Syowa Station, Antarctica. The

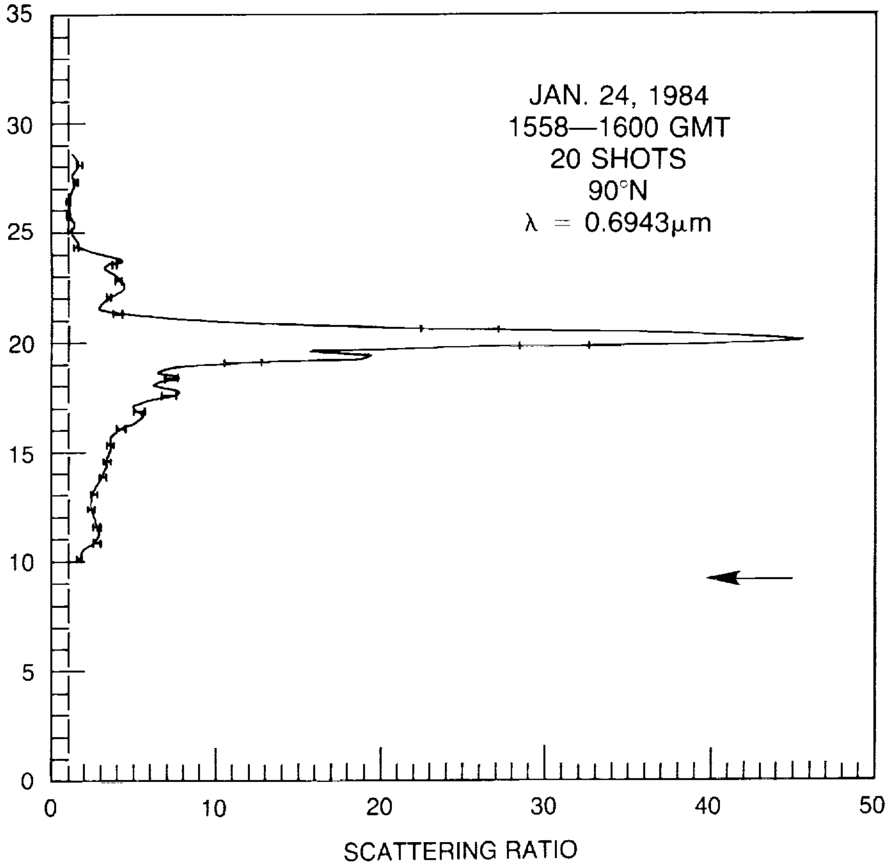

Figure 10.39 Lidar backscatter ratio for a PSC at 90°N measured with the NASA/Langley airborne lidar system (M.P. McCormick, private communication, 1987).

very large backscatter ratio is consistent with a cloud holding up to ~10 large ice crystals per cubic centimeter. On the other hand, most of the SAM–II extinction profiles are consistent with the smaller optical depths associated with nitric acid haze (although this may be due, in part, to the limited latitude range of the SAM–II observations that excludes the coldest polar regions with the greatest likelihood of very dense clouds). Hence, lidar backscatter data provide some supporting evidence for two distinct cloud types.

The depolarization of lidar signals backscattered from PSC's has also been measured in both the Arctic and Antarctic winter regions. Airborne lidar experiments were conducted during January 1984 and January 1986 at high northern latitudes by the Langley research team. The backscatter intensities and depolarization ratios were measured on both occasions (Kent et al., 1986; Poole, 1987; Poole and McCormick, 1988). Independently, Iwasaka (1986) obtained backscatter and depolarization data at Syowa Station (69°S) in the austral winter of 1983.

On January 24, 1984, lidar data were collected along two segments of a flight between Thule, Greenland, and the North Pole. The two segments corresponded to regions in which 50 mb temperatures were about 188 K and 190 K, respectively. Along the segment at the colder temperature, which approached the local frost point of water, the backscatter ratios were 10 to 15 and the depolarization ratios were 0.2 to 0.4. These values would be expected for a cloud of relatively large, irregular ice crystals. On the warmer segment (approximately 2°C above the frost point), the backscatter ratios were smaller, ~5, and the depolarization ratios were less than 0.1. These latter values are consistent with a size distribution of relatively small ice crystals. In regions that were considerably warmer than 190 K, normal stratospheric backscatter ratios in the range of 1.1 to 1.5 were observed, with little depolarization of the signal.

On the 1986 Langley lidar mission, a PSC was encountered at 60°N with local temperatures (at 50 mb) 3°–6°C above the frost point. Again, backscatter ratios showed maximum values of about 5, and the depolarization ratio was never greater than 0.05.

Poole and McCormick (1988) interpreted these observations as indicating a multistage cloud formation process involving both the aerosol haze and cirrus-like ice clouds discussed earlier. They have modeled this formation process and predicted backscatter ratios and depolarizations that are consistent with lidar measurements.

The observations by Iwasaka (1986) are compatible with such an interpretation. At Syowa Station in 1983, the backscatter ratio at altitudes of 10 km to 20 km increased from about 2 to 5 in early June to about 5 to 10 at the end of June. The depolarization ratio over this same period increased from 0.01–0.1 to 0.3–0.6. Simultaneously, the temperature of the region decreased steadily from well above the frost point at the end of May to near the frost point in early July (for an assumed water vapor concentration of 6 ppmv).

10.6.3.2 Radiative Heating of PSC's

It has been suggested that polar stratospheric clouds may cause significant heating of the Antarctic polar stratosphere in spring (e.g., Tung, 1986). Such heating could occur by three processes: 1) absorption of solar visible and near ultraviolet radiation, 2) absorption of solar near infrared radiation, and 3) net absorption of terrestrial longwave (thermal infrared) radiation. Because the expected composition of PSC's in all cases consists of materials that do not absorb visible radiation, and only weakly absorb near ultraviolet radiation, (1) will not be important.

The absorption of solar near-infrared radiation by cloud particles can occur in the near-IR H_2O and HNO_3 bands. Considering the particles to be composed of pure water (ice), and assuming PSC optical depths of 0.01 to 0.1, T. Ackerman (private communication, 1987) has estimated solar heating rates ranging from about 0.001°C to 0.01°C per day (other assumptions are 1 μm radius spherical ice particles uniformly distributed between 10 km and 20 km altitude; surface albedo of 0.5 at all solar wavelengths; solar zenith angle of 75.7°; and a McClatchey subarctic winter temperature profile). By comparison, the heating rate associated with ozone absorption of near-ultraviolet sunlight under the same conditions is roughly 0.5°C per day. The near-infrared absorption of condensed HNO_3 would contribute to the PSC heating (although the corresponding H_2O heating would have to be decreased in accordance with the reduced water-mass fraction of the particles). It is doubtful that cloud particles of mixed composition would produce substantially more heating than pure ice particles. Accordingly, the near-infrared heating rate associated with PSC's should amount only to a few percent of the ozone solar near ultraviolet heating rate. Vapor phase H_2O and HNO_3 also absorb solar radiation; hence, the differential heating in the presence of PSC's also depends on the fraction of these materials that is condensed.

Pollack and McKay (1985) investigated the absorption and emission of longwave radiation by PSC's, and the effects of PSC's on the net heating rates in the polar winter stratosphere. The local net heating rate in the stratosphere is determined mainly by the balance between absorption of upwelling terrestrial radiation, and cloud emission of thermal radiation. The net heating rate depends on the underlying surface temperature, on the tropospheric temperature profile, on the presence and characteristics of cirrus clouds, and on the properties of the PSC's (particle composition, size distribution, and height distribution, and cloud optical depth). For nearly all of the cases considered by Pollack and McKay (1985)—deemed by these authors to represent a comprehensive range of possibilities—the PSC's typically caused a small net longwave cooling of the stratosphere, by up to 1°C per day. In a few cases, warming rates of ~0.07°C per day were found.

On the basis of these studies, it may tentatively be concluded that PSC's are not responsible for significant heating of the polar stratosphere in late winter or early spring, during the time when the ozone hole is forming. Ozone solar absorption provides the primary heating under these conditions.

10.7 CONCLUSIONS

The previous discussion has considered the role of stratospheric aerosols in the remote sensing of the global ozone distribution and long-term trends, and in the Antarctic ozone hole phenomenon. On the basis of the extensive information available on aerosols in the upper atmosphere, the following major conclusions can be drawn.

1. No significant trends that might affect ozone observations can be detected in existing measurements of the global background stratospheric aerosol layer. Likewise, polar stratospheric clouds do not appear to have changed substantially over the early period of their observation (1979 to 1984). However, in 1987 the Antarctic PSC's persisted several weeks longer than usual—well into October—with more sightings of very dense clouds than in previous years. It should be noted that the data records for stratospheric aerosols and PSC's are of a short enough duration that small trends over longer timespans cannot be precluded.

2. The stratospheric aerosol loading is occasionally greatly enhanced by a major volcanic eruption. Such eruptions (for example, El Chichón in 1982), even in remote locations, can perturb the stratosphere worldwide, including the polar regions in both hemispheres, for periods of several years or more. During these volcanic periods, the radiative properties of the atmosphere can be anomalous, complicating the interpretation of remote sensing data.

3. New intercomparisons between SAGE and SME satellite observations indicate that significant aerosol loadings (with respect to remote ozone-sounding measurements) rarely occur above about 35 km—that is, within the altitude region where the accuracy and information content of the SBUV ozone-profiling system is greatest. Hence, background aerosols are not likely to be responsible for ozone errors of more than a few percent in the SBUV layers 6 to 9 (~25 km to 50 km); nor can aerosols explain any long-term trend in the SBUV data. Even so, volcanic aerosols may cause sizeable errors in SBUV ozone profile measurements during relatively short periods following major eruptions. There is little evidence to support the idea of persistent widespread mesospheric aerosol layers (except at the summer mesopause) that might significantly interfere with remote ozone observations.

4. The impact of volcanic aerosols on ground-based Umkehr measurements is greatest in the upper Umkehr layers (7 to 9, above about 30 km) and the lower layers (1 to 3, below about 20 km). The Umkehr data may be corrected for aerosol effects using lidar and satellite data on the vertical and horizontal distributions of particles. Nevertheless, the residual ozone errors in postvolcanic years may exceed several percent at the most sensitive levels. Accordingly, in ozone trend analysis, very careful handling, or neglect, of Umkehr data collected during volcanically disturbed periods is recommended.

5. Direct observations of polar stratospheric cloud properties, together with independent measurements of related physical and chemical parameters, strongly imply that PSC's are intimately involved in the formation of the Antarctic ozone hole. This conclusion is based on the following facts:

- PSC's appear in the proper temporal sequence and spatial configuration to be closely associated with the development of the ozone hole.
- Thermodynamic data suggest that PSC's may be formed through the cocondensation of H_2O, HNO_3, and HCl vapors; cloud particle sedimentation is also consistent with the observed dehydration and denitrification of the winter polar vortex (see Chapter 11).
- Measured PSC optical and morphological properties are compatible with the PSC composition and microphysics inferred above. PSC's are also known to occur in the northern polar winter stratosphere. Accordingly, effects of PSC formation on ozone concentration could be studied in the Northern Hemisphere, as has been done in the Southern Hemisphere. Although much has been learned in the last few years about PSC's and their relation to the ozone hole, considerable uncertainty remains concerning many of the fundamental physical and chemical processes.

Recommendations

A number of logical recommendations follow from the present assessment.

1. Continued monitoring of the global stratospheric aerosol layer is needed, preferably using satelliteborne sensors. Such monitoring not only provides basic scientific information on the

properties and physicochemical effects of atmospheric particles, it also establishes a data base that is essential to remote-sensing system design and operation for the detection of ozone and other terrestrial and atmospheric parameters.

2. Regular lidar aerosol measurements should be carried out at selected Umkehr ozone observation sites to obtain a data set that can be used to correct Umkehr data for variable aerosol properties; such correlative data would greatly improve the precision of the ground-based segment of the long-term ozone-monitoring network.

3. The effects of aerosols on remote-sensing systems should be more carefully accounted for in computational inversion schemes; appropriate algorithms and data requirements should be fully investigated, and, where necessary, more sophisticated approaches implemented.

4. Further research should be pursued to obtain a more complete understanding of the physical chemistry, surface reactions, microphysics, and occurrence of polar stratospheric clouds.

Discussion

The advent of satelliteborne sensors has led to a global description of stratospheric aerosols. The recorded morphology and climatology of these trace atmospheric constituents have become more comprehensive and precise. Through extensive space- and ground-based observations, the evolution of volcanic eruption clouds like that of El Chichón has been characterized in considerable detail.

The degradation by aerosols of remote sensing for ozone (and other parameters) is now well understood. For example, the present analysis confirms potential problems with Umkehr ozone observations during periods that are influenced by volcanic eruptions. Nevertheless, the overall accuracy of Umkehr data for studying ozone climatology and long-term variations would not be compromised by occasional volcanic eruptions when proper account is taken of anomalous aerosol effects. The SBUV sensors are, in general, less susceptible to aerosol effects than Umkehr sensors; studies of global ozone morphology with the SBUV system should not be greatly affected by aerosol-generated errors. Even so, in times and in regions of volcanic disturbance, the SBUV data must be interpreted with care.

Most exciting has been the recent linkage of polar stratospheric clouds to the formation of the Antarctic ozone hole. Scientific analysis indicates that nitric acid and water vapors can condense in the winter polar stratosphere to form nitric acid ice clouds. The resulting denitrification of the stratospheric air is in all likelihood a crucial aspect of the complex chemical process that leads to the formation of the ozone hole.

56-45
53443
p. 85

CHAPTER 11

N92-15463

Observations and Theories Related to Antarctic Ozone Changes

Panel Members

D. Hartmann and R. T. Watson, Co-Chairs
R. A. Cox UN 078125
C. Kolb
J. Mahlman
M. McElroy
A. Plumb
V. Ramanathan
M. Schoeberl — NC 999967
S. Solomon — NJ 920944
R. Stolarski — NC 999967
N. D. Sze
A. Tuck — NJ 920944

PRECEDING PAGE BLANK NOT FILMED

Chapter 11

Observations and Theories Related to Antarctic Ozone Changes

Contents

11.1 INTRODUCTION 669

11.2 OBSERVATIONS 669

- 11.2.1 Ozone Climatology and Trends 669
  - 11.2.1.1 Total Ozone Changes 670
  - 11.2.1.2 Altitude Dependence of Changes in Ozone 685
  - 11.2.1.3 Summary of Ozone Observations 691
- 11.2.2 Morphology of Polar Stratospheric Clouds 692
- 11.2.3 Antarctic Temperature Trends 695
  - 11.2.3.1 Introduction 695
  - 11.2.3.2 Data Intercomparisons 695
  - 11.2.3.3 Rawinsonde Analyses 699
  - 11.2.3.4 Analyzed Fields 704
  - 11.2.3.5 Conclusion 704

11.3 TRANSPORT THEORIES FOR THE ANTARCTIC OZONE HOLE 704

- 11.3.1 Basic Dynamical Concepts and Ozone Transport 704
- 11.3.2 Transport Theories for the Ozone Hole 710
- 11.3.3 Evidence For and Against Transport Theories for the Ozone Hole 713
  - 11.3.3.1 Evidence for a Climate Drift in the Southern Stratosphere 713
  - 11.3.3.2 Evidence for Upward Motion at High Latitudes in Spring 721
- 11.3.4 Summary 724

11.4 CHEMICAL THEORIES AND OBSERVATIONS 725

- 11.4.1 Chemical Theories 725
  - 11.4.1.1 Homogeneous Reactions 725
  - 11.4.1.2 Character and Role of Polar Stratospheric Clouds 729
  - 11.4.1.3 Heterogeneous Reactions 730
  - 11.4.1.4 Summary 734
- 11.4.2 Observations Relevant to Testing the Chemical Theories 734
  - 11.4.2.1 Observational Data Base 734
  - 11.4.2.2 Comparison of Theory and Observations 735
  - 11.4.2.3 Observations of Halogen Species 735
  - 11.4.2.4 Observations of Nitrogen Species 740

11.5 CAN WE EXPLAIN THE OBSERVED SPRINGTIME OZONE TREND OVER ANTARCTICA IN THE LAST 20 YEARS? 743

PRECEDING PAGE BLANK NOT FILMED

PAGE 666 INTENTIONALLY BLANK

11.6 WHAT ARE THE IMPLICATIONS FOR THE GLOBAL EARTH'S SYSTEM OF THE OZONE CHANGES OBSERVED OVER ANTARCTICA? 744

11.7 QUESTIONS FOR THE FUTURE 745

11.8 SUMMARY 746

- 11.8.1 Ozone Observations 746
- 11.8.2 Polar Stratospheric Cloud Observations 747
- 11.8.3 Temperature Observations 747
- 11.8.4 Transport Theories for the Antarctic Ozone Hole 748
- 11.8.5 Chemical Theories and Observations for the Antarctic Ozone Hole 748

11.1 INTRODUCTION

In 1985, there was a report (Farman et al., 1985) of a large, sudden, and unanticipated decrease in the abundance of springtime Antarctic ozone over the last decade. By 1987, ozone decreases of more than 50 percent in the total column, and 95 percent locally between 15 and 20 km, had been observed. A change of this magnitude was not predicted by any of the photochemical models. The scientific community quickly rose to the challenge of explaining this remarkable discovery; theoreticians soon developed a series of chemical and dynamical hypotheses to explain the ozone loss. Unfortunately, there were inadequate observational data to differentiate among the different theories. Consequently, field measurement campaigns were quickly organized to determine the chemical composition and physical structure of the springtime stratosphere over Antarctica and test the theories. Three basic theories were proposed to explain the springtime ozone hole:

- The ozone hole is caused by the increasing atmospheric loading of manmade chemicals containing chlorine (chlorofluorocarbons [CFC's]) and bromine (halons). These chemicals efficiently destroy ozone in the lower stratosphere in the Antarctic because of the special geophysical conditions—of an isolated air mass (polar vortex) with very cold temperatures—that exist there.

- The circulation of the atmosphere in spring has changed from being predominantly downward over Antarctica to upward. This would mean that ozone-poor air from the troposphere—instead of ozone-rich air from the upper stratosphere—would be transported into the lower Antarctic stratosphere.

- The abundance of the oxides of nitrogen in the lower Antarctic stratosphere is periodically enhanced by solar activity. Nitrogen oxides are produced in the upper mesosphere and thermosphere and then transported downward into the lower stratosphere in Antarctica, resulting in the chemical destruction of ozone.

This chapter discusses the climatology and trends of ozone, temperature, and polar stratospheric clouds; the transport and chemical theories for the Antarctic ozone hole; and the observational evidence to test the different theories.

11.2 OBSERVATIONS

11.2.1 Ozone Climatology and Trends

Until recently, attention has focused primarily on the Antarctic springtime variations in total ozone; however, many questions have arisen concerning the overall seasonal and year-to-year variations throughout the Southern Hemisphere. October is the month originally emphasized by Farman et al. (1985) because it is the month of most dramatic effect. This section will discuss the spatial and temporal extent of the changes in both the total column content and the vertical distribution of ozone over and around Antarctica. Ozone changes from year to year, and within a single year, are addressed. The Total Ozone Mapping Spectrometer (TOMS) data shown in this chapter have not been corrected for the drift against the Dobson network, which has been discussed in great detail in earlier chapters. The drift of TOMS data with respect to the Dobson network was reported to be approximately 0.4 percent per year, which corresponds to a total drift of about 3.6 percent from launch in late 1978 to the present.

Consequently, TOMS ozone changes in excess of this can be considered real and not an artifact of the data analysis procedures. Most of the ozone changes discussed in this chapter are significantly greater than the uncertainty in the TOMS calibration, but in identifying the spatial and seasonal extent of the ozone hole phenomenon, it is important to appreciate the accuracy and precision of the TOMS data. Whenever ozone changes are quantitatively discussed in this chapter, an allowance of 10 to 15 Dobson Units (DU) has been made for the TOMS–Dobson network bias, even though the data in the figures have not been corrected.

11.2.1.1 Total Ozone Changes

A significant change in the springtime total ozone content over the Antarctic was first reported by the British Antarctic Survey using the Dobson station data at Halley Bay (76°S, 27°W), with a smaller change seen at the Argentine Islands (65°S, 64°W) (Farman et al., 1985). Figure 11.1 shows the October mean measurements of total ozone from Halley Bay from 1956 through 1987 and the October means of satellite data from satellite overpasses of the Halley Bay station. The 1970 through 1972 satellite data are from the BUV experiment aboard the Nimbus–4 satellite (see, e.g., Hilsenrath and Schlesinger, 1981, and references therein). From 1979 through 1986, October mean data over Halley Bay from the SBUV instrument aboard Nimbus–7 are shown (Stolarski et al., 1986). It is clear from both the ground-based and satellite data shown in Figure 11.1 that the abundance of ozone dropped rapidly after the late 1970's.

Whether the abundance of ozone was already decreasing during the late 1960's and throughout the 1970's, or the decrease started abruptly at the end of the 1970's, is a critical question.

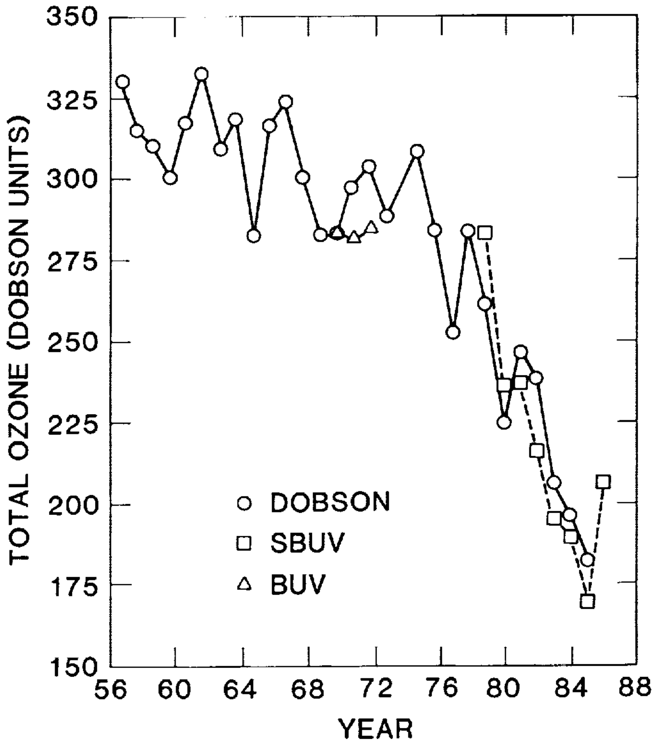

Figure 11.1. October monthly mean total ozone measurements over Halley Bay. Circles are Dobson measurements (Farman et al., 1986). Triangles are Nimbus–4 BUV measurements from 1970 to 1972 and boxes are Nimbus–7 TOMS measurements from 1979 to 1986 (Stolarski et al., 1988).

Inspection of the Halley Bay data tends to suggest that the abundance of ozone was somewhat lower during the 1970's, compared to the late 1950's and 1960's. However, the Halley Bay satellite overpass data indicate little change in total ozone between 1970–1972 and 1979; Table 11.1 shows that there was no significant change in zonal mean ozone from 70°S–80°S from the early 1970's—i.e., 1970–1972, to 1979. Figure 11.2 shows the seasonal deviations in total column ozone from the Argentine Islands, Syowa (69°S, 40°E), Halley Bay, and the South Pole (90°S)

Table 11.1 Zonal mean, minimum, and maximum ozone values for the month of October each year for the 70°S–80°S latitude zone from Nimbus–4 BUV (1970–1972) and from Nimbus–7 SBUV (1979–1984).

Year	Minimum	Mean	Maximum
1970	240	306	484
1971	249	334	482
1972	237	337	539
1979	235	333	515
1980	212	270	467
1981	206	266	422
1982	186	283	494
1983	166	245	479
1984	162	240	446

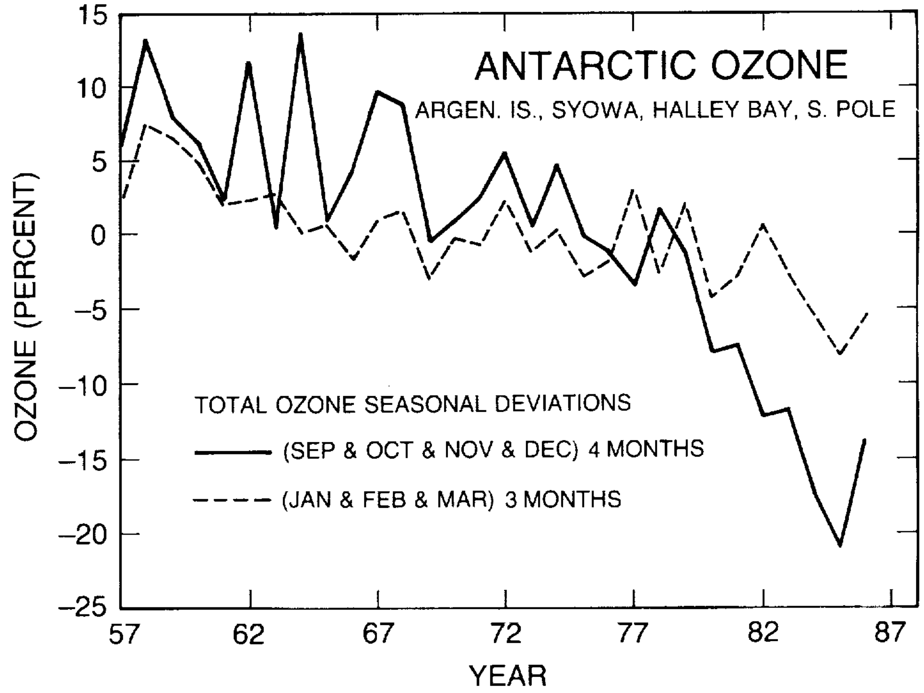

Figure 11.2. Deviation of total ozone from seasonal mean over Argentine Islands, Syowa, Halley Bay, and South Pole stations from 1957 through 1986. Solid line is for spring Sept.–Dec.); dashed line is summer–early fall (Jan.–Mar.) *(Proc. Quadr. Ozone Symp.,* in press).

from 1957 to 1986 for the periods September to December (spring) and January to March (summer). The data appear to indicate a springtime decrease starting in the mid-1970's, with little if any decrease in summertime ozone. Given the high level of interannual variability in Antarctic ozone, it is difficult to draw strong quantitative conclusions about the magnitude of ozone decreases during the 1970's.

Figure 11.3 shows October monthly mean maps for total column ozone for each year from 1979 to 1986; Figures 11.4a and 11.4b show October monthly mean maps for total column ozone for odd and even years, respectively, from 1979 to 1987; Figures 11.5a and 11.5b show September monthly mean maps for total column ozone for odd and even years, respectively, from 1979 to 1987, from the TOMS instrument. The maps are polar orthographic projections with the South Pole at the center and the Equator at the outside edge. The satellite data not only confirm the decrease reported from groundstation data, but demonstrate that the phenomenon is of large regional scale, at least the size of the Antarctic continent. These maps clearly show that the abundance of ozone in 1987 is the lowest since satellite measurements began, and that there has been a decrease of approximately 150 DU in the October mean values of total ozone, and of approximately 100 DU in September's within the region of the ozone minimum that is approximately coincident with the Antarctic continent. They also show that the maximum values of the

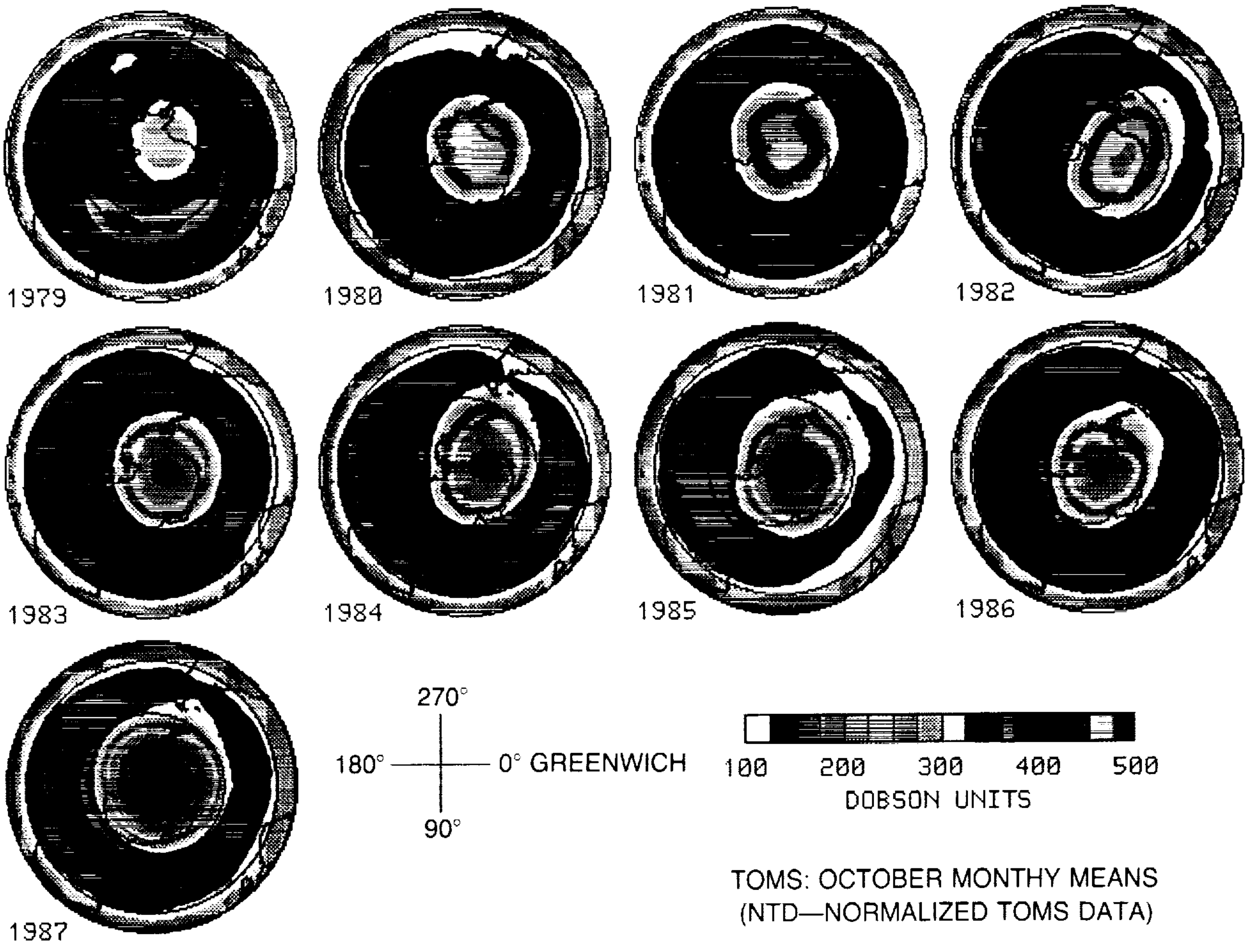

Figure 11.3. TOMS maps of Southern Hemisphere, total ozone for Octobers from 1979 through 1987. Maps are polar orthographic projections with Equator at outside and South Pole at center.

ORIGINAL PAGE
COLOR PHOTOGRAPH

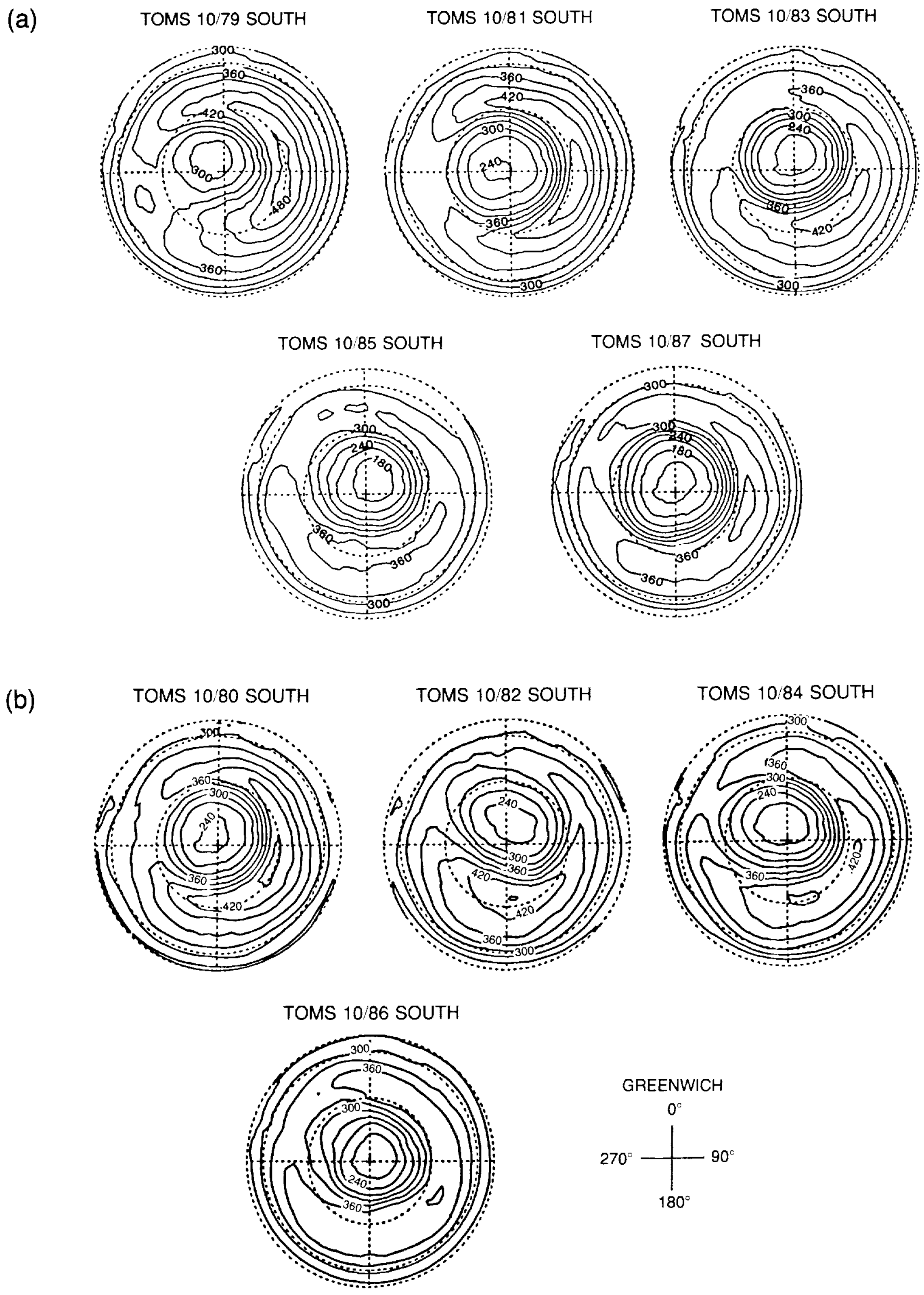
(a)
TOMS 10/79 SOUTH
TOMS 10/81 SOUTH
TOMS 10/83 SOUTH
TOMS 10/85 SOUTH
TOMS 10/87 SOUTH
(b)
TOMS 10/80 SOUTH
TOMS 10/82 SOUTH
TOMS 10/84 SOUTH
TOMS 10/86 SOUTH
GREENWICH
0°
270°
90°
180°

Figure 11.4. Polar orthographic maps of TOMS October mean Southern Hemisphere total ozone for (a) odd years and (b) even years.

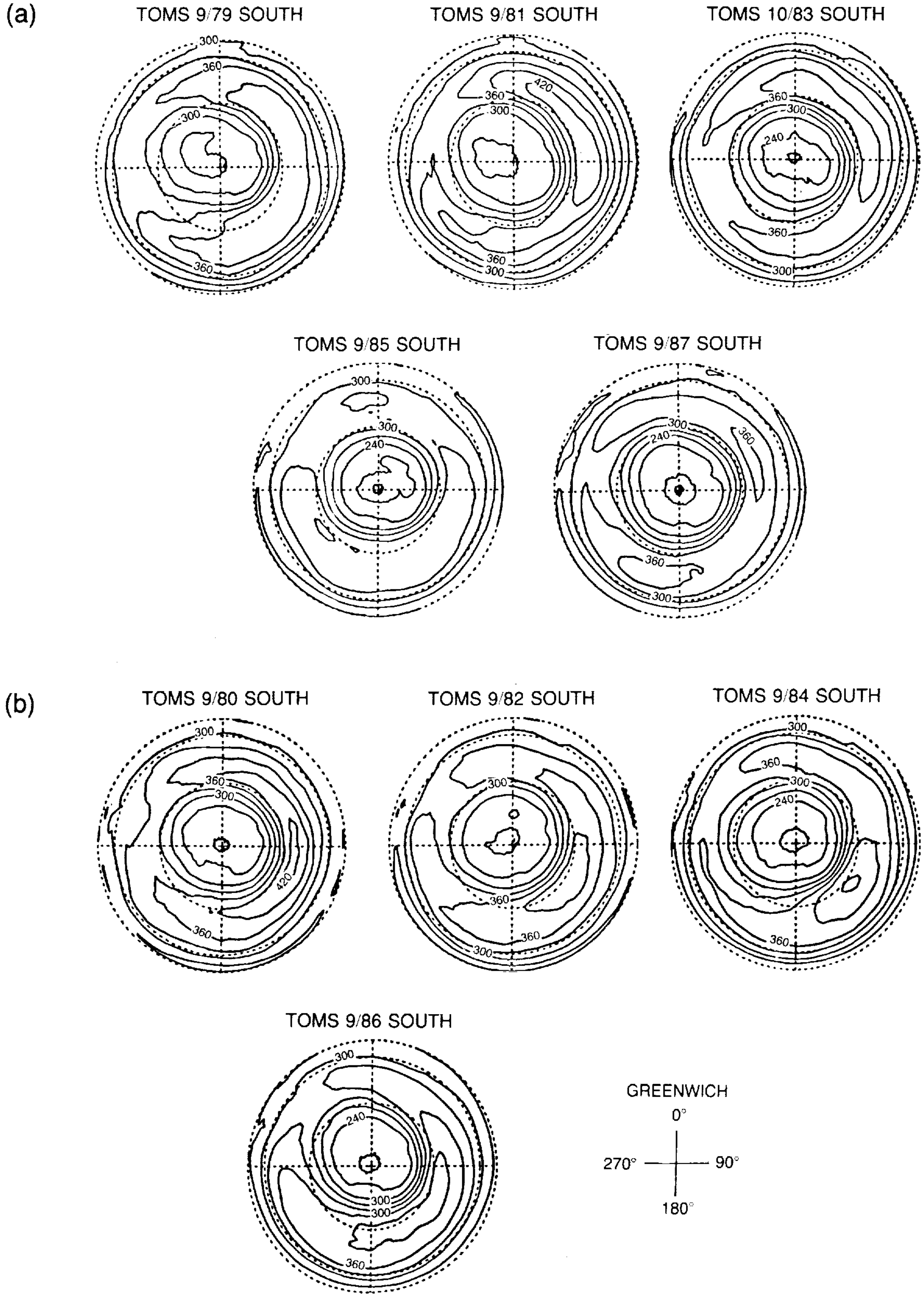
(a)
TOMS 9/79 SOUTH
TOMS 9/81 SOUTH
TOMS 10/83 SOUTH
TOMS 9/85 SOUTH
TOMS 9/87 SOUTH
(b)
TOMS 9/80 SOUTH
TOMS 9/82 SOUTH
TOMS 9/84 SOUTH
TOMS 9/86 SOUTH
GREENWICH
0°
270°
90°
180°
240
300
360
420

Figure 11.5. Polar orthographic maps of TOMS September mean Southern Hemisphere total ozone for (a) odd years and (b) even years.

September and October mean total ozone in the circumpolar ring at about 55°S–60°S have decreased by about 75–100 DU. Thus, the decrease in the maximum is nearly as large as the decrease in the minimum region in absolute DU, but is less than half that in the minimum region in percent (this is shown in greater detail in later figures). Note also, in Figures 11.3, 11.4, and 11.5, that the position of the maximum in the circumpolar ring varies by about 90 degrees in longitude, tending to rotate from about 90°E in 1979 to about 180°E in 1985 and 1986, possibly returning to about 135°E in 1987. This, coupled with the lack of stations in this region, makes it difficult to confirm the reported changes from ground-based Dobson measurements. The only station available for comparison is at MacQuarie Island, Australia, which shows little or no trend (Bojkov, 1986a). This seems to be consistent with the satellite data that indicate that MacQuarie Island is on the edge of the maximum region, which has rotated toward the station while decreasing in magnitude.

Figures 11.6, 11.7, and 11.8 (Krueger et al., 1988) show the daily zonal mean values for total ozone from July 29 through October 7 for 60°S, 70°S, and 80°S, respectively, for the years from 1984 to 1987, with 1979 as a reference year. Table 11.2 shows the monthly zonal mean values for total ozone from August through November from 1978 to 1987 for latitude belts 39°–41°S, 49°–51°S, 59°–61°S, 69°–71°S, and 79°–81°S. The ozone levels in 1987 were between 100 and 150 DU lower than in 1979 at all latitudes south of 70 degrees, and between 75 and 100 DU lower at 60°S. These changes are far in excess of the uncertainty in the TOMS calibration, which, as stated earlier, amounts to about 10–15 DU.

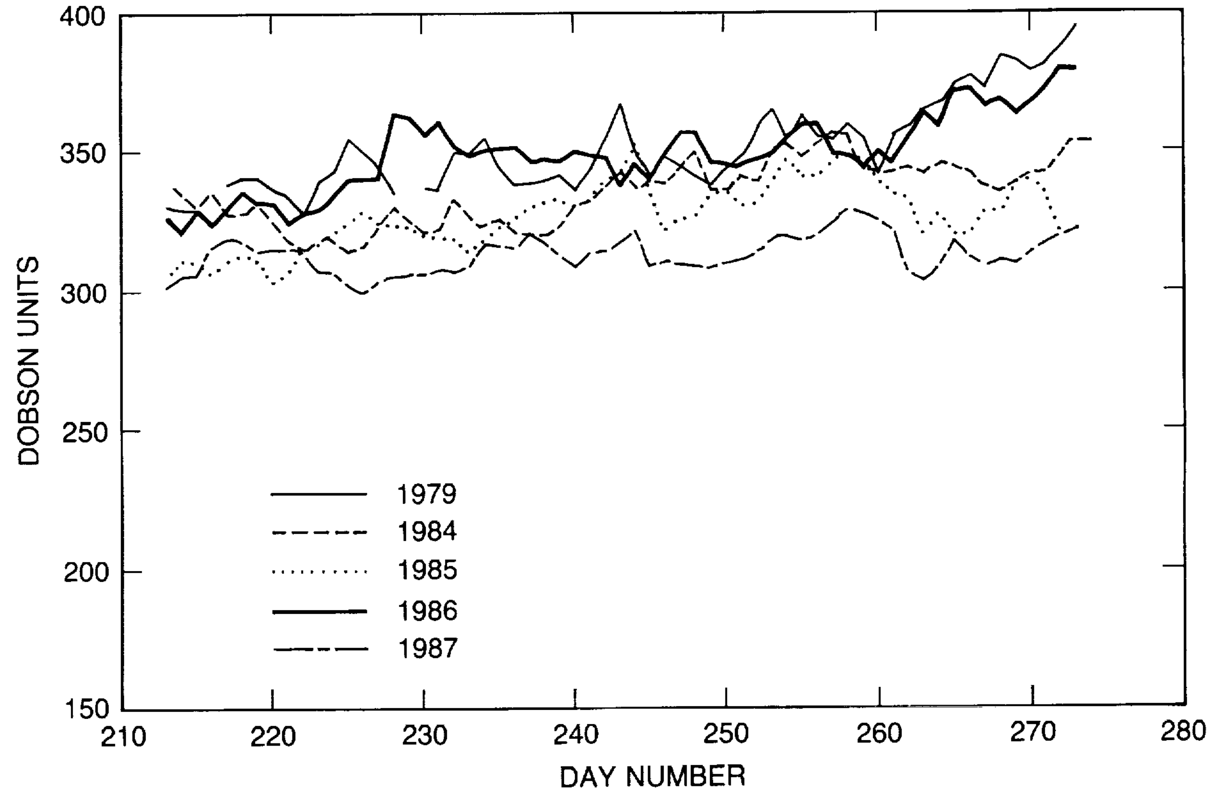

Figure 11.6. Daily zonal mean TOMS total column ozone for latitude band 60°S ±1° from day 210 to day 280, yearly from 1984 to 1987, with 1979 as reference year, using normalized TOMS data (NTD).

Table 11.2 TOMS Total Ozone Monthly Zonal Average

Degrees South Latitude	1978	1979	1980	1981	1982	1983	1984	1985	1986	1987
August										
39–41	–	362	335	354	337	347	354	317	343	323
49–51	–	361	362	362	352	343	359	328	358	326
59–61	–	344	353	339	329	331	323	315	333	301
69–71	–	301	301	304	283	290	265	263	271	249
79–81	–	–	–	–	–	–	–	–	–	–
September										
39–41	–	368	343	363	345	359	364	328	348	338
49–51	–	381	375	395	360	377	370	338	365	348
59–61	–	365	368	371	348	354	341	328	347	306
69–71	–	307	287	296	276	269	261	249	265	216
79–81	–	280	261	274	250	238	227	217	228	196
October										
39–41	–	367	342	362	349	350	349	329	348	339
49–51	–	401	376	397	373	376	375	343	370	358
59–61	–	421	403	401	366	380	365	329	358	326
69–71	–	378	321	307	324	300	290	258	288	215
79–81	–	319	255	255	270	224	225	192	212	157
November										
39–41	336	349	325	337	330	328	326	306	316	324
49–51	371	380	362	362	359	349	356	330	345	342
59–61	397	403	388	390	373	371	376	342	356	333
69–71	397	385	359	369	345	359	347	307	345	248
79–81	379	357	326	323	289	329	296	260	328	195

Careful examination of Figures 11.6–11.8 suggests that the abundance of ozone at the end of the polar night decreased from 1979 to 1987. From Figure 11.7, it appears that the zonal mean abundance of ozone at 70°S at the beginning of August decreased by about 40 to 50 DU. A key question is whether this indicates removal of ozone during the polar night, or whether ozone decreased throughout the year. Figures 11.9, 11.10, and 11.11 show zonal mean total ozone at 60°S, 70°S, and 80°S from 1979 to 1987 for all months of the year. These figures indicate that while the decrease in ozone is largest in the Antarctic spring, ozone decreased by about 40 to 50 DU at each of these latitudes throughout the year. Figures 11.12 and 11.13 (Krueger, private communication) show the October and January monthly mean values of total ozone, respectively, for 1987, the average of 1979 to 1982, and the differences between them. It is clear that at all latitudes, but especially south of about 50°S, total ozone is lower in 1987 than it was between 1979 and 1982 during both October and January.

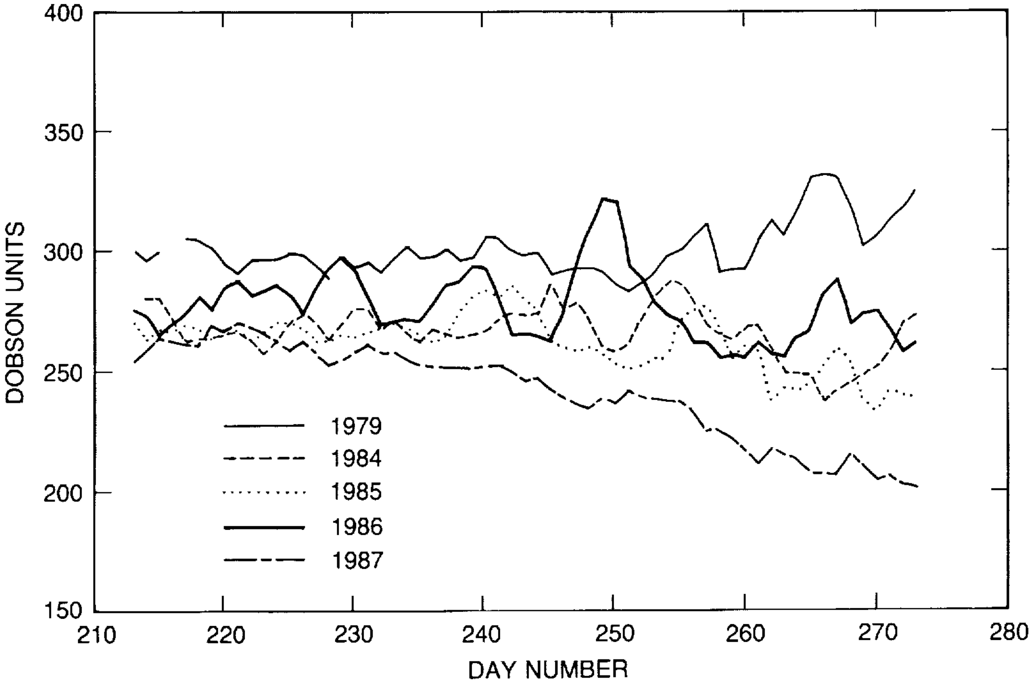

Figure 11.7. Daily zonal mean TOMS total column ozone for latitude band 70°S ±1° from day 210 to day 280, yearly from 1984 to 1987, with 1979 as reference year, using normalized TOMS data (NTD).

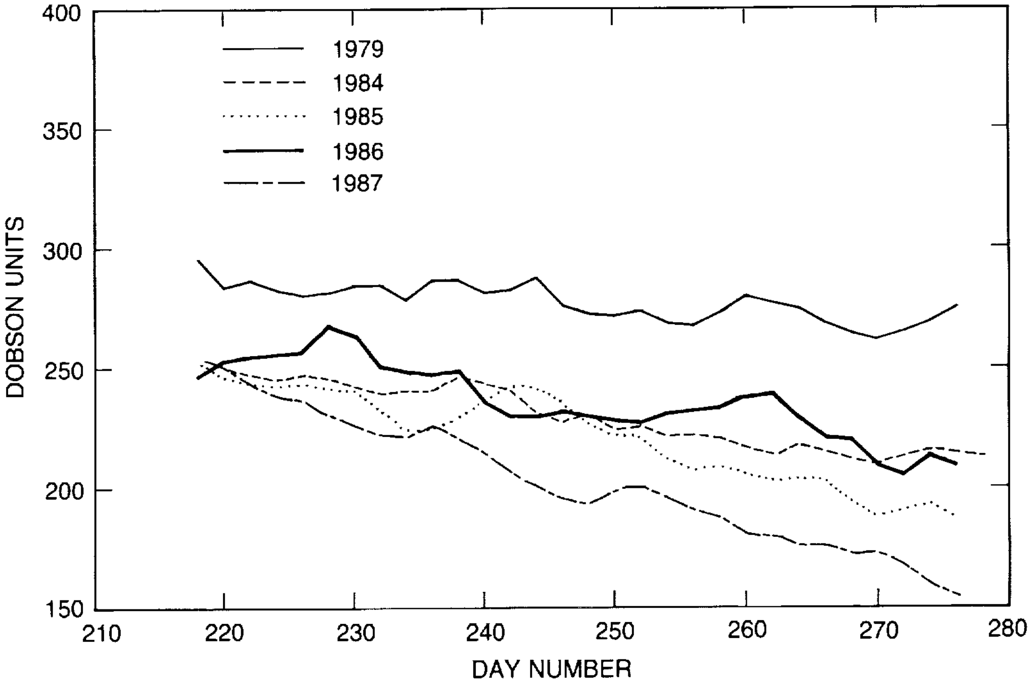

Figure 11.8. Daily zonal mean TOMS total column ozone for latitude band 80°S ±1° from day 210 to day 280, yearly from 1984 to 1987, with 1979 as reference year, using normalized TOMS data (NTD).

Figures 11.12 and 11.13 show September and October mean total ozone as a function of latitude from 1979 to 1987 and clearly demonstrate that ozone decreased in 1987 to a value clearly less than other years at all latitudes south of about 50°S during these months. Figures 11.14 and 11.16 show that the area weighted mean of the total ozone from 44°S to the South Pole has decreased by about 40 to 50 DU over the last 9 years. A similar result is obtained upon examination of total ozone data from 30°S to 70°S. As has already been noted, the TOMS data indicate that within a given year, total ozone is rising during September in the circumpolar maximum region near 60°S in such a way that the area weighted mean of the total ozone remains approximately constant within a given year over the area from 45°S to the South Pole (Schoeberl and Stolarski, 1988), as shown in Figures 11.14 and 11.15. The significance of this observation has been disputed because of the poorly known variations of the transport of ozone from the region below 45°S latitude. In addition, it should be noted that the area weighted mean value of ozone did not remain constant during 1987. Figure 11.16 shows that ozone has decreased between 1986–1987 and 1979–1980 throughout the year and from the South Pole to about 50–60°S.

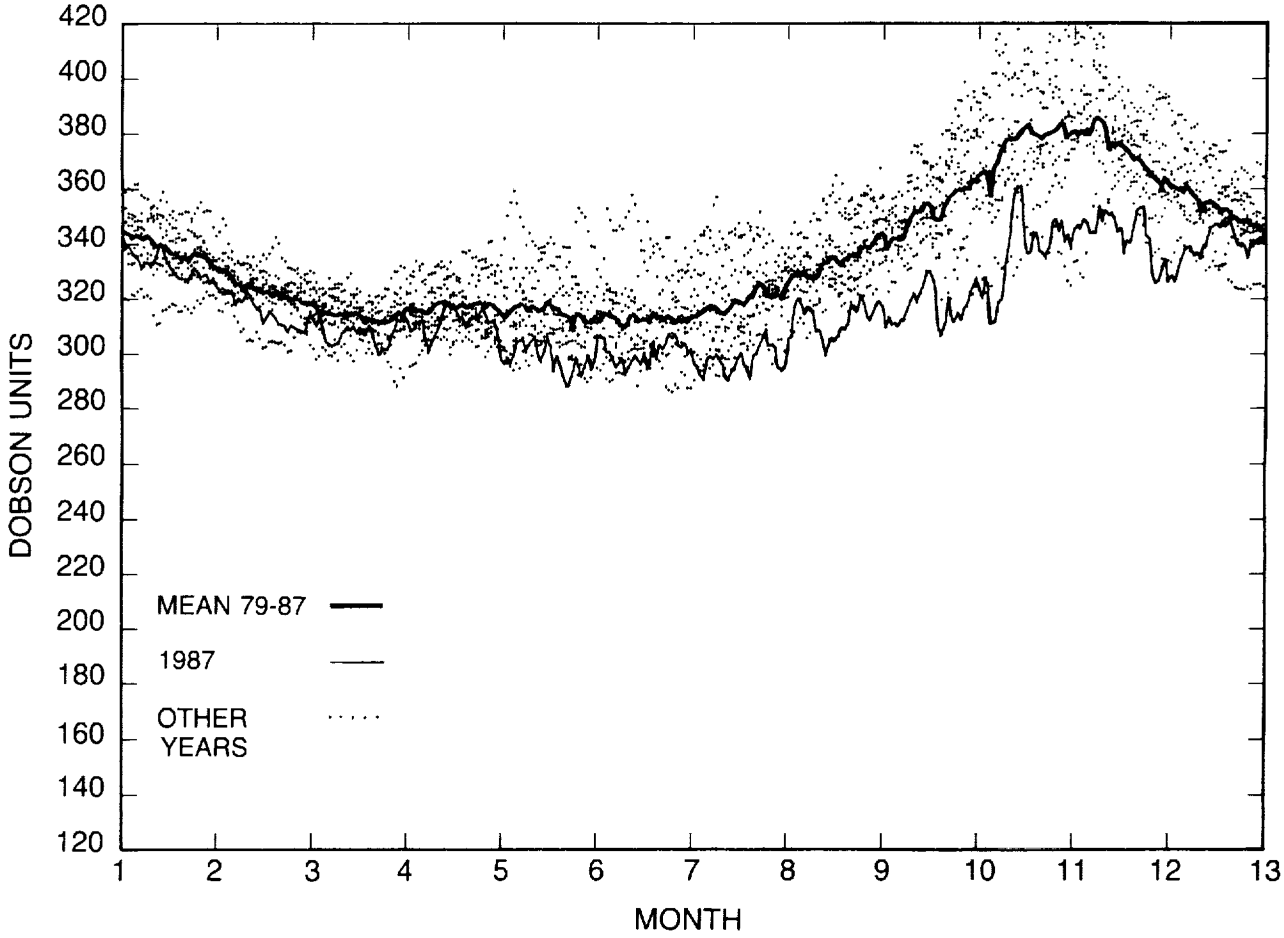

Figure 11.9. Daily zonal mean TOMS total column ozone versus time of year at 60°S for the years 1979 through 1987. Heavy line shows the mean for all years, thin solid line shows 1987, and dots are daily values for all years 1979–1986 (normalized TOMS data used).

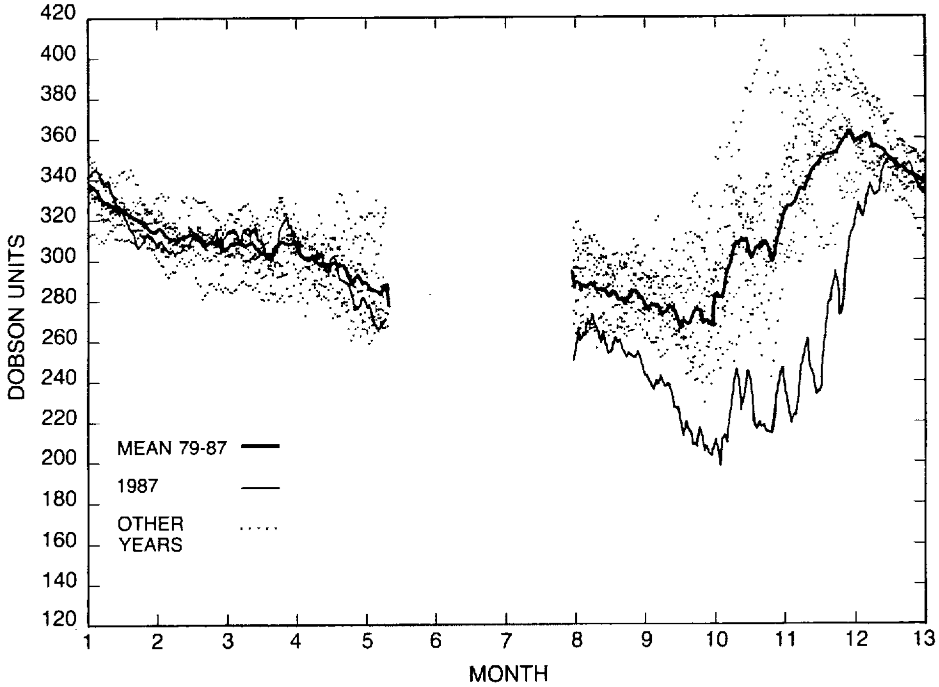

Figure 11.10. Daily zonal mean TOMS total column ozone versus time of year at 70°S for the years 1979 through 1987. Heavy line shows the mean for all years, thin solid line shows 1987, and dots are daily values for all years 1979–1986 (normalized TOMS data used).

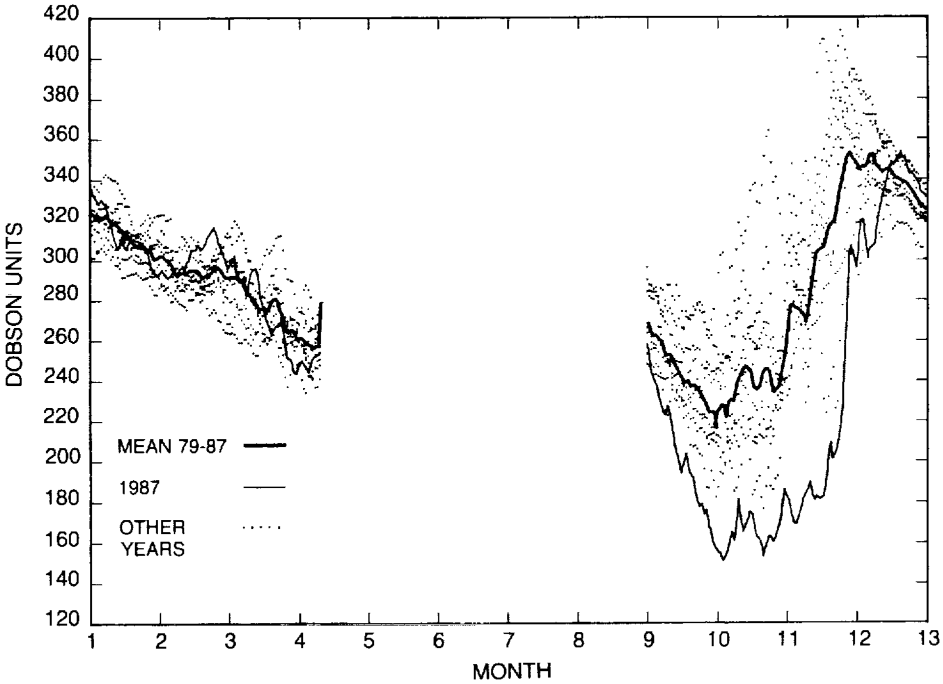

Figure 11.11. Daily zonal mean TOMS total column ozone versus time of year at 80°S for the years 1979 through 1987. Heavy line shows the mean for all years, thin solid line shows 1987, and dots are daily values for all years 1979–1986 (normalized TOMS data used).

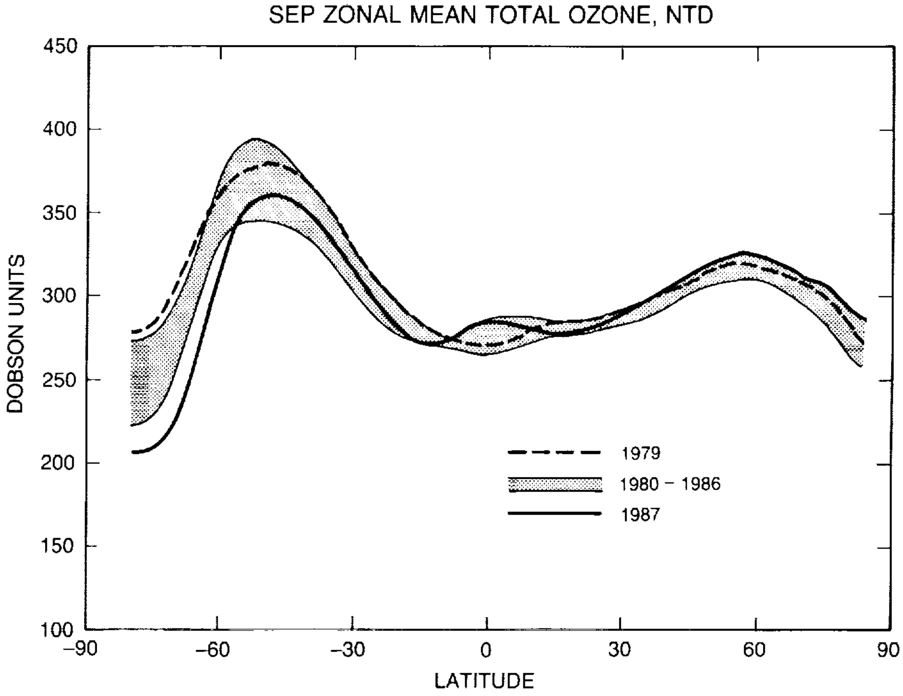

Figure 11.12. Zonally averaged TOMS ozone plotted versus latitude for the month of September from 1979 through 1987, highlighting 1979 with dashed lines and 1987 with a thick black line (normalized TOMS data used). (Schoeberl, 1987, private communication.)

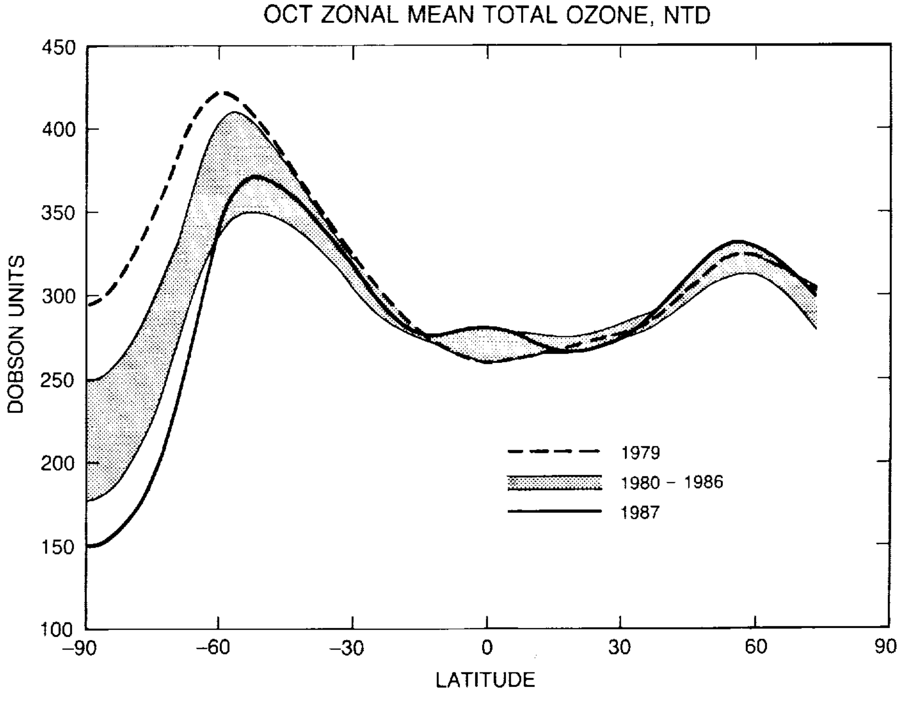

Figure 11.13. Zonally averaged TOMS ozone plotted versus latitude for the month of October from 1979 through 1987, highlighting 1979 with dashed lines and 1987 with a thick black line (normalized TOMS data used). (Schoeberl, 1987, private communication.)

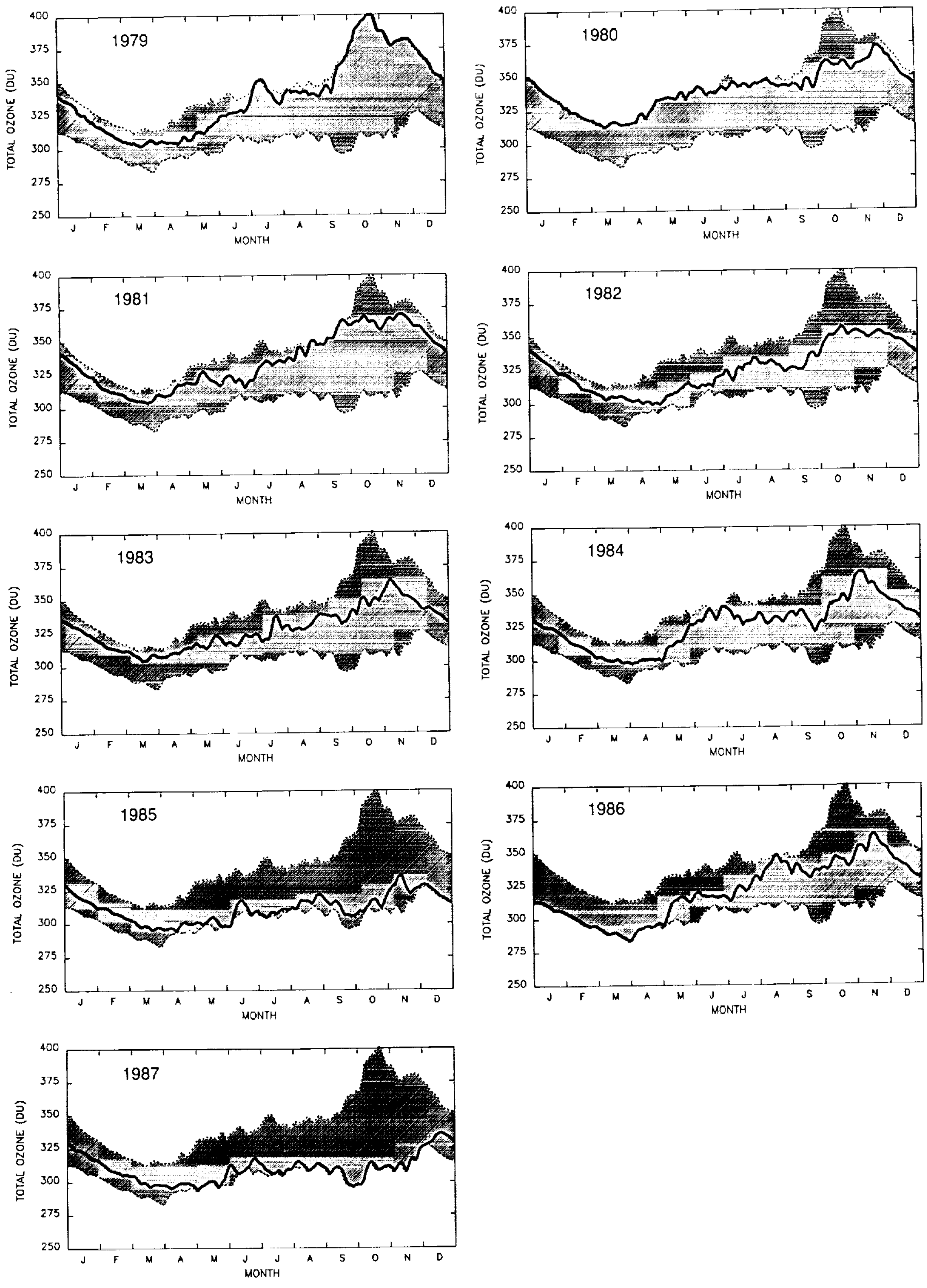

Figure 11.14. Annual progression of TOMS total ozone integrated over the area from 90°S to 44°S plotted for each year from 1979 through 1987. Range of all years is shown as shaded area; solid line in each panel compares individual year to range (normalized TOMS data used). (Schoeberl, 1987, private communication.)

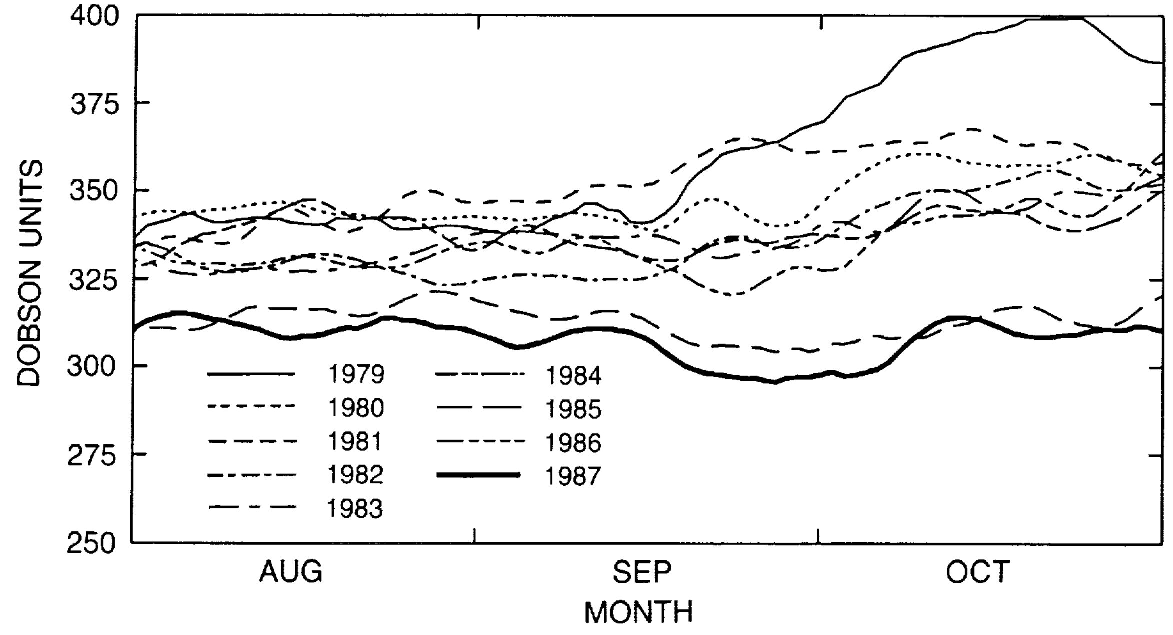

Figure 11.15. Progression of TOMS total ozone integrated over the area from 44°S to 90°S from August through October plotted for each year from 1979 through 1987 (normalized TOMS data used). (Schoeberl, 1987, private communication.)

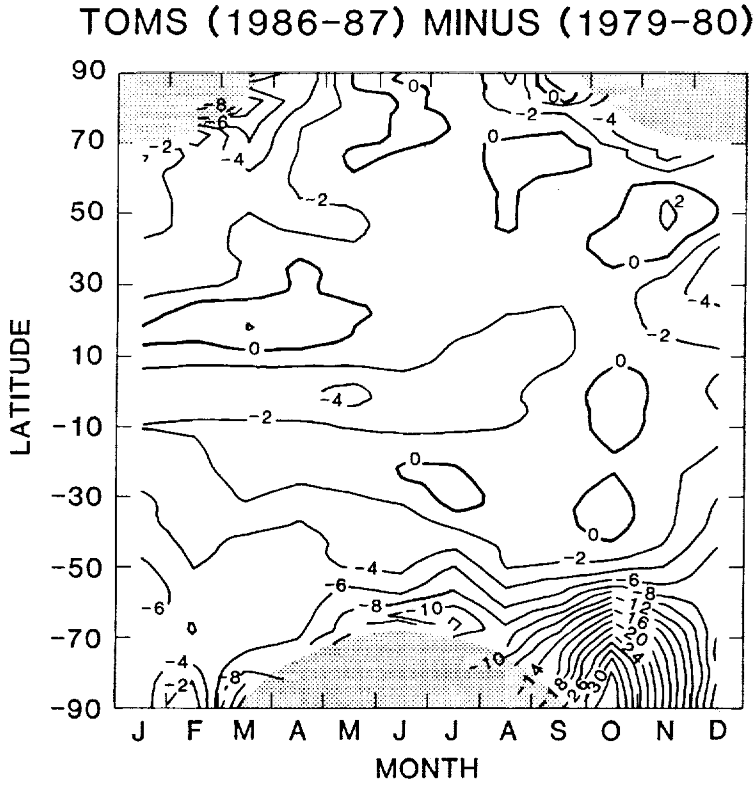

Figure 11.16. Difference between recent 2 years (1986–1987) of TOMS total ozone measurements and first 2 years (1979–1980) as a function of latitude and season. Two years are used to approximately remove the quasi-biennial oscillation.

The development of the minimum occurs mainly during September (Stolarski et al., 1986) when the Sun rises over the polar region. Figures 11.7 and 11.8 clearly demonstrate that the ozone minimum has developed primarily during September in all years since 1979. This behavior has been confirmed by data from McMurdo in Antarctica (Mount et al., 1987; Hofmann et al., 1989) and from the South Pole (Komhyr et al., 1988b). Examination of Figure 11.8 strongly suggests that the rate of ozone decrease during September, within a given year at 80°S, has increased from 1979 to the present. Figure 11.7 is inconclusive as to whether the rate of decrease within a given year of the zonal mean total ozone at 70°S during the late August–September period has increased since 1979. Zonal mean values of ozone at 80°S represent the region of maximum ozone loss—i.e., the ozone hole; hence, Figure 11.8 represents the rate of change of ozone within the region of low ozone. In contrast, the zonal mean values of ozone at 70°S represent a mixture of ozone both within and outside the region of low ozone.

Figures 11.7 and 11.8 also indicate that the period of ozone destruction has lengthened into October, and that the breakdown of the polar vortex now occurs later in the year. Figure 11.17 (Stolarski, private communication) shows four Southern Hemisphere daily total ozone maps for October 15, November 15, November 29, and December 5, 1987. These TOMS images clearly show that the ozone hole lasted until late November/early December in 1987. This is the latest that the region of low ozone has broken down since satellite measurements began. In previous years, it broke down by mid-October to early November; in 1985, the year of the previous lowest ozone, the region of low ozone did not break down until mid-November.

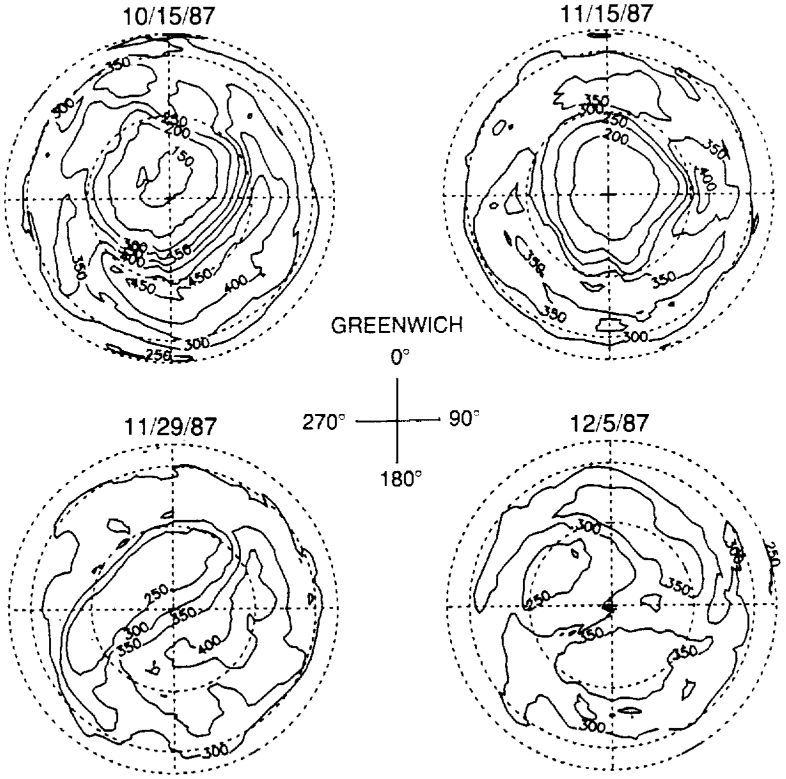

Figure 11.17. Daily TOMS maps of total column ozone in the Southern Hemisphere for October 15, November 15, November 29, and December 5, 1987 (polar orthographic projection). (Stolarski, private communication.)

Figure 11.18 (Stolarski, private communication) shows four Southern Hemisphere daily total ozone maps for August 17, September 5, September 27, and October 5, 1987. These TOMS images clearly show that the abundance of total ozone decreased dramatically over the 6-week period. Total ozone values below 125 DU were observed in early October. However, it is interesting to note that ozone does not change smoothly with time during August, September, and October. In each year since TOMS data have been available, it has been noted that in August and early September, occasional regions appear within the polar vortex where the total ozone content is tens of DU lower than that found in the surrounding area, which is part of the overall polar minimum. In some instances, these "miniholes" formed within 24 hours or less. The miniholes are 5 to 10 degrees in latitudinal and longitudinal extent (an area of several million square kilometers) and last for a few days or more. They seem to occur most frequently in the region just outside the polar night. By mid-September in 1987 they seemed to coalesce into a region of very low total ozone until the minimum was reached in early October. The miniholes are currently thought to be real, even though there is some concern that the amount of ozone they contain is underestimated due to the presence of high cirrus clouds that are always associated with them. Figure 11.19 (Krueger, private communication) shows four daily Southern Hemisphere total ozone maps for September 3–6, 1987. September 3 and 4, respectively, show a relatively uniform abundance of ozone of about 225 DU around the Antarctic continent. September 5 shows the sudden formation of a region with an ozone abundance of less than 200 DU over the Palmer peninsula, surrounded by this general minimum region with ozone amounts of 225 or more DU. September 6 shows that the minihole has moved over the Weddell Sea. The mechanism forming miniholes has yet to be established, and their role and importance in the formation of the ozone hole phenomenon have yet to be determined.

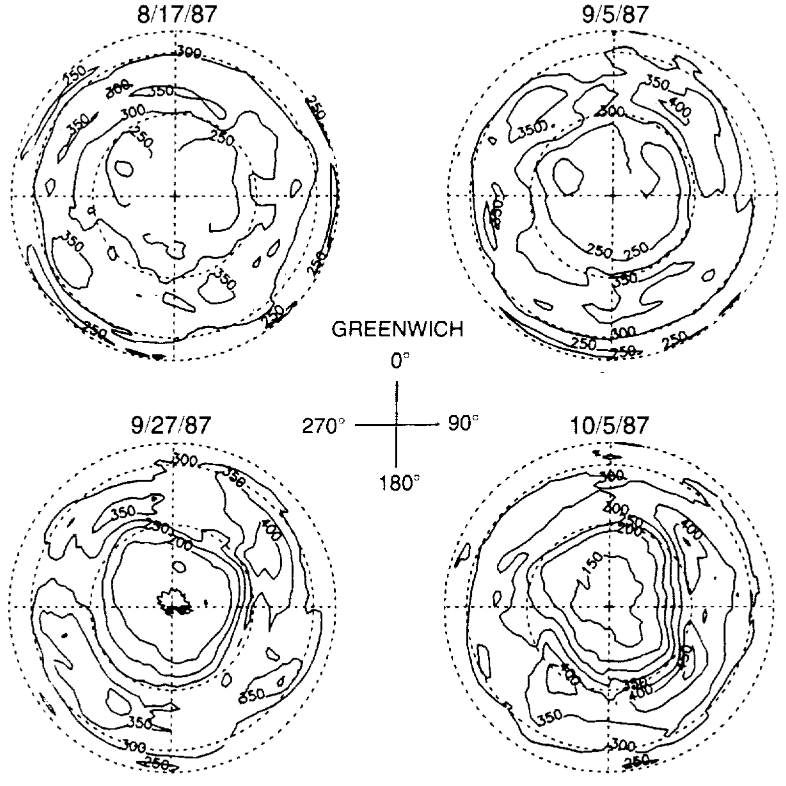

Figure 11.18. TOMS maps of total column ozone in the Southern Hemisphere for August 17, September 5, September 27, and October 5, 1987. (Stolarski, private communication.)

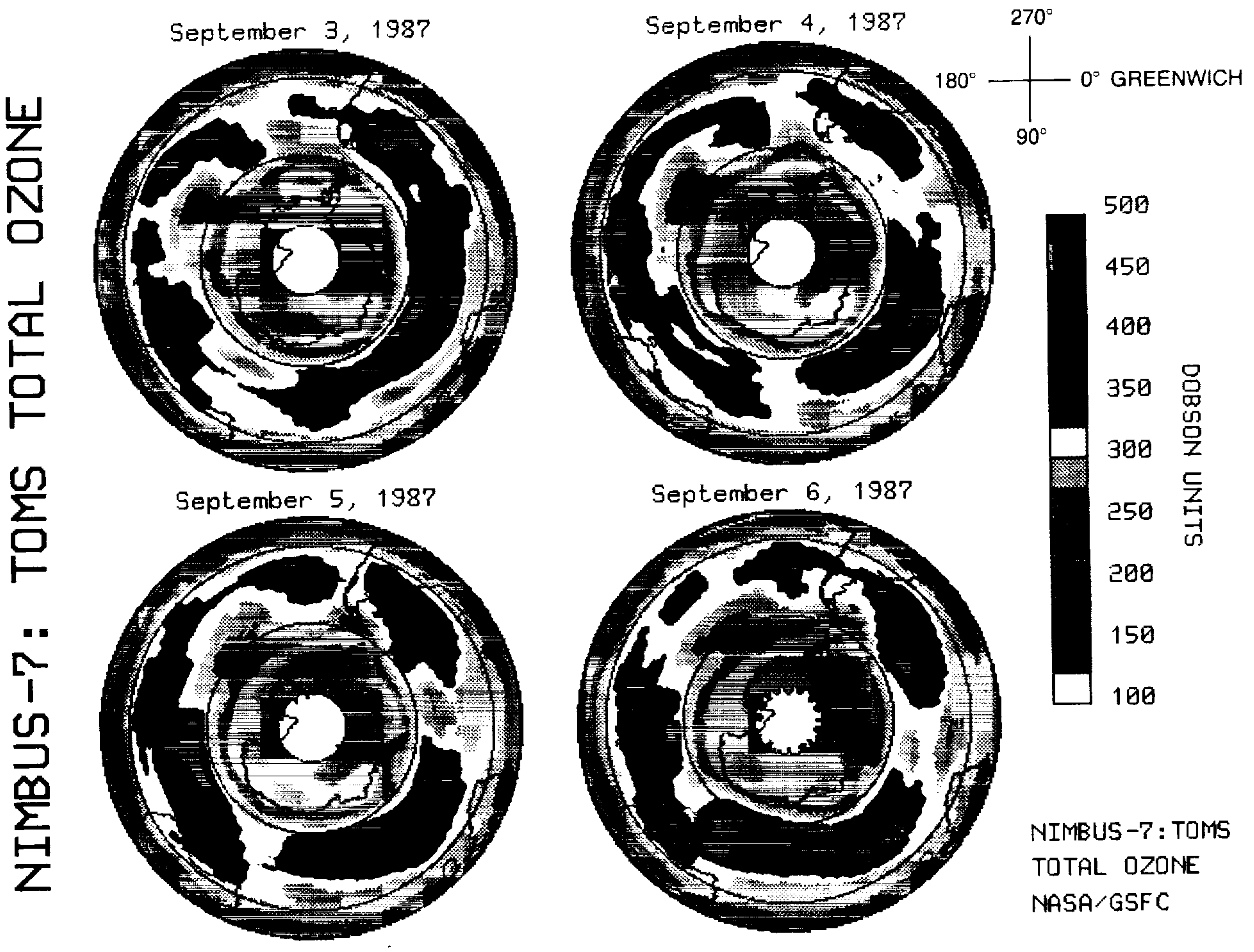
NIMBUS-7: TOMS TOTAL OZONE
September 3, 1987
September 4, 1987
September 5, 1987
September 6, 1987
270°
180°
0° GREENWICH
90°
500
450
400
350
300
250
200
150
100
DOBSON UNITS
NIMBUS-7:TOMS
TOTAL OZONE
NASA/GSFC

Figure 11.19. TOMS maps of total column ozone in the Southern Hemisphere for September 3–6, 1987. (Krueger, private communication.)

The phenomenology of the formation of the total ozone minimum region is beginning to be described in more detail. The circumpolar maximum ring of total ozone is present throughout most of the year. In fall and winter, it surrounds a region of lower total ozone, although the contrast between maximum and minimum total ozone amounts is only about 50 DU. During winter, the contrast between maximum and minimum values increases until an extreme is reached in October, with nearly a 200 DU difference. This general pattern appears to have existed before the appearance of the extreme low October values (London et al., 1976), but the contrast between maximum and minimum values has now increased in the springtime.

11.2.1.2 Altitude Dependence of Changes in Ozone

The first observations of the vertical extent of the depletion of ozone above Antarctica were reported by Chubachi (1984) based on ozonesonde soundings from Syowa. Ozonesonde observations were made from Syowa (Antarctica) from 1966 to 1972, beginning again in 1982. Figure 11.20 shows the vertical distribution of ozone from July through November for 1970 and 1982. From these observations it is clear that ozone was lower in 1982 than in 1970 between about 40

ORIGINAL PAGE
COLOR PHOTOGRAPH

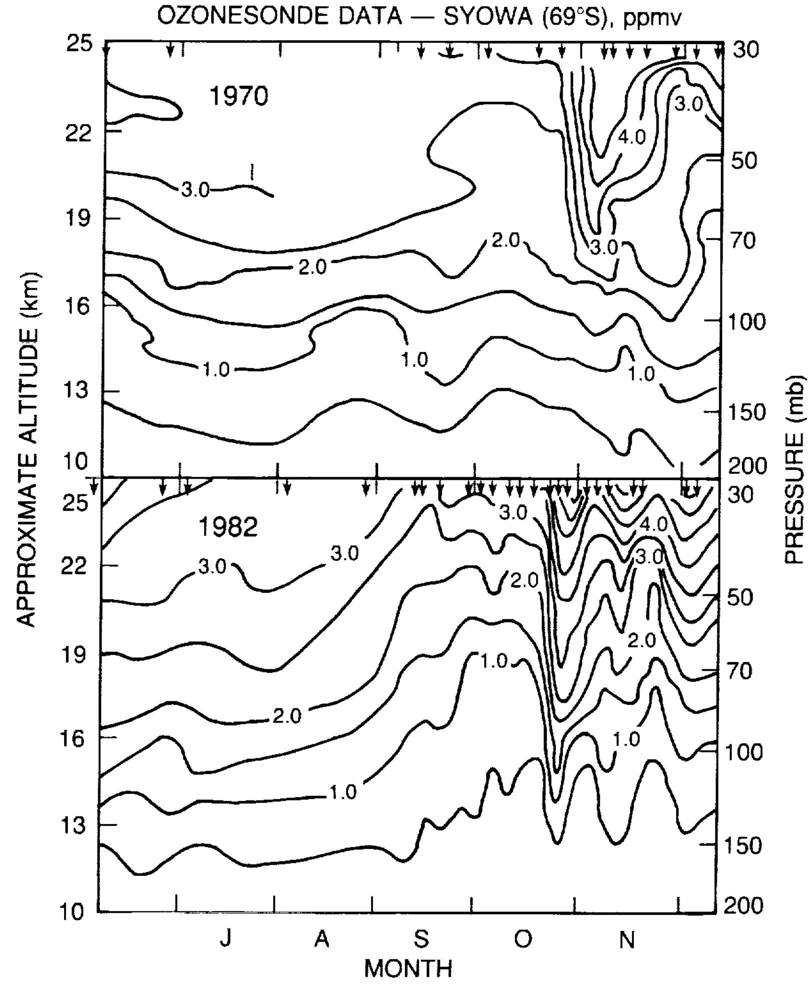

Figure 11.20. Vertical distribution of ozone over Syowa measured by ozonesonde from July through November. Arrows indicate ozonesonde launches during the two time periods. Upper panel shows data for 1970, lower panel for 1982. (Chubachi, 1984.)

and 150 mb, corresponding to about 20 and 13 km, respectively. These findings have largely been confirmed by ozonesonde observations from other stations in Antarctica, including McMurdo (78°S, 146°E) (Hofmann et al., 1986, 1987a, and 1989); Halley Bay (Farman and Gardiner, 1987); Palmer (64°S, 72°W) (Torres and Brothers, 1988); and South Pole (Komhyr et al., 1988b); at the GDR research base near the Soviet station, Novolazarevskaya (71°S, 12°E) (Gernandt, 1987); and by SAGE satellite observations (McCormick and Larsen 1986). The exact altitude range of the ozone depletion varies somewhat between studies. Iwasaka and Kondoh (1987) reported that the ozone decrease extended between 10 and 25 km over Syowa. Hofmann et al. (1986, 1987a) reported the depletion to be confined to a region from about 12 to 22 km above McMurdo in 1986. However, Hofmann et al. (1989), Gardiner (1988), and Torres and Brothers (1988) reported that the region of depleted ozone extended as high as 24 km in 1987.

Balloonsonde observations from McMurdo in 1986 indicated that the minimum began to form in early September near 20–22 km altitude and then to move downward until low ozone was observed from about 12–22 km (Hofmann et al., 1986). Stolarski (1988) has suggested that it is not clear whether this is a true indication of the time behavior of the process or just an indication of a phase change with altitude that tilts toward the east, such that the high-altitude part of the minimum comes over McMurdo first. However, examination of ozonesonde data from other stations such as Syowa (Solomon, 1988), South Pole (Solomon, private communication), and Halley Bay (Jones, private communication) shows that this behavior is observed at all stations; hence, it appears to be a true indication of the temporal behavior of the phenomena. Figure 11.21, from Hofmann et al. (1986), shows the ozone partial pressure as a function of altitude over McMurdo on August 28, 1986, and that measured on October 16, 1986. The difference is seen to be confined mainly to the region between about 10 and 22 km altitude. As stated earlier, this behavior is confirmed by the balloonsonde measurements at the South Pole (Komhyr et al., 1988b). Figure 11.23 from Komhyr et al. (1988a) shows a pair of profiles from the South Pole for August 9, 1986, and for October 7, 1986. At the left of Figure 11.22, these profiles are compared as ozone partial pressures, and at the right as mixing ratios. Connor et al. (1987) reported ozone decreases up to an altitude of 25 km at McMurdo in 1986 using ground-based millimeter-wave spectrometry. Whether there is any significant discrepancy between the ozonesonde and millimeter-wave data is unclear given that the vertical resolution of the latter technique is approximately one scale height, i.e., about 7 km, and that smearing associated with their weighting functions possibly could account for the reported changes at 25 km.

Figure 11.23 shows the vertical distribution of ozone above Halley Bay on August 15, 1987, and October 15, 1987, showing an almost complete loss of ozone between 40 and 100 mb, i.e., 20

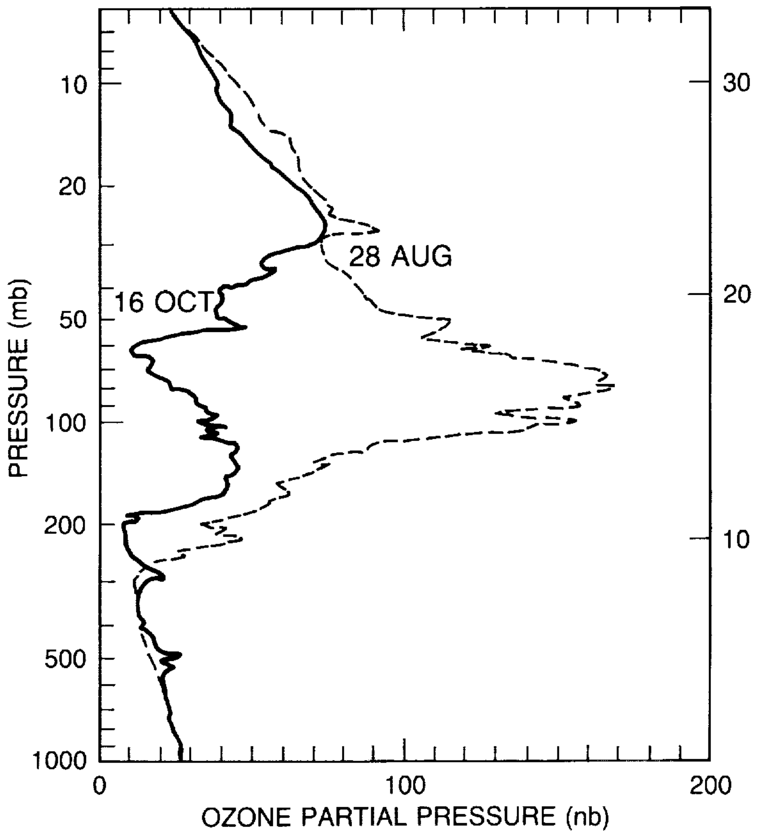

Figure 11.21. Ozone partial pressure as function of altitude over McMurdo as measured by ozonesonde (Hofmann et al., 1986). Shown are August 28 and October 16, 1986.

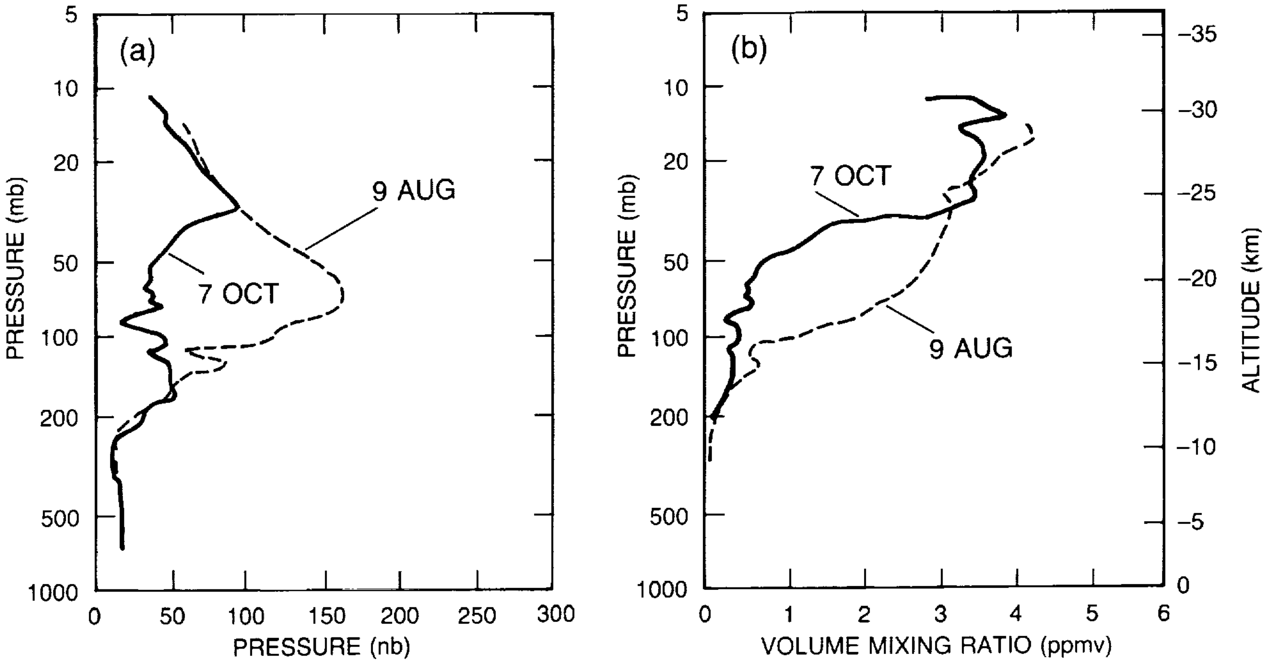

Figure 11.22. Ozone profiles over South Pole measured by ozonesonde for August 9 and October 7, 1986 (Komhyr et al., 1988a). Left panel shows partial pressure; right panel shows mixing ratio.

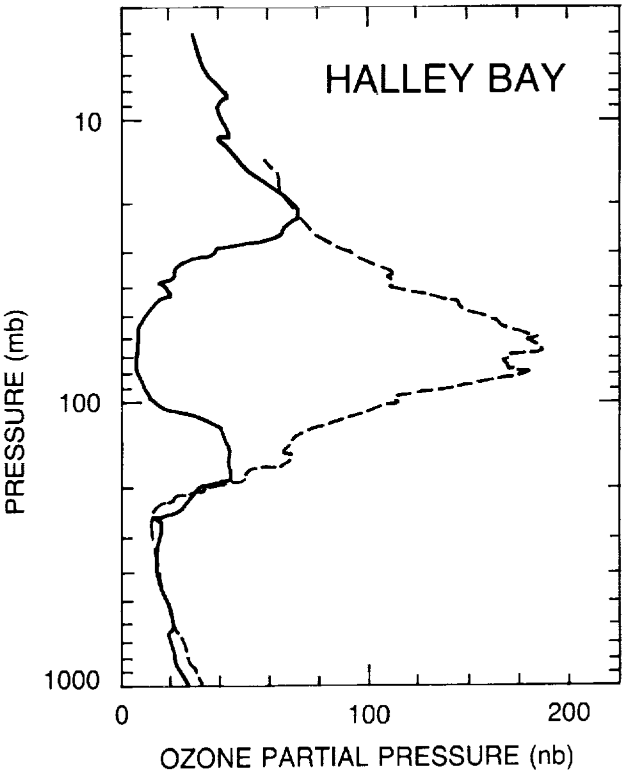

Figure 11.23. Vertical distribution of the ozone partial pressure (nbar) observed at Halley Bay Station on August 15, 1987 (high values), and October 15, 1987 (low values), respectively. (Farman, personal communication, 1987.)

and 15 km. Figure 11.24 shows the vertical distribution of ozone above the Palmer station on October 6, 1987 (high values), and October 9, 1987 (low values), indicating that when the chemically perturbed region of low ozone moves over the Palmer station, the magnitude of the ozone loss is similar to that observed at other stations. Similar results have been reported by Hofmann et al. (1989), Figure 11.25, from McMurdo, and Komhyr et al. (1988b) from the South Pole. Figure 11.26 shows a comparison of SAGE–II and Halley Bay ozonesonde data for October 7, 1987, indicating extremely low values of ozone centered around 75 mb. The 1987 satellite and balloonsonde data clearly indicate that ozone was almost completely removed between 40 and 100 mb, a 5 km altitude region centered near 15 km, and that the altitude region over which ozone decreased ranged from about 14 to 24 km.

During August and September 1987, a campaign was conducted from Punta Arenas, Chile, using a DC–8 and an ER–2 aircraft. The upward-looking lidar aboard the DC–8 of E. Browell and coworkers observed more than a 50 percent decrease in ozone from 14 to 19 km during September 1987 between 77°S and 90°S, but no discernable trend between 12 and 14 km. There was also evidence from the lidar data of a decrease in ozone up to 23 km. The in situ ozone measurements aboard the ER–2 also showed a 50 percent decrease near 18 km during September.

Aikin and McPeters (1986), using SBUV data, reported that the ozone depletion extended up to 1 mb over Antarctica. McCormick and Larsen (1986), using SAGE–I/II data, reported no evidence for a trend in Antarctic springtime ozone above 30 km since 1979, when SAGE–I started to return data.

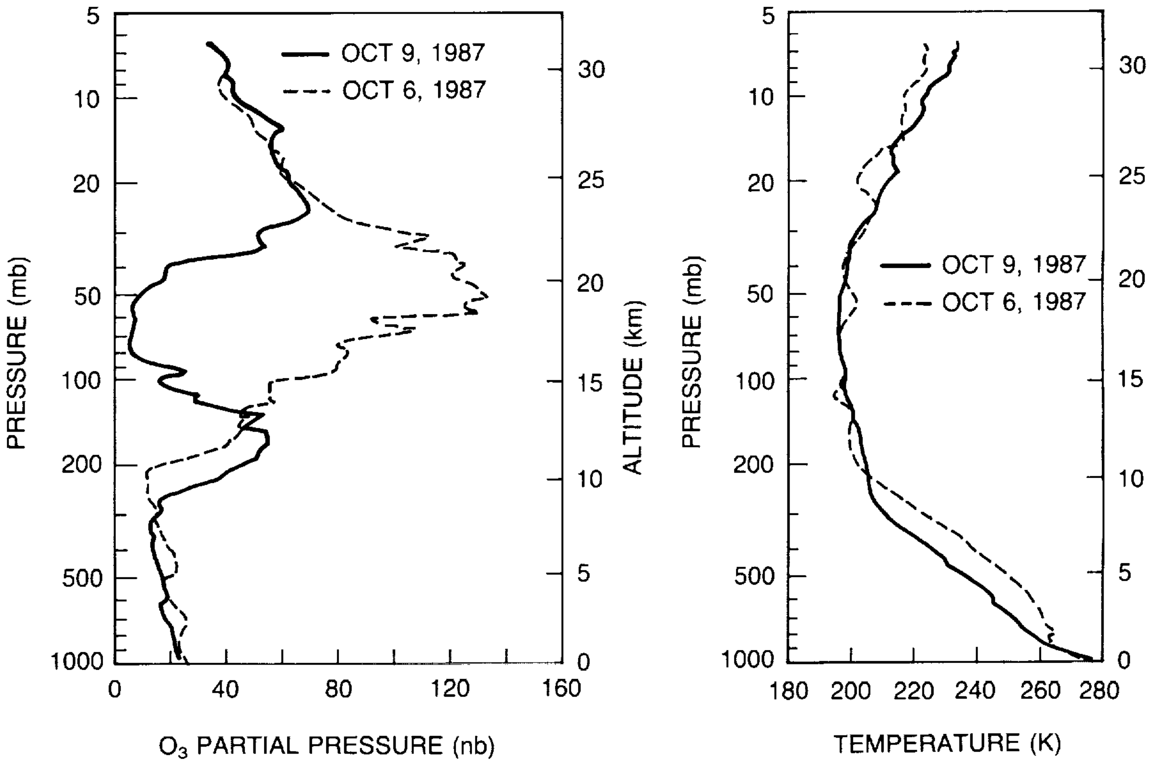

Figure 11.24. (a) Ozone partial pressure over Palmer station on October 6 and 9, 1987; (b) temperature profile for October 6 and 9, 1987, over Palmer Station.

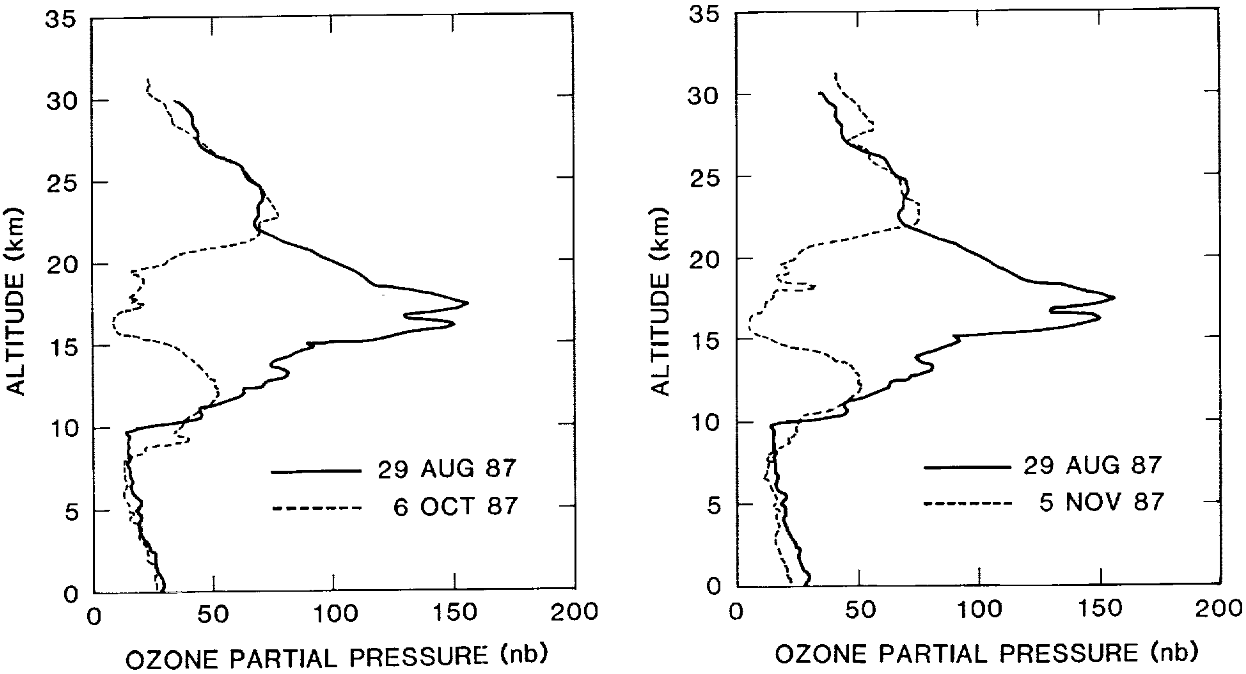

Figure 11.25. Ozone partial pressure over McMurdo measured by ozonesonde (Hofmann et al., 1989); (a) comparison of August 29, 1987, to October 6, 1987, and (b) comparison of August 29, 1987, to November 5, 1987.

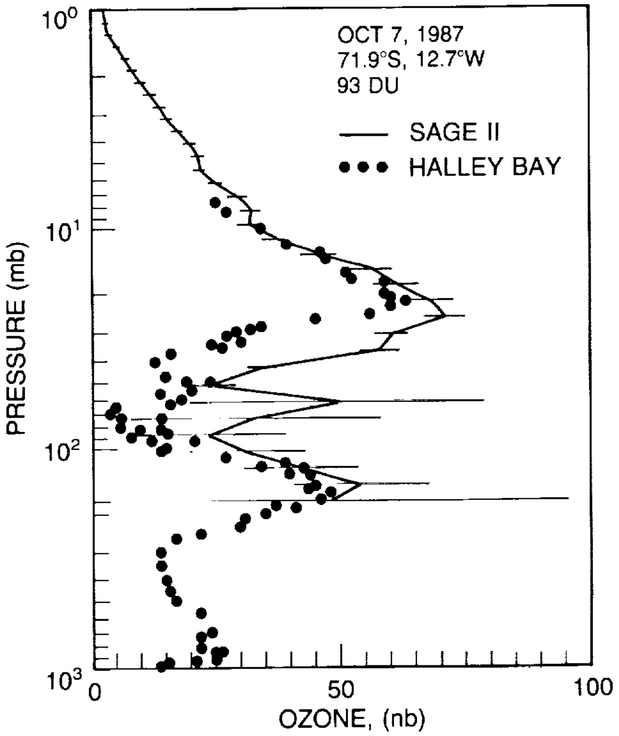

Figure 11.26. Comparison of ozone profiles measured by SAGE with Halley Bay ozonesondes for October 7, 1987. Solid line represents SAGE–II data; dots are ozonesonde data.

One interesting observation is that the 1986 balloonsonde ozone data at McMurdo (Hofmann et al., 1986) show a great deal of structure, primarily in October—i.e., thin layers of less than 1 km thickness in altitude. Figure 11.27, from Hofmann et al. (1986), shows that the vertical distribution of ozone exhibited significant layering and day-to-day variability above McMurdo in 1986. In contrast, the South Pole data show significantly less vertical structure (Komhyr et al., 1988b). Because McMurdo was located near the steep gradient in total ozone for much of the 1986 measurement period, the existence of these layers should not be surprising. They have been measured in previous instances in the Northern Hemisphere (Dütsch, 1974), and are presumably caused by differential advection of air masses with different amounts of ozone.

11.2.1.3 Summary of Ozone Observations

The total ozone changes over high southern latitudes in spring have been measured by several different techniques from the ground and from satellites. The results corroborate one another, providing a clear picture of the changes that have taken place: the development of the minimum occurs mainly during September; the rate of change of ozone within a given Antarctic spring appears to be increasing; the ozone was lower in 1987 than in any previous year since measurements began; the region of low ozone lasted until late November/early December in 1987; the depletion extends to about 50°S; and while the ozone depletion is largest in the Antarctic spring, ozone has decreased at all latitudes south of 50°S throughout the year.

The altitude profiling by balloonborne ozonesondes has shown similar features at a number of stations and is consistent with the SAGE results, providing confidence in their robustness. The ozonesonde and SAGE data seem to indicate that the ozone decrease is confined to a region between about 12 and 24 km.

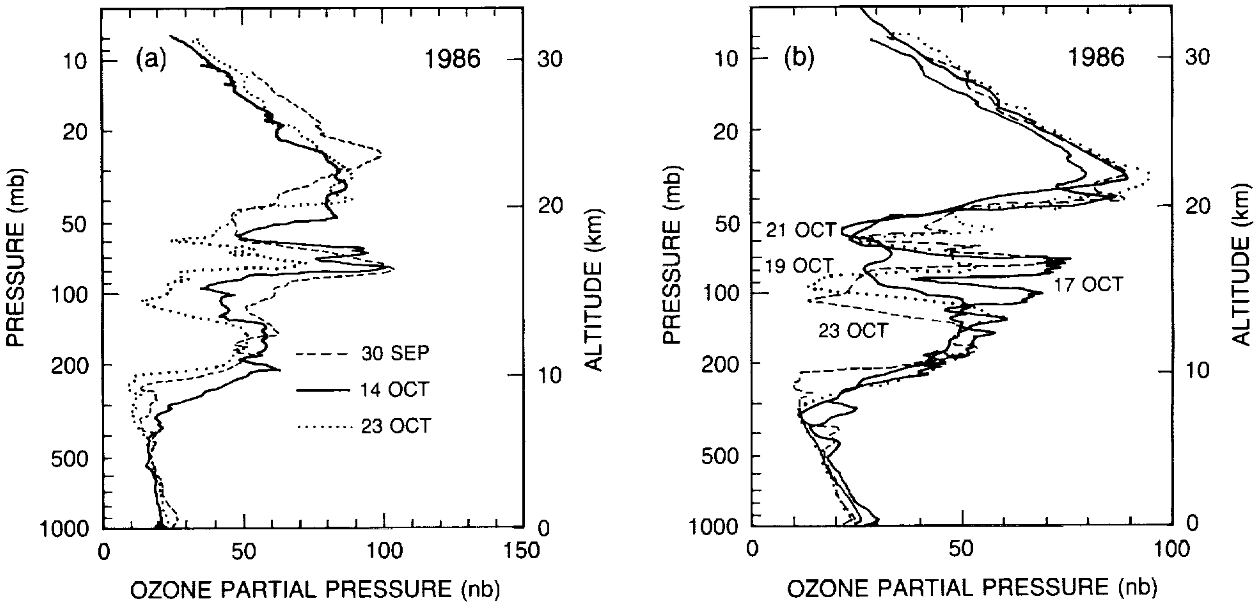

Figure 11.27. Ozonesonde partial pressure measurements for several days over McMurdo during 1986 (Hofmann et al., 1986).

11.2.2 Morphology of Polar Stratospheric Clouds

This section briefly treats Polar Stratospheric Clouds (PSC's), which are discussed in more detail in Chapter 10. Remote-sensing measurements made by the satellite sensor SAM–II, starting in late 1978, have shown that stratospheric clouds occur in both winter polar regions more frequently than had been realized by earlier visual sightings. Named Polar Stratospheric Clouds (McCormick et al., 1982), they were found not to be confined only to the lee side of mountain ranges, but to be strongly associated with synoptic-scale regions of very cold stratospheric temperatures. The first idea put forth to describe the initial data was that the clouds probably formed as a result of the deposition of water vapor onto preexisting stratospheric aerosol droplets (made of sulfuric acid and water) at temperatures below the frost point. Recent studies have proposed that PSC's form by the coupled deposition of nitric acid and water vapors, rather than by the deposition of water vapor alone (McElroy et al., 1986a; Toon et al., 1986; Crutzen and Arnold, 1986). This scenario suggests a possible chemical link between PSC's and the ozone hole. Figure 11.28, from McCormick and Trepte (1987), shows the SAM–II weekly averaged polar stratospheric optical depth record at 1 μm wavelength for October 1978 to December 1986. Both polar regions clearly show that the overall aerosol trend is driven by major volcanic eruptions, which are annotated on the abscissa with their eruption times. The largest increase in this record was caused by the April 1982 eruption of El Chichón. In addition, the Antarctic record clearly shows yearly enhancements in austral winter caused by the presence of PSC's. See, for example, the large order of magnitude enhancement in June–September 1979. This signature is repeated each year, even in the presence of the strong volcanic levels after the El Chichón eruption.

Another feature shown in the Antarctic record of Figure 11.28 is the noticeable minimum occurring each year in October. At this time of the year, the vortex is normally still well formed. Because of the orbit of the Nimbus–7 satellite, SAM–II measurements can be made within the vortex. The minimum indicates that a cleansing has occurred between the pre- and post-PSC period. Subsidence of the air in the altitude region of aerosols and PSC's (10–25 km) is probably not strong enough to cause the observed cleansing over this short period of time, nor is

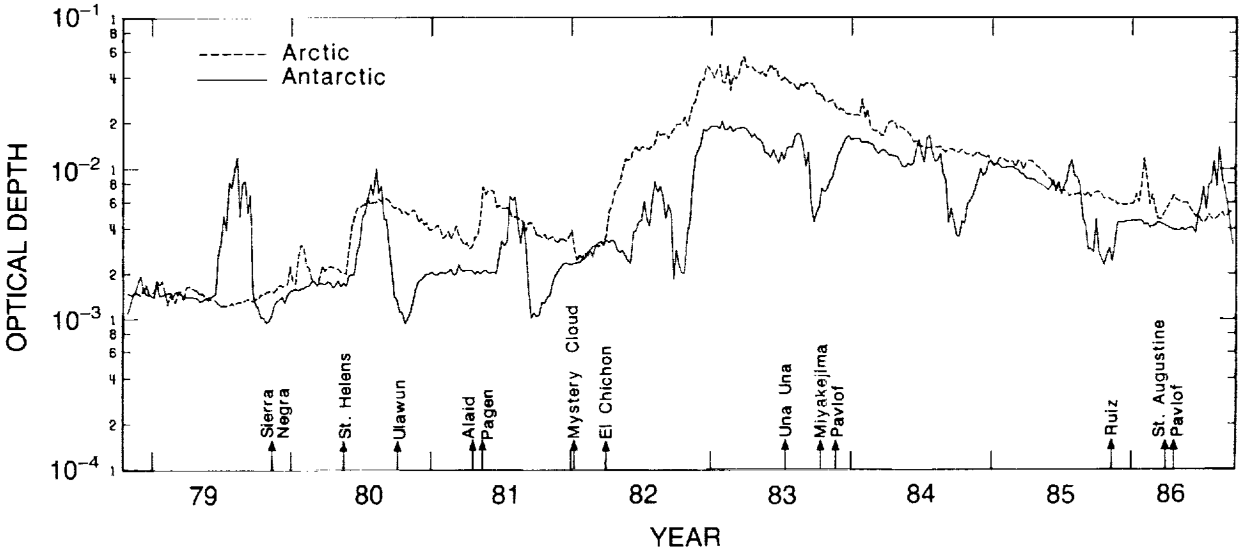

Figure 11.28. SAM–II weekly averaged stratospheric optical depth at 1 μm over the Arctic and Antarctic regions from October 1978 to September 1986 (McCormick and Trepte, 1987).

sedimentation of aerosols or PSC's with small diameters (i.e., equal to or less than 1 μm). However, aerosols or PSC's with larger diameters can sediment at significant rates; for example, a 10 μm diameter particle would fall at a rate of 1–2 km per week.

Figure 11.29 shows the SAM–II weekly averaged aerosol extinction ratio (aerosol extinction divided by molecular extinction) for Antarctica as a function of time for 1980, 1982, and 1984

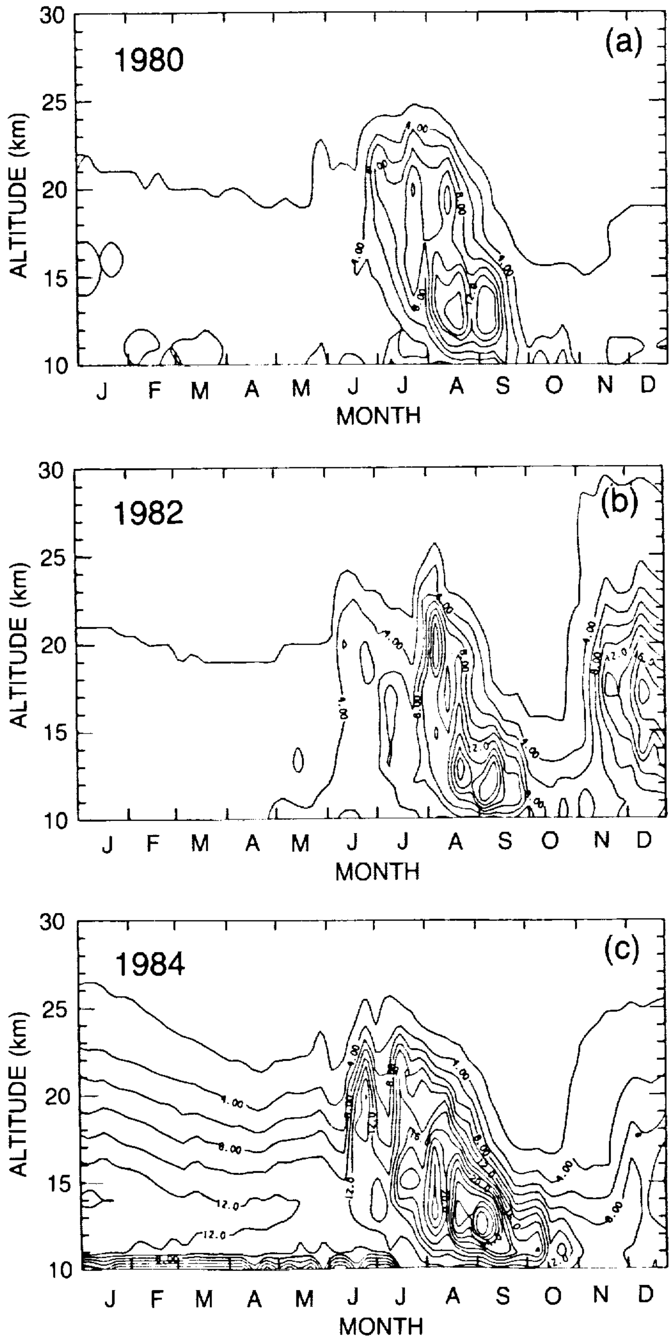

Figure 11.29. Contour plots of SAM–II weekly averaged extinction ratio at 1 μm for (a) 1980, (b) 1982, (c) 1984. (McCormick and Trepte, 1986.)

(McCormick and Trepte, 1986). As previously described, it also shows the vertical extent of PSC's correlated with cold temperatures, the cleansing that occurs during each wintertime period, the relative minimum in October, and the large overall increase in stratospheric aerosols in the Southern Hemisphere that started in about November 1982, after the April 1982 eruption of El Chichón. It should be noted that atmospheric temperatures increase during spring, starting at higher altitudes, resulting in a temporal decrease in the maximum altitude at which PSC's can exist.

Iwasaka et al. (1986) reported lidar aerosol data from Syowa indicating that the abundance of PSC's in September and October had increased from 1983 to 1985 along with a decrease in stratospheric temperatures. McCormick (private communication) reports that the persistence of PSC's in Antarctica has increased since 1984. The 1985 observations show for the first time the occurrence of PSC's at 18 km throughout the end of September. Further, PSC's lasted into October in 1987, at altitudes as high as 18 km and 20 km, in sharp contrast to earlier years. Figures 11.30a,b,c,d show the extinction ratio—i.e., aerosol/molecular extinction at 1.0 μm—at both 18 km and 20 km for 1979 and 1987. Further analysis of all aerosol data is needed to quantify any changes in the PSC's over Antarctica during the last decade or so.

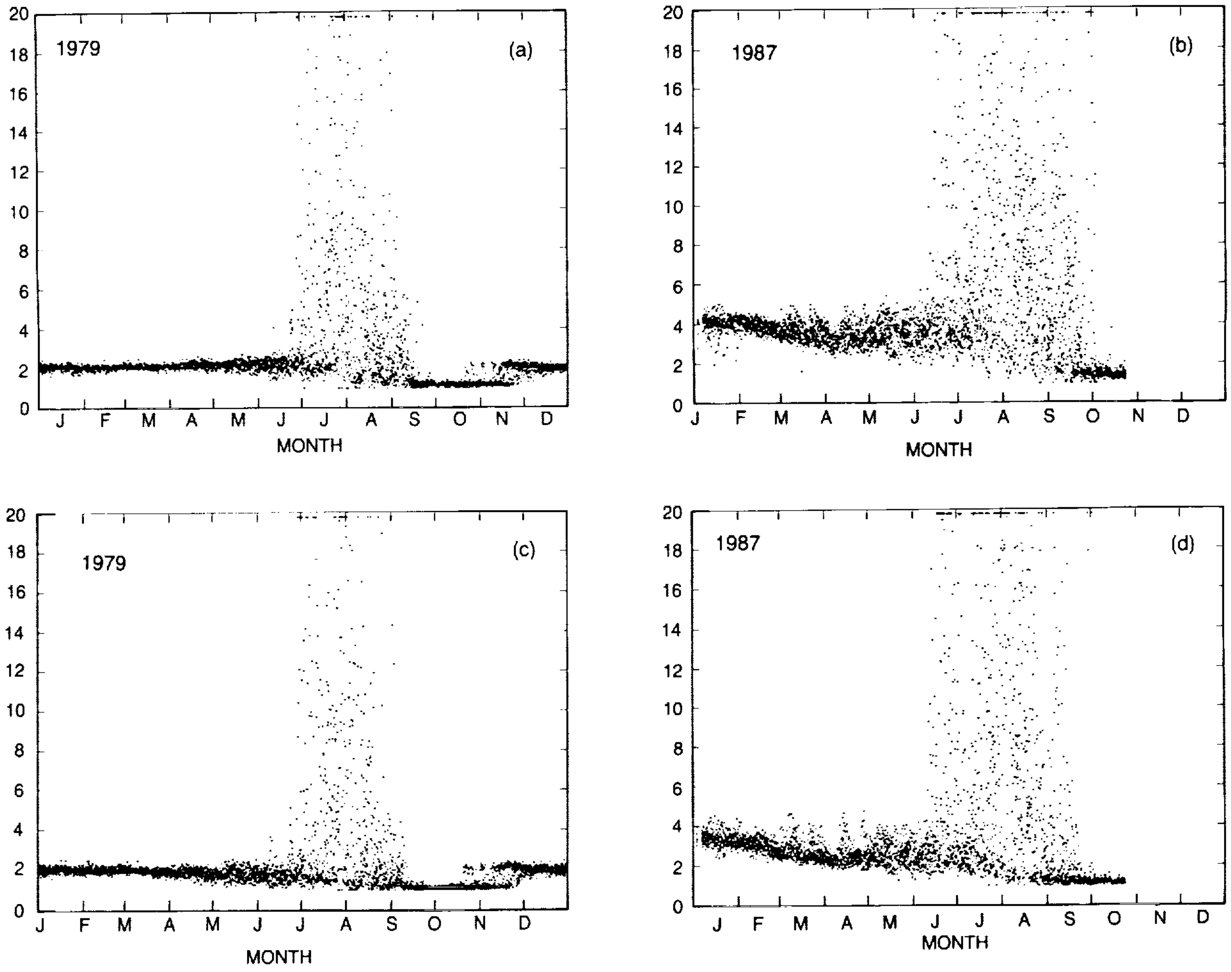

Figure 11.30. SAM–II extinction ratios versus time of year for (a) 1979 at 18 km altitude, (b) 1987 at 18 km altitude, (c) 1979 at 20 km altitude, (d) 1987 at 20 km altitude.

11.2.3 Antarctic Temperature Trends

11.2.3.1 Introduction

Temperature trends that might occur in association with the ozone trends in the south polar region are key in attempting to understand the causes of the observed ozone decline. In the lower stratosphere, both potential temperature and the ozone-mixing ratio have rather long relaxation time scales and both increase with altitude. Therefore, both ozone and temperature tend to decrease locally in response to upward vertical motion and to increase in response to downward motion. Strong correlations between total ozone and dynamical variables such as temperature, geopotential height, and tropopause height are well established in the literature for time scales of days to weeks (e.g., Dobson et al., 1927; Meetham, 1937; Reed, 1950). For periods of at least up to a few weeks, ozone variations associated with vertical motions can be expected to be accompanied by variations in temperature.

Ozone and potential temperature are not perfectly conservative quantities in the lower stratosphere, so that chemical sources of ozone and temperature changes associated with heat transfer by radiation must be considered when the time scale of interest exceeds about a week. A further complication is introduced with the influence of ozone and temperature on each other. Ozone photochemistry is temperature dependent, and ozone itself is a radiatively important constituent in the stratosphere. In the springtime, as the Sun rises over the south polar area, absorption of solar radiation by ozone becomes a principal component of the heat balance in the lower stratosphere.

In this section, evidence for the existence of trends in temperature in the stratosphere over Antarctica will be reviewed. Although monthly averaged temperatures will provide the primary focus, relationships between interannual variability in temperature and total ozone also will be described. The high spatial correlation of the observed changes in total ozone and temperature (which are independent data sets) indicates the generally good precision of the daily global fields. Discussion of what the relationships between ozone and temperature changes might have to say about the cause of the total ozone decline in recent years will be deferred until Section 11.3. General descriptions of the temperature data sets used in this section are given in Chapter 6 (Stratospheric Temperature Trends).

11.2.3.2 Data Intercomparisons

A critical analysis of stratospheric temperature data from a variety of sources shows a greater consistency than previously believed (see Chapter 6). In this section, comparisons between October average U.S. National Meteorological Center (NMC) and radiosonde-observed (RAOB) temperatures are reviewed to document the reliability of these temperature data. In addition, the longer data record available for the RAOB data allows the temperature changes over 1979–1985 to be viewed in the context of the historical record. The quality of temperature retrievals is assessed monthly by NMC. These summaries show mean lower stratospheric daily differences from radiosondes that are generally less than 3 K over Antarctica. Newman and Schoeberl (1986) noted that the NMC October 1979 monthly mean data were underestimations of the radiosondes; this is confirmed in the monthly summaries. The only year in which the NMC data do not give lower temperatures than do the RAOB data is 1982, when the NMC temperatures appear to be higher by about 1 K.

Figure 11.31 (from Newman and Randel, 1988) shows time series of October 100hPa (hecto-Pascals) (1 hPa = 1 mb) temperatures at eight stations around Antarctica, for both NMC (1979–1986) and RAOB (1957–1984) data. These stations were chosen to represent the largest geographical area with the availability of a long time series. Direct comparisons of RAOB to NMC data are available only for 1978–1984, with many of the stations having incomplete records over this period. Nonetheless, the agreement between the two data sets is generally good. Of particular interest is that similar year-to-year changes are observed in both data sets. Figure 11.32 shows similar comparisons at 30hPa; again, overall agreement promotes confidence in the NMC analyses. Although biases are apparent at some stations (such as Casey and Davis in Figure 11.32), comparison of NMC and RAOB data for individual years suggests that the NMC data capture the horizontal temperature structure in the lower-to-middle stratosphere quite accurately. Examples of the horizontal structure of temperature fields are shown in Figure 11.33a,b for October 1983 at 100 and 30hPa. The RAOB temperatures are superimposed for comparison. These are compared to the October 1983 map of TOMS total ozone in Figure 11.33c.

Austin et al. (private communication, 1988) used Microwave Sounding Unit (MSU) channel-24 data to determine lower stratospheric temperature trends. These data provide a measure of temperature in the 50–200hPa region. Using Meeks and Lilley (1963) oxygen transition lines, Newman and Randel (1988) calculated the MSU channel-4 radiances from the

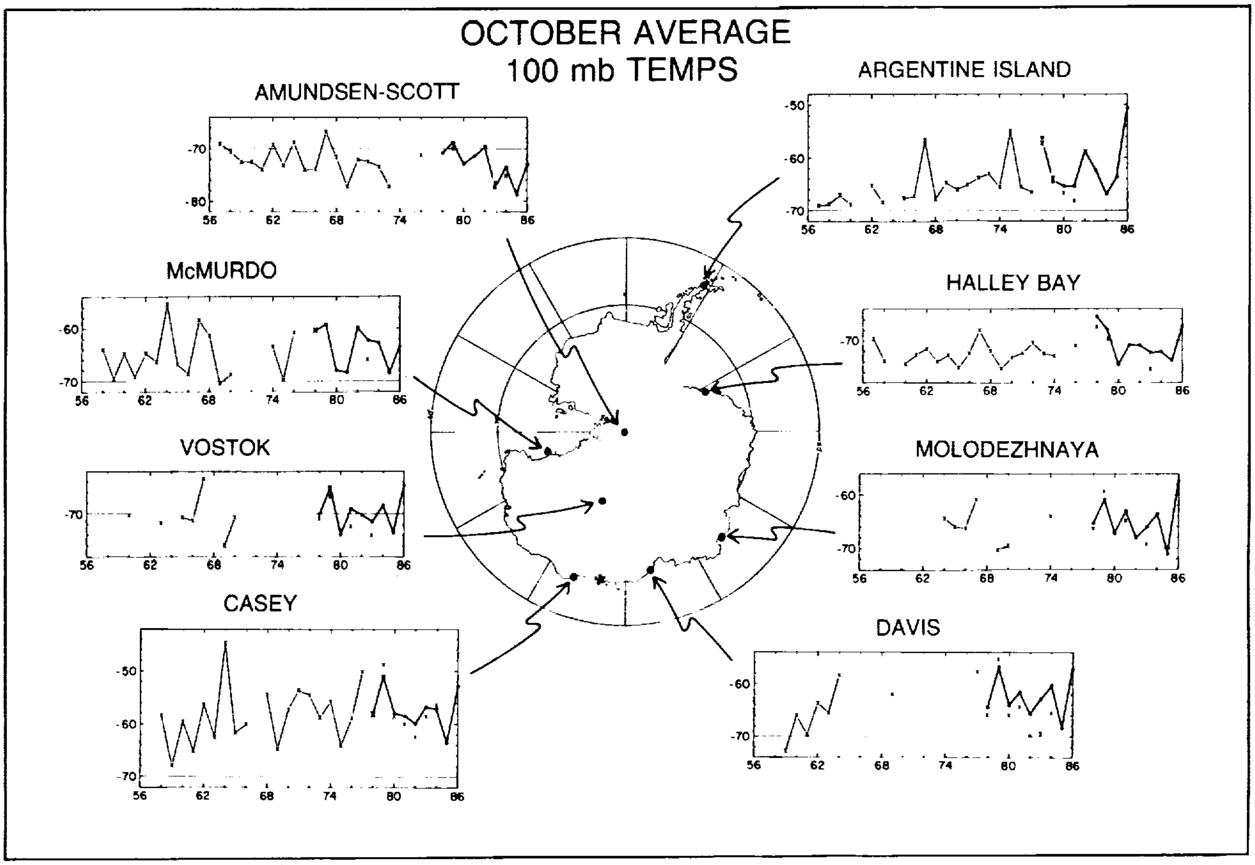

Figure 11.31. Time series of October mean 100 mb (100hPa) temperatures over eight Antarctic stations. Data from 1957–1984 are from rawinsonde observations (RAOB) and data from 1979–1986 are from NMC analyses.

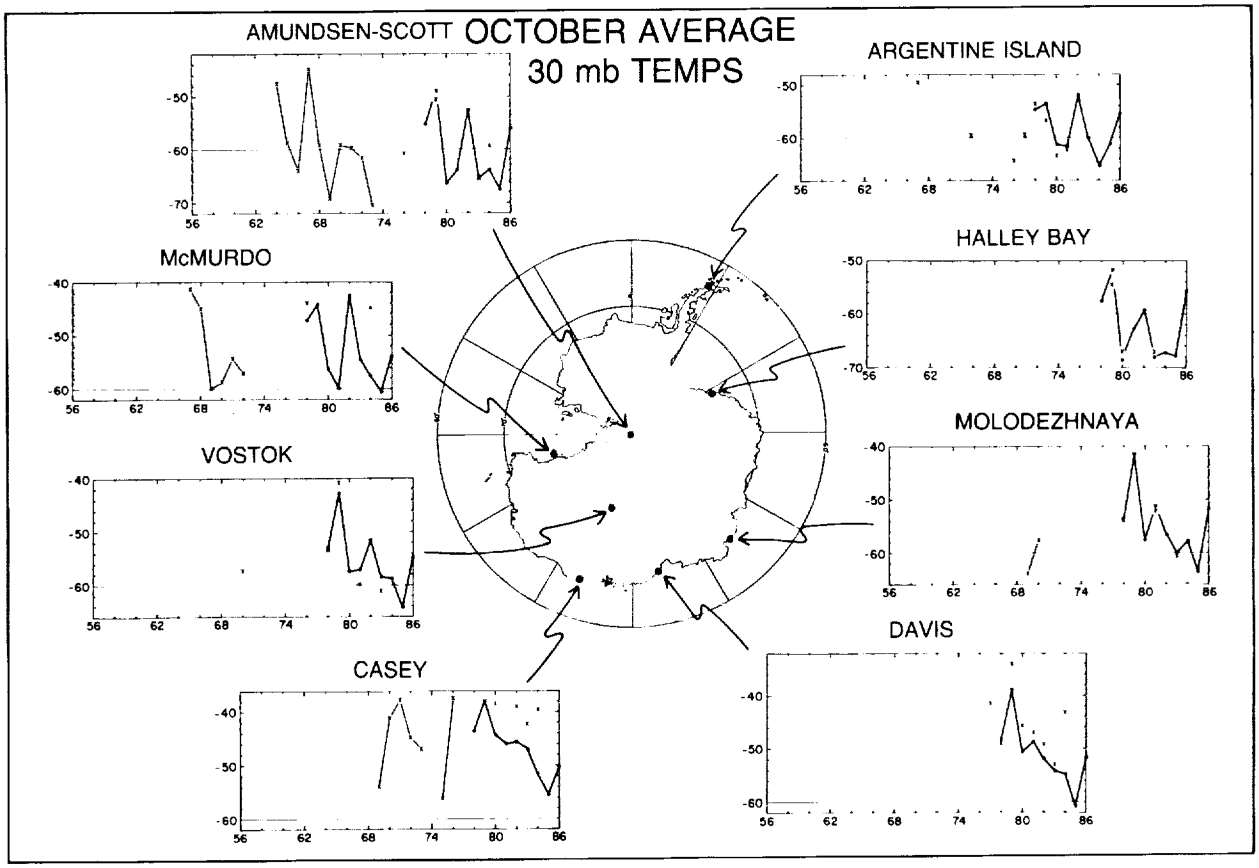

Figure 11.32. Time series of October mean 30 mb (30hPa) temperatures over eight Antarctic stations. Data from 1957–1984 are from rawinsonde observations (RAOB) and data from 1979–1986 are from NMC analyses.

NMC temperature data (see Chapter 6). They found that the MSU radiances simulated from the NMC temperatures were in general agreement, apart from a constant offset. In general, the brightness temperatures from the NMC data were biased 4–7 K higher than the MSU data, either because of the crude weighting function used in the simulation or the poor vertical resolution of the NMC data. The interannual variations of the two data sets match fairly well. The difference between 1979 and 1985 is similar in the two data sets: approximately 8 K in the MSU data and 9.5 K in the NMC data.

Comparison of NMC October 1979 50hPa temperatures to GFDL FGGE* IIIb October 1979 50hPa temperatures (Lau, 1984) shows good agreement. Near the minimum in temperature and ozone, the NMC data were approximately 2 K warmer than the GFDL data, while near the maximum, NMC data were approximately 2 K colder than those from GFDL. In spatial pattern, NMC and GFDL 50hPa temperatures are virtually identical.

One objective of these comparisons is to verify the 1979–1985 temperature changes observed in the NMC data. However, not much RAOB data is available for these later years (Figures 11.31, 11.32, and 11.34). On the other hand, both 1979 and 1983 have numerous reports that make a

---

*Geophysical Fluid Dynamics Laboratory First GARP (Global Atmospheric Research Program) Global Experiment

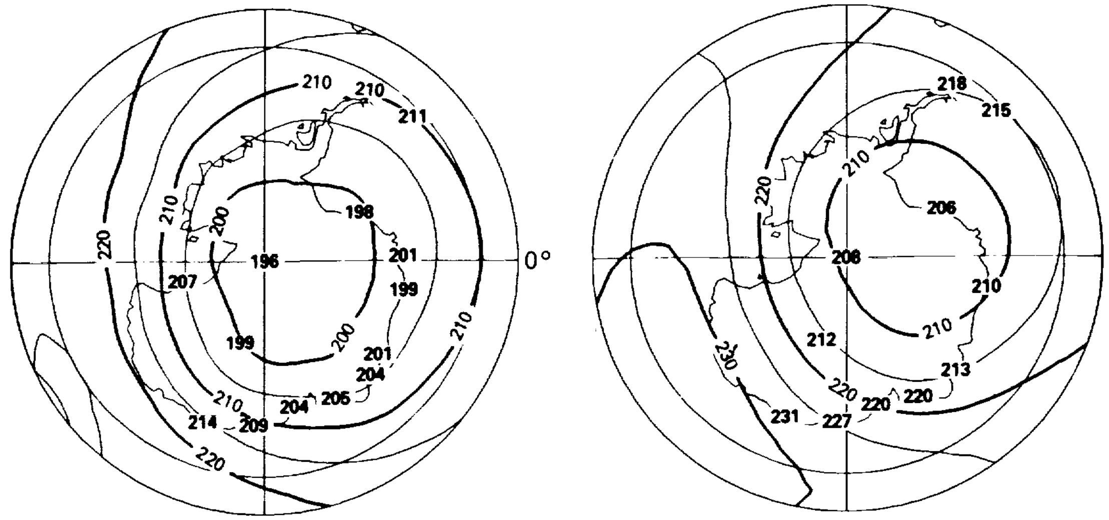

a) 1983 100 mb OCTOBER TEMPERATURE

b) 1983 30 mb OCTOBER TEMPERATURE

210
210
211
198
196
201
199
207
210
200
220
199
200
201
204
206
204
210
214
209
220
0°
218
215
210
220
206
208
210
212
210
213
230
220
220
220
231
227
0°

c) 1983 TOMS OCTOBER TOTAL OZONE

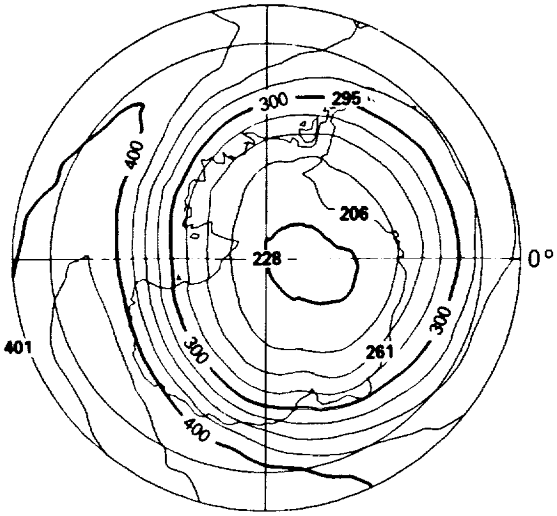

300
295
400
206
228
300
401
300
261
400
0°

Figure 11.33. October 1983 maps of (a) temperature at 100 mb (hPa), (b) temperature at 30 mb (hPa), and (c) TOMS total ozone. Taken from Newman and Randel (1988).

direct comparison possible. Additionally, the 1983–1979 differences are very similar to the temporal trends calculated for 1979–1986 (Figure 11.35). Figure 11.36 (from Newman and Randel, 1988) shows the NMC-observed 1979–1983 differences over the polar region at 100hPa; superimposed over the station locations are values calculated from RAOB data. The patterns and magnitudes are in good overall agreement, with the NMC differences being smaller on the east coast of Antarctica. A similar comparison is shown in Figure 11.36 for 30hPa, with the 1983–1979 differences showing remarkable consistency between these data sources. Again, the NMC differences are somewhat smaller than the RAOB values over the east coast. Inspection of the individual years suggests that this results from the underestimation of temperatures by the NMC retrieval scheme over this region during the warm southern spring of 1979 (see Figures 11.31, 11.32, and 11.34). The good agreement between NMC and RAOB differences in Figure 11.36

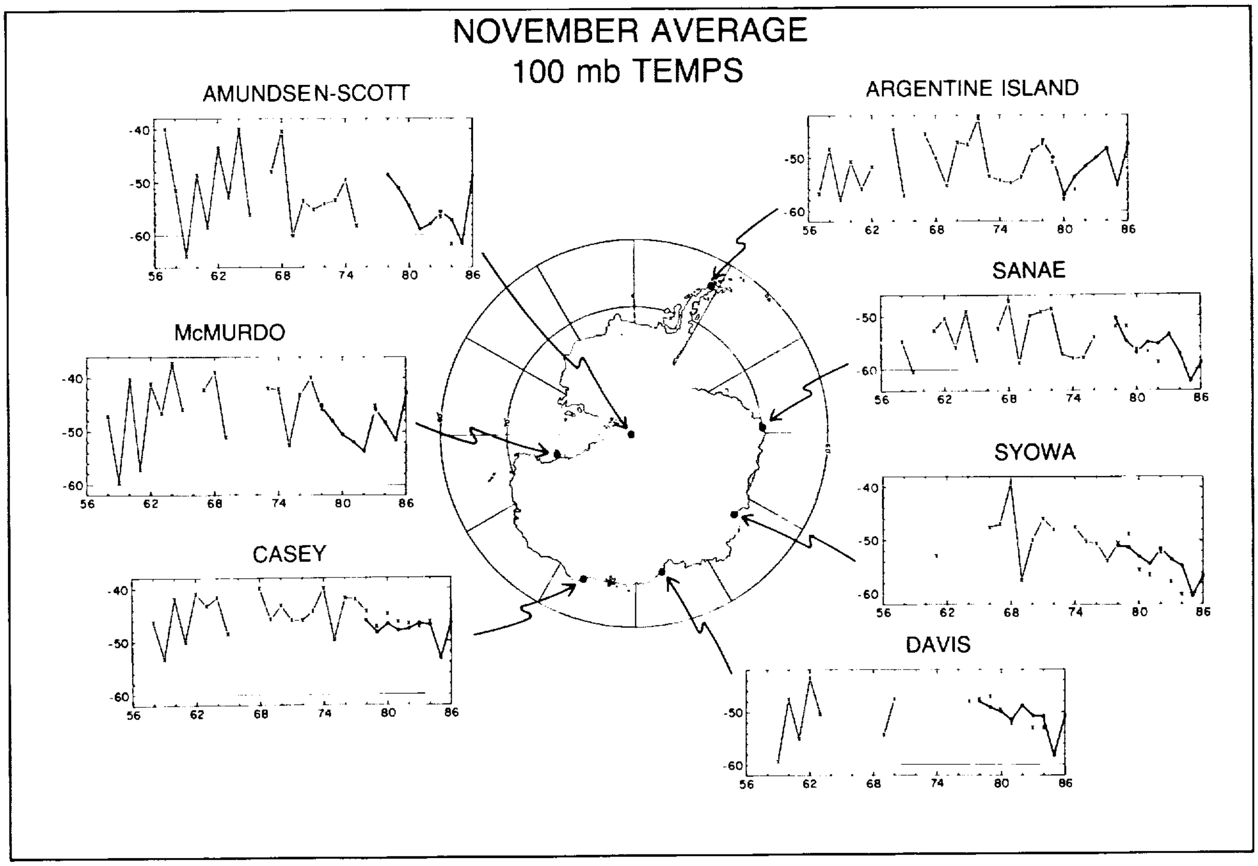

Figure 11.34. Time series of November mean 100 mb (100hPa) temperatures over seven Antarctic stations. Data from 1957–1984 are from rawinsonde observations (RAOB) and data from 1979–1986 are from NMC analyses.

lends confidence to the NMC temperature trends discussed previously. The RAOB's suggest that temperature differences might be slightly larger than those given by NMC values. Note that the highly asymmetric patterns seen in Figure 11.36 clearly caution against the calculation of trends based on values from irregularly spaced station data.

11.2.3.3 Rawinsonde Analyses

In the paper that first announced the recent decline in total ozone over Antarctica, Farman et al. (1985) stated that no corresponding trend in the temperatures at the 100 mb level was measured with rawinsondes over Halley Bay and the Argentine Islands. Sekiguchi (1986) and Chubachi (1986), on the other hand, found a significant recent decline in springtime stratospheric temperatures at Syowa for October and November. Sekiguchi's plots of total ozone and 100hPa temperature, shown in Figure 11.37, suggest that trends in ozone and temperature persist into November and December. The interannual variations of these two quantities are strongly correlated over the 20-year period shown, with 1979 and 1982 appearing as years with relatively high temperatures and ozone in both October and November.

Many authors who have reported declines in south polar stratospheric temperatures in recent years also noted the correspondence with decreasing total ozone (e.g., Sekiguchi, 1986;

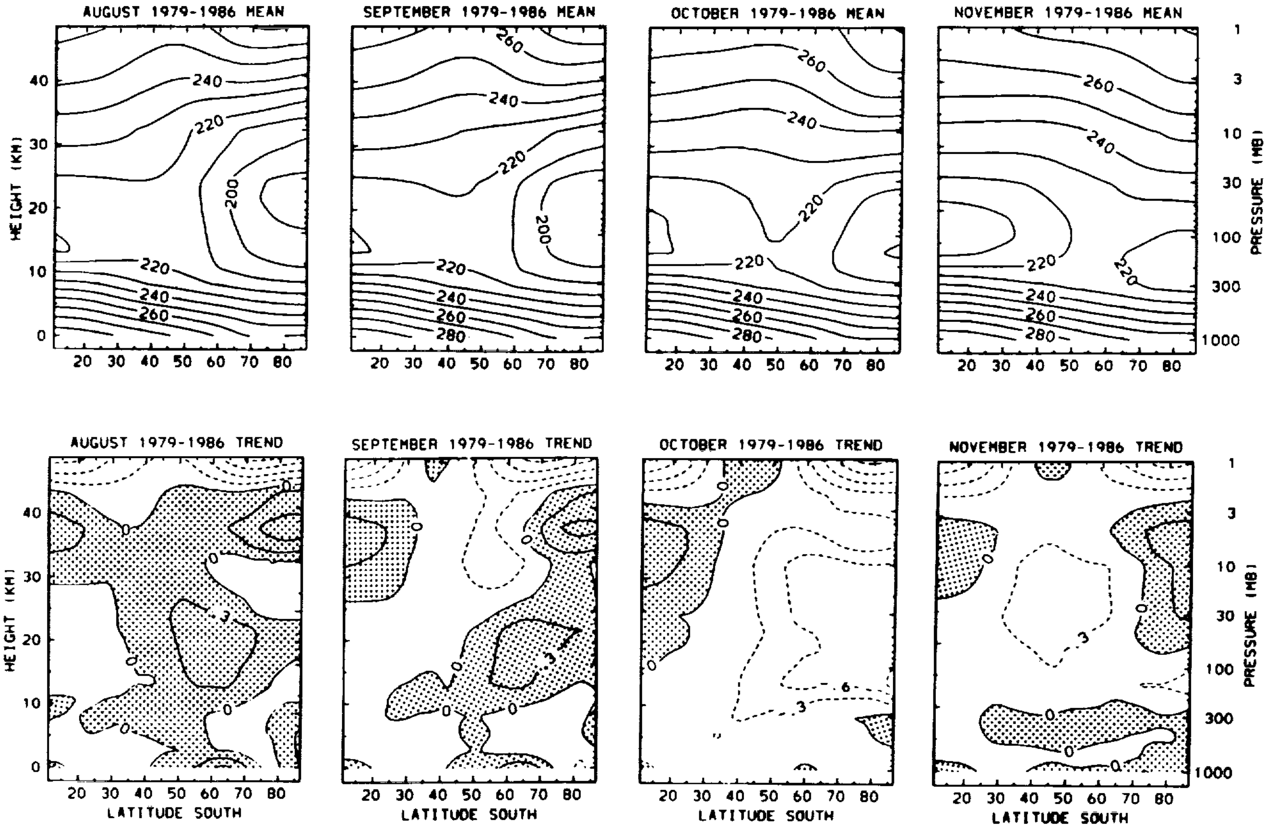

Figure 11.35. NMC 1979–1986 zonal mean temperature averages (top, °K) and 1979–1986 trends (bottom, °K/yr) for August, September, October, and November. Taken from Newman and Randel (1988).

Newman and Schoeberl, 1986; Newman and Randel, 1988; Chubachi, 1986; and Angell, 1986). Temperature and ozone do not decrease monotonically over these years, due to large interannual variability (i.e., the relatively warm, active years of 1979 and 1982, and the cold, quiescent years of 1980, 1983, and 1985; see Farrara and Mechoso, 1986; Shiotani and Gille, 1987; and Newman, 1986). Garcia and Solomon (1987) reemphasized an apparent association of polar temperatures and total ozone with the sign of the equatorial lower stratospheric quasi-biennial oscillation (QBO), although the mechanism for this association is not fully understood (see also Hasebe, 1984). Since the QBO was in opposite phases during 1979 and 1985, some part of the trend estimate over the 1979–1985 period can be attributed to the QBO. This component of the estimated trends is believed to be small, however, so that linear trend analysis can be applied to time series over 1979–1985 to objectively identify large temporal changes over these years.

Angell (1986) considered a composite of rawinsonde temperatures from 16 stations distributed over the Antarctic continent. Some of his results are reproduced in Figure 11.38. Two features are readily apparent: the natural level of interannual variability appears to be much greater in the spring (SON) season, and a consistent decline in temperatures during this season appears to have been sustained since 1979. This cooling trend has a temporal signature similar to the recent trend in total ozone. Both total ozone and lower stratospheric temperature have been below normal and declining approximately linearly with time since about 1980. Angell's time series ended in 1985, a year known to be relatively cold; when combined with the method of smoothing the time series, this gives a very strong suggestion of a cooling trend in recent years.

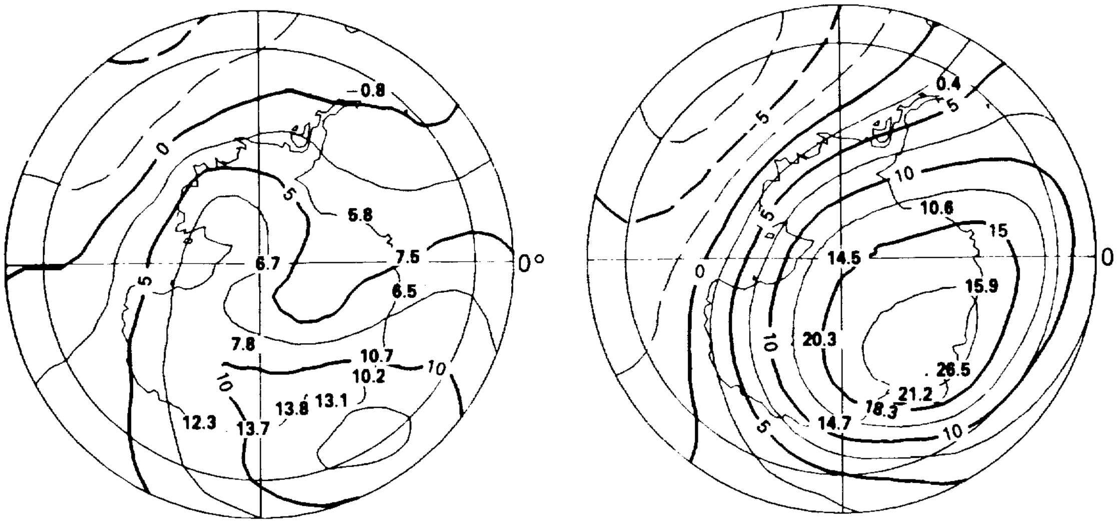

a) OCT. NMC 100 mb TEMP DIFF 79–83

b) OCT. NMC 30 mb TEMP DIFF 79–83

c) OCT. TOMS TOT OZONE DIFF 79–83

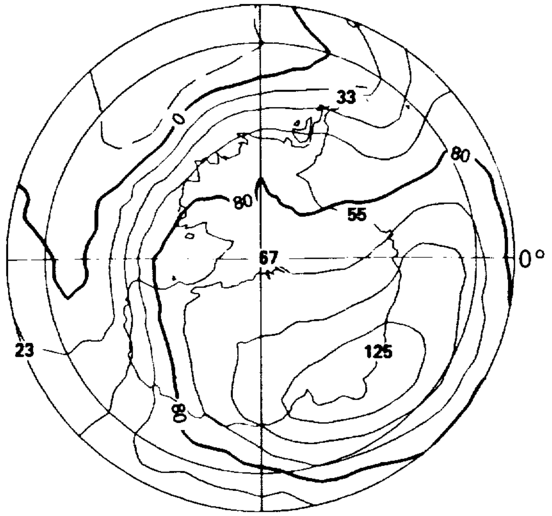

Figure 11.36 NMC temperature differences between 1979–1983 at (a) 100hPa and (b) 30hPa, with RAOB differences superimposed in bold type. The bottom figure shows the TOMS total ozone difference. Taken from Newman and Randel (1988).

Since he used a seasonal rather than a monthly basis in preparing the data, it is impossible to say which months contribute most to the indicated cooling. Evidence presented below suggests that the greatest changes occurred during October and November.

The contrast between the behavior of 100hPa temperatures at Halley Bay, where no trend appears, and Syowa, where for October and November means there does appear to be a trend, is probably related to the large amount of geographic structure in monthly mean temperature changes. Figure 11.31, taken from Newman and Randel (1988), shows time series of October-mean 100hPa temperatures from a selection of stations around Antarctica. It is apparent from this figure that the variations from year to year and from station to station are on the order of

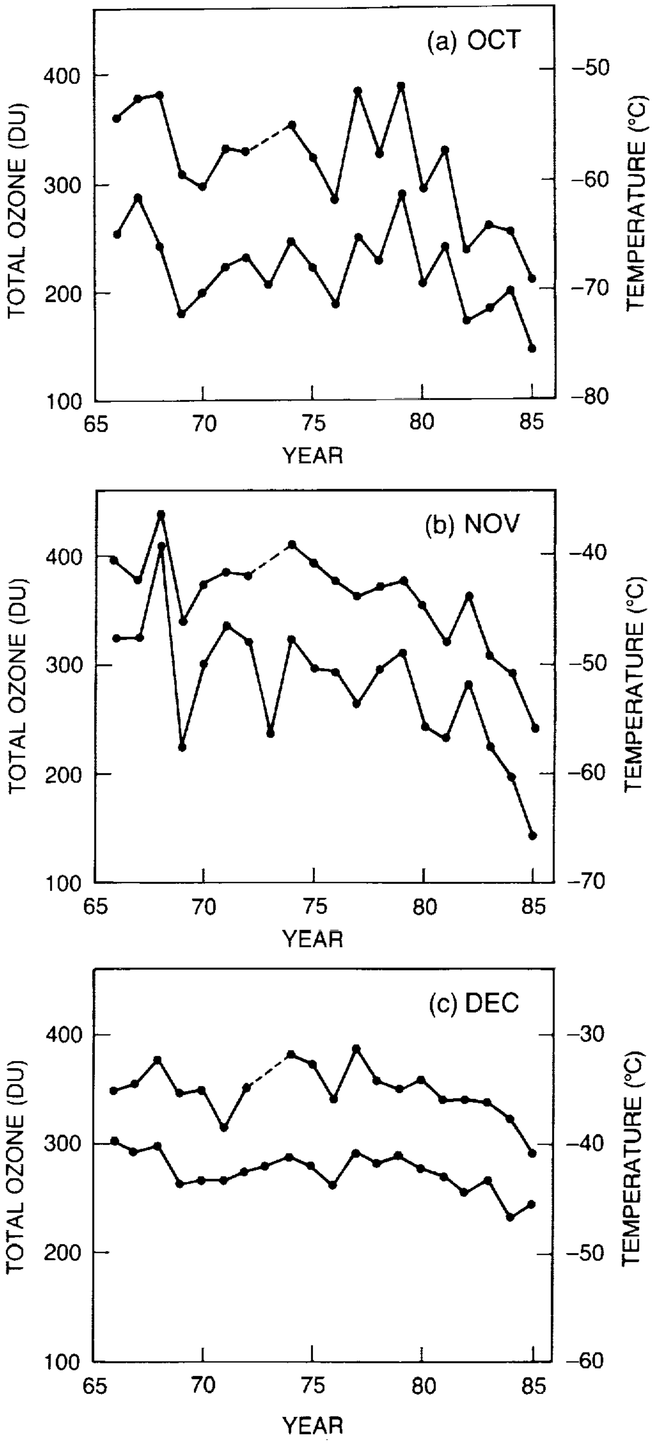

Figure 11.37. Year-to-year change of monthly total ozone amount and 100hPa temperature at Syowa Station: (a) October, (b) November, and (c) December. Taken from Sekiguchi (1986).

10 K—larger than any trend that has occurred during the past 5 to 10 years. These data show that while 1979 was relatively warm, it is not the warmest year in the record. Likewise, while 1985 was cold, several other years were nearly as cold, or colder (such as 1969 and 1973). Stations along the

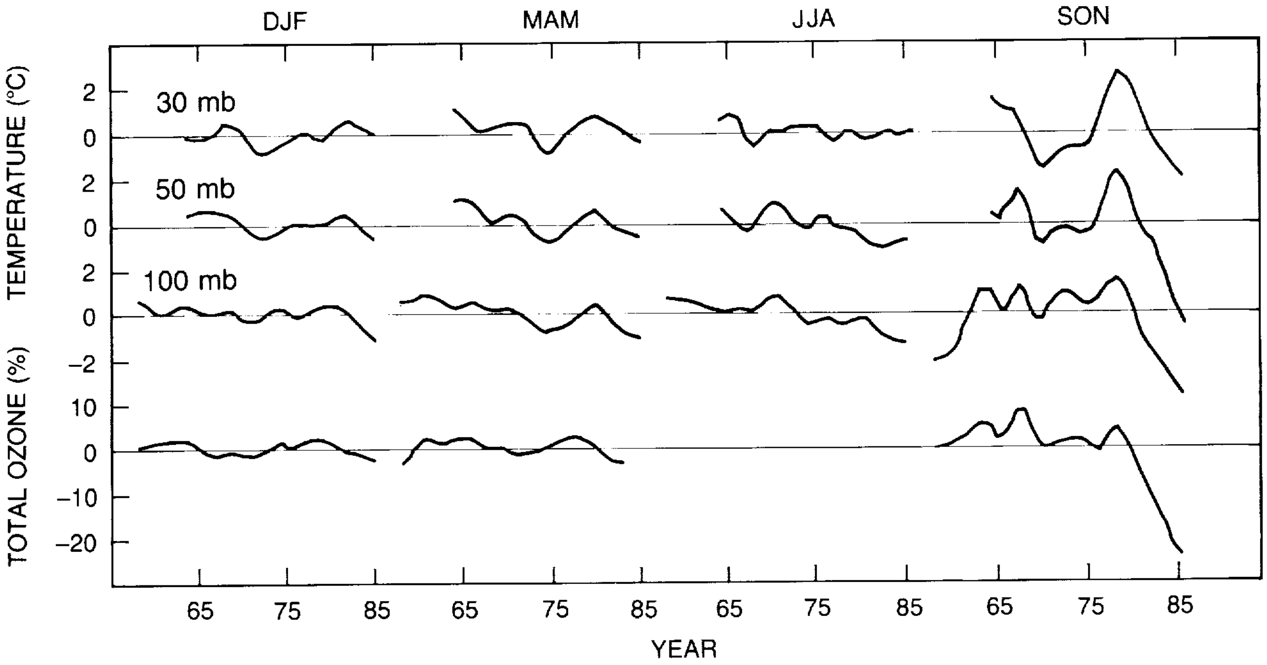

Figure 11.38. Smoothed seasonal (DJF is December–January–February, etc.) temperature deviations at 100, 50, and 30hPa above Antarctica compared with smoothed seasonal total ozone deviations in Antarctica (except for JJA, for which there were insufficient data for analysis). The smoothing involved a 1–2–1 weighting applied twice, except 1–1 at the beginning and end of the record. Taken from Angell (1986).

east Antarctic coast, such as Molodeznaja, Davis, and Casey, show a modest, but consistent, decline between 1979 and 1985, but 1986 was a warm year and breaks the appearance of declining temperatures at these stations. October temperatures at all of the stations shown were significantly higher in 1986 than in 1985. Preliminary data (not shown) indicate that 1987 was again cold. A substantial amount of this year-to-year variability may be associated with the QBO.

Monthly mean temperatures at 100hPa for November are shown in Figure 11.34. The general conclusions are the same as for October. Interannual variability is large, and a succession of years with declining temperatures in east Antarctica was interrupted in 1986 by a relatively warm year at many stations. Although the time series from 1966–1985 at Syowa suggests a long-term downward trend (as discussed in Chubachi, 1986, and Sekiguchi, 1986), data at other stations do not show such a consistent decline. When the temperature variations over 1979–1985 are viewed in longer term perspective, particularly with the inclusion of the warmer 1986 spring, the appearance of a downward trend in recent years is less convincing. October average temperatures for the 30hPa level are shown in Figure 11.32. At this higher level, the amplitude of the year-to-year changes is greater, but the impression of declining temperatures since 1979 is correspondingly stronger and the rise in 1986 is comparatively smaller. Although several stations indicate declining temperatures in recent years, the level of natural interannual variability in station data and the relatively recent onset of the ozone decline make it difficult to determine the existence or magnitude of a secular trend in temperature. The frequent occurrence of cold years recently (1980–1981, 1983–1985) may or may not be associated with a long-term trend.

11.2.3.4 Analyzed Fields

Analyzed maps of temperature based on a combination of rawinsonde and satellite data are available from the NMC. Figure 11.35 (from Newman and Randel, 1988) shows monthly averaged zonal means of temperature and their linear temporal trends (calculated by regression at each point in the latitude–height plane) over 1979–1986, for August through November. The zonal mean temperatures show the substantial seasonal increase in the temperature of the polar lower-to-middle stratosphere between August and November. The morphology and dynamics of the spring warming in the Antarctic stratosphere have been documented by Farrara and Mechoso (1986), Shiotani and Gille (1987), and Mechoso et al. (1988).

A linear temporal trend calculated from a number of years of data is a more robust method for determining decreases with time than a simple difference between any 2 years. The period 1979–1985 has often been used in calculating recent trends because satellite data are readily available for it. Monthly mean temperatures for October show the largest decline over 1979–1985, with large negative trends indicated for much of the lower-to-middle stratosphere poleward of 50°S. November trends show cooling primarily in the polar lower stratosphere near 100hPa. The variation in monthly mean trends in Figure 11.35 suggests that the September–November averages of Angell (1986) give a substantial underestimate of the magnitude of the October temperature change, since no trend is apparent during September. In fact, computations of temperature trends for individual stations by month instead of by season are in excellent agreement with the zonal mean trends shown here (Angell, 1987, private communication).

11.2.3.5 Conclusion

Substantial evidence has been presented for a decline in the temperature of the lower stratosphere over Antarctica since 1979 in October and November. The downward trends appear most strongly in October, when a substantial decline is observed in the middle as well as in the lower stratosphere. During November, the trend is confined to the lower stratosphere, with a maximum negative trend of about 1 K per year, centered at about the 100hPa level. August and September temperatures show little or no trend over 1979–1985. The decline appears in both rawinsonde station data and NMC gridded data that include satellite information.

11.3 TRANSPORT THEORIES FOR THE ANTARCTIC OZONE HOLE

11.3.1 Basic Dynamical Concepts and Ozone Transport

An understanding of the distribution of total ozone requires the integration of chemical, radiative, and dynamical processes. Because the source of ozone in the stratosphere is photodissociation of the oxygen molecule, the largest production of ozone would be expected in the latitude belts with the most intense insolation. If all of the chemical mechanisms for removing ozone from the stratosphere are also included, photochemical processes acting alone would still produce the maximum amount of total ozone in the Tropics. The distribution of the total ozone column with latitude and season bears little resemblance to what would be expected on the basis of the latitudinal and seasonal distribution of the net photochemical source of ozone. Figures 11.39 and 11.40 show the distribution of zonal-mean total ozone with latitude and season as derived from ground-based observations prior to 1974 by Dütsch (1974), and from the TOMS

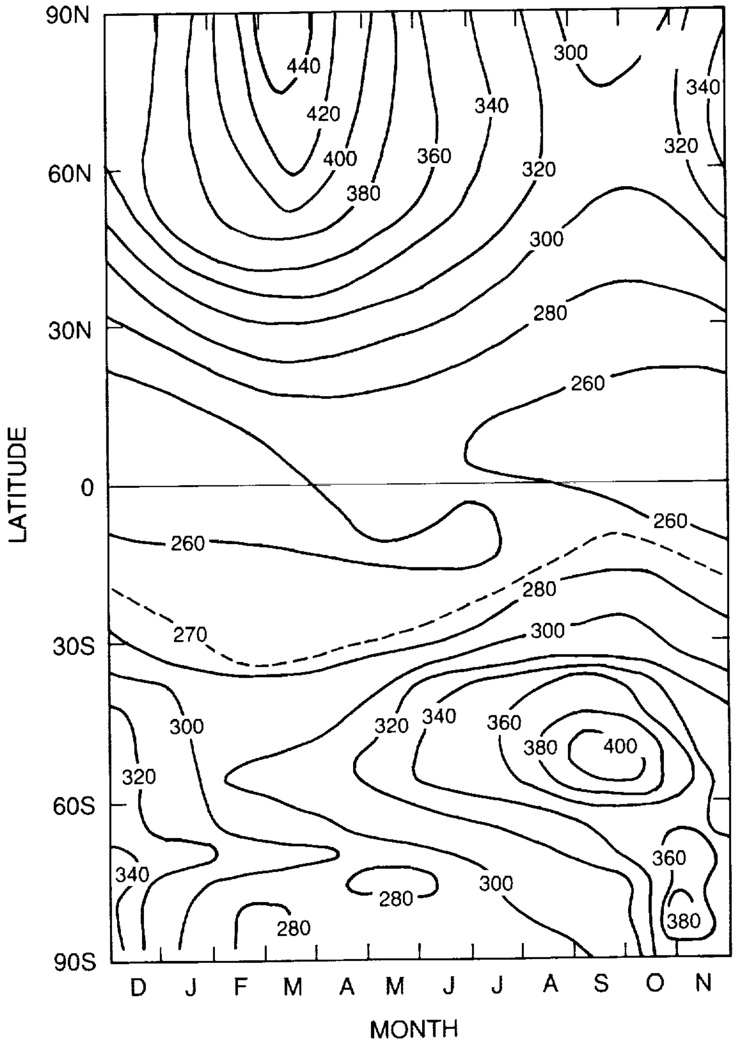

Figure 11.39. Latitude–time contour plots of the annual variation of zonal mean total ozone from Dobson stations before 1974 (from Dütsch, 1974).

instrument on the Nimbus–7 satellite from October 1979 to September 1982 (Bowman and Krueger, 1985). The maximum total ozone occurs not in the Tropics, where the source is greatest, but, rather, in high latitudes. In the polar regions, the maximum occurs not in summer, when the insolation is greatest, but in early spring.

The distribution of total ozone measured by TOMS shown in Figure 11.40 (Bowman and Krueger, 1985) also reveals the dramatic differences between the northern and southern polar regions that have been known since the early 1960's. In the Northern Hemisphere, the maximum ozone column of about 440 DU occurs near the pole around April 1. In the Southern Hemisphere, the maximum of about 400 DU appears off the pole at about 60°S November 1, which is later in the austral spring season than the maximum occurs in the boreal spring. The maximum ozone at the South Pole does not occur until around December 1, and reaches a value of only about 350 DU. Earlier ground-based measurements support the much later and weaker increase of total ozone in the Antarctic than in the Arctic (Dobson, 1966). The dip in total ozone near the South Pole in October shown in Figure 11.40 is the signature of the springtime Antarctic depletion that

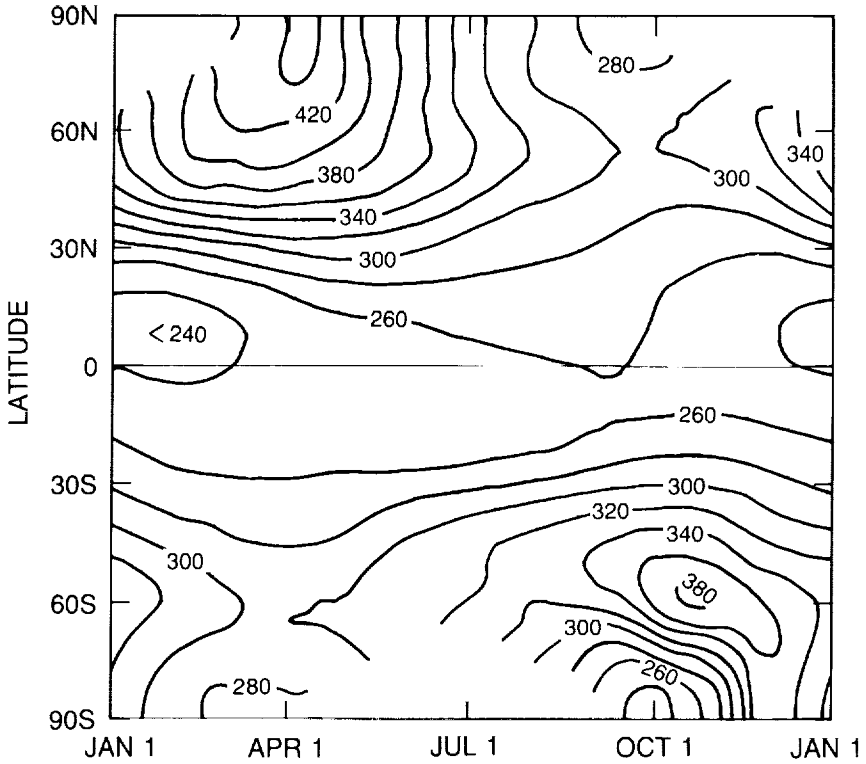

Figure 11.40. TOMS satellite data versus latitude and season between 1979–1982 (from Bowman and Krueger, 1985).

developed sometime after 1975. Earlier data presented by Dobson (1966) for Halley Bay (76°S) and the South Pole show no such depletion, with total ozone values around 280 DU for both September and October (see also Komhyr et al., 1986, and Bojkov, 1986b).

The observation that maximum column ozone amounts are always observed at locations and times that are so strikingly different from those of the maximum photochemical source of odd oxygen was a subject of great interest to pioneers such as Chapman and Dobson. The explanation is well known and well understood, at least in broad outline. It begins with the fact that most of the ozone resides in the lower stratosphere, where photochemical sources and sinks of ozone are normally rather slow, and thus where ozone normally has a long lifetime. The increase during winter of the total ozone column in high latitudes is produced by a downward and poleward transport of ozone from the production region in the middle stratosphere (e.g., Brewer and Wilson, 1968). An early calculation of the meridional circulation in the stratosphere was made by Murgatroyd and Singleton (1958). More recent calculations of the mean meridional circulation in the stratosphere have been made by Dunkerton (1978), Holton and Wehrbein (1980a,b), Gille et al. (1987), and a number of others. Discussions of the processes that maintain these circulations can be found in Chapter 6 of *WMO* (1986) and Chapter 7 of Andrews et al. (1987).

The intensity of meridional mass circulation in the stratosphere is determined by a complex interaction between radiative and dynamical driving. To simplify consideration of these mechanisms, it is often useful to separate the fields of interest into the average around latitude circles, the zonal average or mean, and the deviations therefrom—the eddies. This separation is not without pitfalls, however, since the definition of mean, and hence the division into mean and eddies, is inherently arbitrary, and chosen for mathematical and graphical convenience. In general, the zonal mean and the eddies are neither logically nor physically independent. When the flow becomes distorted and nonlinear processes become dominant, the insight that can be provided by separation into zonal mean and eddies becomes severely limited. If the definition of mean is chosen carefully, the mean motion takes the form of the "transport circulation" or, approximately, the "residual" or "diabatic" circulation (Plumb and Mahlman 1987 discuss the relationship between these; see also *WMO* 1986, Chapter 6). The remaining eddy effects are frequently diffusive and approximately directed along isentropic surfaces. A formulation of the governing fluid dynamical equations that provides the convenience of the zonal mean/eddy decomposition with a minimum amount of potential for confusion is the Transformed Eulerian Mean (TEM) formulation (Andrews and McIntyre, 1976; Boyd, 1976; Edmon et al., 1980). The equations for this formulation and some of its dynamical consequences are given in Chapter 6 of *WMO* (1986). For the purposes of this discussion, it is useful to review several aspects of the zonal-mean mass overturning, or mean meridional circulation, that are especially apparent when viewed in the TEM context.

The mean meridional circulation is a response to the unequal distribution of solar heating, with latitude and the zonal force provided by wave driving. The climate in the stratosphere can vary widely, depending principally upon the amount of forcing of momentum associated with wave propagation from the troposphere. If the wave forcing is strong, as it is in the Northern Hemisphere during winter, then the temperatures will be relatively far from radiatively determined values. In this case, substantial radiative cooling, downward motion, and downward tracer transport will occur in high latitudes. If the wave forcing is weak, then the temperatures in high latitudes during winter will be colder and closer to radiative values, the radiative heat loss will be less, and the downward motion will be relatively weak. The latter case describes the situation in the lower stratosphere of the Southern Hemisphere where the ozone decline has been observed. The relationship between wave driving from below and the zonal mean state in the stratosphere is complicated by the fact that the upward propagating waves are strongly affected by the mean state. Conditions in the stratosphere are achieved by a complex interaction among radiative heating, wave driving from the troposphere, and dynamical processes within the stratosphere. Clear testimony to the potential for strong interactions between the upward propagating planetary waves and the zonal mean state in the stratosphere is given by the occasional major midwinter warmings observed in the Northern Hemisphere.

The difference in the mean mass circulations in the two hemispheres can partially explain the differences in the total ozone behavior between the polar regions in both hemispheres. The greater wave activity in the Northern Hemisphere, which is rooted in the greater east–west variations in continentality and orography there, leads to a stronger mass overturning and, hence, to a stronger downward transport of ozone in high latitudes. To this effect must be added the lateral mixing associated with the upward-propagating planetary waves when they break in the stratosphere. In the Northern Hemisphere, the polar vortex is often completely broken apart in midwinter by the action of upward propagating planetary waves. When this happens, air parcels in the lower stratosphere experience displacements of great distance in latitude that are, to a varying extent, irreversible, and that may lead to major redistributions of chemical species, including ozone. The remarkable differences between the total ozone distributions with latitude and season in the two hemispheres are closely associated with the fact that planetary waves are more intense and more extensive in the Northern Hemisphere, and that major warmings occur there.

In the Southern Hemisphere, thermal and orographic surface boundary conditions are more nearly zonally symmetric than in the Northern Hemisphere, so that the forcing by planetary waves is weaker (Mechoso et al., 1985). The resultant mean state consists of a nearly zonally symmetric vortex with rapid circulation around a relatively cold pole in the troposphere and lower stratosphere (e.g., Harwood, 1975a; Leovy and Webster, 1976; and Hartmann, 1976a,b, 1985). The contrast between the midwinter temperature distributions in the two hemispheres is shown in Figure 11.41a,b. The cold pool of air in the lower stratosphere over Antarctica is quite evident and very different from the much warmer lower stratosphere over the North Pole.

Because of the greater zonal symmetry of the lower boundary forcing, the polar vortex in the Southern Hemisphere is not only stronger, but maintains its integrity throughout the winter and well into the spring season. The final breakdown of the polar vortex is normally complete by April in the Northern Hemisphere, whereas in the Southern Hemisphere, a well-defined vortex in the lower stratosphere may exist until late November. The lower stratospheric polar vortex thus persists about 2 months longer into the spring season in the Southern Hemisphere. The contrast between the springtime circulations is illustrated in Figure 11.41c,d, which shows the zonal wind distributions for October in the south and for April in the north. A strong circumpolar westerly jet is centered at about 10hPa and 70°S, but in the north, the westerly jet has been obliterated by more intense planetary wave activity. The observed morphology and dynamics of the final spring warming in the Southern Hemisphere have been described by Farrara and Mechoso (1986), Shiotani and Gille (1987), and Mechoso et al. (1988).

Another way of viewing the dynamics of the polar vortex is through maps of potential vorticity on potential temperature surfaces (isentropic potential vorticity IPV maps, e.g.; Hoskins et al., 1985). Under adiabatic and frictionless conditions, both potential temperature and the distribution of Ertel's potential vorticity on isentropic surfaces are conservative quantities. Therefore, parcels remain on isentropic surfaces and maintain their potential vorticity as they move laterally on those surfaces. As a result, parcels of air cannot move laterally across IPV contours. The stratospheric polar jet stream is marked on IPV maps as a region of strong gradient. The jet stream axis is thus associated with a region where lateral mixing between high and low latitudes is inhibited to the extent that the flow is frictionless and adiabatic, and the potential vorticity experiences no irreversible mixing associated with Rossby wave breaking (McIntyre and Palmer, 1983). When the vortex is relatively undisturbed by asymmetric forcing associated with planetary waves, and a strong circumpolar jet stream and associated strong meridional gradient of potential vorticity exist, meridional mixing of chemical species can be expected to be weak. Under these conditions, the chemical composition inside and outside the polar vortex can be quite different. Even under very disturbed conditions, the core of the vortex may maintain its integrity, as suggested by numerical simulations of Juckes and McIntyre (1987). The vortex is eroded by wave breaking on its outer edge, with little exchange of air into the center of the vortex. The lower stratosphere of the Southern Hemisphere is, therefore, a nearly unique environment in which extremely cold temperatures are maintained for several months during winter and into the spring season, and where the lateral mixing between air that is inside and outside the polar vortex is inhibited during these months.

Several observed features of the ozone decline over Antarctica suggest that altered transport may be an important factor. First and foremost among these is that the decline occurs in a well-defined layer in the lower stratosphere between approximately 12 and 22 km (see Section 11.2). The decline is greatest in polar regions, with few observable reductions Equatorward of midlatitudes in the Southern Hemisphere. In this region, photochemical sources and sinks are normally considered to be relatively slow, and ozone concentrations are strongly influenced by

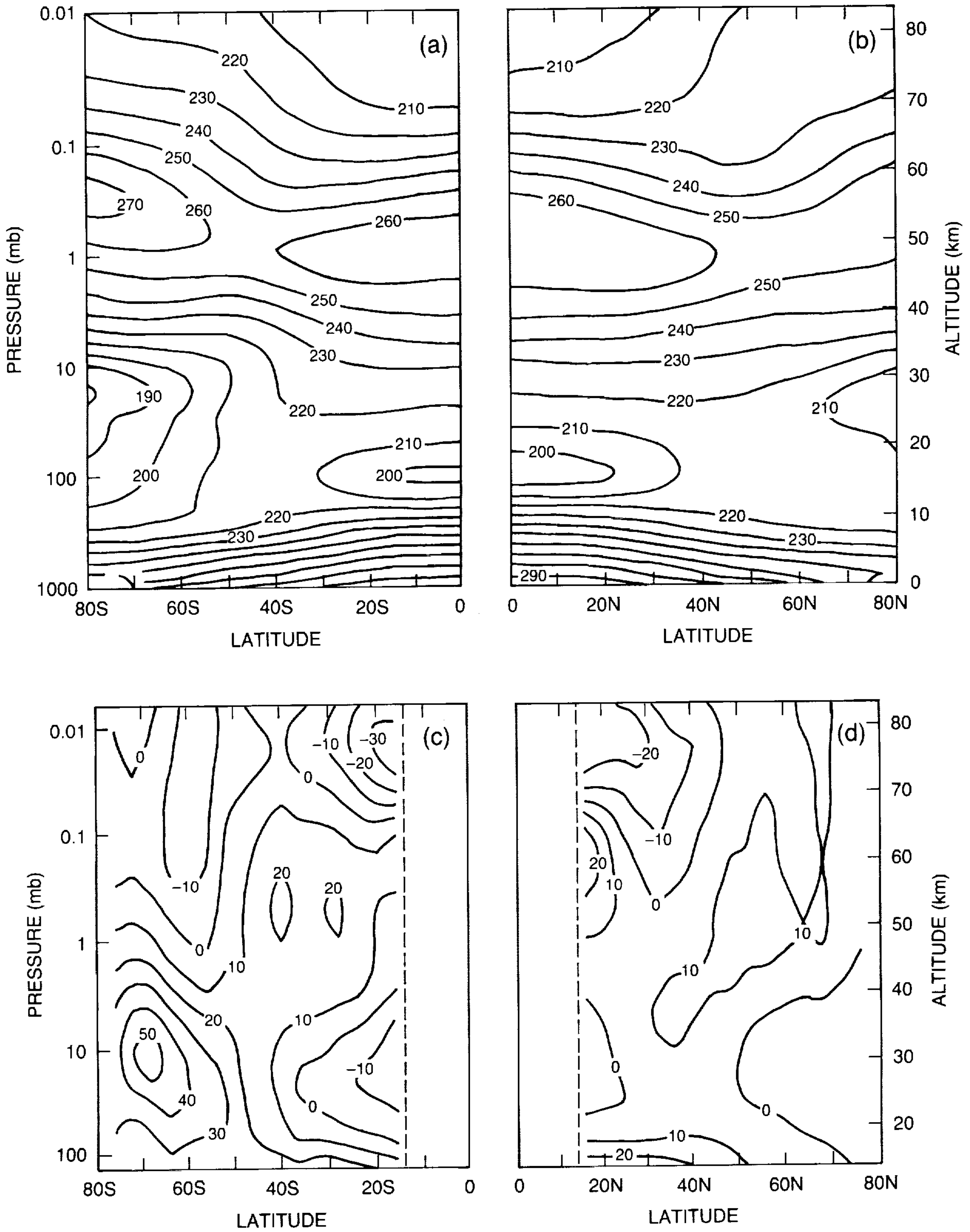

Figure 11.41. Five-year mean climatology of zonal mean temperature (K) for (a) July in the Southern Hemisphere and (b) January in the Northern Hemisphere, and of zonal mean wind (m/s) for c) October in the Southern Hemisphere and d) April in the Northern Hemisphere. Taken from Andrews (1989), who adapted the data from Barnett and Corney (1985).

air motions that move ozone downward and poleward. In polar latitudes, ozone concentrations are generally well above photochemical equilibrium values, as already mentioned (e.g., Dobson, 1930; Jackman et al., 1986). This ozone excess is maintained by transport. Because of their relatively small area and dependence on heat imported from other latitudes, the polar regions experience rather large interannual variability and might be expected to respond sensitively to small changes in climate.

Another important feature of the Antarctic ozone decline is that it is concentrated in the spring season. In recent years, the total ozone over Antarctica has departed rapidly from the climatological annual variation during September, yielding the maximum decrease of a monthly mean from previous decades during October. The monthly mean total ozone then returns to near normal by December. A decline during springtime could be associated with a change in the climate and transport in the lower stratosphere above Antarctica, since spring is the time when the polar vortex in the lower stratosphere is changing rapidly.

A key feature of the ozone distribution in recent years—one not previously observed—is that the total ozone declines in an absolute sense between September and October (Figure 11.40). This requires not merely a reduction in the downward and poleward transport of ozone during the spring season, but that this transport actually fall below the rate at which ozone is being photochemically destroyed in the lower stratosphere. If it is assumed that ozone is conservative in the layer of interest, then, to explain the observed decline, transport must actually remove ozone from the lower stratosphere. Within the context of the zonal mean/eddy decomposition used in the TEM formulation, for example, the removal of ozone must be accomplished either by the mean meridional motions or by mixing by eddies. Published transport theories for the ozone decline have focused on the transport associated with the mean diabatic circulation. Because of the rapid increase with altitude of ozone concentration in the lower stratosphere, the observed total ozone decline over Antarctica can be produced with an upward displacement of about 5 km during September. The alteration in the profile of the ozone-mixing ratio that would result from this uplift is similar to that observed.

11.3.2 Transport Theories for the Ozone Hole

In the previous section, the role of transport in determining the distribution of total ozone was reviewed. Because the depletion is confined to the lower stratosphere, where the gradients of ozone mixing ratio are substantial and transport is known to be important, it is reasonable to hypothesize that transport by atmospheric motions might play an important role in the recent decline of ozone over Antarctica. Because of the importance of arriving at the correct scientific understanding of the observed phenomena, it is essential to evaluate carefully the possibility that the ozone hole has resulted wholly, or in part, from an alteration in the transport of ozone from other latitudes, rather than from enhanced photochemical loss mechanisms. The transport theories for the ozone hole and the evidence for and against them will be reviewed in this section.

The central tenet of the transport theories for the Antarctic ozone depletion is that it is a consequence of reduced transport from lower latitudes. Since ozone exists in high latitudes in the abundance that it does, simply because of transport from its source regions by the atmospheric circulation, any interannual modulation of that circulation would be apparent in the column ozone at high latitudes. While on short time scales transport merely effects a redistribution of ozone, it may, over longer periods, affect the total atmospheric loading by determining how much ozone is removed from the middle stratosphere—where its chemical lifetime is short—and deposited into the lower stratosphere—where much of the total column amount of ozone is located.

To date, most dynamical studies have focused on the possible effects of trends in transport by the mean circulation. Therefore, most of the following discussion will concentrate on this aspect of the problem. Ozone depletion theories that include eddy mixing as well as mean circulations should probably be looked at more carefully in the future. At first sight, it might appear that any quasi-isentropic eddy mixing in high latitudes must increase the column in polar regions where total ozone has a spatial minimum. The isentropes slope steeply upward toward the pole, or, more precisely, toward the temperature minimum, and cross contours of ozone-mixing ratio. Quasi-isentropic transport into the polar region would bring air upward from the lower stratosphere, where ozone is less abundant, and could, therefore, cause a reduction of the high-latitude ozone column. Quasi-isentropic mixing by eddies requires much smaller associated temperature changes than does simple mean ascent.

While a dynamical explanation of the year-to-year decline of Antarctic ozone requires only that the gross effects of transport similarly decline, observations of the springtime seasonal decline place more severe demands on such theories. During this time, the mean motion in the lower stratosphere of high southern latitudes must be upward to bring ozone-poor lower stratospheric air into the high-latitude column. If consideration is limited to mean motions, upward motion appears to be the only alternative to a chemical sink as an explanation of the seasonal depletion. It is not required that the motion be upward everywhere in the polar region, but it is, of course, necessary that it be so where the depletion is occurring.

The mean circulation is driven by eddy transport processes and radiative heating (see *WMO*, 1986, Chapter 6). During transient episodes, such as following polar sunrise in September, both radiative heating and eddy transport are highly transient and could contribute to upward motion that would support the severe ozone decline observed then. Therefore, an interannual trend in high-latitude mean vertical motion could arise from either increased radiative heating or reduced eddy transport. Increased radiative heating might be associated with a trend in aerosol concentration, for example. Reduced eddy transport could be caused by changes in the wave generation processes in the troposphere or altered wave transmission properties of the stratosphere, and would be indicative of a more widespread climate drift in the Southern Hemisphere. In the case of reduced eddy transport of heat, reduced polar ozone should be accompanied by reduced polar temperatures. Evidence of such cooling during October and November and of other aspects of a climate drift, both in the stratosphere and troposphere, is noted in Section 11.3.3, although it is also demonstrated that the cooling of the lower stratosphere could be a radiative response to the ozone decline.

Published theories for the Antarctic ozone decline that invoke altered transport as a primary cause of the reduction during September and October all share certain basic assumptions. They assume that ozone in the lower stratosphere can be considered a conservative quantity on monthly time scales. This assumption requires not merely that there be a reduction of transport into the lower stratosphere, but that ozone actually be exported from the south polar region during September. The method that these theories use to remove ozone from the polar region is transient mean upward motion during the spring season.

Tung et al. (1986) noted that the lower stratosphere over Antarctica is exceedingly cold during the spring season, so that the radiative cooling is probably small when the Sun returns to Antarctica in September. Under these conditions, anomalous upward motion could be induced by a fairly small change in the climate. One mechanism that they proposed for producing this anomalous rising was heating associated with increased aerosol loading of the lower stratosphere. Tung and Yang (1988,1989) used a two-dimensional model to simulate the seasonal and latitudinal distribution of ozone. By using observed temperatures and determining the radiative heating by relaxing to calculated radiative equilibrium temperatures, they were able to obtain a reasonable simulation of conditions prior to 1979. Adding an arbitrary additional heating beginning in 1983 to simulate an assumed heating associated with El Chichón aerosols, they produced a springtime ozone minimum in fair agreement with that shown in Figure 11.40. Tung and Yang (1988,1989) needed an aerosol heating that reached a maximum of 0.5 K per day toward the end of October to produce the decline in total ozone.

Mahlman and Fels (1986) begin with the assumption that a reduction in wintertime planetary wave activity occurred some time after 1979. As outlined above, a reduction in planetary wave activity would result in reduced ozone transport into the polar lower stratosphere via reduced mean mass circulation and reduced eddy mixing. Reduced eddy activity in the stratosphere would also mean that the polar vortex would persist longer into the spring season. Reduced planetary wave activity during winter would produce lower total ozone during the spring season, but cannot by itself explain the observation that a good portion of the ozone decline occurs as an absolute decrease during September. To explain this transient decline, Mahlman and Fels (1986) invoked radiative heating as the Sun returns to Antarctica during spring. If the temperatures in the lower stratosphere are colder than normal in spring, then more polar warming is required to reach temperatures that are in equilibrium with the increasing insolation. Because momentum, as well as heat, must be readjusted to maintain geostrophic balance, part of the solar heating must be used to support vertical motion, while the remainder supports warming. In the absence of anomalous wave forcing, mean Equatorward motion is required to support deceleration of the westerly winds that must occur in association with the decrease of the meridional temperature gradient as the pole is heated. Continuity of mass requires rising motion over the pole to balance Equatorward flow at lower latitudes. Mahlman and Fels (1986) refer to this chain of events as the "flywheel effect."

Rosenfield et al. (1988) calculated total ozone changes following temperature minima in the NMC daily maps. They used observed temperatures and initial ozone profiles to calculate the change in the ozone profiles produced by vertical motions. The vertical motions were determined from the requirement that they balance the thermodynamic effect of the net radiative heating, given the observed temperature changes. Using this scheme, they found that the ozone column decreased during September at about the observed rate, with no need for aerosol heating. They pointed out that this result was very sensitive to the details of the radiative calculation.

Dunkerton (1988) proposed a somewhat different mechanism, which relies on the wave driving provided by tropospheric eddies. Tropospheric synoptic-scale eddies provide a strong deceleration of the mean westerly winds at about 10 km, as opposed to the planetary waves that propagate to much greater altitudes before producing the majority of their effects on the mean flow (e.g., Hartmann et al.; 1984, Mechoso et al., 1985). This intense deceleration requires a poleward mean meridional flow to balance the momentum loss. Dunkerton argued that this wave driving near 10 km induces downward mean flow below 10 km and upward flow above. The upward flow above 10 km is in the correct position to produce the observed ozone decline in the lower stratosphere. He hypothesized that if the planetary wave driving at higher altitudes were reduced, thus decreasing the diabatic sinking in the spring season, then the upward motion induced in the lower stratosphere by the synoptic-scale eddies might be sufficient to produce net upward motion there.

11.3.3 Evidence For and Against Transport Theories for the Ozone Hole

11.3.3.1 Evidence for a Climate Drift in the Southern Stratosphere

If a significant change in the circulation of the Southern Hemisphere stratosphere has occurred during the last 10 years, then this should be reflected in other variables besides total ozone. In particular, it may be expected that if a subtle climate drift were taking place, it would be rooted in some surface condition with a relatively long time scale, such as sea surface temperature or sea ice. In this section, the evidence for changes within the stratosphere is evaluated, and some evidence for tropospheric climate changes is discussed.

Temperature Trends

The participation of dynamical processes in ozone depletion is suggested by the observation of a downward trend in October mean stratospheric temperature at high southern latitudes. As discussed in Section 11.2.3, NMC analyses (Newman and Schoeberl, 1986; Schoeberl et al., 1986) show a negative trend in the Antarctic lower stratosphere of almost 1 K per year around 100hPa and about twice that between 30 and 10hPa (Figure 11.36). Little or no such trend is evident in the September monthly mean temperature. For November, only the trend centered near 100hPa is observed. The existence and structure of temperature trends over Antarctica for the months of September, October, and November of the past 10 years provide crucial clues to the processes contributing to ozone depletion. The structure, relative amplitude, and timing of the ozone and temperature changes provide information on the extent to which ozone depletion causes the temperature decline, or to which both have a common cause, such as an anomalous vertical displacement.

Evidence that the cooling is a radiative response to the ozone decline will be presented below. If we assume for the sake of argument that the cooling is not a radiative response to the ozone depletion, then the most obvious interpretation of the data is that both cooling and depletion are a response to a trend in vertical motion. Interpreted as an indicator of a mean circulation shift, the cooling trend in the Antarctic lower stratosphere implies a secular reduction or even reversal of the climatological mean subsidence there. On a day-to-day basis (and also spatially), a correlation between ozone and temperature is a familiar feature of the observational record and is usually taken to indicate the effects of adiabatic vertical motion on the two. Over short time scales, both ozone and potential temperature usually can be regarded as conservative, so that both respond to vertical motion in the same way, since both are strongly stratified in the vertical and, in the lower stratosphere, increase upward. That such effects can occur on an interannual basis in the south polar regions in spring is illustrated by the quasi-biennial oscillation in ozone and temperature there (Garcia and Solomon, 1987). Tung and Yang (1988, 1989) have estimated that upwelling that adiabatically induces a 2 K decrease in lower stratospheric temperature will cause a 3.5 percent depletion of ozone. Allowing for diabatic effects, they estimate a 7 percent ozone response for the same temperature change (i.e., the same temperature change would require twice the vertical displacement as in the adiabatic case). This is roughly consistent with the observed trends in total ozone and lower stratospheric temperature, though the relationship is sensitive to the assumed vertical gradient of the ozone-mixing ratio.

Even with the long radiative time scales of the lower stratosphere, significant memory in the thermal field is unlikely. The ozone in the Southern Hemisphere lower stratosphere, however, may be sufficiently long-lived for some portion of the springtime depletion to survive through the following year. This might be possible because of ozone's long chemical lifetime there and because, dynamically, the Southern Hemisphere lower stratosphere is relatively isolated from the rest of the atmosphere except in late spring. This possibility was suggested by Mahlman and Fels (1986), who noted that, in simple ozone experiments with the GFDL general circulation/tracer model (Mahlman et al., 1980), October total ozone at 84°S took several years to reach equilibrium with a constant source. There is some evidence of such memory in the observational record. TOMS total ozone data integrated over the area south of 44°S presented in Figure 11.15 suggest that a small part of the springtime ozone depletion may persist through the year. In particular, the very low values at the end of 1985 persist well into 1986 before recovering in May and June, at the beginning of the 1986 winter.

Labitzke (1987) has drawn attention to a sudden and apparently significant change that occurred around 1979 in the October mean geopotential height of the 50 mb surface at the South Pole. In fact, the year-to-year ozone depletion appeared to correlate better with the station geopotential data than with temperature. What this means, on the basis of data from a single station, is difficult to ascertain. The geopotential trend could indicate a change in the position or in the intensity of the circumpolar vortex. There is, in fact, some evidence for both of these possibilities. The synoptic structure of trends in stratospheric temperature or, for that matter, ozone (Figure 11.42), shows changes that are related to shifts in the location of both the polar vortex and the midlatitude anticyclone over the years since 1979. There also appears to have been a trend in the vortex intensity. Austin et al. (private communication, 1988) found a substantial increase in the area enclosed by a given potential vorticity contour on the 1,200 K isentropic surface (about 2hPa), but not at 850 K (about 10hPa), during 1979–1986.

Such changes in the transient, springtime stratospheric circulation could result from changes in the radiative drive (through changes in stratospheric aerosol loading, including PSC's) or in dynamical driving by eddy motions. There are some suggestions that there has indeed been a downward trend in the eddy driving. Nagatani and Miller (1987) argued that the Eliassen–Palm (EP) flux upward through the 100hPa surface of the Southern Hemisphere in September has declined since 1979. Figure 11.43, from Newman and Randel (1988), shows the structure of the northward eddy heat flux and its trend over the period 1979–1985. The poleward eddy heat flux

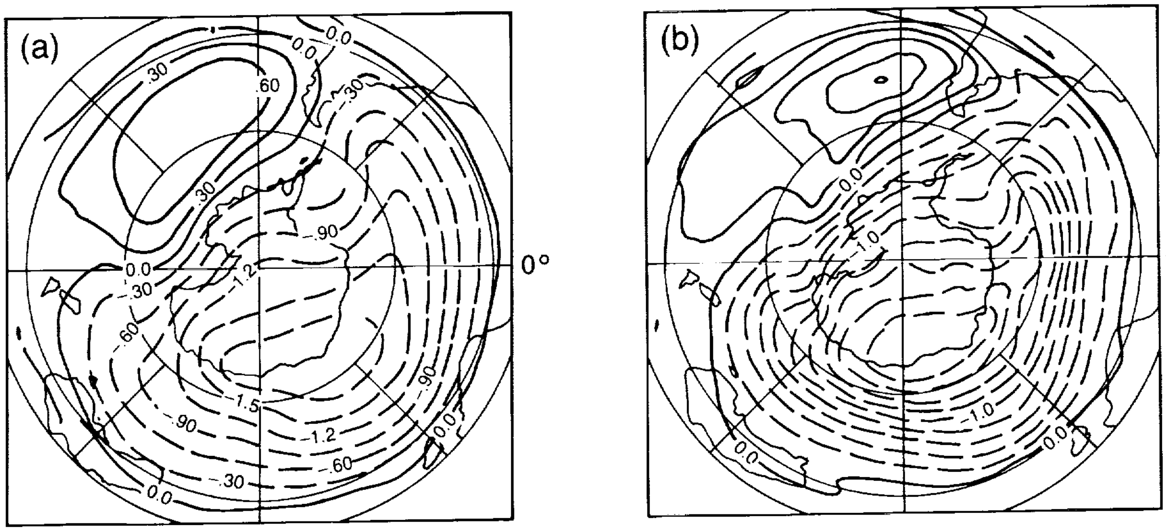

Figure 11.42. (a) October NMC 70 mb temperature trend from 1979 to 1985 and (b) TOMS total ozone trend over the same period. Taken from Newman and Randel (1988).

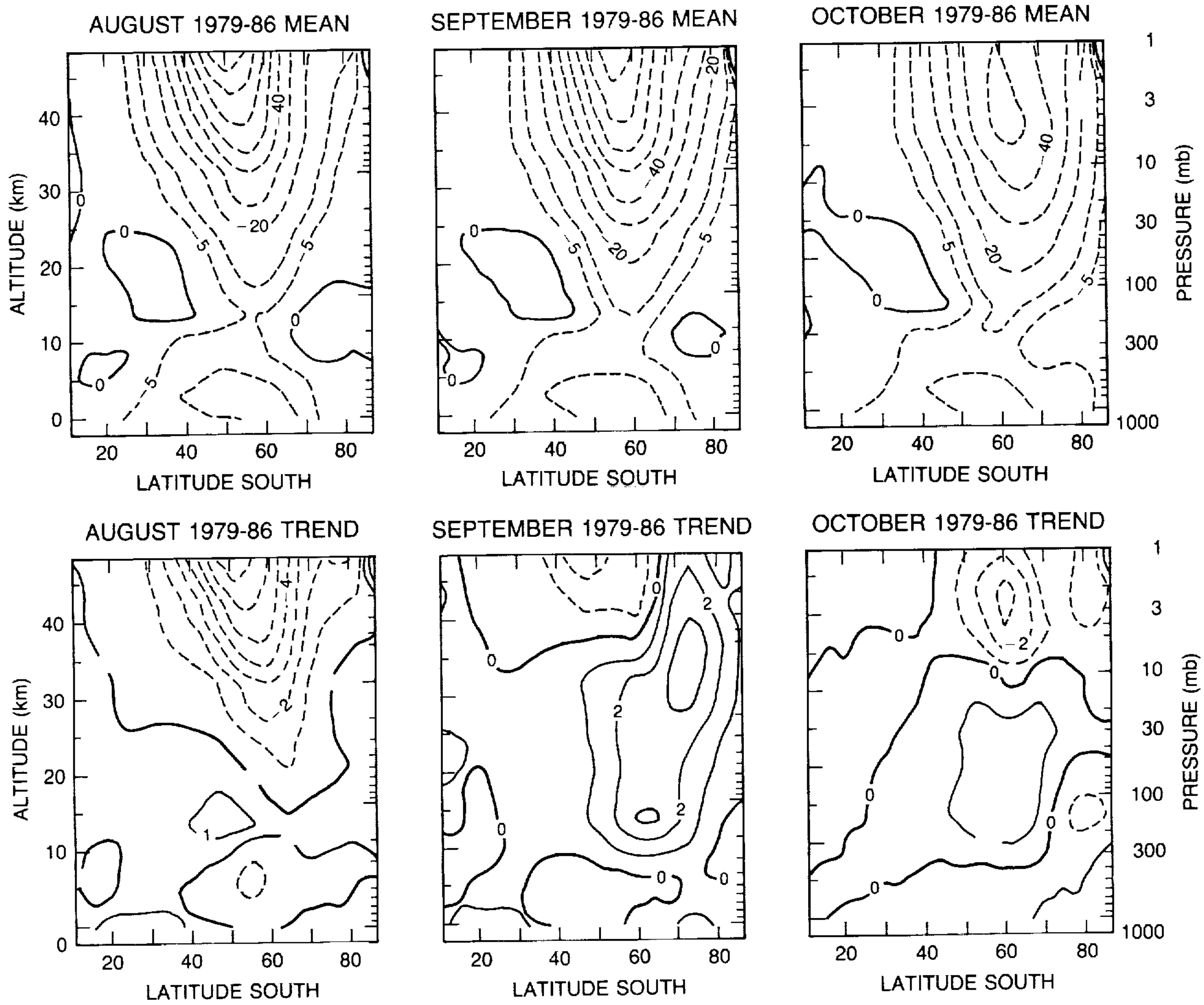

Figure 11.43. Northward eddy heat flux calculated from NMC analyses and averaged over 1979–1985 (top, °K m s^{-1}) and the trend in eddy heat flux (bottom, °K m s^{-1} yr^{-1}) over the same period for August, September, and October. Taken from Newman and Randel (1988).

is proportional to the vertical component of the EP flux, the measure of upward wave propagation. The flux averaged over September has declined everywhere, most markedly in the high-latitude lower stratosphere. Such a decline in the EP flux is qualitatively consistent with the notion that the dynamical driving of the meridional circulation has declined in recent years. October shows a similar, but smaller, decreasing trend. In view of the limited length of the available time series, however, such results should be treated with caution.

Evidence for a Tropospheric Climate Drift

A decline in the upward propagation of wave activity into the stratosphere must be indicative of some change within the troposphere, either in wave generation processes or in transmission characteristics. While direct evidence of such changes has yet to be provided, several examples of trends in key indices of the Southern Hemisphere tropospheric circulation are noteworthy.

Some recent studies have drawn attention to apparent tropospheric and surface temperature trends, especially at high latitudes. Folland et al. (1984) noted an increase in sea surface temperature (SST) over the southern oceans. Austin et al. (private communication, 1988) noted that this increase in winter sea surface temperatures correlates with the decrease in ozone. They also suggested that an increase in the area of the Antarctic sea ice has occurred in recent years. Further, they found evidence for an Equatorward shift of the winter westerlies throughout the troposphere. On the basis of radiosonde data, Danielsen and Houben (unpublished manuscript) found a similar drift of the westerlies in September throughout the depth of the troposphere and lower stratosphere. Unfortunately, it is not clear what significance such trends have for the generation of large-scale planetary waves, since the processes responsible for their generation in the Southern Hemisphere are far from being fully understood.

Unclarified Issues: Causal Mechanisms

An interannual trend in vertical velocity in the springtime southern stratosphere may provide an explanation for the ozone decline; however, the ultimate cause of this climate change has yet to be clarified. Current quantitative dynamical theories (those of Tung and Yang, 1988, 1989; Rosenfield et al., 1988) deduce the mean vertical velocity diagnostically from observed temperatures without attempting to probe the underlying processes driving the circulation. It was noted earlier that the circulation arises from the effects of both radiative and mechanical driving and that interannual trends in the circulation must, therefore, result from trends in one or both of these.

Tung et al. (1986) proposed that increased volcanic aerosols would lead to increased springtime heating in the lower stratosphere. However, these aerosols have, in fact, been decreasing in recent years (McCormick and Trepte, 1986) without any sign of Antarctic ozone returning to normal. Therefore, it seems unlikely that volcanic aerosols can be the cause of the continuing decline of ozone in 1987, though they may have played a role in the early stages of the decline.

On the other hand, Mahlman and Fels (1986) suggested that the circulation change is a response to a decreased dynamical drive, not only allowing the flywheel effect to operate (whereby the transient radiative heating in springtime may drive an upward motion in the polar cap), but also, more generally, resulting in less poleward transport and, therefore, less ozone. The strength of this flywheel effect and its ability to operate on interannual time scales to produce a long-term trend have not been established. Moreover, the temperature trends observed occur for October and November, after the greatest ozone tendency anomaly during September.

Dunkerton (1988) has shown that a transient EP flux convergence in the upper troposphere will drive upward motion in the high-latitude lower stratosphere. Observations suggest, however, that the driving by the tropospheric wave field is relatively steady at this time of year and that the response to steady upper tropospheric driving would be confined to the lower levels. As yet, few theoretical studies of the wave-driven meridional circulation of the springtime southern stratosphere have been made.

Radiative Response to the Ozone Decline

According to the calculations of Shine (1986), some, if not all, of the temperature trend could be a radiative response to the ozone depletion. He found a maximum cooling of 6 K at about 50hPa in response to a 25 percent decrease of column ozone applied to a profile from Syowa between the 250 and 31hPa levels. Calculations similar to Shine's have been completed by several groups for use in this document. Radiatively determined Antarctic temperatures were computed both with and without an ozone depletion. These calculations used the radiative transfer models shown in Table 6.11, Chapter 6. Spring 1986 ozone measured at McMurdo station was used from the surface up to 30 mb (Hofmann et al., 1989). Above 30 mb, ozone climatology given by McPeters et al. (1984) was used. Figure 11.44 shows time–height contours of the ozone-mixing ratios in ppmv.

The calculations began on September 1. The initial temperature profile, from September 1, 1986, NMC data, was located inside the vortex at the 70 mb temperature minimum. The temperatures throughout the next 2 months were determined by time integration, using only radiative heat transfer. In the depleted ozone runs, the ozone-mixing ratios used were those shown in Figure 11.44, while for the undepleted ozone runs, the ozone-mixing ratios were fixed at the September 1 values. The total ozone on September 1 at McMurdo was 218 DU. A Syowa 1982 Antarctic balloon water profile (Iwasaka et al., 1985b) was used from the surface to 116 mb. Above 116 mb, the water vapor was set at 3 ppmv; no clouds were included. In Models 1 and 3, the solar pathlength computations were modified to include Earth's spherical geometry.

Time–height contours of the computed differences in the radiatively determined temperatures for a latitude of 80°S are shown in Figures 11.45, 11.46, and 11.47, for Models 1, 2, and 3, respectively. The models agree with a maximum cooling of −1.5 K by the end of September, and a mean cooling for the month of September of much less than −1 K. The models also agree in predicting a maximum cooling of −6 K to −6.5 K by October 30. In Models 2 and 3, this minimum

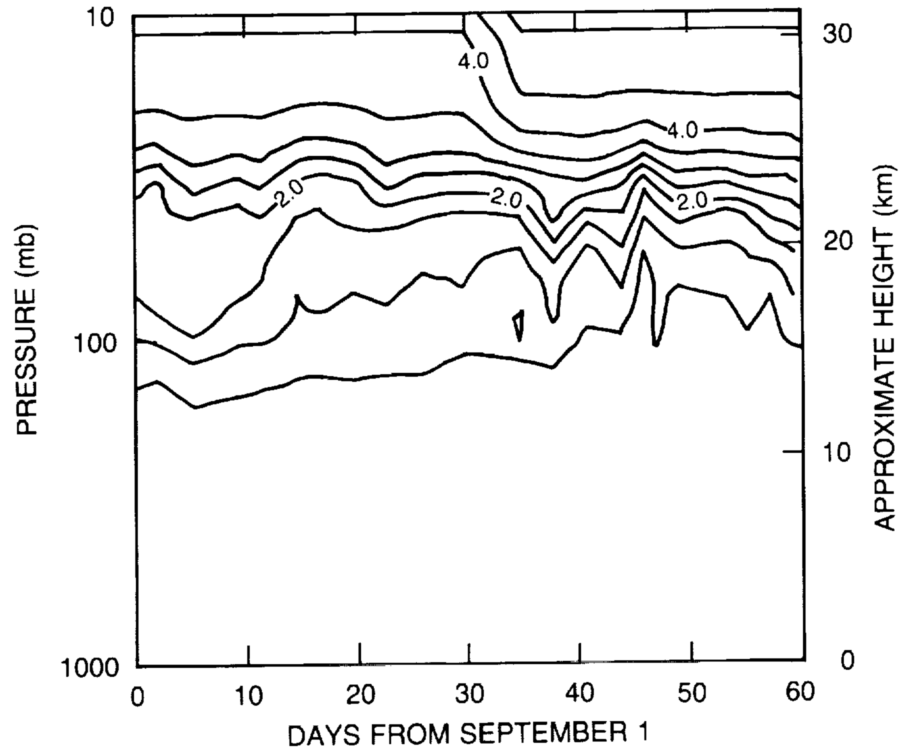

Figure 11.44. Time–height contours of the ozone-mixing ratios used in the radiative heating calculations with depleted ozone. Contours are 0.5 ppmv.

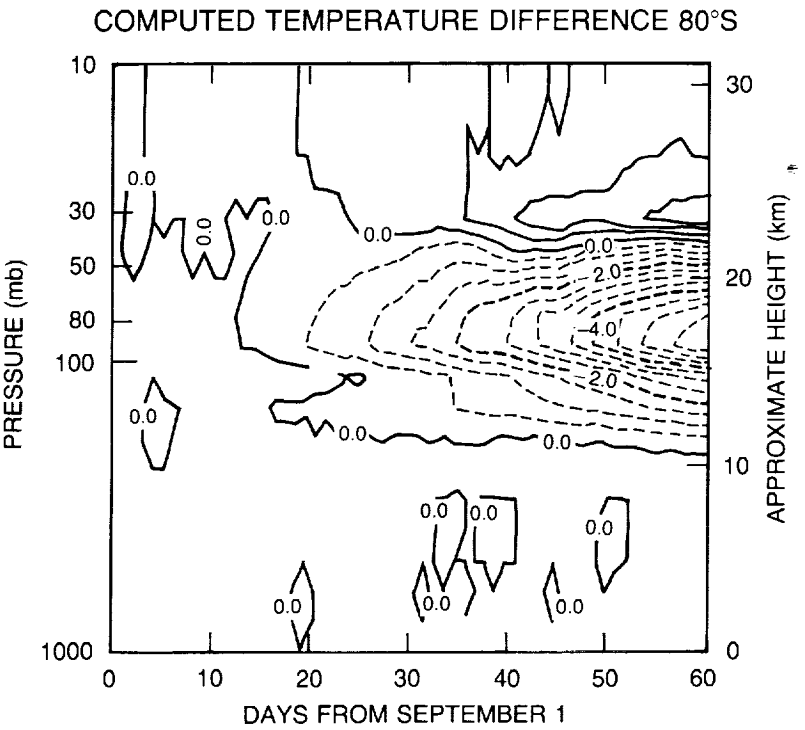

Figure 11.45. Difference of radiatively determined temperatures for depleted and undepleted ozone computed from Model 1, from September 1 through September 30. Units are 0.5 °K.

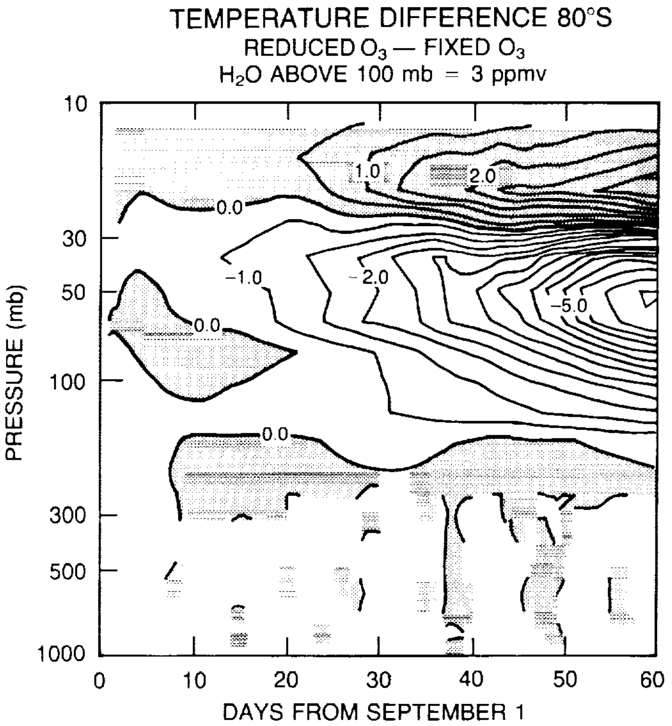

Figure 11.46. Difference of radiatively determined temperatures for depleted and undepleted ozone computed from Model 2, from September 1 through September 30. Units are 0.5 °K.

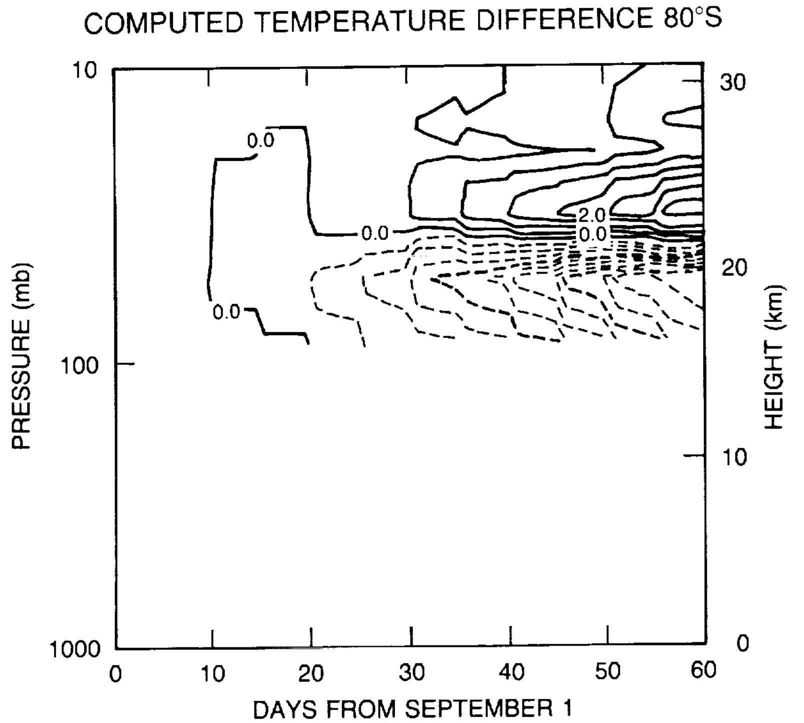

Figure 11.47. Difference of radiatively determined temperatures for depleted and undepleted ozone computed from Model 3, from September 1 through September 30. Units are 0.5 °K.

is found at about 50 mb, while in Model 1, the maximum cooling is at 85 mb. The October monthly mean temperature at the altitude of maximum cooling is predicted to be approximately 4 K colder for the depleted ozone case, relative to the undepleted case. The results of these calculations are similar to those of Shine (1986).

All these calculations predict a warming above the ozone hole that has not been detected in observations. This exceeds 3 K by the end of October in Models 2 and 3. The physical cause of this warming is mainly an increase in the flux of infrared radiation at 9.6 μm that penetrates to midstratospheric levels during periods of depleted ozone in the lower stratosphere. A small contribution is from an increase in the penetrations of reflected radiation from the troposphere (see Shine, 1986).

Further computations were made to test the sensitivity of these conclusions to latitude, water vapor profile, cloud presence, and initial ozone-mixing ratio profile. The maximum cooling on October 30 was about 0.5 K less at 70°S and about 0.5 K greater at 90°S, compared to the runs at 80°S. The use of 1.5 ppmv water vapor above 100 mb (instead of 3.0 ppmv) reduced the October monthly mean cooling by about –1 K in Model 2, while it made very little change in the results of Model 1. The presence of black clouds in the infrared, with a cloud top at 250 mb and a cloud fraction of 1 in Model 1, resulted in a reduction in cooling of about –0.5 K. When the computations were initialized with the ozone rich profile of August 30 (total ozone 270 DU) rather than September 1, Model 3 showed a 60 percent greater cooling. Thus, the predicted cooling appears to be most sensitive to the choice of the initial ozone-mixing ratio profile. Calculations with Model 3 showed that 80 percent of the cooling resulted from decreased absorption of solar radiation, and the rest from decreased absorption of upwelling infrared radiation.

Figure 11.48 shows the differences in two series of temperature profiles—the 1985–1986 mean and the 1979–1980 mean NMC temperatures—collocated with the minimum total ozone, which has a variable latitude and longitude. These data show an October mean difference in excess of 4 K near 100 mb, and roughly agree with the model calculations. The greater day-to-day fluctuation of the observed change is associated with dynamical variability. From these studies, it appears that the year-to-year decrease in Antarctic temperature may result primarily from the ozone reduction. Kiehl et al. (1988) pointed out that the radiative effect of an ozone decline in the lower stratosphere feeds back negatively on the vertical motion. If upward motion produces an ozone decline, the reduced solar heating will tend to suppress the vertical motion or induce sinking.

The importance of the change in radiative heating associated with the ozone decline also provides a possible positive feedback on longer time scales. Once the ozone is reduced in the lower stratosphere, the final spring warming will be delayed because of the reduced radiative heating, assuming that the wave driving is unchanged and relatively weak. The polar vortex, with its cold polar temperatures and capacity for isolating the polar region from mixing, will then persist longer into the spring season. The "filling in" of the ozone hole at the time of the final breakdown of the vortex will thus be delayed, possibly allowing the total ozone to reach lower values than it would have done without the radiative/dynamical feedback from the initial ozone decline. In addition, the warming could be more "radiative," and thereby associated with less lateral mixing. The feedback would be enhanced if the filling in were not complete and memory

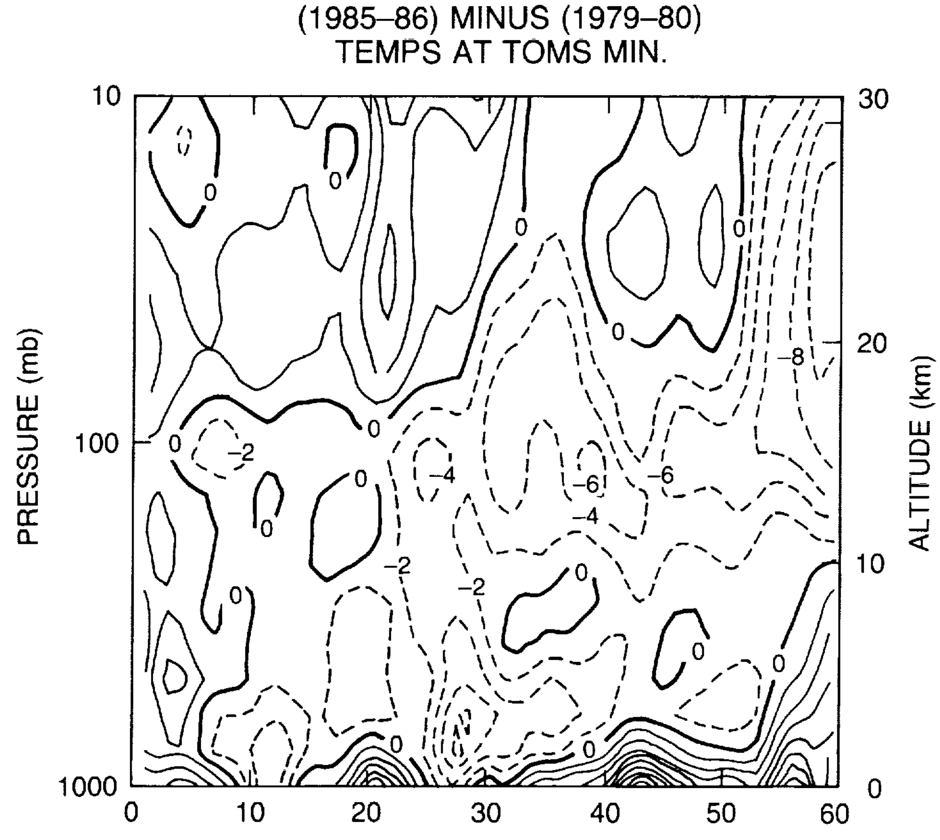

Figure 11.48. The mean of 1985 and 1986 minus the mean of 1979 and 1980 NMC temperature profiles collocated with the total ozone minimum for September 1 to October 30. Units are 2.0 °K.

of the springtime ozone decline persisted into the following year. Memory of the springtime depletion with a time scale of a year would lead to a secular trend for months that are outside the spring season.

When the vertical structure of the radiative temperature change in Figures 11.45 through 11.47 is compared to that of the NMC temperature trends in Figure 11.37, several interesting features are apparent. The radiative temperature changes caused by the ozone decline are centered near 100hPa. The vertical structure is in good agreement with the lower stratospheric trend for November, which also shows maximum trend over the pole at about 100hPa. During October, however, while a similar trend at 100hPa is observed, an additional and larger middle stratospheric trend appears with maximum decrease between the 30 and 10hPa levels. The cooling trend in the middle stratosphere during October is the opposite of the expected radiative warming at these levels and must be associated with altered wave driving. This altered wave driving in the middle stratosphere could be a dynamical response to the radiatively altered lower stratospheric temperature during October, or could arise for an entirely independent reason. The trends in eddy heat flux shown in Figure 11.43 show a significant trend for September, suggesting that the stratospheric temperature trends in the midstratosphere for the October average may be a response to reduced wave driving during the previous month.

11.3.3.2 Evidence for Upward Motion at High Latitudes in Spring

If the observed seasonal springtime ozone decline is to be explained in terms of mean vertical advection, the inferred upward velocity (about 5 km per month or 2 mm per second) cannot be measured directly, but must be inferred from observations of its effects. The most obvious procedure is to track stratospheric tracers. Upper tropospheric wave driving of the mean circulation is sufficient to maintain downward motion at high latitudes below about 10 km above the surface. This downward motion is fed by poleward flow at about the 300hPa level. Any reversed cell with rising over the pole would, therefore, be expected to be confined to the lower stratosphere, and to carry upward concentrations of tracers characteristic of about the 300hPa level or above.

Total Ozone

If the seasonal ozone depletion is indicative of rising motion in high latitudes, then there must be compensating subsidence and dynamically induced increase of the ozone column elsewhere at the same level. There is evidence for this occurring in southern midlatitudes. Stolarski et al. (1986) pointed out that, during September and October of 1979–1982, the midlatitude ozone maximum actually increased and that, in fact, the total ozone integrated over the area south of 44°S merely showed a slow increase. The integrated total ozone is shown in Figure 11.15. The minimum and maximum values south of 30°S for each of the years between 1979 and 1987 are shown in Figure 11.49. In the early years, the maximum increased at the same time that the minimum decreased. This midlatitude compensation is not evident in more recent years. The minimum value during October has continued to decline while the maximum has also decreased, a fact that could indicate one of two things: either there is no upward motion in high latitudes and no compensating ozone increase in midlatitudes and the decrease is caused by a photochemical sink, or the subsidence is occurring over a broader range of latitudes, so that its effects are less apparent. Some evidence for the latter interpretation comes from the calculations of Tung and Yang (1988, 1989), who found that the reverse meridional motion cell deduced from thermodynamic balance extended over a broader range of latitudes year by year and, consequently, that the midlatitude ozone compensation was not evident in later years.

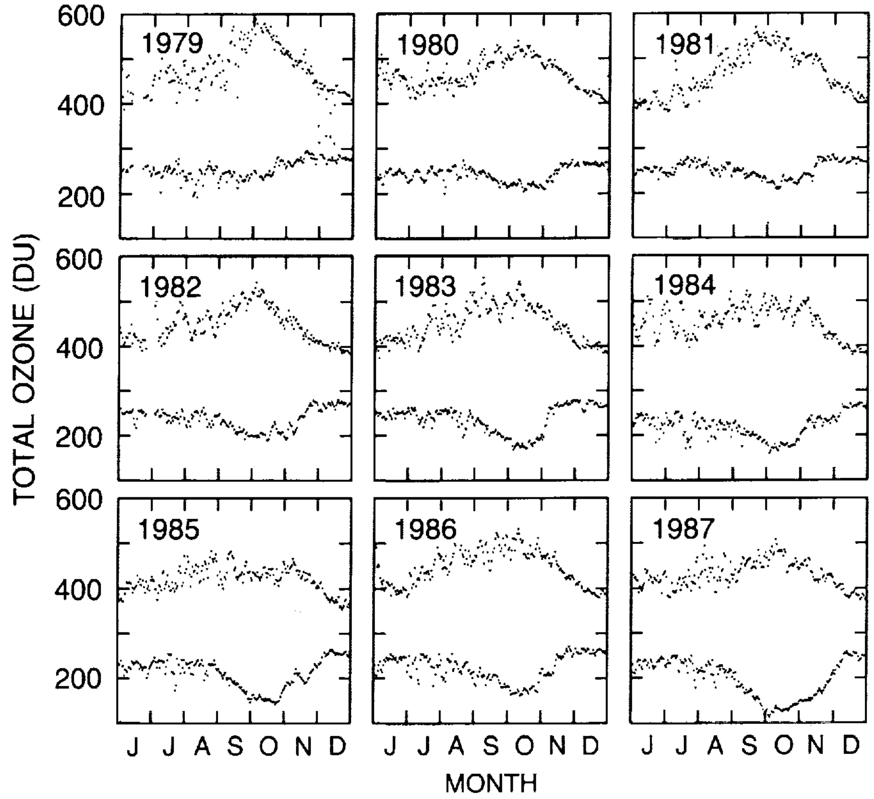

Figure 11.49. Maximum and minimum TOMS total ozone values south of 30°S, plotted as a function of day over the June–December period for each year between 1979 and 1987 (Schoeberl and Stolarski, 1988).

If the ozone depletion is a consequence of a dynamically induced circulation shift, rather than a change in the radiative driving at the end of the polar night, there is no reason that it should be confined to the polar cap. Indeed, the year-by-year depletion of zonal mean ozone in October shown in the TOMS data clearly extends well beyond the Antarctic to about 45°S (Schoeberl et al., 1986; Figures 11.12 and 11.13). Solomon (1988) argued that the midlatitude trend in the TOMS data is inconsistent with the absence of any such trend in the October Dobson data at MacQuarie Island, Invercargill, and Melbourne (Bojkov, 1986a). However, it is clear from the geographic structure of the TOMS trend (Figure 11.42) that this trend has a large planetary wave component that is entirely compatible with a similar structure in the temperature field. The planetary wave component in both the ozone and temperature trends corresponds to an eastward rotation of the October mean planetary wave field since 1979. This component of the ozone trend as measured by TOMS is so large that, while the zonal mean trend is negative in midlatitudes of the Southern Hemisphere, the trend in the South Pacific region is actually positive. The three midlatitude Dobson stations mentioned above are all in the Australia/New Zealand region and, in fact, as evident in Figure 11.42, close to a node in the TOMS trend. Therefore, the absence of a trend at these stations does not undermine the conclusion from the TOMS measurements that a substantial downward trend has occurred in the middle latitudes.

At first sight, the existence of this midlatitude signal appears to support the suggestion that the depletion is a response to a dynamically induced circulation shift, since the direct effects of a radiative change or of chemical depletion would be confined to polar latitudes. Even a localized depletion would be subject to dynamical redistribution during the spring warming, however. If lower stratospheric ozone does indeed possess the long-term memory postulated above, such redistribution of a polar depletion could appear subsequently as a downward trend in mid-latitudes. Therefore, the latitudinal extent of the depletion may, in fact, not provide much insight into the underlying mechanisms of the depletion.

Temperature

By far the best monitored stratospheric quantity is temperature. Observations of temperature can be exploited to infer mean vertical motion through thermodynamic balance. Thus, the upward component can be calculated as the sum of two terms: diabatic (that required to balance radiative heating) and adiabatic (corresponding to the temperature tendency). During mid-winter, the Antarctic lower stratosphere is very close to radiative equilibrium; it seems likely that the diabatic term is upward there as the Sun rises at the end of the polar night. However, it is equally clear that the temperature rises in response to this heating. The two contributions to the calculation of vertical velocity are, therefore, of opposite sign and, in fact, very similar in magnitude. The calculation is thus a delicate one that, since the temperature tendency is reasonably well observed, rests primarily on the accuracy of the calculation of radiative heating.

Rosenfield and Schoeberl (1986) calculated a mean upward diabatic velocity of 0.4 mm per second in October 1980, but concluded that the net mean velocity was weakly downward. Rosenfield et al. (1988), however, deduced that the September mean motion was upward in the Antarctic lower stratosphere and of sufficient magnitude to explain the observed ozone depletion during 1980–1986, but pointed out the sensitivity of their calculation to the specification of surface temperature, tropospheric clouds, and stratospheric aerosols.

Whether or not the zonal mean motion is upward at the pole in spring, there is evidence of upward motion within the planetary wave field in the local temperature minimum. Since the (horizontal) spatial minimum of temperature is displaced from the vortex center (the geopotential minimum), there is a quasi-horizontal flow through the temperature minimum. The flow will, in fact, be almost isentropic (the Lagrangian time scales being short), and so there must be upward motion in the cold region. The implications of this for the Antarctic depletion problem do not appear to have been explored.

Aerosols

The observations of Hofmann et al. (1989) from McMurdo suggest downward motion of lower stratospheric aerosols in October 1986. Some uncertainty in this interpretation is introduced by the comparatively small number of samples taken and the possibility of fallout of the aerosol particles relative to the air.

Long-Lived Trace Gases

Long-lived trace gases of tropospheric origin, such as nitrous oxide (N_2O), F–11 and F–12, are relatively well mixed in the troposphere, but decrease with altitude in the lower stratosphere because they are photolyzed in the upper stratosphere. It would be expected, therefore, that transient upward motion leading to a decrease of ozone in the lower stratosphere would be accompanied by an increase in these gases in the same region in which the ozone depletion occurs. Spectroscopic measurements from McMurdo during spring 1986 showed low values of

N_2O within the vortex (Parrish et al., 1988; Farmer et al., 1987). To interpret such measurements in terms of vertical motion, the time evolution of vertical profiles through the spring season is required. It is possible, for example, that N_2O mixing ratios are low through the lower stratosphere in early spring, in which case the observation of low values would not be an indication of current downward motion, but merely of an earlier downward displacement of air. This appears to be the case, based on preliminary results from the 1987 Punta Arenas (Chile) aircraft campaign.

The ER–2 made 12 sorties out of Punta Arenas (53°S) between August 17 and September 22, 1987. The southernmost latitudes reached were between 68°S and 72°S and were usually inside the core of the vortex. Most tropospheric trace species decreased significantly as the core of the polar vortex was approached at the flight altitude (about 18 km) of the ER–2. Inside the core, N_2O, F–11, and F–12 were observed to remain relatively steady on constant potential temperature surfaces through September, while ozone declined significantly. The flight tracks of the ER–2 aircraft allow crude latitude versus potential temperature cross sections of N_2O and ozone to be drawn for each of the flights between August 17 and September 22, 1987. On the basis of these data, it is difficult to see how the ozone decline could be produced by a simple transport of mass, either by mean upwelling or eddy mixing. While these observations might be unrepresentative of the zonal mean behavior, they do not support the existence of a broad region of near-polar upwelling over this period, strongly suggesting the need of a photochemical sink to explain the ozone decline.

11.3.4 Summary

The polar lower stratosphere of the Southern Hemisphere is very different from that of the Northern Hemisphere. Strong zonal symmetry of surface conditions in the Southern Hemisphere produces a circulation that is much more symmetric and undisturbed by planetary wave activity than that of the Northern Hemisphere. This leads to conditions in the lower stratosphere in which the lower stratospheric polar vortex is relatively intense, maintaining its integrity throughout the winter season and well into spring. Dynamical modeling suggests that relatively little mixing occurs with air at other latitudes, at least at altitudes at which the vortex is sufficiently intense. The air within the polar vortex thus remains very cold and dynamically isolated. When the Sun returns to the South Pole in springtime, temperatures may be near or below radiative equilibrium. Solar heating might, therefore, play a more important role in driving the seasonal change there than it does in the Northern Hemisphere, where temperatures are kept well above radiative equilibrium by stronger wave forcing.

The observed Antarctic ozone decline occurs in the lower stratosphere, where transport by atmospheric motions has a major influence on the ozone-mixing ratio. It is reasonable to suggest that a relatively small climate shift in the Southern Hemisphere could produce a significant change in the total ozone over Antarctica, since the transport of ozone into that region during winter and spring is limited by dynamical constraints associated with the symmetry of the circulation and is very weak in comparison to the almost complete mixing that occurs in the Northern Hemisphere. It is conceivable that colder temperatures at the beginning of spring (produced by weaker wave forcing), or enhanced solar heating during spring (associated with increased aerosols), could lead to transient upwelling during the season that would contribute to the springtime ozone decline. But it is uncertain whether diabatic heating rates would, in reality, be both sufficiently large and suitably distributed in the vertical to produce a significant ozone reduction within the observational constraints.

Evidence from NMC analyses suggests that temperatures in the lower stratosphere over Antarctica have declined from 1979–1985 for the months of October and November; a corresponding decline in the wave driving for September is observed in the same data. Calculations of the radiative temperature change associated with the observed ozone decline suggest that the radiative effect of the ozone decline is comparable in magnitude to the observed trend. The radiative temperature change is largest at the 100hPa level, and its vertical structure in the lower stratosphere is very similar to that of the NMC trend for November. During October, a middle stratospheric temperature decline is observed, in addition to the lower stratospheric decline. This temperature decline in the middle stratosphere is not expected on the basis of radiation alone, but seems more likely to be associated with decreased wave driving during the previous month. Some combination of altered wave driving and radiative response to ozone changes seems necessary to explain the trend observed in NMC data over the 1979–1985 period.

Published attempts to model the springtime Antarctic ozone decline purely as a response to changed transport processes require that low-ozone air be moved into the lower stratosphere from below. Such a movement of air would also imply an increase of long-lived trace species of tropospheric origin such as N_2O, F–11, and F–12. Data from the instruments aboard the ER–2 aircraft show that these trace species remain relatively constant during September as ozone declines significantly, so that transport is unlikely to contribute significantly to the overall decline. These data support the hypothesis that a chemical sink for ozone is required within the polar vortex. However, the role of radiative and dynamical processes in establishing the conditions necessary for the ozone depletion and in controlling the temperature, cloudiness, and precise degree of isolation of the Antarctic ozone hole must be carefully considered.

11.4 CHEMICAL THEORIES AND OBSERVATIONS

11.4.1 Chemical Theories

11.4.1.1 Homogeneous Reactions

In their original paper, Farman et al. (1985) linked the ozone reductions in the Antarctic stratosphere to increasing levels of chlorine from CFC's and other halocarbons. The possible involvement of chlorine and bromine radicals in the ozone reductions has subsequently been the subject of intensive study using theoretical models and field measurements, particularly those made during the 1986 and 1987 ground-based National Ozone Expedition (NOZE) campaigns and the 1987 ER–2 and DC–8 aircraft campaign from Punta Arenas. It quickly became clear that the observed ozone depletion, which occurs predominantly in the lower stratosphere (below 25 km), could not be accounted for by the model chemical schemes in current use to describe the ozone budget in the global stratosphere. These schemes involve partitioning the chlorine between the catalytically active Cl_x species, i.e., Cl and chlorine monoxide radical (ClO), and the inert reservoir molecules hydrochloric acid (HCl), chlorine nitrate ($ClONO_2$), and HOCl, by a series of gas phase photochemical and thermal reactions (*WMO*, 1986). It should be noted that, while HOCl is normally thought of as a reservoir molecule, it can occasionally act as the active form of chlorine (e.g., Scheme A described later in this section). The inert reservoir molecules are the dominant forms of inorganic chlorine in the lower stratosphere at midlatitudes; thus, chlorine is not effective in destroying ozone. In addition, the fraction of chlorine tied up in the organic form is larger at midlatitudes than in the polar regions.

The bulk of the ozone (O_3) column and most of the observed loss over Antarctica occur at altitudes below about 22 km during the early spring weeks (end of August through September and into early October). The low Sun angles characteristic of this season at these latitudes provide an insufficient supply of O atoms to permit catalytic cycles involving recombination of O_3 with O, which dominate the removal of O_3 at midlatitudes. A number of chemical schemes involving ClO, serving as a catalyst for recombination of O_3 with itself, have been suggested and assessed using model calculations; the three most important are:

Scheme A

$$\begin{array}{lcl}
Cl + O_3 & \rightarrow & ClO + O_2 \\
ClO + HO_2 & \rightarrow & HOCl + O_2 \\
HOCl + h\nu & \rightarrow & OH + Cl \\
OH + O_3 & \rightarrow & HO_2 + O_2 \\
\hline
\text{net: } O_3 + O_3 & \rightarrow & 3\,O_2.
\end{array}$$

The reactions in Scheme A were suggested as an explanation of the decrease in Antarctic ozone by P. Solomon et al. (1987). The importance of this scheme appears to be less than Schemes B and C because of the relatively slow rate of photolysis of HOCl. The HO_x radicals produced by photolysis of HOCl in this cycle may also lead to ozone loss through the cycle:

$$\begin{array}{lcl}
OH + O_3 & \rightarrow & HO_2 + O_2 \\
HO_2 + O_3 & \rightarrow & 2O_2 + OH \\
\hline
\text{net: } O_3 + O_3 & \rightarrow & 3\,O_2,
\end{array}$$

but this is apparently less important than the reactions involving ClO.

Scheme B

$$\begin{array}{lcl}
Cl + O_3 & \rightarrow & ClO + O_2 \\
Br + O_3 & \rightarrow & BrO + O_2 \\
BrO + ClO & \rightarrow & Br + Cl + O_2 \\
\hline
\text{net: } O_3 + O_3 & \rightarrow & 3\,O_2.
\end{array}$$

Scheme B was favored by McElroy et al. (1986a). An additional channel for the BrO + ClO reaction is the formation of chlorine dioxide, OClO;

$$BrO + ClO \rightarrow OClO + Br,$$

which could accumulate and become an important form of active chlorine at night. In daylight, OClO is rapidly photolyzed by visible light:

$$OClO + h\nu \rightarrow O + ClO.$$

This sequence produces no net ozone depletion from the BrO + ClO reaction occurring through this channel. However, since this is the only known reaction leading to OClO production in the stratosphere, the observation of significant concentrations of OClO during the Antarctic spring would provide indirect evidence for elevated abundances of ClO and the bromine monoxide radical (BrO), implying that they are involved in the chemical destruction of ozone (Tung et al., 1986; Rodriguez et al., 1986). While other possible OClO formation mechanisms may be possible, such as the photolysis of the Cl_2O_2 dimer, none has yet been demonstrated (discussed later).

Another possible reaction pathway for ClO and BrO leads to the formation of BrCl (Toohey and Anderson, 1988):

$$ClO + BrO \rightarrow BrCl + O_2.$$

This reaction would not affect the efficiency of Scheme B because the BrCl would rapidly photolyze during the daytime to produce chlorine and bromine atoms:

$$BrCl + h\nu \rightarrow Br + Cl,$$

which then rapidly reform ClO and BrO. The reaction would, however, reduce the production of OClO at night because atomic bromine, and hence BrO, would not be reformed and the efficiency of the cycle producing OClO would be reduced (Salawitch et al., 1988a). Current laboratory work is aimed at improving knowledge of the rate and branching ratio for the BrO + ClO reaction for atmospheric conditions. This promises to reduce the uncertainties in the chemistry of the mixed BrO and ClO system. Several studies have confirmed that OClO formation is a major channel from the BrO + ClO reaction (Clyne and Watson, 1977; Friedl and Sander, 1987; Sander and Friedl, 1987; Toohey and Anderson, 1988).

Scheme C (a)

$$\begin{array}{ll}
2[Cl + O_3 & \rightarrow ClO + O_2] \\
ClO + ClO + M & \rightarrow Cl_2O_2 + M \\
Cl_2O_2 + h\nu & \rightarrow Cl + ClOO \\
ClOO + M & \rightarrow Cl + O_2 + M \\
\hline
\text{net: } O_3 + O_3 & \rightarrow 3\,O_2
\end{array}$$

Scheme C (b)

$$\begin{array}{ll}
2[Cl + O_3 & \rightarrow ClO + O_2] \\
ClO + ClO + M & \rightarrow Cl_2O_2 + M \\
Cl_2O_2 + M & \rightarrow Cl_2 + O_2 \\
Cl_2 + h\nu & \rightarrow 2\,Cl \\
\hline
\text{net: } O_3 + O_3 & \rightarrow 3\,O_2.
\end{array}$$

Molina and Molina (1987) were the first to draw attention to the possible importance of the ClO dimer molecule, Cl_2O_2, in Scheme C (a). Rodriguez et al. (1986) and McElroy et al. (1986b) have shown that a combination of Schemes B and C can account for the magnitude of the observed loss of O_3, provided the concentration of ClO is high (close to 1 ppbv), and that for Scheme B to play a dominant role requires an abundance of BrO (in excess of about 10 pptv). Key questions concerning Scheme C (a) are the rate of formation of the Cl_2O_2 dimer, the rate of photolysis, and the identification of the photolytic products of the Cl_2O_2 dimer, none of which is well established (Molina and Molina, 1987; Hayman et al., 1986). Preliminary data suggest that the dimer does photolyze rapidly (Cox and Hayman, 1988; Molina and Molina, 1987). In addition, preliminary and somewhat indirect evidence has been obtained for the production of atomic Cl in the photolysis of Cl_2O_2, rather than ClO and ClO, or Cl and OClO (Cox and Hayman, 1988). If the Cl_2O_2 dimer were to photolyze by either of the latter routes, there would be no catalytic removal of ozone. Consequently, it is essential to define the rate of ClO dimer (Cl_2O_2) formation and the photolysis products of dimer decomposition because only one of several possible routes leads to ozone destruction. Molina and Molina (1987) have proposed an alternate cycle, Scheme C (b), involving the Cl_2O_2 dimer. They propose that the Cl_2O_2 dimer could dissociate thermally to produce molecular chlorine, which would rapidly photodissociate into atomic chlorine and molecular oxygen. The rate and product distribution of the thermal dissociation of the Cl_2O_2 dimer are uncertain, but it appears improbable that this mechanism would be important.

Each of the ozone loss schemes discussed above requires significant release of ClO_x radicals from the main chlorine reservoirs, HCl and $ClONO_2$, which current models, using gas-phase chemistry alone, do not predict. Several theories have been proposed to account for the enhanced ClO abundance. P. Solomon et al. (1987) and McElroy et al. (1986a) point to the possible importance of heterogeneous processes converting the inert reservoir species of chlorine, HCl and $ClONO_2$, to more active forms of chlorine on the surfaces of PSC's. These processes are discussed in Section 11.4.1.3. Crutzen and Arnold (1987) also argued the importance of heterogeneous loss processes involving the PSC's, focusing particularly on the interactions of the nitrogen molecules N_2O_5 and nitric acid (HNO_3). These authors offer an alternative explanation for the release of ClO_x from HCl—through the presence of enhanced abundances of OH. These enhanced OH densities in the polar spring are attributed to a nighttime cosmic ray source of HO_x, augmented by coupling with methane (CH_4) oxidation when sunlight returns.

Krueger et al. (1987) proposed that abnormally high ClO_x and BrO_x radical concentrations could result from increased photolysis rates of the halocarbon source gases due to heterogeneous photolysis on the surface of PSC's and aerosols. Their argument contains several rather tenuous assumptions that are not supported by appropriate experimental laboratory data.

Callis and Natarajan (1986) proposed that ozone loss in the polar stratosphere is catalyzed by abnormally high levels of NO_x. This theory links the currently observed ozone depletion to the 1979 solar maximum, resulting, it is claimed, in the production of large amounts of NO in the mesosphere and thermosphere that would then be transported down to the lower stratosphere. Obviously, if this mechanism were to be correct, then the ozone hole should be periodic. The actual catalytic cycle proposed was the classic NO_x cycle:

$$\begin{array}{ll} NO + O_3 & \rightarrow NO_2 + O_2 \\ O + NO_2 & \rightarrow NO + O_2 \\ \hline \text{net: } O + O_3 & \rightarrow 2\,O_2. \end{array}$$

Several of the gas phase thermal and photochemical reactions not included in previous models of stratospheric chemistry attain new significance in the context of the Antarctic ozone problem, as discussed above. Knowledge of the rate coefficients and pathways of some of these reactions is far from complete. In addition, the extremely low temperatures prevalent in the stratosphere over Antarctica are often significantly outside the range over which measurement of many of the elementary reactions in the HO_x, NO_x, and ClO_x cycles have been carried out. Considerable error may result in the extrapolation of the rate coefficients from higher temperatures, particularly as many of the reactions exhibit non-Arrhenius behavior and have negative temperature dependencies, for example, $HO_2 + O_3$, $HO_2 + ClO$, $HO_2 + HO_2$, and $HO_2 + CH_3O_2$.

11.4.1.2 Character and Role of Polar Stratospheric Clouds

The composition of PSC's is a matter of controversy. It was thought, until recently, that the clouds were composed mainly of water ice, and that individual particles grew by accretion of H_2O on nuclei of hydrated H_2SO_4 (Steele et al., 1983). Toon et al. (1986) argued that the opacity of PSC's would be much larger than that observed if the clouds were composed primarily of H_2O. Toon et al. and Crutzen and Arnold (1986) simultaneously suggested that PSC's might be composed mainly of nitric acid trihydrate ice, $HNO_3 \cdot 3H_2O$; they discussed some of the effects to be expected from incorporation of these species into the condensed phase. Toon et al. also suggested that significant quantities of HCl could condense in PSC's. A direct consequence of cloud formation would be reduction in the gas phase concentrations of the major reservoir species for odd nitrogen and inorganic chlorine. In addition, the presence of HNO_3 and HCl in the solid phase could be important in promoting heterogeneous chemical reactions. If the particles grew large enough to fall out, acids could be removed from the local environment.

McElroy et al. (1986b) presented an alternative analysis of the thermodynamics of H_2O–HNO_3 mixtures that supported the original assertion that condensation in PSC's could provide a significant sink for stratospheric HNO_3 gas. Condensation at temperatures below about 193 K probably involves formation of crystalline phases consisting of mixtures of $HNO_3 \cdot 3H_2O$ and $HNO_3 \cdot H_2O$. Condensation of even a few ppb of H_2O should result in essentially complete removal of gas phase HNO_3. Condensation of HCl requires somewhat lower temperatures, and a solid solution is formed rather than a crystalline hydrate (Wofsy et al., 1988). A reduction in gas phase H_2O by 1 ppm should lead to a reduction in HCl of more than 99 percent. Fallout of particles can provide significant localized sinks for HNO_3, H_2O, and, possibly, HCl and N_2O_5. The first large particles to fall might be expected to be rich in HNO_3. The amount of HNO_3 present in the precipitation might be reduced considerably when an air parcel undergoes subsequent condensation. Precipitation would leave the environment depleted in HNO_3, HCl, and H_2O. The mixing ratios of HNO_3 and HCl in the lower stratosphere are expected, under normal conditions, to rise with increasing altitude. Evaporation of precipitating particles at lower altitudes could be associated with significant enhancement of HNO_3, and possibly HCl, at the deposition altitudes, with small related changes in the abundance of H_2O. There is also a possibility that HNO_4, H_2O_2, and other reservoir molecules could be incorporated and precipitated in the PSC's.

However, a recent study by Poole (1987), with experimental evidence given by Poole and McCormick (1988), has supported the suggestion that these particles have more than one growth mode delineated by temperature. A stage of nitric acid trihydrate deposition is interposed between the two stages of cloud growth assumed in earlier PSC studies—i.e., between the aerosol droplet precursors and ice particles. Figure 11.50 shows the calculations for three temperatures: the end of the precursor stage at about 195 K; just prior to the end of the $HNO_3 \cdot 3H_2O$ deposition stage at about 191 K; and below the frost point at about 189 K. More than 80 percent of the nitric acid and 30 percent of the water vapor supplies may be sequestered in the relatively large 8 μm diameter PSC particles formed at and below the frost point temperature. These large particles would fall at a rate of about 2 km per week (fast enough to produce the October cleansing shown in Figure 11.28), suggesting that PSC's may act as a sink for stratospheric trace gases, in this case HNO_3 and H_2O. It might be possible for other gases to condense like HCl and, at a minimum, to redistribute certain stratospheric gases in altitude.

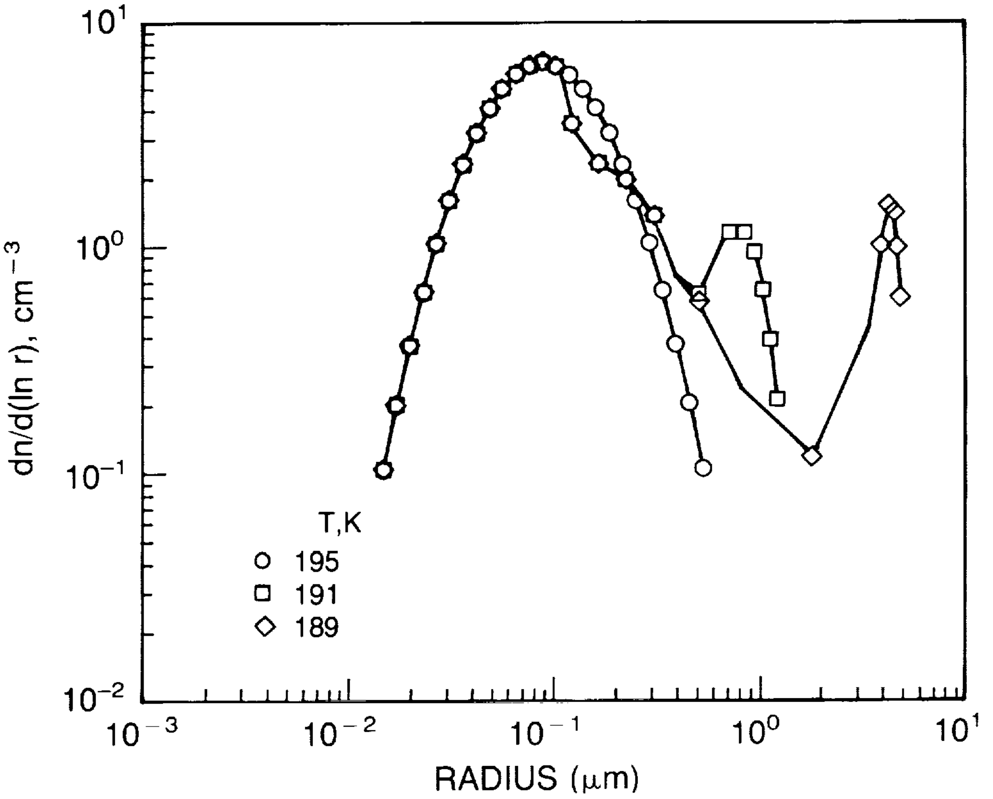

Figure 11.50. Evolution of the nonvolcanic particle size distribution at 70 mb with temperature. Shown are the size distributions at 195 K, 191 K, and 189 K, assuming a cooling rate of 0.5 K/day.

11.4.1.3 Heterogeneous Reactions

The existence of PSC's composed of H_2O, HNO_3, and HCl suggests the possibility of important multiphase (for "heterogeneous") chemical processes. Photochemical theories of the Antarctic ozone hole presume some heterogeneous chemical effects, or at least the microphysical effect of acid condensation and removal. However, not all of these treatments have a quantitative description of specific processes and reaction rates, mainly because of a lack of laboratory data on such reactions and the inadequacy of theoretical approaches in defining the kinetics.

The occurrence of heterogeneous reactions of $ClONO_2$ with H_2O and HCl and of N_2O_5 with water have been known in laboratory systems for some time. The determination of their significance for atmospheric chemistry and their representation in kinetic models presents a considerable challenge.

The heterogeneous processes of current interest include:

$ClONO_2$ (g) + H_2O (s) → HNO_3 (s) + HOCl (g,s)
$ClONO_2$ (g) + HCl (s) → HNO_3 (s) + Cl_2 (g)
N_2O_5 (g) + H_2O (s) → HNO_3 (s) + HNO_3 (s)
HNO_3 (s) and HCl (s) → removal by sedimentation.
N_2O_5 (g) + HCl (s) → HNO_3 (s) + $ClNO_2$ (g).

The efficiency of a heterogeneous reaction is often expressed in terms of the collision efficiency for reaction, g. This is the fraction of the kinetic encounters of a gas molecule with a surface that result in the reaction of interest at the surface. In reality, chemical reactions on solid (ice) particle surfaces are generally multistep processes involving:

- Transport of the reactant species to the surface by diffusion and kinetic motion.
- Absorption on the surface (with physical or chemical bonding).
- Diffusion of the reactants on the surface, or within the bulk of the solid.
- Encounter of the reactants on the surface, with formation of activated complexes and reaction to form products.
- Diffusion of the product species on the surface, or within the solid.
- Possible secondary reactions of product species on the surface.
- Desorption of the product molecules and transport of the products from the vicinity of the particle.

Accordingly, such heterogeneous reactions are much more complex mechanistically than homogeneous gas phase reactions. Often, reactions that are slow in the gas phase can be catalyzed on certain surfaces due to the interaction of the reactants with the surface, which lowers the activation barrier significantly. Nevertheless, such reaction mechanisms have rarely been studied in detail. In the case of heterogeneous reactions of atmospheric interest at low temperatures on HNO_3 and HCl ices, the reaction mechanisms are unknown. Wofsy et al. (1988) pointed out that since a number of chemical bonds are rearranged in the heterogeneous reactions discussed earlier, the lack of a significant activation energy implies a catalytic reaction mechanism. They suggested that the reactions may be acid catalyzed, with protonation of $ClONO_2$ and N_2O_5 giving rise to incipient Cl^+ or $NO_2{}^+$, leaving groups,

$$ClONO_2 + H^+ \rightarrow HNO_3 - Cl^+$$

$$N_2O_5 + H^+ \rightarrow HNO_3 \bullet NO_2{}^+.$$

These powerful oxidant groups should react rapidly with Cl , which can diffuse rapidly through the ice (Molina et al., 1987) to the reaction site on the particle surface. The reaction is essentially an ion–ion recombination, which may be expected to proceed rapidly with no activation barrier. Rowland (1988) also suggested that the reactions might involve partially solvated Cl^- ions in an ice matrix. Because these reactions are rapid, with values of g (collision efficiency) greater than 0.1, it is probably not necessary to understand the details of the heterogeneous reactions to simulate the chemical processes responsible for the depletion of ozone in Antarctica. Accordingly, while a simple representation based on the collision model using empirical data for g is the best that can be done now, it is also appropriate.

The overall rate of a reaction on PSC particles can be estimated using the observed optical extinction of the PSC's (which is related to the available reaction surface area of the PSC's) by the following approximate relation (e.g., Toon et al., 1986):

$$t_R = 1 / (k_e \, v_{th} \, g),$$

where t_R is the reaction time constant (s), k_e is the PSC extinction (cm^{-1}), g is the collision efficiency, and v_{th} is the thermal velocity of the impinging reactant molecules (cm/sec). Since k_e $\sim 10^{-7} - 10^{-8}$/cm and $v_{th} \sim 10^4$ cm/s, $t_R \sim 10^3 - 10^4$/g s. Some typical time constants derived in this way are displayed in Table 11.3.

Table 11.3 Heterogeneous Reactions in PSC's

Reaction	Collision Efficiency, g	Time Constant for Reaction on PSC's (3) (seconds) Extinction 10^{-3}/km	10^{-2}/km
$ClONO_2 + H_2O$ (s) — $HNO_3 + HOCl$	3.2×10^{-4} (1) 0.02 (2) 0.008 (7)	3×10^7 (3) 5×10^5 1.3×10^6	3×10^6 (3) 5×10^4 1.3×10^5
$ClONO_2 + HCl{\bullet}H_2O$ (s) $\rightarrow$ $HNO_3 + Cl_2$	0.05	2×10^5 (3)	2×10^4 (3)
$N_2O_5 + H_2O$ (s) $\rightarrow$ $2HNO_3$ (?)	3.8×10^{-5} (4) 1×10^{-3} (5)	3×10^8 (3) 1×10^7	3×10^7 (3) 1×10^6
$ClO + H_2O$ (s) $\rightarrow$ HCl + ?	3.7×10^{-10} e (3220/T) 3.6×10^{-3} @ 200 K (6)	3×10^6 (3)	3×10^5 (3)
$HCl + H_2O$ (s) $\rightarrow$	>0.1 (8)	2.5×10^4	2.5×10^3
$N_2O_5 + HCl \rightarrow$ $ClONO_2 + HNO_3$			

1. Rossi et al. (1987); for a 95% H_2SO_4–5% H_2O surface at 300 K.

2. Molina et al. (1987); for pure ice, or ice exposed to HCl vapor, at 200 K.

3. The extinction coefficient, K_e(km^{-1}), is related to the reaction time constant, t, by the expression, $t = 1/(k_e v_{th} g)$, where v_{th} = molecular speed and g is the collision efficiency.

4. Baldwin and Golden (1979); lower limit for a 95% H_2SO_4–5% H_2O surface at 300 K.

5. Estimate for nearly pure ice at 200 K.

6. Martin et al. (1980) for 75% H_2SO_4–25% H_2O surface at temperatures down to 230 K.

7. Tolbert et al. (1987) for pure ice at 185 K.

8. Worsnop et al. (1987)

The most significant new work is the studies of $ClONO_2$ reactions on ice and HCl–ice by Molina et al. (1987) and Tolbert et al. (1987), and studies of the sticking coefficients of HCl on ice particles by Worsnop et al. (1987). Recent measurements have shown that sticking coefficients for HCl on ice particles ($g > 0.1$; Worsnop et al., 1987) and for chlorine nitrate on an ice matrix containing HCl ($g > 0.05 - 0.1$; Molina et al., 1987) are much higher than expected based on the limited data, as shown in Table 11.3, where values of collision efficiencies of $\sim 10^{-3}$ to 10^{-5} are reported from earlier studies (e.g., the results of Baldwin and Golden, 1979).

Molina et al. (1987) also derived direct evidence of the following facts:

- HCl vapor readily diffuses into water ice crystals at low temperatures, forming solid solutions that can approach several percent or more of HCl by weight (also see Wofsy et al., 1988); this confirms that HCl may condense directly into PSC ice particles in the polar winter stratosphere.
- The dissolved HCl in solid solution is very mobile within the ice crystal lattice; thus, as in aqueous solutions, the mobility of the HCl molecule greatly enhances its reaction with reactant species on the surface.
- The HNO_3 molecules formed by $ClONO_2$ reactions with ice and HCl ice remain in the condensed phase; hence, the odd nitrogen involved in forming both HNO_3 and $ClONO_2$ can be sequestered in the ice and removed from the local environment. In terms of the polar stratosphere, this result also implies that HNO_3 vapor could condense independently as nitric acid PSC's in accordance with the theories proposed by Toon et al. (1986) and Crutzen and Arnold (1986).
- The HOCl molecules formed by the reaction of $ClONO_2$ and H_2O (ice) are not as tightly bound to the ice surface as HNO_3 and can desorb in minutes (at 200 K); thus, this process probably does not sequester "reactive" chlorine species.

The presence of PSC's, which are a common feature of the nighttime Antarctic stratosphere, may enhance the rate of a number of reactions involving chlorine and nitrogen species. Denitrification of the stratosphere facilitates ozone destruction by ClO_x and BrO_x catalysis because the reactions involving NO and NO_2 (nitrogen dioxide), e.g.,

$$\begin{aligned} ClO + NO &\rightarrow NO_2 + Cl \\ ClO + NO_2 + M &\rightarrow ClONO_2 + M \end{aligned}$$

and

$$\begin{aligned} BrO + NO &\rightarrow NO_2 + Br \\ BrO + NO_2 + M &\rightarrow BrONO_2 + M, \end{aligned}$$

which reduce the concentrations of ClO, are reduced in importance. However, a number of questions regarding multiphase processes require additional study, including:

- The vapor pressures of HNO_3, H_2O, and HCl over mixed ices of these substances at temperatures as low as 180–185 K; the nature of the condensed phases (e.g., the composition and crystal forms) must also be determined.
- The dependence of the heterogeneous reactions described above on temperature and ice composition must be determined quantitatively; the reaction mechanisms must be better delineated.
- Evidence of other global heterogeneous chemical effects should be sought, particularly the possibility of particle-catalyzed chemistry enhanced by volcanic eruptions.

C-4

11.4.1.4 Summary

All current theories that attempt to describe ozone loss in the Antarctic stratosphere in terms of catalytic chemical destruction have the following features:

- Drastic reduction in NO_2 abundance resulting from removal of odd nitrogen (NO_y) as HNO_3 in the condensed phase of PSC's.
- Catalytic cycles involving HOCl, Cl_2O_2, and BrO catalyzing the recombination of O_3 with itself.
- Release of a substantial fraction of the ClO_x contained in the reservoir molecules HCl and $ClONO_2$, either by heterogeneous reactions in PSC's or by enhanced OH abundance.

11.4.2 Observations Relevant to Testing the Chemical Theories

11.4.2.1 Observational Data Base

Our understanding of the chemical composition of the springtime Antarctic atmosphere increased dramatically during 1986 and 1987. Observations of the column content (and in some instances, the vertical distribution) of a large number of species, including O_3, ClO, OClO, $ClONO_2$, HCl, hydrofluoric acid (HF), NO_2, and HNO_3, were made from McMurdo in 1986. These observations clearly demonstrated that the chemical composition of the Antarctic stratosphere in springtime was highly perturbed compared to predictions based on the currently accepted chemical and dynamical theories that are applicable to midlatitudes. The distribution of chlorine species is significantly different from that observed at midlatitudes, as are the abundance and distribution of nitrogen species. At present, it is not clear whether the abundance of total inorganic chlorine is perturbed relative to that expected, or just the partitioning. The preliminary findings from the 1987 ER–2 and DC–8 aircraft campaign based in Punta Arenas are consistent with the observations made last year from McMurdo, and provide a more detailed picture of the chemical composition, dynamic structure, and the complex interplay between them. In addition, it was observed that the amount of total water within some regions of the vortex is significantly lower than anticipated.

The spatial and temporal distribution of a large number of relatively short-lived chemical constituents that play a key role in the chemical reactions affecting ozone abundance were measured from both the ER–2 and DC–8. Instruments aboard the ER–2 gave measurements of the distributions of O_3, ClO, BrO, total NO_y, nitric oxide (NO), and water in the vicinity of the aircraft at altitudes ranging from 12 to 18.5 km above Earth's surface—well into the altitude region where ozone is undergoing depletion. Instruments aboard the DC–8 measured the abundances of H_2O and O_3 in the vicinity of the aircraft, the vertical distribution of O_3 for approximately 10 km above the aircraft, and the total column amounts of O_3, HCl, $ClONO_2$, OClO, BrO, HF, NO, NO_2, HNO_3, and possibly HOCl, as well as of a number of other constituents above the aircraft altitude.

The temporal and spatial distributions of long-lived chemical tracers and dynamical variables were measured to understand atmospheric motions. These included measurements of N_2O, CH_4, chlorofluorocarbons 11 ($CFCl_3$) and 12 (CF_2Cl_2), carbon tetrachloride (CCl_4), and methylchloroform (CH_3CCl_3). In situ measurements of all of these species were made from both the ER–2 and DC–8, and column measurements of most of them from the DC–8. In addition, the vertical distribution of the chlorocarbons provided information about the vertical distribution of inorganic chlorine. Additionally, atmospheric pressure, temperature, lapse rate, and winds were measured aboard the ER–2 to determine the state variables and dynamical structure of the atmosphere.

The size distribution, abundance, and composition of particles were determined by instrumentation aboard the ER–2, and the vertical distribution of aerosols from 12 to 28 km was measured by the DC–8 lidar in an effort to understand the role of heterogeneous processes.

11.4.2.2 Comparison of Theory and Observations

The weight of observational evidence from McMurdo and the aircraft campaign strongly suggests that both chemical and meteorological mechanisms perturb the ozone. Additionally, it is clear that meteorology sets up the special conditions required for the perturbed chemistry. It is evident from the 1987 ER–2 flights that the region of dehydrated and denitrified air maintained a sharply defined latitude gradient throughout most of the campaign. Based on a purely meteorological definition, the vortex edge would be well outside the dehydrated, denitrified region. The meteorological flow must, therefore, have been such as to maintain a kind of "containment vessel" in which the perturbed chemistry could proceed without being influenced by mixing in more normal stratospheric air from outside or below. The concept of mixing at the region of sharp latitudinal gradient is important because it has the potential to supply nitrogen oxides, which would tend to decelerate the chlorine chemistry. The meteorology is thus important in both the termination and initiation phases.

11.4.2.3 Observations of Halogen Species

The data reported from McMurdo in 1986 demonstrated that while the abundance of total chlorine was consistent with that expected, the partitioning of Cl_x was highly perturbed compared with that observed at midlatitudes. The concentrations of HCl were low (Farmer et al., 1987), whereas the concentrations of OClO and ClO were significantly elevated (S. Solomon et al., 1987). Somewhat elevated concentrations of $ClONO_2$ were also observed (Farmer et al., 1987).

The in situ ER–2 data taken from late August until the end of September 1987 at about 18.5 km (the highest altitude at which the plane was flown) showed that the abundance of the chlorine monoxide radical within the polar chemically perturbed region was elevated by a factor of more than 100 relative to that measured at midlatitudes. The abundance of ClO at local solar noon ranged between 0.5 and 1 ppbv. However, the abundance of ClO was observed to decrease rapidly toward lower altitudes, and, while no data were taken at higher altitudes, the observed increase in the abundance of ClO from lower altitudes, coupled with the observed low column abundances of HCl, suggests that the ClO abundance may increase somewhat at altitudes above 18 km. In addition to the steep decrease in ClO abundance at lower altitudes, the abundance of ClO was also observed to decrease dramatically outside the chemically perturbed region. These observations are consistent with the low vertical resolution and low signal-to-noise microwave emission measurements made at McMurdo in 1986 (deZafra et al., 1987; S. Solomon et al., 1987), which reported ClO abundances of about 1 ppbv in the lower stratosphere (Figure 11.51) during September. Figure 11.52, from deZafra et al. (1987), shows the observed temporal behavior of ClO during September and October 1986 from McMurdo. P. Solomon et al. (1987) also reported the diurnal behavior of ClO as shown in Figure 11.53.

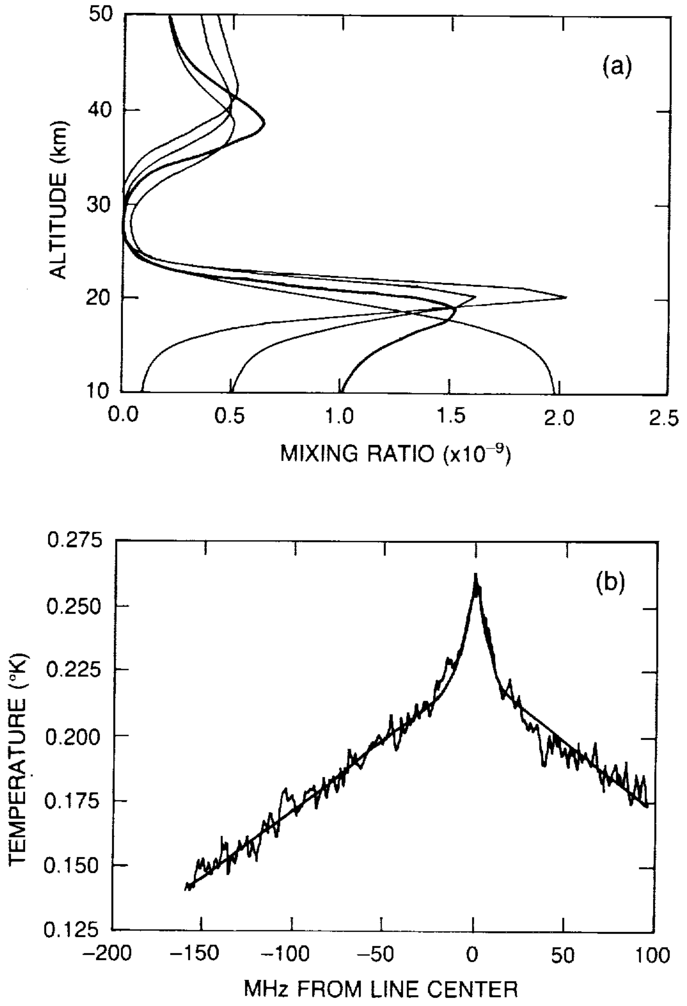

Figure 11.51. Ground-based mm-wave spectral data from McMurdo Station, taken in September 1986. (a) result of four deconvolutions of the ClO emission line at 278 GHz shown in lower panel. Profiles shown result from initial mixing ratio choices of 0.1, 0.5, 1.0, and 2.0 ppbv, constant from 10–60 km, as inputs to the deconvolution algorithm,. The initial choice remains unaltered in the algorithm below ~12 km and dominates the profiles up to ~18 km, but all deconvolutions yield a clearly bimodal structure with a large low-altitude component of ClO the emphasized profile yields the fit to data shown in the lower panel. (b) ClO emission line averaged over a 7-hour period, starting 4 hours after dawn at 20 km and ending 4 hours before sunset at 45 km. Data taken on a nearly daily basis have been averaged over the period 1–22 September. (From de Zafra et al., 1987.)

The in situ aircraft data demonstrated that ClO existed during September 1987, within the chemically perturbed region of the vortex near 18.5 km, at abundances sufficient to destroy ozone if our current understanding of the chlorine–ozone ClO dimer catalytic cycle is correct (Molina and Molina, 1987). The rate of ozone decrease during September at the ER-2's highest altitudes was consistent with simultaneously observed concentrations of ClO. However, as mentioned earlier, our present understanding of key chemical reaction rates and photodissociation products within the catalytic process is incomplete. Once the results of ongoing laboratory studies become available, these in situ ClO data will allow the chemical mechanism to be defined quantitatively and its consequences better understood.

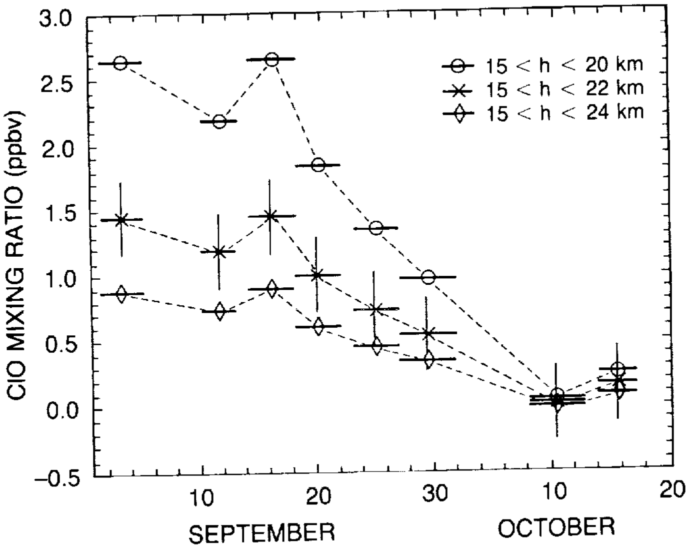

Figure 11.52. Observed trend in lower atmospheric ClO component over McMurdo Station during the period September 1–October 16, 1986. Left-hand scale gives mixing ratio in the form of an average over an altitude span, as determined from line-shape deconvolutions. Different mixing ratio values on a given date result from different assumptions concerning thickness and upper altitude limit of the low-altitude ClO component. Data for October 14–16 are of poorer quality but are included for completeness. Horizontal bars represent averages over 3–5-day periods. (From P. Solomon et al., 1987.)

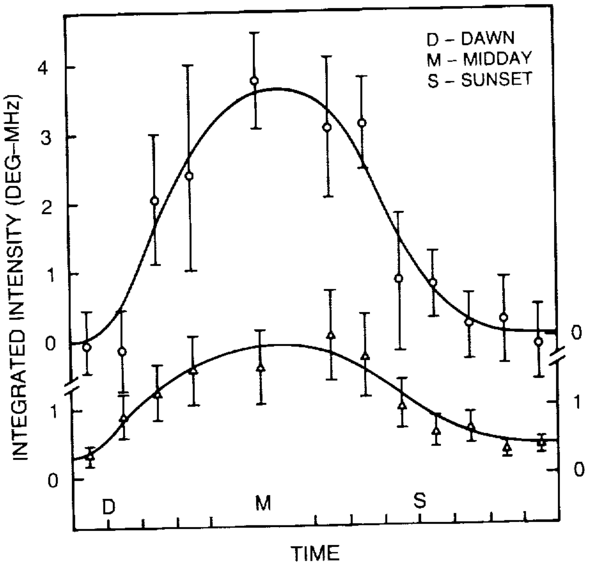

Figure 11.53. Diurnal variation of integrated ClO emission line intensity measured at McMurdo Station in 1986. Data were divided into 2-hour time intervals for analysis, except for the longer midday block. Points D, M, and S along the time axis mark dawn at 20 km, midday, and sunset at 45 km, respectively. The upper curve represents diurnal behavior of the low-altitude component only, integrated over ±100 MHz around the line center. The lower curve represents the upper altitude component only, integrated over ±50 MHz around the line center. A significant fraction of the intensity of the total low-altitude line is lost by the limited bandwidth available for integrating the pressure-broadened line. Curves are freehand fits, and error bars represent one standard deviation uncertainties in retrievals. (From de Zafra et al., 1987.)

There is another line of observational evidence consistent with ozone destruction by chlorine catalysis. In August, a consistent positive correlation between ClO and O_3 was observed, whereas by mid-September, as the ozone concentration was dropping at ER–2 altitudes, a strong anticorrelation developed between ClO and O_3. The anticorrelation was usually present on both large and small scales within the chemically perturbed region.

One observation that is currently difficult to understand is the sharp decrease in the abundance of ClO at lower altitudes where downward trends in ozone were observed. This could be due to a lack of understanding of either the abundance or partitioning of ClO_y, or to dynamical effects. Lack of observations of reactive hydrogen-containing radicals, hydroxyl (OH), and hydroperoxy (HO_2), currently prevents an assessment of their role in the conversion of chlorine reservoir species to ClO. Measurements of HOCl would partly assist in understanding the ClO_y / HO_x interaction.

Chlorine dioxide, which is most likely formed in a reaction sequence involving the ClO radical, was observed both day and night from McMurdo in 1986 at highly elevated concentrations compared to those at midlatitude (P. Solomon et al., 1987). Figure 11.54 shows the observed nighttime vertical column abundance of OClO using direct moonlight visible absorption spectroscopy. Figure 11.55 shows the temporal variation of the vertical column of OClO observed at twilight from August 26, 1986, to October 21, 1986. The preliminary analyses of the 1987 DC–8 and McMurdo observations are consistent with measurements made from McMurdo in 1986. The observed OClO diurnal variation provides useful constraints on the chemical mechanisms controlling the reactive chlorine and reactive bromine levels. Based on preliminary

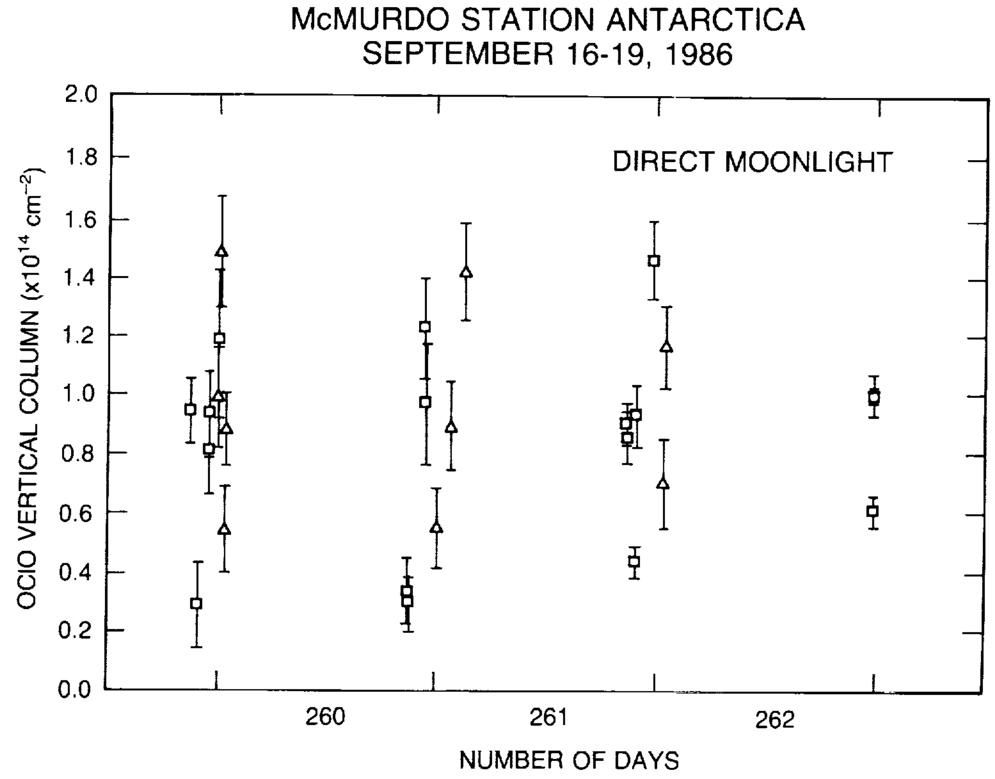

Figure 11.54. OClO vertical column over McMurdo from September 16–19, 1986, measured by direct moonlight. (From S. Solomon et al., 1987.)

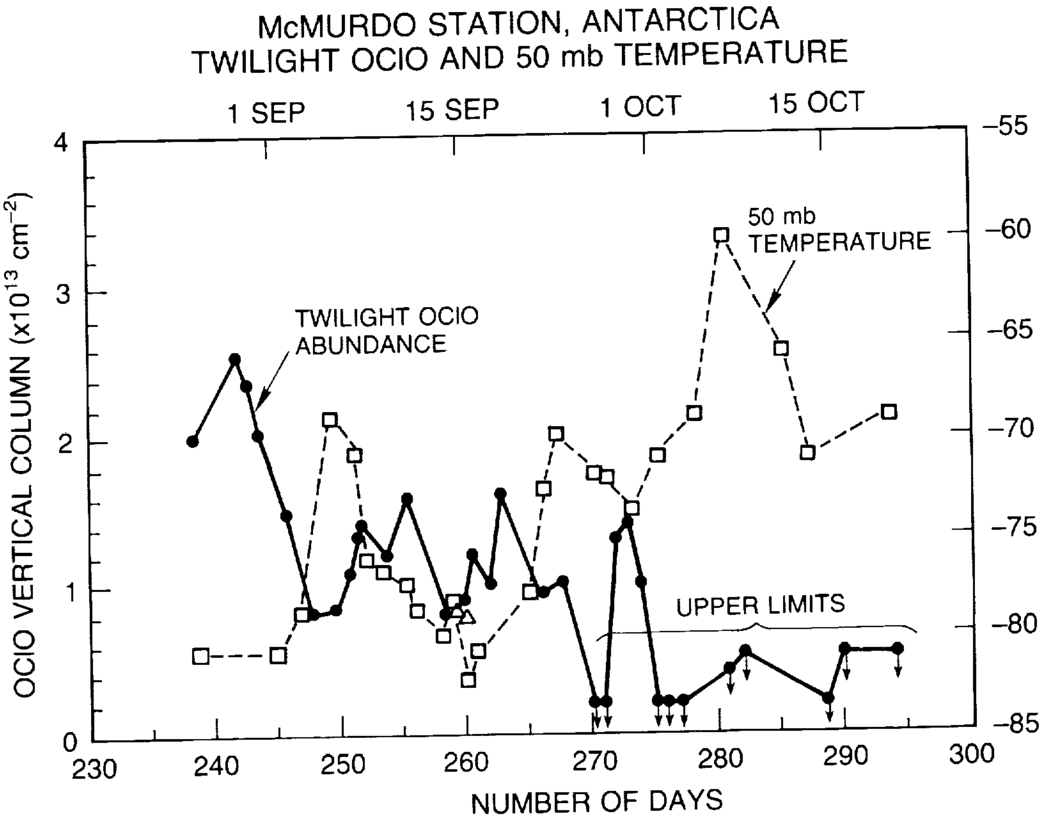

Figure 11.55. OClO vertical column over McMurdo from late August through mid-October 1986 measured during twilight. Also shown is the 50 mb temperature. (From S. Solomon et al., 1987.)

McMurdo data from this year and last, the observed absolute abundances and the diurnal behavior of OClO may be difficult to rationalize with the present chemical mechanisms, particularly in light of new observations that the abundances of BrO are only a few pptv at ER–2 flight altitudes. In addition, it should be noted that there are still significant uncertainties, which are currently being resolved, for the absolute rate constant and branching ratio of the BrO + ClO reaction at lower stratospheric Antarctic conditions. Salawitch et al. (1988a) have simulated OClO abundances, both day and night, for a range of BrO abundances, taking into account different branching ratios for the ClO + BrO reaction. They reported that the observed diurnal variation of OClO is consistent with the ClO + BrO reaction being the sole source of OClO if the reaction has a channel forming BrCl, and if the abundance of BrO is about 10 pptv near 18 km. They concluded that if the ClO + BrO reaction did not have a pathway forming BrCl between 3.5 percent and 14 percent of the time, then the diurnal behavior of OClO implies an additional source of OClO in twilight. This analysis depends critically upon the assumed altitude profiles for the concentrations of both ClO and BrO. Consequently, once the aircraft and McMurdo data become available for both ClO and BrO, a critical analysis of the paper by Salawitch et al. can be performed.

Both the 1986 McMurdo and 1987 DC–8 data demonstrate that the column content of HCl, which is one of the major chlorine reservoirs at midlatitudes, is very low within the chemically perturbed region of the vortex, reaching column contents below 1 × 10^{15} molecules per cm^2 (Farmer et al., 1987). In addition, the column amount ratio of HCl to HF within the chemically perturbed region decreased significantly from a normal midlatitude value of 4 to a value less than unity. Significant concentrations of chlorine nitrate were observed from McMurdo (Farmer et al., 1987). Figure 11.56 shows the vertical column abundances of the chlorine reservoir species, HCl and $ClONO_2$, and their sum, over the McMurdo station during September and October 1986. Table 11.4, from Farmer et al. (1987), tabulates the vertical column abundances of a number of chemical constituents observed at McMurdo station in 1986 using infrared absorption interferometry.

Table 11.4 Observed vertical column abundance (mol. cm^{-2})

Molecule	O_3* ($\times 10^{18}$)	O_3 ($\times 10^{18}$)	NO ($\times 10^{15}$)	NO_2 ($\times 10^{15}$)	HNO_3 ($\times 10^{15}$)	$ClONO_2$ ($\times 10^{15}$)	HCl ($\times 10^{15}$)
Date							
09/08	7.79	8.47±0.20	2.4±0.5	1.4±0.5	19.6±0.5	2.5±0.5	1.56±0.10
09/15	6.15	5.57±0.20	2.6±0.6	1.0±0.4	14.9±0.4	1.8±0.3	1.48±0.10
09/17	5.51	5.98−0.15	2.3±0.4	0.5±0.5	10.9±0.2	1.5±0.2	1.58±0.10
09/20	5.83	5.92−0.15	2.1±1.0		10.8±0.2	2.0±0.2	2.04±0.15
09/24	8.04	8.06−0.20	3.6±0.6	3.0±2.5	16.6±0.5	4.5±0.4	2.69±0.15
09/25	7.04	7.37−0.15	3.1±0.2	1.9±0.4	12.7±0.4	3.7±0.2	2.84±0.10
09/28	6.26	6.44−0.10	3.0±0.2	1.1±0.4	11.2±0.2	3.0±0.2	2.85±0.05
09/30	6.48	6.99−0.15	3.0±0.5	2.2±0.5	14.1±0.2	3.8±0.4	2.88±0.10
10/01	6.26	6.33−0.12	3.5±0.5	2.8±0.5	15.1±0.2	3.7±0.2	2.99±0.10
10/08	7.28	8.55−0.05	3.4±0.3	3.0±0.2	20.0±0.2	3.5±0.1	4.15±0.05
10/12**	6.56	6.95−0.05	3.5±0.4	2.1±0.5	10.2±0.1	3.4±0.5	4.20±0.05
10/15	5.78	5.85−0.05	2.9±0.2	1.9±0.3	11.5±0.2	2.5±0.1	4.17±0.05
10/21	5.13	5.29−0.60	2.8±0.8	2.4±0.6	9.4±0.4	2.4±1.2	3.65±0.25
10/24	5.67	5.55−0.40	3.7±0.5	2.0±1.5	10.7±0.3	1.5±0.8	5.29±0.25

*Latitude-corrected TOMS O_3 column values; see text
**HF = $1.80 \times 10^{15} \pm 0.01$

The bromine monoxide radical was observed at abundances of a few pptv within the chemically perturbed region of the vortex at the flight levels of the ER–2. The abundance of BrO decreased at lower altitudes. Total column measurements of BrO from the DC–8 and from McMurdo in 1987 are currently being analyzed. The low measured abundances of BrO mean that Scheme B is not the dominant catalytic mechanism for ozone destruction. Nevertheless, Scheme B probably accounts for 5 to 10 percent of the ozone destruction at the ER–2 flight levels.

11.4.2.4 Observations of Nitrogen Species

Observations of column amounts of NO, NO_2, HNO_3, and $ClONO_2$ at McMurdo in 1986 demonstrated that the atmosphere was denitrified (Mount et al., 1987; Farmer et al., 1987). Figures 11.57 and 11.58 show the temporal behavior of NO_2 from Mount et al. (1987), and of NO, NO_2, and HNO_3 from Farmer et al. (1987), respectively. The in situ ER–2 observations of the abundance of odd nitrogen, which is the sum of all nitrogen-containing reservoir and radical species, show, like total water, very low values within the chemically perturbed region of the vortex, indicating that the atmosphere has been denitrified as well as dehydrated. Abundances of NO_y of 8–12 ppbv were observed outside the chemically perturbed region, while abundances of 0.5 to 4 ppbv were observed inside the region. A similarly large change was observed for one of

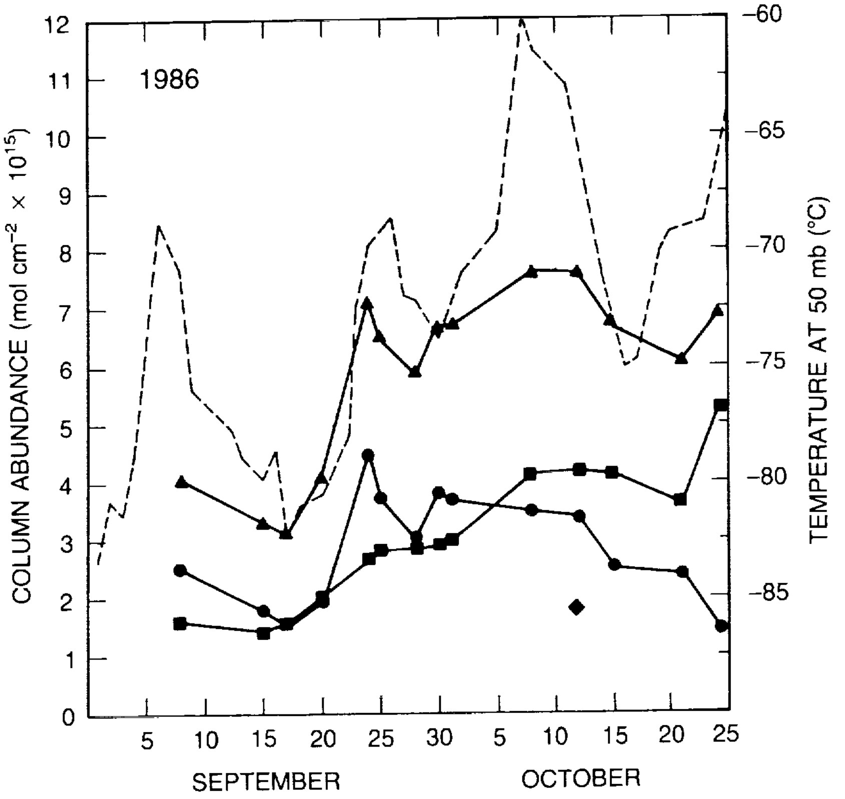

Figure 11.56. Vertical column abundances for the chlorine reservoir species HCl (squares), $ClONO_2$ (circles, and their sum (triangles). The column abundance value for the HF obtained on October 12, 1986, is also shown (diamond). The dotted line shows the temperature at the 50-mb level. (Farmer et al., 1987.)

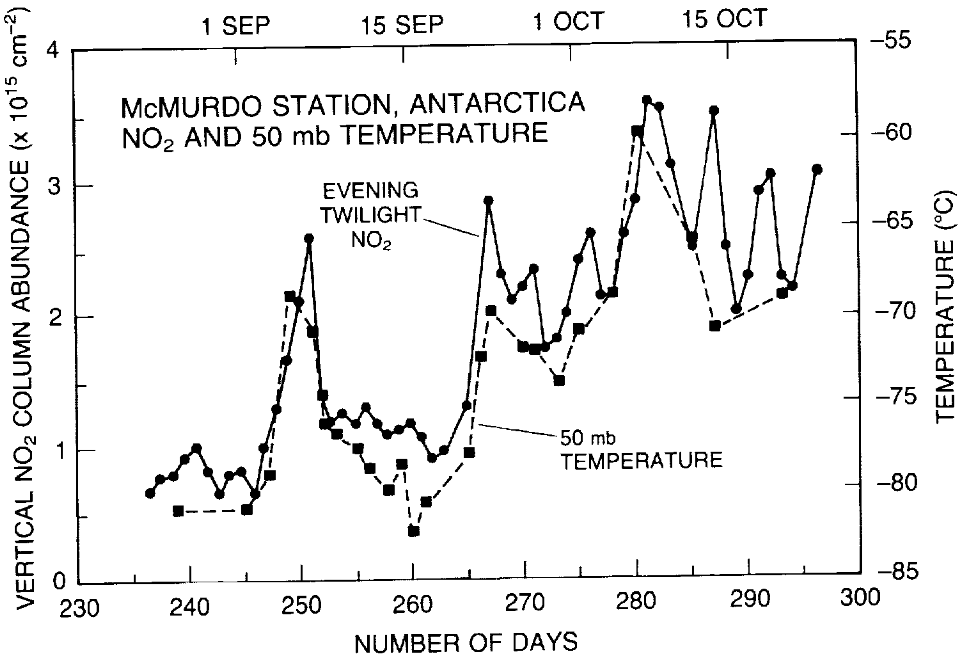

Figure 11.57. NO_2 vertical column over McMurdo from late August through mid-October, 1986, measured during evening twilight compared to 50 mb temperatures (from Mount et al., 1987.)

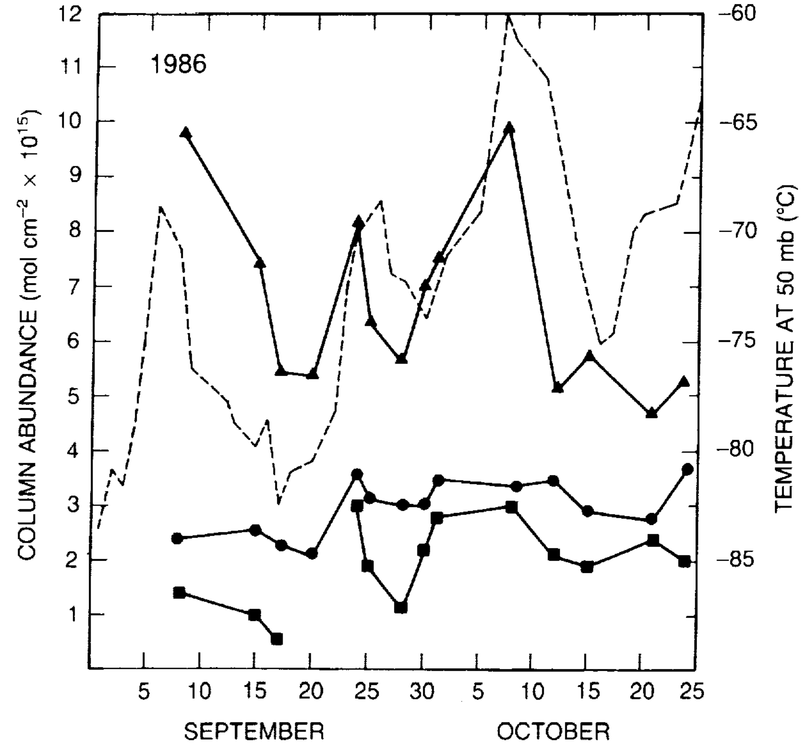

Figure 11.58. Vertical column abundances of HNO_3 (triangles), NO (circles), and NO_2 (squares), over McMurdo Station during September and October 1986. Note that the HNO_3 values are shown at half scale. The dotted line shows the temperature at the 50-mb level. (Farmer et al., 1987.)

the nitrogen components, NO. In addition, some of the NO_y observations suggest that NO_y component species are incorporated into PSC particles; nitrate was observed in the particle phase on some of the filter samples and on some of the wire impactor samples taken in the chemically perturbed region of the vortex. The column measurements of nitric oxide, nitrogen dioxide, and nitric acid made from the DC–8 exhibit a strong decrease in the abundance of these species toward the center of the vortex. These low values of nitrogen species are contrary to all theories requiring elevated levels of nitrogen oxides, such as the proposed solar cycle theory (Callis and Natarajan, 1986).

Observational data showing that air within the chemically perturbed region of the vortex is dehydrated and that the NO_y abundances are very low are consistent with theories that have been invoked whereby the chlorine reservoir species, $ClONO_2$ and HCl, can react on the surfaces of PSC's to enhance the abundance of active chlorine species, i.e., ClO. The observations also support the picture that the abundance of NO_y is low because odd nitrogen can be removed from the atmosphere by being tied up in ice crystals, which can then gravitationally settle to much lower altitudes. Low abundances of NO_y are needed to prevent the rapid reconversion of ClO to $ClONO_2$. This picture is further supported by the observations of low column abundances of HCl, by occasional observations of high levels of nitrate found in the ice particles, and by the visual and lidar observations of high cirrus and polar stratospheric clouds. The meteorology must play a role in the dehydration and denitrification processes. It is crucial to understand whether the necessary low temperatures are maintained radiatively or by ascent, or by some combination of both.

11.5 CAN WE EXPLAIN THE OBSERVED SPRINGTIME OZONE TREND OVER ANTARCTICA IN THE LAST 20 YEARS?

The mean total ozone column in October over the Antarctic station of Halley Bay (see Figure 11.1) exhibits a pronounced interannual variability and an overall weak trend in the 1970's, followed by a substantially faster decrease after 1979. This section will discuss possible explanations for the long-term spring decrease. It is not clear that this highly nonlinear behavior can be quantitatively explained within currently accepted concepts. A doubling of the Cl_x abundance, which probably occurred in the last 15 years or so, cannot, by itself, explain a 50 percent ozone reduction without invoking nonlinear mechanisms not yet included in current atmospheric models. A key question is: If the amount of odd chlorine becomes similar to or larger than the abundance of odd nitrogen, can the nonlinear chemical processes occurring under such conditions explain the rapid development of the springtime ozone hole after the mid-1970's? Wofsy et al. (1988) have a qualitative explanation of the phenomenon. However, there have been no attempts to date to quantitatively model Antarctic ozone over the last 20 years. Wofsy et al. proposed that if the initial concentration of HCl exceeds a critical value—0.5 times the concentration of NO_x before the onset of condensation—i.e.,

$$[HCl] > 0.5\,[NO_x],$$

where $NO_x = NO + NO_2 + NO_3 + 2\,N_2O_5$, high concentrations of reactive chlorine oxide radicals are rapidly produced, accompanied by efficient ozone destruction, by the following sequence of homogeneous and heterogeneous reactions:

$$\begin{array}{ll}
ClNO_3 + HCl\,(s) & \rightarrow Cl_2 + HNO_3\,(s) \\
Cl_2 + h\nu & \rightarrow Cl + Cl \\
2[Cl + O_3 & \rightarrow ClO + O_2] \\
2[ClO + NO_2 + M & \rightarrow ClNO_3 + M] \\
\hline
\text{net}: HCl\,(s) + 2NO_2 + h\nu + 2O_3 & \rightarrow ClNO_3 + HNO_3\,(s) + 2O_2.
\end{array}$$

Production of unreactive $ClNO_3$ and HOCl is favored if HCl concentrations are lower than this value. Therefore, Wofsy et al. suggested that the onset of Antarctic ozone depletion in the mid- to late 1970's may, in part, reflect growth of HCl concentrations beyond this threshold.

Another cause for the abrupt reduction in Antarctic springtime ozone in the late 1970's and 1980's could be a cooling of the winter polar vortex. The consequence of even a slight climatological temperature change could be the production of increased polar stratospheric cloudiness, since heterogeneous nucleation of gases such as HNO_3 occurs only if the temperature becomes sufficiently low. Below a certain "threshold," NO_x and HNO_3 should start to disappear from the gas phase, and heterogeneous processes should become efficient and contribute to the conversion of inert forms of chlorine to active forms. However, it should be noted that there is no evidence for an unprecedented temperature change during late winter and early spring, i.e., August and September. Cold winters have been observed repeatedly in the past, although their frequency appears to have increased recently. In addition, the polar temperature appears to change with the QBO and, possibly, with solar activity (Labitzke and Van Loon, 1988). The amount of particles in the stratosphere has varied by several orders of magnitude on different occasions after the eruption of volcanoes, and there now appears to be some observational evidence of an increase in the PSC amount since the early 1980's (Iwasaka et al., 1986; McCormick, private communication).

11.6 WHAT ARE THE IMPLICATIONS FOR THE GLOBAL EARTH'S SYSTEM OF THE OZONE CHANGES OBSERVED OVER ANTARCTICA?

Besides its dramatic character and sudden appearance, a reason for concern about the ozone hole is that the processes that appear to play a decisive role in the polar environment, and that are not fully understood or included in atmospheric models, could be important at other latitudes and contribute to a global ozone depletion.

Since aerosols are present in the stratosphere at all latitudes, it is important to estimate if the processes involving heterogeneous reactions, and possibly leading to ozone destruction, could also occur in other regions of the atmosphere, for example, the Arctic. To address this problem, it is useful to note that the polar vortex of the Southern Hemisphere is, on average, nearly 10 K colder than the vortex of the Northern Hemisphere and that the composition and physical properties of the aerosols may be significantly different. However, it also should be noted that the average temperature is probably not the important quantity for dehydration. For example, in the Antarctic polar stratosphere, where the temperature reaches 180–190 K at 10–20 km altitude, the frost point of water vapor is reached and large ice particles can form; these may subside and disappear from the stratosphere, leaving the stratosphere dehydrated and denitrified. In the Arctic, where temperatures are in the 190–200 K range, relatively small $HNO_3 \cdot 3H_2O$ particles are expected to form in local regions. The Northern Hemisphere is very different in both the spatial extent of PSC's and meridional flow, and, hence, illumination of air masses exposed to the PSC's. The temperature increases at the end of the winter, essentially as a result of adiabatic processes, resulting in the disappearance of the PSC's before the Sun returns over the North Pole. However, because of the high planetary wave activity in the Northern Hemisphere during winter, the vortex is often significantly displaced from the pole and reaches an illuminated environment where photochemistry could initiate ozone destruction processes. Except for very special configurations where small regions of low temperature are formed, such events should not produce such dramatic ozone changes as observed in the Antarctic: the particles are probably not large enough to subside and remove active nitrogen from the northern polar vortex, and the time required for ClO to destroy ozone is probably longer than the time during which the vortex is illuminated. Finally, because of high dynamical activity and frequent breakdowns of the vortex, substantial transport of ozone from midlatitudes to the polar region occurs during a large portion of the winter; thus, any regions of low ozone formed should rapidly disappear. Measurements of key chemical constituents in the polar region of the Northern Hemisphere should nevertheless confirm these hypotheses and establish whether ozone is substantially changed in geographically limited cold and dynamically undisturbed areas.

The question of possible ozone depletion at midlatitudes as a result of heterogeneous chemistry must also be considered because a substantial number of particles is present at all latitudes inside the so-called Junge layer. These particles, which are small liquid drops, are composed of a mixture of sulfuric acid and water and are thus significantly different from the HNO_3/H_2O particles in the PSC's (or haze). Therefore, the catalytic efficiencies of the particles in the Junge layer and in the PSC's differ, as discussed earlier in the section on heterogeneous processes (see Table 11.3). Furthermore, the mass density of the aerosols in the Junge layer is several orders of magnitude smaller than in the PSC's. Finally, the temperature of the lower stratosphere outside the polar regions is significantly higher (220 K) than in the polar vortex (190–210 K), except over the Tropics, where strong upward motions are present. Processes similar to those hypothesized to explain the formation of the ozone hole over Antarctica, for example, denitrification due to gravitational settling of large particles containing adsorbed nitric acid, are thus unlikely to appear at midlatitudes, although some heterogeneous processes might periodically become important and lead to ozone destruction after large volcanic eruptions, when the amount of particles in the stratosphere is enhanced by several orders of magnitude. If heterogeneous processes are important at midlatitudes, then the concentrations of ClO should be elevated in the Junge layer; this can be evaluated by careful measurements. Calculations of the possible enhancement of ClO in the Junge layer have been performed by Rodriguez et al. (1988). Brune et al. (1988) reported measurements of the vertical distribution of the ClO radical at midlatitudes in the Northern Hemisphere from balloon (24–40 km) and aircraft platforms (15–20 km), as shown in Figure 11.59. It is clear that the abundance of ClO in the peak region of the aerosol layer, i.e., 16 to 20 km, is not significantly elevated as in the chemically perturbed region of the Antarctic ozone hole. This indicates that conversion of inactive reservoir forms of inorganic chlorine—i.e., HCl and $ClNO_3$—to the active form—i.e., ClO—does not appear to be enhanced detectably enhanced (less than a factor of 3 to 5) in this region of the stratosphere.

The possibility of a "dilution effect" of the polar anomaly observed in spring over Antarctica must be considered another possible global implication of the Antarctic ozone hole. Since the chemical lifetime of ozone in the lower stratosphere is of the order of a year, air masses with depleted ozone amounts move toward the Equator as soon as the winter vortex ceases to exist (November and December). As volumes of air with extremely low ozone are transported toward lower latitudes every year, the effects might partly accumulate, and a limited change in the total hemispheric ozone content could become noticeable. At present, this issue is being addressed using both multidimensional theoretical models and the TOMS satellite data by examining changes in total column ozone in both hemispheres.

11.7 QUESTIONS FOR THE FUTURE

The understanding of the mechanisms involved in the rapid decrease of ozone over Antarctica each spring since the late 1970's requires a continuing intense international research effort

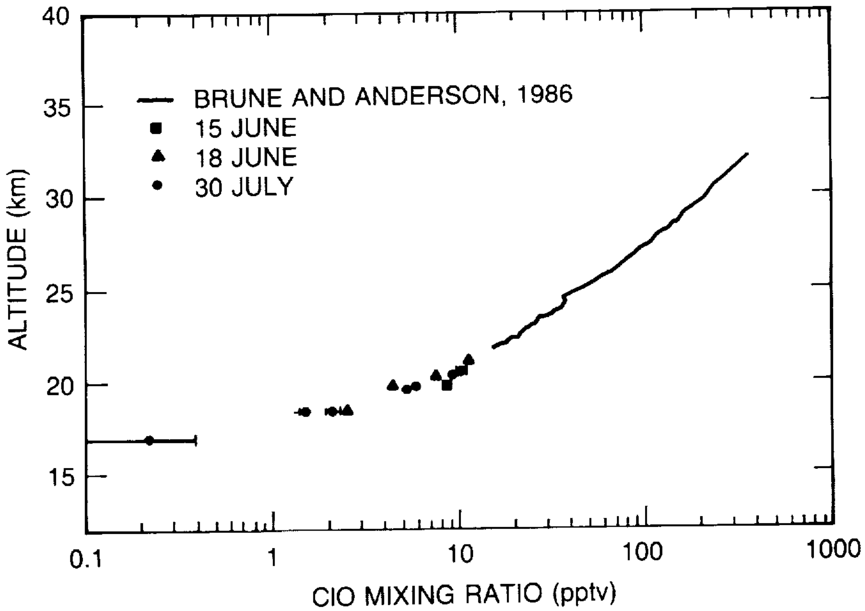

Figure 11.59. ClO mixing ration versus altitude. Symbols are data from the three ER-2 flights; the line represents data from the May 1986 balloon flight. Error bars are 1σ statistical uncertainty. (Brune et al., 1988.)

involving additional field experiments (in the Antarctic and Arctic regions), laboratory work (dealing with homogeneous chlorine chemistry and heterogeneous processes), and modeling studies (involving coupled chemical, dynamical, and radiative models). The following questions should be urgently addressed:

- How is the Antarctic atmosphere preconditioned before ozone is depleted in late winter and early spring? Does the chemical composition change during the polar night?
- Do the observed abundances of ClO and BrO "quantitatively" explain the observed ozone decrease as a function of height and time?
- Can the ozone decrease be explained within a given year? Are the year-to-year changes understood?
- Is the dynamical morphology of the ozone hole understood? Are the relative roles of chemistry and dynamics explained?
- Can the region of depleted ozone become wider and deeper?
- Can mechanisms similar to those occurring in Antarctica destroy ozone at other latitudes (e.g., at the North Pole)? To what extent will the region of low ozone be diluted toward other latitudes in the Southern Hemisphere?
- Can a persistent ozone hole phenomenon change the climate and dynamics of the stratosphere?
- If the climate of the stratosphere is affected, do the changes tend to amplify the ozone hole?
- Can we design field measurements and laboratory experiments that would allow us to understand the composition and formation kinetics of polar stratospheric clouds?
- Can we develop laboratory experiments and theoretical models that allow us to measure and model PSC-induced heterogeneous reaction processes with the same level of accuracy we currently measure and model homogeneous gas phase reaction processes?

11.8 SUMMARY

11.8.1 Ozone Observations

Ground and satellite measurements (using several techniques) of total column ozone over high southern latitudes in springtime corroborate one another and provide a clear picture of the changes that have occurred. A significant change in the springtime total ozone content over the Antarctic was first reported by the British Antarctic Survey using the Dobson station data at Halley Bay (76°S, 27°W), with a smaller change seen at the Argentine Islands (65°S, 64°W) (Farman et al., 1985). The satellite data not only confirm the decrease reported from ground-station data, but demonstrate that the phenomenon is of large regional scale, at least the size of the Antarctic continent. The key aspects of the Antarctic ozone hole are that:

- Ground-based and satellite data clearly show that the abundance of ozone dropped rapidly after the late 1970's. However, given the high level of interannual variability in Antarctic ozone, it is difficult to draw strong quantitative conclusions about the magnitude of ozone decreases during the 1970's.

- The development of the minimum occurs mainly during September.
- The rate of change of ozone within a given Antarctic spring appears to be increasing.
- The region of low ozone over Antarctica persisted until late November/early December 1987.
- Ozone was lower in 1987 at all latitudes south of 60°S than in any previous year since measurements began; the October monthly zonal mean total ozone amounts at 50°S, 60°S, 70°S, and 80°S were 8 percent, 20 percent, 41 percent, and 49 percent lower, respectively, than in 1979.
- In some instances, total column ozone changed dramatically (25–50 DU) over areas as large as several million square kilometers within a matter of a day or two; these reductions lasted for up to a few days.
- The altitude profiling by balloonborne ozonesondes has shown similar features at a number of stations consistent with the SAGE satellite results, providing confidence in the robustness of these results.
- Balloon ozonesonde and SAGE satellite data indicate that the ozone decrease over Antarctica is confined to a region between about 12 and 24 km.
- In October 1987, ozone concentrations between about 15 and 20 km decreased by more than 95 percent of their August values.

11.8.2 Polar Stratospheric Cloud Observations

The vertical extent of PSC's correlates with cold temperatures. Atmospheric temperatures increase during springtime starting at higher altitudes, resulting in a decrease with time of the maximum altitude at which PSC's can exist. The persistence of PSC's in Antarctica has increased since 1984. The 1985 observations show, for the first time, the occurrence of PSC's at 16 km throughout the end of September. Further, in 1987, PSC's lasted into October at altitudes as high as 18 km and 20 km, in sharp contrast to earlier years.

11.8.3 Temperature Observations

Substantial evidence has been presented for a decline since 1979 in the temperature of the lower stratosphere over Antarctica in October and November. The downward trends appear most strongly in October, when a substantial decline is observed in the middle as well as in the lower stratosphere. During November, the trend is confined to the lower stratosphere, with maximum negative trend of about 1 K per year centered at about the 100hPa level. August and September temperatures show little or no trend over the 1979–1985 period. The decline appears in both rawinsonde station data and NMC gridded data that include satellite information.

11.8.4 Transport Theories for the Antarctic Ozone Hole

The polar lower stratosphere of the Southern Hemisphere is very different from that of the Northern Hemisphere. Strong zonal symmetry of surface conditions in the Southern Hemisphere produces a circulation that is relatively symmetric and undisturbed by planetary wave activity; the lower stratosphere in which the lower stratospheric polar vortex is relatively intense, maintaining its integrity throughout winter and into spring. Dynamical modeling suggests that relatively little mixing occurs with air at other latitudes at altitudes where the vortex is sufficiently intense, and the air within the polar vortex thus remains very cold and dynamically isolated. In springtime, temperatures may be near or below radiative equilibrium; thus, solar heating might drive the seasonal change more in the Southern Hemisphere than in the Northern, where temperatures are kept well above radiative equilibrium by stronger wave forcing.

The observed Antarctic ozone decline occurs in the lower stratosphere, where transport by atmospheric motions has a major influence on the ozone-mixing ratio. A relatively small climate shift in the Southern Hemisphere could produce a significant change in the total ozone over Antarctica, since the transport of ozone into that region during winter and spring is limited by dynamical constraints associated with the symmetry of the circulation and is very weak in comparison to the almost complete mixing that occurs in the Northern Hemisphere. While colder temperatures at the beginning of spring, or later enhanced solar heating, could lead to transient upwelling that would contribute to the springtime ozone decline, it is unlikely that diabatic heating rates would be both sufficiently large and suitably distributed to produce the 1987 reduction.

Data suggest a decline in temperatures in the Antarctic lower stratosphere from 1979–1985 for October and November, and a corresponding decline in the wave driving for September. Calculations suggest that the radiative effect of the ozone decline is comparable in magnitude to the observed trend. The radiative temperature change is largest at the 100hPa level; its vertical structure in the lower stratosphere is very similar to that of the November trend. October shows a middle stratospheric temperature decline as well, which appears more likely to be associated with decreased wave driving during the previous month. Some combination of altered wave driving and radiative response to ozone changes seems necessary to explain the 1979–1985 trend.

Models attributing the decline only to changed transport processes require that low-ozone air be moved into the lower stratosphere from below. Such movement would also imply an increase of long-lived trace species of tropospheric origin. Aircraft data show that these trace species remain relatively constant during September as ozone declines significantly, so that transport is unlikely to be a significant contributor. These data support the hypothesis that a chemical sink for ozone is required within the polar vortex. However, the role of radiative and dynamical processes in establishing the conditions necessary for the ozone depletion and in controlling the temperature, cloudiness, and precise degree of isolation of the Antarctic ozone hole must be carefully considered.

11.8.5 Chemical Theories and Observations for the Antarctic Ozone Hole

Two distinctly different classes of chemical theories have been proposed to explain the observed loss of springtime Antarctic ozone. The first suggests that the abundance of the oxides of nitrogen is enhanced periodically by changes in solar activity; the second proposes that the efficiency of reactions involving chlorine and bromine species is enhanced. All current theories that attempt to describe ozone loss in the Antarctic stratosphere in terms of catalytic chemical destruction involving chlorine or bromine have the following features:

- Conversion of a substantial fraction of the Cl_x contained in the reservoir molecules, HCl and $ClONO_2$ into active forms of chlorine, such as ClO, either by heterogeneous reactions in PSC's or by enhanced OH abundance.
- Cycles that effectively catalyze the recombination of O_3 with itself, involving ClO in the rate limiting step with HO_2, itself, or BrO, forming HOCl, the Cl_2O_2 dimer, or Cl and Br, respectively.
- Drastic reduction in NO_2 abundance resulting from removal of NO_y as HNO_3 in the condensed phase of PSC's.

Recent laboratory data have shown conclusively that heterogeneous reactions of $ClONO_2$ (g) and N_2O_5 (g), with H_2O (s) and HCl (s), are rapid enough to play an important role in the chemistry of the Antarctic stratosphere. In particular, HCl was shown to diffuse readily into water ice crystals at low temperatures, forming solid solutions. Dissolved HCl in solid solutions was also shown to be very mobile, greatly enhancing its reactivity with reactant species on the crystal surfaces. The HNO_3 formed by $ClONO_2$ reactions with ice and HCl ice remains in the condensed phase, whereas the chlorinated products desorb into the gas phase.

Our understanding of the chemical composition of the springtime Antarctic atmosphere increased dramatically during 1986 and 1987. Observations of the vertical distribution and column content of a large number of species, including O_3, H_2O, ClO, OClO, $ClONO_2$, HCl, BrO, HF, NO, NO_2, HNO_3, NO_y, N_2O, CH_4, CCl_4, CH_3CCl_3, and CFC's 11 and 12, were made by ground-based observations from McMurdo in 1986 and 1987, and by in situ and remote-sensing techniques from aircraft in Punta Arenas in 1987. In addition, the size distribution, abundance, and composition of particles, the vertical distribution of aerosols from 12 to 28 km, and the size distribution were determined by aircraft, lidar, and balloonsondes, respectively, in an effort to understand the role of heterogeneous processes. The data clearly demonstrated that the chemical composition of the Antarctic stratosphere in springtime was highly perturbed. The distribution of chlorine species and the abundance and distribution of nitrogen species are significantly different from those observed at midlatitudes. It is not clear whether the abundance of total inorganic chlorine is perturbed relative to that expected, or just the partitioning. The amount of total water within some regions of the vortex is also significantly lower than anticipated.

Observational evidence strongly suggests that chemical mechanisms involving chlorine contribute to the formation of the Antarctic ozone hole, and meteorology sets up the special conditions required for the perturbed chemistry. The region of dehydrated and denitrified air maintained a sharply defined latitude gradient throughout the aircraft observation. On a purely meteorological definition, the vortex edge would be well outside the dehydrated, denitrified region. The meteorological flow must, therefore, have maintained a "containment vessel" in which the perturbed chemistry could proceed without being influenced by mixing in more normal stratospheric air from outside or below. Mixing at the region of sharp latitudinal gradient has the potential to supply nitrogen oxides that would tend to decelerate the chlorine chemistry. The meteorology is thus important in both the termination and initiation phases.

There is strong evidence that the chemical composition of the springtime Antarctic stratosphere is highly perturbed compared to midlatitudes. While the abundance of total chlorine is probably consistent with that expected, the partitioning of Cl_x was highly perturbed. The concentrations of HCl were low, the concentrations of OClO and ClO were significantly elevated, and concentration of $ClONO_2$ were somewhat elevated. The fraction of chlorine in an active form was significantly enhanced over that observed at midlatitudes; its abundance within the chemically perturbed region of the Antarctic atmosphere is greater by a factor of 100 to 500 than that measured at comparable altitudes at midlatitudes, reaching about 1 ppbv near 18 to 20 km. Within the chemically perturbed region of the vortex near 18.5 km, the abundance of ClO during September 1987 was sufficient to account for the destruction of ozone if our current understanding of the chlorine–ozone ClO dimer catalytic cycle is correct. The highest aircraft measurements showed the rate of ozone decrease during September to be consistent with simultaneously observed concentrations of ClO. Also consistent with ozone destruction by chlorine catalysis is that, during August, a consistent positive correlation between ClO and O_3 was observed, whereas by mid-September, as the ozone concentration was dropping at aircraft altitudes, a strong anticorrelation developed between ClO and O_3 that was usually present on both large and small scales within the chemically perturbed region.

The bromine monoxide radical was observed at abundances of a few pptv within the chemically perturbed region of the vortex at flight levels. The abundance of BrO decreased at lower altitudes. Total BrO column measurements taken from aircraft and balloonsonde in 1987 are being analyzed. The low measured abundances of BrO mean that the catalytic cycle involving the $BrO + ClO \rightarrow Br + Cl + O_2$ reaction is not the dominant catalytic mechanism for ozone destruction. Nevertheless, Scheme B probably accounts for 5–10 percent of the ozone destruction at flight levels.

The in situ aircraft observations of the abundance of odd nitrogen show, like total water, very low values within the chemically perturbed region of the vortex, indicating that the atmosphere has been denitrified as well as dehydrated. Abundances of NO_y of 8–12 ppbv were observed outside the chemically perturbed region, while abundances of 0.5 to 4 ppbv were observed inside. In addition, some of the NO_y observations suggest that NO_y component species are incorporated into PSC particles; nitrate was observed in the particle phase on some of the filter samples and on some of the wire impactor samples taken in the chemically perturbed region of the vortex. The ground-based and aircraft column measurements of nitric oxide, nitrogen dioxide, and nitric acid exhibit a strong decrease in the abundance of these species toward the center of the vortex. These low values of nitrogen species are contrary to all theories requiring elevated levels of nitrogen oxides, such as the proposed solar cycle theory.

Observational data showing that air within the chemically perturbed region of the vortex is dehydrated and that the NO_y abundances are very low are consistent with theories that have been invoked whereby the chlorine reservoir species can react on the surfaces of PSC's to enhance the abundance of active chlorine species. The observations also support the picture that the abundance of NO_y is low because odd nitrogen can be removed from the atmosphere by being tied up in ice crystals, which can then gravitationally settle to much lower altitudes. Low abundances of NO_y are needed to prevent the rapid reconversion of ClO to $ClONO_2$.

APPENDIX A

Statistical Approaches to Ozone Trend Detection

Panel Members

P. Bloomfield, Chair
D. R. Brillinger
D. W. Nychka
R. S. Stolarski

N C 999967

PRECEDING PAGE BLANK NOT FILMED

Appendix A

Statistical Approaches to Ozone Trend Detection

Contents

1.0 CURRENT STATUS OF STATISTICAL ANALYSES 755

- 1.1 Ground-Based Total Column Ozone 755
- 1.2 Ground-Based Ozone Profiles (Umkehr) 758
- 1.3 Satellite Data 759

2.0 TEMPORAL AND SPATIAL CORRELATION 760

- 2.1 Least-Squares Estimates 760
- 2.2 Interpretation of Standard Error 761
- 2.3 Limitations of the Model 761
- 2.4 An Elementary Model for Temporal Correlation 764
- 2.5 More General Temporal Models 766
- 2.6 Spatial Correlation 767

3.0 SEASONALITY IN OZONE DATA 768

- 3.1 Seasonal Structure in the Mean 769
- 3.2 Seasonal Structure in the Trend 770
- 3.3 Seasonal Structure in the Correlations 771

4.0 SUMMARY 772

PRECEDING PAGE BLANK NOT FILMED

PAGE 752 INTENTIONALLY BLANK

1.0 CURRENT STATUS OF STATISTICAL ANALYSES

The statistical analyses compiled by Reinsel, Tiao, and their coworkers provide the most comprehensive work on trend direction. This group's efforts represent a long-term involvement with ozone data. Their methods have been published in peer-reviewed statistical journals (Reinsel and Tiao, 1987), and previous discrepancies with other approaches have been reconciled (Hill et al., 1986). Stemming from this statistical work are some recent analyses concerning seasonal trends in total ozone for some of the stations in the Dobson network, reported in Chapter 4 of this report. There is a substantial amount of analysis of ozone measurements in the meteorological literature, such as the work by Angell and Korshover (1983b). However, because such studies do not adequately adjust for the short-term correlation in ozone over time, their results are of limited value for drawing conclusions about trends in ozone. For these reasons, this review will concentrate on the methods developed by Reinsel and Tiao.

1.1 Ground-Based Total Column Ozone

The most complete statistical analysis of ground-based ozone measurements is by Reinsel et al. (1987). Based on the measurements of a global network of 36 Dobson spectrophotometers, an average trend of -0.026 ± 0.092 percent per year[1] was estimated over the period 1970–1984[2]. Perhaps the most important aspect of interpreting these results is to distinguish between the average trend associated with these 36 locations and a global trend in total column ozone. They need not be the same. Although satellite data (see Section 1.3) suggest that trend analysis based on the Dobson network is representative of a global trend, more investigation in this area is needed. At present it is uncertain how to extrapolate the average trend among the Dobson network to a global trend for the entire atmosphere.

In order to discuss the assumptions that lead to the average trend cited above and to compare this analysis with other work, it is helpful to describe the statistical model used by Reinsel and Tiao. This model accounts for several factors that influence trend detection: the seasonal behavior of ozone, the relationship of ozone with the solar activity, and short-term autocorrelation within the ozone series. Let Y_t represent the monthly average total ozone recorded from a particular Dobson station. This observation is assumed to have the following decomposition:

$$Y_t = \mu + S_t + \omega X_t + \gamma Z_t + N_t. \tag{1}$$

In the above expression, μ represents a mean level, S_t is a seasonal component, X_t is a ramp function modeling a linear trend in ozone beginning in 1970, Z_t is the monthly average of 10.7 cm solar flux (or a smoothed version of it), and, finally, N_t is a random variable representing the short-term variation in ozone. The parameter ω represents the trend in ozone. Using this statistical model and some assumptions on the short-term variation, it is possible to estimate ω and also derive a measure of the uncertainty in this estimate.

It is well accepted that the monthly fluctuations in ozone are not independent of one another and tend to be positively correlated. One way of accounting for this behavior is to assume that

---

[1] In this appendix all ± limits correspond to 95 percent confidence intervals.

[2] This trend estimate has been updated to -0.05 ± 0.07 percent per year during the longer period of 1970–1986 for a network of 43 Dobson stations (Reinsel, 1988, personal communication).

$\{N_t\}$ is approximated by an autoregressive time series (see Sections 2.4, 2.5, and 3.3 for more detail). Another approach using spectral analysis is given by Bloomfield et al. (1983). This part of the statistical model is necessary in order to obtain reliable measures of uncertainty for the trend estimate. Unfortunately, the trend estimates reported by Angell and Korshover (1983b) and Heath (1986) based on ordinary least-squares are of unknown accuracy because the standard errors (SE's) do not allow for autocorrelation. This issue is discussed at length in Section 2.

The other components in this model are also related to the estimate of ω. Modeling seasonality of the ozone measurements reduces the variance in the data and thus improves the accuracy of the trend estimate. The inclusion of the solar flux reduces bias in the estimate of ω by distinguishing behavior in ozone due to solar cycle from other long-term trends.

The statistical model described above is used by Reinsel and Tiao to obtain trend estimates for each station. Using a random effects model to describe variation between stations, these estimates are combined to yield an average trend for the Dobson network. In order to be able to interpret this estimated average trend, this random effects model will be briefly described. The 36 stations can be divided into seven geographic regions (see Table 1, from Hill et al., 1986). Let $\omega_{i,j}$ denote the actual trend in total ozone for the ith station in the jth region. This trend is assumed to satisfy the equation

$$\omega_{i,j} = \omega + \alpha_j + \beta_{i,j}$$

where ω is the actual "global" trend in ozone, α_j is a zero mean random variable that reflects the variability in trends between different regions, and $\beta_{i,j}$ is a zero mean random variable that reflects the variability of trends within a region. It should be noted that the term $\beta_{i,j}$ not only represents variability due to meteorological effects but also accounts for spurious trends such as calibration problems for particular stations. With this decomposition, the estimated trend for a particular station can be expressed as

$$\hat{\omega}_{i,j} = \omega + \alpha_j + \beta_{i,j} + E_{i,j}$$

where $E_{i,j}$ is the error in the trend estimate due to the variability of the ozone within a station's record.

This "random effects" model can be used to derive an estimate for ω that is a weighted average of the individual trend estimates; a standard error for this estimate can also be calculated. This approach for combining individual trend estimates has an advantage over a simple average because it adjusts for correlation among stations within the same region. The spatial correlation implied by this model, however, has a simple structure that may not be a good approximation of the ozone field. It assumes that all stations within a region are equally correlated while stations in different regions are independent. A more serious problem is interpreting the parameter ω. Although Reinsel et al. (1987) refer to ω as a global trend in ozone, this is an assumption and is not implied by the random effects model. A more precise definition of ω is that it represents the component of trend in total ozone that is common to all the stations used in the analysis.

An alternative to the time domain approach of Reinsel and Tiao can be found in Bloomfield et al. (1983). Rather than using a random effects model to combine estimated trends, a similar model is used to construct an average ozone series. The parameter ω is then estimated from the

Fourier transform of this single series. This frequency domain analysis has the advantage that less need be assumed about the structure of the short- and long-term variation in ozone. One

Table 1. Dobson Network Used in Total Ozone Trend Analysis

Region	Station	Location	Data Period
North America	Resolute, Canada	75°N, 95°W	Jan. 1958–Dec. 1984
	Churchill, Canada	59°N, 94°W	Jan. 1965–Dec. 1984
	Edmonton, Canada*	54°N, 114°W	April 1958–Dec. 1984
	Goose, Canada	53°N, 60°W	Jan. 1962–Dec. 1984
	Caribou, USA	47°N, 68°W	Jan. 1963–Dec. 1984
	Bismarck, USA	47°N, 101°W	Jan. 1963–Dec. 1984
	Toronto, Canada	44°N, 79°W	Jan. 1960–Dec. 1984
	Boulder, USA	40°N, 105°W	Jan. 1964–Dec. 1984
	Nashville, USA	36°N, 87°W	March 1963–Dec. 1984
Europe	Aarhus, Denmark	56°N, 10°E	Jan. 1958–Dec. 1984
	Lerwick, United Kingdom	60°N, 1°W	Jan. 1969–Dec. 1984
	Bracknell, United Kingdom	51°N, 1°W	Jan. 1969–Dec. 1984
	Potsdam, GDR	52°N, 13°E	Jan. 1964–Dec. 1984
	Belsk, Poland	52°N, 21°E	April 1963–Dec. 1984
	Hradec Kralove, Czechoslovakia	50°N, 16°E	Aug. 1961–Dec. 1984
	Hohenpeissenberg, FRG	48°N, 11°E	Jan. 1968–Dec. 1984
	Arosa, Switzerland*	47°N, 10°E	Jan. 1958–Dec. 1984
	Mont Louis, France	42°N, 2°E	March 1962–Dec. 1979
	Vigna di Valle, Italy	42°N, 12°E	Jan. 1958–Dec. 1984
	Cagliari/Elmas, Italy	39°N, 9°E	Jan. 1958–June 1984
	Lisbon, Portugal	39°N, 9°W	Oct. 1967–Dec. 1984
India	Srinagar, India	34°N, 74°E	Feb. 1964–Nov. 1984
	Quetta, Pakistan	30°N, 67°E	Jan. 1964–Dec. 1984
	New Delhi, India	29°N, 77°E	Jan. 1960–Dec. 1984
	Varanasi, India	25°N, 83°E	Jan. 1964–Dec. 1984
	Mount Abu, India	25°N, 73°E	Nov. 1969–Feb. 1982
	Kodaikanal, India*	10°N, 77°E	Jan. 1961–Dec. 1983
Japan	Sapporo	43°N, 141°E	Feb. 1958–Dec. 1984
	Tateno*	36°N, 140°E	Jan. 1958–Dec. 1984
	Kagoshima	32°N, 131°E	Jan. 1960–Dec. 1984
Australia	Brisbane	27°S, 153°E	Jan. 1958–April 1983
	Perth	32°S, 116°E	March 1969–April 1983
	Aspendale*	38°S, 145°E	Jan. 1958–Dec. 1982
	Macquarie Island*	54°S, 159°E	April 1963–Aug. 1981
South America	Huancayo, Peru*	12°S, 75°W	March 1964–Dec. 1984
	Buenos Aires, Argentina*	35°S, 58°W	Oct. 1965–Dec. 1984
Pacific	Mauna Loa, Hawaii*	20°N, 156°W	Jan. 1964–Dec. 1984

*Nine-station network used by Hill et al. (1977).

disadvantage of this model, however, is that stations within a particular region are constrained to having the same spectrum. This assumption is also made among the regional effects. Although this analysis yielded a trend estimate that differed slightly from that of Reinsel and his coworkers, most of the discrepancy can be explained by different sensitivities to extreme ozone values and to the solar variable, by different lengths of data records, and by different methods for modeling the seasonal variance (Hill et al., 1986).

Recent results reported in Chapter 4 suggest that the trend in ozone may depend on the season. For Arosa and several other northern stations, the percent losses in total ozone tended to be greater in the winter. Thus, the estimated trend may be more sensitive to the statistical treatment of the seasonal component than would otherwise have been expected. Another implication of these results is that the sensitivity of the trend estimates may be improved by concentrating on the months in which a larger trend is expected. Because monthly ozone values are autocorrelated, the estimated trends for each month will also be correlated. This feature makes it difficult to interpret the 12 individual trend estimates. However, these estimated monthly trends can be averaged to yield an estimate of the annual trend; a standard error for this estimate can be computed using the dispersion matrix of the individual estimates. Some of the statistical issues of coping with the seasonality in ozone are discussed in Section 3.

1.2 Ground-Based Ozone Profiles (Umkehr)

Statistical analysis of the Umkehr data supplied by some stations in the Dobson network is motivated by the suggestion that the main depletion of ozone due to the release of chlorofluoromethanes (CFM's) will occur at altitudes between 35 to 40 km (Umkehr layers 7 and 8). Trend analysis that concentrates on this segment of the stratosphere may be more sensitive in detecting a depletion due to CFM's than an analysis based on total column ozone. In fact, Reinsel et al. (1987) report a statistically significant negative trend in layers 7 and 8. However, these results need to be qualified in two ways. First, the average trend estimate for a particular layer cannot be interpreted as a global trend, but rather refers to the average ozone in the layer above the Dobson stations taking Umkehr data. Also, Umkehr measurements are sensitive to stratospheric aerosols (see Chapters 3 and 5 of this report). Although Reinsel's method attempts to adjust for aerosols, all the bias caused by the presence of aerosols may not be removed.

The statistical methods applied to the Dobson profile data are similar to the analysis of the total column measurements; therefore, only some specific remarks will be made. To account for the dependence of the Umkehr measurements on aerosols, an additional variable was included in the model (1). This is the atmospheric transmission of solar radiation measured at Mauna Loa, Hawaii. Although these transmission data are specific to the integrated amount of aerosols in the stratosphere over Mauna Loa, it is assumed in Reinsel et al. (1987) that a smoothed and possibly lagged version of this series may be appropriate at other locations. One weakness in this analysis is that the choices for smoothing and lagging the transmission series were not based on a specific statistical model. Nevertheless, the estimated effects due to aerosols on the different ozone layers are in agreement with theoretical predictions. Available aerosol data are discussed in Chapter 10. Reinsel and his coworkers are currently exploring the use of lidar measurements to improve aerosol corrections.

An earlier analysis of Umkehr data by Bloomfield et al. (1982) came to different conclusions from those of Reinsel et al. (1987). Specifically, the earlier analysis detected no significant negative trends. However, the earlier analysis included no attempt to correct for aerosol effects, and was based on older data. Since the statistical methods used were similar to those of Reinsel et al. (1987) in other respects, it is to be expected that an updated analysis would give results largely in agreement with those of the later analysis.

1.3 Satellite Data

The Solar Backscatter Ultraviolet (SBUV) instrument aboard Nimbus–7 provides the most recent and the longest record of ozone measurements from a satellite (see Chapter 5). These data can be used in two different ways to improve trend detection. In contrast to the Dobson network, the Nimbus–7 ozone data provide nearly global coverage. Thus it is fairly simple to construct zonal or global series as aggregations of the raw data. Another use of the satellite data is to assess the global representativeness of the Dobson instrument network. Both of these topics are considered in Reinsel et al. (1988). This work gives an estimate of -0.35 ± 0.28 percent per year for the global trend in total ozone for November 1978 to September 1985, after adjusting for a drift in the SBUV instrument and accounting for solar activity[3]. Comparing the satellite measurements at the locations of the Dobson stations with the full record of measurements suggests that the average trend estimated for this network will be similar to a global trend.

This work uses the same model as that given in (1). The time scale is monthly means, and Y_t should be interpreted as some aggregation of the raw data either over blocks (10 degrees of latitude by 20 degrees of longitude), over zones (bands of 10 degrees latitude), or over the entire surface covered by the satellite (70°S latitude to 70°N latitude). In each of these cases, just as in the Dobson measurements, successive ozone values tend to be correlated. This autocorrelation must be taken into account to derive reliable uncertainty levels for estimated trends. One notable feature of this data set is its short length (7 years) relative to the Dobson data. Since this time series does not even span one solar cycle, the adjustment of the ozone series using a covariate for solar activity (such as 10.7 solar flux) is important. Reinsel et al. (1988) have included such a solar term in their analysis.

Trend analysis using the SBUV data alone is difficult because of an instrument drift (discussed in Chapter 2). Reinsel et al. (1988) estimate a linear drift to be -0.39 ± 0.11 percent per year using the Dobson network[4]. If the satellite data are adjusted by this estimated drift, then the standard error of the estimated trend must also reflect the uncertainty of the drift estimate. Reinsel et al. (1988) include the contribution of the drift uncertainty in the trend standard error, but their method is not entirely satisfactory.

The representativeness of the Dobson network was evaluated by taking a weighted average of all blocks containing the 36 stations used in Reinsel et al. (1988). When this series was subtracted from the global series, no significant trend was found in these differences ($-.06 \pm .12$ percent per year). Although these results suggest that a trend in the Dobson network may be similar to a global trend, there are some problems with this comparison. The blocks are not point measurements of total column ozone but are themselves averages over a substantial amount of surface area. This may cause closer agreement with the global series than might otherwise occur if one used the measurements taken at specific locations. Also, in the actual Dobson analysis, individual trends are estimated for each station and then combined. This differs from first forming an average series from the blocks and then estimating the average trend from this single series.

---

[3] This trend estimate has been updated to -0.28 ± 0.22 percent per year for the period November 1978 through December 1986 (Reinsel, 1988, personal communication).

[4] This drift estimate has been updated to $-.40 \pm 0.11$ percent per year for the period November 1978 through December 1986 (Reinsel, 1988, personal communication).

2.0 TEMPORAL AND SPATIAL CORRELATION

An important contribution of statistical methods to problems such as estimation of trends in ozone data is attaching an appropriate measure of uncertainty to any trend estimate. In this section we shall review the calculation of such measures and discuss their validity.

2.1 Least-Squares Estimates

The calculation of the least-squares slope of a set of data is the most familiar example of trend estimation. Suppose that the data are $y_1, y_2, \ldots, y_n$. Then the least-squares estimate of slope is

$$\hat{\omega} = \frac{\sum_{t=1}^{n} (t - \bar{t})(y_t - \bar{y})}{\sum_{t=1}^{n} (t - \bar{t})^2} \qquad (2)$$

where

$$\bar{t} = (n + 1)/2 \text{ and } \bar{y} = (1/n) \sum_{t=1}^{n} y_t.$$

The full equation of the fitted line is

$$y = \bar{y} + \hat{\omega}(t - \bar{t}).$$

The *residuals* are the vertical distances from the data points (t, y_t) to the line, and are given by

$$r_t = y_t - \hat{y}_t = y_t - \{\bar{y} + \hat{\omega}(t - \bar{t})\}.$$

The *residual sum of squares* is just

$$\sum_{t=1}^{n} r_t^2,$$

and the *residual mean square* is this divided by the *degrees of freedom* $(n-2)$,

$$s^2 = \frac{1}{n-2} \sum_{t=1}^{n} r_t^2.$$

The *standard error* of the slope estimate $\hat{\omega}$ (as it is usually calculated) is

$$SE(\hat{\omega}) = \frac{s}{\sqrt{\sum_{t=1}^{n} (t - \bar{t})^2}}, \qquad (3)$$

and it is common for the estimated slope to be reported as "$\hat{\omega} \pm SE(\hat{\omega})$" or, for reasons described in the next section, as "$\hat{\omega} \pm 2\, SE(\hat{\omega})$". But what meaning can be attached to such a report?

2.2 Interpretation of Standard Error

We can give a firm interpretation to a standard error such as $SE(\hat{\omega})$ only by reference to some *model* for the randomness in the data. The simplest such model is

$$y_t = \mu + \omega(t - \bar{t}) + \epsilon_t, \tag{4}$$

where $\{\epsilon_1, \epsilon_2, \ldots, \epsilon_n\}$ are random errors, independently drawn from a Gaussian distribution with mean value 0 and variance σ^2. The constants μ, ω, and σ are the (statistical) *parameters* of the model, and $\bar{y}$, $\hat{\omega}$, and s are *estimates* of these parameters. The implication of such a model is that the observed set of data $\{y_1, y_2, \ldots, y_n\}$ is only one out of an infinitely large set of possible data sequences, each with different values of the ϵ's. The observed data are a *sample* (of size 1) from the *population* of possible sequences.

Since each possible sequence gives rise to a different value of $\hat{\omega}$, the model implies a distribution for $\hat{\omega}$, called its *sampling distribution*. The variance of this distribution is

$$\mathrm{var}(\hat{\omega}) = \frac{\sigma^2}{\sum_{t=1}^{n} (t - \bar{t})^2}, \tag{5}$$

and, consequently, the standard error calculated in (3) can be regarded as an estimate of the square root of this variance.

It follows that for an appropriate constant $t_{n-2}^{.95}$, the range of values

$$\hat{\omega} \pm t_{n-2}^{.95} SE(\hat{\omega})$$

has a 95 percent chance of containing the "true" slope value, ω, or, in a certain sense,

$$Pr\{\hat{\omega} - t_{n-2}^{.95} SE(\hat{\omega}) \leq \omega \leq \hat{\omega} + t_{n-2}^{.95} SE(\hat{\omega})\} = .95 \tag{6}$$

Since the tabulated values for $t_{n-2}^{.95}$ are all at least 1.96, and for $n > 60$ are at most 2, the interval is often approximated by

$$\hat{\omega} \pm 2SE(\hat{\omega}).$$

Thus, "2σ" limits can be interpreted as giving an approximate 95 percent confidence interval.

2.3 Limitations of the Model

Evidently the credibility of the standard error (3) depends on the credibility of the model (4), in light of the data. It is often clear by cursory inspection that the Gaussian distribution is not a good model for the distribution of the errors ϵ_t. The Gaussian distribution is symmetric about its center and has relatively short tails, behavioral aspects that are often not shared by real data. However, it is known that the confidence interval statement (6) is not drastically affected by such deviations from the model (the effects of such deviations in the simpler case of estimating a mean are discussed by Benjamini, 1983).

A more serious problem is that the model (4) states that the data are *independent* of each other, and hence *uncorrelated*. In many sets of real data, however, especially those collected sequentially in time (*time series* data), cursory inspection reveals *serial* (or *temporal*) *correlation* in the data. Unfortunately, the effect of correlations among the data, including serial correlation, is generally to invalidate any confidence interpretation of the conventional standard error formula (3).

How is correlation visible? Positive correlation among consecutive observations means that a value higher than expected (that is, one with a positive error ϵ) is likely to be followed by another observation with a positive ϵ. Such *persistence* of deviations above or below what is expected is characteristic of many real series, including ozone data and most of the related meteorological data. Figure 1 shows annual mean ozone levels at Arosa, Switzerland, 1933 to 1982, from Birrer (1975) and Dütsch (1984b). Also shown is the (least-squares) regression line for the data, with equation

$$y = 336.4 - 0.1648\,(\text{year} - 1957.5).$$

The occurrence of several values in a row above or below the regression line is evidence of positive serial correlation, though it is less strong in this series than in many. Figure 2 shows the same data with least-squares lines fitted through data for several successive 10-year periods. This is essentially the same as the analysis of Bishop and Hill (1982). The coefficients of the lines are given in Table 2. The average of the nine SE's is 0.819, whereas the standard deviation of the calculated trends is 1.199. Thus the calculated trends show 46 percent more variation than their standard errors suggest they should. For series with stronger correlation between consecutive values, such as monthly station data and regional or global average series, the actual variability can exceed the estimated standard error by much more than in this case.

Where does this leave us? The standard formula (3) is, in general, meaningful only in the context of the model (4), but this model is untenable for most of the data we need to analyze for trend. Evidently we need a more tenable model, and a new formula for standard error that has the desired confidence interpretation (6) in the context of that model.

We shall see that other models may suggest other formulas for slope estimates, as well as for their standard errors. In general, these other slope estimates differ little from the ordinary least-squares estimates (2), and, in fact, (2) is asymptotically efficient in the presence of stationary autocorrelated noise (Grenander, 1954). Thus, the problem lies mainly in obtaining valid standard errors, not in calculating the slope estimate itself.

Table 2. Coefficients of least-squares lines

Start year	End year	Centercept[a]	Slope	SE (slope)
1933	1942	340.633	1.526	1.276
1938	1947	338.458	−0.678	1.397
1943	1952	335.892	1.753	0.676
1948	1957	337.450	0.224	0.799
1953	1962	339.600	0.490	0.747
1958	1967	337.976	−1.915	0.754
1963	1972	335.576	0.643	0.727
1968	1977	334.392	−1.166	0.578
1973	1982	330.375	0.044	0.440

[a] The *centercept* of the line is its height at the midpoint of the interval to which it is fit.

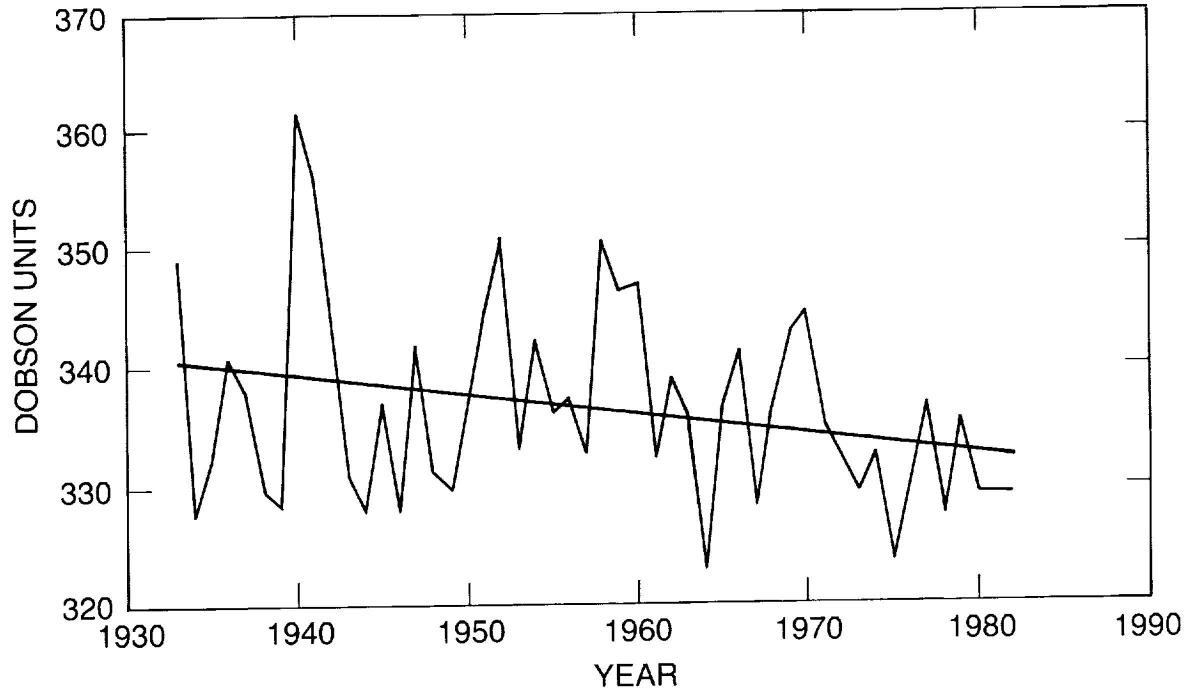

Figure 1: Annual mean ozone levels at Arosa, Switzerland, 1983–1982. (Unweighted averages of monthly means, with missing months replaced by least-squares estimates.)

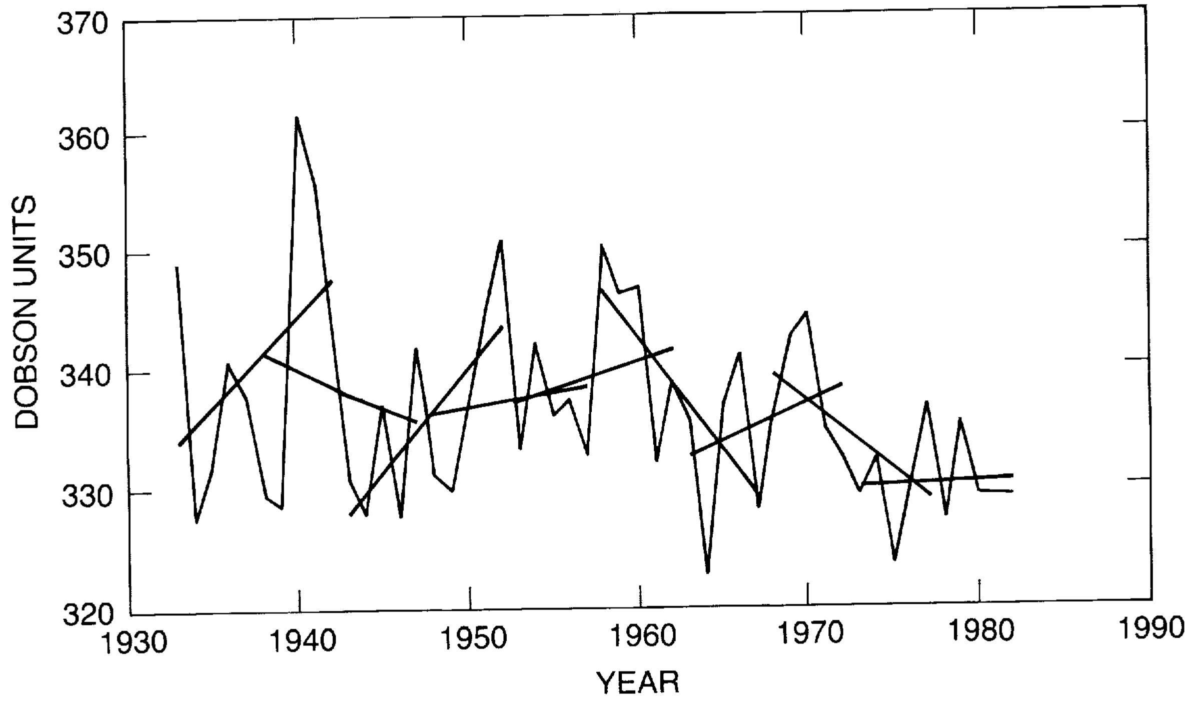

Figure 2: Arosa data with least-squares fitted lines.

2.4 An Elementary Model for Temporal Correlation

Models for serially correlated data have been discussed extensively in the statistical literature (see, for example, Box and Jenkins, 1976). One of the simplest is the (first-order) *autoregressive model*

$$\eta_t = \phi\eta_{t-1} + \epsilon_t, \ |\phi| < 1, \tag{7}$$

where the ϵ's are, as in (4), independent from mean 0 and variance σ^2. If we introduce the *backshift operator* B, defined by

$$B\eta_t = \eta_{t-1},$$

and more generally

$$B^h\eta_t = \eta_{t-h}, \ -\infty < h < \infty,$$

the model (7) may be written

$$\eta_t = \phi B\eta_t + \epsilon_t$$

whence

$$(1 - \phi B)\eta_t = \epsilon_t$$

and

$$\eta_t = (1 - \phi B)^{-1}\epsilon_t.$$

For this model, the serial covariances (or *autocovariances*) are

$$\gamma_h = \mathrm{cov}\,(\eta_t, \eta_{t-h}) = \frac{\sigma^2\phi^{|h|}}{1 - \phi^2}, \ -\infty < h < \infty$$

and the serial correlations are

$$\rho_h = \mathrm{corr}\,(\eta_t, \eta_{t-h}) = \phi^{|h|}, \ -\infty < h < \infty. \tag{8}$$

Since ϕ can be arbitrarily close to 1, this model can display correlations that are also close to 1, and that die away very slowly as the time separation h increases.

Now suppose that we wish to estimate a trend in the presence of correlated errors with the structure (7). That is, suppose that we wish to estimate ω in the equation

$$y_t = \mu + \omega(t - \bar{t}) + \eta_t,$$

where $\{\eta_t\}$ satisfies (7). If we know the value of ϕ, the simplest solution is to construct a new set of data

$$\begin{aligned} y_t^* &= y_t - \phi y_{t-1} \\ &= \{\mu + \omega(t - \bar{t}) + \eta_t\} - \phi\{\mu + \omega(t - 1 - \bar{t}) + \eta_{t-1}\} \\ &= (1 - \phi)(\mu + \omega/2) + \omega(1 - \phi)(t - \bar{t} - 1/2) + \eta_t - \phi\eta_{t-1} \\ &= (1 - \phi)(\mu + \omega/2) + \omega(1 - \phi)(t - \bar{t} - 1/2) + \epsilon_t, \end{aligned}$$

for $t = 2, \ldots, n$. If we write

$$x_t^* = (1 - \phi)(t - \bar{t} - 1/2)$$

and

$$\mu^* = (1 - \phi)\mu + (1 - \phi)\omega/2,$$

then the modified data satisfy

$$y_t^* = \mu^* + \omega x_t^* + \epsilon_t,$$

which is in the same form as the original equation (4), with errors ϵ_t that are now *uncorrelated*. It is therefore legitimate to estimate ω by least-squares, and to report its standard error as in equation (3). The resulting estimate is

$$\hat{\omega}_{ar1} = \frac{\sum_{t=2}^{n} x_t^*(y_t^* - \bar{y}^*)}{\sum_{t=2}^{n} x_t^{*2}}$$

with standard error

$$SE(\hat{\omega}_{\mathrm{ar1}}) = \frac{s_{ar1}}{\sqrt{\sum_{t=2}^{n} x_t^{*2}}}$$

where

$$s_{ar1}^2 = \frac{1}{n-3}\sum_{t=2}^{n}(y_t^* - \bar{y}^* - \hat{\omega}_{ar1}x_t{}^*)^2.$$

It may be shown that if n is large and $|\phi|$ is not close to 1, the new slope estimate $\hat{\omega}_{ar1}$ is very close to the estimate $\hat{\omega}$ of equation (2). However, the new standard error may be quite different from the earlier version, and is typically larger. In fact, we can show that if n is large and $|\phi|$ is not close to 1, then the (valid) standard error of $\hat{\omega}_{ar1}$ is larger than the (invalid) standard error of the least-squares estimate $\hat{\omega}$ by the factor

$$\sqrt{(1 + \phi)/(1 - \phi)}.$$

For the Arosa annual average data, the estimated value of ϕ is around 0.25, which would make this factor approximately 1.29. Since we observed 46 percent more variation among the slopes than was suggested by the least-squares standard error, rather than 29 percent, there is even more variability among the calculated trends than is predicted by the model (7).

Reinsel et al. (1987) found the month-to-month correlation for SBUV total ozone column data averaged from 70°S to 70°N to be around 0.84, which would make this factor 3.39. Thus, for ozone data averaged over a large region, in this case most of the globe, the effect of ignoring serial correlation can be a reported standard error of less than a third of its true value. Reinsel et al. (1988) give several illustrations of the difference between the valid and invalid standard errors.

In practice, of course, we will not know the value of ϕ, but it may be estimated from residuals and, provided the series length is adequate, used essentially as if it were known. An iterative procedure in which ϕ and ω are updated alternately was suggested by Cochrane and Orcutt (1949), and has been shown to yield maximum conditional likelihood estimates (Sargan, 1964). The procedure is discussed by Shumway (1988, Section 3.5).

2.5 More General Temporal Models

Equation (7) is often not the appropriate model for a given set of data; in practice, serial correlations may not show the simple exponential decay of equation (8). However, it is the simplest of a family of models (the *ARMA* family) that can be used in this way to model serial correlation and to provide valid standard errors for parameter estimates. The ARMA model of order *(p,q)* has the form

$$\eta_t = \sum_{r=1}^{p} \phi_r \eta_{t-r} + \sum_{s=0}^{q} \theta_s \epsilon_{t-s}. \tag{9}$$

In terms of the backshift operator, this may be written

$$\eta_t = \frac{\theta(B)}{\phi(B)} \epsilon_t$$

where the polynomials $\phi(z)$ and $\theta(z)$ are defined by

$$\phi(z) = 1 - \sum_{r=1}^{p} \phi_r z^r,\ \theta(z) = \sum_{s=0}^{q} \theta_s z^s.$$

The constraint $|\phi| < 1$ in the first-order model is generalized to the requirements

$$\phi(z) \neq 0 \text{ for } |z| \leq 1,\ \theta(z) \neq 0 \text{ for } |z| < 1.$$

For this model, the autocorrelations

$$\rho_h = \mathrm{corr}(\eta_t, \eta_{t-\mathrm{h}})$$

cannot be written down explicitly, but satisfy the difference equation

$$\rho_h = \sum_{r=1}^{p} \phi_r \rho_{h-r}, \mathrm{h} > q.$$

They therefore still decay to zero at an exponential *rate* as $h \rightarrow \infty$, but not as a simple exponential *sequence*.

As in the case of the AR(1) model (7), the slope of a trend line should be estimated not by ordinary least-squares, but by some method that takes the covariance structure of the data into account. Various methods are available, and some are implemented in the more complete statistical packages. It is again true that the slope estimate itself is generally close to the one obtained by ordinary least-squares, but its standard error may be very different when calculated appropriately. The approximate ratio of the correct standard error to the incorrect one can again be calculated, but it is more easily expressed in terms of the *power spectrum* of the model than its autocovariances.

The power spectrum of a stationary time series is the function whose Fourier coefficients are the autocovariances

$$s(f) = \sum_{h=-\infty}^{\infty} \gamma_h \epsilon^{-2\pi i f h}, 0 \leq f < 1,$$

from which it follows that

$$\gamma_h = \int_0^1 e^{2\pi i f h} \, s(f) df, \ -\infty < h < \infty.$$

The power spectrum of the ARMA(p, q) model (9) is

$$s_{ARMA}(f) = \sigma^2 \frac{|\theta(e^{2\pi i f})|^2}{|\phi(e^{2\pi i f})|^2}.$$

Grenander (1954) showed that the variance of the sampling distribution of a trend estimated from a stretch of data of length n is, for large n, approximately

$$\text{var}(\hat{\omega}) = \frac{s(0)}{\sum_{t=1}^{n} (t - \bar{t})^2}, \tag{10}$$

Comparison with equation (5) shows that the factor σ^2 in the numerator has been replaced by s(0), the power spectrum evaluated at zero frequency. Equation (10) can be used as the basis for computing the approximate standard error of the trend estimate, or merely to get an indication of how much the standard error differs from the result given by the formula (3), the ratio being just

$$\sqrt{s(0) \,/ \int_0^1 s(f) df}\,.$$

2.6 Spatial Correlation

In the previous sections we discussed the complications that arise when we analyze data collected over time, with correlation among observations that are close together in time (serial correlation, or *temporal* correlation). Measurements made close together in *space* also tend to be correlated, and when such measurements are analyzed jointly, their *spatial* correlation also needs to be taken into account.

One general approach to analysis of spatiotemporal data is based on models generalized from the strictly temporal models described above. However, this approach requires the data to be collected on a regular grid of locations, and to show some homogeneity in their correlation structure. One or both of these features is absent in most of the data that have been collected in studies of ozone and other atmospheric trends. However, more ad hoc solutions can be found for certain problems.

One such problem is the need to combine quantities calculated from data collected at different locations. Suppose that $\hat{\theta}_1$ and $\hat{\theta}_2$ are estimates of similar quantities at two locations. Each $\hat{\theta}$ might be a trend estimate, or an average ozone level over a decade, or a change in such an average from one decade to the next. The standard error of the average

$$\hat{\theta}_. = (\hat{\theta}_1 + \hat{\theta}_2)/2$$

is given by

$$SE\,(\hat{\theta}_.) = \sqrt{\mathrm{var}\,(\hat{\theta}_.)}$$

where

$$\mathrm{var}(\hat{\theta}_.) = (1/4)\,\{\mathrm{var}(\hat{\theta}_1) + \mathrm{var}(\hat{\theta}_2) + 2\mathrm{cov}(\hat{\theta}_1, \hat{\theta}_2)\}.$$

The two variance terms can usually be obtained from the analysis of the data for locations 1 and 2 separately, but the covariance term depends on the joint behavior of the two sets of data, and therefore can be calculated only from a joint analysis. While this is not a difficult analysis to carry out, it is not one that the commonly available statistical packages are set up to handle. Reinsel and Tiao (1987) describe a method that amounts to doing just this, in their analysis of an entire Dobson network, but the method is not easy to implement with standard software. As a result, it is more convenient to calculate summary statistics for a number of locations in a slightly different way.

Consider, for instance, the problem of calculating an average trend for all Dobson stations in a certain latitude band. Since it is straightforward to calculate a trend for each station, it might seem that the way to proceed is to simply combine the individual trends. However, to compute the standard error for this average we would need to know all the covariances among the individual station trends. We can, instead, form an average ozone time series for the band, then estimate the trend in this single series. The standard error of the resulting estimate may then be obtained in the usual way. The estimated trend in the average series is, in general, close to the average of the individual trends, and may actually be a more appropriate quantity to consider.

The weakness of this approach is that the analysis of the average series can account only for the statistical fluctuations that are visible in the average. Thus, phenomena that induce spurious trends in the individual station records, for example instrument drift, pass undetected, while in Reinsel and Tiao's approach they show up as variations among the individual trend estimates. As a result, the standard error obtained from analysis of an average series may need to be inflated to allow for such phenomena, while the standard error calculated from Reinsel and Tiao's method automatically allows for them. Neither approach can handle spurious trends common to all stations, so in either case some allowance must be made for these.

3.0 SEASONALITY IN OZONE DATA

In this section we review various ways in which ozone data show seasonal behavior, the problems such behavior raises, and some of the solutions used.

3.1 Seasonal Structure in the Mean

Seasonal structure is one aspect of many time series that needs to be considered when estimating a trend. It is usually easy to separate seasonal behavior from trend, so the issue is not one of confusion between the two so much as estimating the size of the random errors in the data.

There are two basic strategies for coping with seasonality in the mean. One is to use *seasonal adjustment* to remove the seasonal behavior, and then to estimate trend from the *seasonally adjusted* data. The second is to fit a model that includes both seasonal structure and a trend term, so that both parts are estimated simultaneously. The former is preferred in exploratory analysis as it allows more flexibility in estimating the trend. For instance, a graph of the adjusted data will often suggest what kind of trend is actually present, and will typically provide a preliminary estimate of its magnitude. By contrast, simultaneous estimation is preferable when a model has been chosen and its parameters are being estimated. One advantage of simultaneous estimation is that it usually provides standard errors for all estimated parameters, as well as their correlations.

In either case, it is necessary to specify the seasonal structure to be removed or incorporated into the model, respectively. The simplest approach is to allow an arbitrary mean for each month[5]. If we write the data as

$$y_t = S_t + z_t,$$

where S_t and z_t represent the seasonal and nonseasonal parts of the data, respectively, then this amounts to putting

$$S_t = \mu_i \text{ if data month } t \text{ falls in calendar month } i,\ i = 1,2,\ldots 12.$$

Here, μ_1 is the mean of January data, μ_2 is the mean of February data, and so on.

This approach has the merits of simplicity and ease of interpretation, but in short series it may be undesirable to use as many as 12 parameters to describe seasonal structure. An alternative approach is to use a sine-cosine expansion. In this case, we put

$$S_t = \mu + \sum_{j=1}^{J} \{A_j \cos(2\pi jt/12) + B_j \sin(2\pi jt/12)\}$$

where $J \leq 5$, using $2J + 1$ parameters. Often $J = 1$ or $J = 2$ is sufficient, corresponding to fitting an annual wave with three parameters, or annual and semiannual waves requiring five parameters, respectively. If we set $J = 6$ with the constraint $B_6 = 0$, there are again 12 parameters; this is effectively the same as allowing an arbitrary set of monthly means.

Figure 3 shows the results of these two approaches for the monthly Arosa data. The asterisks indicate the monthly means; the curve is constructed from a sine-cosine expansion with $J = 2$ (estimated by ordinary least-squares). This two-frequency model fits most of the monthly means

---

[5] For ease of exposition we deal only with the case of monthly data. The modifications necessary for other types of seasonal behavior are clear.

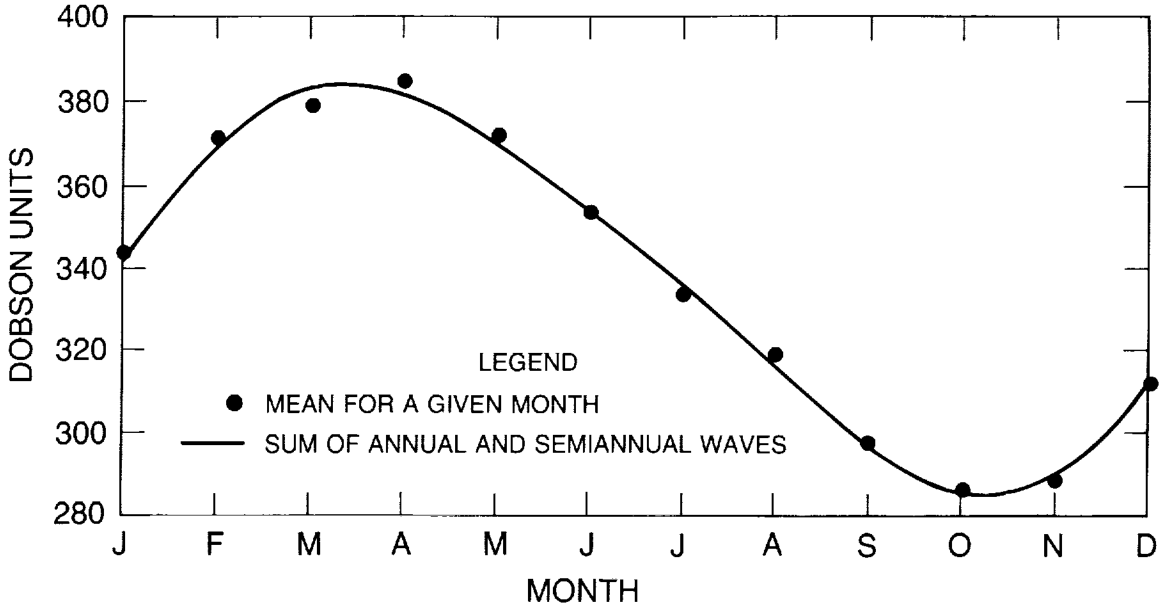

Figure 3: Seasonal structure of monthly Arosa data.

well in the graph, but the lack of fit in March and April could be critical in a trend study (see Section 3.2 below).

3.2 Seasonal Structure In the Trend

The issue of seasonal structure in the mean of a series discussed in the previous section may also extend to estimating a trend, if theory or observation suggests that the trend may vary from season to season.

Suppose, for instance, that trend is being measured by a ramp function such as

$$
\begin{aligned}
\mathrm{r}_t &= \begin{cases} \lambda & \text{if } t < t_0 \\ \lambda + \omega\,(t - t_0) & \text{if } t \geq t_0 \end{cases} \\
&= \lambda + \omega\,(t - t_0)_+,
\end{aligned}
$$

where $(t - t_0)_+$ is defined by

$$
(t - t_0)_+ = \begin{cases} 0 & \text{if } t < t_0 \\ (t - t_0) & \text{if } t \geq t_0. \end{cases}
$$

The function r_t has the constant level λ up to month t_0, and increases with slope ω units per month after month t_0. As in the previous section, we have various ways of allowing the magnitude of the trend to vary from month to month. The simplest is to replace the single λ by 12 λ's and the single ω by 12 ω's:

$$
r_t = \lambda_i + \omega_i\,(t - t_0)_+ \text{ if data month } t \text{ falls in calendar month } i.
$$

Seasonal trend estimates of this form are reported in Chapter 4.

Again, however, we might not want to allow completely arbitrary variation in the trends from one month to the next. One alternative would be to use sine-cosine expansions as before:

$$r_t = \lambda_0 + \sum_{j=1}^{J}\{A_j\cos(2\pi jt/12) + B_j\sin(2\pi jt/12)\}$$
$$+ \left[\, \omega_0 + \sum_{j=1}^{J}\{C_j\cos(2\pi jt/12) + D_j\sin(2\pi jt/12)\}\right](t - t_0)_+.$$

Notice that we have used the same number of terms in each expansion. Statistical considerations such as lack of significance of some coefficients might suggest dropping terms from one sum but not the other, but care would have to be used. Omission of significant terms from one sum would introduce bias into estimates of coefficients in the other, and possibly into other coefficients in the same sum. In particular, bias could arise if a sine-cosine expansion were used for, say, the level term, and arbitrary constants were used for the trend, since using arbitrary constants is effectively the same as taking $J = 6$ (and omitting the final sine term).

3.3 Seasonal Structure in the Correlations

In Section 2 we have discussed the use of time-series models to represent the correlation among measurements such as ozone columns at different times at the same location (or geographical region). One way in which those models are not sufficiently general is that they have *stationary* covariance structure:

$$\operatorname{cov}(y_t, y_{t-h}) = \text{a function only of } h.$$

However, most ozone time series have covariances that depend on the season as well as the time separation h. This is most easily seen in the monthly dependence of the standard deviation. As was mentioned in Section 1.1, failure to allow for such seasonality in covariance structure distorts any analysis by placing equal weight on the more variable winter data and the less variable summer data.

Two approaches have emerged for coping with this problem. Reinsel and his coworkers have developed and exploited a method that can be described as seasonally weighted least-squares, while the values reported in Chapter 4 were obtained essentially by standardization of the data before fitting the trend model. The two approaches may be compared in terms of a corresponding model for the noise term η_t. In each case, the analysis may be interpreted as using a modified ARMA model (cf. equation 9). Reinsel's approach corresponds to the model

$$\eta_t = \frac{\theta(B)}{\phi(B)}(\sigma_t\epsilon_t),$$

while the approach used in this report corresponds to

$$\eta_t = \sigma_t \frac{\theta(B)}{\phi(B)}\epsilon_t.$$

In each case, the scale factors σ_t are periodic, and reflect the seasonal dependence of the standard deviation of the noise η_t and of the innovations ϵ_t, respectively. Both general models appear plausible, but studies of which fits ozone data better have not been performed in depth.

4.0 Summary

Ready, widespread acceptance of the results of a scientific investigation depends critically on the credibility of the study, and, in the case of a data-oriented study, this in turn depends largely on two factors: the quality of the data on which the study is based and the quality of the subsequent analysis of those data. Data quality for each of the measuring systems is discussed in the relevant chapters; here we offer only broad comments. The primary focus of this appendix is on data analysis techniques, about which we offer more specific suggestions.

- *Trend estimates*—There are many ways to qualify the trend in a set of data, including fitting a straight line, fitting a ramp (or hockey stick) function, or comparing averages over different time windows. In each case, the resulting quantity should be accompanied by an appropriate standard error.

- *Standard errors*—A standard error has meaning only in the context of being a model for the way in which the data were sampled. If the data show evidence of spatial or temporal correlation, the sampling model must reflect this. Computer software for building the required sampling models and calculating the corresponding trend estimates and standard errors is widely available and should be used more extensively.

- *Current results*—Trend estimates based on fitting ramp functions reported in Chapter 4, and those of Reinsel, Tiao, and their coworkers, adequately account for serial correlation and its seasonal structure, and represent state-of-the-art estimates. Estimates of trends from Total Ozone Mapping Spectrometer (TOMS) data, also reported in Chapter 4, allow for serial correlation, but not for its seasonal structure. Although not state of the art, the results should be close. Standard errors of other trend estimates obtained by least-squares fitting without allowance for serial correlation may be incorrect by factors of more than three.

- *Ground-based total ozone column data*—It has been demonstrated that the quality of Dobson total ozone column data can be improved substantially by retroactive application of corrections based on calibration changes. This is best carried out by complete recalculation of each day's data on the basis of corrected algorithms, but useful improvements can be made by correcting monthly averages. Stations should be urged to give a higher priority to such adjustments to historical data, and to ensuring publication of the adjusted data by the World Ozone Center.

- *Ground-based ozone profile data*—The largest remaining question about the quality of the ozone profile data obtained by the Umkehr technique is the impact of aerosols. This question will have to be resolved before the Umkehr network can fulfill its dual roles of providing ground-based information about trends in ozone profiles and of providing ground truth for the validation of satelliteborne instruments.

- *Satellite ozone measurements*—The realization that the effect of diffuser plate degradation on Nimbus-7 cannot be uniquely separated from other instrument changes underscores the difficulty of maintaining measurement stability with satellite-based systems. This illustrates the continuing need for cross-checking all types of measurements, a need about which there has been a tendency to become complacent.

Omit
to
End

APPENDIX B

List of Contributors

PRECEDING PAGE BLANK NOT FILMED

Appendix B

List of Contributors

Ozone Trends Panel

D. Albritton	NOAA Aeronomy Laboratory, Boulder, CO
P. Bloomfield	North Carolina State University, Raleigh
R. Bojkov	Atmospheric Environment Service, Downview, Ontario, Canada
D. Ehhalt	Institute for Chemistry, Julich, Federal Republic of Germany
P. Fraser	CSIRO, Aspendale, Australia
J. Gille	NCAR, Boulder, CO
D. Hartmann	University of Washington, Seattle, WA
R. Hudson	NASA/Goddard Space Flight Center, Greenbelt, MD
I.S.A. Isaksen	University of Oslo, Oslo, Norway
H. Johnston	University of California, Berkeley
J. Mahlman	NOAA Geophysical Fluid Dynamics Laboratory, Princeton, NJ
J.J. Margitan	Jet Propulsion Laboratory/NASA Headquarters, Washington, DC
M.P. McCormick	NASA/Langley Research Center, Hampton, VA
M. McFarland	E.I. DuPont de Nemours & Company, Wilmington, DE
F. Ormond, **Executive Secretary**	ARC/NASA, Washington, DC
C. Rodgers	Oxford University, Oxford, England
F.S. Rowland	University of California, Irvine
M. Schoeberl	NASA/Goddard Space Flight Center, Greenbelt, MD
R. Stolarski, **Vice Chair**	NASA/Goddard Space Flight Center, Greenbelt, MD
R. Turco	R&D Associates, Marina del Rey, CA
R.T. Watson, **Chair**	NASA Headquarters, Washington, DC

Reviewers

J. Barnett	Oxford University, Oxford, England
R.J. Cicerone	NCAR, Boulder, CO
S. Fels	NOAA, Geophysical Fluid Dynamics Laboratory, Princeton, NJ
N. Krull	Federal Aviation Administration, Washington, DC
M.J. Kurylo	NBS/NASA Headquarters, Washington, DC
M. McIntyre	University of Cambridge, Cambridge, England
G. Megie	Service d'Aeronomie, CNRS, Verrieres, le Buisson, France
M. Prather	Goddard Institute for Space Studies, New York, NY
H. Rodhe	University of Stockholm, Sweden
A. Schmeltekopf	NOAA, Environmental Research Laboratory, Boulder, CO
N. Sundararaman	World Meteorological Organization, Geneva, Switzerland
G. Visconti	University of Aquila, Aquila, Italy
S. Wofsy	Harvard University, Cambridge, MA

PRECEDING PAGE BLANK NOT FILMED

PAGE 774 INTENTIONALLY BLANK

Working Groups

Executive Summary

Robert T. Watson, NASA Headquarters, Washington, DC, Chair

Ozone Trend Panel Members
Ozone Trend Panel Reviewers

Chapter 1 Introduction

Robert T. Watson, Chair, Ozone Trends Panel

Chapter 2 Spacecraft Instrument Calibration and Stability

J. Gille, Chair, National Center for Atmospheric Research, Boulder, Colorado

P. Feldman	Johns Hopkins University, Baltimore, Maryland
R. Hudson	NASA/Goddard Space Flight Center, Greenbelt, Maryland
J. Lean	Naval Research Laboratory, Washington, D.C.
R. Madden	National Bureau of Standards, Gaithersburg, Maryland
L. McMaster	NASA/Langley Research Center, Hampton, Virginia
G. Mount	NOAA, Boulder, Colorado
G. Rottman	LASP, University of Colorado, Boulder
P.C. Simon	Institute d'Aeronomie Spatiale de Belgique, Brussels, Belgium

Chapter 3 Information Content of Ozone Retrieval Algorithms

C. Rodgers, Chair, Oxford University, Oxford, England

P.K. Bhartia	Science Applications Research, Lanham, Maryland
W.P. Chu	NASA/Langley Research Center, Hampton, Virginia
R. Curran	NASA Headquarters, Washington, D.C.
J. DeLuisi	NOAA, Boulder, Colorado
J. Gille	NCAR, Boulder, Colorado
R. Hudson	NASA/Goddard Space Flight Center, Greenbelt, Maryland
C. Mateer	Atmospheric Environment Service, Downsview, Ontario, Canada
D. Rusch	University of Colorado, Boulder
R.J. Thomas	University of Colorado, Boulder
R. Turco	R&D Associates, Marina del Rey, California
W. Wiscombe	NASA/Goddard Space Flight Center, Greenbelt, Maryland

Chapter 4 Trends in Total Column Ozone Measurements

F.S. Rowland, Chair, University of California, Irvine

J. Angell	NOAA, Rockville, Maryland
W. Attmannspacher	Deutscher Wetterdienst, Hohenpeissenberg, Federal Republic of Germany

P. Bloomfield	North Carolina State University, Raleigh
R. Bojkov	Atmospheric Environment Service, Downsview, Ontario, Canada
N. Harris	University of California, Irvine
W. Komhyr	NOAA, Boulder, Colorado
M. McFarland	E.I. DuPont de Nemours & Company, Wilmington, Delaware
R. McPeters	NASA/Goddard Space Flight Center, Greenbelt, Maryland
R. Stolarski	NASA/Goddard Space Flight Center, Greenbelt, Maryland

Chapter 5 Trends in Ozone Profile Measurements

H. Johnston, Chair, University of California, Berkeley

A. Aikin	NASA/Goddard Space Flight Center, Greenbelt, Maryland
R. Barnes	Chemal, Inc., Wallops Island, Virginia
S. Chandra	NASA/Goddard Space Flight Center, Greenbelt, Maryland
D. Cunnold	Georgia Institute of Technology, Atlanta, Georgia
J. DeLuisi	NOAA, Boulder, Colorado
J. Gille	NCAR, Boulder, Colorado
R. Hudson	NASA/Goddard Space Flight Center, Greenbelt, Maryland
M.P. McCormick	NASA/Langley Research Center, Hampton, Virginia
L. McMaster	NASA/Langley Research Center, Hampton, Virginia
A.J. Miller	NOAA/NWS/Climate Anaylsis Center, Washington, D.C.
R. Nagatani	NOAA/NWS/Climate Anaylsis Center, Washington, D.C.
W. Planet	NOAA NESDIS, Washington, D.C.
E. Remsberg	NASA/Langley Research Center, Hampton, Virginia
D. Rusch	University of Colorado, Boulder
C. Trepte	ST Systems Corporation, Hampton, Virginia
R. Veiga	NRC/NSF, Hampton, Virginia
P. Wang	STC, Hampton, Virginia
C. Wellemeyer	ST Systems Corporation, Lanham, Maryland
J. Zawodny	NASA/Langley Research Center, Hampton, Virginia

Chapter 6 Trends in Stratospheric Temperature

M. Schoeberl, Chair, NASA/Goddard Space Flight Center, Greenbelt, Maryland

J. Angell	NOAA, Rockville, Maryland
J. Barnett	Oxford University, Oxford, England
B. Boville	NCAR, Boulder, Colorado
S. Chandra	NASA/Goddard Space Flight Center, Greenbelt, Maryland
S. Fels	NOAA, Geophysical Fluid Dynamics Laboratory, Princeton, New Jersey
E. Fleming	ARC Corporation, Landover, Maryland
M. Gelman	NOAA/NWS/Climate Anaylsis Center, Washington, D.C.
K. Labitzke	Free University of Berlin, Federal Republic of Germany
A.J. Miller	NOAA/NWS/Climate Anaylsis Center, Washington, D.C.
J. Nash	British Meteorological Office, England
P.A. Newman	NASA/Goddard Space Flight Center, Greenbelt, Maryland
V. Ramaswamy	Princeton University, Princeton, New Jersey

J. Rosenfield	NASA/Goddard Space Flight Center, Greenbelt, Maryland
F. Schmidlin	NASA, Wallops Island, Virginia
M. Schwarzkopf	NOAA, Geophysical Fluid Dynamics Laboratory, Princeton, New Jersey
K. Shine	Oxford University, Oxford, England

Chapter 7 Theory and Observations

I.S.A. Isaksen, Chair, University of Oslo, Oslo, Norway

R. Eckman	University of Cambridge, Cambridge, England
A. Lacis	Goddard Institute for Space Studies, New York, New York
M. Ko	AER, Inc., Cambridge, Massachusetts
M. Prather	Goddard Institute for Space Studies, New York, New York
J. Pyle	University of Cambridge, Cambridge, England
H. Rodhe	University of Stockholm. Stockholm, Sweden
F. Stordal	University of Oslo, Oslo, Norway
R. Stolarski	NASA/Goddard Space Flight Center, Greenbelt, Maryland
R. Turco	R&D Associates, Marina del Rey, California
D. Wuebbles	Lawrence Livermore National Laboratories, Livermore, California

Chapter 8 Trends in Source Gases

D. Ehhalt, Chair, Institute for Chemistry, Julich, Federal Republic of Germany
P. Fraser, Cochair, CSIRO, Aspendale, Australia

D. Albritton	NOAA, Boulder, Colorado
R.J. Cicerone	NCAR, Boulder, Colorado
M.A.K. Khalil	Oregon Graduate Center, Beaverton, Oregon
M. Legrand	CNRS, France
Y. Makide	University of Tokyo, Japan
F.S. Rowland	University of California, Irvine
L.P. Steele	CIRES, University of Colorado/NOAA, Boulder, Colorado
R. Zander	University of Liege, Liege–Ougree, Belgium

Chapter 9 Trends in Stratospheric Minor Constituents

R. Stolarski, Chair, NASA/Goddard Space Flight Center, Greenbelt, Maryland

W.P. Chu	NASA/Langley Research Center, Hampton, Virginia
M.T. Coffey	NCAR, Boulder, Colorado
W.S. Heaps	NASA/Goddard Space Flight Center, Greenbelt, Maryland
J.A. Kaye	NASA/Goddard Space Flight Center, Greenbelt, Maryland
M.P. McCormick	NASA/Langley Research Center, Hampton, Virginia
R. Zander	University of Liege, Liege–Ougree, Belgium

Chapter 10 Trends in Aerosol Abundances and Distributions

R.P. Turco, Chair, R & D Associates, Marina del Rey, California
M.P. McCormick, Cochair, NASA/Langley Research Center, Hampton, Virginia

R.T. Clancy	LASP, University of Colorado, Boulder
R. Curran	NASA Headquarters, Washington, D.C.
J. DeLuisi	NOAA/ERL, Boulder, Colorado
P. Hamill	San Jose State University, San Jose, California
G. Kent	STC, Hampton, Virginia
J.M. Rosen	University of Wyoming, Laramie
O.B. Toon	NASA/Ames, Moffett Field, California
G. Yue	NASA/Langley Research Center, Hampton, Virginia

Chapter 11 Observations and Theories Related to Antarctic Ozone Changes

D. Hartmann, Cochair, University of Washington, Seattle, Washington
R.T. Watson, Cochair, NASA Headquarters, Washington, D.C.

R.A. Cox	AERE, Harwell, England
C. Kolb	Aerodyne, Billerica, Massachusetts
J. Mahlman	NOAA, Geophysical Fluid Dynamics Laboratory, Princeton, New Jersey
M. McElroy	Harvard University, Cambridge, Massachusetts
A. Plumb	CSIRO, Aspendale, Australia
V. Ramanathan	University of Chicago, Chicago, Illinois
M. Schoeberl	NASA/Goddard Space Flight Center, Greenbelt, Maryland
S. Solomon	NOAA, Boulder, Colorado
R. Stolarski	NASA/Goddard Space Flight Center, Greenbelt, Maryland
N.D. Sze	AER, Inc., Cambridge, Massachusetts
A. Tuck	NOAA, Boulder, Colorado

Appendix A: Statistical Approaches to Ozone Trend Detection

P. Bloomfield, Chair, North Carolina State University, Raleigh

D.R. Brillinger	University of California, Berkeley
D. Nychka	North Carolina State University, Raleigh
R. Stolarski	NASA/Goddard Space Flight Center, Greenbelt, Maryland

Acknowledgments

S. Chandra, Proofreading; Research Assistance—References	NASA/Goddard Space Flight Center, Greenbelt, MD
E. Fleming, Proofreading; Research Assistance—References	NASA/Goddard Space Flight Center, Greenbelt, MD
R.F. Hampson, Proofreading; Research Assistance—References	National Institute of Standards and Technology, Gaithersburg, MD
J.L. Hostetter, Research Assistance—References	ARC Professional Services Group, Washington, DC
C. Jackman, Proofreader; Research Assistance—References	NASA/Goddard Space Flight Center, Greenbelt, MD
J. Lynch, Proofreading	ST Systems Corporation, Lanham, MD
J. Lund, Typesetting	Systems Publications, Inc., Hyattsville, MD
R. Mills, Editorial Supervision and References	ST Systems Corporation, Lanham, MD
M. Tarlton, Jr., Graphics and Design	ST Systems Corporation, Lanham, MD
V. Vahlberg, Research Assistance—References	ST Systems Corporation, Lanham, MD
C. Wheal, Proofreading	ST Systems Corporation, Lanham, MD

APPENDIX C

Ozone Trends Panel Working Group Meetings

PRECEDING PAGE BLANK NOT FILMED

Appendix C

Ozone Trends Panel Working Group Meetings

Date	Meeting and Place	Chair
12/15–16, 1986	OZONE TRENDS PANEL NASA/GSFC, Greenbelt, MD	R.T. Watson
1/21, 1987	Data Intercomparisons Satellite–Satellite— Preliminary Meeting NASA/LaRC, Hampton, VA	H. Johnston
2/12–13	Algorithms Boulder, CO	C. Rodgers
2/19–20	Calibrations Instrument Performance NASA/GSFC, Greenbelt, MD	J. Gille
3/9–10	Data Intercomparisons S–S NASA/LaRC, Hampton, VA	H. Johnston
3/12–13	Dobson–Umkehr Intercomparisons Newport Beach, CA	F.S. Rowland
3/19–20	Calibrations Instrument Performance NASA/GSFC, Greenbelt, MD	J. Gille
3/23–24	OZONE TRENDS PANEL Boulder, CO	R.T. Watson
4/14–15	Algorithms LASP, Boulder, CO	C. Rodgers
5/4–5	Other Trends in Stratosphere— Preliminary Meeting NASA/LaRC, Hampton, VA	R. Stolarski
5/12–13	Dobson–Umkehr S–Ground Intercomparisons Atmospheric Environment Service Downsview, Ontario, Canada	F.S. Rowland
5/17	Satellite–Satellite Intercomparisons NASA/GSFC, Greenbelt, MD	H. Johnston
5/21–22	Theory and Observations Oslo, Norway	I. Isaksen
5/21–22	Calibrations Instrument Performance Johns Hopkins University Baltimore, MD	J. Gille

PRECEDING PAGE BLANK NOT FILMED

PAGE 782 INTENTIONALLY BLANK

WORKING GROUP MEETINGS

5/25	Aerosols Marine del Rey, CA	R. Turco
6/18–19	OZONE TRENDS PANEL NASA/GSFC, Greenbelt, MD	R.T. Watson
6/23–25	Antarctic Ozone Symposium/WS NASA/Ames, Moffett Field, CA	R.T. Watson D. Hartmann
7/8–9	Temperature NASA/GSFC, Greenbelt, MD	M. Schoeberl
7/20	Aerosols Boulder, CO	R. Turco
7/20–21	Statistics Raleigh, NC	P. Bloomfield
7/27–28	Calibrations Boulder, CO	J. Gille
7/30–31	Dobson–Umkehr Intercomparisons Newport Beach, CA	F.S. Rowland
8/22	Theory and Observations Oslo, Norway	I. Isaksen
8/29	Source Gases Petersborough, Canada	D. Ehhalt
9/9–10	Satellite–Satellite Intercomparisons Oakland, CA	H.S. Johnston
9/14–16	Algorithms Somers Point, NJ	C. Rodgers
9/15–17	Theory and Observations Oslo, Norway	I. Isaksen
9/21–23	Calibrations Boulder, CO	J. Gille
9/30	Dobson–Umkehr Intercomparisons NASA/GSFC, Greenbelt, MD	F.S. Rowland
10/1–2	OZONE TRENDS PANEL NASA/GSFC, Greenbelt, MD	R.T. Watson
10/14–15	Temperature NASA/GSFC, Greenbelt, MD	M. Schoeberl
10/15	Source Gases Europe	D. Ehhalt

11/9–11/13	OZONE TRENDS PANEL Editorial and Peer Review Meeting St. Croix, Switzerland	R.T. Watson
1/27–29, 1988	OZONE TRENDS PANEL and Peer Reviewers	R.T. Watson
March	Chapter Summaries Completed	All
3/15	Executive Summary of Ozone Trends Panel Released	
June	Extended chapter summaries received for *NASA Reference Publication 1208, Present State of Knowledge of the Upper Atmosphere 1988: An Assessment Report*	
August	*NASA RP 1208* Published	
October 1989	Preparation of *Report of the International Ozone Trends Panel—1988, Report No. 18,* World Meteorological Organization Global Ozone Research and Monitoring Project	

APPENDIX D

List of Figures

PAGE 786 INTENTIONALLY BLANK

PRECEDING PAGE BLANK NOT FILMED

Appendix D

List of Figures

Figure 2.1 Periods of available data for satellite ozone-measuring systems. 12
Figure 2.2 Reflectivity as a function of wavelength for uncoated aluminum surfaces, one of which was exposed to an oil-pumped vacuum system, and the other (control sample) not. 13
Figure 2.3 Effect of UV irradiation on evaporated DC 705 oil. The effective layer thickness is ≅200Å, evaporated onto an aluminum surface coated with MgF_2 (enlarged 700 times). 14
Figure 2.4 Mass accumulation as a function of time in orbit for illuminated and shadowed quartz microbalances on the SCATHA spacecraft. 14
Figure 2.5 Bond energy of likely breaks of methyl phenyl siloxane (silicone rubber). 15
Figure 2.6 Reflectance at 270 nm of an uncoated oxidized aluminum plate as a function of the thickness of a carbon film deposited on its surface. ... 15
Figure 2.7 Schematic diagram of the SBUV instrument. 19
Figure 2.8a The measured degradation of the SBUV instrument, Fm(t)/Fm(0), for 1978–1987. 21
Figure 2.8b The same as for Figure 2.8a, except for the six longest wavelengths. .. 21
Figure 2.9 Values of $r(\lambda)$ determined during the four frequent deployment periods by CPH. 27
Figure 2.10 Values of $S(\lambda)$ determined during the four frequent deployment periods by CPH. 28
Figure 2.11a Percent difference between solar observation data and models. 30
Figure 2.11b As in 2.11a, but for the six longest wavelengths. 30
Figure 2.12 Comparison at 340 nm between the measured solar irradiance, irradiance corrected for diffuser degradation, Earth radiance from 20°N–20°S, and albedo, as a function of time. 32
Figure 2.13a Relative diffuser reflectivity as a function of time for the OPT (CPH) and quasi-linear models, for the six shortest wavelengths. 35
Figure 2.13b As in 13a, but for the six longest wavelengths. 35
Figure 2.14a Relative spectrometer degradation as a function of time for the OPT (CPH) and quasi-linear models, for the six shortest wavelengths. 36
Figure 2.14b As in 14a, but for the six longest wavelengths. 36
Figure 2.15a The percent difference in the calculated albedo between the quasi-linear models and the exponential (CPH) fits for the six shortest wavelengths. 37
Figure 2.15b The same as 15b, but for the six longest wavelengths. 37
Figure 2.16 Geometry of the earthshine observations. 39
Figure 2.17 Example of ratio of earthshine signal to direct solar irradiance as a function of subsatellite latitude. 39
Figure 2.18a Comparison of diffuser reflectivity relative to 1978 versus wavelength, determined from earthshine measurements, and given by the models, for December 1983. 40
Figure 2.18b As in 18a, but for December 1984. 40
Figure 2.18c As in 18a, but for December 1985. 40
Figure 2.19 Wavelength pairs for total ozone determination. 41

PAGE 788 INTENTIONALLY BLANK

PRECEDING PAGE BLANK NOT FILMED

FIGURES

Figure 2.20 Archived SBUV total ozone minus total ozone determined from SBUV D-pair wavelengths, 1980–1987 (from Bhartia, unpublished). 42
Figure 2.21 Uncertainty in ozone change determined from SBUV data over 8 years. 43
Figure 2.22 Uncertainty in rate of ozone change determined from SBUV data over 8 years. 44
Figure 2.23 Midlatitude vertical distributions of ozone change from 1978–1986 determined from SBUV data, for several models of diffuser degradation. ... 45
Figure 2.24 TOMS optical diagram. 47
Figure 2.25 Diagram of TOMS scanning swath. 48
Figure 2.26 Diffuser reflectivity vs. wavelength; comparison of model predictions for TOMS wavelengths. 51
Figure 2.27 SAGE–II sensor assembly. 54
Figure 2.28 SAGE–II spectrometer layout. 55
Figure 2.29 Data acquisition mode for solar extinction experiment during sunset event. 56
Figure 2.30 Sensitivity of ozone retrieval to variation of scan mirror reflectivity variation with angle. 58
Figure 2.31 Sensitivity of SAGE–II ozone retrieval to reference altitude errors (%/km), as a function of altitude. 59
Figure 2.32 Combined systematic errors in SAGE ozone profiles. 61
Figure 2.33 Uncertainty in SAGE ozone changes. 62
Figure 2.34 Uncertainty in ozone change determined from SAGE–I/SAGE–II differences. 64
Figure 2.35 SME orbit and scan geometry. 65
Figure 2.36 The geometry of limb viewing with the UVS on SME. Z_o is the minimum ray height of the 3.5 km vertical resolution of the measurement. 67
Figure 2.37 Schematic drawing of the SME UV spectrophotometer. 68
Figure 2.38 (a) Random altitude-dependent errors associated with noise and data compression and temperature and pressure. (b) Systematic altitude-dependent errors associated with uncertainties in instrument sensitivity, instrument polarization, dead-time constants, and ozone cross-sections. (c) The altitude-dependent error from combined random and systematic errors. 69
Figure 2.39 (a) Example of IR horizon sensor trigger altitudes vs. latitude. (b) Altitude corrections vs. latitude. 71
Figure 2.40 NIR physical processes. 74
Figure 2.41 Optical scheme of the near-infrared spectrometer. 75
Figure 2.42 Normalized NIR photodiode sensitivity through the mission. 75
Figure 2.43 Total systematic error on ozone data estimated from input errors. 76
Figure 2.44 UV and NIR 0.75 mb mixing ratio with time. No correction for sensitivity drift of UV LW channel. 77
Figure 2.45 UV and NIR 0.75 mb mixing ratio with time. Correction for sensitivity drift of UV LW channel. 78
Figure 2.46 NIR 0.75 mb mixing ratio with time using the bus horizon sensors. ... 79
Figure 2.47 Ozone mixing ratios for June 1982–1986 for the UV instrument. 79
Figure 2.48 Schematic drawing of LIMS optical train. 82
Figure 2.49 Normalized instantaneous FOV functions for the six LIMS channels. .. 84
Figure 2.50 Normalized spectral response curves for LIMS channels. 85
Figure 2.51a LIMS primary calibration curve for channel 3. 87
Figure 2.51b Departure of curve in 2.51a from linearity. 87

Figure 2.52 LIMS detector temperature vs. time (expressed in orbit number). One week is approximately 100 orbits. 88
Figure 2.53 Percent variation of indicated scale factor around an orbit for LIMS carbon dioxide (temperature) and ozone channels. 89
Figure 2.54 (a) Scale factor for narrow CO_2 channel as a function of time during LIMS missions. (b) Scale factor for wide CO_2 channel as a function of time during LIMS missions. (c) Scale factor for wide O_3 channel as a function of time during LIMS missions. (d) RMS noise in O_3 channel as a function of time during LIMS missions. 90
Figure 2.55 Uncertainty in total change determined by the various experiments over their lifetimes, as functions of altitude. For SBUV, the uncertainty is half of the range between models of high and low diffuser degradation. 100
Figure 2.56 Uncertainties of trends determined by various experiments over their lifetimes, as functions of altitude. For SBUV, the uncertainty is half of the range between models of high and low diffuser degradation. 101
Figure 2.57 Midlatitude vertical distributions of ozone change from 1978–1986 determined from SBUV data, for several models of diffuser degradation. 102

Figure 3.1 Aerosol profile from SAGE–I: average ratio of aerosol to Rayleigh extinction at 292 nm, for 5°S in summer 1980. 127
Figure 3.2 Calculated SBUV spectral signature for the Figure 3.1 aerosol profile. 128
Figure 3.3 The effect of the Fig. 3.1 aerosol on the SBUV-retrieved ozone profile. 129
Figure 3.4 SBUV averaging kernels for retrieved layer amounts. 131
Figure 3.5 (a) rms error in the SBUV profile due to a 1 percent random error in D_λ. (b) increase in ozone due to an increase in D_λ of 1 percent at all wavelengths. (c) rms scale error due to a 2 percent random error in $r(\lambda)$, after 8 years' operation. (d) increase in ozone due to a 5 percent increase in $r(\lambda)$ at all wavelengths. 132
Figure 3.6 Change in ozone relative to the SBUV archived data, due to the diffuser degradation models M1, M2, and L, as defined in Chapter 2. 133
Figure 3.7 Sensitivity of the SBUV retrieved layer amounts to errors in the mean layer temperatures. The curves are labeled with the layer in which the temperature is perturbed and are offset by multiples of 0.05%/K for clarity. 133
Figure 3.8 Sensitivities of the SBUV-retrieved layer amounts to errors in (a) surface reflectivity (b) surface pressure (c) Rayleigh-scattering coefficient (d) ozone absorption coefficient. 134
Figure 3.9 Umkehr averaging kernels for retrieved layer amounts. 140
Figure 3.10 Sensitivity of the Umkehr retrieval to absorption coefficient errors. 141
Figure 3.11 Changes in Umkehr retrievals due to the following absorption coefficient assumptions: (a) changing the coefficient ratio to the Bass–Paur value, keeping the difference unchanged. (b) Bass–Paur values at −44°C. (c) Bass–Paur values, including temperature dependence. 142
Figure 3.12 Sensitivity of Umkehr-retrieved ozone to atmospheric temperature changes. The curves are labeled with the number of the layer in which the temperature is perturbed by 20K and are offset by 1%/20K for clarity. 143
Figure 3.13 Sensitivity of Umkehr-retrieved ozone to Rayleigh-scattering coefficient errors. 144
Figure 3.14 Sensitivity of the Umkehr-retrieved profile to errors in the total ozone measurement. 144

Figure 3.15 Sensitivity of the Umkehr-retrieved profile to surface reflectivity errors. 145

Figure 3.16 Effect on the ozone profile of changing the method of calculating the multiple-scattering correction. 146

Figure 3.17 Sensitivity of the Umkehr-retrieved profile to SO_2 in the lower half of layer 1. 146

Figure 3.18 Averaging kernels for SAGE–II. Curves are not plotted for all altitudes. 152

Figure 3.19 Random error of a single SAGE–II profile due to instrument noise only. 153

Figure 3.20 Sensitivity of the SAGE retrieval to altitude reference error. 153

Figure 3.21 Sensitivity of SAGE retrieval to atmospheric temperature errors. Curves are labeled with the pressure level (mb) at which the NMC temperature is perturbed and are offset by multiples of 0.1%/K for clarity. 154

Figure 3.22 Averaging kernels for SME–NIRS at selected altitudes. (a) Slit tilt = 0°. (b) Slit tilt = 10°. (c) Slit tilt = 25°. Curves are labeled (1) 0.001 mb, (2) 0.0032 mb, (3) 0.01 mb, (4) 0.032 mb, (5) 0.1 mb, (6) 0.316 mb, and (7) 1 mb. 163

Figure 3.23 SME–NIRS sensitivities to model parameters at slit tilt = 0°. Units are percent ozone per percent parameter, except where stated. (a) $J_{3,\infty}$ (b) τ_{UV} (c) τ_{762} (d) $\tau_{1.27}$ (e) $J_{S,\infty}$ (f) A_s (g) A_D (h) k_D (i) k_N (j) k_O (k) k_s (l) Cal (m) Altitude reference (percent ozone per 0.01 km) (o) Solar zenith angle (percent ozone per 0.01 radian). 164

Figure 3.24 Sensitivity of SME–NIRS retrievals to temperature errors. (a) Density on a height scale (b) Mixing ratio on a log pressure scale. Plotted are the perturbations in the profile due to a 1K temperature change at (1) 90 km, (2) 82 km, (3) 74 km, (4) 66 km, (5) 58 km, and (6) 50 km. 165

Figure 3.25 LIMS ozone averaging kernels at three selected altitudes. 169

Figure 3.26 Sensitivity of LIMS-retrieved ozone to temperature errors at selected altitudes. 170

Figure 3.27 Sensitivity of LIMS-retrieved ozone to a 1K temperature change at all levels, a 1 percent radiance calibration error, and a 1 percent registration pressure error. 170

Figure 3.28 SBUV spectral signature for a Gaussian ozone depletion of 10 percent centered at 3 mb, with a width of 10 km at half maximum. 171

Figure 3.29 Umkehr measurement signature for a Gaussian-shaped depletion with a maximum of 25 percent and a half width of about 14 km centered at 3 mb (squares). Stratospheric aerosol signature (triangles). (a) Total ozone 200 DU. (b) Total ozone 300 DU. (c) Total ozone 400 DU. 173

Figure 4.1 Geographical distribution of Dobson stations with long records. 190

Figure 4.2 Total ozone monthly deviations at Mauna Loa (1957–1986). Calculated from the data published in *Ozone Data for the World*, showing the apparent disruption in the data in 1976–1977. 198

Figure 4.3 Geographical distribution of the M–83 filter ozonometers in the USSR (the numbers correspond to those given in Table 4.7). 200

Figure 4.4 The top panel shows the percentage difference between measurements of the Dobson Spectrophotometer and the TOMS instrument at Arosa, Switzerland. The middle and bottom panels show the actual measurements of the Dobson and the TOMS instruments, respectively. 206

Figure 4.5 Monthly mean biases (Dobson–TOMS)/Dobson and their respective intra-station standard deviations ($\pm 1\sigma$). 208

Figure 4.6 Monthly mean (Dobson–TOMS)/Dobson differences after the monthly biases have been removed. Stations where the σ of the monthly mean is less than 5 percent have not been included. 211

Figure 4.7 Fractional distribution of 71 Dobson stations and 21 M–83 filter stations according to the (station–TOMS)/station monthly mean differences in 1 percent intervals. More than two-thirds of the Dobsons, but only half of the M–83 stations, have less than 2 percent mean difference with the network average transferred via TOMS; 22 percent of all stations have differences ⩾ 3 percent. 212

Figure 4.8 Fractional distribution of 92 stations according to the relative variability (σ in percent of the total ozone at a given station) of their monthly mean differences with TOMS. 213

Figure 4.9 Monthly differences between ozone measured at Huancayo and by TOMS (BR is bias removed), showing a slow upward drift during the first 4 years and a sharp decline in October 1982 (result of calibration). The σ of the differences forming each monthly point is about 2.6 percent. 214

Figure 4.10 Monthly (Dobson–TOMS)/Dobson differences for Bracknell indicating a downward rift between 1981 and 1984, followed by a sudden upward shift. The σ of the differences forming each monthly point is about 5.6 percent and is among the largest in the network. 215

Figure 4.11 Monthly (Dobson–TOMS)/Dobson differences for Singapore showing a strong downward drift between 1980–1983, when, as a result of calibration, the instrument is stabilized but at a level about 7 percent too low. The σ of differences forming each monthly point is about 2.4 percent. . 215

Figure 4.12 Monthly (Dobson–TOMS)/Dobson differences for Brisbane showing a downward drift until the end of 1980, followed by a sudden drop of about 5 percent. Only after calibration in early 1985 is the instrument restored to a state of agreement with the rest of the ozone network. The σ of the differences forming each monthly point is about 4.5 percent. 216

Figure 4.13 Monthly (Dobson–TOMS)/Dobson differences for Shiangher (near Beijing). The σ of the differences forming each monthly point is about 2.1 percent. 216

Figure 4.14 Monthly (Dobson–TOMS)/Dobson differences for Potsdam indicating a μ dependence as well as a shifting (in 1982–1983) of the level of ozone measured by the groundstation. The σ of the differences forming each monthly point is about 4.2 percent. 217

Figure 4.15 Monthly (Dobson–TOMS)/Dobson differences for Hobart showing an extremely large μ dependence and an erroneously low ozone level for the entire period of comparison. The σ of the differences forming each monthly point is about 4.7 percent. 218

Figure 4.16 Monthly (Dobson–TOMS)/Dobson differences for Hohenpeissenberg. The top panel indicates a well-pronounced μ dependence until 1985. The bottom panel shows the same monthly differences after removal of the μ-dependent variations and application of the instrument calibration procedures, indicating a very stable course, except too low by about 2.5 percent. This difference would be reduced by about 1 percent if an altitude correction is applied to the TOMS data. The σ of the differences forming each monthly point is about 2.8 percent, and is among the smallest in the network. 219

FIGURES

Figure 4.17 Monthly (Dobson–TOMS)/Dobson differences for Churchill indicating a constant difference of about 2.3 percent during most months, except for the winter (December and January are too low by about 7 and 5 percent, respectively). The σ of the differences forming each monthly point is about 5.1 percent. 220

Figure 4.18 Daily differences for Aarhus indicating extremely great scattering. The σ of the difference forming the monthly points (not plotted) is about 9.1 percent, the second largest in the network. 220

Figure 4.19 Daily differences for Toronto indicating stable direct-Sun readings (the σ of the differences of the monthly values is only about 2.2 percent) and very great scattering of the zenith-sky readings. The σ of the differences forming the monthly points from all observations (not plotted) is about 4.6 percent. 221

Figure 4.20 Comparison of the Belsk station-revised ozone data and the "fast" revised record, including corrections found during the August 1986 intercomparisons. The data are plotted as monthly deviations that have been normalized and smoothed by taking the 12-month running mean. 222

Figure 4.21 The Belsk total ozone record as it was originally published in *Ozone Data for the World*. The data are plotted as normalized monthly ozone deviations that have been smoothed. 223

Figure 4.22 The 12-month running means of the total ozone measurements taken at Varanasi and New Delhi and recorded in *Ozone Data for the World*. 224

Figure 4.23 The monthly total ozone deviations (a smooth plot of the actual deviation divided by the particular month's interannual standard deviation) for Tateno and Kagoshima that are recorded in *ODW*. 225

Figure 4.24 The monthly total ozone deviations (as in Figure 4.23) for Potsdam and Belsk. The Potsdam data are taken from *ODW*, and the Belsk data are the station-corrected set that was also published in *ODW* and that replaced the original values reported to *ODW*. 225

Figure 4.25 The monthly deviations (as in Figure 4.23) for the originally published Belsk total ozone record and for the 100 mb temperature. 226

Figure 4.26 The monthly deviations (as in Figure 4.23) for the fast-revised Belsk total ozone record and for the 100 mb temperature. 227

Figure 4.27 The monthly deviations (as in Figure 4.23) for the station-revised Belsk total ozone record and for the 100 mb temperature. Since the station has, to date, revised the data only through December 1981, a provisional adjustment has been applied to the more recent data published in *ODW*. 227

Figure 4.28 The monthly deviations (as in Figure 4.23) of the 100 mb temperature are plotted against the total ozone data from Churchill. In the upper panel, the ozone values published in *ODW* are shown, and in the lower panel the provisionally revised total ozone data set is plotted. 228

Figure 4.29 The provisionally revised total ozone data and the 100 mb temperatures for Bismarck are plotted. 229

Figure 4.30 Intercomparison of TOMS overpass measurements of total ozone with World Primary Standard Dobson ozone measurements at Mauna Loa Observatory, Hawaii, June 29, 1979. 234

Figure 4.31 The variation of the (TOMS minus Dobson) percentage difference with time given for three different types of Dobson measurements. 235

Figure 4.32 Average total ozone distribution for 1957–1975 derived from ground-based measurements. 237

Figure 4.33 Variation of total ozone with latitude and season. 238
Figure 4.34 Long-term means of the monthly total ozone values at Arosa, Switzerland, for August 1931–July 1986. The associated interannual standard deviations for each month are shown as ± 1 sigma vertical bars. 239
Figure 4.35 (a) Differences in the long-term monthly means at Arosa between August 1931–December 1969 and January 1970–July 1986. (b)–(f) Differences in the long-term monthly means at five other stations between the period prior to December 1975 and the period from January 1976 on. 240
Figure 4.36 Differences in the means of the 4-month "winter" season (DJFM) for the 11-year periods from January 1965–December 1975 and January 1976–December 1986 are plotted for 19 Northern Hemisphere stations. Data are taken from *ODW*. 241
Figure 4.37 Differences in the means of the 4-month "summer" season (MJJA) for the 11-year periods from January 1965–December 1975 and January 1976–December 1986 are plotted for 19 Northern Hemisphere stations. Data are taken from *ODW*. 242
Figure 4.38 Differences in the means of the 4-month "winter" season (DJFM) for the 11-year periods from January 1965–December 1975 and January 1976–December 1986 are plotted for 19 Northern Hemisphere stations. Provisionally revised data are used. 244
Figure 4.39 Differences in the means of the 4-month "summer" season (MJJA) for the 11-year periods from January 1965–December 1975 and January 1976–December 1986 are plotted for 19 Northern Hemisphere stations. Provisionally revised data are used. 244
Figure 4.40 Changes in monthly average ozone total amounts at Bismarck, North Dakota, between January 1963–December 1974 and January 1975–December 1986. Using (a) the data as published in *Ozone Data for the World* and (b) the provisionally revised data, with monthly average corrections for instrument calibrations applied to the data recorded in *Ozone Data for the World*. 246
Figure 4.41 Description of trend (a) monotonic, year-round (hockey stick) and (b) separate hockey stick models for each calendar month. 252
Figure 4.42 Smoothed sunspot cycle 1957–1986 255
Figure 4.43 50 mbar Singapore wind speed, 1957–1986 256
Figure 4.44 Ozone decreases caused by the atmospheric nuclear bomb tests as calculated by the 2-D LLNL photochemical model for five different latitude bands. 256
Figure 4.45 Ozone changes for various stations between 1970 and 1986. The statistical model used allowed for effects of the solar cycle and the quasi-biennial oscillation, and data from 1965 (or when the station started making total ozone measurements if it did so after 1965) to 1986 were used. The ozone change in each month was assumed to have occurred in a linear fashion after 1969. The monthly ozone changes plotted are not trends; they are found by multiplying the calculated trend by the 17-year period over which the loss was assumed to have occurred. (a) Arosa, Switzerland, (b) Aspendale, Australia, (c) Belsk, Poland, (d) Bismarck, USA, (e) Boulder, USA, (f) Bracknell, UK, (g) Caribou, USA, (h) Edmonton, Canada, (i) Goose Bay, Canada, (j) Hohenpeissenberg, FRG, (k) Hradec Kralove, Czechoslovakia, (l) Leningrad, USSR, (m) Lerwick, UK, (n) Mauna Loa, 264
USA, (o) Sapporo, Japan, (p) Tateno, Japan, (q) Toronto, Canada. 269

Figure 4.46 Phase of total ozone maximum. 270
Figure 4.47 Quasi-biennial oscillation of total ozone (Dobson Units—DU) in the mean values of Northern Hemisphere (NH), Southern Hemisphere (SH), globe (GL), and zonal mean values (ZM). 278
Figure 4.48 The calculated coefficients for the quasi-biennial term are plotted for 31 stations. At all latitudes except those between 30–39°N, the Singapore wind speed was kept concurrent with the total ozone (so that they are anticorrelated in northern latitudes). Between 30–39°N, a 6-month phase lag was imposed on the Singapore wind speed. 279
Figure 4.49 Variation of annual total ozone percentage deviations for the three latitude bands 53–64°N, 40–52°N, and 30–39°N. The most northerly band has the highest ozone values. 282
Figure 4.50 Variation of winter total ozone percentage deviations for the three latitude bands 53–64°N, 40–52°N, and 30–39°N. 283
Figure 4.51 Variation of summer total ozone percentage deviations for the three latitude bands 53–64°N, 40–52°N, and 30–39°N. 284
Figure 4.52 Ozone changes for the three latitude bands 53–64°N, 40–52°N, and 30–39°N between 1970 and 1986. 286
Figure 4.53 Annual total ozone cycles at Belsk and Bismark. The points represent the 10-day averages at each station calculated from 24 years of measure. .. 288
Figure 4.54 The points using the symbol ● are the differences in the monthly averages for the periods January 1963–December 1974 and January 1975–December 1986 for a combined series of the data from Belsk and Bismarck. The equivalent results when only Belsk was taken as operating in the former period are shown with the symbol ☐, while those for the case where just Bismarck was taken for the first period have the symbol ▲. In all cases, both stations' data were used in the second period. 289
Figure 4.55 The total ozone trends for the individual months are shown for the latitude band between 53°N and 64°N illustrating the effect of the addition of successive years of data. 292
Figure 4.56 The total ozone trends for the individual months are shown for the latitude band between 40°N and 52°N illustrating the effect of the addition of successive years of data. 293
Figure 4.57 The total ozone trends for the individual months are shown for the latitude band between 30°N and 39°N illustrating the effect of the addition of successive years of data. 294
Figure 4.58 Distribution of the changes between 1980 and 1986 in the 36 monthly trend coefficients for the three latitude bands shown in Figures 4.55, 4.56, and 4.57. 294
Figure 4.59 The total ozone trends for the individual months are shown for the latitude band between 53°N and 64°N illustrating the effect of the addition of successive years of data. 295
Figure 4.60 The total ozone trends for the individual months are shown for the latitude band between 40°N and 52°N illustrating the effect of the addition of successive years of data. The ozone change in each month was assumed to have occurred in proportion to the organochlorine burden of the troposphere, i.e., in a nonlinear fashion until the year shown, and the data used were from 1965 until the year shown. The statistical model used allowed for effects of the solar cycle and the quasi-biennial oscillation. The monthly ozone *trends* are given in DU/yr. 296

Figure 4.61 The total ozone trends for the individual months are shown for the latitude band between 30°N and 39°N illustrating the effect of the addition of successive years of data. 297
Figure 4.62 Distribution of the changes between 1980 and 1986 in the 36 monthly trend coefficients for the three latitude bands shown in Figures 4.59, 4.60, and 4.61. 297
Figure 4.63 Ozone changes for four regional averages composed from the USSR M–83 data taken between 1972 and 1986. 298
Figure 4.64 Variation of total ozone with latitude and season derived from TOMS measurements between 1979 and 1987. 299
Figure 4.65 Variation of total ozone with latitude and season derived from TOMS for each year from 1979 to 1987. 300
Figure 4.66 Globally averaged total ozone from November 1978–December 1987 derived from TOMS measurements. The solid line is a simple linear least squares fit of the data with a slope of -0.4% yr^{-1}. 301
Figure 4.67 (a) Deseasonalized global total ozone derived from TOMS. (b) Deseasonalized total ozone between 53°N and 53°S derived from TOMS. Percentage deviations from the seasonal means are plotted. 302
Figure 4.68 Zonal means of total ozone derived from TOMS for the areas between (a) 0–53°N and (b) 0–53°S. Percentage deviations from the seasonal means are plotted. 304
Figure 4.69 Zonal means of total ozone derived from TOMS for various latitude bands are plotted as percentage deviations from the weekly means. (a) 53–65°S, (b) 39–53°S, (c) 29–39°S, (d) 19–29°S, (e) 0–19°S, (f) 0–19°N, (g) 19–29°N, (h) 29–39°N, (i) 39–53°N, (j) 53–65°N. 305–306
Figure 4.70 Changes by month and latitude in total ozone between 1979–1980 and 1986–1987 as measured with TOMS on the Nimbus–7 satellite (2-year averages are used to minimize differences originating with the QBO). . 307
Figure 4.71 (a-l) TOMS maps of monthly (January through December) total ozone change averaged from 1979 through 1987. 308–314

Figure 5.1 Global averages of SBUV ozone data for November 1978 to September 1984 using data between 70°S and 70°N with equal surface weighting, including Umkehr layers 6 to 9. 391
Figure 5.2 The SBUV weekly mean mixing ratios at 1.0 mb (about 50 km) for latitudes 10°N and 40°N. 392
Figure 5.3 The trend in SBUV ozone mixing ratio as a function of height for three periods, January 1979 to March 1982 (pre-El Chichón period), January 1979 to December 1984, and January 1979 to October 1986. For each period, the percentage change is computed using a least square fit of a time series containing the annual, semiannual, and linear trend terms. 392
Figure 5.4 The percentage change in ozone mixing ratio as a function of altitude and latitude from 1979–1986. The percentage change is computed for each pressure and latitude, as in Figure 5.3. 393
Figure 5.5 SAGE–I and SAGE–II yearly latitudinal coverage. 397
Figure 5.6 Cluster means of SAGE–I and SBUV at 40°S. 398
Figure 5.7 Cluster means of SAGE–I and SBUV at the Equator. 399
Figure 5.8 Cluster means of SAGE–I and SBUV at 40°N. 400

Figure 5.9 Cluster means of SAGE–II and SBUV at 40°S. 401
Figure 5.10 Cluster means of SAGE–II and SBUV at the Equator. 402
Figure 5.11 Cluster means of SAGE–II and SBUV at 40°N. 403
Figure 5.12 Time average of the cluster means. The averaging period for SAGE–I was October 24, 1979, to October 23, 1981. The averaging period for SAGE–II was October 24, 1984, to October 23, 1986. The corresponding SBUV data were similarly averaged. 404
Figure 5.13 The average of the percentage difference between SAGE–I and –II and SBUV cluster means with SBUV the reference. The averaging period was identical to that used for Figure 5.12. 405
Figure 5.14 Time averages of the percentage difference between SAGE–I and –II and SBUV cluster means with SBUV the reference. Averaging was done over all latitude bands for the time period used in Figure 5.12. 406
Figure 5.15 Averages of the percentage difference between the cluster means of SAGE–II and SAGE–I (SAGE–I the reference) or SBUV (1984–1986) and SBUV (1979–1981) (SBUV 1979–1981 the reference). Percentage differences were computed at SAGE–I and SAGE–II intersections. For each latitude band there were approximately eight intersections and thus eight percentage differences averaged to produce one point on the graph. 407
Figure 5.16 Latitudinally averaged mean percentage difference between SAGE–II and SAGE–I (SAGE–I the reference) or between SBUV (1984–1986) and SBUV (1979–1981) (SBUV 1979–1981 the reference). 408
Figure 5.17 Mean percentage difference between SAGE–II and SAGE–I at the geometric altitudes of SAGE (SAGE–I is the reference). For each latitude band approximately eight intersections were available from which to compute percentage differences. The average percentage difference along with its standard error are plotted. The standard error reflects only the variation between the eight percentage differences in a given latitude band. 409
Figure 5.18 Mean percentage difference between SAGE–II and SAGE–I at the geometric altitudes of SAGE (SAGE–I is the reference). All intersections occurring between 20°N to 50°N (or 20°S to 50°S) were combined into one sample. The percentage difference at each intersection was computed. These percentage differences were averaged and plotted for each altitude. The sample standard error was also computed and plotted as the horizontal bar at each point. Within each hemisphere, approximately 2,500 SAGE–I profiles and 6,000 SAGE–II profiles were used in computing the statistics. 410
Figure 5.19 Direct presentation of ozone observations (Dobson units) from the Umkehr station at Tateno (36°N) in the lower panel and collocated SBUV ozone observations in the upper panel from 1979 through 1986 for Umkehr layer 6. 413
Figure 5.20 Same as 5.19, except for Umkehr layer 7. 414
Figure 5.21 Same as 5.19, except for Umkehr layer 8. 415
Figure 5.22 Ratio of Umkehr ozone measurements in layer 8 to collocated SBUV measurements for 7 years after launching of SBUV in November 1978. Eleven Umkehr stations are included. 416
Figure 5.23 Aerosol-corrected Umkehr observations (Arosa, Belsk, Lisbon, and Tateno) plotted as a function of time in comparison with zonal average SAGE–II and SBUV data at 40°N latitude. This figure is a copy of Figure 5.11 with the Umkehr data added. 420

Figure 5.24 Plots of monthly average ozone concentration vs. time in Umkehr layer 6 for five Umkehr stations for precisely 7 years, including 1979 through 1986. 421
Figure 5.25 Same as 5.24, except it is for layer 7. 422
Figure 5.26 Same as 5.24, except it is for layer 8. 425
Figure 5.27 Comparison of zonal mean ozone layer amount calculated from the SBUV, SAGE–I, and LIMS observations for the case of March 1979 SAGE–I sunrise (Table 5.9). 428
Figure 5.28 Same as Figure 5.27 except for April 1979 SAGE–I sunset. 428
Figure 5.29 Percentage difference of zonal mean ozone layer amount of SBUV, SAGE–I, and LIMS from the average for the case of March 1979 SAGE–I sunrise (Table 5.9). 429
Figure 5.30 Same as Figure 5.29 except for April 1979 SAGE–I sunset. 430
Figure 5.31 SME UVS (+) and SBUV (*) average (0° to 60°N) mixing ratios at 1.0 mb for May, June, July, and August. 432
Figure 5.32 Envelope of maximum (2σ) trend of ozone mixing ratios from the UVS instrument of SME for June 1982 to 1986 at 0.75 mb. The error bars denote the range of the data (2σ) resulting from uncertainty in the determination of UVS sensitivity change with time. 433
Figure 5.33 Ozone concentration versus altitude for SMM (UVSP) and for SAGE–II. 434
Figure 5.34 Sunset ozone concentrations from the SMM instrument in the 53–57 km region plotted as a function of time for 20°N. Each point represents a weekly mean. The SBUV and SMM data were taken at different local times; at these altitudes, ozone changes during the diurnal cycle. 435
Figure 5.35 Same as Figure 5.34, except at 20°S. 435
Figure 5.36 Average ozone vertical profile based on ROCOZ–A and chemical ozonesondes at Natal, Brazil, in March and April 1985. Middle panel: SAGE–II minus ROCOZ–A, vertical profile of ozone percentage difference at Natal in 1985 as a function of geometrical altitude. Right panel: SBUV minus ROCOZ–A, vertical profile of ozone percentage difference at Natal in 1985 at Umkehr layers and as a function of pressure. 440

Figure 6.1 Intercomparison of different radiosondes at night. a. Temperature differences from a standard defined by the U.S. and Finnish instruments. b. As in (a), but reported on standard pressure surfaces. 449
Figure 6.2 Weighting functions for satellite temperature instruments: a. MSU, SSU; b. Synthesized SSU channels. 451
Figure 6.3 Temperature changes in the 2 mb NMC analyses, as inferred from rocket comparisons, comparison of analyses around change dates, and regression, as explained in text. 456
Figure 6.4 Monthly 2 mb average temperature (a, unadjusted; b, adjusted to rocket; c, adjusted to joints) deviations from the long-term monthly averages for the Equator. Time runs from October 1978 (month 1) to April 1986 (month 91). 457
Figure 6.5 As in Figure 6.4, but for 30°N. 457
Figure 6.6 Temperature variation (K) in the 30–100 mb layer of "north temperate" latitudes, where a 1–2–1 weighting (1–1 at beginning and end of record) has been applied twice to successive seasonal deviations from the mean. 462
Figure 6.7 Seasonal temperatures with the long-term seasonal averages removed and smoothed 1–2–1 in time. 463

Figure 6.8 Seasonal temperatures with the long-term seasonal averages removed and smoothed 1–2–1 in time. 464
Figure 6.9 Seasonal temperatures with the long-term seasonal averages removed and smoothed 1–2–1 in time. 465
Figure 6.10 Seasonal temperatures with the long-term seasonal averages removed and smoothed 1–2–1 in time. 466
Figure 6.11 Seasonal temperatures with the long-term seasonal averages removed and smoothed 1–2–1 in time. 467
Figure 6.12 Seasonal temperatures with the long-term seasonal averages removed and smoothed 1–2–1 in time for SSU channel 47X centered at approximately 0.5 mb for a) Northern Hemisphere average, b) Southern Hemisphere average, c) global average, and d) 30°S–30°N average. 468
Figure 6.13 Seasonal temperatures with the long-term seasonal averages removed and smoothed 1–2–1 in time for the 30–35 km layer average of station rocket data and the corresponding zonal average of SSU channel 25 centered at approximately 15 mb for a) Ascension Island (9°S, 14°W), b) Cape Canaveral (28°N, 81°W), and c) Kwajalein (9°N, 168°E). 469
Figure 6.14 Seasonal temperatures with the long-term seasonal averages removed and smoothed 1–2–1 in time for the 30–35–40 km layer average of station rocket data and the corresponding zonal average of SSU channel 26 centered at approximately 6 mb. 470
Figure 6.15 Seasonal temperatures with the long-term seasonal averages removed and smoothed 1–2–1 in time for the 40–45–50 km layer average of station rocket data and the corresponding zonal average of SSU channel 27 centered at approximately 2 mb and SSU channel 36X centered at approximately 1.5 mb. 471
Figure 6.16 Seasonal temperatures with the long-term seasonal averages removed and smoothed 1–2–1 in time for the 50–55 km layer average of station rocket data and the corresponding zonal average of SSU channel 47X centered at approximately 0.5 mb 471
Figure 6.17 Summary of global stratospheric temperature differences (1985 and 1986 minus the average of 1979 and 1980). 475
Figure 6.18 As in 6.17, except for Tropics and including rocket stations. Kwajalein Island (KI; 9°N, 168°E), Ascension Island (AI; 9°S, 14°W), and Cape Canaveral (CC; 28°N, 81°W). 475
Figure 6.19 1970–1986 linear regressions from Free University of Berlin data at 30 mb, and Angell and Korshover (1983a) climate zones from the 100–30 mb thicknesses. 476
Figure 6.20 Seasonal changes in tropospheric and stratospheric Northern Hemisphere temperature (degrees Celsius per 10 years) between 1973 and 1985 based on linear regression applied to rocketsonde data primarily in the Western Hemisphere (values above 25 km) and radiosonde data around the entire hemisphere. 477
Figure 6.21 Rocket observations for 30–55 km region at Ascension Island. 479
Figure 6.22 Same as 6.21 except for Kwajalein. 480
Figure 6.23 Same as 6.21 except for Barking Sands. 481
Figure 6.24 Same as 6.21 except for Cape Canaveral. 482
Figure 6.25 Same as 6.21 except for Pt. Mugu. 483
Figure 6.26 Same as 6.21 except for Primrose Lake. 484

Figure 6.27 Fractional decrease between 1979 and 1986 SBUV zonal mean monthly mean ozone mixing ratios. 486
Figure 6.28 Radiative equilibrium temperature differences computed by the three models for the June summer polar case. The differences plotted are computed using 1986 and 1979 ozone data. 487
Figure 6.29 As in Figure 6.28 except for the March equatorial case. 487
Figure 6.30 Radiative equilibrium computation for SAGE-observed ozone. 488
Figure 6.31 Changes in solar heating rates due to variations in the ultraviolet flux between solar minimum and solar maximum based on Heath and Schlesinger (1986) and Chapter 7 of this report. Units are degrees Kelvin per day. 489
Figure 6.32 Changes in radiative–convective equilibrium temperature due to changes in the solar ultraviolet flux over a solar cycle. 490
Figure 6.33 Effect of aerosols with an optical depth of 0.08 on a) solar heating rate, b) infrared heating rate, and c) temperature, for a tropical profile. 491
Figure 6.34 Changes in the net heating rate as a function of unimodal sulfate aerosol optical depth in a tropical atmosphere. 492
Figure 6.35 Aerosol-induced perturbations in radiative–convective equilibrium temperature as a function of unimodal sulfate aerosol optical depth. 493

Figure 7.1 Ozone-mixing ratio (ppmv) as a function of latitude and altitude for January from (a) LIMS and SBUV observations for 1979, (b) Calculations using Oslo 2-D model, (c) Calculations using AER 2-D model, (d) Calculations using Cambridge 2-D model, (e) Calculations using LLNL 2-D model. 514–515

Figure 7.2 Altitude profile of ozone-mixing ratios for January in the Tropics from LIMS observations and the four 2-D models. 516
Figure 7.3 Total column ozone abundance (Dobson Units) as a function of latitude and season for (a) TOMS observations averaged 1979–1986, (b) Oslo, (c) AER, (d) Cambridge, and (e) LLNL models. 516–517

Figure 7.4 Total odd nitrogen (NO_y in ppbv) as a function of latitude for summer from LIMS observations and from the four 2-D models for (a) 3 mb, (b) 16 mb, and (c) 30 mb. Also shown are results from ATMOS. 519
Figure 7.5 Altitude profiles of ClO mixing ratio for July, 30°N, from measurements and from four 2-D models. 520
Figure 7.6 Timeline of percent change in globally averaged column ozone from model calculations for the three cases described in Table 7.1: (1) trace gas emissions only, (2) trace gases plus solar cycle, and (3) trace gases, solar cycle, and atmospheric nuclear tests for the (a) Oslo, (b) AER, (c) Cambridge, and (d) LLNL models. 523
Figure 7.7 Calculated change (%) in column ozone changes as a function of time and latitude during the atmospheric nuclear tests. Results from the LLNL 2-D model are shown for 1962–1963. 524
Figure 7.8 Calculated change (%) in column ozone from 1979–1985 as a function of latitude and month from the Oslo model. The results demonstrate the effect of solar cycle (maximum to minimum) alone, neglecting all other influences. 525

Figure 7.9 Calculated change (%) in column ozone from 1979–1985 as a function of latitude and month, considering trace gases only (case 1). Calculations are from the (a) Oslo, (b) AER, and (c) LLNL models. 526

Figure 7.10 Timeline of percent change in column ozone from 1965 to 1985 for the latitude bands (a) 52–64°N, (b) 40–52°N, and (c) 30–40°N. 528

Figure 7.11 TOMS data for column ozone integrated from 65°S to 65°N are shown for 1978–1987. The TOMS satellite data have been normalized to the ground-based Dobson network. 529

Figure 7.12 Observed change (%) in column ozone from TOMS data, the average of 1985–1986 minus the average of 1979–1980. The TOMS data have been recalibrated and do not reflect the currently archived data: TOMS data for 1985 and 1986 have been increased by approximately 4 percent to account for drift with respect to Dobson network. 529

Figure 7.13 Calculated change (%) in column ozone as a function of latitude and season from 1979–1985, including effects of trace gases and solar cycle. Calculations are from the (a) Oslo, (b) AER, (c) Cambridge, and (d) LLNL models. 530

Figure 7.14 Observed change (%) in column ozone between the 11-year (solar-cycle) averages 1965–1975 and 1976–1986 for (a) summer season (May–June–July–August) and (b) winter season (December–January–February–March). Points representing values from single stations are plotted as a function of station latitude. Results from two 2-D models (Oslo and AER) are also shown. 531

Figure 7.15 Calculated height–latitude changes (%) in ozone from July 1979 to July 1985 for solar cycle only from the Oslo model (a), and solar cycle plus trace gases (case 2) from the (b) Oslo, (c) AER, (d) Cambridge, and (e) LLNL models. 533

Figure 7.16 Observed changes (%) in stratospheric ozone profiles from different instruments over 1979–1986. Differences between SAGE–I (1979–1980) and SAGE–II (1984–1985) measurements are shown for northern and southern latitudes (20°–50°). Umkehr observations from 1979–1986 are limited to northern midlatitudes. 535

Figure 7.17 Model calculations (Oslo) of globally averaged column ozone (Dobson Units) from 1979 extended to 1991 for the large and small solar-cycle variations. 538

Figure 8.1 Monthly mean mixing ratios of CCl_3F measured with HP5840 and HP5880 gas chromatographs on porosil columns at the ALE–GAGE stations between July 1978 and June 1986. 549

Figure 8.2 Monthly mean mixing ratios of CCl_2F_2 measured with HP5840 and HP5880 gas chromatographs on porosil columns at the ALE–GAGE stations between July 1978 and June 1986. 550

Figure 8.3 Monthly mean mixing ratios of CH_3CCl_3 measured with HP5840 and HP5880 gas chromatographs on silicone columns at the ALE–GAGE stations between July 1978 and June 1986. 551

Figure 8.4 Monthly mean mixing ratios of CCl_4 measured with HP5840 and HP5880 gas chromatographs on silicone columns at the ALE–GAGE stations between July 1978 and June 1986. 552

Figure 8.5 Trends of atmospheric concentrations of CCl_2FCClF_2 (CFC–113) observed in Hokkaido, Japan, and as a global average of six sampling sites. 556

Figure 8.6 The global distribution of CCl_2FCClF_2 in 1985 from six sampling sites (Barrow, Alaska; Cape Meares, Oregon; Mauna Loa, Hawaii; Cape Matatula, American Samoa; Cape Grim, Tasmania; South Pole). 556
Figure 8.7 Monthly mean $CHClF_2$ observations (pptv) at Cape Grim, Tasmania, from the Oregon Graduate Center flask sampling program. 557
Figure 8.8 Monthly mean CH_3Cl observations (pptv) at Cape Grim, Tasmania, from the Oregon Graduate Center flask sampling program. 557
Figure 8.9 Measured and predicted cumulative increases of chlorinated source gases in the troposphere over the past decade and up to 1990. The concentrations are given as chlorine atom equivalents. 558
Figure 8.10 Monthly mean concentrations of $CBrF_3$ and $CBrClF_2$ at Cape Meares, Oregon, over the last decade. Concentrations of $CBrF_3$ have increased exponentially at 18(± 1) percent/yr and linearly for $CBrClF_2$ at 0.12(± 0.01) pptv/yr. 559
Figure 8.11 Observations of $CBrClF_2$ (pptv) in the Southern Hemisphere at Cape Grim, Tasmania, and at the South Pole. 560
Figure 8.12 The monthly and globally averaged concentrations of N_2O based on ALE–GAGE data collected using in situ gas chromatographs at Adrigole, Cape Meares, Barbados, Samoa, and Cape Grim, and flask data from Barrow and Mauna Loa. 561
Figure 8.13 N_2O measurements obtained from ice cores. 561
Figure 8.14 Results from four long-term, methane measurement programs based upon gas chromatography and flame ionization detection: (a) the Commonwealth Scientific and Industrial Research Organisation, Australia (CSIRO); (b) the Geophysical Monitoring for Climate Change program of the National Oceanic and Atmospheric Administration (NOAA); (c) the Institute of Atmospheric Sciences, Oregon Graduate Center (OGC); and (d) the University of California at Irvine (UC). 563
Figure 8.15 Time series of monthly mean methane concentrations measured by flask sampling from aircraft in the mid-troposphere (3.5 to 5.5 km altitude) over the southeastern Australian region. 563
Figure 8.16 Zonally averaged representation of the variations in atmospheric methane concentrations in the remote marine boundary layer for the 4-year period May 1983 to April 1987. 564
Figure 8.17 Summary of methane concentrations measured in air bubbles extracted from ice cores in both Greenland and Antarctica. Data are from several investigations, and differing methods of extracting the air from the ice have been used. 565

Figure 8.18 Hemispheric and global averages of deseasonalized CO concentrations. 566

Figure 8.18 Hemispheric and global averages of deseasonalized CO concentrations. . . 566

Figure 8.19 Monthly mean CO observations in the Southern Hemisphere from Samoa, Cape Grim, Mawson, and the South Pole. 567
Figure 8.20 Nitrate (NO_3^-) trends over the last 100 years: (a) Dye 3, South Queensland, (b) South Pole, Antarctica. 568

FIGURES

Figure 9.1. Solar occultation measurements of daytime mixing ratios of NO_2 in ppbv by the SAGE and SAGE–II (preliminary data) instruments. 576

Figure 9.2. NO_2 column amounts above 12 km from a number of ground- and aircraft-based measurements. 578

Figure 9.3. NO_2 column amounts above 24 km from indicated satelliteborne experiments. 579

Figure 9.4. Monthly averaged NO_2 slant column amounts at Lauder, New Zealand (45°S, 170°E). 580

Figure 9.5. SBUV NO data showing column amount of NO above 1 mb in molecules per cm^2 as a function of time for the period 1979 to 1986 in the indicated latitude ranges. 581

Figure 9.6. Plot of total odd nitrogen measured by ATMOS on 5/1/85, at 30°N, LIMS descending node $NO_2 + HNO_3$, and LIMS descending node $NO_2 + HNO_3$ plus twice the N_2O_5 inferred from a photochemical model. 583

Figure 9.7. Time series plot of column amount of hydrogen chloride (HCl) measured from the ground, aircraft, or shuttle during the period 1976 to 1987. .. 584

Figure 9.8. Time series plots of column amount of hydrogen fluoride (HF) measured from the ground, aircraft, or space during the period 1976 to 1987. ... 587

Figure 9.9. Time series of midday ClO column abundances above 30 km measured by ground-based millimeter wave spectrometry taken from Hawaii. 588

Figure 9.10. Time series of stratospheric H_2O vapor measurements made by frost-point hygrometer measurements. (a) 60 mb mixing ratios obtained from balloon flights launched at Washington, D.C. (1963 to 1980), and Boulder, Colorado (since 1980). (b) Representative stratospheric humidity measured on aircraft flights over southern England near 50°N from 1972 to 1980. (c) Mean 15 to 21 km water vapor mixing ratio (ppmm) over Mildura and Alice Springs, Australia, from 1973 to 1979. 590

Figure 9.11. Time series of normalized monthly OH column amounts from indicated groundstations. (a) Fritz Peak, Colorado. (b) Boca Raton, Florida. 591

Figure 10.1 Geometries for ozone passive remote sensing. Configurations for both space-based and ground-based sensors are indicated. 606

Figure 10.2 Decrease in direct solar transmission due to aerosol turbidity (extinction) at Mauna Loa, Hawaii, from 1958 to 1986, based on broad-band solar pyrheliometer measurements. 610

Figure 10.3 Integrated lidar backscatter intensities over the decade 1974 to 1985 for a wavelength 0.6943 μm at two sites: (a) Mauna Loa; (b) Hampton, VA. .. 612

Figure 10.3 Integrated lidar backscatter intensities over the decade 1974 to 1985 for a wavelength 0.6943 μm at two sites: (a) Mauna Loa; (b) Hampton, Virginia. 612

Figure 10.4 Simultaneously measured aerosol and ozone profiles over Minneapolis, Minnesota, on December 22, 1965. 613

Figure 10.5 Aerosol vertical profiles obtained with the six-channel dustsonde. 614

Figure 10.6 Time development of the peak mass mixing ratio of the stratospheric aerosol layer over Laramie, Wyoming, during the entire period of regular dustsonde operations at that site. 615

Figure 10.7 Optical depth of aerosols in the polar stratosphere at a wavelength of 1 micron measured by the SAM–II satellite from October 1978 through September 1986. 617
Figure 10.8 Global distribution of the aerosol optical depth (measured at a wavelength of 1 μm) roughly 2.5 months after the eruption of Mount St. Helens in May 1980. 618
Figure 10.9 Contours of inferred vertical and temporal variations in the aerosol extinction at a wavelength of 6.8 μm (given in units of 10^{-4} km^{-1}, with values indicated on the contours) from SME infrared radiometer data for the first year following the El Chichón eruption of April 4, 1982. 619
Figure 10.10 Contours of volume-scattering ratios at a wavelength of 440 nm from the SME visible spectrometer for observations at 40°N, the Equator, and 40°S, covering the period 1982 through mid-1986. 620
Figure 10.11 Time–longitude contours of SME visible-wavelength (440 nm) volume-scattering ratios at equatorial latitudes, for altitudes of 37.5 km and 30.5 km. 621
Figure 10.12 Comparison of extinction ratios (here, the ratio of aerosol extinction to molecular Rayleigh extinction, at a wavelength of 450 nm) from SAGE–II limb extinction measurements converted to extinction (volume scattering) using two distinct aerosol size distributions. 623
Figure 10.13 Balloonborne dustsonde measurements of the vertical concentration profile of particles with radii greater than 0.15 μm over Laramie, Wyoming. 627
Figure 10.14 Integrated lidar aerosol backscatter intensity (in units of 10^{-4} sr^{-1}) for the stratosphere (i.e., from the tropopause upward) versus latitude from an aircraft survey. 628
Figure 10.15 Perspective plot of the integrated stratospheric lidar backscatter intensity versus latitude for different times after the El Chichón eruption. 631
Figure 10.16 Time development of the global-average stratospheric aerosol optical depth, referred to the zenith, at a wavelength of 1 μm. Data were obtained from the SAGE and SAM–II satellite systems. 632
Figure 10.17 Illustration of the geometry for zenith Umkehr observations of scattered solar radiation, with the Sun at an elevation of 0°. 633
Figure 10.18 Normalized contribution functions (i.e., the relative vertical intensity profiles for primary scattered radiation, which are related to the weighting functions of Chapter 3) for the Umkehr C (311.4 and 332.4 nm) wavelength pair at several solar zenith angles. 634
Figure 10.19 Residual, or aerosol-induced, Δ N-values in the Umkehr C-pair measurement versus solar zenith angle for three aerosol fields. 635
Figure 10.20 Model profiles for aerosol concentration that have been used in ozone/aerosol Umkehr error calculations. 635
Figure 10.21 Errors in Umkehr ozone measurements resulting from stratospheric aerosol interference. 637
Figure 10.22 Monthly averaged midlatitude stratospheric aerosol optical depth (above 15 km) versus time, as compiled from lidar measurements at four sites in the United States, Wales, Germany, and France. 638
Figure 10.23 Illustration of the geometry for SBUV nadir observations of scattered solar radiation. 639
Figure 10.24 A polar stratospheric cloud extinction profile obtained from SAM–II data for January 23, 1979, at 68.7°N and 27°W. 642

Figure 10.25 Average aerosol extinction profile for January 1979 in the Northern Hemisphere. The data correspond to all of the SAM–II observations for that month. 643
Figure 10.26 Histogram showing the longitudinal distribution of PSC events in the Southern Hemisphere for the winters of 1979–1981 based on SAM–II observations. 645
Figure 10.27 Averaged altitude of the maximum aerosol (PSC) extinction (on the vertical profile of extinction) for SAM–II satellite measurements over Antarctica during 13 weeks of a winter season. 646
Figure 10.28 Frequency of cloud sightings by the SAM–II detector as a function of the minimum stratospheric temperature in the vicinity of the clouds, during the austral winter of 1981. 646
Figure 10.29 Detailed SAM–II extinction measurements at 50 mb over a 130-day period during the austral winter and spring of 1981. 647
Figure 10.30 An expanded plot of a segment of the data in Figure 10.29. 648
Figure 10.31 Temperature variations at 50 mb for the same period and geographical locations as in Figure 10.30. 648
Figure 10.32 Histograms of the statistical characteristics of the total ensemble of Southern Hemisphere PSC's having extinctions greater than 2×10^{-3} detected by the SAM–II satellite in 1986. 649
Figure 10.33 As in Figure 10.32, except for the PSC's observed in the Northern Hemisphere in 1986. 650
Figure 10.34 Extinction ratios at 18 km versus time as measured by the SAM–II system in the Southern Hemisphere (i.e., the total extinction including aerosol effects obtained by the satellite limb sensor, divided by the extinction caused by molecular Rayleigh scattering obtained from an atmospheric model; ratios that exceed unity are associated with aerosol extinction). 652
Figure 10.35 Relative frequency (in percent) of observed aerosol extinction ratios at 18 km for 1979 and 1985 through 1987 (as in Figures 10.34a–d) for two specific intervals: (a) September 10 to 20 and (b) September 20 to 30. 653
Figure 10.36 Freezing-point curves for nitric acid aqueous solutions as a function of the nitric acid weight percent of the solution at a pressure of 1 atmosphere. 655
Figure 10.37a Vapor pressures of HNO_3 over aqueous solutions and ices of various compositions as a function of temperature (1000/T). 656
Figure 10.37b Same as Figure 10.37a, except for the H_2O vapor pressures. 657
Figure 10.38 HNO_3 vapor pressures over aqueous HNO_3 solutions and solid phases. 658
Figure 10.39 Lidar backscatter ratio for a PSC at 90°N measured with the NASA/Langley airborne lidar system 660

Figure 11.1 October monthly mean total ozone measurements over Halley Bay. ... 670
Figure 11.2 Deviation of total ozone from seasonal mean over Argentine Islands, Syowa, Halley Bay, and South Pole stations from 1957 through 1986. . 671
Figure 11.3 TOMS maps of Southern Hemisphere, total ozone for Octobers from 1979 through 1987. Maps are polar orthographic projections with Equator at outside and South Pole at center. 672
Figure 11.4 Polar orthographic maps of TOMS October mean Southern Hemisphere total ozone for (a) odd years and (b) even years. 673
Figure 11.5 Polar orthographic maps of TOMS September mean Southern Hemisphere total ozone for (a) odd years and (b) even years. 674

Figure 11.6 Daily zonal mean TOMS total column ozone for latitude band 60°S ±1° from day 210 to day 280, yearly from 1984 to 1987, with 1979 as reference year, using normalized TOMS data (NTD). 675
Figure 11.7 Daily zonal mean TOMS total column ozone for latitude band 70°S ±1° from day 210 to day 280, yearly from 1984 to 1987, with 1979 as reference year, using normalized TOMS data (NTD). 677
Figure 11.8 Daily zonal mean TOMS total column ozone for latitude band 80°S ±1° from day 210 to day 280, yearly from 1984 to 1987, with 1979 as reference year, using normalized TOMS data (NTD). 677
Figure 11.9 Daily zonal mean TOMS total column ozone versus time of year at 60°S for the years 1979 through 1987. 678
Figure 11.10 Daily zonal mean TOMS total column ozone versus time of year at 70°S for the years 1979 through 1987. 679
Figure 11.11 Daily zonal mean TOMS total column ozone versus time of year at 80°S for the years 1979 through 1987. 679
Figure 11.12 Zonally averaged TOMS ozone plotted versus latitude for the month of September from 1979 through 1987. 680
Figure 11.13 Zonally averaged TOMS ozone plotted versus latitude for the month of October from 1979 through 1987. 680
Figure 11.14 Annual progression of TOMS total ozone integrated over the area from 90°S to 44°S plotted for each year from 1979 through 1987. 681
Figure 11.15 Progression of TOMS total ozone integrated over the area from 44°S to 90°S from August through October plotted for each year from 1979 through 1987 (normalized TOMS data used). 682
Figure 11.16 Difference between recent 2 years (1986–1987) of TOMS total ozone measurements and first 2 years (1979–1980) as a function of latitude and season. Two years are used to approximately remove the quasi-biennial oscillation. 682
Figure 11.17 Daily TOMS maps of total column ozone in the Southern Hemisphere for October 15, November 15, November 29, and December 5, 1987 (polar orthographic projection). 683
Figure 11.18 TOMS maps of total column ozone in the Southern Hemisphere for August 17, September 5, September 27, and October 5, 1987. 684
Figure 11.19 TOMS maps of total column ozone in the Southern Hemisphere for September 3–6, 1987. 685
Figure 11.20 Vertical distribution of ozone over Syowa measured by ozonesonde from July through November. 686
Figure 11.21 Ozone partial pressure as function of altitude over McMurdo as measured by ozonesonde. Shown are August 28 and October 16, 1986. 687
Figure 11.22 Ozone profiles over South Pole measured by ozonesonde for August 9 and October 7, 1986. 688
Figure 11.23 Vertical distribution of the ozone partial pressure (nbar) observed at Halley Bay Station on August 15, 1987 (high values), and October 15, 1987 (low values), respectively. 688
Figure 11.24 (a) Ozone partial pressure over Palmer station on October 6 and 9, 1987; (b) temperature profile for October 6 and 9, 1987, over Palmer Station. ... 689
Figure 11.25 Ozone partial pressure over McMurdo measured by ozonesonde; (a) comparison of August 29, 1987, to October 6, 1987, and (b) comparison of August 29, 1987, to November 5, 1987. 690

Figure 11.26 Comparison of ozone profiles measured by SAGE with Halley Bay ozonesondes for October 7, 1987. 690
Figure 11.27 Ozonesonde partial pressure measurements for several days over McMurdo during 1986. 691
Figure 11.28 SAM–II weekly averaged stratospheric optical depth at 1 μm over the Arctic and Antarctic regions from October 1978 to September 1986. ... 692
Figure 11.29 Contour plots of SAM–II weekly averaged extinction ratio at 1 μm for (a) 1980, (b) 1982, (c) 1984. 693
Figure 11.30 SAM–II extinction ratios versus time of year for (a) 1979 at 18 km altitude, (b) 1987 at 18 km altitude, (c) 1979 at 20 km altitude, (d) 1987 at 20 km altitude. 694
Figure 11.31 Time series of October mean 100 mb (100hPa) temperatures over eight Antarctic stations. Data from 1957–1984 are from rawinsonde observations (RAOB) and data from 1979–1986 are from NMC analyses. 696
Figure 11.32 Time series of October mean 30 mb (30hPa) temperatures over eight Antarctic stations. Data from 1957–1984 are from rawinsonde observations (RAOB) and data from 1979–1986 are from NMC analyses. 697
Figure 11.33 October 1983 maps of (a) temperature at 100 mb (hPa), (b) temperature at 30 mb (hPa), and (c) TOMS total ozone. 698
Figure 11.34 Time series of November mean 100 mb (100hPa) temperatures over seven Antarctic stations. Data from 1957–1984 are from rawinsonde observations (RAOB) and data from 1979–1986 are from NMC analyses. 699
Figure 11.35 NMC 1979–1986 zonal mean temperature averages (top, °K) and 1979–1986 trends (bottom, °K/yr) for August, September, October, and November. 700
Figure 11.36 NMC temperature differences between 1979–1983 at (a) 100hPa and (b) 30hPa, with RAOB differences superimposed in bold type. The bottom figure shows the TOMS total ozone difference. 701
Figure 11.37 Year-to-year change of monthly total ozone amount and 100hPa temperature at Syowa Station: (a) October, (b) November, and (c) December. . 702
Figure 11.38 Smoothed seasonal temperature deviations at 100, 50, and 30hPa above Antarctica compared with smoothed seasonal total ozone deviations in Antarctica. 703
Figure 11.39 Latitude–time contour plots of the annual variation of zonal mean total ozone from Dobson stations before 1974. 705
Figure 11.40 TOMS satellite data versus latitude and season between 1979–1982. ... 706
Figure 11.41 Five-year mean climatology of zonal mean temperature (K) for (a) July in the Southern Hemisphere and (b) January in the Northern Hemisphere, and of zonal mean wind (m/s) for c) October in the Southern Hemisphere and d) April in the Northern Hemisphere. 709
Figure 11.42 (a) October NMC 70 mb temperature trend from 1979 to 1985 and (b) TOMS total ozone trend over the same period. 714
Figure 11.43 Northward eddy heat flux calculated from NMC analyses and averaged over 1979–1985 (top, °K m s^{-1}) and the trend in eddy heat flux (bottom, °K m s^{-1} yr^{-1}) over the same period for August, September, and October. 715
Figure 11.44 Time–height contours of the ozone-mixing ratios used in the radiative heating calculations with depleted ozone. Contours are 0.5 ppmv. 717
Figure 11.45 Difference of radiatively determined temperatures for depleted and undepleted ozone computed from Model 1, from September 1 through September 30. Units are 0.5 °K. 718

Figure 11.46 Difference of radiatively determined temperatures for depleted and undepleted ozone computed from Model 2, from September 1 through September 30. Units are 0.5 °K. 718
Figure 11.47 Difference of radiatively determined temperatures for depleted and undepleted ozone computed from Model 3, from September 1 through September 30. Units are 0.5 °K. 719
Figure 11.48 The mean of 1985 and 1986 minus the mean of 1979 and 1980 NMC temperature profiles collocated with the total ozone minimum for September 1 to October 30. Units are 2.0 °K. 720
Figure 11.49 Maximum and minimum TOMS total ozone values south of 30°S, plotted as a function of day over the June–December period for each year between 1979 and 1987. 722
Figure 11.50 Evolution of the nonvolcanic particle size distribution at 70 mb with temperature. Shown are the size distributions at 195 K, 191 K, and 189 K, assuming a cooling rate of 0.5 K/day. 730
Figure 11.51 Ground-based mm-wave spectral data from McMurdo Station, taken in September 1986. 736
Figure 11.52 Observed trend in lower atmospheric ClO component over McMurdo Station during the period September 1–October 16, 1986. 737
Figure 11.53 Diurnal variation of integrated ClO emission line intensity measured at McMurdo Station in 1986. 737
Figure 11.54 OClO vertical column over McMurdo from September 16–19, 1986, measured by direct moonlight. 738
Figure 11.55 OClO vertical column over McMurdo from late August through mid-October 1986 measured during twilight. Also shown is the 50 mb temperature. 738
Figure 11.56 Vertical column abundances for the chlorine reservoir species HCl, $ClONO_2$, and their sum. The column abundance value for the HF obtained on October 12, 1986, is also shown. 741
Figure 11.57 NO_2 vertical column over McMurdo from late August through mid-October, 1986, measured during evening twilight compared to 50 mb temperatures 741
Figure 11.58 Vertical column abundances of HNO_3, NO, and NO_2, over McMurdo Station during September and October 1986. 742
Figure 11.59 ClO mixing ration versus altitude. 745

Appendix

Figure 1 Annual mean ozone levels at Arosa, Switzerland, 1933–1982 763
Figure 2 Arosa data with least-squares fitted lines 763
Figure 3 Seasonal structure of monthly Arosa data 770

APPENDIX E

List of Tables

PRECEDING PAGE BLANK NOT FILMED

PAGE 810 INTENTIONALLY BLANK

Appendix E

List of Tables

Table 2.1 SBUV r and s values 27
Table 2.2 Comparison of SBUV and TOMS r values for combined periods 1–2 .. 29
Table 2.3 Coefficients for the quasi-linear model 33
Table 2.4 Model values of diffuser D after 8 years 43
Table 2.5 Midlatitude ozone changes (1978–1986) for different diffuser degradation models 44
Table 2.6 Model values of diffuser D after 8 years 50
Table 2.7 Range of uncertainty in total ozone 52
Table 2.8 SAGE instrument characteristics 55
Table 2.9 Errors of SAGE–I and SAGE–II 61
Table 2.10 Errors in the difference between SAGE–I and SAGE–II 64
Table 2.11 Characteristics of LIMS channels 85
Table 2.12 Comparison of important features between SBUV–2 and SBUV 93
Table 3.1 Sensitivity of retrieved total ozone to diffuser plate reflectivity, $d \ln \Omega / d \ln D_\lambda$, for TOMS at two view angles, θ, and for SBUV. The reference atmosphere contains 280 Dobson Units (DU) of ozone, surface reflectivity is 0.3, and the solar zenith angle is 45°. 118
Table 3.2 Sensitivity of retrieved total ozone to Diffuser plate model error scenarios. The basic state is as for Table 3.1. The details of the scenarios are discussed in the text. 119
Table 3.3 Layer numbers used by SBUV and Umkehr retrievals 124
Table 3.4. Effective ozone absorption coefficients for Dobson C-Pair 137
Table 3.5. Averaging kernel peak heights and widths 140
Table 3.6 Summary of retrieval characteristics 175
Table 4.1 Ultraviolet wavelength pairs used for atmospheric ozone measurements with Dobson spectrophotometers (wavelengths in nanometers). 185
Table 4.2 Possible causes of error in ozone trends from Dobson stations; estimates of the effects on the determined trends due to instrumental and other experimental causes. 189
Table 4.3 Dobson stations for which preliminary revised ozone data are available over time periods long enough for trend analysis. 191
Table 4.4 Other Dobson stations for which the records are too short for trend analysis, have major interruptions in their records, or are otherwise unsuitable at the present time for analysis on an individual basis. 192
Table 4.5 Primary and secondary standard Dobson ozone spectrophotometers. . 194
Table 4.6 Summary of results of calibrations of world standard Dobson spectrophotometer No. 83 with standard lamps and by means of direct-Sun observations at Mauna Loa Observatory. 195
Table 4.7 USSR M–83 ozone stations. 199
Table 4.8 Six-month average bias (Dobson–TOMS)/Dobson centered at February 1 and August 1 of each year as deduced from all and from only direct-Sun observations. 209
Table 4.9 Stations with variability of their monthly mean differences with TOMS ≥ 3 percent. 213
Table 4.10 Provisionally revised station data used in the time series analyses. 230

812 INTENTIONALLY BLANK

PRECEDING PAGE BLANK NOT FILMED

Table 4.11 Results of trend analyses of the monthly ozone values at Belsk, Poland, for the period 3/63–7/86. 232
Table 4.12 Changes in average total ozone concentrations as measured at individual Dobson stations over the 22-year period 1965–1986, inclusive. 243
Table 4.13 Parameter values for several linear ramp statistical calculations with ozone data from Bismarck. 248
Table 4.14 Statistical analyses of ozone data from Bismarck. 250
Table 4.15 Monthly means and standard deviations at Bismarck (in DU). 259
Table 4.16 Winter and summer trends for individual stations 262
Table 4.17 Average monthly ozone changes for different continents, 1970–1986 270
Table 4.18 Average monthly ozone changes for different continents, 1976–1986. 272
Table 4.19 Average monthly ozone changes, 1970–1986 (data for 1957–1986). 274
Table 4.20 Statistical evaluations of ozone depletion from atmospheric nuclear testing using data from individual stations 276
Table 4.21 Monthly trends in ozone when allowance is made for depletion by nuclear testing. 277
Table 4.22 Statistical evaluation of ozone variations in response to the solar sunspot cycle. 281
Table 4.23 Monthly coefficients (in DU/yr) for the three latitude bands for 1965–1986 data. 285
Table 4.24 Monthly coefficients (in DU/yr) for the same bands as in Table 4.23 for 1957–1986 data. 287
Table 4.25 Different ways of calculating an annual rate of loss. 290
Table 4.26 Variance and covariance of the monthly trend estimates used in calculating seasonal averages. 296
Table 4.27 Percentage changes in total column ozone (measured by TOMS on Nimbus–7, calibrated by comparison with ground-based measurements) 303
Table 5.1 Ozone measuring systems and periods of available data 387
Table 5.2 SAGE systematic errors 395
Table 5.3 SAGE errors affecting the precision and repeatability of ozone measurements for a vertical resolution of 1 km 395
Table 5.4 Comparison of important features between SBUV–2 and SBUV 411
Table 5.5 SBUV trend collocated with 11 Umkehr stations, the trend of the difference (SBUV–Umkehr), and the derived Umkehr trend for 1979 to 1986 417
Table 5.6 Corrections for aerosols applied to Umkehr data on the basis of lidar measurements and DeLuisi's model 419
Table 5.7 Linear least-squares ozone trends in Umkehr layers 6, 7, and 8 from January 1, 1979, to December 31, 1986 423
Table 5.8 Sensitivity study of the effect of three different assumed size distributions for aerosols: the distribution function based on observed aerosols and two widely different arbitrary distributions 424
Table 5.9 The beginning and ending dates (in 1979) and latitudes of four cases of longitudinal progression of the SAGE–I observations 427
Table 5.10 Estimated overall percentage differences of the calculated zonal mean ozone layer amount of SBUV, SAGE–I, and LIMS with respect to the average of these instruments 431
Table 5.11 Reproducibility of satellite and rocket systems in measuring upper stratospheric ozone near Natal, Brazil, during periods of atmospheric stability in 1979 and 1985 438
Table 5.12 Replication of upper stratospheric ozone by sets of three instruments 439

Table 6.1 Sensitivity of measured SSU brightness temperatures to 8 ppmv CO_2 increase and 10 percent ozone decrease at all levels 454
Table 6.2 Global daily 1200 GMT temperature and height fields history of changes 455
Table 6.3 Rocketsonde launch sites having data available for trend analysis 458
Table 6.4 Example of arcasonde and datasonde measurements of same temperature profiles and appropriate corrections 459
Table 6.5 100–50 mb layer mean temperature changes 1986/1985–1980/1979 472
Table 6.6 100–30 mb layer mean temperature changes 1986/1985–1980/1979 472
Table 6.7 30–10 mb layer mean temperature changes 1986/1985–1980/1979 473
Table 6.8 10–5 mb layer mean temperature changes 1986/1985–1980/1979 473
Table 6.9 5–1 mb layer mean temperature changes 1986/1985–1980/1979 474
Table 6.10 0.5 mb layer mean temperature changes 1986/1985–1979/1980 474
Table 6.11 Radiative transfer models used in this section 486
Table 6.12 Dependence of radiative convective equilibrium temperatures on cloud properties 493
Table 6.13 Comparison of calculated cooling from one-dimensional radiative–photochemical models near to the level of peak cooling 496
Table 6.14 Comparison of calculated cooling from one-dimensional radiative–photochemical models at about 30 mb (24 km) 497
Table 7.1 Factors included in model simulations 504
Table 7.2 Trace gas scenarios adopted for 1950–1991 504
Table 7.3 Fluorocarbon emission fluxes (10^9g/yr) used in models for 1950–1991 .. 505
Table 7.4 Assumed peak-to-peak variation of UV radiation during a solar cycle as a function of wavelength 506
Table 7.5 Relative magnitude of solar cycles 507
Table 7.6 Limited set of nuclear tests used in model calculations 508
Table 7.7 Characteristics of 2-D models used in calculations of Chapter Seven 509–510
Table 7.8 Total chlorine mixing ratio (Cl_y in ppb) in the upper stratosphere at 30°N for July 520
Table 7.9 Calculated temperature changes in 1985 vs. 1979 for Oslo model, Case 3. Values are given for July at the equator 521
Table 7.10 Calculated trends in ozone at Umkehr levels 5–9 for 1970–1981; trace gas scenario only 534
Table 8.1 Updated global trends and tropospheric concentrations of source gases for 1986. Where appropriate and available, lifetimes are also tabulated. ... 547
Table 8.2 Annual mean halocarbon concentrations (pptv) observed at the GAGE sites in 1985. the data must be regarded as preliminary. The global average is the mean of the four GAGE sites. CCl_3F data were collected on a porosil column. 548
Table 8.3 Halocarbon growth rates (pptv/yr) observed at the ALE–GAGE sites over the period 1978 to June 1986. the data must be regarded as preliminary. Adrigole ceased operation in 1984. Growth rates were obtained by least squares linear regression; the numbers in parentheses are single standard deviations. The global average is the mean of growth rates observed at Oregon, Barbados, Samoa, and Cape Grim. CCl_3F data are from the porosil column. 548
Table 8.4 Halocarbon growth rates (%/yr) observed at the GAGE sites in 1985. Data are obtained from Tables 8.1 and 8.2. 553

Table 8.5 Annual mean halocarbon concentrations and trends observed at (a) Hokkaido, Japan (42° to 45°N) (Makide et al., 1987a), and (b) Oregon, USA (45°N) (GAGE data), in 1985. Concentrations are in pptv, annual increases (pptv/yr) were obtained by linear regression, and the number in parentheses is one standard deviation. Data at both sites were collected from 1979 to 1986. 554
Table 8.6 Annual mean CCl_3F and CCl_2F_2 concentrations (pptv) and increases (pptv/yr, %/yr) observed at the five Geophysical Monitoring for climatic change stations. 555
Table 8.7 Comparison of growth rates of atmospheric methane. For all data sets except UC the growth rates are given by the slope of a least squares linear fit to 12-month running mean methane values calculated from the monthly data. The values in parentheses are the standard errors of these slopes. The growth rate for the UC data was found by a least squares linear fit to the actual data over the period specified. 564
Table 10.1 Properties of atmospheric aerosols and clouds 600
Table 10.2 Time constants for aerosol processes 608
Table 10.3 Sites of long-term aerosol lidar observations 611
Table 10.4 Long-term aerosol measurements from satellites 616
Table 10.5 Observational methods used to study the stratospheric effects of the El Chichón volcanic eruption 624–625
Table 10.6 Volcanic eruptions known to have injected material into the stratosphere 630
Table 10.7 Aerosol impact on Umkehr and SBUV measurement systems, in order of importance of aerosol properties to each system 636
Table 10.8 Observed PSC properties: 1979 to 1981 644
Table 11.1 Zonal mean, minimum, and maximum ozone for the month of October each year for the 70°S–80°S latitude zone from Nimbus–4 BUV (1970–1972) and from Nimbus–7 SBUV (1979–1984). 671
Table 11.2 TOMS total ozone monthly zonal average 676
Table 11.3 Heterogeneous reactions in PSC's 732
Table 11.4 Observed vertical column abundance (mol. cm^{-2}) 740

Appendix

Table 1 Dobson networks used in total ozone trend anaylsis 757
Table 2 Coefficients of least-squares lines 762

APPENDIX F

Major Acronyms

PRECEDING PAGE BLANK NOT FILMED

Appendix F

Major Acronyms

AER, Inc.	Atmospheric and Environmental Research, Incorporated
AERE	Atomic Energy Research Establishment (UK)
AFCRL	Air Force Cambridge Research Laboratories
AFGL	Air Force Geophysical Laboratory
AGU	American Geophysical Union
AIAA	American Institute of Aeronautics and Astronautics, Inc.
NOAA/AL	Aeronomy Laboratory
ARC	Ames Research Center (NASA)
ATMOS	Atmospheric Trace Molecule Spectroscopy Experiment
AVHRR	Advanced Very High Resolution Radiometer
BOIC	Balloon Ozone Intercomparison Campaign
BUV	Backscatter Ultraviolet Spectrometer
CFC	Chlorofluorocarbon
CFM	Chlorofluoromethane
CIMO	Commission on Instrument and Method of Observation
CIRA	COSPAR International Reference Atmosphere
CMA	Chemical Manufacturers Association
CMRN	Cooperative Meteorological Rocketsonde Network
CNRS	Centre National de la Recherche Scientifique (France)
COSPAR	Committee on Space Research
CPOZ	Compressed Profile Ozone
CSIRO	Commonwealth Scientific and Industrial Research Organization
DCA	Detector capsule assembly
DU	Dobson Unit
ECC	Electrochemical cell (ozonesonde)
EGA	Emissivity growth approximation
EMR	Electromagnetic radiation
ENSO	El Niño–Southern Oscillation
EOS	Earth Observing System
ERBS	Earth Radiation Budget Satellite
ERL	Environmental Research Laboratory (NOAA)
FGGE	First GARP Global Experiment
FOV	Field of view
FRG	Federal Republic of Germany
GARP	Global Atmospheric Research Program
GDR	German Democratic Republic
GFDL	Geophysical Fluid Dynamics Laboratory
GHRS	Goddard High Resolution Spectrograph

PAGE 818 INTENTIONALLY BLANK

PRECEDING PAGE BLANK NOT FILMED

ACRONYMS

GMCC	Geophysical Monitoring for Global Change (NOAA)
GMT	Greenwich Mean Time
GSFC	Goddard Space Flight Center (NASA)
HIRS	High Resolution Infrared Radiation Sounder
hPa	hectoPascals
IAGA/IAMAP	International Association for Geomagnetism and Aeronomy/International Association for Meteorology and Atmospheric Physics
ICSU	International Council of Scientific Unions
IFC	Inflight calibrator
IFOV	Instrument field of view
IGY	International Geophysical Year
INPE	Brazilian space agency
IOC	International Ozone Commission
IPV	Isentropic potential vorticity
IR	Infrared
JPL	Jet Propulsion Laboratory
LAMAT	LIMS Map Archival Tapes
LaRC	Langley Research Center (NASA)
LASP	Laboratory for Atmospheric and Space Physics (University of Colorado)
LIMS	Limb Infrared Monitor of the Stratosphere
LLNL	Lawrence Livermore National Laboratory
LRIR	Limb Radiance Inversion Radiometer
LTE	Local Thermodynamic Equilibrium
MAP	Middle Atmosphere Program
MSU	Microwave Sounding Unit
NASA	National Aeronautics and Space Administration
NBS	National Bureau of Standards (now NIST)
NCAR	National Center for Atmospheric Research
NDSC	Network for the Detection of Stratospheric Change
NESDIS	National Environmental Satellite Data and Information Service
NIR	Near infrared
NMC	National Meteorological Center
NMHC	Nonmethane hydrocarbons
NOAA	National Oceanic and Atmospheric Administration
NOZE	National Ozone Expedition
NRC	National Research Council
NRL	Naval Research Laboratory
NSSDC	National Space Science Data Center
ODW	Ozone Data for the World
OGO	Orbiting Geophysical Observatory
OPT	Ozone Processing Team
PMR	Pressure Modulated Radiometer
PMT	Photomultiplier tube
PSC	Polar Stratospheric Cloud
QBO	Quasi-Biennial Oscillation

RAOB	Rawinsonde Observation
ROCOZ	Rocket Ozonesonde
SAGE	Stratospheric Aerosol and Gas Experiment
SAM–II	Stratospheric Aerosol Measurement
SAMS	Stratospheric and Mesospheric Sounder
SAO	Smithsonian Astrophysical Observatory (Cambridge, MA)
SBUV	Solar Backscatter Ultraviolet Spectrometer
SCOSTEP	Scientific Committee on Solar Terrestrial Physics
SCR	Selective Chopper Radiometer
SIRIS	Stratospheric InfraRed Interferometer Spectrometer
SME	Solar Mesosphere Explorer
SMM	Solar Maximum Mission
SPIE	International Society for Optical Engineering
SSU	Stratospheric Sounding Unit
THIR	Temperature Humidity Infrared Radiometer
TIROS	Television and Infrared Observation Satellite
TOMS	Total Ozone Mapping Spectrometer
TOVS	TIROS Operational Vertical Sounder
UARS	Upper Atmosphere Research Satellite
UKMO	United Kingdom Meteorological Office
UNEP	United Nations Environment Program
UVS	Ultraviolet Spectrometer
UVSP	Ultraviolet Spectrometer and Polarimeter
VTPR	Vertical Temperature Profile Radiometer
WMO	World Meteorological Organization
WODC	World Ozone Data Center

APPENDIX G

Chemical Formulae and Nomenclature

PRECEDING PAGE BLANK NOT FILMED

PAGE 822 INTENTIONALLY BLANK

Appendix G

Chemical Formulae and Nomenclature

Symbol	Name
O	Atomic oxygen
O_2	Molecular oxygen
O_3	Ozone
O_x	Odd oxygen (O, O(^{1}D), O_3)
N_2	Molecular nitrogen
N_2O	Nitrous oxide
NO	Nitric oxide
NO_2	Nitrogen dioxide
NO_3	Nitrogen trioxide, nitrate radical
NO_y	Odd nitrogen (NO, NO_2, NO_3, N_2O_5, $ClONO_2$, HNO_4, HNO_3)
NOx	Oxides of nitrogen (NO, NO_2, NO_3)
N_2O_5	Dinitrogen pentoxide
HNO_2, HONO	Nitrous acid
HNO_3, $HONO_2$	Nitric acid
HNO_4, HO_2NO_2	Peroxynitric acid
NH_3	Ammonia
H_2O	Water vapor
H_2O_2	Hydrogen peroxide
OH, HO	Hydroxyl radical
HO_2	Hydroperoxyl radical
HO_x	Odd hydrogen (OH, HO_2, H_2O_2)
CO	Carbon monoxide
CO_2	Carbon dioxide
CS_2	Carbon disulfide
COS, OCS	Carbonyl sulfide
SO_2	Sulfur dioxide
SF_6	Sulfur hexafluoride
H_2SO_4	Sulfuric acid
HF	Hydrogen fluoride
HCl	Hydrogen chloride
HCN	Hydrogen cyanide
HOCl	Hypochlorous acid
Cl	Chlorine atom
ClO	Chlorine monoxide
$ClONO_2$, $ClNO_3$	Chlorine nitrate
Cl_x	Odd chlorine, inorganic chlorine
CH_4	Methane
C_2H_6	Ethane
C_3H_8	Propane
C_2H_4	Ethylene
C_2H_2	Acetylene

Symbol	Name
CH_2O	Formaldehyde
CH_3CHO	Acetaldehyde
$(CH_3)_2CO$	Acetone
CH_3O_2H	Methyl hydroperoxide
CH_2CHCHO	Acrolein
C_2Cl_4	Tetrachloroethylene
CH_3Cl	Methyl chloride
CH_2Cl_2	Dichloromethane
$CHCl_3$	Chloroform, trichloromethane
CFC	Chlorofluorocarbon
HC	Hydrocarbon
NMHC	Nonmethane hydrocarbons
PAN	Peroxyacetylnitrate
CH_3CCl_3	Methyl chloroform
C_2F_6	Hexafluoroethane
CCl_4	Carbon tetrachloride (FC–10)
CCl_3F	Trichlorofluoromethane (FC–11)
CCl_2F_2	Dichlorodifluoromethane (FC–12)
$CClF_3$	Chlorotrifluoromethane (FC–13)
CF_4	Tetrafluoromethane (FC–14)
$CHCl_2F$	Dichlorofluoromethane (FC–21)
$CHClF_2$	Chlorodifluoromethane (FC–22)
CCl_2FCClF_2	Trichlorotrifluoroethane (FC–113)
$CClF_2CClF_2$	Dichlorotetrafluoroethane (FC–114)
$CClF_2CF_3$	Chloropentafluoroethane (FC–115)
CF_3CF_3	Hexafluoroethane (FC–116)
CH_3CN	Methyl cyanide
CH_3I	Methyl iodide
Br	Bromine atom
BrO	Bromine monoxide
Br_x	Odd bromine, inorganic bromine
$CBrF_3$	Trifluorobromomethane
$CHBr_3$	Bromoform, tribromomethane
CH_3Br	Methyl bromide
CH_2Br_2	Dibromomethane
$CHBr_2Cl$	Dibromochloromethane
$C_2H_4Br_2$	Dibromoethane
$CBrClF_2$	Halon 1211 (BCF) FC–12B1
CF_3Br	Halon 1301 FC–13B1

PAGE 824 INTENTIONALLY BLANK

PRECEDING PAGE BLANK NOT FILMED

APPENDIX H

Pressure—Altitude Conversion Chart

PRECEDING PAGE BLANK NOT FILMED

PAGE 826 INTENTIONALLY BLANK

Appendix H

Pressure–Altitude Conversion Chart

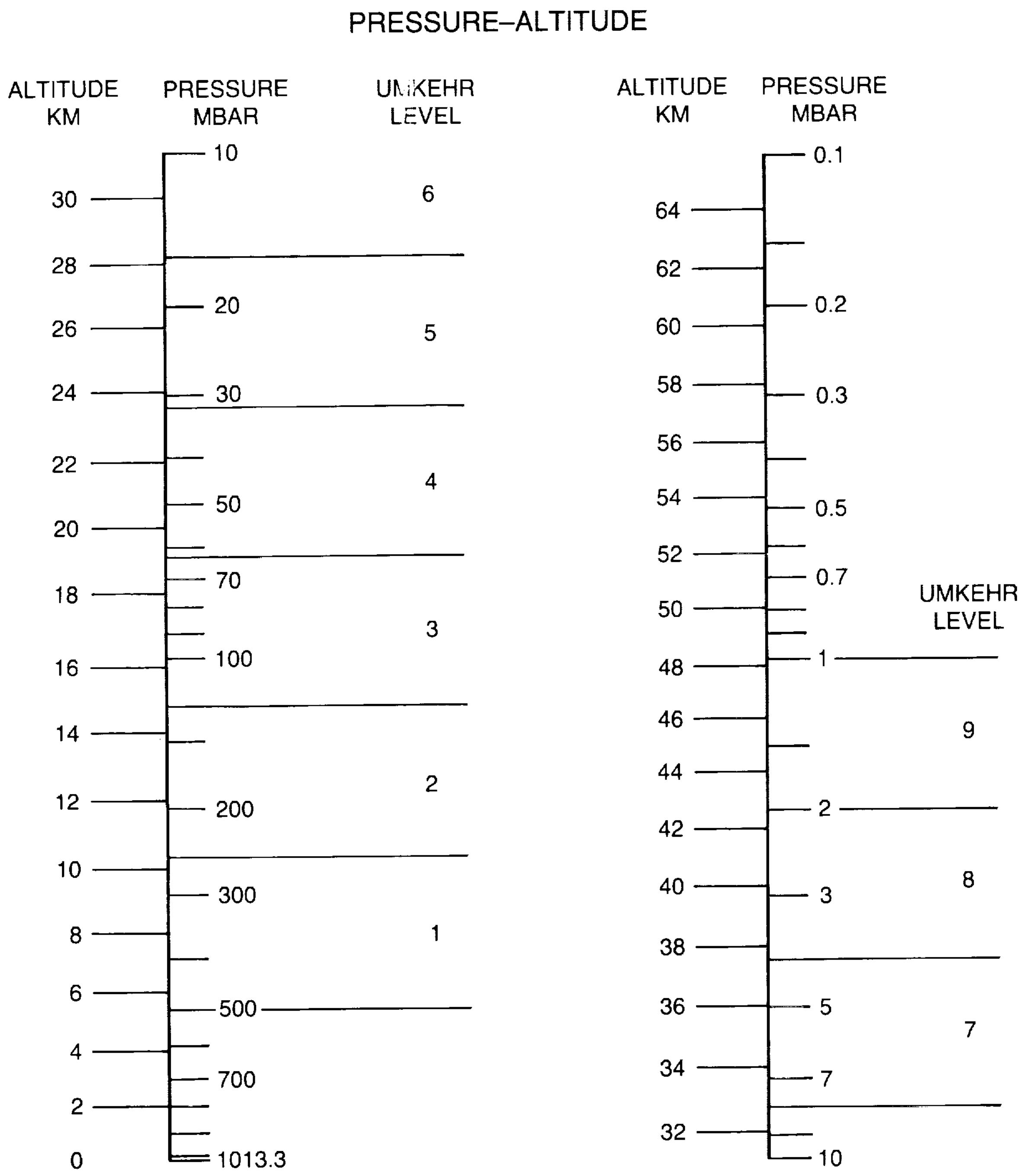

Altitudes are based on U.S. Standard Atmosphere, 1976. The actual altitude for a given pressure may differ by as much as 2 km, depending on season, latitude, and short-term variations.

PAGE 828 INTENTIONALLY BLANK

PRECEDING PAGE BLANK NOT FILMED

R

References

Appendix: References

Adriani, A., F. Congeduti, G. Fiocco, and G.P. Gobbi, One year lidar observations of the stratospheric aerosol at Frascati, March 1982–March 1983, *Geophys. Res. Lett.*, *10*, 1005–1008, 1983.

Aikin, A.C., and R.D. McPeters, Meteoric material and the behavior of upper stratospheric polar ozone, *Geophys. Res. Lett.*, *13*, 1300–1303, 1986.

Aikin, A.C., B. Woodgate, and H.J.P. Smith, Atmospheric ozone determination by solar occultation using the UV spectrometer on the Solar Maximum Mission, *Appl. Optics*, *21*, 2412–2424, 1982.

Aikin, A.C., B. Woodgate, and H.J.P. Smith, Equatorial ozone profiles from the Solar Maximum Mission—A comparison with theory, *Planet. Space Sci.*, *32*, 503–513, 1984.

Anderson, S., and K. Mauersberger, Calibration of a mass spectrometer experiment for ozone, *Rev. Sci. Instrum.*, *52*, 1025–1028, 1981.

Andreji, P.D., Evaluation of various factors affecting homogeneity of the total ozone time-series, in *Proc. Quadr. Ozone Symposium—1988*, Göttingen, edited by R.D. Bojkov and P. Fabian, Deepak Publ., USA, in press.

Andrews, D.G., Some comparisons between the middle atmosphere dynamics of the Southern and Northern Hemispheres, *Pure Appl. Geophys.*, *130*, 213–232, 1989.

Andrews, D.G., and M.E. McIntyre, Planetary waves in horizontal and vertical shear: The generalized Eliassen–Palm relation and the mean zonal acceleration, *J. Atmos. Sci.*, *33*, 2031–2048, 1976.

Andrews, D.G., J.R. Holton, and C.B. Leovy, Extratropical zonal-mean circulation, in *Middle Atmospheric Dynamics*, pp. 295–312, Academic Press, Orlando, Florida, 1987.

Angell, J.K., The close relation between Antarctic total-ozone depletion and cooling of the Antarctic low stratosphere, *Geophys. Res. Lett.*, *13*, 1240–1243, 1986.

Angell, J.K., Rocketsonde evidence for a stratospheric temperature decrease in the Western Hemisphere during 1973–85, *Mon. Weather Rev.*, *115*, 2569–2577, 1987a.

Angell, J.K., Seasonal differences in the trend of total ozone and contributions from tropospheric and stratospheric layers, *Mon. Weather Rev.*, *115*, 753, 1987b.

Angell, J.K., and J. Korshover, Global analysis of recent total ozone fluctuations, *Mon. Weather Rev.*, *104*, 63–75, 1976.

Angell, J.K., and J. Korshover, Global ozone variations: An update into 1976, *Mon. Weather Rev.*, *106*, 725–737, 1978.

Angell, J.K., and J. Korshover, Global temperature variations in the troposphere and stratosphere, *Mon. Weather Rev.*, *11*, 901–921, 1983a.

Angell, J.K., and J. Korshover, Global variation in total ozone and layer-mean ozone: An update through 1981, *J. Clim. and Appl. Meteor.*, *22*, 1611–1627, 1983b.

Angell, J.K., J. Korshover, and W.G. Planet, Ground-based and satellite evidence for a pronounced total-ozone minimum in early 1983 and responsible atmospheric layers, *Mon. Weather Rev.*, *113*, 641–646, 1985.

Atkinson, R.J., and J.R. Easson, Re-evaluation of the Australian total ozone record, in *Proc. Quadr. Ozone Symposium—1988*, Göttingen, edited by R.D. Bojkov and P. Fabian, Deepak Publ., USA, in press.

Avaste, O.A., A.V. Fedynsky, G.M. Grechko, V.I. Sevastyanov, and Ch.I. Willmann, Advances in noctilucent cloud research in the space era, *PAGEOPH*, *118*, 528–580, 1980.

Bailey, P.L., and J.C. Gille, Inversion of limb radiance measurements: An operational algorithm, *J. Geophys. Res.*, *91*, 2757–2774, 1986.

REFERENCES

Baldwin, A.C., and D.M. Golden, Heterogeneous atmospheric reactions—Sulphuric acid aerosols as tropospheric sinks, *Science, 206*, 562–563, 1979.

Ball Aerospace Systems Division, *SBUV/2 Technical Description, Document Number B6802-10, Revision B*, Boulder, Colorado, 40 pp., November 16, 1981.

Bandeen, W.R., and R.S. Fraser, Radiative effects of the El Chichón volcanic eruption: Preliminary results concerning remote sensing, *NASA Tech. Memorandum 84959*, 1982.

Barnes, R.A., Changes in SBUV ozone profiles near Natal, Brazil, from 1979 to 1985, *J. Geophys. Res., 93*, 1704–1707, 1988.

Barnes, R.A., and P.G. Simeth, Design of a rocket-borne radiometer for stratospheric ozone measurements, *Rev. Sci. Instrum., 57*, 544–550, 1986.

Barnes, R.A., A.R. Bandy, and A.L. Torres, Electrochemical concentration cell ozonesonde accuracy and precision, *J. Geophys. Res., 90*, 7881–7887, 1985.

Barnes, R.A., A.C. Holland, and H.S. Lee, An improved rocket ozonesonde (ROCOZ–A) 2. Preparation of stratospheric ozone profiles, *J. Geophys. Res., 91*, 14521–14531, 1986.

Barnes, R.A., A.C. Holland, and V.W.J.H. Kirchhoff, Equatorial ozone profiles from the ground to 52 km during the Southern Hemisphere autumn, *J. Geophys. Res., 92*, 5573–5583, 1987.

Barnett, J.J., and M.E. Corney, Middle atmosphere reference model derived from satellite data, edited by K. Labitzke, J.J. Barnett, and B. Edwards, *Handbook for MAP, Vol. 16*, pp. 47–85, SCOSTEP, Urbana, Illinois, 1985.

Barnett, J.J., and M.E. Corney, Temperature comparisons between the Nimbus–7 SAMS, rocket/radiosondes and the NOAA–6 SSU, *J. Geophys. Res., 89*, 5294–5302, 1984.

Barnett, J.J., R.S. Harwood, J.T. Houghton, C.G. Morgan, C.D. Rodgers, and E.J. Williamson, *Atmospheric Physics Memorandum*, Clarendon Laboratory, University of Oxford, England, 1974.

Barth, C.A., The ultraviolet spectroscopy of planets, in *The Middle Ultraviolet: Its Science and Technology*, edited by A.E.S. Green, pp. 177–218, John Wiley and Sons, New York, 1966.

Barth, C.A., R.W. Sanders, R.J. Thomas, B.M. Jakosky, and R.A. West, Formation of the El Chichón aerosol cloud, *Geophys. Res. Lett., 10*, 993–996, 1983.

Basher, R.E., Review of the Dobson spectrophotometer and its accuracy, *WMO Ozone Report #13*, 1982.

Bass, A.M., and R.J. Paur, The ultraviolet cross-sections of ozone: I. The measurements, in *Atmospheric Ozone, Proceedings of the Quadrennial Ozone Symposium*, Halkidiki, Greece, September 3–7, 1984, edited by C.S. Zerefos and A. Ghazi, pp. 606–610, D. Reidel, Dordrecht, The Netherlands, 1985.

Bass, A.M., A.E. Ledford, Jr., and A.H. Laufer, Extinction coefficients of NO_2 and N_2O_4, *J. of Res. of the N.B.S–A. Phys. and Chem., 80A*, 143–166, 1976.

Bates, D.R., Rayleigh scattering by air, *Planet. Space Sci., 32*, 785–790, 1984.

Bauer, E., A catalog of perturbing influences on stratospheric ozone, 1955–1975, *J. Geophys. Res., 84*, 6929–6940, 1979.

Benjamini, Y., Is the "t test" really conservative when the parent distribution is long-tailed? *J. Amer. Statist. Assoc., 78*, 645–654, 1983.

Bhartia, P.K., K.F. Klenk, V.G. Kaveeshwar, S. Ahmad, A.J. Fleig, R.D. McPeters, and C.L. Mateer, Algorithm for Vertical Ozone Profile Determination for the Nimbus–4 BUV Data Set, in *Proceedings of the 4th Conference on Atmospheric Radiation*, pp. 27–32, American Meteorological Society, Boston, MA, 1981.

Bhartia, P.K., K.F. Klenk, C.K. Wong, D. Gordon, and A.J. Fleig, Intercomparison of the Nimbus 7 SBUV/TOMS total ozone data sets with Dobson and M83 results, *J. Geophys. Res., 89*, 5239–5248, 1984.

Bhartia, P.K., C.K. Wong, and A.J. Fleig, An evaluation of the performance of Umkehr stations by SBUV experiment, in *Atmospheric Ozone, Proceedings of the Quadrennial Ozone Symposium,* Halkidiki, Greece, September 3–7, 1984, edited by C.S. Zerefos and A. Ghazi, pp. 229–233, D. Reidel, Dordrecht, The Netherlands, 1985.

Bhartia, P.K., S. Taylor, and A.J. Fleig, Estimation of errors in the long-term change in ozone reported by the SBUV/TOMS instruments—A new way of looking at the old data, *Proc. Quadr. Ozone Symposium—1988,* Göttingen, edited by R.D. Bojkov and P. Fabian, Deepak Publ., USA, in press.

Birrer, W., *Homogenisierung und Diskussien der Totalozon–Missreihe von Arosa 1926–1971,* Laboratorium für Atmosphärenphysik, 1975.

Bishop, L., and W.J. Hill, Analyzing total ozone for natural and man-made trend variability, *Geophys. Res. Lett., 9,* 485–488, 1982.

Blackmon, M.L., J.E. Geosler, and E.J. Pitcher, A general circulation model study of January climate anomaly patterns associated with interannual variation of equatorial Pacific sea surface temperatures, *J. Atmos. Sci., 40,* 1410–1425, 1983.

Blake, D.R., and F.S. Rowland, Continuing worldwide increase in tropospheric methane, 1978 to 1987, *Science, 239,* 1129–1131, 1988.

Blake, D.R., and F.S. Rowland, World-wide increase in tropospheric methane, *J. Atmos. Chem., 4,* 43–62, 1986.

Bloomfield, P., M.L. Thompson, and S. Zeger, A statistical analysis of Umkehr measurements of 32–46 km. ozone, *J. Appl. Meteorol., 21,* 1828–1837, 1982.

Bloomfield, P., G. Oehlert, M.L. Thompson, and S. Zeger, A frequency domain analysis of trends in Dobson total ozone records, *J. Geophys. Res., 88,* 8512–8522, 1983.

Bojkov, R.D., Computing the vertical ozone distribution from its relationship with total ozone amount, *J. Appl. Meteor., 8,* 284–292, 1969a.

Bojkov, R.D., Differences in Dobson spectrophotometer and filter ozonometer measurements of total ozone, *J. Appl. Meteor., 8,* 362–368, 1969b.

Bojkov, R.D., Global total ozone distribution (1957–1965), NCAR manuscript presented at the Ozone Symposium, Monaco, 1968.

Bojkov, R.D., The 1979–1985 ozone decline in Antarctica as reflected in ground based observations, *Geophys. Res. Lett., 13,* 1236–1239, 1986a.

Bojkov, R.D., The 1983 and 1985 anomalies in ozone distribution in perspective, *Mon. Weather Rev., 115,* 2187–2201, 1987b.

Bojkov, R.D., On the long-term changes of tropospheric ozone, in *Proc. Quadr. Ozone Symposium—1988,* Göttingen, edited by R.D. Bojkov and P. Fabian, Deepak Publ., USA, in press.

Bojkov, R.D., Ozone changes at the surface and in the free troposphere, in *Tropospheric Ozone—Regional and Global Scale Interactions,* edited by I.S.A. Isaksen, pp. 83–96, D. Reidel, Norwell, Massachusetts, 1988b.

Bojkov, R.D., Ozone changes at the surface and in the troposphere, in *Tropospheric Ozone: Proceedings of the NATO Workshop,* edited by I.S.A. Isaksen, pp. 83–96, D. Reidel, Boston, 1987a.

Bojkov, R.D., Ozone variations in the Northern polar region, *Meteorol. Atmos. Phys., 38,* 117–130, 1988a.

Bojkov, R.D., Spring ozone change in the Antarctic and the role of the polar vortex, *Adv. Space Res., 136,* 89–98, 1986b.

Bojkov, R.D., Surface ozone during the second half of the nineteenth century, *J. Clim. Appl. Meteor., 25,* 343–352, 1986c.

Bojkov, R.D., and W. Attmannspacher, Ozone variability and trends from ozone soundings at Hohenpeissenberg, paper presented at the Quadrennial Ozone Symposium, Göttingen, August 8–17, 1988.

Bojkov, R.D., and C.L. Mateer, On the relative quality and performance of the Global Ozone Observing System total ozone measurements, in *Atmospheric Ozone, Proceedings of the Quadrennial Ozone Symposium*, Halkidiki, Greece, September 3–7, 1984, edited by C.S. Zerefos and A. Ghazi, pp. 335–340, D. Reidel, Dordrecht, The Netherlands, 1985.

Bojkov, R.D., and G.C. Reinsel, Trends in tropospheric ozone concentration, in *Atmospheric Ozone, Proceedings of the Quadrennial Ozone Symposium*, Halkidiki, Greece, September 3–7, 1984, edited by C.S. Zerefos and A. Ghazi, pp. 775–781, D. Reidel, Dordrecht, The Netherlands, 1985.

Bojkov, R.D., C.L. Mateer, and A.L. Hansson, Comparison of ground-based and Total Ozone Mapping Spectrometer measurements used in assessing the performance of the Global Ozone Observing System, *J. Geophys. Res.*, *93*, 9525–9533, 1988.

Borucki, W.J., and W.L. Chameides, Lightning: Estimates of the rates of energy dissipation of nitrogen fixation, *Rev. Geophys.*, *22*, 363–372, 1984.

Bowman, K.P., and A.J. Krueger, A global climatology of total ozone from the Nimbus–7 Total Ozone Mapping Spectrometer (TOMS), *J. Geophys. Res.*, *90*, 7967–7976, 1985.

Box, G.E.P., and G.M. Jenkins, *Time Series Analysis, Forecasting and Control*, 575 pp., Holden–Day, San Francisco, 1976.

Boyd, J.P., The noninteraction of waves with the zonally averaged flow on a spherical Earth and the interrelationships of eddy fluxes of energy, heat and momentum, *J. Atmos. Sci.*, *33*, 2285–2291, 1976.

Brasseur, G., and A. De Rudder, Theoretical prediction of perturbations in the middle atmosphere related to the increasing emission of greenhouse gases, *Adv. Space Res*, *6*, 51–54, 1986.

Brasseur, G., and P.C. Simon, Stratospheric chemical and thermal response to long-term variability in solar UV irradiance, *J. Geophys. Res.*, *86*, 7343–7362, 1981.

Brasseur, G., and S. Solomon, *Aeronomy of the Middle Atmosphere*, D. Reidel, Boston, 441 pp., 1984.

Brewer, A.W., A replacement for the Dobson spectrophotometer? *Pure and Applied Geophys.*, *106–108*, 919–927, 1973.

Brewer, A.W., and J.R. Milford, The Oxford–Kew ozonesonde, *Proc. Roy. Soc. London*, *A256*, 470–495, 1960.

Brewer, A.W., and A.W. Wilson, The regions of formation of atmospheric ozone, *Quart. J. Roy. Meteorol. Soc.*, *94*, 249–265, 1968.

Bridges, J.M., and W.R. Ott, Vacuum ultraviolet radiometry. 3: The argon mini-arc as a new secondary standard of spectral radiance, *Appl. Opt.*, *16*, 367–376, 1977.

Brownscombe, J.L., J. Nash, G. Vaughan, and C.F. Rogers, Solar tides in the middle atmosphere. I: Description of satellite observations and comparison with theoretical calculations at equinox, *Quart. J. Roy. Meteorol. Soc.*, *111*, 677–689, 1985.

Bruhl, C., *Ein effizientes Model für global Klima- und Luftzusammensetzunganderungen durch menschlishe activäten*, Doctorate Thesis, University of Mainz, Federal Republic of Germany, 1987.

Bruhl, C., and P.J Crutzen, Scenarios of possible changes in atmospheric temperatures and ozone concentrations due to man's activities, estimated with a one-dimensional coupled photochemical climate model, *Climate Dynamics*, *2*, 173–203, 1988.

Brune, W.H., and J.G. Anderson, In situ observations of midlatitude stratospheric ClO and BrO, *Geophys. Res. Lett.*, *13*, 1391–1394, 1986.

Brune, W.H., E.M. Weinstock, J.J. Schwab, R.M. Stimpfle, and J.G. Anderson, Stratospheric ClO: In situ detection with a new approach, *Geophys. Res. Lett.*, *12*, 441–444, 1985.

Brune, W.H., E.M. Weinstock, and J.G. Anderson, Midlatitude ClO below 22 km altitude: Measurements with a new aircraft-borne instrument, *Geophys. Res. Lett., 15*, 144–147, 1988.

Burnett, C.R., K.R. Minschwaner, and E.B. Burnett, Vertical column abundance measurements of atmospheric hydroxyl from 26°, 40°, and 65°N, *J. Geophys. Res., 93*, 5241–5254, 1988.

Cabannes, J., and J. Dufay, Les variations de la quantité d'ozone contenue dans l'atmosphere, *J. Phys. Rad., Ser. 6, 8*, 353–364, 1927.

Cadle, R.D., C.S. Kiang, and J.F. Louis, The global scale dispersion of the eruption clouds from major volcanic eruptions, *J. Geophys. Res., 81*, 3125–3132, 1976.

Cadle, R.D., F.G. Fernald, and C.I. Frush, Combined use of lidar and numerical diffusion models to estimate the quantity and dispersion of volcanic eruption clouds in the stratosphere: Vulcán Fuego, 1974, and Augustine, 1976, *J. Geophys. Res., 82*, 1783–1786, 1977.

Callis, L.B., and M. Natarajan, The Antarctic ozone minimum: Relationship to odd nitrogen, odd chlorine, the final warming and the 11-year solar cycle, *J. Geophys. Res., 91*, 10771–10796, 1986.

Callis, L.B., J.C. Alpert, and M.A. Geller, An assessment of thermal, wind, and planetary wave changes in the middle atmosphere due to 11-year in flux variations, *J. Geophys. Res., 90*, 2273–2282, 1985a.

Callis, L.B., M. Natarajan, and J.M. Russell, III, Estimates of the stratospheric distribution of odd nitrogen from the LIMS data, *Geophys. Res. Lett., 12*, 259–262, 1985b.

Callis, L.B., M. Natarajan, R.E. Boughner, J.M. Russell III, and J.D. Lambeth, Stratospheric photochemical studies using Nimbus 7 data 2. Development of inferred trace specie distributions, *J. Geophys. Res., 91*, 1167–1197, 1986.

Cebula, R.P., H. Park, and D.F. Heath, Characterization of the Nimbus–7 SBUV radiometer for the long term monitoring of stratospheric ozone, *J. Atm. Oceanic Technology, 5*, 215–227, 1988.

Chandra, S., Recent trends in stratospheric ozone inferred from Nimbus–7 SBUV spectrometer, National Workshop on Ozone, April 13–15, 1987, pp. 33–44, National Physical Laboratory, New Delhi, 1988.

Chandra, S., Solar-induced oscillations in the stratosphere: A myth or reality?, *J. Geophys. Res., 90*, 2331–2339, 1985.

Chang, J.S., W.H. Duewer, and D.J. Wuebbles, The atmospheric nuclear tests of the 1950's and 1960's: A possible test of ozone depletion theories, *J. Geophys. Res., 94*, 1755–1765, 1979.

Chemical Manufacturers Association (CMA), Production, sales and calculated release of CFC–11 and –12 through 1984, *Report of Fluorocarbon Program Panel*, Washington, D.C., 1985.

Chemical Manufactures Association (CMA), World production and release of chlorofluorocarbons 11 and 12 through 1981, *Report FPP 83–F*, Washington, D.C., 1982.

Chu, W.P., Inversion of SAGE II Measurements, in *Abstracts of the 6th AMS Conference on Atmospheric Radiation*, pp. J49–J51, Williamsburg, Virginia, May 13–16, 1986.

Chu, W.P., Inversion technique for SAGE II data, Workshop on Remote Sensing Retrieval Methods, Dec. 15–18, 1987, Williamsburg, Virginia, 1988.

Chu, W.P., SAGE II inversion algorithm, *J. Geophys. Res., 94*, 8339–8351, 1989.

Chu, W.P., and M.P. McCormick, Inversion of stratospheric aerosol and gaseous constituents from spacecraft solar extinction data in the 0.38–1.0μm wavelength region, *Appl. Opt., 18*, 1404–1413, 1979.

Chu, W.P., and M.P. McCormick, SAGE observations of stratospheric nitrogen dioxide, *J. Geophys. Res., 91*, 5465–5476, 1986.

Chu, W.P., M.P. McCormick, J. Lenoble, C. Brogniez, and P. Pruvost, SAGE II inversion algorithm, *J. Geophys. Res., 94*, 8339–8351, 1989.

Chubachi, S., On the cooling of stratospheric temperatures at Syowa, Antarctica, *Geophys. Res. Lett., 13*, 1221–1223, 1986.

Chubachi, S., Preliminary results of ozone observations at Syowa Station from February 1982 to January 1983, *Mem. Natl. Inst. Polar Res., Spec. Issue No. 34, Proceedings of the Sixth Annual Symposium of Polar Meteorology and Glaciology,* National Institute of Polar Research, Tokyo, Japan, p. 13, 1984.

Chubachi, S., and R. Kajawara, Total ozone variations at Syowa, Antarctica, *Geophys. Res. Lett., 13,* 1197–1198, 1986.

Cicerone, R.J., How has the atmospheric concentration of CO changed? in *The Changing Atmosphere,* edited by F.S. Rowland and I.S.A. Isaksen, Dahlem Konferenzen, Berlin, November 1–6, 1987, pp. 49–61, John Wiley and Sons, Ltd., Chichester, England, 1988.

Cicerone, R.J., L.E. Heidt, and W.H. Pollock, Measurements of atmospheric methyl bromide (CH_3Br) and bromoform ($CHBr_3$), *J. Geophys. Res., 93,* 3745–3749, 1988.

Clancy, R.T., El Chichón and "mystery cloud" aerosols between 30 and 55 km: Global observations from the SME visible spectrometer, *Geophys. Res. Lett., 13,* 937–940, 1986.

Clavelin, J.L., and P. Mirabel, Determination des pressions partielles du melange eau–acide nitrique, *J. Chimie Phys., 76,* 533–537, 1979.

Clemesha, B.R., and D.M. Simonich, Lidar observations of the El Chichón dust cloud at 23°S, *Geophys. Res. Lett., 10,* 321–324, 1983.

Clyne, M.A.A., and R.T. Watson, Kinetic studies of diatomic free radicals using mass spectrometry, Part 4—The BrO + ClO and BrO + ClO reactions, *J. Chem. Soc., Faraday Trans. I., 73,* 1169–1187, 1977.

CMA: see Chemical Manufacturer's Association

Cochrane, D., and G.H. Orcutt, Applications of least-squares regression to relationships containing autocorrelated errors, *J. Amer. Statist. Assoc., 44,* 32–61, 1949.

Coffey, M., On the temporal change of stratospheric NO_2, *Geophys. Res. Lett., 15,* 331–334, 1988.

Connor, B.J., J.W. Barrett, A. Parish, P.M. Solomon, R.L. DeZafra, and M. Jaramillo, Ozone over McMurdo Station, Antarctica, austral spring 1986: Altitude profiles for the middle and upper stratosphere, *J. Geophys. Res., 92,* 13221–13230, 1987.

Conway, T.J., P. Tans, L.S. Waterman, K.W. Thoning, K.A. Masarie, and R.H. Gammon, Atmospheric carbon dioxide measurements in the remote global troposphere, 1981–1984, *Tellus, 40B,* 81–115, 1988.

Cowley, J.R., and G.M. Lawrence, Earth limb altitude determination for the Solar Mesosphere Explorer, paper presented at 21st AIAA Aerospace Sciences Meeting, January 10–13, Reno, Nevada, 1983.

Cox, R.A., and G.D. Hayman, Stability and photochemistry of ClO dimers formed at low temperature in the gas phase, Polar Ozone Workshop, *NASA Conf. Publ. 10014,* pp. 256–258, Snowmass, Colorado, 1988.

Coy, L., An unusually large westerly amplitude of the quasi-biennial oscillation, *J. Atmos. Sci., 36,* 174, 1979.

Craig, H., and C.C. Chou, Methane: The record in polar ice cores, *Geophys. Res. Lett., 9,* 1221–1224, 1982.

Craig, R.A., *The Upper Atmosphere—Meteorology and Physics,* 209 pp., Academic Press, New York, 1965.

Craig, R.A., J.J. DeLuisi, and I. Stuetzer, Comparison of chemiluminescent and Umkehr observations of ozone, *J. Geophys. Res., 72,* 1667–1671, 1967.

Crutzen, P.J., Tropospheric ozone: An overview, in *Tropospheric Ozone: Proceedings of the NATO Workshop,* edited by I.S.A. Isaksen, pp. 3–32, D. Reidel, Boston, 1987.

Crutzen, P.J., and F. Arnold, Nitric acid cloud formation in the cold Antarctic stratosphere: A major cause for the springtime "ozone hole," *Nature, 324,* 651–655, 1986.

Crutzen, P.J., I.S.A. Isaksen, and G.C. Reid, Solar proton events: Stratospheric sources of nitric oxide, *Science, 189,* 457–459, 1975.

Cunnold, D.M., R.G. Prinn, R.A. Rasmussen, P.G. Simmonds, F.N. Alyea, C.A. Cardelino, A.J. Crawford, P.J. Fraser, and R.D. Rosen, The Atmospheric Lifetime Experiment 3. Lifetime methodology and application to three years of CCl_3F data, *J. Geophys. Res.*, *88*, 8379–8400, 1983a.

Cunnold, D.M., R.G. Prinn, R.A. Rasmussen, P.G. Simmonds, F.N. Alyea, C.A. Cardelino, and A.J. Crawford, The Atmospheric Lifetime Experiment 4. Result for CCl_2F_2 based on three years of data, *J. Geophys. Res.*, *88*, 8401–8414, 1983b.

Cunnold, D.M., M.C. Pitts, and C.R. Trepte, An intercomparison of SAGE and SBUV ozone observations for March and April 1979, *J. Geophys. Res.*, *89*, 5249–5262, 1984.

Cunnold, D.M., R.G. Prinn, R.A. Rasmussen, P.G. Simmonds, F.N. Alyea, C.A. Cardelino, A.J. Crawford, P.J. Fraser, and R.D. Rosen, Atmospheric lifetime and annual release estimates for CCl_3F and CCl_2F_2 from five years of ALE data, *J. Geophys. Res.*, *91*, 10797–10817, 1986.

Cunnold, D.M., W.P. Chu, R.A. Barnes, M.P. McCormick, and R.E. Veiga, Validation of SAGE II ozone measurements, *J. Geophys. Res.*, *94*, 8447–8460, 1989.

Danielsen, E.F., and H. Houben, Dynamics of the Antarctic stratosphere and implications for the ozone hole, unpublished manuscript.

Dave, J.V., Effect of aerosol on estimation of total ozone in an atmospheric column from the measurement of its ultraviolet radiance, *J. Atmos. Sci.*, *35*, 899–911, 1978.

Dave, J.V., Multiple scattering in a non-homogeneous, Rayleigh atmosphere, *J. Atmos. Sci.*, *22*, 273–279, 1964.

Dave, J.V., and P.M. Furukawa, Scattered radiation in the ozone absorption bands at selected levels of a terrestrial, Rayleigh atmosphere, *Meteorol. Mon.*, *7 (29)*, 1966.

Dave, J.V., and C.L. Mateer, A preliminary study on the possibility of estimating total atmospheric ozone from satellite measurements, *J. Atmos. Sci.*, *24*, 414–427, 1967.

Dave, J.V., J.J. DeLuisi, and C.L. Mateer, Results of a comprehensive theoretical examination of the optical effects of aerosols on the Umkehr measurement, *Special Environmental Report 14*, pp. 15–22, World Meteorological Organization, Geneva, 1979.

Dave, J.V., C.L. Mateer, and J.J. DeLuisi, An examination of the effect of haze on the Short Umkehr method for deducing the vertical distribution of ozone, in *Proc. Quadr. Ozone Symp.*, pp. 222–229, National Center for Atmospheric Research, Boulder, Colorado, 1980.

Deirmendjian, D., On volcanic and other particulate turbidity anomalies, *Adv. Geophys.*, *16*, 267–296, 1973.

DeLuisi, J.J., A study of the effect of haze upon Umkehr measurements, *Quart. J. Roy. Meteorol. Soc.*, *95*, 181–187, 1969.

DeLuisi, J.J., Umkehr vertical ozone profile errors caused by the presence of stratospheric aerosols, *J. Geophys. Res.*, *84*, 1766–1770, 1979.

DeLuisi, J.J., and C.L. Mateer, On the application of the optimum statistical inversion technique to the evaluation of Umkehr observations, *J. Appl. Meteor.*, *10*, 328–334, 1971.

DeLuisi, J.J., and J. Nimira, Preliminary comparison of satellite BUV and surface-based Umkehr observations of the vertical distribution of ozone in the upper stratosphere, *J. Geophys. Res.*, *83*, 379–384, 1977.

DeLuisi, J.J., C.L. Mateer, and D.F. Heath, Comparison of seasonal variations of upper stratospheric ozone concentrations revealed by Umkehr and Nimbus 4 BUV observations, *J. Geophys. Res.*, *84*, 3728–3732, 1979.

DeLuisi, J.J., T. DeFoor, K. Coulson, F. Fernald, and K. Thorne, *Lidar Observations of Stratospheric Aerosol Over Mauna Loa Observatory: 1974–1981, NOAA Data Report ERL ARL-4*, 107 pp., NOAA Environmental Research Laboratories, Boulder, Colorado, 1982.

DeLuisi, J.J., E.G. Dutton, K.L. Coulson, T.E. DeFoor, and B.G. Mendonca, On some radiative features of the El Chichón volcanic stratospheric dust cloud and a cloud of unknown origin observed at Mauna Loa, *J. Geophys. Res.*, *88*, 6769–6772, 1983.

DeLuisi, J.J., C.L. Mateer, and P.K. Bhartia, On the correspondence between standard, short Umkehr, and solar backscattered ultraviolet vertical ozone profiles, *J. Geophys. Res.*, *90*, 3845–3849, 1985.

DeMore, W.B., and M. Patapoff, Comparison of ozone determinations by ultraviolet photometry and gas phase titration, *Environ. Sci. Technol.*, *10*, 897–899, 1976.

DeMore, W.B., J.J. Margitan, M.J. Molina, R.T. Watson, D.M. Golden, R.F. Hampson, M.J. Kurylo, C.J. Howard, and A.R. Ravishankara, Chemical kinetics and photochemical data for use in stratospheric modeling, evaluation number 7, *JPL Publication 85–37*, 226 pp., Jet Propulsion Laboratory, Pasadena, California, 1985.

deZafra, R.L., A. Parrish, P.M. Solomon, and J.W. Barrett, Quantitative observations of stratospheric chlorine monoxide as a function of latitude and season during the period 1980–1983, in *Atmospheric Ozone, Proceedings of the Quadrennial Ozone Symposium*, Halkidiki, Greece, September 3–7, 1984, edited by C.S. Zerefos and A. Ghazi, pp. 206–209, D. Reidel, Dordrecht, The Netherlands, 1985.

deZafra, R.L., M. Jaramillo, A. Parrish, P.M. Solomon, B. Connor, and J. Barrett, High concentrations of chlorine monoxide at low altitudes in the Antarctic spring stratosphere, I, Diurnal variation, *Nature*, *328*, 408–411, 1987.

Dianov-Klokov, V.I., and L.N. Yurganov, A spectroscopic study of the global spacetime distribution of atmospheric CO, *Tellus*, *33*, 262–273, 1981.

Dobson, G.M.B., Adjustment and calibration of ozone spectrophotometer, *Ann. IGY*, *5*, 90–114, 1957b.

Dobson, G.M.B., Annual variation of ozone in Antarctica, *Quart. J. Roy. Meteorol. Soc.*, *92*, 549–552, 1966.

Dobson, G.M.B., The development of instruments for measuring atmospheric ozone during the last fifty years, *J. Phys. E: Sci. Instrum.*, *6*, 938–939, 1973.

Dobson, G.M.B., Measurements of the amount of ozone in the Earth's atmosphere and its relation to other geophysical conditions, Part IV, *Proc. Roy. Soc. London*, *A 129*, 411–433, 1930.

Dobson, G.M.B., Observers handbook for the ozone spectrophotometer, *Ann. IGY*, *5*, 46–89, 1957a.

Dobson, G.M.B., A photoelectric spectrophotometer for measuring the amount of atmospheric ozone, *Proc. Phys. Soc. London*, *43*, 324–339, 1931.

Dobson, G.M.B., and D.N. Harrison, Measurements of the amount of ozone in the Earth's atmosphere and its relation to other geophysical conditions, *Proc. Roy. Soc. London*, *A 110*, 660–693, 1926.

Dobson, G.M.B., and C.W.B. Normand, Determination of the constants, etc., used in the calculation of the amount of ozone from spectrophotometer measurements and the accuracy of the results, *Ann. IGY*, *16*, 161–191, 1962.

Dobson, G.M.B., D.N. Harrison, and J. Lawrence, Measurements of the amount of ozone in the Earth's atmosphere and its relation to other geophysical conditions, Part II, *Proc. Roy. Soc. London*, *A 114*, 521–541, 1927.

Dobson, G.M.B., D.N. Harrison, and J. Lawrence, Measurements of the amount of ozone in the Earth's atmosphere and its relation to other geophysical conditions, Part III, *Proc. Roy. Soc. London*, *A 122*, 456–486, 1929.

Douglass, A.R., and R.S. Stolarski, The use of atmospheric measurements to constrain model predictions of ozone change from chlorine perturbations, *J. Geophys. Res.*, *92*, 6662–6674, 1987.

Douglass, A.R., R.B. Rood, and R.S. Stolarski, Interpretation of ozone temperature correlations 2. Analysis of SBUV ozone data, *J. Geophys. Res.*, *90*, 10693–10708, 1985.

Drayson, S.R., P.L. Bailey, H. Fischer, J.C. Gille, A. Girard, L.L. Gordley, J.E. Harries, W.G. Planet, E.E. Remsberg, and J.M. Russell, Spectroscopy and transmittances for the LIMS experiment, *J. Geophys. Res.*, *89*, 5141, 1984.

Dreschhoff, G.A., E.J. Zeller, and B.C. Parker, Past solar activity variation reflected in nitrate concentrations in Antarctic ice, in *Weather and Climate Responses to Solar Variations*, edited by B.M. McCormac, pp. 225–236, Colorado University Press, Boulder, 1983.

Dunkerton, T.J., Body force circulation and the Antarctic ozone minimum, *J. Atmos. Sci.*, *45*, 427–438, 1988.

Dunkerton, T.J., On the mean meridional mass motions of the stratosphere and mesosphere, *J. Atmos. Sci.*, *35*, 2325–2333, 1978.

Dütsch, H.U., The ozone distribution in the atmosphere, *Can. J. Chem.*, *52*, 1491–1504, 1974.

Dütsch, H.U., Total ozone trend in the light of ozone soundings: The impact of El Chichón, in *Atmospheric Ozone, Proceedings of the Quadrennial Ozone Symposium*, Halkidiki, Greece, September 3–7, 1984, edited by C.S. Zerefos and A. Ghazi, pp. 263–268, D. Reidel, Dordrecht, The Netherlands, 1984a.

Dütsch, H.U., An update of the Arosa ozone series to the present using a statistical instrument calibration, *Quart. J. Roy. Meteorol. Soc.*, *110*, 1079–1096, 1984b.

Dutton, E.G., and J. DeLuisi, Spectral extinction of direct solar radiation by the El Chichón cloud during December, 1982, *Geophys. Res. Lett.*, *10*, 1013–1016, 1983.

Dvoryashina, E.V., V.I. Dianov–Klokov, and L.N. Yurganov, Variations of the content of carbon monoxide in the atmosphere in the period from 1970 to 1982, *Journal of the Academy of Sciences USSR, Atmospheric and Oceanic Physics*, *20*, 27–33, 1984.

Dziewulska–Losiowa, A., M. Degorska, and B. Rajewska–Wiech, The normalized total ozone data record, Belsk, 1963–1981, *Publ. Inst. Geophys., Ser. D, Pol. Acad. Sci.*, *18 (169)*, 23–73, 1983.

Eck, T.F., P.K Bhartia, P.H. Hwang, and L.L. Stowe, Reflectivity of the Earth's surface and clouds in ultraviolet from satellite observations, *J. Geophys. Res.*, *92*, 4287–4296, 1987.

Eckerle, K.L., Modification of an NBS reference spectrophotometer, *Natl. Bur. Stand. (U.S.) Tech. Note 913*, 43 pp., 1976.

Eckman, R.S., J.D. Haigh, and J.A. Pyle, An important uncertainty in coupled chlorine–carbon dioxide studies of atmospheric ozone modification, *Nature*, *329*, 616–619, 1987.

Edmon, H.J., B.J. Hoskins, and M.E. McIntyre, Eliassen–Palm cross sections for the troposphere, *J. Atmos. Sci.*, *37*, 2600–2616, 1980. (See also *Corrigendum*, *38*, 1115, 1981, esp. the second-to-last item.)

Ehhalt, D.H., R.J. Zander, and R.A. Lamontagne, On the temporal increase of tropospheric CH_4, *J. Geophys. Res.*, *88*, 8442–8446, 1983.

Elansky, N.R., A. Ya Arabov, A.S. Elokhov, and I.A. Senik, Spatial and temporal variability of the NO_2 total content based on annual observation data, in *Atmospheric Ozone, Proceedings of the Quadrennial Ozone Symposium*, Halkidiki, Greece, September 3–7, 1984, edited by C.S. Zerefos and A. Ghazi, pp. 157–162, D. Reidel, Dordrecht, The Netherlands, 1985.

Etheridge, D.M., G.I. Pearman, and F. de Silva, Atmospheric trace gas variations as revealed by air trapped in an ice-core from Law Dome, Antarctica, *Annals of Glaciology*, *10*, 28–33, 1987.

Evans, W.F.J., Depletion of the Arctic ozone hole by the notching mechanism during spring 1986, Paper A12–02, Spring AGU Meeting, *EOS*, *68*, 272, 1987.

Evans, W.F.J., and J.B. Kerr, Estimates of the amount of sulphur dioxide injected into the stratosphere by the explosive volcanic eruptions: El Chichón, mystery volcano, Mt. St. Helens, *Geophys. Res. Lett.*, *10*, 1049–1051, 1983.

Evans, W.F.J., I.A. Asbridge, J.B. Kerr, C.L. Mateer, and R.A. Olafson, The effects of SO_2 on Dobson and Brewer total ozone measurements, in *Proc. Quadrennial Ozone Symposium*, edited by J. London, pp. 48–56, International Ozone Commission, Boulder, Colorado, 1980.

Fabian, P., R. Borchers, S.A. Penkett, and N.J.D. Prosser, Halocarbons in the stratosphere, *Nature, 216*, 135–136, 1981.

Fabry, C., and M. Buisson, L'absorption de l'ultraviolet par l'ozone et la limite du spectre solaire, *J. Phys. Rad., Ser. 5, 3*, 196–226, 1913.

Fabry, C., and M. Buisson, Etude de l'extremité ultraviolette du spectre solaire, *J. Phys. Rad., Ser. 6, 2*, 197–226, 1921.

Fahey, D.W., C.S. Eubank, G. Hubler, and F.C. Fehsenfeld, Evaluation of a catalytic reduction technique for the measurement of total reactive odd-nitrogen, NO_y, in the atmosphere, *J. Atmos. Chem., 3*, 435–468, 1985.

Fairchild, C.E., E.J. Stone, and G.M. Lawrence, Photofragment spectroscopy of ozone in the UV region 270–310 nm and at 600 nm, *J. Chem. Phys., 69*, 3632, 1978.

Farkas, E., *Proc. Quadr. Ozone Symposium—1988*, Göttingen, edited by R.J. Bojkov and P. Fabian, Deepak Publ., USA, in press.

Farman, J.C., and B.G. Gardiner, Ozone depletion over Antarctica, *Nature, 329*, 574, 1987.

Farman, J.C., B.G. Gardiner, and J.D. Shanklin, Large losses of ozone in Antarctica reveal seasonal ClO_x/NO_x interaction, *Nature, 315*, 207–210, 1985.

Farmer, C.B., G.C. Toon, P.W. Schaper, J.F. Blavier, and L.L. Lowes, Stratospheric trace gases in the spring 1986 Antarctic atmosphere, *Nature, 329*, 126, 1987.

Farrara, J.D., and C.R. Mechoso, An observational study of the final warming in the Southern Hemisphere stratosphere, *Geophys. Res. Lett., 13*, 1232–1235, 1986.

Federal Coordinator for Meteorological Services and Supporting Research, *The National Plan for Stratospheric Monitoring 1987–1997*, Department of Commerce, NOAA, Washington, D.C., 1988.

Feister, U., and W. Warmbt, Long-term surface ozone increase at Arkona, in *Atmospheric Ozone, Proceedings of the Quadrennial Ozone Symposium*, Halkidiki, Greece, September 3–7, 1984, edited by C.S. Zerefos and A. Ghazi, pp. 782–787, D. Reidel, Dordrecht, The Netherlands, 1985.

Fels, S.B., and M.D. Schwarzkopf, The simplified exchange approximation: A new method for radiative transfer calculations, *J. Atmos. Sci., 32*, 1475–1488, 1975.

Fels, S.B., J.D. Mahlman, M.D. Schwarzkopf, and R.W. Sinclair, Stratospheric sensitivity to perturbations in ozone and carbon dioxide: Radiative and dynamical response, *J. Atmos. Sci., 37*, 2265–2297, 1980.

Findlay, F.D., and D.R. Snelling, Collisional deactivation of $O_2(^1\Delta g)$, *J. Chem. Phys., 55*, 545–551, 1971.

Finger, F.G., H.M. Woolf, and C.E. Anderson, A method for objective analysis of stratospheric constant-pressure charts, *Mon. Weather Rev., 93*, 619–638, 1965.

Finger, F.G., M.E. Gelman, F.J. Schmidlin, R. Leviton, and B.W. Kennedy, Compatibility of meteorological rocketsonde data as indicated by international comparison tests, *J. Atmos. Sci., 32*, 1705–1714, 1975.

Fiocco, G., and G. Grams, Observations of the aerosol layer at 20 km by optical radar, *J. Atmos. Sci., 21*, 323–324, 1964.

Fleig, A.J., K.F. Klenk, P.K. Bhartia, K.D. Lee, C.G. Wellemeyer, and V.G. Kaveeshwar, Vertical ozone profile results from Nimbus–4 data, in *Proc. Fourth Conference on Atmospheric Radiation*, pp. 20–26, AMS, Toronto, Ontario, June 16–18, 1981.

Fleig, A.J., P.K. Bhartia, C.K. Wong, and C.L. Mateer, Comparison of Nimbus–7 TOMS and ground-station total ozone measurements, *Index 17, XV–XVII*, World Meteorol. Organ. World Ozone Data Cent., Toronto, Canada, 1982.

Fleig, A.J., P.K. Bhartia, C.G. Wellemeyer, and D.S. Silberstein, Seven years of total ozone from the TOMS instrument—A report on data quality, *Geophys. Res. Lett., 13*, 1355–1358, 1986a.

Fleig, A.J., P.K. Bhartia, and D.S. Silberstein, An assessment of the long-term drift in SBUV total ozone data, based on comparison with the Dobson network, *Geophys. Res. Lett., 13,* 1359–1362, 1986b.

Fleig, A.J., D.S. Silberstein, C.G. Wellemeyer, R.P. Cebula, and P.K. Bhartia, An assessment of the long-term drift in TOMS total ozone data, based on comparison with the Dobson network, in *Proc. Quadr. Ozone Symposium—1988,* Göttingen, edited by R.D. Bojkov and P. Fabian, Deepak Publ., USA, in press.

Fogle, B., and B. Haurwitz, Noctilucent clouds, *Space Sci. Rev., 6,* 278–340, 1966.

Folland, C.K., D.E. Parker, and F.E. Kates, Worldwide marine temperature fluctuations 1856–1981, *Nature, 310,* 670–673, 1984.

Foot, J.S., Aircraft measurements of the humidity in the lower stratosphere from 1977 to 1980 between 45°N and 65°N, *Quart. J. Roy. Meteorol. Soc., 110,* 303–319, 1984.

Fowle, F.E., Atmospheric ozone: Its relation to some solar and terrestrial phenomena, *Smith's. Misc. Coll., 81, No. 11,* 1929.

Fox, R.J., G.W. Grams, B.G. Schuster, and J.A. Weinman, Measurements of stratospheric aerosols by airborne laser radar, *J. Geophys. Res., 78,* 7789–7801, 1973.

Fraser, P.J., and N. Derek, Atmospheric halocarbons and nitrous oxide, 1982–1985, in *Baseline 85, Baseline Atmospheric Program (Australia) 1985,* edited by B.W. Forgan and P.J. Fraser, pp. 44–47, Bureau of Meteorology/CSIRO, 1987.

Fraser, P.J., G.I. Pearman, and P. Hyson, The global distribution of atmospheric carbon dioxide 2. A review of provisional background observations, 1978–1980, *J. Geophys. Res., 88,* 3591–3598, 1983.

Fraser, P.J., P. Hyson, R.A. Rasmussen, A.J. Crawford, and M.A.K. Khalil, Methane, carbon monoxide and methylchloroform in the Southern Hemisphere, *J. Atmos. Chem., 4,* 3–42, 1986a.

Fraser, P.J., N. Derek, R. O'Brien, R. Shepherd, R.A. Rasmussen, and A.J. Crawford, Atmospheric halocarbons and nitrous oxide, 1976–1984, in *Baseline 83–84, Baseline Atmospheric Program (Australia) 1983–1984,* edited by R.J. Francey and B.W. Forgan, pp. 43–49, Bureau of Meteorology/CSIRO, 1986b.

Fraser, P.J., P. Hyson, S. Coram, R.A. Rasmussen, A.J. Crawford, and M.A.K. Khalil, Carbon monoxide in the Southern Hemisphere, in *Proceedings of the 7th World Clean Air Congress, 2,* pp. 341–352, Sydney, Australia, August 1986, 1986c.

Fraser, P.J., R.A. Rasmussen, and M.A.K. Khalil, Atmospheric observations of chlorocarbons, nitrous oxide, methane and carbon monoxide from the Oregon Graduate Center (OGC) flask sampling program, 1984–1985, in *Baseline 85, Baseline Atmospheric Program (Australia) 1985,* edited by B.W. Forgan and P.J. Fraser, pp. 57–55, Bureau of Meteorology/CSIRO, 1987a.

Fraser, P.J., S. Coram, and N. Derek, Atmospheric methane, carbon monoxide and carbon dioxide by gas chromatography, 1978–1985, in *Baseline 85, Baseline Atmospheric Program (Australia) 1985,* edited by B.W. Forgan and P.J. Fraser, pp. 48–50, Bureau of Meteorology/ CSIRO, 1987b.

Frederick, J.E., G.N. Seraphino, and A.R. Douglass, An analysis of the annual cycle in upper stratospheric ozone, *J. Geophys. Res., 89,* 9547–9555, 1984.

Frederick, J.E., R.P. Cebula, and D.F. Heath, Instrument characterization for the detection of long-term changes in stratospheric ozone: An analysis of the SBUV/2 radiometer, *J. Atmos. Ocean. Tech., 3,* 472, 1986.

Friedl, R.R., and S.P. Sander, Kinetic and product studies of the reaction ClO + BrO using discharge flow-mass spectroscopy, Paper delivered at the Eighteenth International Symposium on Free Radicals, Oxford, England, 1987.

Gandin, L.S., Objective analysis of meteorological fields, *GIMIZ Gidrometeorologicheskoe Izdatel'stvo,* Leningrad, 1963.

Gandrud, B.W., M.A. Kritz, and A.L. Lazrus, Balloon and aircraft measurements of stratospheric sulfate mixing ratio following the El Chichón eruption, *Geophys. Res. Lett.*, *10*, 1037–1040, 1983.

Garcia, R., and S. Solomon, A possible relationship between interannual variability in Antarctic ozone and the quasi-biennial oscillation, *Geophys. Res. Lett.*, *14*, 848–851, 1987.

Garcia, R.R., S. Solomon, R.G. Roble, and D.W. Rusch, A numerical study of the response of the middle atmosphere to the 11 year solar cycle, *Planet. Space Sci.*, *32*, 411–423, 1984.

Gardiner, B.G., Comparative morphology of the vertical ozone profile in the Antarctic spring, *Geophys. Res. Lett.*, *8*, 901–904, 1988.

Geller, M.A., M.–F. Wu, M.E. Gelman, Troposphere–stratosphere (surface—55 km) monthly winter general circulation statistics for the Northern Hemisphere—Four year averages, *J. Atmos. Res.*, *40*, 334–342, 1983.

Gelman, M.E., and R.M. Nagatani, Objectives analyses of height and temperature at the 5, 2, and 0.4 mb levels using meteorological rocketsonde and satellite radiation data, *Space Research XVII*, *17*, 122, 1977.

Gelman, M.E., A.J. Miller, R.M. Nagatani, and H.D. Bowman II, Mean zonal wind and temperature structure during the PMP–1 winter periods, *Adv. Space Res.*, *2*, 159–162, 1983.

Gelman, M.E., A.J. Miller, K.W. Johnson, and R.M. Nagatani, Detection of long-term trends in global stratospheric temperature from NMC analyses derived from NOAA satellite data, *Adv. Space Res.*, *6*, 17–25, 1986.

Gernandt, H., The vertical ozone distribution above the GDR-research base, Antarctica in 1985, *Geophys. Res. Lett.*, *14*, 84–86, 1987.

Gille, J.C., and L.V. Lyjak, Radiative heating and cooling rates in the middle atmosphere, *J. Atmos. Sci.*, *43*, 2215–2229, 1986.

Gille, J.C., and J.M. Russell, III, The limb infrared monitor of the stratosphere: Experiment description, performance, and results, *J. Geophys. Res.*, *89*, 5125–5140, 1984.

Gille, J.C., P.L. Bailey, and J.M. Russell III, Temperature and composition measurements from the LRIR and LIMS experiments on Nimbus 6 and 7, *Phil. Trans. Roy. Soc. London Ser. A*, *296*, 205–218, 1980.

Gille, J.C., J.M. Russell, P.L. Bailey, L.L. Gordley, E.E. Remsberg, J.H. Lienesch, W.G. Planet, F.B. House, L.V. Lyjak, and S.A. Beck, Validation of temperature retrievals obtained by the Limb Infrared Monitoring of the Stratosphere (LIMS) experiment on Nimbus–7, *J. Geophys. Res.*, *89*, 5147–5160, 1984a.

Gille, J.C., J.M. Russell, III, P.L. Bailey, E.E. Remsberg, L.L. Gordley, W.F.J. Evans, H. Fischer, B.W. Gandrud, A. Girard, J.E. Harries, and S.A. Beck, Accuracy and precision of the nitric acid concentrations determined by the Limb Infrared Monitor of the Stratosphere experiment on Nimbus–7, *J. Geophys. Res.*, *89*, 5179–5190, 1984b.

Gille, J.C., C.M. Smythe, and D.F. Heath, Observed ozone response to variations in solar ultraviolet radiation, *Science*, *225*, 315–317, 1984c.

Gille, J.C., L. Lyjak, and A.K. Smith, The global residual mean circulation in the middle atmosphere for the northern winter period, *J. Atmos. Sci.*, *44*, 1437, 1987.

GMCC, 1986a, see Schnell, R.C.

GMCC, 1986b, see Schnell, R.C., and R.M. Rosson.

Goldman, A., F.J. Murcray, R.D. Blatherwick, and D.G. Murcray, Quantification of HCl from high-resolution, ground-based infrared solar spectra in the 3000 cm^{-1} region, *J. Quant. Spec. Rad. Trans.* *30*, 385–387, 1986.

Gooding, J.L., D.S. Clanton, E.M. Gabel, and J.L. Warren, El Chichón volcanic ash in the stratosphere: Particle abundance and size distribution after the 1982 eruption, *Geophys. Res. Lett.*, *10*, 1033–1036, 1983.

Gordley, L.L., and J.M. Russell, Rapid inversion of limb radiance data using an emissivity growth approximation, *Appl. Opt.*, *20*, 807, 1981.

Götz, F.W.P., A.R. Meetham, and G.M.B. Dobson, The vertical distribution of ozone in the atmosphere, *Proc. Roy. Soc. London*, *A145*, 416–446, 1934.

Graedel, T.E., and J.E. McRae, On the possible increase of the atmospheric methane and carbon monoxide concentrations during the last decade, *Geophys. Res. Letts.*, *7*, 977–979, 1980.

Grant, K.E., P.S. Connell, and D.J. Wuebbles, Monte Carlo uncertainty analysis of change in atmospheric ozone concentrations from large trace gas perturbations, *EOS*, *66*, 838, 1985.

Gray, L.J., and J.A. Pyle, A two dimensional model of the quasi-biennial oscillation of ozone, Polar Ozone Workshop, *NASA Conf. Publ. 10014*, 306 pp., Snowmass, Colorado, 1988.

Grenander, U., On the estimation of regression coefficients in the case of an autocorrelated disturbance, *Ann. Math. Statist.*, *25*, 252–272, 1954.

Gustin, G.P., On the methodology of total ozone measurements in the global network, *Proc. Main Geophys. Obs. Leningrad*, *406*, 63–75, 1978.

Gustin, G.P., Universal ozonometer, *Proc. Main Geophys. Obs. Leningrad*, *141*, 83–98, 1963.

Gustin, G.P., S.A. Sokolenko, and V.A. Kovalyov, Total-ozone measuring instruments used at the USSR station network, in *Atmospheric Ozone, Proceedings of the Quadrennial Ozone Symposium*, Halkidiki, Greece, September 3–7, 1984, edited by C.S. Zerefos and A. Ghazi, pp. 543–546, D. Reidel, Dordrecht, The Netherlands, 1985.

Haigh, J.D., Radiative heating in the lower stratosphere and the distribution of ozone in a two-dimensional model, *Quart. J. Roy. Meteorol. Soc.*, *110*, 167–185, 1984.

Hamill, P., The time dependent growth of H_2O–H_2SO_4 aerosols by heteromolecular condensation, *J. Aerosol Sci.*, *6*, 475–482, 1975.

Hamill, P., and L.R. McMaster (Eds.), *Polar Stratospheric Clouds: Their Role in Atmospheric Processes, NASA CP–2318*, 72 pp., Hampton, VA, 1984.

Hamill, P., O.B. Toon, and R.P. Turco, Characteristics of polar stratospheric clouds during the formation of the Antarctic ozone hole, *Geophys. Res. Lett.*, *13*, 1288–1291, 1986.

Hamill, P., R.P. Turco, and O.B. Toon, Formation and properties of nitric acid polar stratospheric clouds, *J. Atmos Chem.*, *7*, 287–315, 1988.

Hamilton, K.P., *Stratospheric Circulation Statistics, NCAR Tech. Note TN–191–STR*, National Center for Atmospheric Research, Boulder, Colorado, 1982.

Hansen, J.E., W.C. Wang, and A.A. Lacis, Mt. Agung provides best of a global climate perturbation, *Science*, *199*, 1065–1068, 1978.

Hanson, D., and K. Mauersberger, Precision ozone vapor pressure measurements, *J. Chem. Phys.*, *83*, 326–328, 1985.

Hanson, D., and K. Mauersberger, The vapor pressure of solid and liquid ozone, *J. Chem. Phys.*, *85*, 4669–4672, 1986.

Hao, W.M., S.C. Wofsy, M.B. McElroy, J.M. Beer, and M.A. Toqan, Sources of atmospheric nitrous oxide from combustion, *J. Geophys. Res.*, *92*, 3098–3104, 1987.

Harris, N.R.P., and F.S. Rowland, Trends in total ozone measurements at Arosa, *EOS*, *67*, 875, 1986.

Harris, N.R.P., and F.S. Rowland, *Trends in Total Ozone Measurements at Arosa*, American Geophys. Union, San Francisco, 1988.

Harris, O.D., and G.W. Adams, Where does the $O(^1D)$ energy go? *J. Geophys. Res.*, *88*, 4918–4928, 1983.

Hartley, W.N., On the absorption of solar rays by atmospheric ozone, *J. Chem. Soc.*, *39*, 111–128, 1881b.

Hartley, W.N., On the absorption spectrum of ozone, *J. Chem. Soc.*, *39*, 57–61, 1881a.

C-5

Hartmann, D.L., The dynamical climatology of the stratosphere in the Southern Hemisphere during late winter 1973, *J. Atmos. Sci.*, *33*, 1789–1802, 1976b.

Hartmann, D.L., Some aspects of stratospheric dynamics, in *Advances in Geophysics, 28A*, edited by B. Saltzman, vol. ed. S. Manabe, pp. 219–247, Academic Press, Orlando, Florida, 1985.

Hartmann, D.L., The structure of the stratosphere in the Southern Hemisphere during late winter 1973 as observed by satellite, *J. Atmos. Sci.*, *33*, 1141–1154, 1976a.

Hartmann, D.L., C.R. Mechoso, and K. Yamazaki, Observations of wave mean-flow interaction in the Southern Hemisphere, *J. Atmos. Sci.*, *41*, 351–362, 1984.

Harwood, R.S., The temperature structure of the Southern Hemisphere stratosphere August–October 1971, *Quart. J. Roy. Meteorol. Soc.*, *101*, 75–91, 1975.

Harwood, R.S., and J.A. Pyle, a two-dimensional mean circulation model for the atmosphere below 80 km, *Quart. J. Roy. Meteorol. Soc.*, *101*, 723–747, 1975.

Hasebe, F., The global structure of the total ozone fluctuations observed on the time scales of two to several years, in *Dynamics of the Middle Atmosphere*, edited by J.R. Holton and T. Matsuno, pp. 445–464, Terra Publishers, Tokyo, 1984.

Hasebe, F., Interannual variations of global total ozone revealed from Nimbus IV BUV and ground-based observations, *J.Geophys. Res.*, *88*, 6819, 1983.

Hayman, G.D., J.M. Davies, and R.A. Cox, Kinetics of the reaction ClO + ClO → products and its potential relevance to Antarctic ozone, *Geophys. Res. Lett.*, *13*, 1347, 1986.

Hearn, A.G., The absorption of ozone in the ultra-violet and visible regions of the spectrum, *Proc. Phys. Soc. (London)*, *78*, 932–940, 1961.

Heath, D.F., Non-seasonal changes in total column ozone from satellite observations, 1970–1986, *Nature*, *332*, 219–227, 1988.

Heath, D.F., Testimony before the Subcommittee on Health and the Environment of the House Committee on Energy and Commerce, 1986.

Heath, D.F., and B.M. Schlesinger, The Mg 280-nm doublet as a monitor of changes in solar ultraviolet irradiance, *J. Geophys. Res.*, *91*, 8672–8682, 1986.

Heath, D.F., and B.M. Schlesinger, Temporal variability of UV solar spectral irradiance from 160–400 nm over periods of the evolution and rotation regions from maximum to minimum phases of the sunspot cycle, in *IRS 84: Current Problems in Atmospheric Radiation, Proceedings of the International Radiation Symposium*, Perugia, Italy, edited by G. Fiocco, pp. 315–319, A. Deepak, Hampton, Virginia, 1984.

Heath, D., A.J. Krueger, and C.L. Mateer, The Backscatter Ultraviolet (BUV) Spectrometer experiment, in *The Nimbus IV User's Guide*, edited by R.R. Sabatini, pp. 149–171, NASA, Greenbelt, Maryland, 1970.

Heath, D.F., C.L. Mateer, and A.J. Krueger, The Nimbus–4 Backscatter Ultraviolet (BUV) atmospheric ozone experiment—Two years' operation, *PAGEOPH*, *106–108*, 1238–1252, 1973.

Heath, D.F., A.J. Krueger, H.A. Roeder, and B.D. Henderson, The Solar Backscatter Ultraviolet and Total Ozone Mapping Spectrometer (SBUV/TOMS) for Nimbus G, *Opt. Eng.*, *14*, 323–331, 1975.

Heath, D.F., A.J. Krueger, and H. Park, The Solar Backscatter Ultraviolet (SBUV) and Total Ozone Mapping Spectrometer (TOMS) experiment, in *The Nimbus–7 User's Guide*, edited by C.R. Madrid, NASA Goddard Space Flight Center, Greenbelt, MD., 175–211, 1978.

Herron, M.M., Impurities sources of F, Cl, NO_3, and SO_4 in Greenland and Antarctic precipitation, *J. Geophys. Res.*, *87*, 3052–3060, 1982.

Heymsfield, A.J., Ice particles observed in a cirriform cloud at −83°C and implications for polar stratospheric clouds, *J. Atmos. Sci.*, *43*, 851–855, 1986.

Hill, W.J., P.N. Sheldon, and J.J. Tiede, Analyzing world-wide ozone for trends, *Geophys. Res. Lett.*, *4*, 21–24, 1977.

Hill, W.J., G.W. Oehlert, and G.C. Reinsel, Trend analysis sensitivity studies of Dobson total ozone data through 1984, *J. Geophys. Res.*, *91*, 14515–14520, 1986.

Hilsenrath, E., and B.M. Schlesinger, Total ozone seasonal and interannual variations derived from the 7 year Nimbus-4 BUV data set, *J. Geophys. Res.*, *86*, 12087–12096, 1981.

Hilsenrath, E., P.J. Dunn, and C.L. Mateer, Standard ozone profiles from balloon and rocket data for satellite and theoretical model input, Presented at IAGA/IAMAP Joint Assembly, Seattle, 1977.

Hilsenrath, E., W. Attmannspacher, A. Bass, W. Evans, R. Hagemeyer, R.A. Barnes, W. Komhyr, K. Mauersberger, J. Mentall, M. Proffitt, D. Robbins, S. Taylor, A. Torres, and E. Weinstock, Results from the balloon ozone inter-comparison campaign (BOIC), *J. Geophys. Res. 91*, 13137–13152, 1986.

Hofmann, D.J., Perturbations to the global atmosphere associated with El Chichón volcanic eruption of 1982, *Rev. Geophys.*, *25*, 743–759, 1987.

Hofmann, D.J., and J.M. Rosen, Antarctic observations of stratospheric aerosol and high altitude condensation nuclei following the El Chichón eruption, *Geophys. Res. Lett.*, *12*, 13–16, 1985.

Hofmann, D.J., and J.M. Rosen, On the temporal variation of stratospheric aerosol size and mass during the first 18 months following the 1982 eruption of El Chichón, *J. Geophys. Res.*, *89*, 4883–4890, 1984.

Hofmann, D.J., and J.M. Rosen, Stratospheric sulfuric acid fraction and mass estimate for the 1982 volcanic eruption of El Chichón, *Geophys. Res. Lett.*, *10*, 313–316, 1983b.

Hofmann, D.J., and J.M. Rosen, Sulfuric acid droplet formation and growth in the stratosphere after the 1982 eruption of El Chichón, *Science*, *222*, 325–327, 1983, 1983a.

Hofmann, D.J., J.M. Rosen, T.J. Pepin, and R.G. Pinnick, Stratospheric aerosol measurements I: Time variations at northern mid-latitudes, *J. Atmos. Sci.*, *32*, 1446–1456, 1975.

Hofmann, D.J., J.M. Rosen, J.W. Harder, and S.R. Rolf, Ozone and aerosol measurements in the springtime Antarctic stratosphere in 1985, *Geophys. Res. Lett.*, *13*, 1252–1255, 1986.

Hofmann, D.J., J.W. Harder, S.R. Rolf, and J.M. Rosen, Balloon-borne observations of the development and vertical structure of the Antarctic ozone hole in 1986, *Nature*, *326*, 59–62, 1987a.

Hofmann, D.J., J.M. Rosen, J.W. Harder, and S.R. Rolf, Observations of the decay of the El Chichón stratospheric aerosol cloud in Antarctica, *Geophys. Res. Lett.*, *14*, 614–617, 1987b.

Hofmann, D.J., J.M. Rosen, and J.W. Harder, Aerosol measurements in the winter/spring Antarctic stratosphere: I. Correlative measurements with ozone, *J. Geophys. Res.*, *93*, 665–676, 1988.

Hofmann, D.J., J.W. Harder, J.M. Rosen, J.V. Hereford, and J.R. Carpenter, Ozone profile measurements at McMurdo Station, Antarctica, during spring 1987, *J. Geophys. Res.*, 1989, in press.

Holland, A.C., R.A. Barnes, and H.S. Lee, Improved rocket ozonesonde (ROCOZ–A) 1. Demonstration of precision, *Appl. Opt.*, *24*, 3286–3295, 1985.

Holton, J.R., and W.M. Wehrbein, A numerical model of the zonal mean circulation of the middle atmosphere, *Pure Appl. Geophys.*, *118*, 284–306, 1980b.

Holton, J.R., and W.M. Wehrbein, The role of forced planetary waves in the annual cycle of the zonal mean circulation of the middle atmosphere, *J. Atm. Sci.*, *37*, 1968–1983, 1980a.

Hood, L.L., The temporal behavior of upper stratospheric ozone at low latitudes: Evidence from Nimbus 4 BUV data for short-term responses to solar ultraviolet variability, *J. Geophys. Res.*, *89*, 9557–9568, 1984.

Hoskins, B.J., M.E. McIntyre, and A.W. Robertson, On the use and significance of isentropic potential vorticity maps, *Quart. J. Roy. Meteorol. Soc.*, *111*, 877–946, 1985.

Houghton, J.T., Absorption and emission by carbon dioxide in the mesosphere, *Quart. J. Roy. Meteorol. Soc., 95*, 1–20, 1969.

Howard, C.J., and K.M. Evenson, Kinetics of the reaction of HO_2 with NO, *Geophys. Res. Lett., 4*, 437–441, 1977.

Hunter, W.R., Optical contamination: Its prevention in the XUV spectrographs flown by the Naval Research Observatory in the Apollo telescope mount, *Appl. Opt., 16*, 909–916, 1977.

Hyson, P., Stratospheric water vapour over Australia, *Quart. J. R. Meteorol. Soc., 109*, 285–294, 1983.

Isaksen, I.S.A., and O. Hov, Calculations of trends in the tropospheric ozone concentrations of O_3, OH, CO, CH_4 and NO_x. *Tellus, 39B*, 271–283, 1987.

Isaksen, I.S.A., and F. Stordal, Antarctic ozone depletion: 2–D model studies, *Geophys. Res. Lett., 13*, 1327–1330, 1986a.

Isaksen, I.S.A., and F. Stordal, Ozone perturbations by enhanced levels of CFCs, N_2O and CH_4: A two-dimensional model study including uncertainty estimates, *J. Geophys. Res., 91*, 5249–5263, 1986b.

Iwasaka, Y., Non-spherical particles in the Antarctic polar stratosphere—Increase in particulate content and stratospheric water vapor budget, *Tellus, 38B*, 364–374, 1986.

Iwasaka, Y., and K. Kondoh, Depletion of Antarctic ozone: Height of ozone loss and its temporal changes, *Geophys. Res. Lett., 14*, 87–90, 1987.

Iwasaka, Y., T. Ono, and A. Nonura, Changes in aerosol content and temperature in the Antarctic spring stratosphere: Lidar measurement at Syowa station (69° 00′ S, 30° 35′ E) in 1883, 1984, and 1985, *Geophys. Res. Lett., 13*, 1407–1410, 1985a.

Iwasaka, Y., A. Ono, and A. Saitoh, Measurements of water vapor content in the polar stratosphere: Syowa Station, Spring 1983, *Mem. Nat. Inst. Polar Research, Tokyo, Spec. Issue No. 39*, 51–55, 1985b.

Iwasaka, Y., T. Hirasawa, and H. Fukunishi, Lidar measurement on the Antarctic stratospheric aerosol layer (II) The changes of layer, height, and thickness in winter, *J. Geomag. Geoelectr., 38*, 99–109, 1986.

Iwasaka, Y., T. Ono, and A. Nonura, Lidar measurements of Antarctic stratospheric aerosols during 1983, 1984, and 1985: Effect of volcanic eruption of El Chichón, *Mem. Natl. Inst. Polar Res., Spec. Issue No. 47*, 56–61, 1987.

Jackman, C.H., J.E. Frederick, and R.S. Stolarski, Production of odd nitrogen in the stratosphere and mesosphere: An intercomparison of source strengths, *J. Geophys. Res., 85*, 7495–7505, 1980.

Jackman, C.H., R.S. Stolarski, and J.A. Kaye, Two-dimensional monthly average ozone balance from Limb Infrared Monitor of the stratosphere and stratospheric and mesospheric sounder data, *J. Geophys. Res., 91*, 1103–1116, 1986.

Jager, H., R. Reiter, W. Carnuth, and S. Jian, Stratospheric aerosol layers during 1982 and 1983 as observed by lidar at Garmisch–Partenkirchen, 12th International Laser Radar Conference, Aix-en-Provence, France, August 13–17, 1984, *Abstracts*, pp. 207–210, 1984.

Jakosky, B.M., G.E. Thomas, D.W. Rusch, C.A. Barth, G.M. Lawrence, J.J. Olivero, R.T. Clancy, R.W. Sanders, and B.G. Knapp, Solar Mesosphere Explorer observations of stratospheric and mesospheric water vapor, *MECA Workshop on Atmospheric H–b2–sO Observations of Earth and Mars: Physical Processes, Measurements, and Interpretations*, Houston, Texas, edited by S.M. Clifford and R.M. Haberle, Lunar and Planetary Inst., Houston, Texas, 1988.

Johnson, K.W., and M.E. Gelman, Trends in the upper stratospheric temperatures as observed by rocketsondes (1965–1983), in *Handbook for MAP*, edited by S. Kato, SCOSTEP, Urbana, Illinois, 18, 24–27, 1985.

Johnston, P.V., and R.L. McKenzie, NO_2 observations at 45° during the decreasing phase of solar cycle 21, from 1980 to 1987, *J. Geophys. Res., 94*, 3473–3486, 1989.

Juckes, M.N., and M.E. McIntyre, A high-resolution one-layer model of breaking planetary waves in the stratosphere, *Nature, 328*, 590–596, 1987.

Junge, C.E., C.W. Chagnon, and J.E. Mason, Stratospheric aerosols, *J. Meteorol., 18*, 81–108, 1961.

Keating, G.M., The response of ozone to solar activity variations. A review, *Solar Physics, 74*, 321–347, 1981.

Keating, G.M., G.P. Brasseur, J.Y. Nicholson III, and A. De Rudder, Detection of the response of ozone in the middle atmosphere to short-term solar ultraviolet variations, *Geophys. Res. Lett., 12*, 449–452, 1985.

Kent, G.S., Dispersion characteristics of volcanically injected aerosol as seen by SAGE I, SAM II and SAGE II, Conference on Atmospheric Radiation, Williamsburg, Virginia, May 13–16, 1986, *Abstracts*, pp. 54–55, 1986.

Kent, G.S., and M.P. McCormick, SAGE and SAM II measurements of global stratospheric aerosol optical depth and mass loading, *J. Geophys. Res., 89*, 5303–5314, 1984.

Kent, G.S., C.R. Trepte, U.O. Farrukh, and M.P. McCormick, Variation in the stratospheric aerosol associated with the north cyclonic polar vortex as measured by the SAM II satellite sensor, *J. Atmos. Sci., 42*, 1536–1551, 1985a.

Kent, G.S., P.H. Wang, U.O. Farrukh, A. Deepak, and E.M. Patterson, Development of a global model for atmospheric backscatter at CO_2 wavelengths, *NASA Final Report*, Contract NAS8–35594, 1985b.

Kent, G.S., L.R. Poole, and M.P. McCormick, Characteristics of Arctic polar stratospheric clouds as measured by airborne lidar, *J. Atmos. Sci., 43*, 2149–2161, 1986.

Kerr, J.B., I.A. Asbridge, and W.F.J. Evans, Intercomparison of total ozone measured by the Brewer and Dobson spectrophotometers at Toronto, *J. Geophys. Res.*, 93, 11129–11140, 1988a.

Kerr, J.B., I.A. Asbridge, and W.F.J. Evans, Long-term intercomparison between the Brewer and Dobson spectrophotometers at Canadian network stations, in *Proc. Quadr. Ozone Symposium—1988*, Göttingen, edited by R.D. Bojkov and P. Fabian, Deepak Publ., USA, in press.

Khalil, M.A.K., and R.A. Rasmussen, The atmospheric lifetime of methylchloroform (CH_3CCl_3), *Tellus, 36B*, 317–332, 1984a.

Khalil, M.A.K., and R.A. Rasmussen, Atmospheric methane: Trends over the last 10,000 years, *Atmos. Environ., 21*, 2445–2452, 1987c.

Khalil, M.A.K., and R.A. Rasmussen, Carbon monoxide in the Earth's atmosphere: Increasing trend, *Science, 224*, 54–56, 1984b.

Khalil, M.A.K., and R.A. Rasmussen, Carbon monoxide in the Earth's atmosphere: Indications of a global increase, *Nature, 332*, 242–245, 1988.

Khalil, M.A.K., and R.A. Rasmussen, Chlorocarbons in the Southern Hemisphere: Concentrations and temporal trends, in *Baseline 85, Baseline Atmospheric Program (Australia) 1985*, edited by B.W. Forgan and P.J. Fraser, pp. 26–29, Bureau of Meteorology/CSIRO, 1987a.

Khalil, M.A.K., and R.A. Rasmussen, Increase and seasonal cycles of nitrous oxide in the Earth's atmosphere, *Tellus*, 35B, 161–169, 1983a.

Khalil, M.A.K., and R.A. Rasmussen, Increase of $CHClF_2$ in the Earth's atmosphere, *Nature, 292*, 823–824, 1981.

Khalil, M.A.K., and R.A. Rasmussen, Interannual variability of atmospheric methane: Possible effects of the El Niño–Southern Oscillation, *Science, 232*, 56–58, 1986.

Khalil, M.A.K., and R.A. Rasmussen, Nitrous oxide: Trends and global mass balance over the last 3,000 years, *Annals of Glaciology, 10*, 73–79, 1987b.

Khalil, M.A.K., and R.A. Rasmussen, Secular trends of atmospheric methane, *Chemosphere, 11*, 877–883, 1982.

Khalil, M.A.K., and R.A. Rasmussen, Sources, sinks and seasonal cycles of atmospheric methane, *J. Geophys. Res., 88*, 5131–5144, 1983b.

Khalil, M.A.K., and R.A. Rasmussen, The trend of bromochlorodifluoromethane (CB_rClF_2) and the concentrations of other bromine containing gases at the South Pole, *Antarctic Journal of the United States: 1985 Review*, pp. 206–207, 1985.

Khalil, M.A.K., R.A. Rasmussen, and R. Gunawardena, Atmospheric bromine in the polar regions, in *Geophysical Monitoring for Climatic Change No. 15 Summary Report 1986*, edited by R. Schnell, pp. 123–125, NOAA, Boulder, Colorado, 1986.

Kiang, C.S., and P. Hamill, H_2SO_4–HNO_3–H_2O ternary system in the stratosphere, *Nature, 250*, 401–402, 1974.

Kiehl, J.T., and B.A. Boville, The radiative–dynamical response of a stratospheric–tropospheric general circulation model to changes in ozone, *J. Atmos. Sci., 45*, 1798–1817, 1988.

Kiehl, J.T., B.A. Boville, and B.P. Briegleb, Response of a general circulation model to a prescribed Antarctic ozone hole, *Nature, 332*, 522–525, 1988.

Klenk, K.F., Absorption coefficients of ozone for the backscatter U.V. experiment, *Appl. Opt., 19*, 236–242, 1980.

Klenk, K.F., P.K. Bhartia, A.J. Fleig, V.G. Kaveeshwar, R.D. McPeters, and P.M. Smith, Total ozone determination from the Backscatter UV Experiment (BUV), *J. Appl. Meteorol., 21*, 1672–1684, 1982.

Kley, D., A. Volz, and F. Mülheims, Ozone measurements in historic perspective: Tropospheric ozone, regional and global scale interactions, edited by I.S.A. Isaksen, *NATO ASI Series C, Vol. 227*, pp. 63–72, D. Reidel, Dordrecht, The Netherlands, 1988.

Knollenberg, R.G., and D. Huffman, Measurements of the aerosol size distributions in the El Chichón cloud, *Geophys. Res. Lett., 10*, 1025–1028, 1983.

Ko, M.K.W., K.K. Tung, D.K. Weinstein, and N.D. Sze, A zonal-mean model of stratospheric tracer transport in isentropic coordinates: Numerical solutions for nitrous oxide and nitric acid, *J. Geophys. Res., 90*, 2313–2329, 1985.

Ko, M.K.W., M.B. McElroy, D.K. Weisenstein, and N.D. Sze, Lightning: A possible source of stratospheric odd nitrogen, *J. Geophys. Res., 91*, 5395–5404, 1986.

Kobayashi, J., and Y. Toyama, On various methods of measuring the vertical distribution of atmospheric ozone 2, *Papers in Meteor. and Geoph., 17*, 97–112, 1966.

Köhler, U., and W. Attmannspacher, Long time intercomparison between Brewer and Dobson spectrophotometer at the Hohenpeissenberg, *Beitr. Phys. Atmosph., 59*, 85–96, 1986.

Komhyr, W.D., A carbon–iodine sensor for atmospheric soundings, *Proc. Ozone Symp.*, Albuquerque, New Mexico, pp. 26–30, 1965.

Komhyr, W.D., Electrochemical concentration cells for gas analysis, *Ann. Geophys., 25*, 203–210, 1969.

Komhyr, W.D., Operations handbook: Ozone observations with the Dobson spectrophotometer, *WMO Ozone Report #6*, 125 pp., 1980.

Komhyr, W.D., and R.D. Evans, Dobson spectrophotometer total ozone measurement errors caused by interfering absorbing species such as SO_2, NO_2, and photochemically produced O_3 in polluted air, *Geophys. Res. Lett. 7*, 157–160, 1980.

Komhyr, W.D., and T.B. Harris, Development of an ECC ozonesonde, *NOAA Tech. Rep. ERL 200–APCL 18*, 54 pp., Natl. Oceanic and Atmos. Admin., Boulder, Colorado, 1971.

Komhyr, W.D., S.J. Oltmans, A.N. Chopra, R.K. Leonard, T.E. Garcia, and C. McFee, Results of Umkehr, ozonesonde, total ozone, and sulfur dioxide observations in Hawaii following the eruption of El Chichón volcano in 1982, in *Atmospheric Ozone, Proceedings of the Quadrennial Ozone Symposium*, Halkidiki, Greece, September 3–7, 1984, edited by C.S. Zerefos and A. Ghazi, pp. 305–310, D. Reidel, Dordrecht, The Netherlands, 1985.

Komhyr, W.D., R.D. Grass, and R.K. Leonard, Total ozone decrease at South Pole, Antarctica, 1964–1985, *Geophys. Res. Lett.*, *13*, 1248–1251, 1986.

Komhyr, W.D., R.D. Grass, and R.K. Leonard, Dobson spectrophotometer No. 83: A standard for total ozone measurements, manuscript of the NOAA Air Resources Laboratory, Boulder, Colorado, 36 pp., 1987.

Komhyr, W.D., R.D. Grass, and R.K. Leonard, Calibration history of world standard Dobson spectrophotometer 83 and total ozone trends at Mauna Loa Observatory, Hawaii, and at American Samoa, South Pacific, *Proc. Quadr. Ozone Symposium—1988*, Göttingen, edited by R.D.Bojkov and P. Fabian, A. Deepak, USA, in press.

Komhyr, W.D., P.R. Franchois, S.E. Kuester, P.J. Reitelbach, and M.L. Fanning, ECC ozonesonde observations at South Pole, Antarctica, during 1987, *NOAA Data Report ERL ARL–15*, Boulder, CO, 319 pp., 1988a.

Komhyr, W.D., S.J. Oltmans, and R.D. Grass, Atmospheric ozone at South Pole, Antarctica, in 1986, *J. Geophys. Res.*, *93*, 5167–5184, 1988b.

Komhyr, W.D., R.D. Grass, and R.K. Leonard, Total ozone, ozone vertical distribution, and stratospheric temperatures at South Pole, Antarctica, in 1986 and 1987, *J. Geophys. Res.*, *94*, 11429–11436, 1989.

Krueger, A.J., Sighting of El Chichón sulfur dioxide clouds with the Nimbus 7 total ozone mapping spectrometer, *Science*, *220*, 1377–1379, 1983.

Krueger, A.J., and R.A. Minzner, A mid-latitude ozone model for the 1976 U.S. Standard Atmosphere, *J. Geophys. Res.*, *81*, 4477, 1976.

Krueger, A.J., and M.R. Schoeberl, TOMS observations of total ozone in the 1986 Arctic spring, *Geophys. Res. Lett.*, *14*, 527–530, 1987.

Krueger, A.J., P.E. Ardanuy, F.S. Sechrist, L.M. Penn, D.E. Larko, S.D. Doiron, and R.N. Galimore, The 1987 airborne Antarctic ozone experiment, *NASA Ref. Pub. 1201*, 252 pp., NASA/Goddard Space Flight Center, Greenbelt, MD, 1988.

Krumins, M.V., and W.C. Lyons, Corrections for the upper atmosphere temperatures using a thin film loop mount, *NOLTR 72–152*, Naval Ordnance Laboratory, White Oak, Silver Spring, Maryland, 1972.

Labitzke, K., Sunspots, the QBO, and the stratospheric temperature in the north polar region, *Geophys. Res. Lett.*, *14*, 535–537, 1987.

Labitzke, K., and H. van Loon, Associations between the 11-year solar cycle, the QBO and the atmosphere. Part I: The troposphere and stratosphere in the Northern Hemisphere in winter, *J. Atm. Terr. Phys.*, *50*, *3*, 197–206, 1988.

Labitzke, K., J.J. Barnett, and B. Edwards, Atmospheric structure and its variation in the region 20 to 120 km, Draft of a new reference middle atmosphere, *Handbook for MAP, Vol. 16*, 318 pp., SCOSTEP, Urbana, Illinois, 1985.

Labitzke, K., G. Brasseur, B. Naujokat, and A. De Rudder, Long-term temperature trends in the stratosphere: Possible influence of anthropogenic gases, *Geophys. Res. Lett.*, *12*, 52–55, 1986a.

Labitzke, K., B. Naujokat, and J.K. Angell, Long-term temperature trends in the middle stratosphere of the Northern Hemisphere, *Adv. Space Res.*, *6*, 7–16, 1986b.

Labs, D., and H. Neckel, The radiation of the solar photosphere from 2000Å to 100 microns, *Z. Astrophy.*, *69*, 1–73, 1968.

Lacis, A.A., and J.E. Hansen, A parameterization for the absorption of solar radiation in the Earth's atmosphere, *J. Atmos. Sci.*, *31*, 118–133, 1974.

Laird, C.M., Solar particle flux and nitrate in South Pole snow, in *Weather and Climate Responses to Solar Variations*, edited by B.M. McCormac, pp. 237–242, Colorado, Assoc. Univ. Press, Boulder, 1983.

Lait, L.R., M.R. Schoeberl, and P.A. Newman, Quasi-biennial modulation of the Antarctic ozone depletion, *J. Geophys. Res.*, *94*, 11559–11571, 1989.

Lal, S., R. Borchers, P. Fabian, and B.C. Kruger, Increasing abundance of $CBrClF_2$ in the atmosphere, *Nature, 216*, 135–136, 1985.

Larsen, J.C., M.P. McCormick, L.R. McMaster, and W.P. Chu, Observations of atmospheric water vapor with the SAGE II instrument, MECA Workshop on Atmospheric H_2O Observations of Earth and Mars, Houston, Texas, July 1986.

Lau, N.-C., Circulation statistics based on FGGE level III-B analyses produced by GFDL, *NOAA Data Report, ERL GFDL-5*, 427 pp., NOAA Fluid Dynamics Laboratory, Princeton, NJ, 1984.

Lazrus, A.L., R.D. Cadle, B.W. Gandrud, J.P. Greenberg, B.J. Huebert, and W.I. Rose, Jr., Sulfur and halogen chemistry of the stratosphere and of volcanic eruption plumes, *J. Geophys. Res., 84*, 7869–7875, 1979.

Lean, J., Solar ultraviolet irradiance variations: A review, *J. Geophys. Res., 92*, 839–868, 1987.

Legrand, M.R., and R.J. Delmas, The ionic balance of Antarctic snow: A 10-year detailed record, *Atmos. Environ., 18*, 1867–1874, 1984.

Legrand, M.R., and R.J. Delmas, Relative contributions of tropospheric and stratospheric sources to nitrate in Antarctic snow, *Tellus, 38*, 236–249, 1986.

Leovy, C.B., and P.J. Webster, Stratospheric long waves: Comparison of thermal structure in the Northern and Southern Hemispheres, *J. Atmos. Sci., 33*, 1624–1638, 1976.

List, R.J., *Smithsonian Meteorological Tables, 6th Edition*, 527 pp., Smithsonian Institution Press, Washington, D.C., 1951.

Lockwood, G.W., N.M. White, D.T. Thompson, and H. Tug, Spectrally resolved measurements of the El Chichón cloud, May 1982–August 1983, *Geof. Int., 23–3*, 351–362, 1984.

Logan, J.A., Tropospheric ozone—Seasonal behaviour, trends and anthropogenic influence, J. *Geophys. Res., 90*, 10463–10482, 1985.

London, J., Radiative energy sources and sinks in the stratosphere and mesosphere, in *Proceedings of the NATO Advanced Study Institute on Atmospheric Ozone: Its Variations and Human Influence*, edited by Nicolet and Aiken, pp. 703–721, U.S. Department of Transportation, Washington, D.C., 1980.

London, J., R.D. Bojkov, S. Oltmans, and J.I. Kelley, Atlas of the global distribution of total ozone, July 1957–June 1967, *NCAR Technical Note NCAR/TN/113 STR*, National Center for Atmospheric Research, Boulder, Colorado, 1976.

Lovelock, J.E., Methylchloroform in the troposphere as an indicator of OH radical abundance, *Nature, 267*, 32, 1977.

Luther, F.M., Monthly values of eddy diffusion coefficients in the lower stratosphere, *UCRL Report No. 74616, AIAA Paper No. 73–498*, presented to the AIAA/AMS Conference on the Environmental Impact of Aerospace Operations in the High Atmosphere, Denver, 1973.

Madden, R.P., Reflecting films for the vacuum ultraviolet, in *Physics of Thin Films*, Vol. 1, edited by G. Hass, pp. 123–186, Academic Press, New York, 1963.

Mahlman, J.D., and S.B. Fels, Antarctic ozone decreases: A dynamical cause?, *Geophys. Res. Lett., 13*, 1316–1319, 1986.

Mahlman, J.D., and L.J. Umscheid, Comprehensive modeling of the middle atmosphere: The influence of horizontal resolution, *Trans. Processes in Middle Atmos.*, edited by G. Visconti and Rolando Garcia, pp. 251–266, 1987.

Mahlman, J.D., and L.J. Umscheid, Dynamics of the middle atmosphere: Successes and problems of the GFDL "SKYHI" general circulation model, in *Dynamics of the Middle Atmosphere*, edited by J.R. Holton and T. Matsuno, pp. 501–525, Terra Sci. Publ. Co., Tokyo, 1984.

Mahlman, J.D., H.B. Levy II, and W.J. Moxim, Three-dimensional tracer structure and behavior as simulated in two ozone precursor experiments, *J. Atmos. Sci., 37*, 655–685, 1980.

Mahlman, J.D., D.G. Andrews, H.U. Dütsch, D.L. Hartmann, T. Matsuno, R.J. Murgatroyd, and J.F. Noxon, Transport of trace constituents in the stratosphere, *Handbook for MAP, Vol. 3*, edited by C.F. Sechrist, J., 14–43, SCOSTEP, Urbana, Illinois, 1981.

Mahlman, J.D., D.G. Andrews, D.L. Hartmann, T. Matsuno, and R.G. Murgatroyd, Transport of trace constituents in the stratosphere, in *Dynamics of the Middle Atmosphere*, edited by J.R. Holton and T. Matsuno, pp. 387–416, Terrapub, Tokyo, 1984.

Makide, Y., and F.S. Rowland, Tropospheric concentrations of methylchloroform, CH_3CCl_3, in January 1978 and estimates of atmospheric residence times for hydrocarbons, *Proc. Nat. Acad. Sci., USA, 78*, 5933–5937, 1981.

Makide, Y., A. Yokohata, Y. Kubo, and T. Tominaga, Atmospheric concentrations of halocarbons in Japan in 1979–1986, *Bull. Chem. Soc. Japan, 60*, 571–524, 1987a.

Makide, Y., Y. Kubo, Y. Tojima, and T. Tominaga, The increase of the atmospheric concentration of CFC–113 (CCl_2FCClF_2), 54th Annual Meeting, Chemical Society of Japan, Tokyo, 1–4 April 1987, *Abstracts, 1*, R8, 1987b.

Manabe, S., and R.W. Weatherald, Thermal equilibrium of the atmosphere with a given distribution of relative humidity, *J. Atmos. Sci., 24*, 241–259, 1967.

Mankin, W.G., and M.T. Coffey, Increased stratospheric hydrogen chloride in the El Chichón cloud, *Science, 226*, 170–172, 1984.

Mankin, W.G., and M.T. Coffey, Latitudinal distributions and temporal changes of stratospheric HCl and HF, *J. Geophys. Res., 88*, 10776–10784, 1983.

Marche, P., and C. Meunier, Atmospheric trace species measured above Haute-Provence observatory, *Planet. Space Sci., 31*, 731–733, 1983.

Marche, P., A. Barbe, C. Secroun, J. Corr, and P. Jouve, Ground-based spectroscopic measurement of HCl, *Geophys. Res. Lett., 7*, 869–872, 1980.

Martin, L.R., H.S. Judeikis, and M. Wu, Heterogeneous reactions of Cl and ClO in the stratosphere, *J. Geophys. Res., 85*, 5511–5518, 1980.

Massie, S.T., J.A. Davidson, C.A. Cantrell, A.H. McDaniel, J.C. Gille, V.G. Kunde, J.C. Brasunas, W.C. Maguire, A. Goldman, and M.M. Abbas, Atmospheric infrared emission of $ClONO_2$ observed by a balloon-borne Fourier spectrometer, *J. Geophys. Res., 92*, 14806–14814, 1987.

Mastenbrook, H.J., and S.J. Oltmans, Stratospheric water vapor variability for Washington, DC/Boulder, Colorado: 1964–82, *J. Atmos. Sci., 40*, 2157–2165, 1983.

Mateer, C.L., On the information content of Umkehr observations, *J. Atmos. Sci., 21*, 370–381, 1964.

Mateer, C.L., A review of some aspects of inferring the ozone profile from inversion of ultraviolet radiance measurements, in *Mathematics of Profile Inversion*, edited by L. Colin, pp. 1–2 to 1–25, *NASA Tech. Memo. TM X–62*, 150 pp., Greenbelt, Maryland, 1972.

Mateer, C.L., and H.U. Dütsch, *Uniform Evaluation of Umkehr Observations From the World Ozone Network, Part I. Proposed Standard Umkehr Evaluation Technique*, 105 pp., National Center for Atmospheric Research, Boulder, Colorado, 1964.

Mateer, C.L., J.J. DeLuisi, and C.C. Porco, The short Umkehr method, part I: Standard ozone profiles for use in the estimation of ozone profiles by the inversion of short Umkehr observations, *NOAA Tech. Memo. ERL ARL–86*, 20 pp., NOAA Air Resources Laboratories, Silver Spring, MD, 1980.

Mateer, C.L., D.F. Heath, and A.J. Krueger, Estimation of total ozone from satellite measurements of backscattered ultraviolet Earth radiances, *J. Atmos. Sci., 28*, 1307–1311, 1971.

Mauersberger, K., D. Hanson, J. Barnes, and J. Morton, Ozone vapor pressure and absorption cross section measurements: Introduction of an ozone standard, *J. Geophys. Res., 92*, 8480–8482, 1987.

Mauldin, L.E., III, and W.P. Chu, Optical degradation due to contamination on the SAGE/SAGE II spaceflight instruments, in *Proc. Society of Photo-optical Instrumentation Engineers*, Arlington, Virginia, May 4–6, 1982.

Mauldin, L.E., III, N.H. Zaun, M.P. McCormick, J.H. Guy, and W.R. Vaughn, Stratospheric Aerosol and Gas Experiment II instrument: A functional description, *Opt. Eng., 24*, 307–321, 1985a.

Mauldin, L.E., III, M.P. McCormick, L.R. McMaster, and W.R. Vaughn, The Stratospheric Aerosol and Gas Experiment II (SAGE II) design and in-orbit performance, in *Proc. Society of Photo-optical Instrumentation Engineers, Arlington, Virginia, Vol. 589, Instrumentation for Remote Sensing From Space*, pp. 104–111, 1985b.

McClatchey, R.A., R.W. Fenn, J.E.A. Selby, F.E. Volz, and J.S. Garind, Optical properties of the atmosphere, *Environ. Res. Papers, AFCRL–71–0279*, Air Force Cambridge Research Laboratories, Bedford, Massachusetts, 1971.

McCormick, M.P., El Chichón: Lidar and satellite measurements versus time and latitude, Topical Meeting on Optical Remote Sensing of the Atmosphere, January 15–18, 1985, Incline Village, Nevada, *Technical Digest*, pp. TuA2–1 to TuA2–5, 1985.

McCormick, M.P., Lidar measurements of the El Chichón stratospheric aerosol climatology, 12th International Laser Radar Conference, Aix-en-Provence, France, August 13–17, 1984, *Abstracts*, pp. 207–210, 1984.

McCormick, M.P., and J.C. Larsen, Antarctic springtime measurements of ozone, nitrogen dioxide, and aerosol extinction by SAM II, SAGE, and SAGE II, *Geophys. Res. Lett., 13*, 1280–1283, 1986.

McCormick, M.P., and T.J. Swissler, Stratospheric aerosol mass and latitudinal distribution of the El Chichón eruption cloud for October, 1982, *Geophys. Res. Lett., 10*, 877–880, 1983.

McCormick, M.P., and C.R. Trepte, Polar stratospheric optical depth observed between 1978 and 1985, *J. Geophys. Res., 92*, 4297–4307, 1987.

McCormick, M.P., and C.R. Trepte, SAM II measurements of Antarctic PSC's and aerosols, *Geophys. Res. Lett., 13*, 1276–1279, 1986.

McCormick, M.P., P. Hamill, T.J. Pepin, W.P. Chu, T.J. Swissler, and L.R. McMaster, Satellite studies of the stratospheric aerosol, *Bull. Amer. Meteorol. Soc., 60*, 1038–1046, 1979.

McCormick, M.P., G.S. Kent, G.K. Yue, and D.M. Cunnold, SAGE measurements of the stratospheric aerosol dispersion and loading from the Soufriere volcano, *NASA Tech. Paper 1922*, 23 pp., NASA/Langley Research Center, Hampton, VA, 1981.

McCormick, M.P., H.M. Steele, P. Hamill, W.P. Chu, and T.J. Swissler, Polar stratospheric cloud sightings by SAM II, *J. Atmos. Sci., 39*, 1387–1397, 1982.

McCormick, M.P., C.R. Trepte, and G.S. Kent, Spatial changes in the stratospheric aerosol associated with the north polar vortex, *Geophys. Res. Lett., 10*, 941–944, 1983.

McCormick, M.P., T.J. Swissler, E. Hilsenrath, A.J. Krueger, and M.T. Osborn, Satellite and correlative measurements of stratospheric ozone: Comparison of measurements made by SAGE, ECC balloons, chemiluminescent, and optical rocketsondes, *J. Geophys. Res., 89*, 5315–5320, 1984a.

McCormick, M.P., T.J. Swissler, W.H. Fuller, W.H. Hunt, and M.T. Osborn, Airborne and ground-based lidar measurements of the El Chichón stratospheric aerosol from 90°N to 56°S, *Geof. Int., 23–2*, 187–221, 1984b.

McElroy, M.B., R.J. Salawitch, and S.C. Wofsy, Antarctic ozone: Chemical mechanisms for the spring decrease, *Geophys. Res. Lett., 13*, 1296–1299, 1986a.

McElroy, M.B., R.J. Salawitch, S.C. Wofsy, and J.A. Logan, Reductions of Antarctic ozone due to synergistic interactions of chlorine and bromine, *Nature, 321*, 759–762, 1986b.

McIntyre, M.E., and T.N. Palmer, Breaking planetary waves in the stratosphere, *Nature, 305*, 593–600, 1983.

McIntyre, M.E., and T.N. Palmer, A note on the concept of wave breaking for Rossby and gravity waves, *PAGEOPH, 123*, 964–975, 1985.

McIntyre, M.E., and T.N. Palmer, The "surf-zone" in the stratosphere, *J. Atmos. Terr. Phys.*, *46*, 825–850, 1984.

McKenzie, R.L., and P.V. Johnston, Springtime stratospheric NO_2 in Antarctica, *Geophys. Res. Lett.*, *11*, 73–75, 1984.

McMaster, L.R., Stratospheric Aerosol and Gas Experiment (SAGE II), in *Abstracts of the 6th AMS Conference on Atmospheric Radiation*, pp. J46–J48, Williamsburg, Virginia, 1986.

McPeters, R.D., The climatology of nitric oxide in the upper stratosphere and mesosphere as measured by SBUV, in *Abstracts of the 19th General Assembly of the IUGG*, pp. 7–13, Vancouver, Canada, 1987.

McPeters, R.D., The climatology of nitric oxide in the upper stratosphere, mesosphere, and thermosphere from 1979 through 1986, *J. Geophys. Res.*, *94*, 3461–3472, 1989.

McPeters, R.D., A nitric oxide increase observed following the July 1982 solar proton event, *Geophys. Res. Lett.*, *13*, 667–670, 1986.

McPeters, R.D., and A. Bass, Anomalous atmospheric spectral features between 300 and 310 nm interpreted in light of new ozone absorption coefficients measurements, *Geophys. Res. Lett.*, *9*, 227–230, 1982.

McPeters, R.D., and W.D. Komhyr, Long-term changes in SBUV/TOMS relative to the world primary standard Dobson instrument, *Proc. Quadr. Ozone Symposium—1988*, Göttingen, edited by R.D. Bojkov and P. Fabian, A. Deepak, USA, in press.

McPeters, R.D., D.F. Heath, and P.K. Bhartia, Average ozone profiles for 1979 from Nimbus 7 SBUV instrument, *J. Geophys. Res.*, *89*, 5199–5214, 1984.

McPeters, R.D., R.D. Hudson, P.K. Bhartia, and S.L. Taylor, The vertical ozone distribution in the Antarctic ozone minimum measured by SBUV, *Geophys. Res. Lett. 13*, 1213–1216, 1986.

Mechoso, C.R., D.L. Hartmann, and J.D. Farrara, Climatology and interannual variability of wave, mean-flow interaction in the Southern Hemisphere, *J. Atmos. Sci.*, *42*, 2189–2206, 1985.

Mechoso, C.R., A. O'Neill, V.D. Pope, and J.D. Farrara, A study of the stratospheric final warming of 1982 in the Southern Hemisphere, *Quart. J. Roy. Meteorol. Soc.*, *114*, 1365–1384, 1988.

Meeks, M.L., and A.E. Lilley, The microwave spectrum of oxygen in the Earth's atmosphere, *J. Geophys. Res.*, *68*, 1683–1703, 1963.

Meetham, A.R., Correlation of atmospheric ozone with other geophysical phenomena, *Quart. J. Roy. Meteorol. Soc.*, *Suppl. to 62*, 59–66, 1936.

Meetham, A.R., The correlation of the amount of ozone with other characteristics of the atmosphere, *Quart. J. Roy. Meteorol. Soc.*, *63*, 289–307, 1937.

Megie, G., G. Aucellar, and J. Pelon, Lidar measurements of ozone vertical profiles, *Appl. Opt.*, *24*, 3453–3463, 1985.

Menzies, T., A re-evaluation of laser heterodyne radiometer ClO measurements, *Geophys. Res. Lett.*, *10*, 729–732, 1983.

Mielenz, K.D., K.L. Eckerle, R.P. Madden, and J. Reader, New reference spectrophotometer, *Appl. Opt.*, *12*, 1630–1641, 1973.

Miller, A.J., and F.J. Schmidlin, Rocketsonde repeatability and stratospheric variability, *J. Appl. Meteor.*, *10*, 320–327, 1971.

Molina, L.T., and M.J. Molina, Absolute absorption cross sections of ozone in the 185- to 350-nm wavelength range, *J. Geophys. Res.*, *91*, 14501–14508, 1986.

Molina, L.T., and M.J. Molina, Production of Cl_2O_2 from the self-reaction of the ClO radical, *J. Phys. Chem.*, *91*, 433–436, 1987.

Molina, M.J., T.-L. Tso, L.T. Molina, and F.C.-Y. Wang, Antarctic stratospheric chemistry of chlorine nitrate, hydrogen chloride, and ice: Release of active chlorine, *Science*, *238*, 1253–1257, 1987.

Mount, G.H., *The SME Ultraviolet Ozone Spectrometer—A Users Guide*, Laboratory for Atmospheric and Space Physics Internal Report, University of Colorado, Boulder, 50 pp., 1982.

Mount, G.H., D.W. Rusch, J.F. Noxon, J.M. Zandony, and C.A. Barth, Measurements of stratospheric NO_2 from the Solar Mesosphere Explorer satellite, 1. An overview of the results, *J. Geophys. Res., 89*, 1327–1340, 1984.

Mount, G., R. Sanders, A. Schmeltekopf, and S. Solomon, Visible spectroscopy at McMurdo Station, Antarctica: 1. Overview and daily variations of NO_2 and O_3, austral spring, 1986, *J. Geophys. Res., 92*, 8320–8328, 1987.

Mroz, E.J., A.S. Mason, and W.A. Sedlacek, Stratospheric sulfate from El Chichón and the mystery volcano, *Geophys. Res. Lett., 10*, 873–876, 1983.

Murcray, F.J., F.H. Murcray, A. Goldman, D.G. Murcray, and C.P. Rinsland, Infrared measurements of several nitrogen species above the South Pole in December 1980 and November–December 1986, *J. Geophys. Res., 92*, 13373–13376, 1987.

Murgatroyd, R.J., and F. Singleton, Possible meridional circulations in the stratosphere and mesosphere, *Quart. J. Roy. Meteorol. Soc., 84*, 225–234, 1958.

Muzio, L.J., and J.C. Kramuch, An artifact in the measurement of N_2O from combustion sources, *Geophys. Res. Lett., 15*, 1369–1372, 1988.

Nagatani, R.M., and A.J. Miller, The influence of lower stratospheric forcing on the October Antarctic ozone decrease, *Geophys. Res. Lett., 14*, 202–205, 1987.

Nash, J., Extension of explicit radiance observations by the stratospheric sounding unit into the lower stratosphere and lower mesosphere, *Quart. J. Roy. Meteorol. Soc., 114*, 1153–1171, 1988.

Nash, J., and J.L. Brownscombe, Validation of the stratospheric sounding unit, *Adv. Space Res., 2, 6*, 59–62, 1983.

Nash, J., and G.F. Forrester, Long-term monitoring of stratospheric temperature trends using radiance measurements obtained by the TIROS–N series of NOAA spacecraft, *Adv. Space Res., 6*, 37–43, 1986.

Nash, J., and F.J. Schmidlin, *Final Report of the WMO International Radiosonde Intercomparison, Report 30*, WMO, 120 pp., 1987.

Nastrom, G.D., and A.D. Belmont, Periodic variations in stratospheric–mesospheric temperatures from 20–65 km at 80° N to 30° S, *J. Atmos. Sci., 32*, 1715–1722, 1975.

Natarajan, M., L.B. Callis, and J.E. Nealy, Solar UV variability: Effects on stratospheric ozone, trace constituents and thermal structure, *Pure Appl. Geophys., 119*, 750–779, 1980/81.

National Research Council (NRC), *The Effects on the Atmosphere of a Major Nuclear Exchange*, 193 pp., National Academy Press, Washington, D.C., 1985.

Naujokat, B., Long-term variations in the stratosphere of the Northern Hemisphere during the last two sunspot cycles, *J. Geophys. Res., 86*, 9811–9816, 1981.

Naujokat, B., An update of the observed quasi-biennial oscillation of the stratospheric winds over the tropics, *J. Atmos. Sci., 43*, 1873, 1986.

Naylor, J.A., Error evaluation of a rocket meteorological temperature sounding system, *Contractor Report*, University of Utah to NASA/Wallops Flight Center, Virginia, 1976.

Neftel, A., J. Beer, H. Oeschger, F. Zurcher, and R.C. Finkel, Sulphate and nitrate concentrations in snow from South Greenland 1895–1978, *Nature, 314*, 611–614, 1985.

Newman, P.A., The final warming and polar vortex disappearance during the Southern Hemisphere spring, *Geophys. Res. Lett., 13*, 1228–1231, 1986.

Newman, P.A., and W.J. Randel, Coherent ozone-dynamical changes during the Southern Hemisphere spring, 1979–1986, *J. Geophys. Res., 93*, 12585–12606, 1988.

Newman, P.A., and M.R. Schoeberl, October Antarctic temperature and total ozone trends from 1979–1985, *Geophys. Res. Lett., 13*, 1206–1209, 1986.

Noxon, J.F., E.C. Whipple, Jr., and R.S. Hyde, Stratospheric NO_2, 1. Observational method and behavior at mid-latitude, *J. Geophys. Res., 84*, 5047–5065, 1979.

NRC: See National Research Council

Ny, T.-Z., and Choong S.P., L'absorption de la lumiere par l'ozone entre 3050 et 2150 Å, *C.R. Acad. Sci. Paris, 196*, 916–918, 1933.

Ny, T.-Z., and Choong S.P., L'absorption de la lumiere par l'ozone entre 3050 et 3400 Å (region des bandes de Huggins), *C.R. Acad. Sci. Paris, 195*, 309–311, 1932.

Oberbeck, V.R., E.F. Danielsen, K.G. Snetsinger, G.V. Ferry, W. Fong, and D.M. Hayes, Effect of the eruption of El Chichón on stratospheric aerosol size and composition, *Geophys. Res. Lett., 10*, 1021–1024, 1983.

Oehlert, G., Trends in Dobson total ozone: An update through 1983, *J. Geophys. Res., 91, D2*, 2675–2679, 1986.

Ohring, G., K. Gallo, A. Gruber, W. Planet, L. Stowe, and J.D. Tarpley, Climate and Global Change: Chapter 6 of NOAA Satellite Data, *EOS, 70*, 41, p. 889, 1989.

Olsen, R.O., F.J. Schmidlin, D.U. Wright, and J.K. Luers, Comparison of atmospheric temperatures derived from falling sphere and grenade experiments conducted at Wallops Island in 1975, in *COSPAR Space Research, XIX*, 111–114, 1979.

Oltmans, S.J., Water vapor profiles for Washington, DC; Boulder, CO; Palestine, TX; Laramie, Wy; and Fairbanks, AK; during the period 1974 to 1985, *NOAA Data Report ERL ARL-7*, NOAA, Silver Spring, Maryland, 1986.

Osantowski, J.F., Contamination sensitivity of typical mirror coatings—A parametric study, *Proc. SPIE 338*, 80–86, 1983.

Oslik, N., *Solar Backscattered Ultraviolet Radiometer Version 2 User's Guide, SASC Document No. SASC-T-5-5085-017-84*, ST Systems Corp., Lanham, Maryland, 1984.

Owens, A.J., C.H. Hales, D.L. Filkin, C. Miller, and M. McFarland, Multiple scenario ozone change calculations: The subtractive perturbation approach, in *Atmospheric Ozone, Proceedings of the Quadrennial Ozone Symposium*, Halkidiki, Greece, September 3–7, 1984, edited by C.S. Zerefos and A. Ghazi, pp. 82–86, D. Reidel, Dordrecht, The Netherlands, 1985.

Ozone Data for the World, Atmospheric Environment Service, Department of the Environment in cooperation with the World Meteorological Organization, Downsview, Ontario.

Palmer, K.F., and D. Williams, Optical constants of sulfuric acid; application to the clouds of Venus?, *Appl. Opt., 14*, 208–219, 1975.

Park, H., and D.F. Heath, Nimbus 7 SBUV/TOMS calibration for the ozone measurement, in *Atmospheric Ozone, Proceedings of the Quadrennial Ozone Symposium*, Halkidiki, Greece, September 3–7, 1984, edited by C.S. Zerefos and A. Ghazi, pp. 412–416, D. Reidel, Dordrecht, The Netherlands, 1985.

Parrish, A., P. Solomon, L. deZafra, M. Jaramillo, B. Connor, and J. Barrett, Extremely low N_2O concentration in the springtime stratosphere at McMurdo Station, Antarctica, 1988, *Nature*, 332, 53, 1988.

Parsons, C.L., J.C. Gerlach, and M.E. Williams, An intercomparison of ground-based total ozone instruments, *J. Appl. Meteorol., 21*, 708–724, 1982.

Paur, R.J., and A.M. Bass, The ultraviolet cross-sections of ozone: II. Results and temperature dependence, in *Atmospheric Ozone, Proceedings of the Quadrennial Ozone Symposium*, Halkidiki, Greece, September 3–7, 1984, edited by C.S. Zerefos and A. Ghazi, pp. 611–616, D. Reidel, Dordrecht, The Netherlands, 1985.

Pearman, G.I., D. Etheridge, F. de Silva, and P.J. Fraser, Evidence of changing concentrations of atmospheric CO_2, N_2O and CH_4 from air bubbles in Antarctic ice, *Nature, 320*, 248–250, 1986.

Penndorf, R.B., Tables of the refractive index for standard air and the Rayleigh scattering coefficient for the spectral region between 0.2mu and 20.0mu and their application to atmospheric optics, *J. Opt. Soc. Am., 47*, 176, 1957.

Penney, C.M., Study of temperature dependence of the Chappuis band absorption of ozone, *NASA CR 158977*, 1979.

REFERENCES

Perry, R.A., Kinetics of the reactions of the NCO radicals with H_2 and NO using photolysis-laser induced fluorescence, *J. Chem. Phys.*, *82*, 5485–5488, 1985.

Peterson, K.R., An empirical model for estimating world-wide deposition from atmospheric nuclear detonations, *Health Physics*, *18*, 357–378, 1970.

Pick, D.R., and J.L. Brownscombe, Early results based on the stratospheric channels of TOVS on the TIROS–N series of operational satellites, *Adv. Space Res.*, *1*, 247–260, 1981.

Pickering, S.U., Isolation of two predicted hydrates of nitric acid, *J. Chem. Soc.*, *63*, 436–443, 1893.

Pinnick, R.G., and D.J. Hofmann, Efficiency of light-scattering aerosol particle counters, *Appl. Optics*, *12*, 2593–2597, 1973.

Pinnick, R.G., J.M. Rosen, and D.J. Hofmann, Measured light scattering properties of individual aerosol particles compared to Mie scattering theory, *Appl. Optics*, *12*, 37–41, 1973.

Pitari, G., and G. Visconti, Two-dimensional tracer transport: Derivation of residual mean circulation and eddy transport tensor from a 3-D model data set, *J. Geophys. Res.*, *90*, 8019–8032, 1985.

Pitari, G., M. Verdecchia, and G. Visconti, A transformed Eulerian model to study possible effects of the El Chichón eruption on the stratospheric circulation, *J. Geophys. Res.*, *92*, 10961–10975, 1987.

Plumb, R.A., and J.D. Mahlman, The zonally averaged transport characteristics of the GFDL general circulation/transport model, *J. Atmos. Sci.*, *44*, 298–327, 1987.

Pollack, J.B., and T.P. Ackerman, Possible effects of the El Chichón cloud on the radiation budget of the northern tropics, *Geophys. Res. Lett.*, *10*, 1057–1060, 1983.

Pollack, J.B., and C.P. McKay, The impact of polar stratospheric clouds on the heating rates of the polar winter stratosphere, *J. Atmos. Sci.*, *42*, 245–262, 1985.

Pollack, J.B., O.B. Toon, C. Sagan, A. Summers, B. Baldwin, and W. VanCamp, Volcanic explosions and climate change: A theoretical assessment, *J. Geophys. Res.*, *81*, 1071–1083, 1976.

Poole, L.R., *Airborne Lidar Studies of Arctic Polar Stratospheric Clouds*, Ph.D. Dissertation, University of Arizona, Tuscon, 1987.

Poole, L.R., and M.P. McCormick, Airborne lidar observations of Arctic polar stratospheric clouds: Indications of two distinct growth modes, *Geophys. Res. Lett.*, *15*, 21–23, 1988.

Post, M.J., Atmospheric infrared backscattering profiles: Interpretation of statistical and temporal properties, *NOAA Tech. Memorandum ERL WPL-122*, 113 pp., NOAA, Boulder, CO, 1985.

Prather, M.J., Continental sources of halocarbons and nitrous oxide, *Nature*, *317*, 221–225, 1985.

Prather, M.J., European sources of halocarbons and nitrous oxide: Update 1986, *J. Atmos. Chem.*, *6*, 375–406, 1988.

Prather, M.J., M.B. McElroy, and S.C. Wofsy, Reductions in ozone at high concentrations of stratospheric halogens, *Nature*, *312*, 227–231, 1984.

Prinn, R.G., P.G. Simmonds, R.A. Rasmussen, R.D. Rosen, F.N. Alyea, C.A. Cardelino, A.J. Crawford, D.M. Cunnold, P.J. Fraser, and J.E. Lovelock, The Atmospheric Lifetime Experiment 1. Introduction, instrumentation and overview, *J. Geophys. Res.*, *88*, 8353–8367, 1983a.

Prinn, R.G., R.A. Rasmussen, P.G. Simmonds, F.N. Alyea, D.M. Cunnold, B.C. Lane, C.A. Cardelino, and A.J. Crawford, The Atmospheric Lifetime Experiment 5. Results for CH_3CCl_3 based on three years of data, *J. Geophys. Research*, *88*, 8415–8426, 1983b.

Prinn, R.G., D. Cunnold, R. Rasmussen, P. Simmonds, F. Alyea, A. Crawford, P. Fraser, and R. Rosen, Atmospheric trends in methylchloroform during 1978–1985 and the global-average OH concentration, *Science*, *238*, 945–950, 1987.

Prinn, R.G., D. Cunnold, R. Rasmussen, P. Simmonds, F. Alyea, A. Crawford, P. Fraser, and R. Rosen, Atmospheric trends and emissions of nitrous oxide deduced from nine years of ALE–GAGE data, 1988, in preparation.

Pruppacher, H.R., and J.D. Klett, *Microphysics of Clouds and Precipitation*, D. Reidel, Dordrecht, The Netherlands, 1978.

Pyle, J.A., A calculation of the possible depletion of ozone by chlorofluorocarbons using a two-dimensional model, *PAGEOPH, 118*, 355–377, 1980.

Ramaswamy, V., and J.T. Kiehl, Sensitivities of the radiative forcing due to large loadings of smoke and dust aerosols, *J. Geophys. Res., 90*, 5597–5613, 1985.

Ramaswamy, V., and V. Ramanathan, Solar absorption by cirrus clouds and the maintenance of the upper troposphere thermal structure, *J. Atmos. Sci., 46*, 2293–2310, 1989.

Raper, O.F., C.B. Farmer, R. Zander, and J.H. Park, Infrared spectroscopic measurements of halogenated sink and reservoir gases in the stratosphere with the ATMOS instrument, *J. Geophys. Res., 92*, 9851–9858, 1987.

Rasmussen, R.A., and M.A.K. Khalil, Atmospheric methane (CH_4): Trends and seasonal cycles, *J. Geophys. Res., 86*, 9826–9832, 1981.

Rasmussen, R.A., and M.A.K. Khalil, Atmospheric methane in recent and ancient atmospheres: Concentrations, trends and interhemispheric gradients, *J. Geophys. Res., 89*, 11599–11605, 1984.

Rasmussen, R.A., and M.A.K. Khalil, Atmospheric trace gases: Trends and distributions over the last decade, *Science, 232*, 1623–1624, 1986.

Rasmussen, R.A., and J.E. Lovelock, The Atmospheric Lifetime Experiment 2. Calibration, *J. Geophys. Res., 88*, 8369–8378, 1983.

Reed, R.J., The role of vertical motions in ozone-weather relationships, *J. Meteorology, 1*, 263–267, 1950.

Reed, R.J., The structure and dynamics of the 26-month oscillation, Paper presented at the 40th anniversary meeting of the Amer. Met. Soc., Boston, 1960.

Reed, R.J., W.J. Campbell, L.A. Rasmussen, and D.G. Rogers, Evidence of downward-propagating annual wind reversal in the equatorial stratosphere, *J. Geophys. Res., 66*, 813–818, 1961.

Reinsel, G.C., Analysis of total ozone data for the detection of recent trends and the effects of nuclear testing during the 1960's, *Geophys. Res. Lett., 8*, 1227–1230, 1981.

Reinsel, G.C., and G.C. Tiao, Impact of chlorofluoromethanes on stratospheric ozone: A statistical analysis of ozone data for trends, *J. Am. Stat. Assoc., 82*, 20–30, 1987.

Reinsel, G.C., G.C. Tiao, M.N. Wang, R. Lewis, and D. Nychka, Statistical analysis of stratospheric ozone data for the detection trend, *Atmos. Environ., 15*, 1569–1577, 1981.

Reinsel, G.C., G.C. Tiao, J.J. DeLuisi, C.L. Mateer, A.J. Miller, and J.E. Frederick, An analysis of upper stratospheric Umkehr ozone profile data for trends and the effects of stratospheric aerosols, *J. Geophys. Res., 89*, 4833–4840, 1984.

Reinsel, G.C., G.C. Tiao, A.J. Miller, D.J. Wuebbles, P.S. Connell, C.L. Mateer, and J. Deluisi, Statistical analysis of total ozone and stratospheric Umkehr data for trends and solar cycle relationship, *J. Geophys. Res., 92*, 2201–2209, 1987.

Reinsel, G.C., G.C. Tiao, S.K. Ahn, M. Pugh, S. Basu, J.J. Deluisi, C.L. Mateer, A.J. Miller, P.S. Connell, and D.J. Wuebbles, An analysis of the 7 year record of SBUV satellite ozone data: Global profile features and trends in total ozone, *J. Geophys. Res., 93*, 1689–1703, 1988.

Reiter, R., H. Jager, W. Carnuth, and W. Funk, The El Chichón cloud over central Europe, observed by lidar at Garmisch–Partenkirchen during 1982, *Geophys. Res. Lett., 10*, 1001–1004, 1983.

Remsberg, E.E., J.M. Russell III, L.L. Gordley, P.L. Bailey, W.G. Planet, and J.E. Harries, The validation of Nimbus 7 LIMS measurements of ozone, *J. Geophys. Res., 89*, 5161–5178, 1984.

Rinsland, C.P., and J.S. Levine, Free tropospheric carbon monoxide concentrations in 1950 and 1951 deduced from infrared total column amount measurements, *Nature, 318*, 250–254, 1985.

REFERENCES

Rinsland, C.P., J.S. Levine, and T. Miles, Concentration of methane in the troposphere deduced from 1951 infrared solar spectra, *Nature, 318,* 245–249, 1985.

Robbins, R.C., L.A. Cavanagh, L.J. Salas, and E. Robinson, Analysis of ancient atmospheres, *J. Geophys. Res., 78,* 5341–5344, 1973.

Robock, A., and M. Matson, Circumglobal transport of the El Chichón volcanic dust cloud, *Science, 221,* 195–197, 1983.

Rodgers, C.D., A General Error Analysis for Profile Retrieval, 1988, in preparation.

Rodgers, C.D., Retrieval of atmospheric temperature and composition from remote measurements of thermal radiation, *Rev. Geophys. and Space Phys. 14,* 609–624, 1976.

Rodriguez, J.M., M.K.W. Ko, and N.D. Sze, Chlorine chemistry in the Antarctic stratosphere: Impact of OClO and Cl_2O_2 and implications for observations, *Geophys. Res. Lett., 13,* 1292–1295, 1986.

Rodriguez, J.M., M.K.W. Ko, and N.D. Sze, Antarctic chlorine chemistry: Possible global implications, *Geophys. Res. Lett., 15,* 257–260, 1988.

Roewe, D.A., J.C. Gille, and P.L. Bailey, Infrared limb scanning in the presence of horizontal temperature gradients: An operational approach, *Appl. Opt., 21,* 3775–3783, 1982.

Rood, R.B., and A.R. Douglass, Interpretation of ozone temperature correlations—Theory, *J. Geophys. Res., 90,* 5733–5743, 1985.

Rosen, J.M., Correlation of dust and ozone in the stratosphere, *Nature, 209,* 1342, 1966.

Rosen, J.M, The vertical distribution of dust to 30 kilometers, *J. Geophys. Res., 69,* 4673–4676, 1964.

Rosen, J.M., The boiling point of stratospheric aerosols, *J. Appl. Meteorol., 10,* 1044–1046, 1971.

Rosen, J.M., Simultaneous dust and ozone soundings over North and Central America, *J. Geophys. Res., 73,* 479–486, 1968.

Rosen, J.M., and D.J. Hofmann, Balloon-borne measurements of condensation nuclei, *J. Appl. Meteorol., 16,* 56–62, 1977.

Rosen, J.M., and D.J. Hofmann, Optical model of stratospheric aerosol: Present status, *Appl. Optics, 25,* 410–419, 1986.

Rosen, J.M., and D.J. Hofmann, Unusual behavior in the condensation nuclei concentration at 30 km, *J. Geophys. Res., 88,* 3725–3731, 1983.

Rosen, J.M., D.J. Hofmann, and J.W. Harder, Aerosol measurements in the winter/spring Antarctic stratosphere 2: Impact on polar stratospheric cloud theories, *J. Geophys. Res., 93,* 677–686, 1988.

Rosenfield, J.E., and M.R. Schoeberl, A computation of stratospheric heating rates and diabatic circulation for the Antarctic spring, *Geophys. Res. Lett., 13,* 1339–1342, 1986.

Rosenfield, J.E., M.R. Schoeberl, and P.A. Newman, Antarctic springtime ozone depletion computed from temperature observations, *J. Geophys. Res., 93,* 3833–3849, 1988.

Rossi, M.J., R. Malhotra, and D.M. Golden, Heterogeneous chemical reaction of chlorine nitrate and water on sulfuric-acid surfaces at room temperature, *Geophys. Res. Lett., 14,* 127–130, 1987.

Rottman G.J., C.A. Barth, R.J. Thomas, G.H. Mount, G.M. Lawrence, D.W. Rusch, R.W. Sanders, G.E. Thomas, and J. London, Solar spectral irradiance 120 to 190 nm, October 13, 1981–January 3, 1982, *Geophys. Res. Lett. 9,* 587–590, 1982.

Rowland, F.S., Some aspects of chemistry in the springtime Antarctic stratosphere, edited by F.S. Rowland and I.S.A. Isaksen, in *The Changing Atmosphere,* Dahlem Konferenzen, November 1–6, 1987, pp. 121–140, John Wiley and Sons, Ltd., Chichester, England, 1988.

Rowland, F.S., N.R.P. Harris, R.D. Bojkov, and P. Bloomfield, Statistical error analysis of ozone trends Winter depletion in the Northern Hemisphere, in *Proc. Quadr. Ozone Symposium—1988,* Göttingen, edited by R.D. Bojkov and P. Fabian, A. Deepak, USA, in press.

Rusch, D.W., and R.T. Clancy, A comparison of ozone trends from SME and SBUV satellite observations and model calculations, *Geophys. Res. Lett.*, *15*, 776–779, 1988.

Rusch, D.W., G.H. Mount, C.A. Barth, R.J. Thomas, and M.T. Callan, Solar Mesosphere Explorer Ultraviolet Spectrometer: Measurements of ozone in the 1.0–0.1 mbar region, *J. Geophys. Res.*, *89*, 11677–11687, 1984.

Russell, J.M., and S.R. Drayson, The inference of atmospheric ozone using satellite observations in the 1042 cm^{-1} band, *J. Atmos. Sci.*, *29*, 376–390, 1972.

Russell, J.M., III, and J.C. Gille, The Limb Infrared Monitor of the Stratosphere (LIMS) experiment, in *The Nimbus 7 Users' Guide*, edited by C.R. Madrid, pp. 71–103, NASA/Goddard Space Flight Center, Greenbelt, MD, 1978.

Russell, P.B., M.P. McCormick, T.J. Swissler, W.P. Chu, J.M. Livingston, W.H. Fuller, J.M. Rosen, D.J. Hofmann, L.R. McMaster, D.C. Woods, and T.J. Pepin, Satellite and correlative measurements of the stratospheric aerosol. II: Comparison of measurements made by SAM II, dustsondes and airborne lidar, *J. Atmos. Sci.*, *38*, 1295–1312, 1981.

Russell, J.M., III, C.B. Farmer, C.P. Rinsland, R. Zander, L. Froidevaux, G.C. Toon, B. Gao, J. Shaw, and M. Gunson, Measurements of odd nitrogen compounds in the stratosphere by the ATMOS experiment on Spacelab 3, *J. Geophys. Res.*, *93*, 1718–1736, 1988.

Salawitch, R.J., S.C. Wofsy, and M.B. McElroy, Chemistry of OClO in the Antarctic stratosphere: Implications for bromine, *Planet. Space Sci.*, *36*, 213–224, 1988a.

Salawitch, R.J., S.C. Wofsy, and M.B. McElroy, Influence of polar stratospheric clouds on the depletion of ozone over Antarctica, *Geophys. Res. Lett.*, *15*, 871–874, 1988b.

Sander, S.P., and R.R. Friedl, Kinetics and product studies of the BrO + ClO reaction: Implications for Antarctic chemistry, *Geophys. Res. Lett.*, *15*, 887–890, 1988

Sander, S.P., and R.R. Friedl, Kinetic studies of the reaction BrO + ClO: Products by flash photolysis, Paper delivered at the Eighteenth International Symposium of Free Radicals, Oxford, England, 1987.

Sanford, J.L., On the nature of persistent stratospheric clouds in the Antarctic, *Tellus*, *29*, 530–534, 1977.

Sargan, J.D., Wages and prices in the United Kingdom: A study in econometric methodology, in *Econometric Analysis for National Economic Planning*, edited by P.E. Hart, G. Mills, and J.K. Whittaker, pp. 25–54, Butterworth, London, 1964.

Schlesinger, M.E., and J.F.B. Mitchell, Climate model simulations of the equilibrium response to increased carbon dioxide, *Rev. Geophys.*, *25*, 760–798, 1987.

Schmidlin, F.J., Intercomparison of temperature, density, and wind measurements from in situ and satellite techniques, *Adv. Space Res.*, *4*, 101–110, 1984.

Schmidlin, F.J., Repeatability and measurement uncertainty of the United States meteorological rocketsonde, *J. Geophys. Res.*, *86*, 9599–9603, 1981.

Schnell, R.C. (Ed.), *Geophysical Monitoring for Climatic Change, No. 14, Summary Report 1985*, NOAA, Air Resources Laboratory, Boulder, CO, pp. 57–60, 1986a.

Schnell, R.C. (Ed.), *Geophysical Monitoring for Climatic Change, No. 14, Summary Report 1985*, NOAA, Air Resources Laboratory, Boulder, CO, pp. 37–42, 1986b.

Schoeberl, M.R., and R.S. Stolarski, Reply to Elliott and Rowland, *Geophys. Res. Lett.*, *15*, 198–199, 1988.

Schoeberl, M.R., and D.F. Strobel, The response of the zonally averaged circulation to stratospheric ozone reductions, *J. Atmos. Sci.*, *35*, 1751–1757, 1978.

Schoeberl, M.R., A.J. Krueger, and P.A. Newman, The morphology of Antarctica total ozone as seen by TOMS, *Geophys. Res. Lett.*, *13*, 1217–1220, 1986.

Schuster, G., R. Rood, and M. Schoeberl, Quasi-biennial and inter-annual variability in high resolution Total Ozone Data (TOMS), in *Proc. Quadr. Ozone Symposium—1988*, Göttingen, edited by R.D. Bojkov and P. Fabian, Deepak Publ., USA, in press.

Schwarzkopf, M.D., and S.B. Fels, Improvements to the algorithm for computing CO_2 transmissivities and cooling rates, *J. Geophys. Res.*, *90*, 10541–10550, 1985.

Seiler, W., H. Giehl, E.G. Brunke, and E. Halliday, The seasonality of CO abundance in the Southern Hemisphere, *Tellus*, *36B*, 250–254, 1984.

Sekiguchi, Y., Antarctic ozone change correlated to the stratospheric temperature field, *Geophys. Res. Lett.*, *13*, 1202–1205, 1986.

Self, S., M.R. Rampino, and J.J. Barbera, The possible effects of large 19th and 20th century volcanic eruptions on zonal and hemispheric surface temperatures, *J. Volcan. Geotherm. Res.*, *11*, 41–60, 1981.

Shah, G.M., and W.F.J. Evans, Latitude survey of aerosol optical thickness of the El Chichón eruption cloud in May 1983, *Geophys. Res. Lett.*, *12*, 255–258, 1985.

Shapiro, M.A., R.C. Schnell, F.P. Parungo, S.J. Oltmans, and B.A. Bodhaine, El Chichón volcanic debris in an Arctic tropopause fold, *Geophys. Res. Lett.*, *11*, 421–424, 1984.

Shettle, E.P., and R.W. Fenn, Models for the aerosols of the lower atmosphere and the effects of humidity variations on their optical properties, *Rep. AFGL-TR-79-0214*, 94 pp., 1979.

Shi, G.Y., W.C. Wang, M.K.W. Ko, and M. Tanaka, Radiative heating due to stratospheric aerosols over Antarctica, *Geophys. Res. Lett.*, *13*, 1335–1338, 1986.

Shibasaki, K., N. Iwagami, and T. Ogawa, Stratospheric nitrogen dioxide observed by ground-based and balloonborne techniques at Syowa Station (69.0°S, 39.6°E), *Geophys. Res. Lett.*, *13*, 1268–1271, 1986.

Shibata, T., M. Fujiwara, and M. Hirono, The El Chichón volcanic cloud in the stratosphere: Lidar observations at Fukuoka and numerical simulation, *J. Atmos. Terr. Phys.*, *46*, 1121–1146, 1984.

Shine, K.P., The middle atmosphere in the absence of dynamical heat fluxes, *Quart. J. Roy. Meteorol. Soc.*, *113*, 603–633, 1987.

Shine, K.P., On the modelled thermal response of the Antarctic stratosphere to a depletion of ozone, *Geophys. Res. Lett.*, *13*, 1331–1334, 1986.

Shiotani, M., and J.C. Gille, Dynamical factors affecting ozone mixing ratios in the Antarctic lower stratosphere, *J. Geophys. Res.*, *92*, 9811–9824, 1987.

Shumway, R.H., *Applied Statistical Time Series Analysis*, Prentice–Hall, Englewood Cliffs, New Jersey, 1988.

Simkin, T., L. Siebert, L. McClelland, D. Bridge, C. Newhall, and J.H. Latter, *Volcanoes of the World*, 232 pp., Smithsonian Institution, Washington, D.C., 1981.

Simmonds, P.G., F.N. Alyea, C.A. Cardelino, A.J. Crawford, D.M. Cunnold, B.C. Lane, J.E. Lovelock, R.G. Prinn, and R.A. Rasmussen, The Atmospheric Lifetime Experiment 6. Results for carbon tetrachloride based on three years of data, *J. Geophys. Res.*, *88*, 8427–8441, 1983.

Simmonds, P.G., D.M. Cunnold, F.N. Alyea, C.A. Cardelino, A.J. Crawford, R.G. Prinn, P.J. Fraser, R.A. Rasmussen, and R.D. Rosen, Carbon tetrachloride lifetimes and emissions determined from daily global measurements during 1978–1985, *J. Atmos. Chem.*, *7*, 35–58, 1988.

Singer, S.F., and R.C. Wentworth, A method for the determination of the vertical ozone distribution from a satellite, *J. Geophys. Res.*, *62*, 299–308, 1957.

Singh, H.B., Preliminary estimates of average tropospheric OH concentrations in the Northern and Southern Hemispheres, *Geophys. Res. Lett.*, *4*, 453–456, 1977.

Smith, D.Y., E. Shiles, and M. Inokuti, The optical properties of metallic aluminum, in *Handbook of Optical Constants of Solids*, edited by E.D. Palik, pp. 369–406, Academic Press, Orlando, Florida, 1985.

Smith, W.L., H.M. Woolf, C. Hayden, D.Q. Wark, and L.M. McMillan, TIROS–N operational vertical sounder, *Bull. Amer. Meteor. Soc.*, *60*, 1177–1197, 1979.

Solomon, S., The mystery of the Antarctic ozone hole, *Rev. Geophysics, 26,* 131–148, 1988.

Solomon, S., and R.R. Garcia, On the distributions of long-lived tracers and chlorine species in the middle atmosphere, *J. Geophys. Res., 89,* 11633–11644, 1984a.

Solomon, S., and R.R. Garcia, Transport of thermospheric NO to the upper stratosphere?, *Planet. Space Sci., 32,* 399–409, 1984b.

Solomon, S., R.R. Garcia, F.S. Rowland, and D.J. Wuebbles, On the depletion of Antarctic ozone, *Nature, 321,* 755–758, 1986a.

Solomon, S., J.T. Keihl, B.J. Kerridge, E.E. Remsberg, and J.M. Russell III, Evidence for nonlocal thermodynamic equilibrium in the v_3 mode of mesospheric ozone, *J. Geophys. Res., 91,* 9865–9876, 1986b.

Solomon, P.M., B. Connor, R. deZafra, A. Parrish, J. Barrett, and M. Jaramillo, Observations of high concentrations of chlorine monoxide in the lower stratosphere during the Antarctic spring, II, Secular variation, *Nature, 328,* 411–413, 1987.

Solomon, S., G.H. Mount, R.W. Sanders, and A.L. Schmeltekopf, Visible spectroscopy at McMurdo Station, Antarctica: 2 Observations of OClO, *J. Geophys. Res., 92,* 8329–8338, 1987.

Spinhirne, J.D., El Chichón eruption cloud: Latitudinal variation of the spectral optical thickness for October 1982, *Geophys. Res. Lett., 10,* 881–884, 1983.

St. John, D.S., S.P. Bailey, W.H. Fellner, J.M. Minor, and R.D. Snee, Time series search for trend in total ozone measurements, *J. Geophys. Res., 86,* 7299–7311, 1981.

St. John, D.S., S.P. Bailey, W.H. Fellner, J.M. Minor, and R.D. Snee, Time series analysis of stratospheric ozone, *Commun. Statist. Theory Methods, 11,* 1293–1333, 1982.

Stauffer, B., G. Fischer, A. Neftel, and H. Oeschger, Increase of atmospheric methane recorded in Antarctic ice, *Science, 229,* 1386–1388, 1985.

Steele, H.M., and P. Hamill, Effects of temperature and humidity on the growth and optical properties of sulphuric acid water droplets in the stratosphere, *J. Aerosol Sci., 12,* 515–527, 1981.

Steele, H.M., P. Hamill, M.P. McCormick, and T.J. Swissler, The formation of polar stratospheric clouds, *J. Atmos. Sci., 40,* 2055–2067, 1983.

Steele, L.P., P.J. Fraser, R.A. Rasmussen, M.A.K. Khalil, T.J. Conway, A.J. Crawford, R.H. Gammon, K.A. Masarie, and K.W. Thoning, The global distribution of methane in the troposphere, *J. Atmos. Chem., 5,* 125–171, 1987.

Stolarski, R.S., The Antarctic ozone hole, *Sci. Am., 258,* 20–26, 1988.

Stolarski, R.S., Changes in ozone over the Antarctic, in *The Changing Atmosphere,* Dahlem Konferenzen, edited by F.S. Rowland and I.S.A. Isaksen, pp. 105–120, John Wiley and Sons Ltd., Chichester, England, 1988.

Stolarski, R.S., and A.R. Douglass, Sensitivity of an atmospheric photochemistry model to chlorine perturbations including consideration of uncertainty propagation, *J. Geophys. Res., 91,* 7853–7864, 1986.

Stolarski, R.S., and M.R. Schoeberl, Further interpretation of satellite measurements of Antarctic total ozone, *Geophys. Res. Lett. 13,* 1210–1212, 1986.

Stolarski, R.S., A.J. Krueger, M.R. Schoeberl, R.D. Peters, P.A. Newman, and J.C. Alpert, Nimbus 7 SBUV/TOMS measurements of the springtime Antarctic ozone decrease, *Nature, 322,* 808–811, 1986.

Stolarski, R.S., A.J. Krueger, and M.R. Schoeberl, Total ozone trends from TOMS data, in *Proc. Quadr. Ozone Symp.—88,* Göttingen, Deepak Publ., USA, in press.

Stordal, F., Isaksen, I.S.A., and Hornveth, K., 1985, A diabatic circulation two-dimensional model with photochemistry simulations of ozone and long-lived tracers with surface sources, *J. Geophys. Res., 90,* 5757–5776, 1985.

Strand, O.N., and E.R. Westwater, Statistical estimation of the numerical solution of a Fredholm integral equation of the first kind, *J. Assoc. Comp. Mach., 15,* 100–114, 1968.

Streit, G.E., C.J. Howard, A.L. Schmeltekopf, J.A. Davidson, and H.I. Schiff, Temperature dependence of the O(^{1}D) rate constants for reactions with O_2, N_2, CO_2, O_3 and H_2O, *J. Chem. Phys.*, *65*, 4761–4764, 1976.

Strong, A.E., Monitoring El Chichón aerosol distribution using NOAA–7 satellite AVHRR sea surface temperature, *Geof. Int.*, *23–2*, 129–142, 1984.

Swissler, T.J., M.P. McCormick, and J.D. Spinhirne, El Chichón eruption cloud, comparison of lidar and optical thickness measurements for October 1982, *Geophys. Res. Lett.*, *10*, 885–888, 1983.

Sze, N.D., Anthropogenic CO emissions: Implications for the atmospheric CO–OH–CH_4 cycle, *Science*, *195*, 673–675, 1977.

Taylor, S L., P.K. Bhartia, V.G. Kaveeshwar, K.F. Klenk, A.J. Fleig, and C.L. Mateer, Role of multiple scattering in ozone profile retrieval from satellite measurements in the ultraviolet, in *Remote Sensing of Atmospheres and Oceans*, edited by A. Deepak, pp. 219–231, Academic Press, New York, 1980.

Thomas, G.E., Solar Mesosphere Explorer measurements of polar mesospheric clouds (noctilucent clouds), *J. Atmos. Terr. Phys.*, *46*, 819–824, 1984.

Thomas, G.E., B.M. Jakosky, R.A. West, and R.W. Sanders, Satellite limb-scanning thermal infrared observations of the El Chichón stratospheric aerosols: First results, *Geophys. Res. Lett.*, *10*, 997–1000, 1983.

Thomas, R.J., C.A. Barth, D.W. Rusch, and R.W. Sanders, Solar Mesosphere Explorer Near-Infrared Spectrometer: Measurements of 1.27μ radiances and the inference of mesospheric ozone, *J. Geophys. Res.*, *89*, 9569–9580, 1984.

Thomas, R.W.L., and A.C. Holland, Simple relationship between UV radiation backscattered by the Earth's atmosphere and the vertical ozone profile, *Appl. Opt. 16*, 2581–2583, 1977.

Thompson, A.M., and R.J. Cicerone, Possible perturbations to atmospheric CO, CH_4 and OH, *J. Geophys. Res.*, *91*, 10853–10864, 1986.

Tiao, G.C., G.C. Reinsel, J.H. Frederick, G.M. Allenby, C.L. Mateer, A.J. Miller, and J.J. DeLuisi, A statistical trend analysis of ozonesonde data, *J. Geophys. Res.*, *91*, 13121–13136, 1986.

Tolbert, M.A., M.J. Rossi, R. Malhotra, and D.M. Golden, Reaction of chlorine nitrate with hydrogen chloride and water at Antarctic stratospheric temperatures, *Science*, *238*, 1258–1260, 1987.

Tolson, R.H., Spatial and temporal variations of monthly mean total columnar ozone derived from 7 years of BUV data, *J. Geophys. Res.*, *86*, 4788–4796, 1981.

Toohey, D.W., and J.G. Anderson, Formation of BrCl (3πo +) in the reaction of BrO with ClO, *J. Phys. Chem.*, *92*, 1705, 1988.

Toon, O.B., and J.B. Pollack, A global average model of atmospheric aerosols for radiative transfer calculations, *J. Appl. Meteor.*, *15*, 225–246, 1976.

Toon, O.B., P. Hamill, R.P. Turco, and J. Pinto, Condensation of HNO_3 and HCl in the winter polar stratosphere, *Geophys. Res. Lett.*, *13*, 1284–1287, 1986.

Torres, A.L., and A.R. Bandy, Performance characteristics of the electrochemical concentration cell ozonesonde, *J. Geophys. Res.*, *83*, 5501–5504, 1978.

Torres, A.L., and G. Brothers, Ozone measurements above Palmer Station, Antarctica, Polar Ozone Workshop, *NASA Conf. Publ. 10014*, pp. 42–44, Snowmass, Colorado, 1988.

Tung, K.K., On the relationship between the thermal structure of the stratosphere and the seasonal distribution of ozone, *Geophys. Res. Lett.*, *13*, 1308–1311, 1986.

Tung, K.K., and H. Yang, Dynamic variability of column ozone, *J. Geophys. Res.*, *93*, 11123–11128, 1988.

Tung, K.K., and H. Yang, Dynamical component of seasonal and year-to-year changes in Antarctic and global ozone, *J. Geophys. Res.*, *93*, 12537–12559, 1989.

Tung, K.K., M.K.W. Ko, J.M. Rodriguez, and N.D. Sze, Are Antarctic ozone variations a manifestation of dynamics or chemistry?, *Nature, 322,* 811–814, 1986.

Turco, R.P., R.C. Whitten, and O.B. Toon, Stratospheric aerosols: Observation and theory, *Rev. Geophys. Space Phys., 20,* 233–279, 1982.

Turco, R.P., O.B. Toon, and P. Hamill, Heterogeneous physicochemistry of the polar ozone hole, *J. Geophys. Res., Special Issue,* 1989, in press.

Twomey, S., *Atmospheric Aerosols,* 302 pp., Elsevier, Amsterdam, The Netherlands, 1977.

Twomey, S., On the numerical solution of Fredholm integral equations of the first kind by the inversion of the linear systems produced by quadrature, *J. Assoc. Comp. Mach., 10,* 97–101, 1963.

Twomey, S., B. Herman, and R. Rabinoff, An extension to the Chahine method of inverting the radiative transfer equation, *J. Atmos. Sci., 34,* 1085–1096, 1977.

Uchino, O., On dispersion processes of the El Chichón dust particles in the lower stratosphere, *J. Meteor. Soc. Japan, 63,* 288–293, 1985.

Valentini, J.J., D.P. Gerrity, D.L. Phillips, J.C. Neih, and K.D. Tabor, CARS spectroscopy of $O_2(^1\Delta/g)$ from the Hartley band photodissociation of O_3: Dynamics of the dissociation, *J. Chem. Phys., 86,* 6745–6756, 1987.

van Loon, H., and K. Labitzke, The Southern Oscillation, Part V: The anomalies in the lower stratosphere of the Northern Hemisphere in winter and a comparison with the Quasi-Biennial Oscillation, *Mon. Weather Rev., 115,* 357–369, 1987.

Vassey, A., and E. Vassey, Effect of temperature on the absorption spectrum of ozone: Chappuis bands, *J. Chem. Phys., 16,* 1163–1164, 1948.

Vedder, J.F., E.P. Condon, E.C.Y. Inn, K.D. Tabor, and M.A. Kritz, Measurements of stratospheric SO_2 after the El Chichón eruptions, *Geophys. Res. Lett., 10,* 1045–1048, 1983.

Veryard, R.G., and Ebdon, R.A., Fluctuations in tropical stratospheric winds, *Meteor. Mag., 90,* 125–143, 1961.

Vierkorn–Rudolph, B., K. Bachmann, B. Schwarz, and F.X. Meixner, Vertical profiles of hydrogen chloride in the troposphere, *J. Atmos. Chem., 2,* 47–63, 1984.

Vigroux, E., Contribution a l'étude experimentale de l'absorption de l'ozone, *Ann. Phys., 8,* 709–762, 1953.

Vigroux, E., Determination des coefficients moyens d'absorption de l'ozone en vue des observations concernant l'ozone atmospherique a l'aide du spectrometre Dobson, *Ann. Phys., 2,* 209–215, 1967.

Vupputuri, R.K.R., Potential effects of anthropogenic trace gas emissions on atmospheric ozone, temperature structure and surface climate, in *Measuring the Greenhouse Effect, Report ARD87–2,* edited by W.F.J. Evans, A.J. Forester, and D.I. Wardle, pp. 147–156, Atmospheric Environment Service, Canada, 1987.

Wagner, N.K., Theoretical accuracy of a meteorological thermistor, *J. Appl. Meteor., 3,* 461–469, 1964.

Wallace, J.M, General circulation of the tropical lower stratosphere, *Rev. Geophys. Space Phys., 11,* 191–222, 1973.

Wang, W–C, D.J. Wuebbles, W.M. Washington, R.G. Isaacs, and G. Molnar, Trace gases and other potential perturbations to global climate, *Rev. Geophys., 24,* 110–140, 1986.

Wardle, D.J., C.D. Walshaw, and T.W. Wormell, A new instrument for atmospheric ozone, *Nature, 199,* 1177–1178, 1983.

Waters, J.W., J.C. Hardy, R.F. Jarnot, and H.M. Pickett, Chlorine monoxide radical, ozone, and hydrogen peroxide: Stratospheric measurements by microwave limb sounding, *Science, 214,* 61–64, 1981.

Watson, R.T., M.A. Geller, R.S. Stolarski, and R.F. Hampson, Present state of knowledge of the upper atmosphere: An assessment, *NASA Reference Publication RP 1162*, NASA/Goddard Space Flight Center, Greenbelt, MD, 1986.

Wayne, R.P., Reactions of singlet molecular oxygen in the gas phase, in *Singlet O_2, Vol 1, Physical–Chemical Aspects*, edited by A.A. Frimer, pp. 81–175, CRC Press, Boca Raton, Florida, 1985.

Weinstock, E.M., M.J. Phillips, and J.G. Anderson, In situ observation of ClO in the stratosphere: A review of recent results, *J. Geophys. Res.*, *86*, 7273–7278, 1981.

Weiss, R.F., The temporal and spatial distribution of tropospheric nitrous oxide, *J. Geophys. Res.*, *86*, 7185–7195, 1981.

Wellemeyer, C.G., A.J. Fleig, and P.K. Bhartia, Internal comparisons at SBUV and TOMS total ozone measurements, *Proc. Quadr. Ozone Symposium—1988*, Göttingen, edited by R.D. Bojkov and P. Fabian, Deepak Publ., USA, in press.

Witteborn, F.C., K. O'Brien, H.W. Crean, J.B. Pollack, and K.H. Bilski, Spectroscopic measurements of the 8- to 13-micrometer transmission of the upper atmosphere following the El Chichón eruptions, *Geophys. Res. Lett.*, *10*, 1009–1012, 1983.

WMO, Report of the meeting of experts on the assessment of performance characteristics of various ozone observing systems, World Meteorological Organization Ozone Project, *Report No. 9*, WMO, Boulder, Colorado, 1980.

WMO, Report of the meeting of experts on sources of errors in detection of ozone trends, World Meteorological Organization Ozone Project, *Report No. 12*, WMO, Toronto, 48 pp., 1982.

WMO, *Atmospheric Ozone, Assessment of Our Understanding of the Processes Controlling its Present Distribution and Change, Report No. 16*, World Meteorological Organization Global Ozone Research and Monitoring Project, in three volumes, Washington D.C., 1986.

Wofsy, S.C., M. Molina, R.J. Salawitch, L.E. Fox, and M.B. McElroy, Interactions between HCl, NO_x, and H_2O ice in the Antarctic stratosphere: Implications for ozone, *J. Geophys. Res.*, *93*, 2442–2450, 1988.

Woodgate, B.R., E.A. Tandberg–Hanssen, E.C. Bruner, J.M. Beckers, J.C. Brandt, W. Henze, C.L. Hyder, M.W. Kalet, P.J. Kenny, E.D. Knox, A.G. Michalitsianos, R. Rehse, R.A. Shine, and H.D. Tinsley, The ultraviolet spectrometer and polarimeter on the Solar Maximum Mission, *Sol. Phys.*, *65*, 73–90, 1980.

Woods, D.C., and R.L. Chuan, Size-specific composition of aerosols in the El Chichón volcanic cloud, *Geophys. Res. Lett.*, *10*, 1041–1044, 1983.

Worsnop, D.R., M.S. Zahniser, P. Davidovits, C.C. Kolb, Heterogeneous reaction kinetics of importance to stratospheric chemistry, *Report No. ARIRR #613*, 1987.

Wuebbles, D.J., A theoretical analysis of the past variations in global atmospheric composition and temperature structure, *UCRL–53423*, Lawrence Livermore National Laboratory, Livermore, CA, 1983a.

Wuebbles, D.J., *A Theoretical Analysis of the Past Variations in Global Atmospheric Composition and Temperature Structure*, Ph.D. Thesis, University of California, Livermore, 1983b.

Wuebbles, D.J., Trends in ozone and temperature structure: Comparison of theory and measurement, in *Atmospheric Ozone, Proc. Quadrennial Ozone Symposium*, Halkidiki, Greece, September 3–7, 1984, edited by C.S. Zerefos and A. Ghazi, pp. 87–91, D. Reidel, Dordrecht, The Netherlands, 1985.

Wuebbles, D.J., M.C. MacCracken, and F.M. Luther, A proposed reference set of scenarios for radiatively active atmospheric constituents, U.S. Department of Energy, Carbon Dioxide Research Division, *Technical Report 015*, 54 pp., Washington, DC, 1984.

Wuebbles, D.J., P.S. Cornell, K.E. Grant, R. Tarp, and K.E. Taylor, Initial results with the LLNL 2-D chemical-radiative-transport model of the troposphere and stratosphere, Lawrence Livermore National Laboratory Report, *CID–21145*, 14 pp., Livermore, California, 1987.

Yue, G.K., M.P. McCormick, and W.P. Chu, A comparative study of aerosol extinction measurements made by the SAM II and SAGE satellite experiments, *J. Geophys. Res., 89,* 5321–5327, 1984.

Yue, G.K., M.P. McCormick, W.P. Chu, P. Wang, and M.T. Osborn, Comparative studies of aerosol extinction measurements made by the SAM II and SAGE II satellite experiments, *J. Geophys. Res., 94,* 8412–8424, 1989.

Zander, R., and Ph. de Moulin, Spectroscopic evidence for the presence of the v_4–Q branch of chlorine nitrate ($ClONO_2$) in ground-based infrared solar spectra, *J. Atmos. Chem., 6,* 191–200, 1988.

Zander, R., G. Roland, L. Delbouille, A. Sauval, C.B. Farmer, and R.H. Norton, Column abundance and long-term trend of hydrogen chloride (HCl) above the Jungfraujoch station, *J. Atmos. Chem., 5,* 395–404, 1987a.

Zander, R., G. Roland, L. Delbouille, A. Sauval, C.B. Farmer, and R.H. Norton, Monitoring of the integrated column of hydrogen fluoride above the Jungfraujoch station since 1977—The HF/HCl column ratio, *J. Atmos. Chem., 5,* 385–394, 1987b.

Zander, R., G. Roland, L. Delbouille, A.J. Sauval, P. Marche, F. Karcher, M. Amoudei, and B. Dufour, Concentrations of hydrogen chloride and hydrogen fluoride during the MAP/GLOBUS comparison of September 1983, *Planet. Space Sci., 35,* 665–672, 1987c.

Zander, R., Ph. de Moulin, D.H. Ehhalt, and U. Schmidt, Secular increase of the column abundance of methane above the Jungfraujoch station, 1989, in preparation.